Photoswitchable Ligands Enable Thermodynamic Disequilibration of Metal-Organic Assemblies

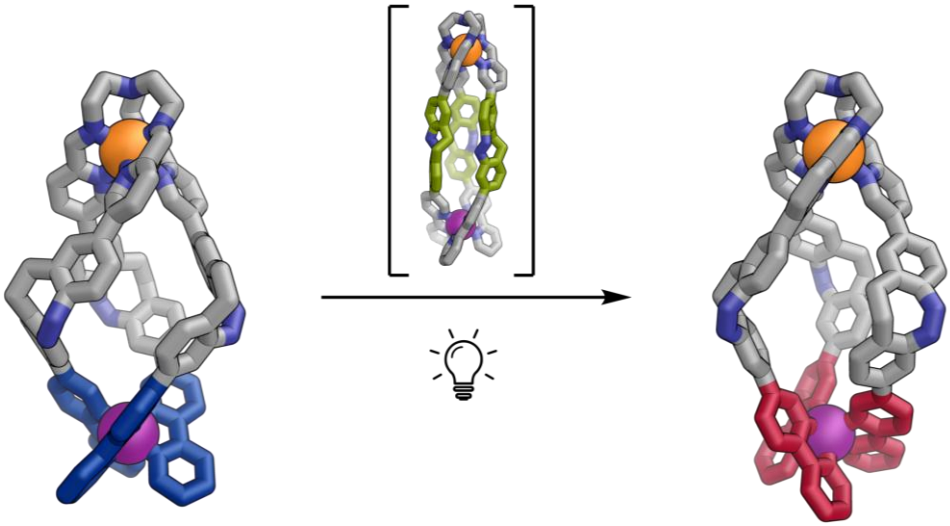

DISSERTATION

zur

Erlangung des Doktorgrades (Dr. rer. nat.)

der

Mathematisch-Naturwissenschaftlichen Fakultät

der

Rheinischen Friedrich-Wilhelms-Universität Bonn

vorgelegt von

Maximilian Johannes Notheis

aus

Dormagen

Bonn, 2025

Angefertigt mit Genehmigung der Mathematisch-Naturwissenschaftlichen Fakultät
der Rheinischen Friedrich-Wilhelms-Universität Bonn

Gutachterin/Betreuerin: Dr. Larissa K. S. von Krbek
Gutachter: Prof. Dr. Arne Lützen

Tag der Promotion: **31.03.2026**

Erscheinungsjahr: **2026**

Danksagung

Zuallererst möchte ich mich bei Dr. Larissa K. S. von Krbek für die wunderbare Unterstützung während der letzten fünf Jahre bedanken. Dein felsenfestes Vertrauen in mich und meine Fähigkeiten sowie Deine kontinuierlichen Ermutigungen haben mich zu dem Chemiker gemacht, der ich heute bin. Ich bin stolz, dass ich Dir auf diesem Abschnitt Deiner akademischen Laufbahn helfen konnte und durfte.

Ebenso möchte ich mich bei Prof. Dr. Arne Lützen bedanken, der mich ermutigt hat den Schritt in eine Juniorforschungsgruppe zu wagen. Selbst nachdem ich Ihre Gruppe verlassen hatte, standen Sie mir mit unzähligen hilfreichen Ratschlägen zur Seite und haben so ebenfalls zum Erfolg meiner Forschungsprojekte beigetragen.

Ein weiterer Dank gilt Prof. Dr. Thomas Bredow und PD Dr. Hagelücken für die Bereitschaft meiner Promotionskommission beizutreten.

Ohne die tatkräftige Unterstützung, die ich aus der Zentralanalytik und den Werkstätten der Chemischen Institute erfahren habe, wäre diese Arbeit nicht möglich gewesen. Daher bedanke ich mich herzlich bei:

- Ulrike, Dipl.-Ing Karin Prochnicki und Dr. Senada. Nozinovic aus der NMR-Abteilung für das nette Miteinander und die Berücksichtigung meiner vielen Sonderwünsche.
- PD Dr. Marianne Engeser und Karin Peters-Pflaumbaum für die Durchführung und hilfreichen Besprechungen der massenspektroskopischen Analysen.
- Andreas Schneider für die Durchführung der HPLC-Messungen.
- Dipl.-Ing. Bernhard Klöckner und dem gesamten Personal der Elektronik-Werkstatt für ihre Begeisterungsfähigkeit für meine Ideen zum Bau der 3D-gedruckten Lichtquellen, deren fundamentale Weiterentwicklung, sowie deren Serienfertigung.
- Dem gesamten Personal der mechanischen Werkstatt für ihre exzellente Arbeit und Unterstützung, vom Bau der 3D-gedruckten Lichtquellen bis zum Anschleifen der Glasfaserkabel.

Ein besonderer Dank gilt dem AK Krbek für die großartige Stimmung. Es gab keinen einzigen Tag, an dem ich nicht freudig zu Euch ins Labor gekommen bin. Danke Ruben, für das Donnerstagsproblem und den Roadtrip nach der Island Konferenz. Danke Lidón, für deine gute Laune, die sich selbst von meinem Musikgeschmack nicht vertreiben lässt, und die tolle

Zeit in Labor 5.102. Danke Vigan, dass du meine Begeisterung für Diazocine auch nach dem Doppel-Diazocin-Debakel noch teilst. Danke Anne, für Deine Motivation, die mich auch heute noch mitreißt. Danke Justin, eines Tages werden wir hoffentlich rausfinden, was er da eigentlich im Stutzen hat. Danke auch an Wiebke, Johannes, Jonathan, Vivi, Parveen und Khyati.

Ebenso bedanke ich mich bei:

- AK-Menche: Vielen Dank Jonas, für das viele Feedback und die abendliche Gesellschaft im Labor. Außerdem danke an: Max, Max, Max und Max sowie Pascal, Hoang, Alex, Christina, Raphi, Tim, Torben, Leon, Johannes, Florian, Ceire, Simon, Timon, Tragi, Edgar, Vivi, Gero, Niklas.
- AK Lützen für den fachlichen Austausch und die unterhaltsamen Abende: Basti, Erik, Daniel, Anne, Lukas, Marvin, Clemens, Jan, Anh Tu, Wing-Si, Hannah, Lena, Ayla, Fee, Tom, Leon, Marc, Lea, Fraz, Hanna.
- Meinen Freunden dafür, dass Sie mir auch weiterhin zuhören, wenn ich über meine Forschung rede: Henrik, Marcel, Michael, Annika, Lukas, Aaron, Basti, Daniel, Marc.
- Kirstin, Thomas, Lea und Martin dafür, dass ihr immer an mich geglaubt habt.
- Meinen Eltern für ihre bedingungslose Unterstützung.
- Meiner Freundin Hannah, dafür, dass sie immer für mich da ist.

La lutte elle-même vers les sommets suffit à remplir un cœur d'homme. Il faut imaginer Sisyphe heureux.

Der Kampf gegen Gipfel vermag ein Menschenherz auszufüllen. Man muss sich Sisyphus als glücklich vorstellen.

Albert Camus

Abstract

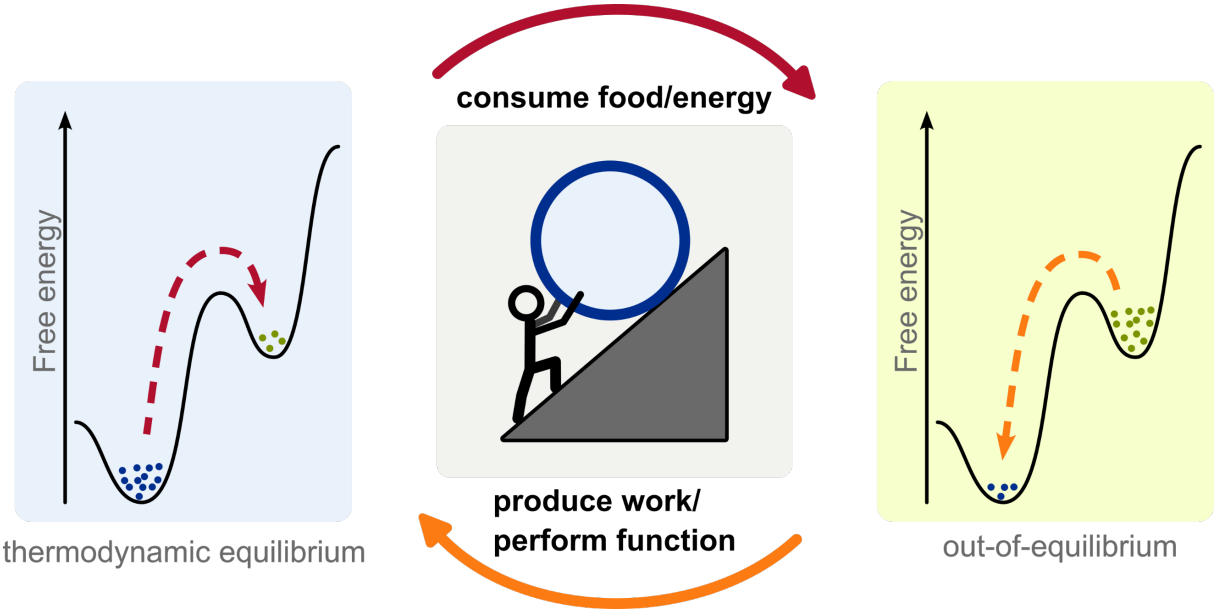

Living organisms need a constant supply of energy to sustain life. The molecular reason for this can be found in the operating mechanism of biological systems that perform extraordinary functions like absorbing nutrients and distributing them across the organism, self-healing, movement, and reproduction. These intricate biological systems do not reside in the thermodynamic minimum. Instead, a constant energy supply is needed to sustain meta-stable states far away from the thermodynamic minimum. The innate energy of these states is harnessed to perform work, enabling the complex behaviors of living organisms.

A fundamental understanding of how to access and sustain meta-stable states in artificial systems and materials is a step towards extending life-like behaviors to inanimate objects, opening numerous perspectives from more sustainable self-repairing materials to medical applications in targeted drug release. Systems making use of phase boundaries to stabilize meta-stable states such as dynamic droplets and nanocrystals have recently been described in literature. However, the systematic use of dynamic and reversible metal-ligand interactions to stabilize meta-stable states remains an underexplored approach.

This dissertation establishes light-driven reaction networks, specifically energy ratchets, as a foundational mechanism to accumulate meta-stable states in self-assembled metal-organic structures. Furthermore, it explores how the innate energy of the meta-stable state can be harnessed in enabling macroscale spatio-temporal control over nanoscale chemical transformations.

Initial work focused on the design, synthesis and investigation of photoresponsive building blocks. Firstly, a family of novel twelve-membered macrocyclic azobenzenes was investigated, yielding new insights on using backbone flexibility to tune photochromic properties. Secondly,

a reliable gram-scale synthesis of 2,8-dihalogenated diazocine was established. This was followed by selective, stepwise Suzuki couplings to access asymmetrically functionalized diazocine building blocks that combine a large geometry change during switching with favorable photochemical properties.

A one-pot sub-component self-assembly using one of the tailor-made building blocks resulted in selective formation of high-fidelity, low-symmetry, heterobimetallic helicates. The final structure contains two distinct coordination sites, enabling quantitative formation of self-sorted Fe/Zn and Zn/Co heterobimetallic helicates. The precise metal distribution is enabled by a complex reaction network during self-assembly that amplifies differences in metal-ligand bond strength and exchange kinetics. This separates the metals into the two coordination sites as a result of kinetic and thermodynamic factors.

Investigating the photoresponsive behavior of the helicates revealed a light-driven energy-ratchet mechanism. Photoisomerization of the diazocine units transiently reshapes the assemblies' energy landscape, enabling rapid reconfiguration of the initial structure into a mixture of metastable isomeric states. These become kinetically trapped upon back-isomerization, enabling the accumulation of meta-stable high-energy atropisomers. Continuous white-light irradiation operates the energy ratchet autonomously by exciting both switching transitions simultaneously. This amplifies a minor photostationary state into a dominant, long-lived meta-stable diastereomer. Additionally, operation of the ratchet accelerates regioselective metal-cation exchange (Zn_2**L** → ZnFe**L**), providing spatiotemporal control over selective metal ion capture.

Nature shows us that complex behavior is a result of complex systems. The incorporation of energy ratchets into metal-organic cages elevates them into a realm of complexity that is usually reserved for enzymes. These results pave the way towards larger photoresponsive cages for molecular machines that operate under out-of-equilibrium conditions, thus enabling life-like behaviors such as controlled catalysis, active transport, or macroscale directed movement.

Table of Contents

1 Introduction: from Supramolecular to Systems Chemistry

As chemists, our perspective on life is focused on the single molecule. However, when looking closely at the molecules in living organisms one quickly realizes that single molecules by themselves cannot possibly enable the functioning of such a complex organism. Only when multiple molecules come together and interact in very specific ways, function starts to emerge.

Understanding and predicting these intermolecular interactions is the domain of supramolecular chemistry. Instead of covalent bonds where a pair of electrons is shared between atoms, weak and reversible interactions like hydrogen bonds, van-der-Waals interactions, π-π-interactions, and electrostatic interactions govern the formation and operation of multi-molecule structures. Structures of higher complexity are spontaneously formed when two or more building blocks interact on a supramolecular level in a complementary way. This thermodynamically downhill process is termed self-assembly. The geometry of the self-assembled structures is encoded in the functional groups of the building blocks. Thus, enabling highly selective catalysis, regulation, transport and recognition processes in living organisms.[1]

1.1 Artificial Molecular Machines

Among the most notable developments by supramolecular chemists are artificial molecular machines. These are molecules with similar functions as biological machines like motor proteins or molecular pumps and work by transforming an energy input into an output of work. Their development earned Jean-Pierre Sauvage, Fraser Stoddart and Ben Feringa the 2016 Nobel prize in chemistry. These artificial machines enabled new insights into how motion can be generated on a molecular scale, but chemists are still struggling to bridge the gap between these nano scale movements and real-world functions.[2]

Taking another look at biological machinery and how it operates reveals that it is not just a single motor working away. Instead, the motor protein is part of a larger system. This system directs the movement and allows regulation of its activity and provides spatial and temporal control over the motion, transports fuel to and waste away from the motor, with all parts coexisting in a confined space and possessing structural order. This is where the concepts of “systems chemistry” provide an opportunity to add the missing dimensions of alignment, directionality, signaling, communication, compartmentalization, fuel, temporal and spatial control, and more, to artificial molecular machines.[2]

1.2 Systems Chemistry - Translating Molecular Interactions into Real World Functions

Supramolecular chemistry enables understanding complex biochemical systems through rationalizing intramolecular interactions. Systems chemistry takes another step towards complexity by exploring how these interactions give rise to emergent properties. Systems chemistry seeks to emulate both the complexity and functionality of biological systems by creating networks of interacting and interconverting molecules that respond to external stimuli and carry out a specific function.[3]

Supramolecular chemistry usually deals with thermodynamically driven “equilibrium” self-assembly with products in the absolute thermodynamic minimum. However, in biological systems, many processes occur far from thermodynamic equilibrium, allowing the system to perform work and adapt to external stimuli. One such system can be found in the cytoskeleton where microtubule formation relies on the continuous input of energy. When the energy supply ceases, the microtubules disintegrate.[4] Similarly, systems chemistry aims to create artificial multi component systems that harness energy to drive non-equilibrium processes to generate a metastable out-of-equilibrium state that serves as the basis for the function of the system, thereby advancing the fields of artificial molecular machines and smart materials.

1.3 A Complex Biological System: The Visual Cycle in Vertebrates

One system utilizing out-of-equilibrium (bio)chemistry can be found in the visual cycle of vertebrates where the absorption of a photon is translated into a synaptic signal (**Figure 1**). Its discovery earned G. Wald the 1967 Nobel prize in medicine.[5] The system is based on meta-stable 11-*cis*-retinal that is formed from the thermodynamically most stable all-*trans*-retinal in a complex biochemical isomerisation.[6] The 11-*cis*-retinal then self-assembles into an opsin protein through reversible imine bond formation, forming rhodopsin. This protein could be compared to a spring-loaded mousetrap with the energy rich 11-*cis*-retinal being analogous to a loaded spring. As soon as a photon hits the rhodopsin, it is set off. Absorption of a photon triggers the back-isomerization of the chromophore to all-*trans*-retinal within just 1 ps.[7] This isomerization triggers a drastic conformational change of the opsin protein which in turn triggers a complex network of biochemical reactions, ultimately resulting in the hyperpolarization of the cell and transmission of a nerve impulse. The system automatically resets through a feedback loop that is part of the biochemical reaction network, liberating the all-trans-retinal from its protein residue so that the cycle can start anew. [8]

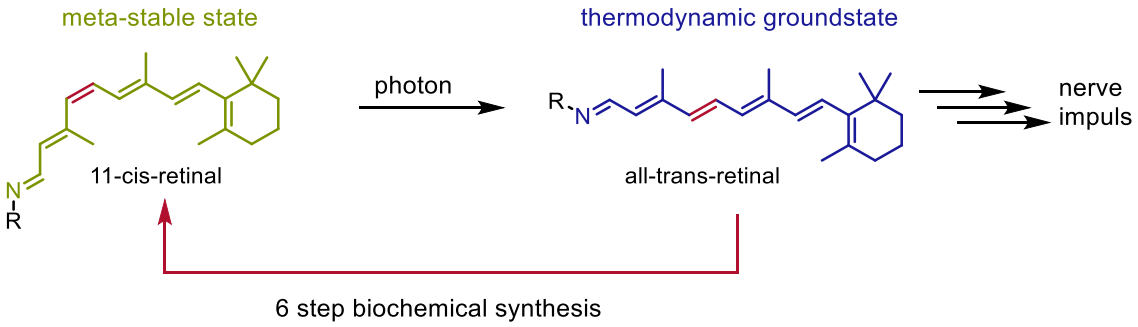

Figure 1. *Photochemical isomerization of opsin bound meta-stable 11-cis-retinal to all-trans-retinal triggers a reaction cascade that results in the transmission of a nerve impulse, enabling vision in vertebrates. Following photoisomerization to thermodynamically more stable all-trans-retinal undergoes a six-step biochemical synthesis to regenerate meta-stable 11-cis-retinal.*

1.4 A Systems Chemistry Approach to Photoresponsive Metal-Organic Cages

Biology demonstrates that complex functions emerge from complex networks of (bio)chemical reactions. Systems chemistry provides a toolbox of concepts that empower chemists to replicate these life-like properties in artificial structures. The goal of this thesis is to bring self-assembled metal-organic cages into the world of systems chemistry by exploring ways to reliably generate out-of-equilibrium structures. Like meta-stable 11-*cis*-retinal in the visual cycle, these high-energy structures can return to low energy states, releasing the stored energy in the process. Therefore, these high-energy cage assemblies have been brought up as promising candidates for controllable molecular machines that mimic the complexity found in nature[9] where this energy release is harnessed to produce work.[10,11] This thesis will focus on using light as an energy source to drive the metal-organic assemblies out of thermodynamic equilibrium, as this is a waste free way to impart energy into the system that can be precisely controlled, both spatially and temporally. Therefore, a secondary goal of this thesis is to develop molecular photoswitches and an understanding of how to synthesize them.

2 Theoretical Background

2.1 Photoswitches

The irradiation of photoresponsive molecules represents an ideal way to take chemical systems out of equilibrium. Light is a convenient energy source as it is trivial to control the energy influx by modulating the irradiation wavelength, intensity, timing, and location. Nature typically uses energy rich molecules like ATP to power out of equilibrium processes and has evolved elegant strategies to remove waste, regenerate fuel and control its distribution. These properties are exceedingly difficult to reproduce in artificial fuel driven systems that have no such way of getting rid of the waste generated during operation, with accumulated waste often hindering their function. When using light, the only by-product generated is heat with no additional reagents being needed that could complicate both functioning and analysis of the system. Another advantage is that light is non-invasive compared to the addition of energy rich and reactive fuels that could also enable unwanted side reactions.

2.1.1 Relevant Properties of Photoswitches

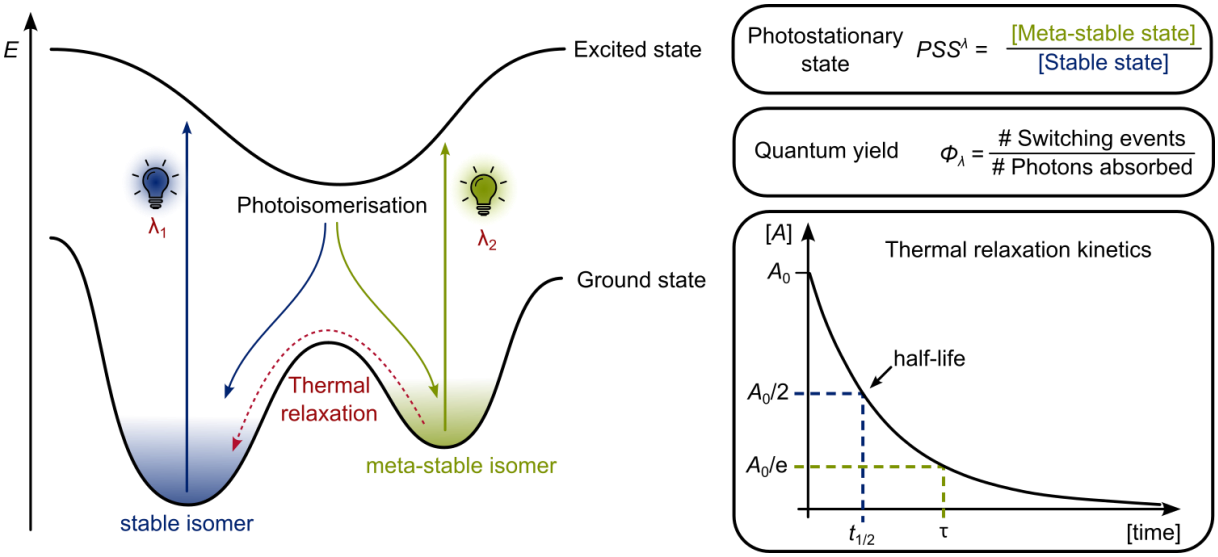

Figure 2. *Generalized depiction of the energy surfaces of a photochromic molecule. The stable isomer can be excited to an excited state with light of wavelength λ_1. This exited state can relax to the ground state of either the stable or the meta-stable isomer. Continuous irradiation enriches the meta-stable isomer until an equilibrium photostationary state (PSS^{λ}) is reached. Thermal relaxation to the stable isomer is determined by the barrier height between the two isomers and follows first-order kinetics, described by the half-life ($t_{1/2}$) or mean lifetime (τ). Switching back to the stable isomer can be achieved with light of wavelength λ_2. The efficiency of photoswitching depends on the quantum yield (Φ_{λ}) and molar extinction coefficient (ε_{λ}), as well as light intensity.*[12]

Photoswitches are photochromic molecules that can be reversibly switched between two isomers using light. Irradiation of the thermodynamically most stable isomer with light of the appropriate wavelength (**Figure 2**: λ_1) excites the molecule into an excited state. Relaxation

can occur either back to the ground state of the stable, or to the meta-stable isomer. Since the stable isomer is continuously excited, the meta-stable isomer is enriched during continued irradiation. Eventually, a steady state (**Figure 2**: photostationary state at irradiation wavelength λ; PSS^{λ}) will be reached where the ratio between the two isomers remains constant. When the irradiation ceases, thermal relaxation to the stable isomer will occur, following first-order kinetics. This process can be described using the half-life (**Figure 2**: $t_{1/2}$) or the mean lifetime (**Figure 2**: τ) which can range from milliseconds[13] to thousands of years[14] depending on the activation barrier. Alternatively, most photoswitches can be switched back from their meta-stable isomer by irradiation with another wavelength of light that selectively excites the meta-stable isomer (**Figure 2**: λ_2). The PSS is generally below 100% in both switching directions because the absorption spectra of the two isomers overlap and some photons induce reverse switching until a dynamic equilibrium is established. The steady state of this equilibrium is the PSS. Therefore, a large band separation and minimal spectral overlap between the two isomers is favorable for selective photoswitching. A second factor detrimental to obtaining the maximum PSS is the spectrum of the light employed for switching. Typically, LEDs are used as they emit close to monochromatic light with narrow half-widths ($\lambda_{1/2}$ = 10 to 50 nm). When a more precise excitation is needed, laser light or usage of a monochromator can further reduce the half-width of the excitation light to less than one nanometer.

The rate of photoswitching depends on the quantum yield (**Figure 2**: Φ_{λ}) that describes how likely an absorbed photon triggers isomerization. The molar extinction coefficient (**Figure 2**: ε_{λ}) describes how likely a photon is to be absorbed in the first place. A high quantum yield and high molar extinction coefficient are desirable as this results in fast switching, reducing the time needed until the photostationary state is reached. Additionally, switching rates depend on the light intensity and the overlap of the photoactive absorbance band(s) with the spectral profile of the light.

2.1.2 Azobenzene and the Photophysics of its Switching Process

Azobenzene (**Figure 3**) was already found to be a photoswitch in 1937 by G. S. Hartley.[15] Due to its long history and well understood properties, it is often the first molecule that is chosen by chemists when developing new photo-responsive proteins, drugs, molecular machines, or materials.[16] It boasts multiple advantages over the also well-known stilbenes such as a much greater resistance to photodegradation, not needing deep UV-light for the isomerization, and faster switching. If stored in the dark, azobenzene exists as the more stable *E*-isomer. When exposed to UV-light (λ = 365 nm), it readily switches to the *Z*-isomer, reaching a good PSS^{365} of 91% *Z*.[17] Back switching occurs when exposing the sample to visible light which switches

most of the meta-stable *Z*-isomer back to the stable *E*-isomer, reaching a PSS^{vis} of 21% *Z*. Complete return to the *E*-isomer is only possible by thermal relaxation in the dark.[18]

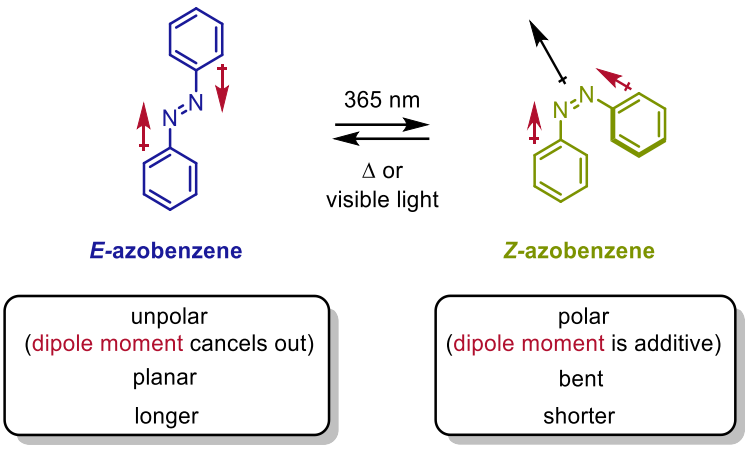

Figure 3. *Comparison of the chemical structures of E- and Z-azobenzene with C-N dipole moments highlighted in red.*

The UV-vis spectrum of *E*-azobenzene (**Figure 4**, **A**, blue line) shows a very intense absorbance band around λ = 350 nm that corresponds to its ππ* transition ($h\nu_1$). This is the band that is targeted during the irradiation with λ_{irr} = 365 nm where absorption of a photon of appropriate energy excites an electron from an occupied π-orbital (HOMO) into an unoccupied π*-orbital (LUMO).[19] In a simplified Jablonski diagram (**Figure 4**, **C**), this transition corresponds to a excitation from the electronic ground state (S_0) to the second excited state (S_2). This excited state decays very fast to the first excited state (S_1) through an S_2/S_1 canonical intersection (CI_3). No direct isomerization from *E* → *Z*-azobenzene is possible from the S_2 state.

The isomerization from *E*- to *Z*-azobenzene is proposed to occur at the S_1/S_0 canonical intersections where the relaxation forks to either *Z*-S_0 or *E*-S_0. The ratio between relaxation to *Z*-S_0 or *E*-S_0 determines the quantum yield of the switching process with CI_1 having a higher likelihood of relaxation to the *Z*-S_0 state than CI_2.[20]

From the S_1 state of *E*-azobenzene, two different $S_1 \rightarrow S_0$ relaxation pathways utilizing different canonical intersections (CI_1 and CI_2) are possible following $S_2 \rightarrow S_1$ relaxation. The preferred pathway is the $S_1 \rightarrow CI_2 \rightarrow S_0$ relaxation process which involves the canonical intersection CI_2. This can only be reached without a significant barrier from where the wave packet is deposited after $S_2 \rightarrow S_1$ relaxation but not from the S_1 energy minimum, resulting in two different isomerization pathways with differing quantum yields following S_2 or S_1 excitation, violating

Kasha's rule.[21,22] The second relaxation process ($S_1 \rightarrow CI_1 \rightarrow S_0$) is directly accessible from the S_1 energy minimum.

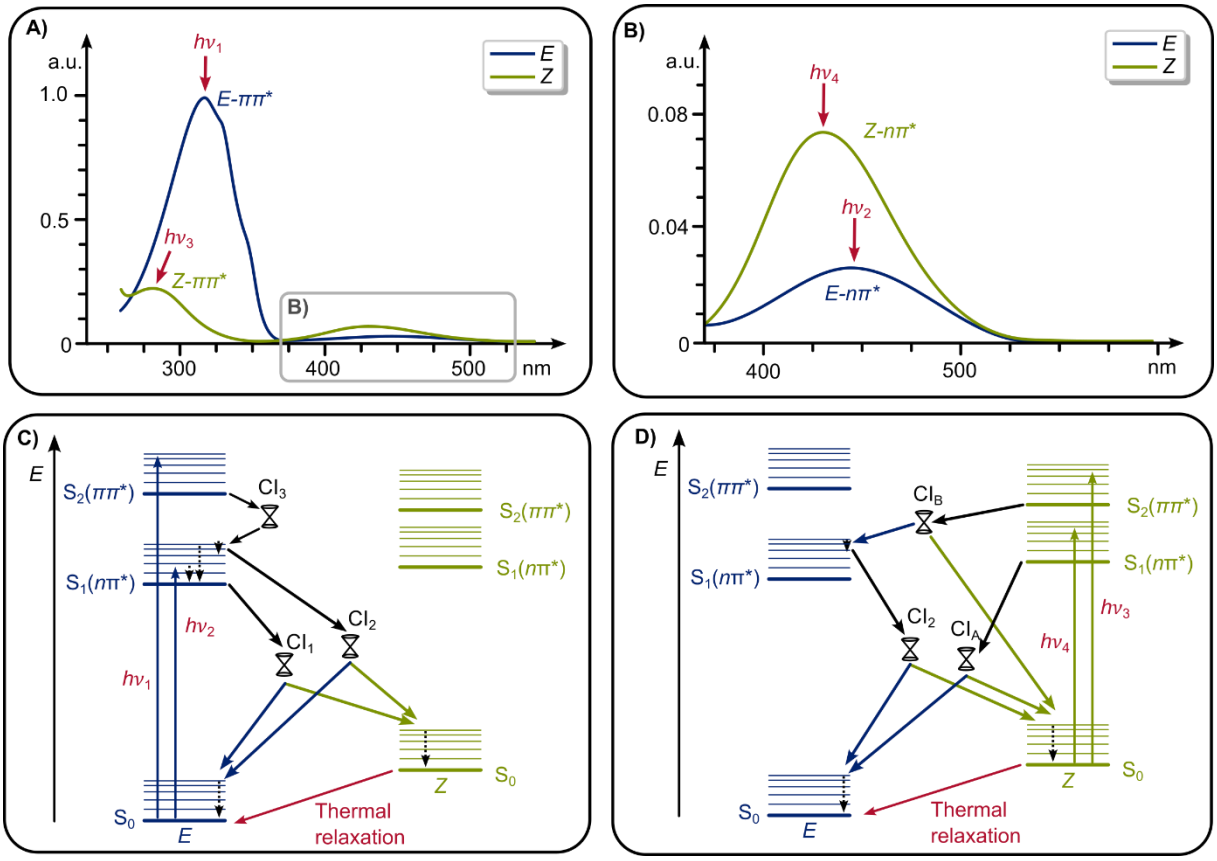

Figure 4. *Experimental UV-vis spectra of E- and Z-azobenzene (**A**, **B**).[23,24] Simplified Jablonski diagrams for E→Z switching (**C**) and Z→E switching (**D**) of azobenzene. Relative energy levels and isomerization mechanisms were obtained via ultrafast time-resolved fluorescence and transient absorption in both the UV-visible and the IR regions, femtosecond spectroscopy, as well as quantum chemical calculations.[20,25–27]*

Besides the very intense ππ* transition band, a much weaker band can be found around λ = 450 nm (**Figure 4**, **B**, blue line). This band corresponds to an nπ* transition that is symmetry forbidden in accordance with the Laporte rule for centrosymmetric molecules.[28] Despite this being a forbidden transition, an absorbance band is observed due to vibronic coupling where asymmetric vibrational modes influence the symmetry of the electronic structure. This process is not very efficient, resulting in "weakly allowed" transitions with much lower molar extinction coefficients, as is the case for the nπ* transition. Exciting the *n*π* band of *E*-azobenzene ($h\nu_2$) will excite the molecule to its S_1 state (**Figure 4**, **C**). Following the Franck-Condon principle that implies vertical excitation/relaxation,[29] the wave packet is deposited on a different position on the energy hypersurface of S_1 following the $S_0 \rightarrow S_1$ transition than it would be following a $S_2 \rightarrow S_1$ transition, giving access to only one of the two

S_1/S_0 canonical intersections (CI_1) where photoisomerization can occur. The quantum yield for *E*→*Z* switching is higher following $S_1n\pi^*$ excitation, as only CI_1 can be reached, which shows a greater preference for relaxation to *Z*-S_0. This results in an increased quantum yield of Φ_{S1} = 20% to 35% compared to Φ_{S2} = 5% to 15% following $S_2\pi\pi^*$ excitation (depending on solvent polarity and viscosity).[30] However, irradiation of the $S_1n\pi^*$ transition to induce photoswitching switching is unfavorable due to the very low intensity of the absorbance band and large overlap with the much more intense $n\pi^*$ transition band of *Z*-azobenzene, which results in reduced photostationary states.[20]

The aromatic conjugation in *Z*-azobenzene is broken as one of the phenyl rings is twisted out of plane. This is reflected in its UV-vis spectrum (**Figure 4**, **A**, green line) that shows a much less intense (= lower molar extinction coefficient) $\pi\pi^*$ transition of higher energy (= blue shifted) when compared to the fully conjugated *E*-azobenzene. Even though this band allows for the direct isomerization of *Z*-azobenzene to *E*-azobenzene by a complex relaxation mechanism involving population of an S_1 state in *E*-azobenzene (**Figure 4**, **D**), it is typically not used for photoisomerization. Due to the overlap with the much more intense $\pi\pi^*$ transition band of *E*-azobenzene this band is hard to selectively excite. Furthermore, using deep UV-light for switching is not ideal as it is much more likely to trigger photodegradation processes.

The second absorption band in *Z*-azobenzene at λ = 450 nm corresponds to its $n\pi^*$ transition (**Figure 4**, **B**, $h\nu_4$). Just like in *E*-azobenzene, this transition is symmetry forbidden but experiences a stronger vibronic coupling, resulting in a greater oscillator strength and a three-fold more intense absorbance band. Irradiation of *Z*-azobenzene with blue light (λ = 450 nm) excites it from its electronic ground state S_0 to the first excited state S_1 (**Figure 4**, **D**). Like for *E*-azobenzene, a canonical intersection (CI_A) can be reached where either isomerization (*Z*-S_1→*E*-S_0) or relaxation to the electronic ground state (*Z*-S_1→*Z*-S_0) can occur.[20]

The exact mechanism of the isomerization from a geometrical viewpoint has been a source of disagreement for decades, despite extensive experimental and computational investigations.[31]

It has been observed that the quantum yield for the switching is about twice as high when exciting the $S_1n\pi^*$ transition as compared to excitation of the $S_2\pi\pi^*$ transition. If both relaxations occurred through the same mechanism, this could not be possible. Experimental and computational data seems to suggest a predominantly rotational pathway in $S_1n\pi^*$ through CI_1 and a nonrotational pathway in $S_2\pi\pi^*$, enabled by CI_2.[32] However, these two mechanisms are unable to fully explain all experimental and computational observations by themselves.[30] This leads to proposals that a mixed process like the hula-twist or inversion-assisted torsion is taking place.[20,33] An overview of the molecular motions proposed for this isomerization is depicted in **Figure 5**. Substituents on the aromatic rings can completely change the energy

hypersurfaces of the S_n states and therefore further increase the complexity of the isomerization mechanism, making it almost futile to try to propose a generally applicable mechanism.[34] A detailed summary and discussion of *E*-azobenzene photoisomerization was published by Tarnovsky and coworkers in 2022.[30]

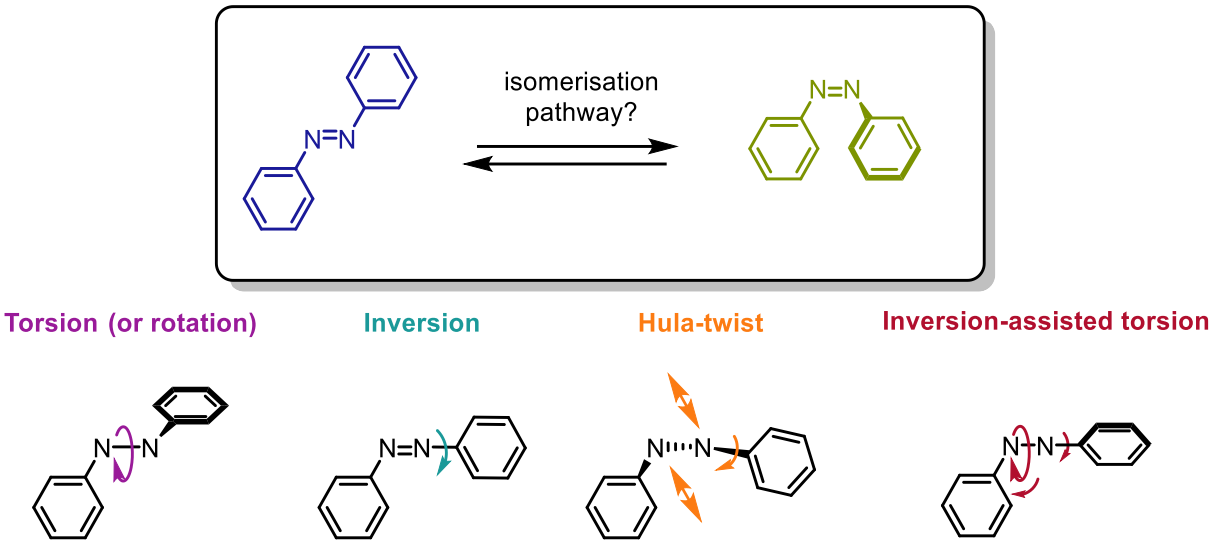

Figure 5. *Schematic representation of the molecular motions for azobenzene E → Z isomerisation: torsion (or rotational), inversion (or non-rotational), hula-twist, and inversion-assisted rotation.*

Summarizing the photophysical processes in *E*- and *Z*-azobenzene and how to best harness them as a chemist trying to use light to control azobenzene:

- The $S_1n\pi^*$ and $S_2\pi\pi^*$ transitions of both isomers can, in principle, be used for photoisomerization.
- For *E* → *Z* switching it is best to target the *E*-azobenzene $\pi\pi^*$ transition ($h\nu_1$) due to its high extinction coefficient and good band separation, allowing for selective switching.
- For *Z* → *E* switching targeting the $n\pi^*$ transition of *Z*-azobenzene ($h\nu_4$) typically gives the best results. Despite the small band separation and unwanted co-excitation of *E*-azobenzene, the much stronger vibrational coupling in *Z*-azobenzene makes this an effective way to switch.
- It may often be helpful to irradiate a shoulder instead of the maximum of the targeted band as this often increases the selectivity of the photoexcitation.
- The overlapping $n\pi^*$ transitions in the visible range typically result in isomerization under ambient light, so azobenzene samples that are not stored and handled in the dark will always contain both isomers, typically with 10-30% *Z*-isomer present.[30]

2.1.3 Azobenzene Derivatives

Azobenzenes are generally good photoswitches that reach good photostationary states when switching from *E* → *Z*. Their structure-function relationship is well understood (**Figure 6**) which allows chemists to fine-tune the properties of the switch for specific applications. Drawbacks of azobenzenes include the usually non-quantitative back switching due to an overlap of the nπ* transitions of *E*-and *Z*-azobenzene which can be a problem for use cases where the switch needs to be fully switched off.

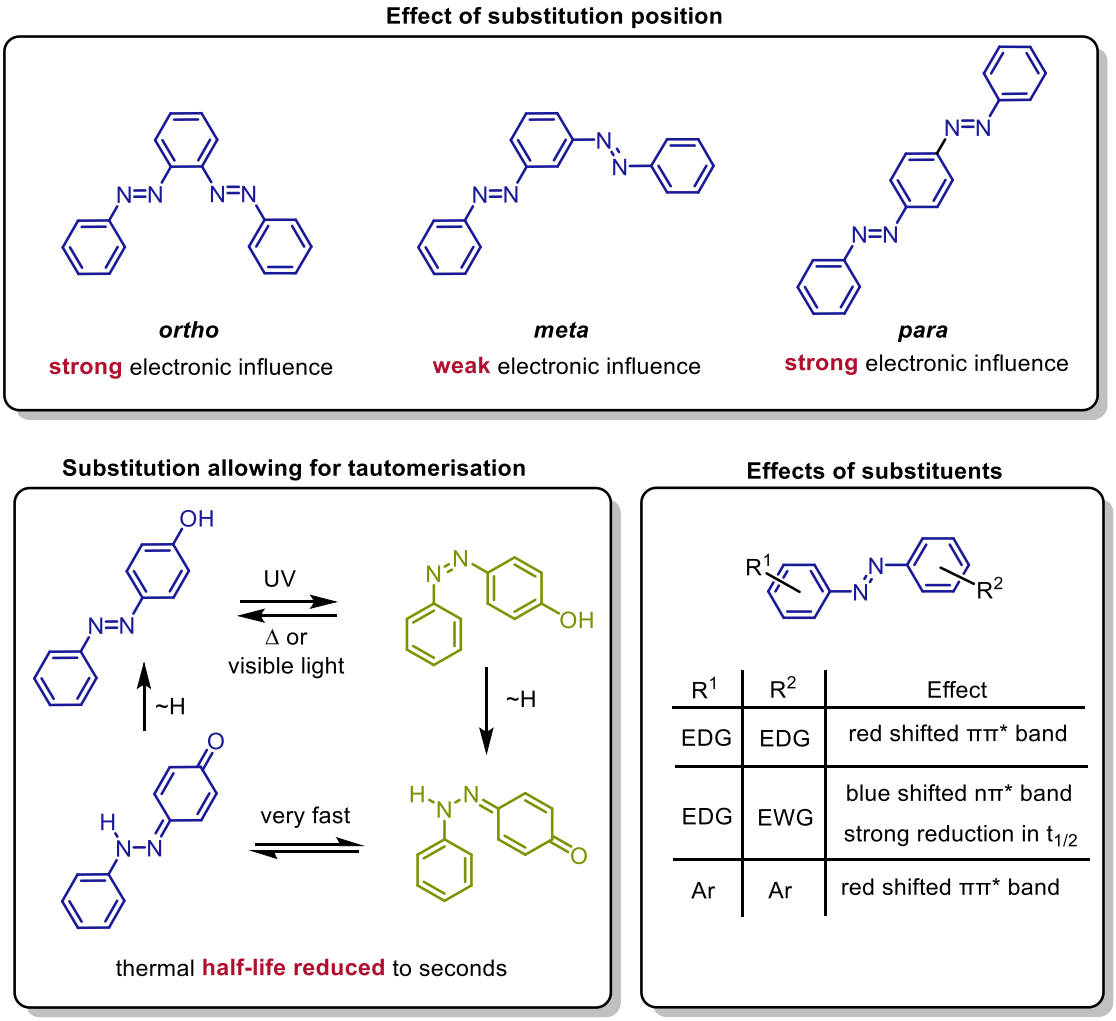

Figure 6. *The magnitude of substituent effects correlates with the degree of electronic coupling.*[35] *Substituents that enable tautomerization of the N=N double bond to an N-N single bond reduce the half-life of azobenzenes drastically.*[13] *The position of the ππ* transition can be influenced by substituent effects with electron donating groups (EDG) or aromatic substituents resulting in a red shift. Mixing EDG with electron withdrawing groups (EWG) creates a push-pull system that will drastically reduce the thermal half-life of the Z-state.*[36]

The properties of azobenzenes can be tuned by substitution of the phenyl-H atoms. Bis-azobenzenes are a great example of how the substitution position affects the switching properties. When comparing azobenzene to *ortho* bis-azobenzene,[35] the absorbance maximum of the ππ* transition is blue-shifted, and the quantum yield is reduced. The most drastic change can be observed in the thermal half-life that is shortened from multiple days to just 1.6 milliseconds. This drastic change is caused by an intramolecular excitonic interaction between the azo groups that enables this ultra-fast relaxation. In the case of *meta* bis-azobenzene,[35] no significant deviations from azobenzene can be observed in absorbance maxima, quantum yield, and thermal half-life as the *meta*-substitution pattern minimizes the electronic interaction between the two azo groups. The *para* bis-azobenzene[35] shows a redshifted ππ* transition, drastically reduced quantum yield, and a slightly reduced half-life of 10 hours. To summarize the observations, it can be said that the *para* and *ortho*-position should be used when attempting to tune the switching properties, but the *meta*-position is the best option when connecting the azobenzene core to another molecule and interference with the switching behavior is not intended.

A class of substitutions to keep in mind are substituents containing protic H atoms as they will drastically reduce the thermal half-life of the metastable state by enabling tautomerization of the N=N double bond. In the tautomerized state, *E*/*Z* isomerization is very fast as almost no barrier exists for the rotation around the single bond (**Figure 6**).[13]

Substitution with electron donating and/or aromatic groups will result in red shifted ππ* absorbance band, bringing the excitation wavelengths into the visible range, eliminating the need for UV-light in the excitation process. A mixed donor/acceptor substitution pattern will drastically reduce the thermal half-life as the push-pull system increases the sigma character of the N=N double bond, lowering the barrier for thermal isomerization (**Figure 6**).[36]

Many azobenzene derivatives with improved properties have been published with tetra-*ortho* substitution,[37] heteroaromatic,[38] and BF_2-azobenzenes[39] being examples of especially effective modifications. Their structures, excitation wavelengths, photostationary states, and thermal half-lives can be seen in **Figure 7**. The **tetra-*ortho* substitution**[37] shifts the nπ* band into the visible range, with the *E*-nπ* band being affected stronger than the *Z*-nπ* band. This interchanges the position of the absorbance maxima and excitation of the redshifted shoulder allows selective *E*→*Z* switching using green light (λ = 500 nm). The *ortho*-substituents also interfere with thermal relaxation as the steric crowding increases the isomerization barrier, leading to exceptionally long thermal half-lives in the range of years instead of days. The photostationary states remain similar to those of azobenzene. **Heteroaryl azobenzenes**[38] do not show a particularly strong redshift, but the increased band gaps allow for exceptionally selective excitation, leading to superior photostationary states of for both *E*→*Z* and *Z*→*E*

switching, with almost quantitative switching being observed. The thermal half-life remains similar to that of azobenzene. **Azo-BF_2 switches**[39] exhibit a structure reminiscent of BODIPY chromophores. This results in an extreme redshift of the ππ* band by around 310 nm, allowing switching with near-infrared light of λ = 710 nm. The thermal half-life of these switches is reduced to a few minutes, and they will decompose in solution by hydrolysis on a timescale of hours.

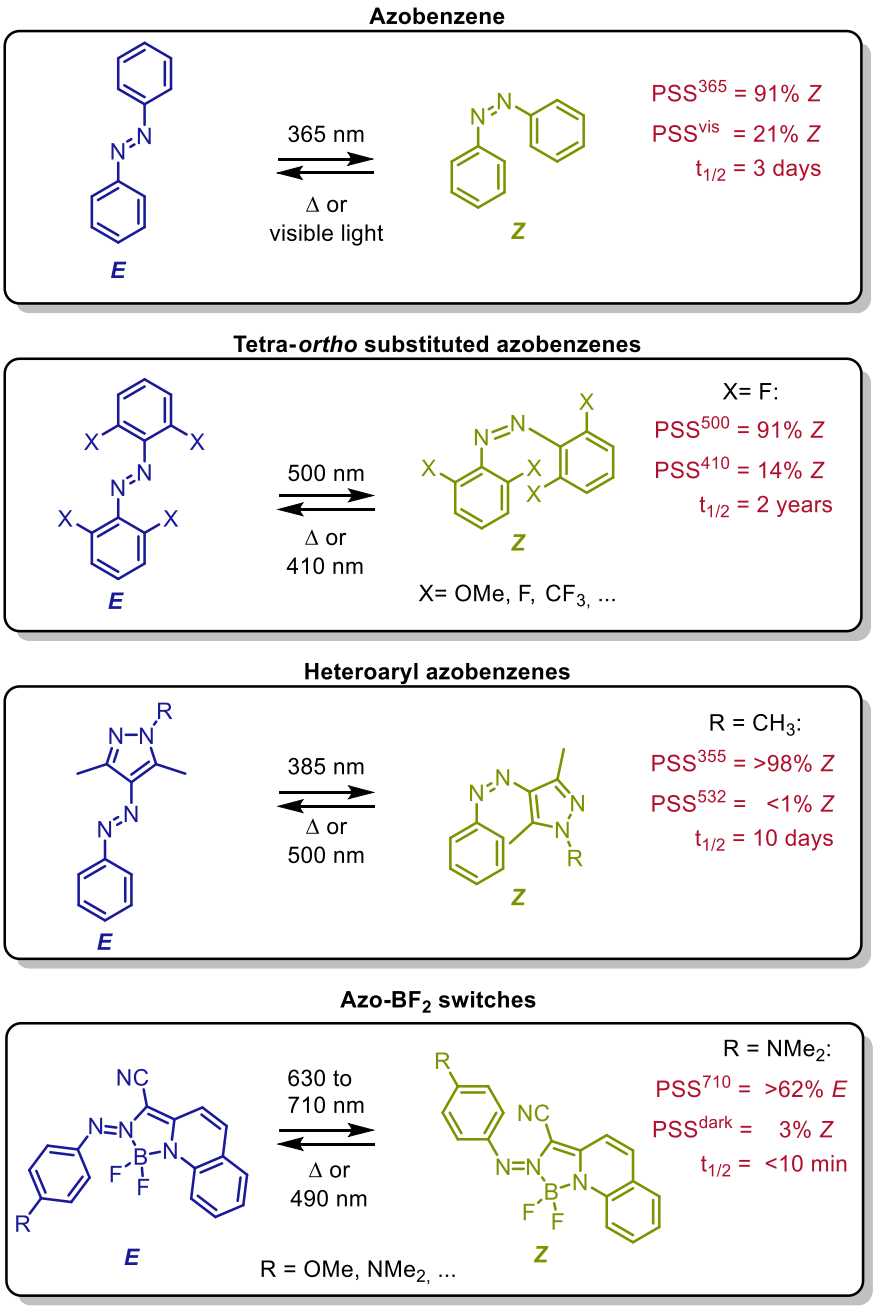

Figure 7. *Comparison of the photochemical properties of azobenzene,[40,41] a tetraorthofluoro azobenzene,[37] a heteroarylazobenzene,[38] and an azo-BF_2 switch.[39]*

It can be concluded that substitution patterns with exceptional properties are available. Thermal half-lives can range from seconds to years, visible light switching is common, and near quantitative switching has been achieved, allowing chemists to pick and choose structural motives depending on their desired properties. While not all combinations (e.g. near-infrared switching AND long half-life) have yet been reported, new azobenzene derivatives expanding the range of available properties continue to be of interest to the academic world.

2.1.4 Diazocines

One class of azobenzene derivative that will be discussed in detail are based on 11,12-dihydrodibenzo[*c*,*g*][1,2]diazocine where two *ortho*-substituents are connected, resulting in an eight-membered ring structure (**Figure 8**). These are usually referred to by the shortened name "diazocine". Note that in IUPAC nomenclature, the term "diazocine" refers to a class of unsaturated eight membered rings containing two nitrogen and six carbon atoms, a much larger group of compounds.[42,43]

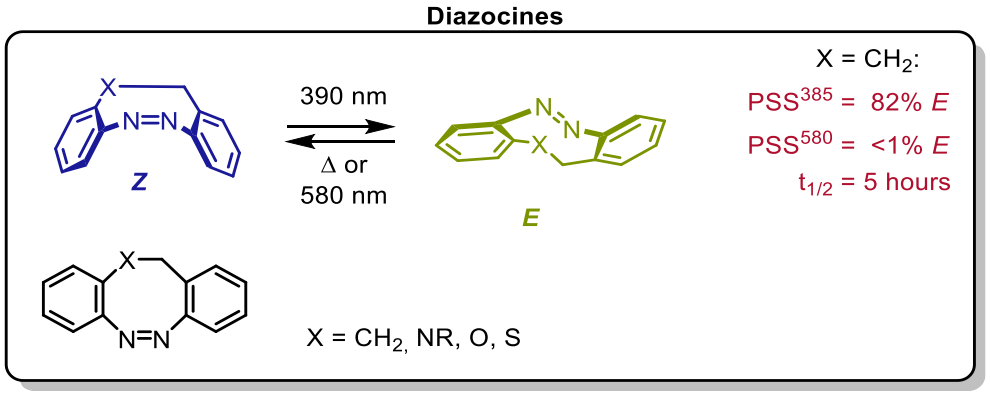

Figure 8. *Photochemical properties of 11,12-dihydrodibenzo[c,g][1,2]diazocines ("diazocines") determined in methanol.*[44]

The parent compound was first synthesized in 1910 by French chemist Duval,[45] but its photochromic properties were only discovered and investigated in 2009 by F. Temps and R. Herges.[46] The ring strain drastically changes the energy landscape of the switching process, resulting in the U-shaped *Z*-isomer being thermodynamically more stable than the almost planar *E*-diazocine. This is a unique feature compared to non-cyclic azobenzene derivatives where the inverse stability is observed.

A comparison of the three-dimensional structures of *E*- and *Z*-isomers of diazocine and azobenzene can be seen in **Figure 9**. Azobenzene is a fully planar in its *E*-state, with the whole

molecule being in aromatic conjugation. In the *Z*-state of azobenzene, the two phenyl rings are almost orthogonal to each other with rotation around the N-C bond resulting in a propeller/petal-like shape. Breaking the aromatic conjugation results in the *Z*-isomer being 49.0 kJ/mol lower in energy than *E*-azobenzene. The ethyl bridge induces strain into the diazocine structure with none of its isomers containing two fully coplanar phenyl rings, meaning that the aromatic conjugation is reduced in all isomers. The three most stable isomers can be classified according to the shape of the eight-membered ring. Due to stiff aromatic rings, it behaves more like a six-membered ring with the *Z*-boat configuration having the least ring strain and being the most stable isomer. The *E*-isomer can take on either a chair-like or a twisted geometry, with the twisted geometry being slightly favored at respective relative energies compared to *Z*-diazocine of 31.8 kJ/mol (twist) and 43.1 J/mol (chair). At room temperature, the isomerization between the two *E*-isomers exhibits almost no barrier and interconversion is practically instantaneous.[47,48]

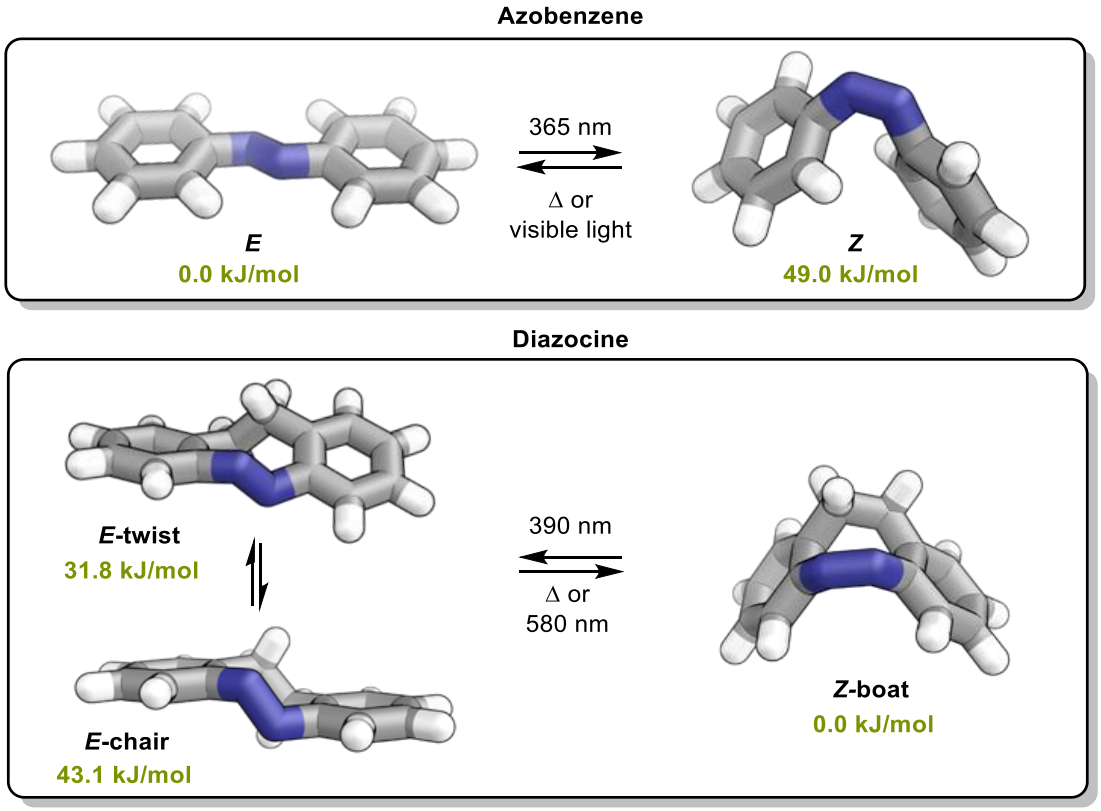

Figure 9. *Three dimensional representations of isomers of azobenzene and diazocine. The geometries were optimized and relative energies calculated at B3LYP/6-31G* level (green).*[47,48]

The ring strain strongly affects the energy of the $S_1n\pi^*$ transition, that is found around λ = 450 nm for both *E*- and *Z*-azobenzene. In *Z*-diazocine, the $n\pi^*$ band is strongly blue shifted to λ = 404 nm with the $n\pi^*$ band of the *E*-isomer experiencing a strong redshift to λ = 490 nm,

resulting in an excellent band separation that enables selective photoexcitation. A comparison of the UV-vis spectra of diazocine and azobenzene with the spectral profiles of different LEDs can be seen in **Figure 10**. UV light irradiation (λ = 390 nm) allows *Z*→*E* switching in diazocine with an excellent photostationary state of up to 90% *E*-diazocine while *E*→*Z* switching is quantitative with both white and green (λ = 500 nm) light. This quantitative back-switching is a property not often observed in azobenzene derived switches and is useful in applications where full conversion to the OFF state is required.[44]

Another notable improvement over azobenzene can be found in the drastically improved quantum yield for both switching directions with $\Phi_{Z\rightarrow E}$ = 72% and $\Phi_{E\rightarrow Z}$ = 50%.[46] This increase for the *E*→*Z* switching stems in part from avoiding the less-efficient isomerization after $S_2\pi\pi^*$ excitation. Furthermore, the ring strain reduces conformational degrees of freedom which in turn disfavors unproductive vibrational relaxation pathways of the electronic excited state S_1, thereby increasing the likelihood of an isomerization event.[47]

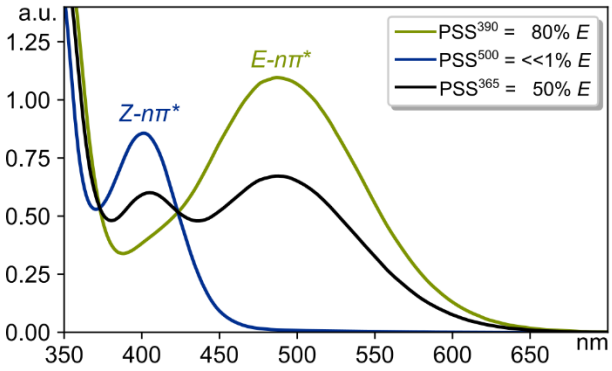

Figure 10: *Experimental UV-vis spectra of diazocine (1mM, MeCN, 25°C) after irradiation with different wavelengths for one minute.*

A comparison of the UV-vis spectra of diazocine and azobenzene with the spectral profiles of different LEDs used for photo switching can be seen in **Figure 11**. As a reminder, azobenzene can be switched from *E*→*Z* using UV-light (λ = 365 nm) by $S_2\pi\pi^*$ excitation and from *Z*→*E* by $S_1n\pi^*$ excitation using for example blue light (λ = 430 nm). The *E*→*Z* switching works well due to the much more intense $\pi\pi^*$ band in *E*-azobenzene but is rather inefficient due to additional non-productive vibrational relaxation pathways. Back-switching of azobenzenes is a lot less selective, as the *E*-$n\pi^*$ and *Z*-$n\pi^*$ transitions are barely separated and cannot be targeted separately due to their large overlap. Back switching is, however, still possible, as the $n\pi^*$ transition in *E*-azobenzene is much less intense, but this results in non-complete deactivation of the *Z*-isomer.

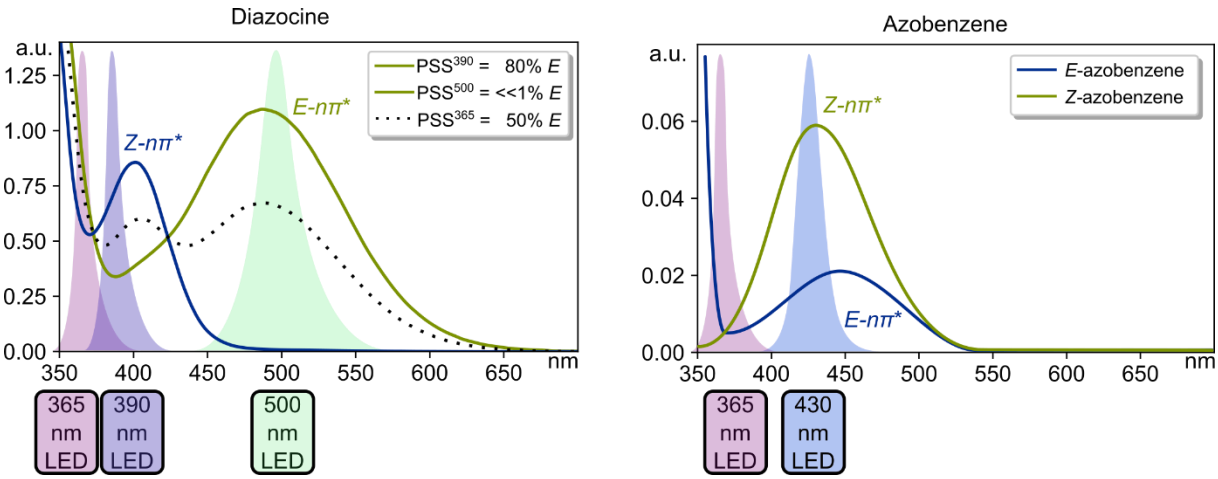

Figure 11. *Experimental UV-vis spectra of diazocine (left, 1mM, MeCN, 25°C) and literature spectrum of azobenzene (right)[23,24] overlayed with the spectral profiles of the LEDs used for photoswitching.*

In comparison, diazocine and its large band separation of the *E*- and *Z*-nπ* bands allows selective S_1 photoexcitation with deep blue light (λ = 390 nm) or green light (λ = 500 nm). UV-light (λ = 365 nm) excites both isomers as there is a significant overlap in their ππ* bands, resulting in a worse photostationary state of around 50% *E*.[49] Despite the strained ring structure, diazocines are very stable and show no photodegradation even after hours of irradiation or hundreds of switching cycles. Solid diazocine is extraordinarily stable, it can still photo isomerize and can even be sublimated. Diazocines are well soluble in most solvents from cyclohexane to acetonitrile and acetonitrile. The solutions will not show any decomposition effects, even when exposed to air, heat, light, or all three at once. Only aggressive chemical environments such as strong acids, bases, oxidants, or reductants will result in decomposition.

Despite their favorable properties, diazocines have only recently started to see widespread use as photoresponsive molecules, likely due to their challenging synthesis. A bar chart of the number of publications containing diazocines from 1950 to today (August 2025) can be seen in **Figure 12**. The publications can be roughly divided into four periods in which a different prevailing theme can be observed in the publications. The first group (**Figure 12**, orange) was published before the photochromic properties had been reported and focused on the synthesis of novel structural motives and description of the physicochemical properties of diazocines.[43]

The second group of publications (**Figure 12**, blue) starts with the 2009 publication of Temps and Herges,[46] where the photochromic properties of diazocine were investigated for the first time. This was followed by a first wave of publications that focused on quantum chemical descriptions of the photoisomerization process. A first application was also published during this period with the 2012 paper by Woolley who integrated a diazocine linker into a peptide strand and could reversibly use it to change from a folded to a helical arrangement.[50]

Seemingly, interest in diazocines faded again. This was likely due to the difficult synthetic access with early publications boasting yields of 4%[46] and 8%[50] in the cyclisation step (**Figure 13**).

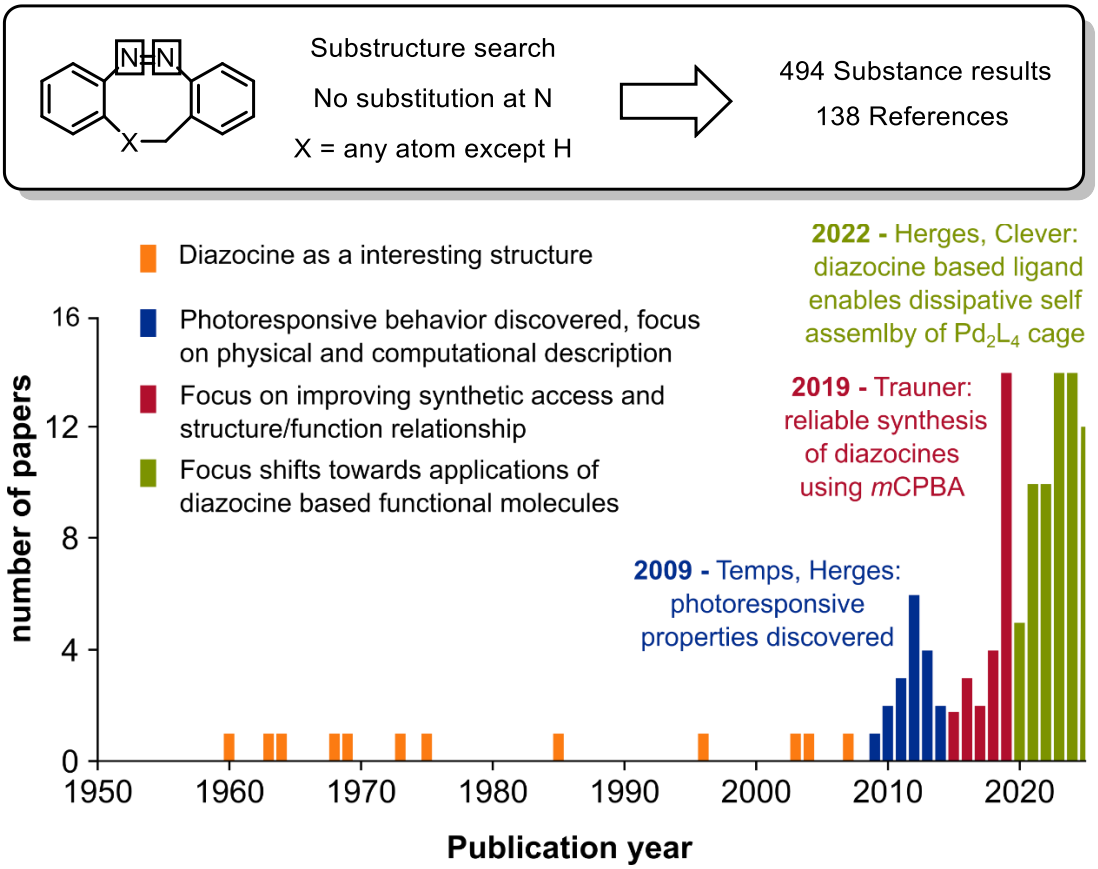

Figure 12. *Number of publications per year on diazocines (obtained from https://scifinder-n.cas.org/ on 02.08.2025).*

This lack of synthetic access was the focus of the third group of publications (**Figure 12**, red) from 2015 to 2019 where improvements to synthetic strategies are the most common topic. The scope of diazocines was extended to hetero atom (O, S, N) bridged diazocines that boasted improved photophysical properties.[51] Besides this, a few computational investigations and the first application of diazocines in photo pharmacology were reported.[52]

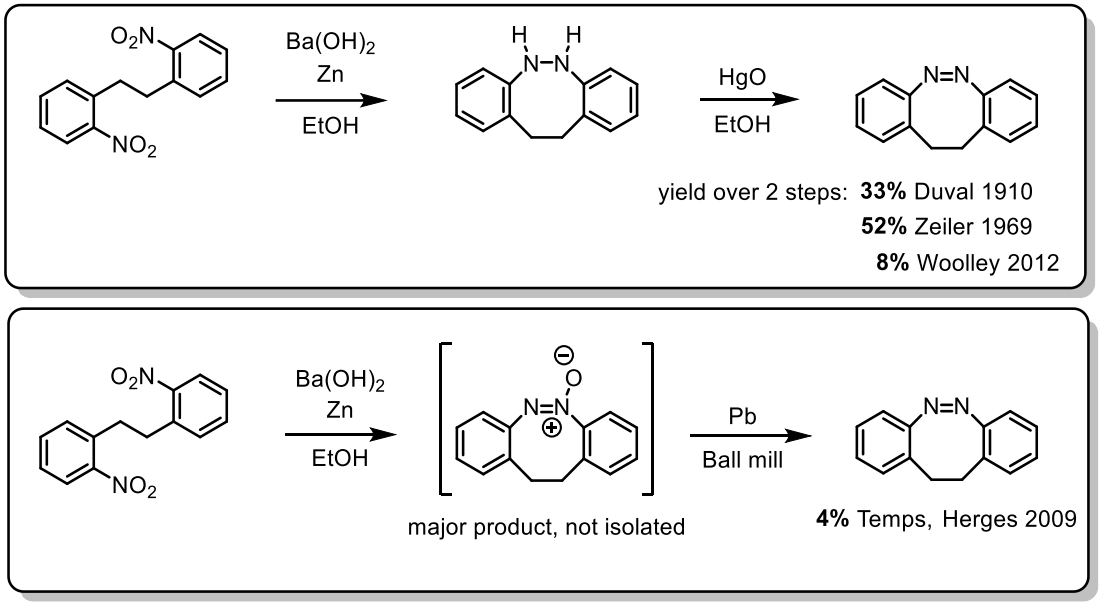

Figure 13. *Reductive diazocine synthesis as published by Duval in 1910,[45] by Zeiler in 1969,[43] by Herges in 2009,[46] and Woolley in 2012.[50] The synthesis requires a large excess of heavy metals and yields are not easily reproducible.*

Two notable publications could drastically improve both the yield and diversity of substituents for diazocines were published by Herges and by Trauner in 2019 (**Figure 14**). Herges reported optimizations to the reductive pathway that improved the yield of the cyclization to 56% and that of the dinitrophenyl-ethane substrate to >90%.[53]

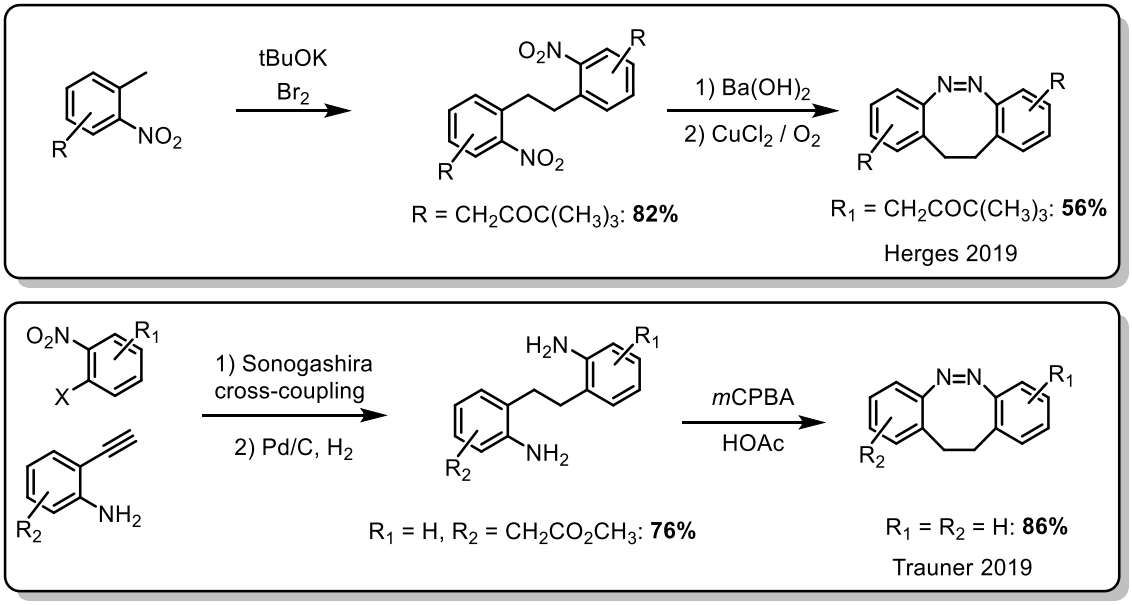

Figure 14. *Improved synthesis of diazocines published by Herges in 2019[53] and by Trauner in 2019.[49]*

Trauner followed a different pathway that involves the oxidation of a bis-aniline to furnish the diazocine in an intramolecular Bayer Mills reaction. This bis-aniline could be obtained with a

diverse set of substituents in 70-80% yield by consecutive Sonogashira coupling and alkyne/nitro reduction. Oxidation to the diazocine using *m*CPBA proceeds with high yields for many substituents, furnishing the unsubstituted diazocine in 86% yield.[49]

After reliable access had been established and a broad set of derivatives was prepared, the interest in the field continued to rise with around half of the publications on diazocines having been published in the last four years (2020-2024). This represents the fourth phase (**Figure 12**, green) in diazocine development where the structure is well understood and its properties of being an excellent photoswitch are being made use of. This does, however, not mean that development of new synthetic methodologies or detailed investigations into its photophysical properties have stopped, as this type of work is still being actively investigated. Today, the most employed synthetic strategy is the oxidative approach using *m*CPBA with an increasing number of application-oriented projects being published. Enabled by the systematic understanding of their photophysical properties, diazocines have been used in photoresponsive polymers,[54] proteins,[55] DNA-binders,[56] molecular tweezers,[57,58] pain medication,[59] covalent organic frameworks,[60] and metal-organic cages.[61,62]

2.1.5 External Influences on Diazocine Properties

The photophysical properties of unsubstituted diazocine have been investigated and reported in multiple publications, but each publication reported slightly different values for the *Z*→*E* switching and the thermal half-life (**Figure 15**).[44,46,49,51] The reason for this is likely not inaccurate measurements, but the fact that each publication used slightly different experimental conditions and therefore observed different results. For example, the photostationary state is influenced by the solvent polarity. Non-polar solvents stabilize the less polar *E*-isomer, while polar solvents stabilize the *Z*-isomer with its higher dipole moment. This results in a lowered PSS when changing from n-hexane to acetone, DMSO or even methanol. The thermal half-life obviously depends on the temperature of the measurement, that differs between publications. In addition to the thermal influence, it can be observed that protic solvents accelerate thermal relaxation by H-bond interactions with the azo-nitrogen lone-pairs, a mechanism that was also observed for azobenzene.[12] The quantum yields can differ significantly depending on the excitation wavelength that was used, with *E*→*Z* switching showing a doubling in quantum yield at λ = 520 nm as compared to λ = 385 nm. Therefore, it is important to check the measurement conditions before reaching any conclusions on the effect that substitution and derivatization have on diazocine switches.

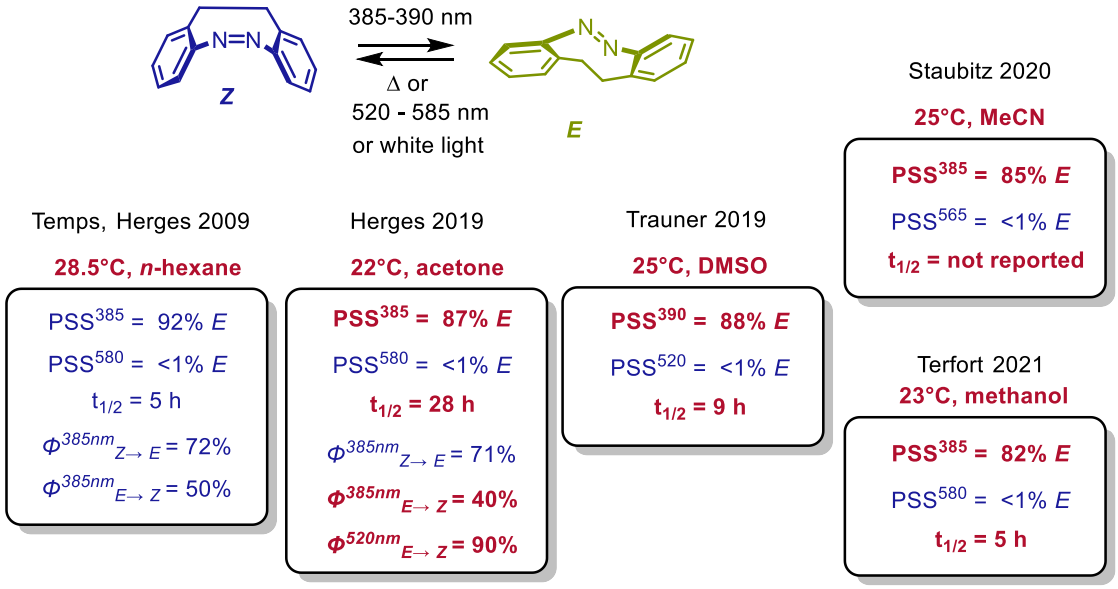

Figure 15. *Overview of photochemical properties of diazocines as determined by Temps and Herges in 2009,[46] Herges in 2019,[51] Trauner in 2019,[49] Staubitz in 2020,[63] and by Terfort in 2021.[44] Discrepancies between the publications are marked in red.*

2.1.6 Properties of Diazocine Derivatives

The synthesis of new diazocine derivatives has seen considerable interest in literature, both for broadening the scope of properties in diazocines as well as to add functional groups that allow them to be incorporated into larger structures.

Backbone modifications to the ethylene spacer can be seen in **Figure 16** and have focused on either incorporating a hetero atom or on increasing its rigidity. Incorporation of hetero atoms reduces the thermal half-life for nitrogen[51] and oxygen[64] and increases it for sulfur.[64] The photostationary states of all bridged derivatives are lower in the *Z* → *E* switching than that of the parent diazocine, with sulfur and nitrogen bridged diazocine seeing the strongest decrease. Back switching remains close to quantitative for all derivatives. While the additional bridging in the backbone has a minor influence on the photostationary state, a large influence is observed for the quantum yield.[47] As previously discussed, the quantum yield increases when increasing the rigidity of the structure as this disfavors unproductive vibrational relaxation pathways from the electronic excited states, resulting in higher quantum yield for most processes.

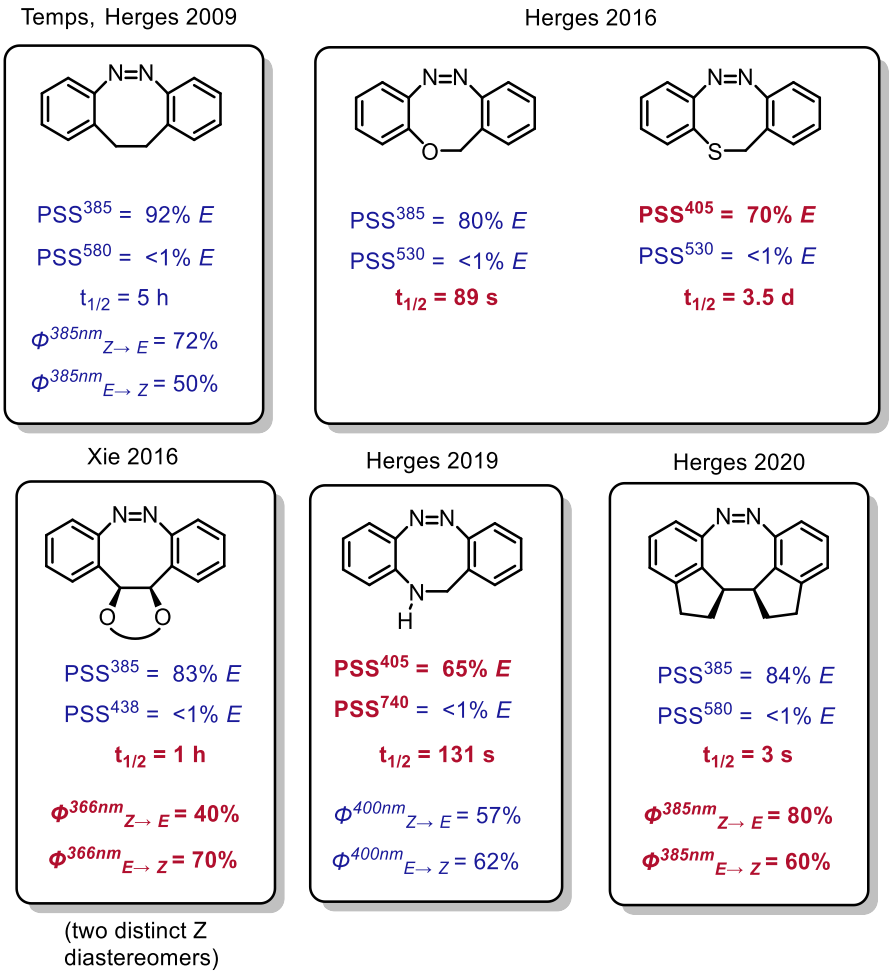

Figure 16. *Overview over the photochemical properties of bridge modified diazocine derivatives published by Temps and Herges in 2009,[46] Xie in 2016,[65] Herges in 2016,[64] 2019,[51]and 2020.[47] Strongly affected properties are marked in red.*

Surprisingly, to date the first reported unsubstituted diazocine still holds the record for the best photostationary state. No derivative that could improve in this property has been reported to date (April 2025). This might be explained by a closer look at the effect of substituents on diazocine properties. A brief overview over some of the reported diazocine derivatives with their photostationary states can be seen in **Figure 17**.

The substituents can be divided into two groups. Group one includes substituents with +I, -I and -M effects and the photoswitching is typically slightly worse than for unsubstituted diazocine but remains excellent. Thermal half-lives are highly tunable with strongly electron withdrawing substituents in the *ortho* or *para*-positions of the azo bridge drastically accelerating the thermal relaxation. Some specific substitutions, such as 2,9-difluoro diazocine, will unpredictably result in drastically reduced photostationary states. The reason for this can be found in the spectral overlap of the *E*- and *Z*-states that surprisingly much stronger for the difluoro system than for mono-fluoro diazocines, thus inhibiting selective photoexcitation. While

the first group of substituents will usually not result in an increased overlap of the *E*- and *Z*-spectra and therefore retain the excellent photoswitching properties, the substituents of the second group (+M effect) such as ethers and amines will reliably reduce the band gaps between the *E*-S_1/*Z*-S_2 and *E*-S_2/*Z*-S_2 transitions. Therefore, just a single methoxy group will reduce the photostationary state drastically and +M substituents should be avoided on diazocines. This is in stark contrast to azobenzenes, where methoxy substituted azobenzenes represent excellent switches.[66]

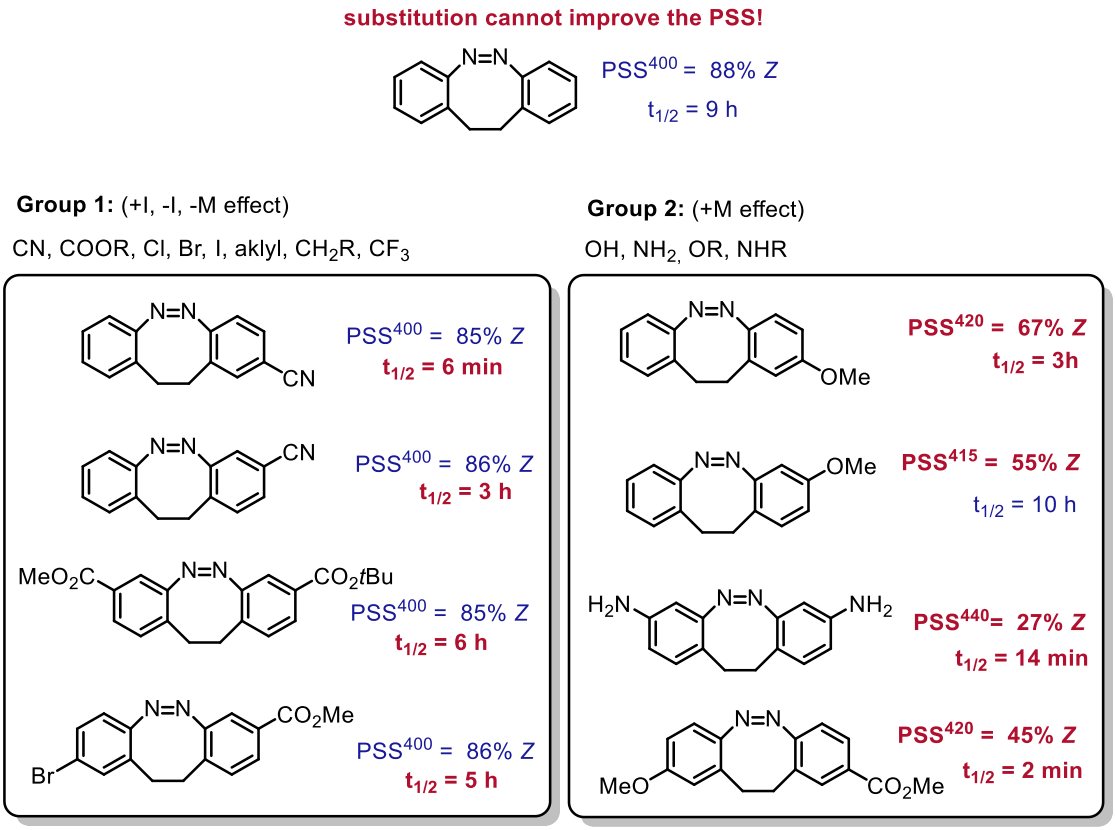

Figure 17. *Substituted diazocines and their photochemical properties.*[49]

Extending the π system of the diazocine results in a redshifted nπ* absorbance band but lowers the PSS for *Z* → *E* switching drastically (**Figure 18**). Thermal half-lives can be tuned with larger aromatic systems exhibiting longer thermal half-lives. The authors reported reduced irradiation times for larger aromatic systems, indicating that the photoswitching quantum yield is increased. Without exact measurements, this remains a qualitative observation.

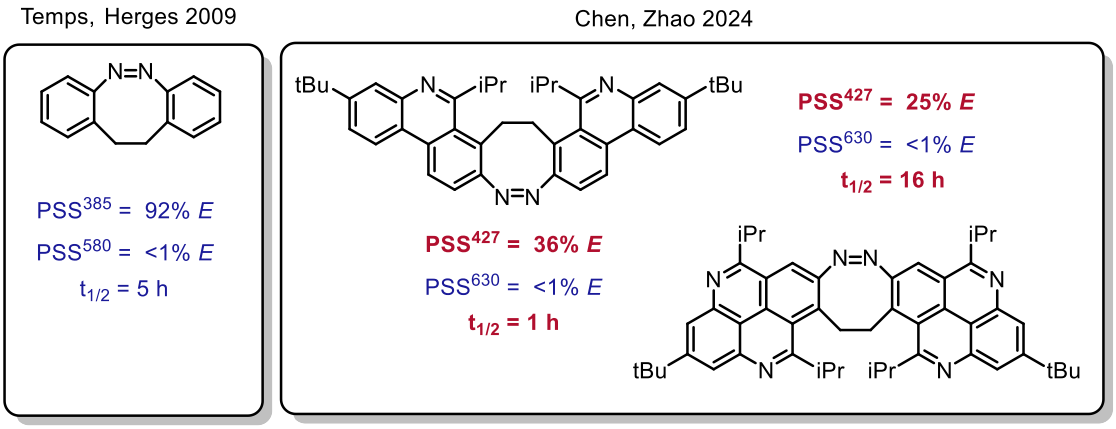

Figure 18. *Comparison of the photochemical properties of unsubstituted diazocine[46] with those of π-fused diazocines published by Chen and Zhao in 2024.[67]*

2.1.7 Synthesis of Diazocines

Excellent photostationary states, high quantum yields, and the inverted stability of the *E*- and *Z*-state make diazocines an ideal building block for photoresponsive system, the only drawback being their nontrivial synthesis. However, recent research efforts could alleviate this by establishing reliable procedures for the synthesis of diazocines. As previously mentioned, the most reliable synthetic strategy is the oxidative intramolecular Baeyer Mills reaction of ethylene bridged bisanilines, where a freshly titrated solution of the oxidant *m*CPBA is slowly added over twelve hours to the aniline via syringe pump. This controlled addition is necessary to avoid undesired oxidation pathways that will result in overoxidation to the azoxy compound, as can be seen in **Figure 19**. This method is reliable, but functional groups such as nitrogen bearing heterocycles are not compatible with this strategy as they will readily react with the oxidant to form N-oxides.[49]

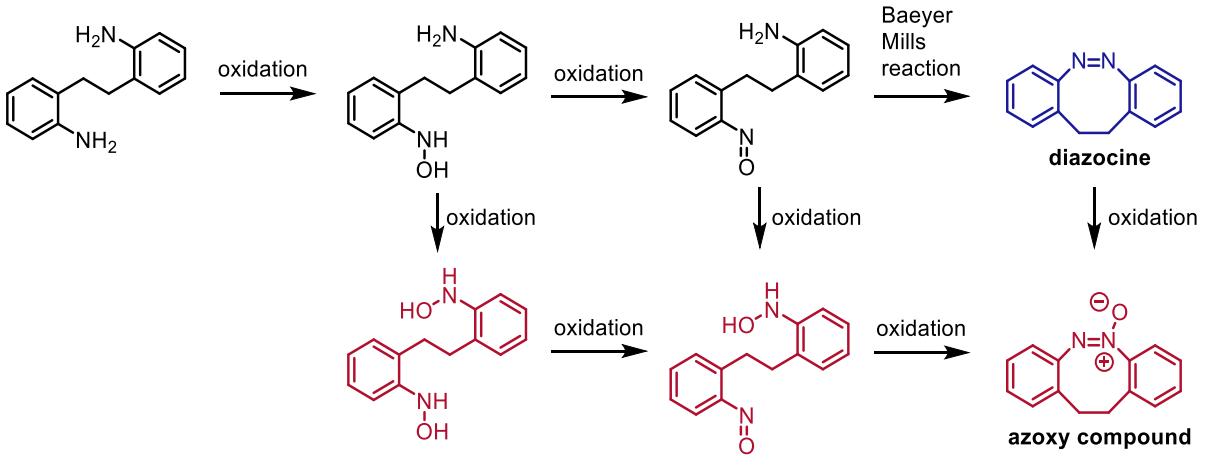

Figure 19. *Oxidative synthesis of diazocines requires two consecutive oxidation steps followed by an intramolecular Baeyer-Mills reaction. Unselective oxidation or overoxidation will result in the formation of azoxy-diazocine.[49]*

Despite other methods being available, the reductive synthesis of diazocines remains a viable strategy. Like the oxidative pathway, it is not trivial to stop the reaction at the right oxidation state. Most reductive processes yield either the azoxy compound or the hydrazide, requiring a secondary oxidation/reduction step to yield the desired diazocine (**Figure 20**). This strategy can tolerate many functional groups, provided they are not overly sensitive towards the reductive conditions. [44,46,68]

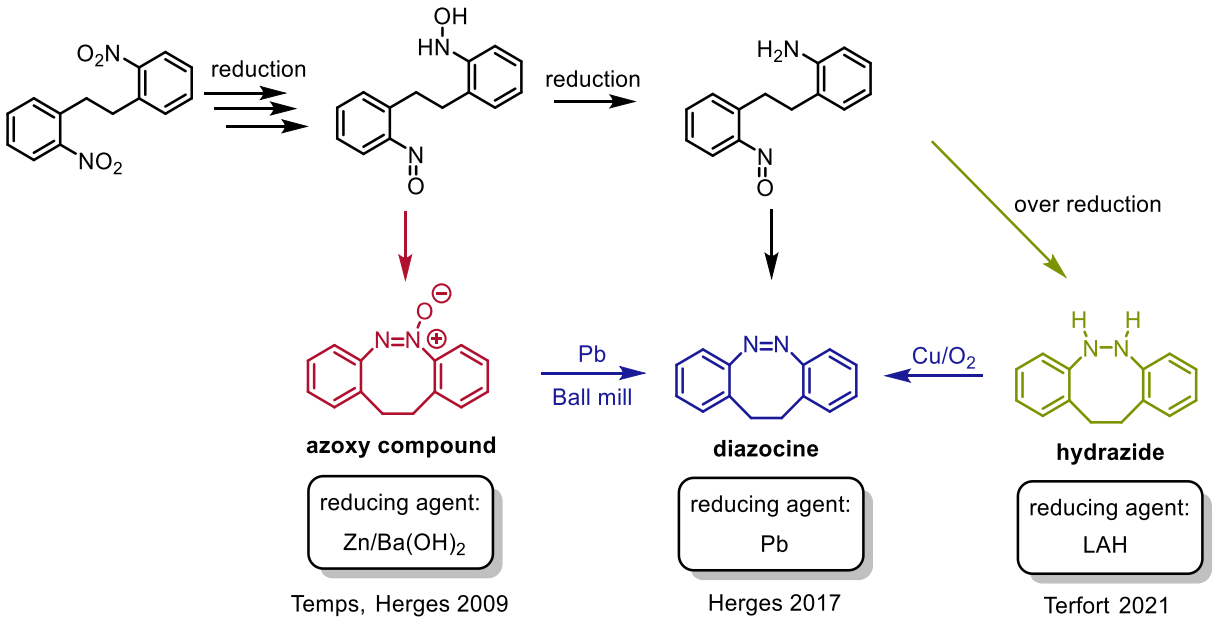

Figure 20. *Reductive synthesis of diazocines published by to Temps and Herges 2009,[46] by Herges in 2017,[68] and by Terfort in 2021.[44] The outcome of the reaction depends on the reducing agent used and a second oxidation/reduction step might be required to obtain the target compound.*

Disadvantages of the reductive pathway are generally lower yields than those of the oxidative pathway and asymmetrically substituted diazocines being much harder to synthesize. An overview of the common synthetic approaches for the dinitro and dianiline precursors can be seen in **Figure 21**. The asymmetric dinitro precursor needs a statistical benzylic coupling reaction that entails a challenging separation process.[53] The bis-aniline precursor of the oxidative strategy can be easily synthesized bearing asymmetric substitution patterns by utilizing a Sonogashira cross-coupling reaction followed by a palladium on charcoal catalyzed hydrogenation,[49] as long as the substituents are compatible with those reaction conditions. Despite all of this, the reductive strategy has advantages. Terfort and colleagues published an extraordinarily fast synthetic route that allows the synthesis of disubstituted diazocines in two steps with a combined reaction time of just 35 minutes, starting from cheap and readily available substituted nitrotoluenes.[44]

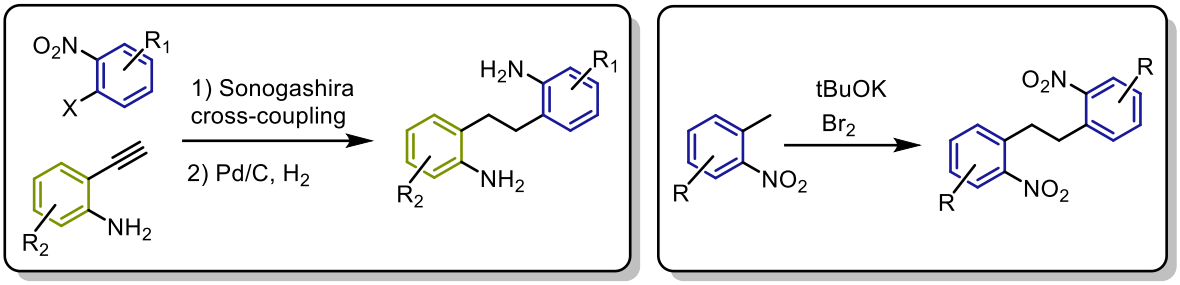

Figure 21. *Synthesis of dianiline[49] and dinitro[53] precursors for the synthesis of diacozines.*

Additional synthetic strategies have been published recently but have not yet found widespread adaption, an overview can be seen in **Figure 22**. Diazocines have been synthesized using a photocatalytically active cobalt cage,[69] electrochemically in the presence of carbon dioxide,[70] utilizing a cascade C-N coupling with BOC protected hydrazine,[63] and via nickel catalyzed nitrene dimerization.[71] While requiring exotic reagents or non-standard experimental setups, these methods offer unique advantages such as near-quantitative yields (electrochemical and photo redox approach) or avoiding strongly oxidizing or reducing conditions (C-N coupling and nitrene dimerization).

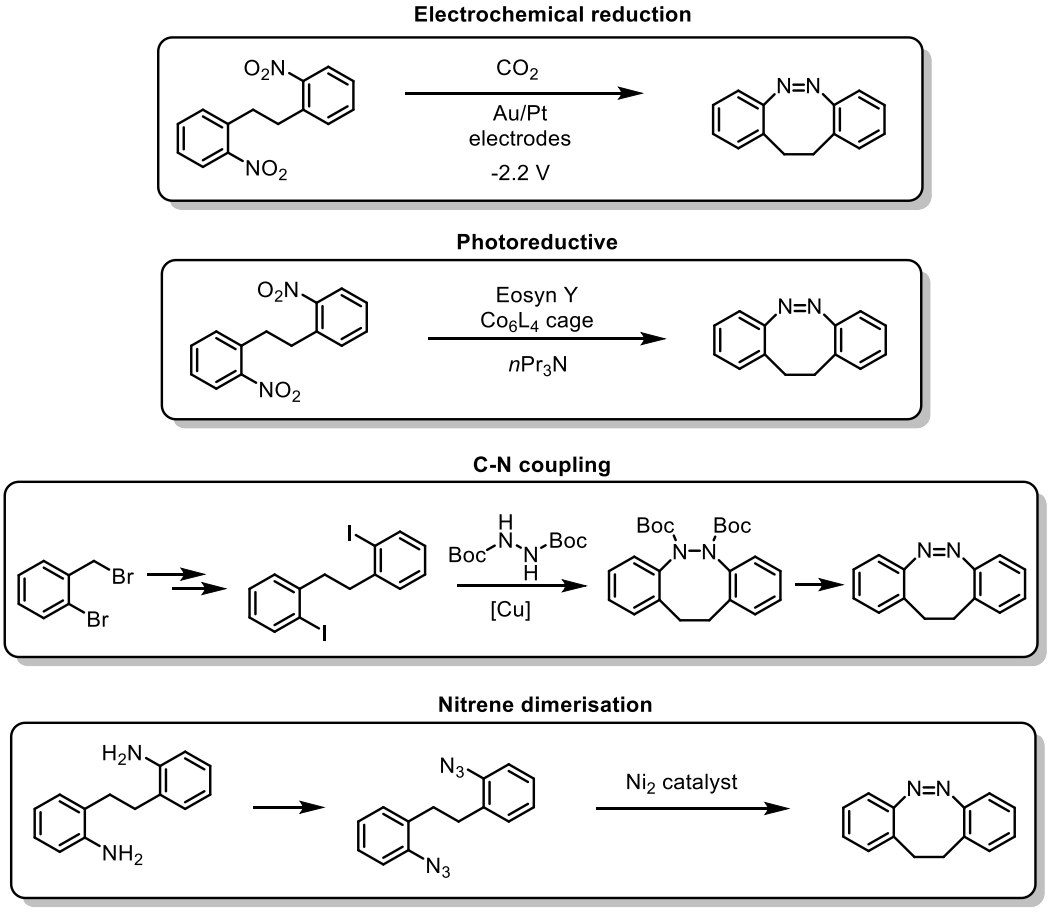

Figure 22. *Additional synthetic strategies for the synthesis of diazocines include electrochemical reduction,[70] photoreductive synthesis,[69] cascade C-N coupling,[63] and nitrene dimerization.[71]*

2.1.8 Other Photoswitches

Aside from azobenzene and its derivatives, commonly used photoswitches include dithienylethenes (DTE)[72] and stiff stilbenes[73] (**Figure 23**).

The thermodynamically favoured open state of DTE switches can undergo a photochemically induced cyclisation when exposed to UV-light, resulting in the metastable closed state. These closed states contain a much larger aromatic system, resulting in an intense absorbance in the visible range. Exciting this absorbance with light will revert the switch into its original open state. One disadvantage is the need for high energy UV-light that favours side reactions and decomposition of the switch. This problem can be partially overcome by the fluorine substitution of the cyclopropane backbone, as this stops homolytic C-H bond cleavage and consecutive oxidation. One interesting property is the large energy barrier for back isomerisation, resulting in long to very long thermal half-lives. Specific examples exhibit a thermal half-life of more than 100 000 years at room temperature, resulting in a truly bistable system without any thermal relaxation.[72]

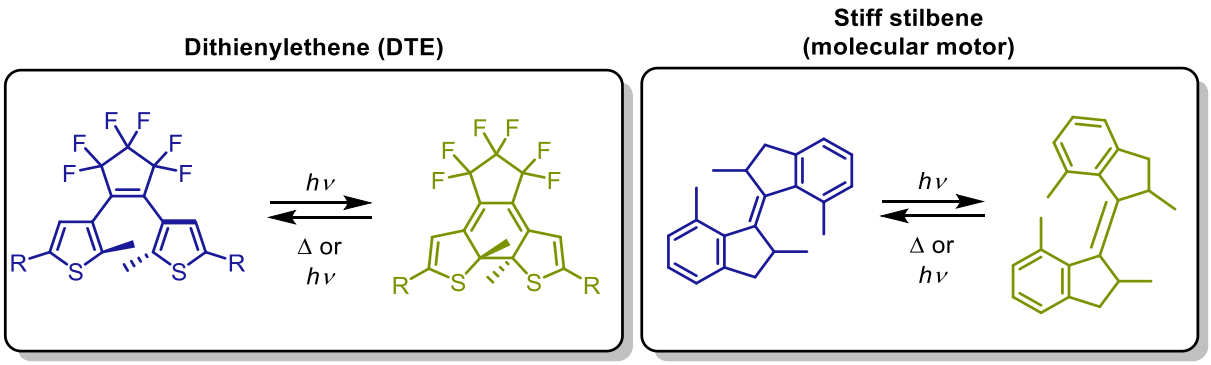

Figure 23. *Chemical structures of DTE[72] and stiff stilbene molecular switches.[73]*

Stiff stilbenes represent a class of fused ring derivatives of stilbene. Exposure to UV light induces photoisomerization to the *Z*-isomer with high quantum yields. Like DTE switches, stiff stilbenes both show a high thermal stability and typically need high energy UV light to switch that might enable in side reactions, but steric crowding around the alkene stops potential side reactions like oxidation that are commonly observed for regular stilbene. Stiff stilbenes have found particular success in their use as molecular motors, for example in the “four-wheeled” molecule published by Feringa and coworkers that uses four enantiopure stiff-stilbenes to move across a surface in a linear fashion, resembling the structure of a car chassis with four wheels.[74]

2.2 Self-Assembly

Living organisms rely on large and ordered supramolecular structures such as lipid bilayers, DNA helixes, and multiprotein complexes. The formation of these structures is enabled by self-assembly processes. Self-assembly describes the spontaneous formation of large and highly ordered structures from smaller building blocks through reversible aggregation reactions where building blocks interact in a complementary manner. These complementary interactions are non-covalent supramolecular interactions such as hydrogen bonding, van der Waals forces, and metal-ligand interactions. They are much weaker than covalent bonds and can be broken easily, but once the structure has formed the sum of many weak interactions is considerable and can result in extraordinarily stable structures.

A famous example are DNA strands, where a nucleobase will only interact with its complementary partner, but not any other molecule, resulting in the selective formation of the famous double helical structure (**Figure 24**, **A**). The interaction is governed by non-covalent hydrogen bonds that could be cleaved easily in a single base pair. However, the DNA helix consists of thousands to billions of base pairs and is therefore an extraordinarily stable structure. The self-assembly process is governed by the formation of supramolecular interactions that represent a net gain in energy, and the resulting ordered structure is dictated by the maximization of the absolute energy gain (**Figure 24**, **B**). The self-assembly process is a network of equilibrium reactions, with each step being reversible. This makes the process thermodynamically driven and enables error correction (**Figure 24**, **C**). Therefore, the shape of the resulting structure is encoded within the building blocks and their complementary interactions (**Figure 24**, **D**). One of the main advantages of self-assembly is that it can be used to construct large supramolecular structures from small building blocks in just one step, reducing the synthetic effort drastically.[75]

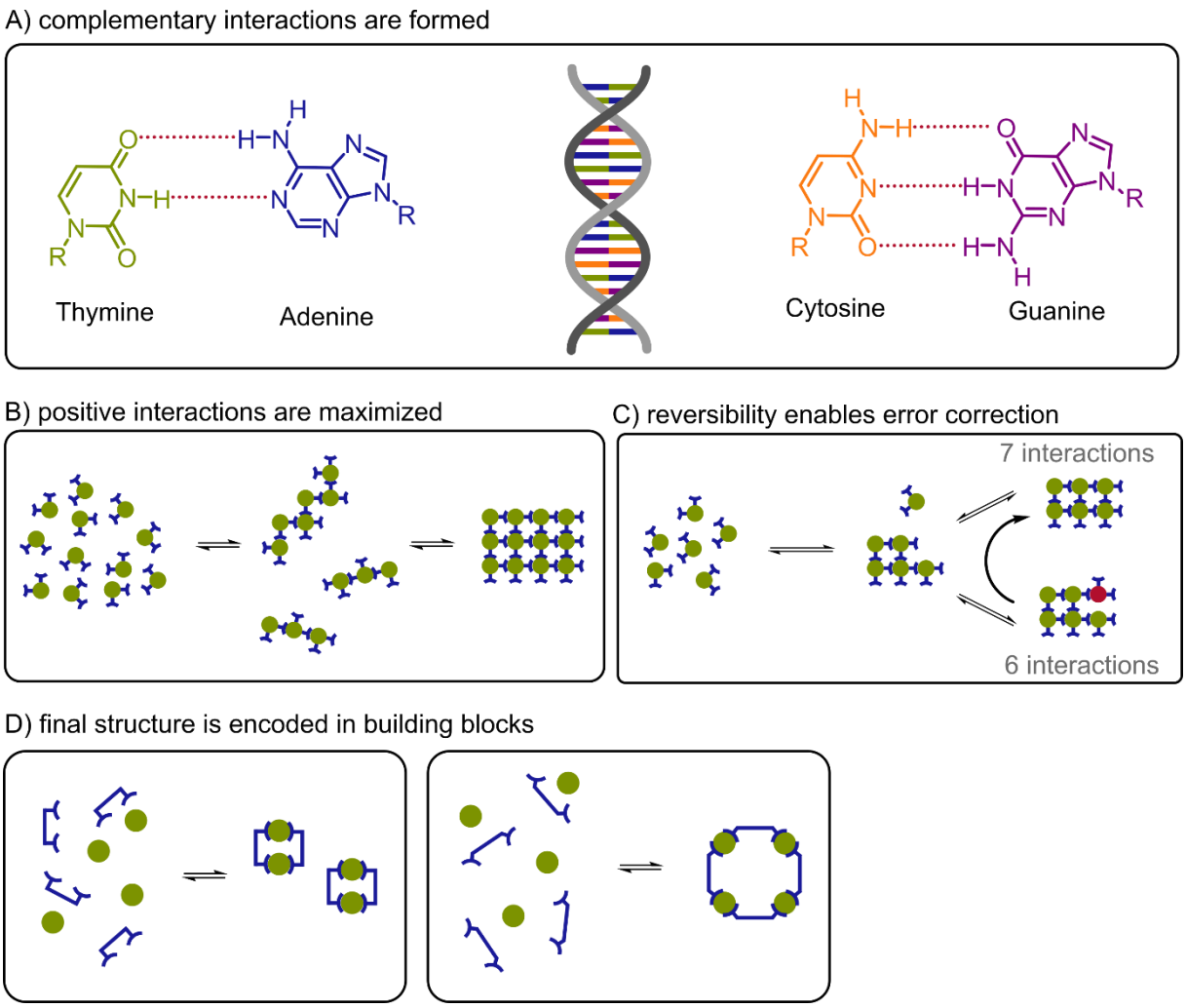

Figure 24. A) *The DNA double helix is formed and stabilized by complementary hydrogen bonding interactions between thymine/adenine and cytosine/guanine.* ***B)*** *During the self-assembly process, supramolecular bonds are formed with the structure trending towards the thermodynamic minimum.* ***C)*** *Bond formation is reversible, allowing for error correction and preferential formation of a structure where the positive interactions are maximized.* ***D)*** *The final structure of the assembly is governed by the shapes of the building blocks and the directionality of the supramolecular interactions.*

2.2.1 Energy Profiles of Self-Assembly

The “default” case when talking about self-assembly is equilibrium self-assembly (**Figure 25**, **A**). The building blocks represent a higher energy state on the energy hypersurface of the system while the final assembly resides in the global minimum. This is the preferred approach for synthetic chemists self-assembling large molecular structures, as the outcome is predictable. The building blocks that are part of the assembly are in equilibrium with those in solution, allowing for the dynamic exchange of building blocks, enabling error correction, and allowing the system to “find” its own minimum structure.[76]

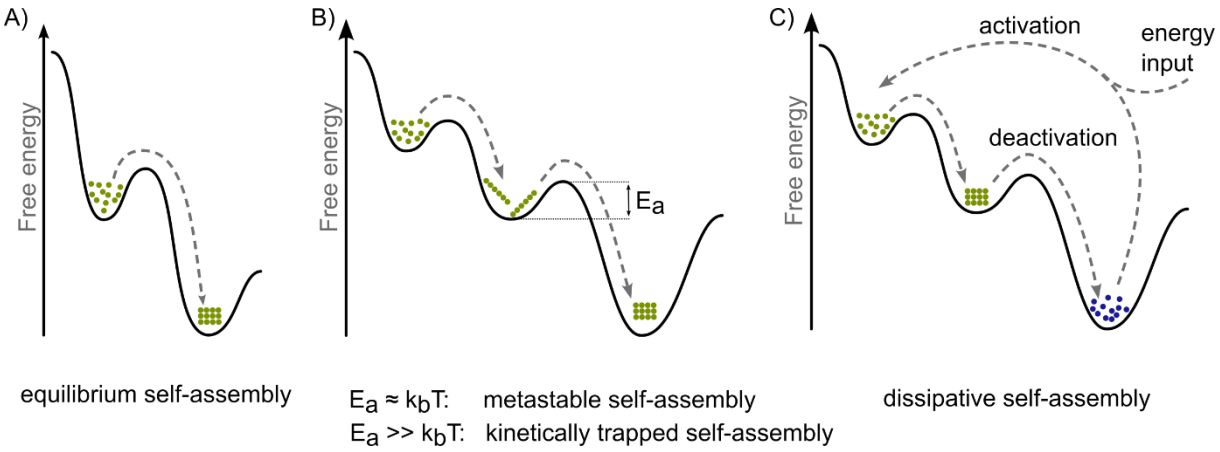

Figure 25. *Energy profiles of self-assembly processes.* ***A)*** *Equilibrium self-assembly describes the "default" case where building blocks self-assemble into a lower energy structure by forming supramolecular interactions.* ***B)*** *Intermediates or side products of the self-assembly process may have considerable activation barriers to form the thermodynamically most stable structure. If this activation barrier is large, the structure is kinetically trapped, if it is small the structure is metastable.* ***C)*** *Dissipative self-assembly requires an endothermic activation of the building block before it can participate in the self-assembly process. Deactivation of the building block can occur in the self-assembled structure and results in its disassembly.*[76]

Residing in the thermodynamic minimum limits properties of the assembly and especially biological self-assembled systems need to be adaptable, perform work, and dynamically assemble and disassemble at the right time and place. One such example can be found in the microtubules of eukaryotes during cell division, as they need to form, perform their task, and then disassemble again to allow normal functioning of the cell.[4] The mechanism by which this behavior is enabled is out-of-equilibrium self-assembly. The easiest way to attain out-of-equilibrium self-assembly is to consider an intermediate of the self-assembly process, where an activation energy barrier (E_a) needs to be overcome to transform the intermediate into the final product (**Figure 25**, **B**). If the energy barrier is lower than the thermal energy provided to the system (k_bT), this state is metastable and exhibits a short lifetime. If the activation barrier is greater than the thermal energy, the intermediate is kinetically trapped, and longer lifetimes are possible. This state might possess drastically different properties than the minimum structure and may transform into the minimum structure when appropriate external stimuli are applied. However, this transformation will be irreversible and once all metastable and kinetically trapped structures are gone, they cannot be reformed.[76]

This is where dissipative self-assembly adds an additional step to the self-assembly process, as it uses inactive building blocks that reside in the thermodynamic minimum and need to be activated under energy consumption to form the active building block, that will then self-assemble into the target structure (**Figure 25**, **C**).[76] The deactivation reaction is occurring spontaneously and as soon as the energy input stops and all activated building blocks are

used up, the structure disassembles into its inactive building blocks. This process allows microtubules to form and disassembly dynamically. The GDP-tubulin protein is the inactive building block, and ATP is used as an energy source to turn the GDP-tubulin into GTP-tubulin that can actively assemble into microtubules. If the energy input is sufficient and enough GTP-tubulin is available, the microtubules grow. In the microtubules, the hydrolysis of GTP-tubulin to GDP-tubulin occurs at an accelerated rate, starting from the bottom of the tubules and working its way to the top. As soon as the hydrolysis front reaches the top of the microtubule, it instantly disassembles and releases the inactive GDP-tubulin proteins.[4]

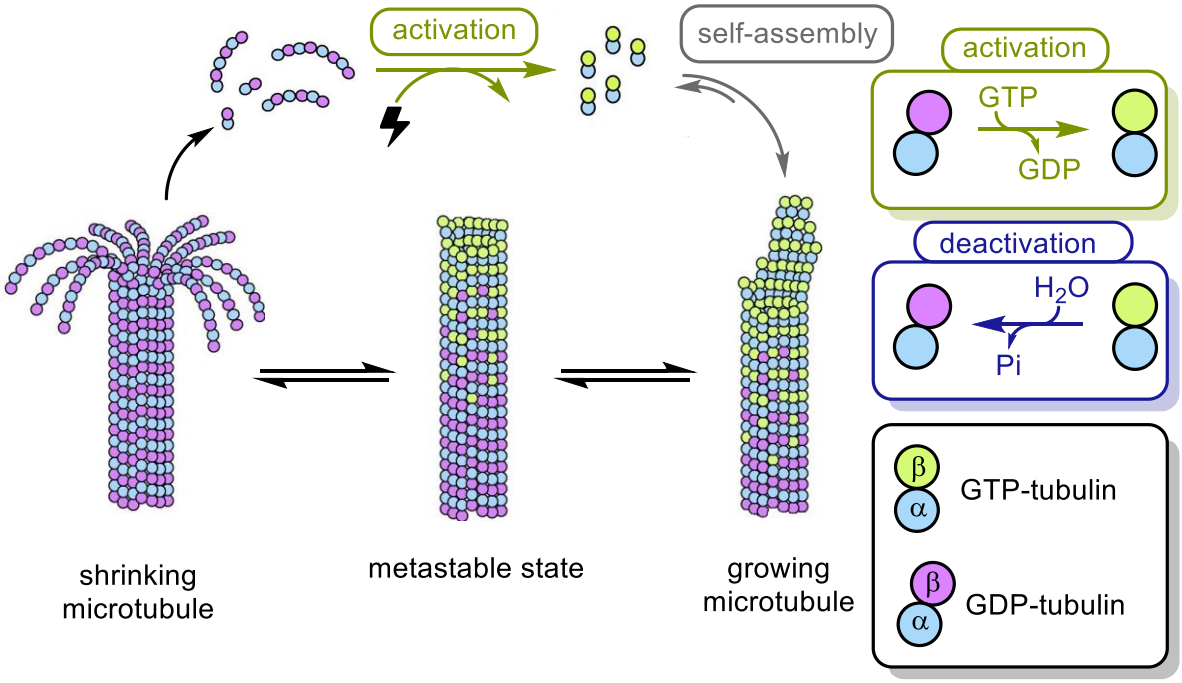

Figure 26. *Dissipative self-assembly of a microtubule from activated GTP-tubulin. The tubule grows as long as sufficient GTP-tubulin is available. Inside of the tubule the linear GTP-tubulin hydrolyzes to bent GDP-tubulin. If the hydrolysis is faster than tubule growth and the hydrolysis front reaches the top of the tubule, it rapidly disassembles.*[4]

2.2.2 Targeted Self-Assembly of Three-Dimensional Structures

To reliably synthesize large molecular structures, supramolecular chemists have developed methods to encode the cage geometry in its building blocks. The molecular library approach[77] by Stang and the molecular paneling approach[78] by Fujita rely on organic ligands with at least two coordination sites and transition metal cations that act as directing groups thanks to their known orbital geometries. Especially Pd(II) and Pt(II) have been successfully employed in this approach, as they reliably form square planar coordination geometries, effectively allowing for the arrangement of four ligands in 90° angles. The shape of free binding sites of both the ligand and the metal determines the geometry of the resulting structure. A table for two dimensional assemblies using two bidentate building blocks can be seen in **Figure 27**.

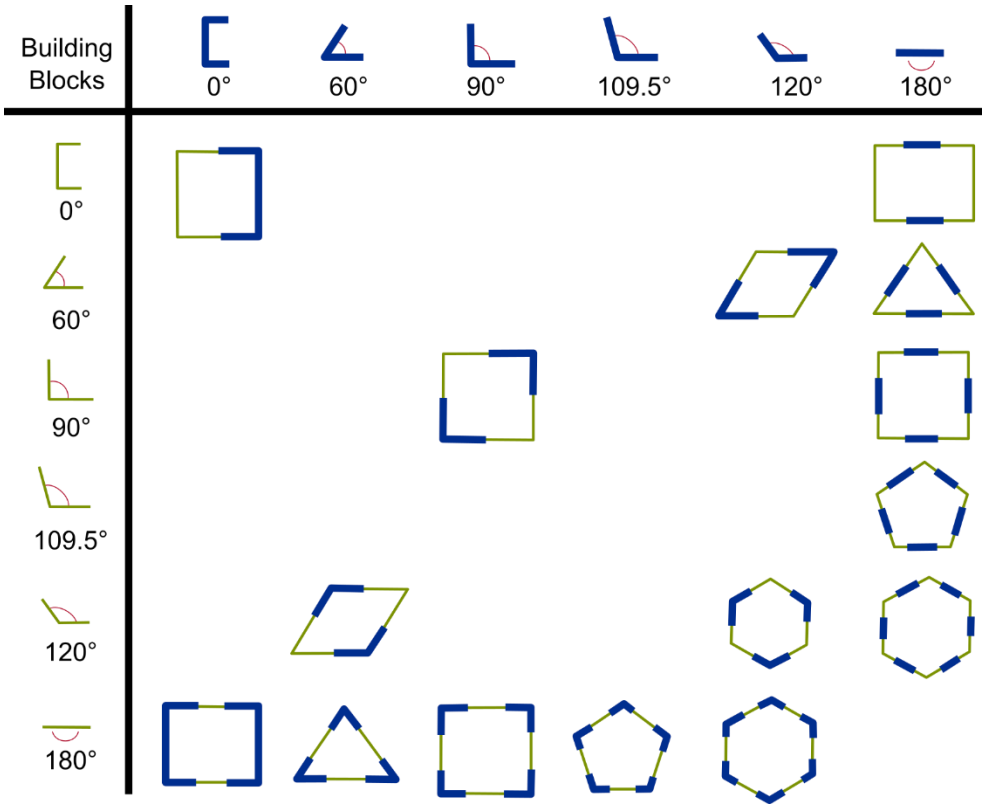

Figure 27. *Representation of two-dimensional structures derived from the molecular library approach.*[77]

For example, as can be seen in **Figure 28**, combining a bidentate ligand with parallel binding sites with *trans*-$PdCl_2$ results in the formation of a two-dimensional molecular square. However, when unprotected palladium is used, a Pd_2L_4 lantern shaped complex is formed. This approach enables the design and construction of two- and three-dimensional structures with both differing sizes and symmetries.[79]

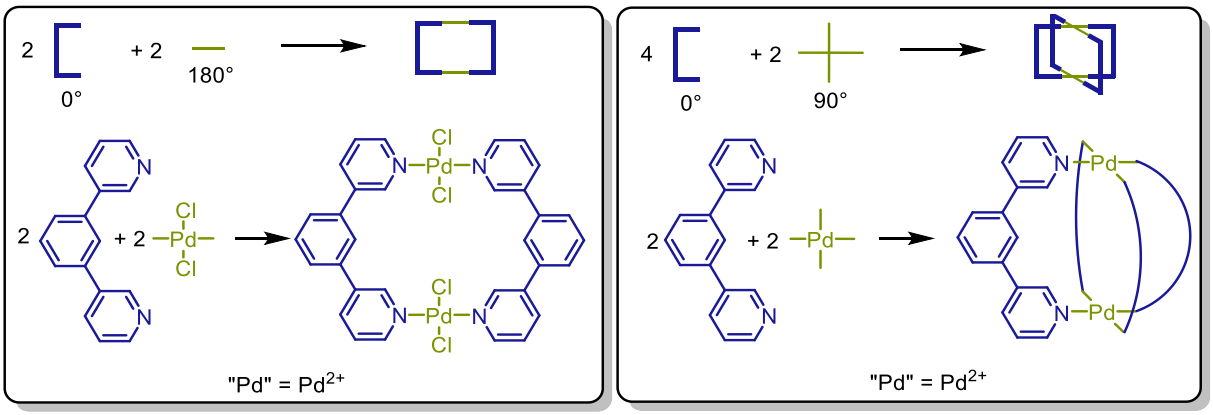

Figure 28. *Self-assembly of palladium complexes guided by the molecular library approach.*[79]

A second important approach for the rational design of large supramolecular structures is the symmetry interaction approach[80] by Raymond that describes how chelating ligands can be used in combination with tetrahedral or octahedral metal cations to predictably and reliably synthesize large supramolecular structures. It establishes the coordinate vector, the approach angle and the chelate plane as relevant descriptors of the coordination sphere of the metal ion to intricately discuss the incorporation of metal coordination geometries into Platonic and Archimedean solids (**Figure 29**). It has been successfully employed to design and synthesize face and edge capped tetrahedral[80–83] and cubic[84–86] metal-organic cages. For example, in 2010 Cashion and coworkers published a ligand with antiparallel coordinate vectors.[83] Upon addition of octahedral Fe(II) ions it readily self-assembles into a tetrahedral Fe4L6 cage.

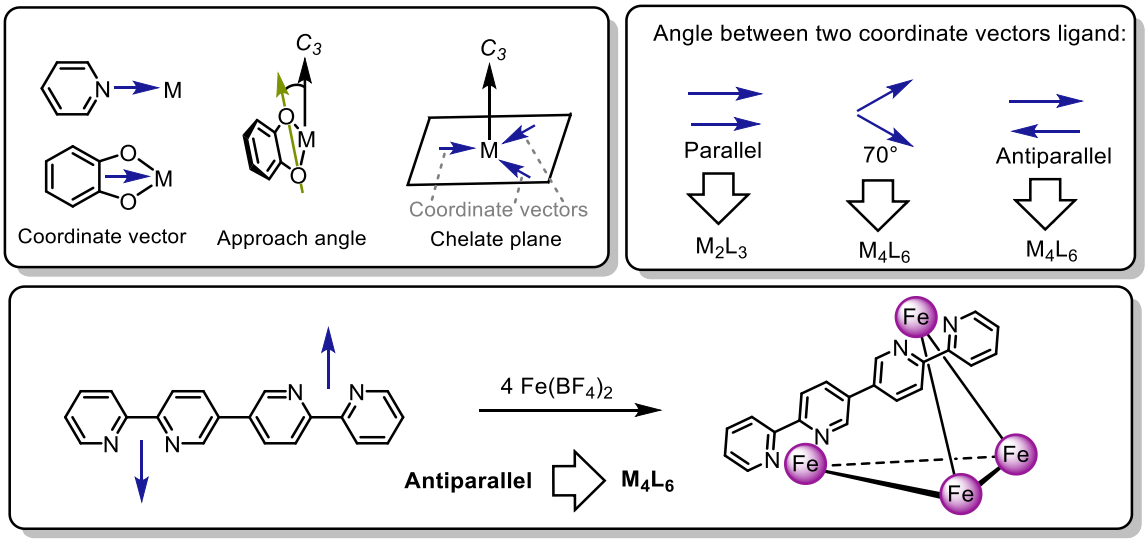

Figure 29. *Important concepts of the symmetry interaction approach by Raymond*[80] *and an example with coordinate vectors shown in the ligand.*

2.2.3 Subcomponent Self-Assembly

The synthesis of ligands with coordination motives in a specific orientation to each other can be time consuming and expensive, as it typically requires multi-step syntheses. This makes modifying an already established structure to incorporate a new functional group like a chromophore or photoswitch difficult, as the synthesis of the ligand must be restarted from scratch. One way to minimize the synthetic effort is the subcomponent self-assembly approach developed by Nitschke.[81] It combines dynamic covalent chemistry with the self-assembly step and subcomponents of the ligand are combined with the metal in a one-pot reaction. The two subcomponents undergo a dynamic (=reversible) bond formation, typically pyridine carboxaldehyde and aniline forming an imine bond in a condensation reaction. A complex equilibrium between the aldehyde, imine, and other species such as the aminal exists that is further complicated by metal coordination, as all parts of the ligand mixture can interact with the metal center. The metal cation mediates the formation of its own ligand through Lewis acidic activation of the carbonyl group, thereby accelerating the imine condensation. All reactions involved in cage formation are equilibrium reactions, thereby allowing for error correction. Heating the mixture for a prolonged time will result in efficient self-assembly of both ligand and complex since positive interactions are maximized in the cage structure. Metastable or kinetically trapped states might be formed initially (**Figure 25**), but heating provides the activation energy needed to convert them into the product. The maximum occupancy rule[87] and cooperativity effects[88,89] drive the reaction to the thermodynamic minimum, selectively forming the metal-organic cage.[90]

A famous example of subcomponent self-assembly is the formation of an M_4L_6 tetrahedron from six equivalents of a sulfonated benzidine, twelve equivalents of pyridine carboxaldehyde, and four equivalents of iron(II) sulfate (**Figure 30**).[91] Despite the ligand by itself being sensitive towards hydrolysis, the subcomponent self-assembly is carried out in water as a solvent. Due to cooperativity effects the cage represents a thermodynamically and kinetically stable structure that does not readily hydrolyze.

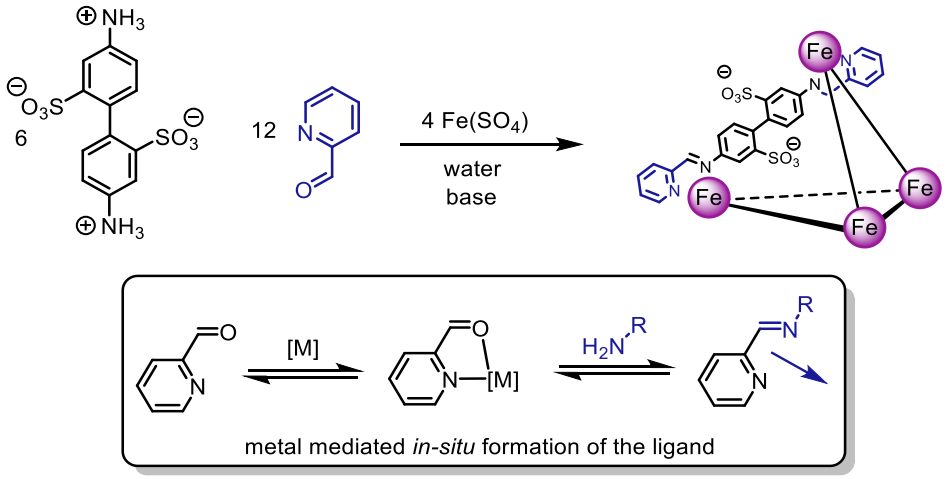

Figure 30. *Subcomponent self-assembly of a Fe_4L_6 tetrahedron.*[91]

2.2.4 Heteroleptic and Heterometallic Self-Assembled Metal-organic Cages

To mimic the sophisticated and highly asymmetric cavities of enzymes that enable their unparalleled selectivity, supramolecular chemists have turned to heteroleptic and heterometallic cages with reduced symmetry.[92] The step-up in sophistication is accompanied by an increasingly difficult synthesis and achieving non-statistical incorporation of the ligands is far from trivial. Even when only one simple structure (e.g. M_2L_4) is formed, six different homoleptic and heteroleptic cages might form simultaneously (**Figure 31**).

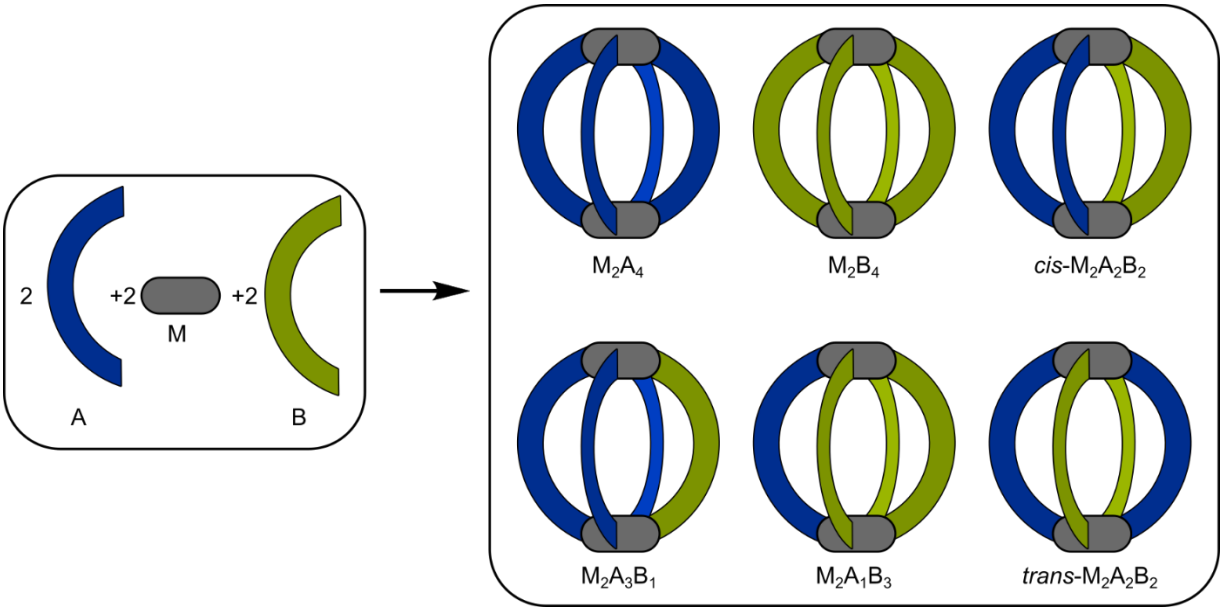

Figure 31. *Potential outcomes of the mixed self-assembly of two equivalents of a metal M, two equivalents of a ligand A, and two equivalents of a second ligand B.*[92]

Self-sorting of the ligands ideally results in the formation of a single species. However, this is far from trivial and supramolecular chemists have expanded the concepts of the molecular library, molecular paneling, and symmetry interaction approaches into strategies that can facilitate the formation of just a single desired species. These include (**Figure 32**):[92]

a) Coordination sphere engineering where steric bulk is incorporated close to the metal center.
b) Shape complementarity where two ligands that are distorted and prefer forming heteroleptic capsules are used.
c) The use of non-symmetric ligands that use driving forces such as charge separation to direct ligand orientation.
d) Backbone steric hindrance where bulky backbones direct the ligand into specific sites in the structure that allows them to maximize the distance to their neighbors.

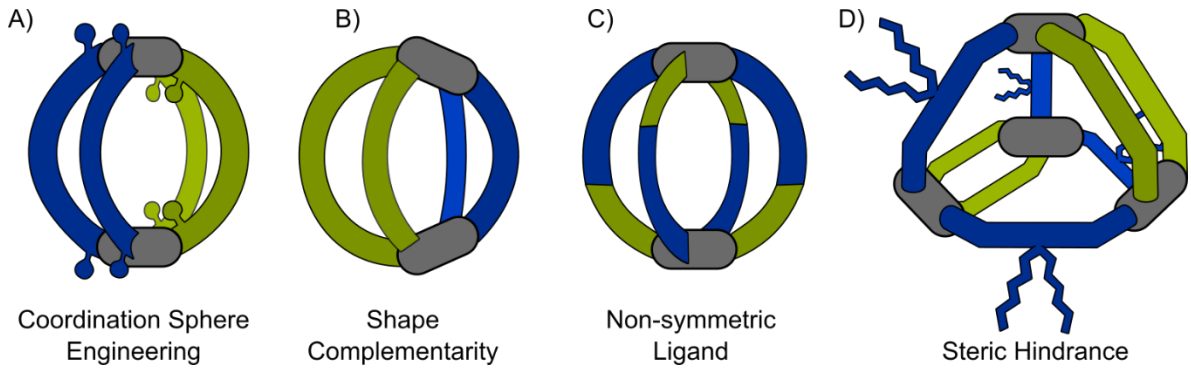

Figure 32. *Different strategies for the selective synthesis of heteroleptic capsules.*[92]

For example, using two different ligands where one has divergent coordinate vectors at an angle of 60°, and the other one has divergent coordinate vectors at an angle of 120° allows the selective formation of the *cis*-$Pd_2A_2B_2$ cage (**Figure 33**). Other heteroleptic cages such as *trans*-$Pd_2A_2B_2$, $Pd_2A_3B_1$, and $Pd_2A_1B_3$ or homoleptic cages Pd_2A_4 and Pd_2B_4 are not formed, making this an example of integrative self-sorting.[93]

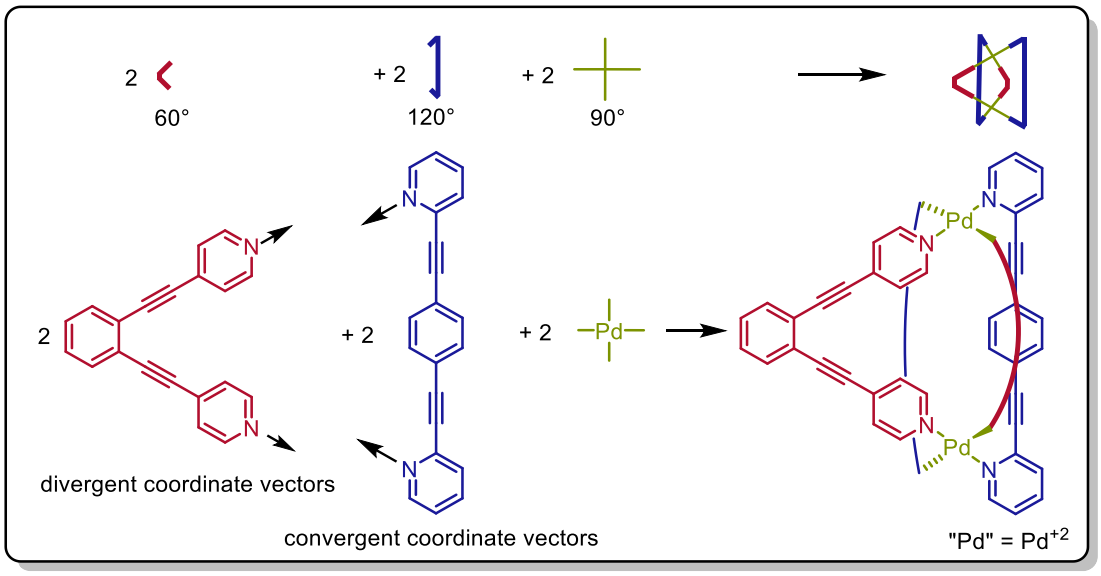

Figure 33. *Self-sorting of a self-assembled $Pd_2A_2B_2$ heteroleptic cage enabled by shape complementary ligands.*[93]

Careful combination of multiple ligands allowed the Clever group to synthesize a $Pd_2A_1B_1C_1D_1$ heteroleptic cage bearing four different ligands in a one pot self-assembly reaction (**Figure 34**). A mixture of shape complementarity and supramolecular interactions between the ligand strands result in the integratively self-sorted cage being the thermodynamically favored structure and therefore, the only product.[94]

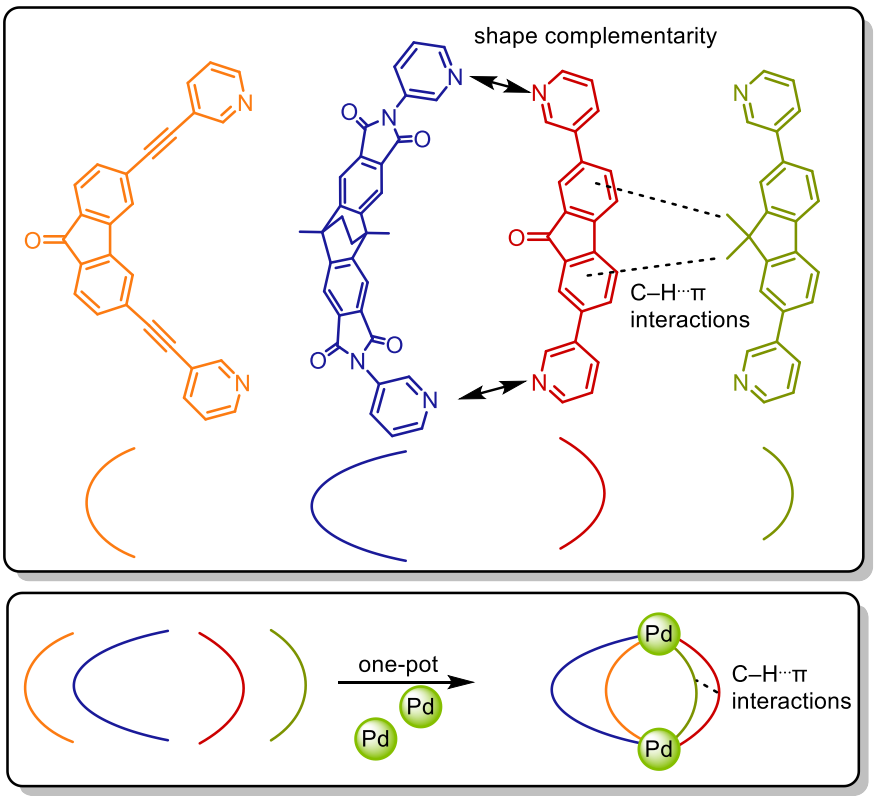

Figure 34. *Self-sorting in a self-assembled Pd_2ABCD heteroleptic cage.*[94]

Like heteroleptic structures where multiple different ligands are used, heterometallic structures using different metals represent an increase in the fidelity of metal-organic cages. Just as was the case for heteroleptic cages, this increase in fidelity coincides with increased synthetic effort in ensuring the metals are not just statistically distributed throughout the structure (**Figure 35**). This is especially likely when using metals that prefer the same coordination environment, like square planar Pd(II)/Pt(II) or octahedral Co(II)/Fe(II).

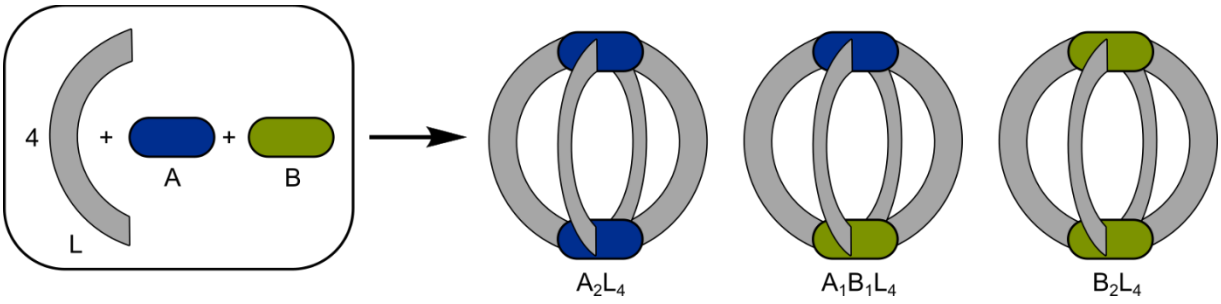

Figure 35. *Potential outcomes of the mixed self-assembly of 1 equivalent of A, one equivalent of B and four equivalents of L.*[92]

Sometimes, stepwise addition of the metals can result in the formation of the desired complex. A commonly employed strategy is the complex-as-a-ligand approach.[95] With this two-step approach, kinetically inert metal-ligand complexes are formed from one metal in the first step. These are used as a ligand in the second complexation step where the kinetically inert precomplex can be treated like a covalent molecule and the design strategies presented earlier (molecular library, symmetry interaction) may be applied. Candidates for the formation of such inert metal-ligand complexes are metals with slow ligand exchange kinetics such as Pt(II) or highly chelating ligands with up to six coordination sites. Additionally, the reaction conditions such as temperature or pH may be altered in the second step to reduce the kinetic lability of the first metal complex.[95]

Crowley and coworkers synthesized a heterobimetallic $PdPtL_4$ lantern shaped cage using sub-component self-assembly and the complex-as-a-ligand approach (**Figure 36**).[96] In the first step, they used pyridine carboxaldehyde and Pt(II) to synthesize a Pt(II) complex bearing four aldehyde functional groups. Ligand exchange on Pt(II) is slow since Pt(II)-N bonds are strong and associative ligand exchange mechanisms are disfavored. Therefore, the reaction needs to be carried out at 60 °C. In the second step, they added four equivalents of a hydrazone bearing pyridyl ligand and one equivalent of Pd(II). Since Pd(II) undergoes ligand exchange on a much faster timescale, this reaction can be carried out at 25 °C where the Pt(II) moiety is kinetically inert. The hydrazone and aldehyde subcomponents react in an imine condensation, forming the final ligand with Pd(II) ions binding to the four remaining pyridines.

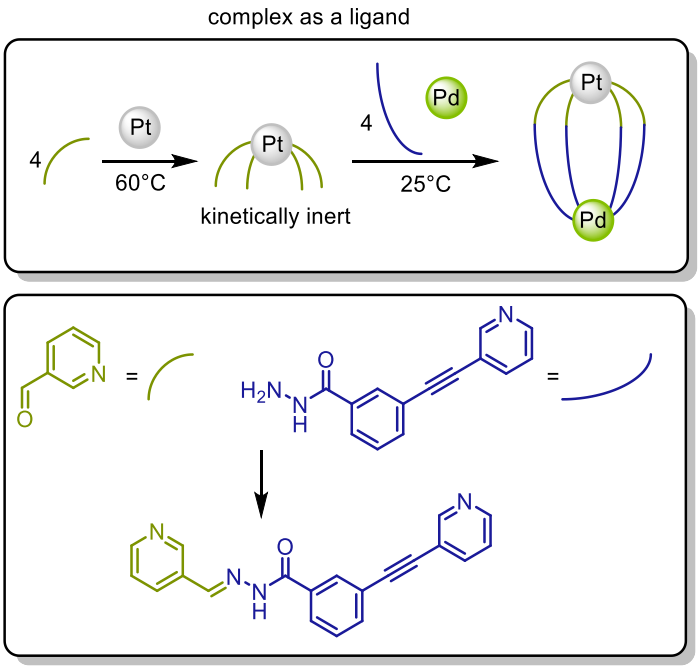

Figure 36. *Two step synthesis of a heteroleptic and heterometallic cage using the complex-as-a-ligand approach.*[96]

Alternatively, orthogonal binding sites enable the one-pot formation of heterometallic architectures (**Figure 37**). Careful design of the system allows the construction of large and high-fidelity structures in just one step, from simple building blocks. Lützen and coworkers synthesized a $Fe_2L_2Pd_3L^*_3$ heterometallic bipyramidal cage in a one-pot subcomponent self-assembly reaction utilizing three equivalents of *cis* protected Pd(II), two equivalents of a triamine, six equivalents of an organic pre-ligand and two equivalents of Fe(II).[97] Three pre-ligands react with the triamine, forming a single six-fold coordinating ligand. This structure contains an octahedral binding site that is preferentially occupied by the Fe(II) ions, while three pyridines point outwards, away from the Fe(II) ion. These pyridines coordinate to the *cis* protected palladium units which results in the formation of a bipyramid where two tripodal Fe(II) corners are dimerized by three bridging *cis* protected Pd(II) moieties. The final structure contains two octahedral binding sites in the tips of the bipyramid that are occupied by the Fe(II) ions while three square planar binding sites in the corners of the base of the bipyramid are occupied by the Pd(II) ions. This structure is an interesting example of how high-fidelity metal-organic structures can be self-assembled in just a single step.

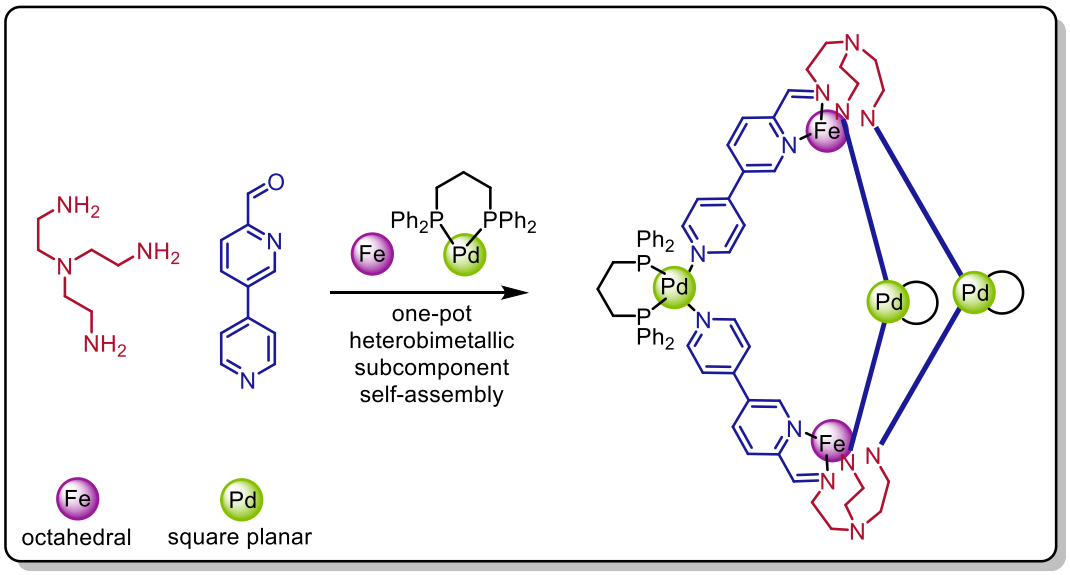

Figure 37. *One-pot sub-component self-assembly of a heterobimetallic bipyramidal cage.*[97]

2.3 Photoresponsive Self-Assembled Metal Complexes

2.3.1 Designing Photoresponsive Self-Assembled Complexes

The first prerequisite for the design of photoresponsive cages is an excellent understanding of design principles such as the symmetry interaction and molecular library approaches as well as sub-component self-assembly and self-sorting. These concepts were discussed in detail in Chapter **2.2**. Without the comprehensive literature that exists on these systems, the design of photoresponsive cages would be impossible.

Apart from the supramolecular design concepts the photoswitch must be well understood. This includes optimal wavelengths for switching, photostationary states, thermal half-lives, and molecular changes during the switching process (especially geometry). These properties were discussed extensively in Chapter **2.1**.

"Static" cages, that have been previously reported, are an excellent starting point for the design of photoresponsive cages. Inserting a photoswitch into their structure without disturbing the general geometry of the binding sites too much will generally allow for the synthesis of photoswitch-containing structures. Especially structures formed using sub-component self-assembly are ideal, as using different subcomponents is straightforward, drastically minimizing synthetic effort. One example where this was done was published in 2021 by the group of Stefankiewicz who replaced the 4,4-diamino-biphenyl subcomponent with 4,4-diamino-azobenzene in the subcomponent self-assembly of an M_4L_6 tetrahedron (**Figure 38**).[98] The parent structure was published by the Nitschke group and discussed earlier (**Figure 30**).[91]

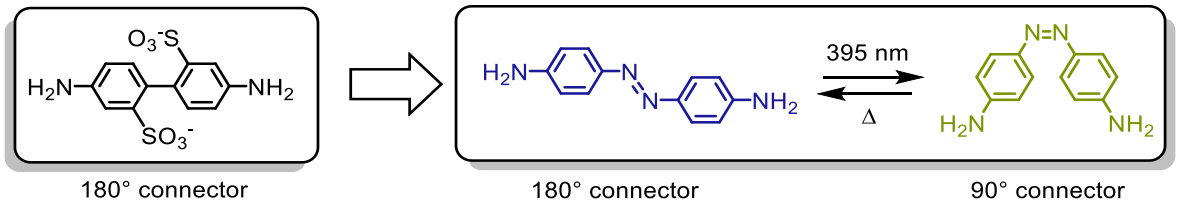

Figure 38. *Replacing subcomponents of literature known sub-component self-assembled structures with isostructural photoswitchable building blocks allows for the synthesis of photo switch containing cages with minimal synthetic effort. The 4,4-diamino-biphenyl subcomponent was used in the synthesis of an M4L6 tetrahedron.[91] The Stefankiewicz group replaced it with an 4,4-diamino-azobenzene, that can switch between an isostructural linear E-state and a bent Z-state.[98]*

The geometry of the *E*-4,4-diamino-azobenzene strongly resembles that of the parent diamino building block, both could be understood as bidentate 180° linkers in the context of the molecular library approach. Photoswitching of the stable *E*-azobenzene will result in the metastable *Z*-azobenzene, where the two amines are now connected at a 90° angle. This drastic change can be expected to lead to the formation of a different structure.

To get a better understanding of what type of structure might be formed we can look at the coordinate vectors of the self-assembled ligand in both the *E*- and *Z*-state and compare them to non-switchable ligands, that exhibit a similar relative orientation of the coordinate vectors (**Figure 39**).

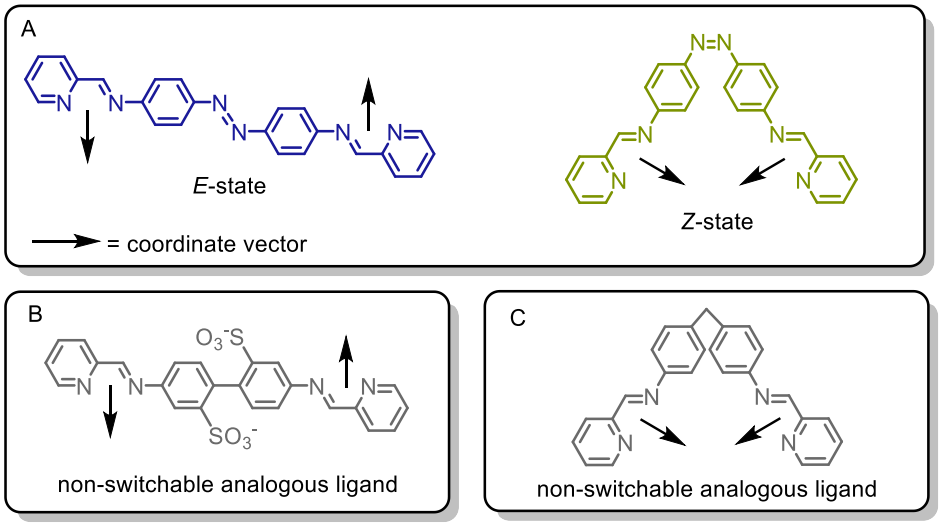

Figure 39. *Comparison of the coordinate vectors of the E and Z-state of the azobenzene based ligand (**A**) and isostructural non-switchable ligands for the E-state (**B**)[91] and the Z-state (**C**).[99]*

The *E*-state of the azobenzene ligand is directly analogous to a ligand published by the Nitschke group in 2008 and exhibits the same antiparallel arrangement of the coordinate vectors (**Figure 39 B**).[91] It is therefore expected, that the sub-component self-assembly of the azobenzene derived sub-component will also result in the formation of an M_4L_6 tetrahedron (**Figure 40**, **A** and **B**). The bent *Z*-azobenzene ligand with its strongly convergent coordinate vectors is analogous to a 4,4-diaminodiphenylmethane based ligand (**Figure 39**, **C**). It was published by Ichikawa in 1997 and readily self-assembles into a triply stranded M_2L_3 helicate (**Figure 40**, **D**).[99] Ab-into geometry optimizations are an excellent way to estimate if the synthesis of these cages can be successful. Especially low-cost semi-empirical methods like Grimmes GFN2-xTB[100] that produce good geometries can help in quickly screening possible synthetic targets.[101] Indeed, quantum chemical simulations predict a reasonable geometry for an M_2L_3 helicate of the *Z*-azobenzene ligand (**Figure 40**, **C**). However, this consideration remains purely theoretical as no photoresponsive behavior was observed for the *E*-azobenzene M_4L_6 tetrahedron. While the ligand can readily undergo photoisomerization, it cannot do so after the addition of the metal salt, as this results in the formation of a rigid structure where the azobenzenes are locked into their *E* configuration. For them to undergo *E*- to *Z*-isomerization the coordinative bonds would need to be broken. This represents a large energy barrier that cannot be overcome with the available energy. Therefore, photoswitching

is completely inhibited and the M_4L_6 tetrahedron does not exhibit any photoresponsive behavior (**Figure 41**).[98]

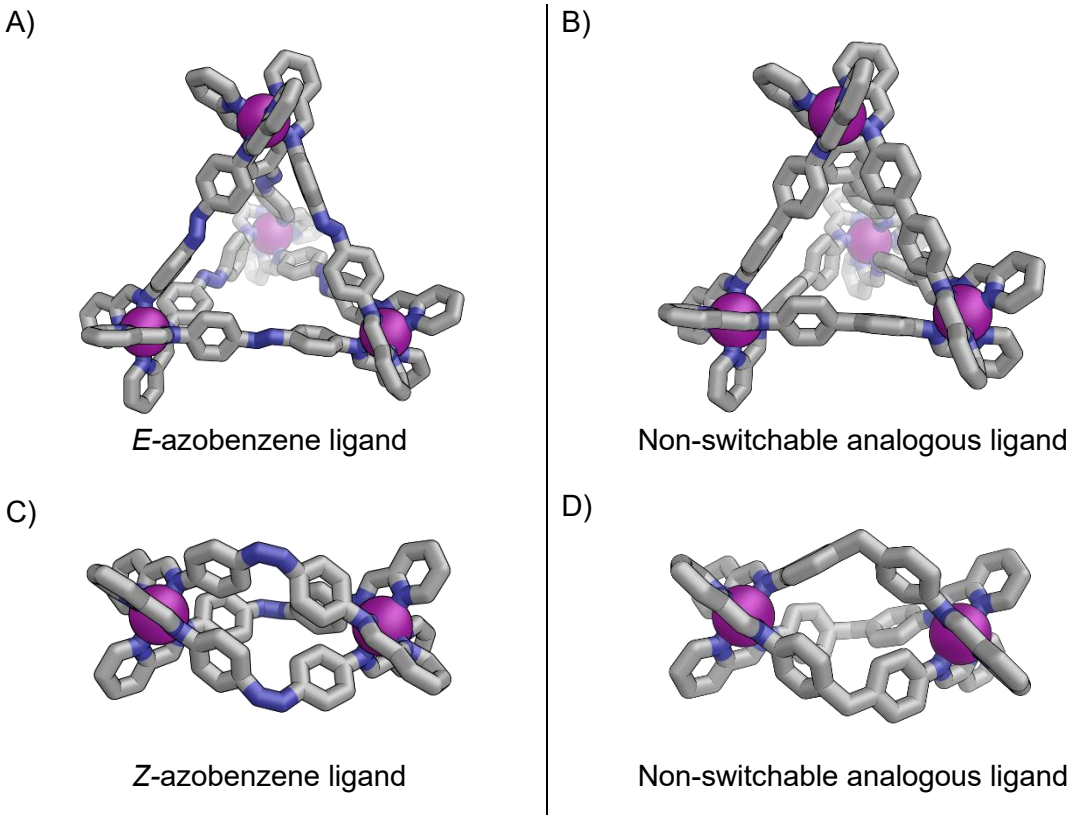

Figure 40. *Three dimensional structures of azobenzene based assemblies and comparison to the structures formed by analogous ligands. All geometries were optimized on GFN2-xTB level using M=Fe^{2+}.* ***A)*** *In its E-state, the azobenzene derived ligand forms a M_4L_6 tetrahedron. This structure is experimentally confirmed and is the same structure that was formed by an analogous non-switchable ligand (**B** sulfonate groups omitted for clarity).[91]* ***C)*** *In its Z-state, the azobenzene ligand could hypothetically form an M_2L_3 helicate.* ***D)*** *An analogous non-switchable ligand that exhibits similar coordinate vectors was experimentally confirmed to form an M_2L_3 helicate.[99]*

As can be seen from this example, incorporating photoswitches as structural building blocks into discrete self-assembled structures will not necessarily yield photoresponsive structures. The synthesis of metal-organic cages that can undergo reversible photoisomerization is far from trivial. This is evidenced by the low number and recency of published examples where these structures can undergo reversible photoisomerization.[102] Challenges include upholding reliable photoswitching after incorporation into the structure and correctly predicting the geometry of both states so that the cage design principles outlined in Chapter **2.2.2** may be applied. One way around these problems can be the incorporation of switches in the interior[103] or exterior[104,105] of the structure, but this may also reduce the magnitude of the changes to the structure during switching. Successful incorporation of molecular photoswitches into a discrete self-assembled metal-organic cage without hampering photoswitching has only been achieved

for dithienylethene[72] (DTE) by the Clever[106] group in 2012, for crowded alkenes[73] by the Feringa group in 2019,[107] and recently for azobenzene derived switches by the groups of Beves[108] and Clever[61] , both in 2022. Since then, more examples using azobenzene and its derivatives have been published.[10,109–111]

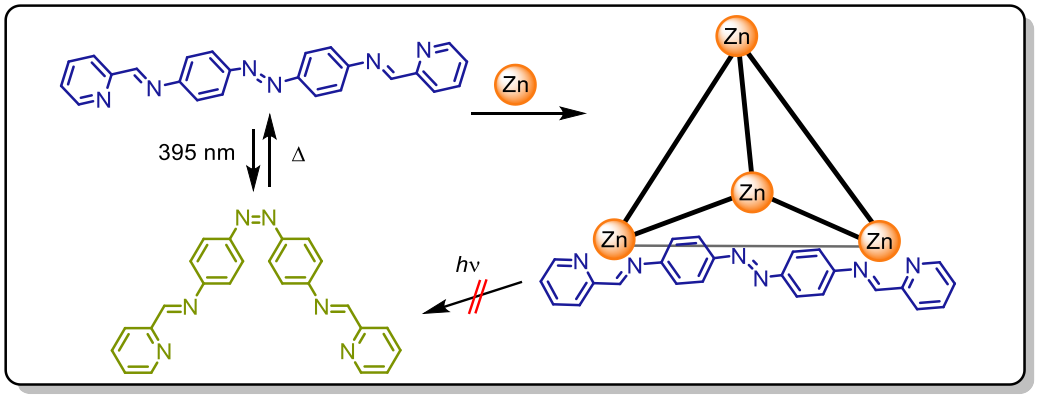

Figure 41. *The azobenzene ligand can be photoswitched if no metal is present, but as soon as the M_4L_6 tetrahedron is formed, no photoswitching can be observed.*[112]

2.3.2 Considerations for Photoresponsive Building Blocks

To showcase how easily photoswitching properties of azobenzenes may be hampered by the incorporation into self-assembled structures, two well understood examples from literature will be discussed here.

In 2021 the group of Bogliotti published a Ruthenium(II) complex with a pyridine-azobenzene ligand,[113] where the azo-nitrogen can directly bind to the metal center (**Figure 42**, **A**). Switching the ligand into its metastable *Z*-isomer prior to complexation affords the *Z*-ligand complex, where the N=N double bond is part of a seven-membered metallacycle. This will switch into the *E*-state when exposed to visible light, with the ruthenium now binding to one of the azobenzene nitrogens and one of the pyridines being unmasked.[114] This switching process correlates with a large gain in Gibbs free energy (approx. 90 kJ/mol) due to the elimination of ring strain. Photochemical *E* → *Z*-isomerization is not possible, as overcoming the strain and the need to cleave and reform a Ru-N bond results in no accessible pathways for the *E* → *Z* conversion on the energy hypersurface of the S_1 state, despite quantum chemical calculations showing that the $S_1n\pi^*$ transition needed for the switching process (see Chapter **2.1.2**) is accessible for the *E*-complex.[113]

In a second example from 2015, the groups of Schalley and Hecht published a dicationic azobenzene that forms a pseudo[2]rotaxane with a bridged divalent crown ether receptor (**Figure 42**, **B**).[112] The azobenzene can freely photoswitch if the receptor is not present. The

distance between the two binding sites in the receptor results in a high binding affinity for *E*-azobenzene. This strong binding affinity completely stops *E* → *Z* isomerization, as the switching process would need to involve the dissociation of one of the binding sites, as the *Z*-azobenzene derivative has a bent geometry that cannot interact with both receptors at once. Thus, despite the S_1 state being accessible through the nπ* transition, no photoswitching is observed as the energy barrier on the energy hypersurface is too large.

This indicates that incorporation into rigid structures will usually not disturb the general accessibility of the switched state but instead impose a large barrier on the isomerization pathway and that a certain degree of flexibility is required for successful and reversible switching. It must be kept in mind that the design principles for metal-organic cages assume stiff and inflexible ligands and that balancing these requirements is crucial.

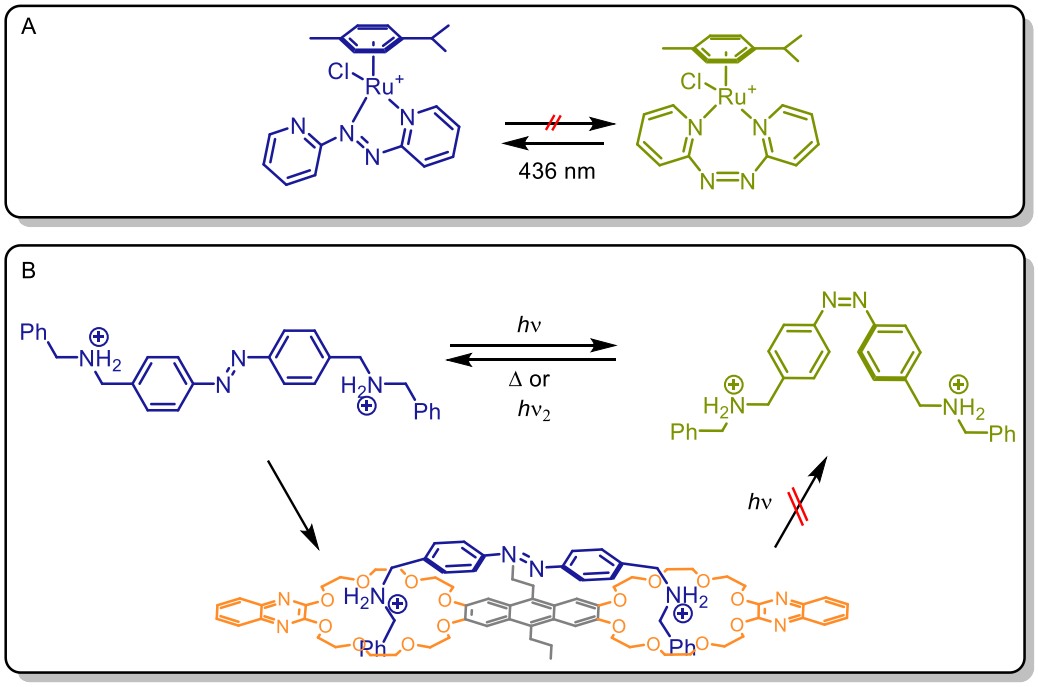

Figure 42. A) *Photoswitching of azobenzene can be inhibited by sufficiently large energy barriers on the isomerization pathway. Ruthenium(II) complex with a pyridine-azobenzene ligand,[113] where the azo-nitrogen directly binds to the metal center. The complex undergoes a switch from the Z-isomer to the E-state when exposed to visible light. Photochemical E → Z isomerization is not possible due to the strain and the need to cleave and reform a Ru-N bond.* ***B)*** *Dicationic azobenzene forming a pseudorotaxane with a bridged divalent crown ether receptor.[112] The azobenzene can freely photoswitch if the receptor is not present. The receptor binds to E-azobenzene, completely stopping E → Z isomerization due to the need to dissociate one of the binding sites. Despite the* S^1 *state being accessible in both examples through the nπ* transition, no photoswitching is observed due to the large energy barrier on the energy hypersurface*

2.3.3 DTE Based Capsule

The first example of a discrete self-assembled metal-organic cage incorporating photo switches as structural building blocks that could be reversibly switched between two different states was published in 2013 by the Clever group (**Figure 43**).[106]

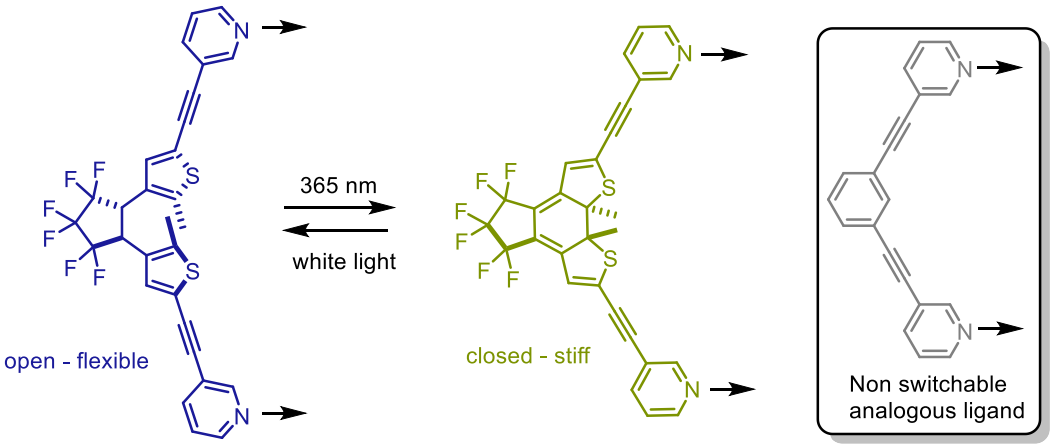

Figure 43. *Open and closed states of a photo switchable DTE based ligand.[106] Both states exhibit parallel coordinate vectors and can be compared to a non-switchable building block (grey, right) that was found to form a Pd_2L_4 lantern.[115] It is therefore no surprise, that both the open and closed state will also form Pd_2L_4 lantern shaped complexes.*

They synthesized a DTE based ligand, that self-assembles into a Pd_2L_4 lantern shaped complex in the presence of Pd^{2+} ions. This cage can reversibly switch between a flexible open-ring cage and a rigid closed-ring cage upon irradiation with UV or white light (**Figure 44**).

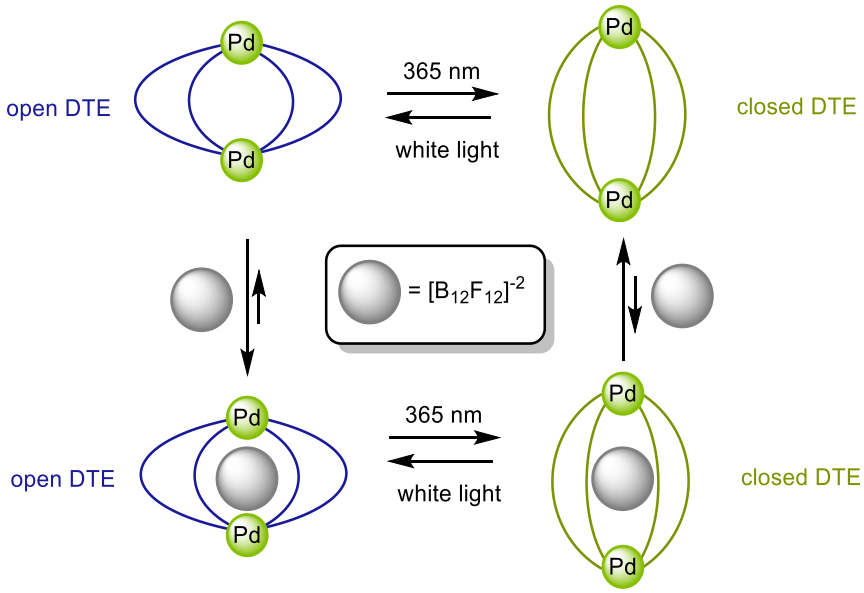

Figure 44. *Lantern shaped Pd_2L_4 capsule based on DTE photoswitches will undergo reversible photoisomerization from the thermodynamically more stable open form (blue, top left) when exposed to UV-light (λ = 365 nm) to yield the less flexible closed form of the ligand (green, top right). These two structures exhibit different binding affinities to a $B_{12}F_{12}^{2-}$ guest.*

The closed form exhibits a remarkably similar binding geometry to a non-switchable ligand, that is well known to form Pd_2L_4 lantern shaped cages.[115] This similarity was potentially used as an inspiration during the design of the photoswitchable ligand to ensure reliable self-assembly of a metal-organic cage. The flexible open form of the ligand seems to exhibit slightly convergent coordinate vectors at first glance, but its flexibility allows the formation of Pd_2L_4 cages with a helical arrangement of the ligands and an offset between the two metal centers.[116] The ability to switch between the open and closed forms allows for dynamic control over the encapsulation of $B_{12}F_{12}^{2-}$ guest molecules, as there is a significant difference in guest binding strength between the two forms, with the flexible form showing a much stronger affinity for the guest molecule. The encapsulation process is found to be entropy-driven and endothermic, governed by the release of ordered solvent from the interior of the cage.[106]

2.3.4 Azobenzene Based Metal-Organic Cages

The first publication on azobenzene derived photoresponsive metal-organic cages that can be switched using visible light was published by the Beves group in 2022 (**Figure 45**).[108]

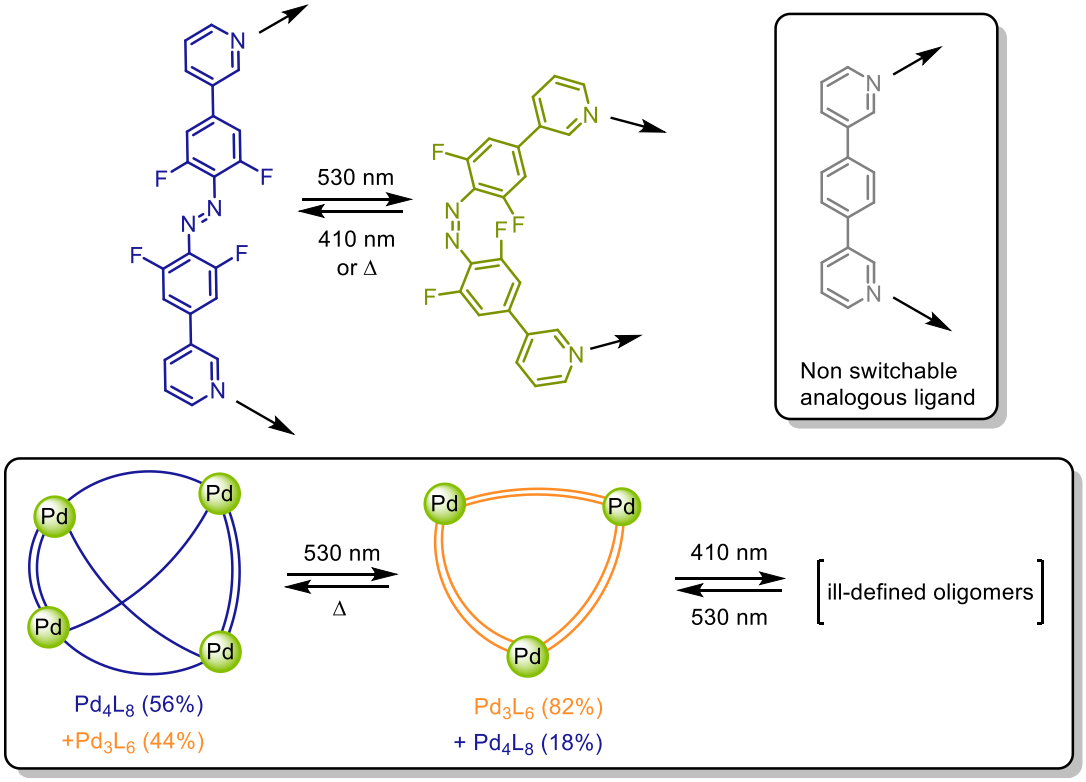

Figure 45. *A photo switchable ligand that self-assembles into a mixture of Pd_3L_6 and Pd_4L_8 cages.[108] Photoswitching of the cage mixture with green light (λ = 530 nm) shifts the distribution of Pd_3L_6 and Pd_4L_8 cages. Thermal relaxation will reform the initial distribution. Irradiation with blue light (λ = 410 nm) will not reform the initial state but instead lead to the disassembly of the cages. A mixture of Pd_3L_6 and Pd_4L_8 cages was also formed from an analogous non switchable ligand (grey, top right).[117]*

The Beves group used an *ortho*-tetrafluoro azobenzene switch bearing two 3-pyridyl substituents. The *E* ground state with its divergent coordinate vectors can be compared to a 1,4-di(3-pyridyl)benzene ligand that was used by the Fujita group to form mixtures of Pd_3L_6 and Pd_4L_8 cages.[117] Indeed, this comparison with a non-switchable analogous ligand proves valuable, as the *E*-state of the *ortho*-tetrafluoro azobenzene ligand forms a mixture of $Pd_4(E\text{-}L)_8$ and $Pd_3(E\text{-}L)_6$ cages. Complexation drastically transforms the energy surface of the switch, as it would undergo nearly quantitative switching when no Pd(II) was present, but no measurable amount of the *Z*-ligand can be observed upon irradiation after complexation, showcasing how photoswitching can be altered by metal complexation. However, exposing the mixture to blue light increases the amount of the $Pd_3(E\text{-}L)_6$ complex from 44% to 82%. Switching back to the initial state was not possible, as irradiation with blue light (λ = 410 nm) resulted in the disassembly of the cage. Instead, thermal relaxation by heating the mixture in the dark could revert the system to its starting point of 44% $Pd_3(E\text{-}L)_6$ complex. The authors postulate that the dynamic nature of coordinative bonds results in a small amount of free ligand, and that this can photoswitch, in turn affecting the distribution between $Pd_4(E\text{-}L)_8$ and $Pd_3(E\text{-}L)_6$.This showcases some of the pitfalls potentially encountered when attempting to synthesize photoswitchable cages, such as incomplete and irreversible switching.

In their next publication in 2022, the Beves group changed the ligand architecture slightly by replacing the pyridine moieties with *iso*-quinoline groups (**Figure 46**).[102] This subtle change has an extraordinarily large effect on the structures this ligand can form. In its *E* ground state, the ligand exhibits slightly converging coordinate vectors and strongly converging coordinate vectors in the *Z*-state. A non-switchable ligand analogous to the *E* ground state had been found to reliably form Pd_2L_4 lantern shaped cages by the Clever group.[118] This comparison proves valuable again, as the *iso*-quinoline decorated switchable ligand also forms a $Pd_2(E\text{-}L)_4$ lantern shaped cage.

When exposed to green light (λ = 530 nm), the ligand switches into its *Z*-state where its two arms come close enough together to coordinate the same palladium ion, resulting in the near quantitative formation of a monometallic $Pd(Z\text{-}L)_2$ complex. This change is completely reversible. Either thermal relaxation or irradiation with blue light (λ = 405 nm) will quantitatively reform the $Pd_2(E\text{-}L)_4$ lantern shaped cage. Excitingly, better switching is observed in the cage than for the free ligand with both higher PSS and a longer half-life. This shows that carefully tuning the ligand to form stable metal-organic complexes in both states can drastically improve the switching properties. The two switchable structures differ greatly, as the $Pd_2(E\text{-}L)_4$ lantern exhibits a cavity that could be used for host-guest chemistry while the monometallic $Pd(Z\text{-}L)_2$ complex would not be able to act as a host. At least in theory, this system represents a host that can be turned off and on at will, an exciting property for potential applications such as

photopharmacology.[10,119] In reality no binding to the cavity was observed, as all investigated guest molecules bound to the outside of the cage.[102]

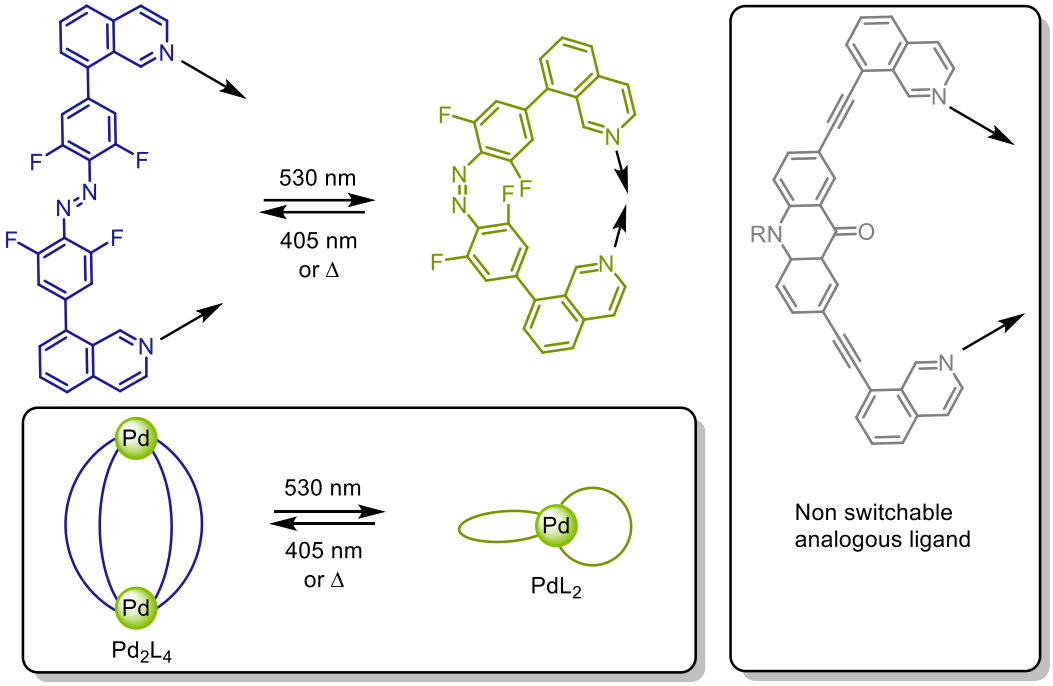

Figure 46. *A photoswitchable ligand that self-assembles into a Pd_2L_4 lantern shaped cage under ambient conditions.[102] Irradiation with green light (λ = 530 nm) will quantitatively yield a PdL_2 complex. This process is completely reversible either by irradiation with blue light (λ = 405 nm) or thermal relaxation. An analogous ligand to the E-state also self-assembles into Pd_2L_4 lantern shaped cages.[118]*

The third iteration of this system was published by Beves and Lusby in 2024 (**Figure 47**).[120] The coordinating group of the ligand had been changed to an ethinyl pyridine and the attachment to the azobenzene was moved from the *para* the *meta*-position. Additionally, the complex is heteroleptic and consists of two different ligands with a second, non-switchable ligand being added. While the azobenzene based ligand exhibits convergent coordinate vectors in its *E* ground state, the second ligand exhibits divergent coordinate vectors. This second ligand had previously been used in combination with a shape complementary and non-switchable ligand bearing convergent coordinate vectors to synthesize heteroleptic $Pd_2L_2L^*_2$ cages by the Hiraoka group.[93] Similarly, the *E* ground state of the azobenzene ligand is shape-complementary to the second ligand and a $Pd_2(E\text{-}L)_2L^*_2$ lantern shaped cage is formed, showcasing how even intricate non-switchable cages can be used to inspire the design of photoresponsive architectures. When exposed to green light (λ = 530 nm), the *ortho*-tetrafluoro azobenzene ligand switches quantitatively into its *Z*-state. Like in the *Z*-state of the *iso*-quinoline based ligand, the two pyridines are close enough together to form a $Pd(Z\text{-}L)_2$ monometallic complex, leaving the secondary ligand to form a $Pd_4L^*_8$ complex. Again, this

change is fully reversible either by thermal relaxation or irradiation with blue light (λ = 405 nm) and the heteroleptic cage is reformed quantitatively.

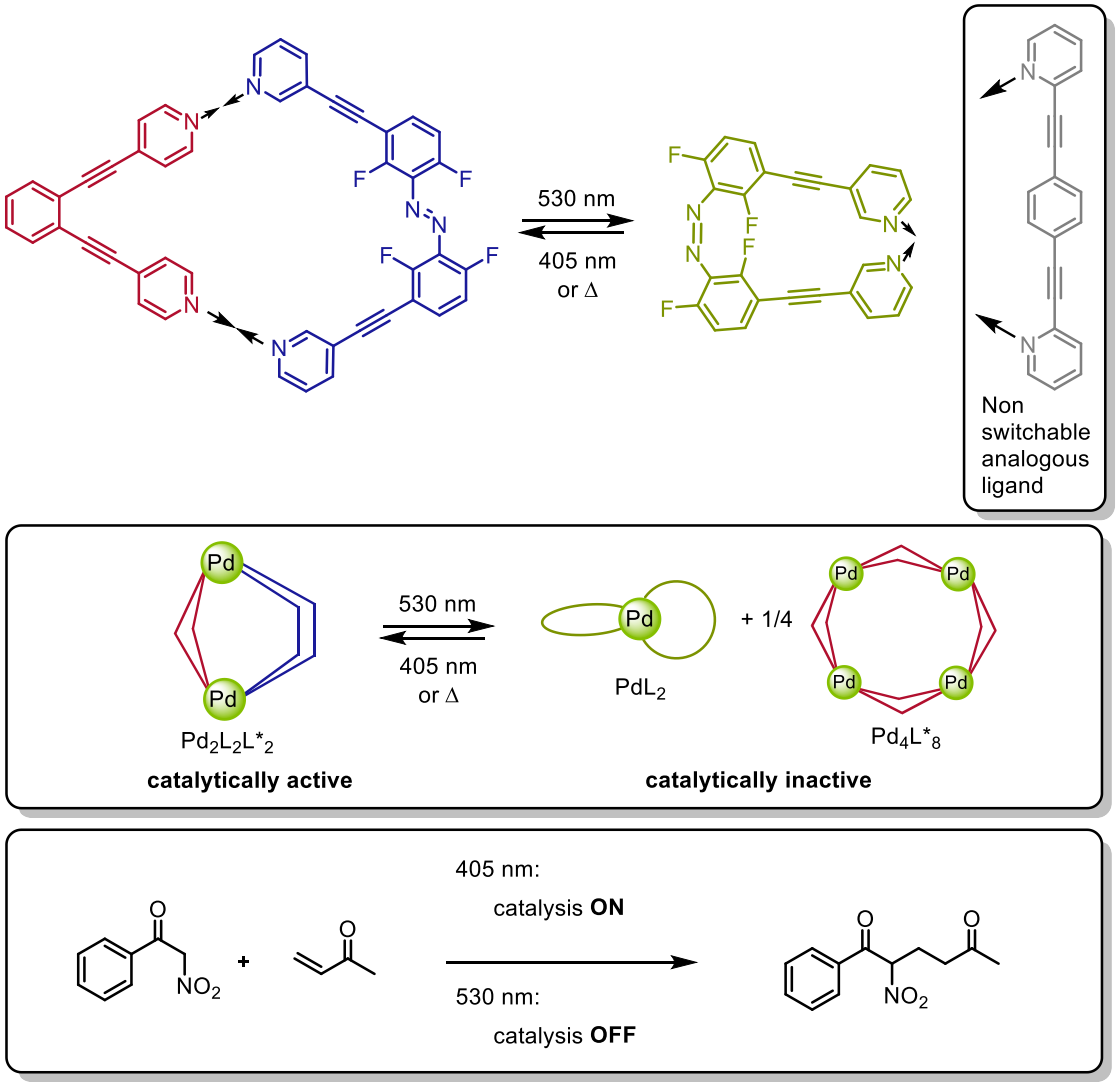

Figure 47. *A photo switchable ligand was used to self-assemble a heteroleptic cage, potentially inspired by a ligand with analogous coordinate vectors (left, grey).*[93] *The $Pd_2L_2L^*_2$ cage catalyzes the Michael addition between methyl vinyl ketone and benzoyl nitromethane. After 530 nm irradiation, the cage disassembles into PdL_2 and $Pd_4L^*_8$ cages that are not catalytically active anymore. Catalytic activity can be restored by 405 nm irradiation.*

While the successful self-sorting and formation of a heteroleptic cage is far from trivial and requires excellent understanding of cage design, the increase in fidelity that comes with it can be worth the effort. In this case, the cavity of the third iteration of *ortho*-tetrafluoro azobenzene based cages published by the Beves group exhibits a cavity that can catalyze the Michael addition between methyl vinyl ketone and benzoyl nitromethane. Combined with the ability to use light to disassemble the cage, this represents a powerful stimuli responsive system, where

the catalytic activity can be switched on or off, mimicking the high fidelity control that biological systems have over enzyme activity. This adaptability enables many of the complex properties found in biochemical systems and this example paves the way for systems chemistry to start reproducing the complex behavior of biological systems.[9]

Sixteen researchers (from students to professor level) were involved in gradually improving the capabilities and complexity of these azobenzene based ligands over three publications until a photo switchable catalytically active cavity could be achieved (**Figure 48**). This showcases that the successful synthesis of photo-responsive metal-organic structures is far from trivial but also demonstrates how powerful the incorporation of photo switchable ligands into metal-organic architectures is in pushing the boundaries of enabling life-like properties. The photo switchable moiety remained unchanged throughout the optimization process, indicating that *ortho*-tetrafluoro azobenzene is an excellent switch for this application. It is a fully symmetric molecule that is synthetically easily accessible, can reach high PSS for switching both ways, and can be operated using visible light. The first publication laid the groundwork for understanding the behavior of switchable ligands that were perfected in the second publication with the third publication adding heteroleptic cage design to the mix and enabling a functional cavity.

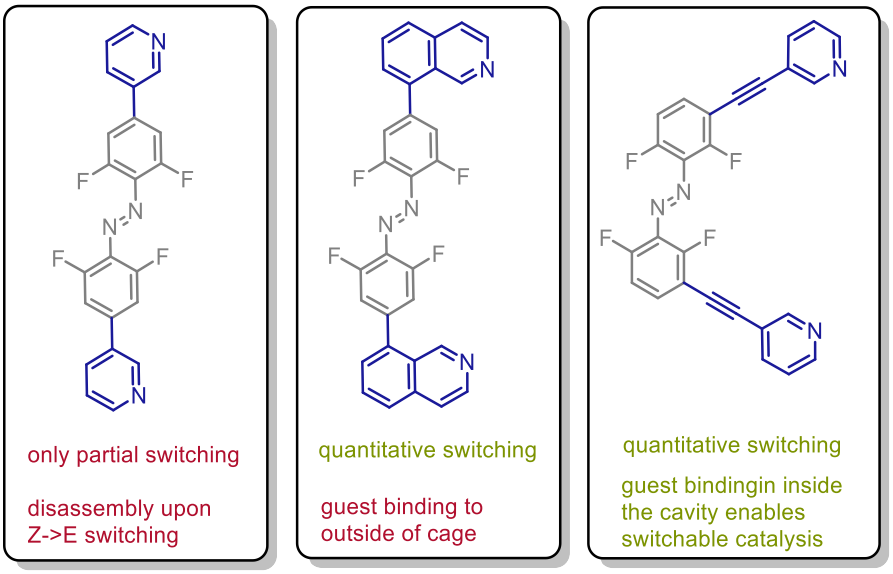

Figure 48. *Three iterations of an ortho-tetrafluoro azobenzene based ligand. The first iteration (left) helped researchers establish how photoswitches might behave in metal-organic cages, but the system showed both incomplete and irreversible switching.[108] The second iteration (middle) enabled the Z-state to form a stable Pd(Z-L)$_2$ complex, which seemed to be a key enabler of quantitative switching, as this effectively sinks the ligand in an inactive structure.[102] The third iteration (right) showed that a heteroleptic architecture was necessary to obtain the desired host-guest interactions and successful self-sorting was enabled by shape complementary ligands.[120]*

2.3.5 Diazocine Based Metal-Organic Cages

As previously discussed in Chapter **2.1.4**, diazocines are cyclic azobenzene derivatives that show an inverted stability of the *E*- and *Z*-states, with the U-shaped *Z*-state being the thermodynamically most stable state. This inverted stability makes diazocines interesting building blocks for metastable metal-organic cages that only form with the metastable linear building block after irradiation. The big advantage of this approach is the much simpler design when compared to metastable assemblies derived from azobenzene, where the metastable state is both flexible and bent, which makes using the design principles outlined in Chapter **2.2.2** much more difficult and complicates predictions of the assembly's structure.

The Clever and Herges groups published a diazocine based ligand in 2022[61] that can be reversibly switched from its stable *Z*-state into its metastable *E*-state. In the presence of Pd(II) ions both a $Pd_2(Z\text{-L})_4$ lantern shaped cage and ill-defined oligomers are formed (**Figure 49**). Irradiation with blue light (λ = 405 nm) switches the ligand into its *E*-state, resulting in the dissipative assembly of a metastable $Pd_2(E\text{-L})_4$ lantern shaped cage. As soon as the irradiation ceases, this metastable cage starts to disassemble, reforming the mixture of *Z*-cage and ill-defined oligomers. Due to the elongated shape of the metastable $Pd_2(E\text{-L})_4$ lantern it can bind disulfonate guests while the stubby $Pd_2(Z\text{-L})_4$ lantern cannot bind these guests. This enables the light triggered release of a guest molecule, an exciting property in the context of photopharmacology.[61]

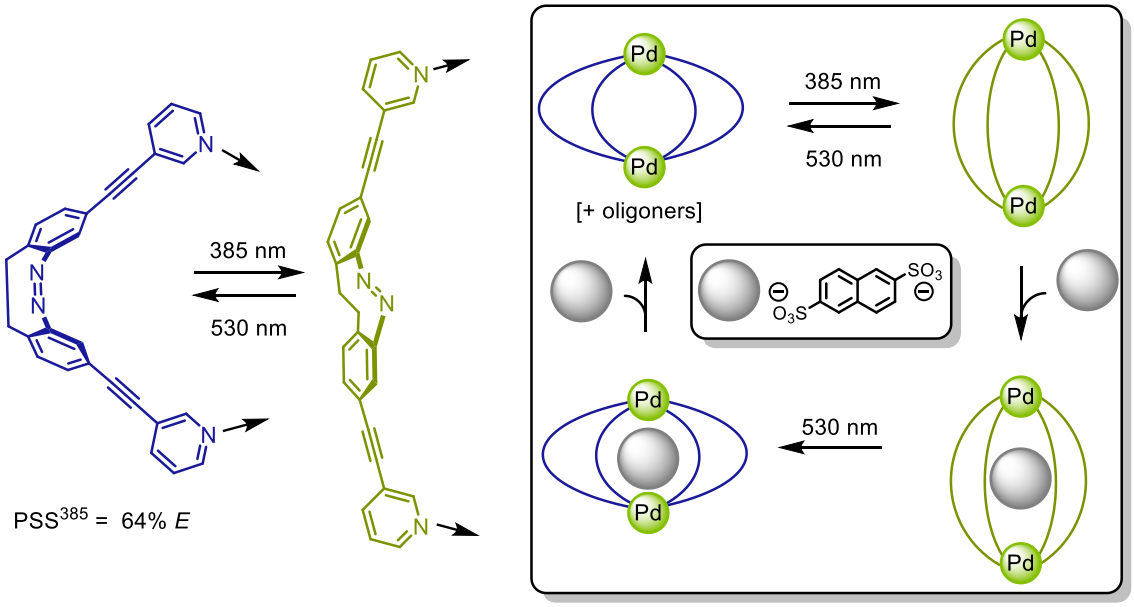

Figure 49. *In its Z-ground state, a diazocine based ligand forms a mixture of Z-Pd_2L_4 cage and ill-defined oligomers. Exposure to 385 nm light switches the ligand into its E-form where the E-Pd_2L_4 cage is formed exclusively. Due to the elongated shape, E-Pd_2L_4 binds a disulfonate guest while back switching to Z-Pd_2L_4 releases this bound guest molecules from the smaller cage.*[61]

A second structure was published in 2023 by the McConnel and Herges groups.[62] This structure uses diazocine based ligands in the self-assembly of Co_2L_3 helicates. The structure is very sensitive towards the substitution pattern at the diazocine core since this has a strong influence on the coordinate vectors in both the *E*- and Z-states. If the triazole moiety is attached in the *meta*-position of the diazocine unit (L^{meta}, **Figure 50**, **A**), the coordinate vectors end up convergent and no complex formation is observed.

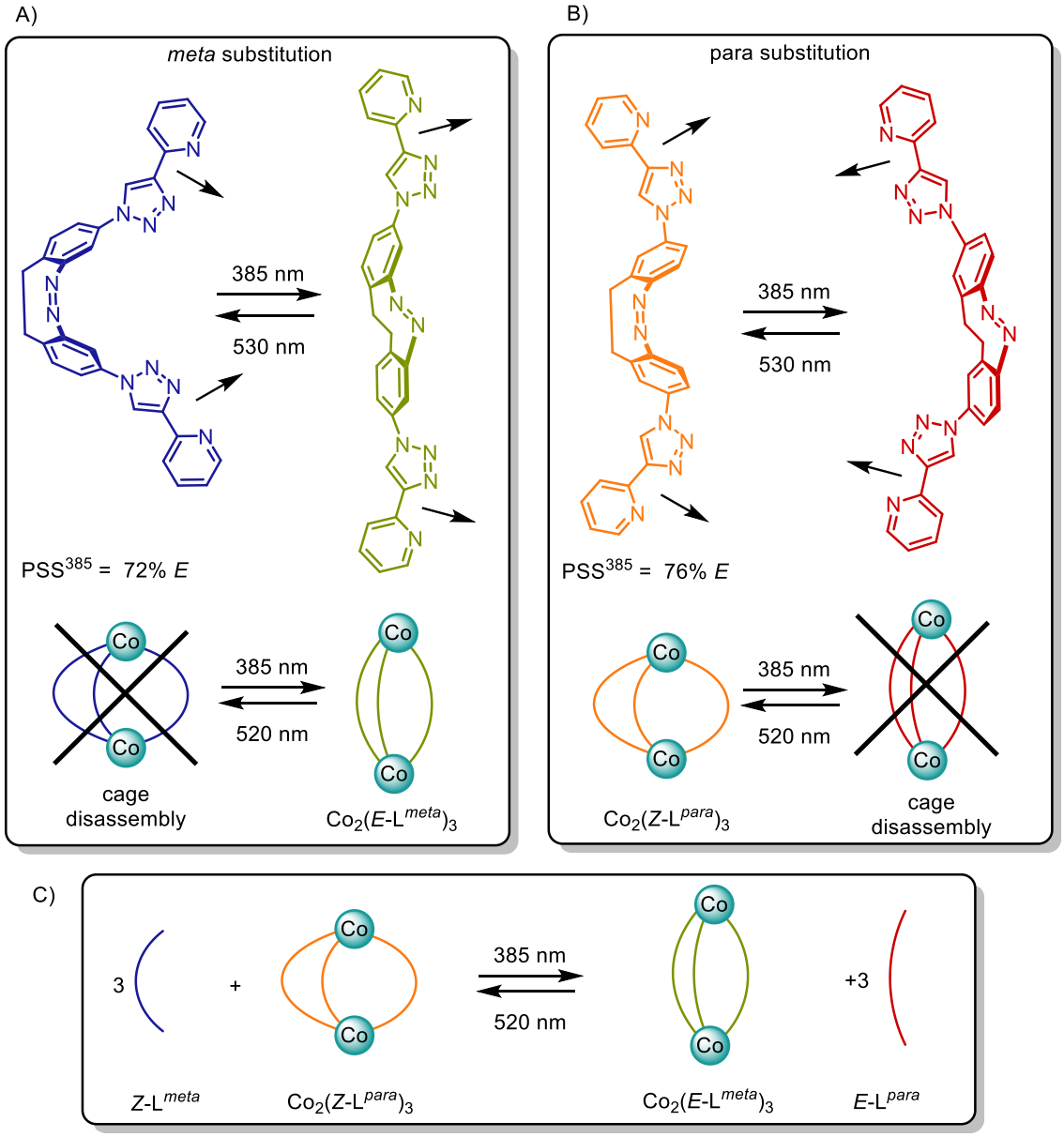

Figure 50. A) *A meta-substituted diazocine based ligand (L^{meta}) forms no cage with cobalt(II) ions in its Z ground state, but irradiation with 385 nm light result in the formation of a $Co_2L^{meta}{}_3$ helicate. It can be reversibly destroyed and reformed using 520 nm and 385 nm irradiation.* ***B)*** *A para-substituted diazocine based ligand (L^{para}) forms a $Co_2L^{para}{}_3$ helicate with cobalt(II) ions in its Z ground state that can be disassembled by irradiation with 385 nm and reformed by 520 nm irradiation.* ***C)*** *A mixture of cobalt(II) ions, L^{meta}, and L^{para} result in the formation of the $Co_2L^{para}{}_3$ helicate and free L^{meta}. Irradiation with 385 nm results in the formation of $Co_2L^{meta}{}_3$ three equivalents of L^{para}. The process is fully reversible by irradiation with 520 nm light.*

Irradiation with UV-light (λ = 385 nm) switches L^{meta} into its linear *E*-state where the coordinate vectors are now slightly divergent, which is a preferred orientation for helical structures where the intertwining of ligands distorts the ligand and results in parallel coordinate vectors (**Figure 29**). The exact opposite behavior is observed when the triazole moiety is attached in the *para*-position of the diazocine nitrogen atoms (L^{para}, **Figure 50**, **B**). The *Z* ground state exhibits slightly divergent coordinate vectors, thereby favoring the formation of the triply stranded helicate in the ground state. Irradiation with UV-light (λ = 385 nm) switches L^{para} into its *E*-state and results in a structure with convergent coordinate vectors, leading to the complete disassembly of the helicate. Mixing three equivalents each of the two ligands with two equivalents of a cobalt salt creates a dynamic system (**Figure 50**, **C**). Under ambient conditions, both ligands exist in the thermodynamically more stable *Z*-state, where a $Co_2L^{para}_3$ helicate is formed and three equivalents of L^{meta} are left over. Irradiation with UV-light (λ = 385 nm) switches the ligands into their *E*-state, resulting in the formation of $Co_2L^{meta}_3$ and three equivalents of free L^{para}. This process is perfectly reversible and irradiation with green light (λ = 520 nm) restores the initial composition of $Co_2L^{para}_3$ and three equivalents of L^{meta}.

2.4 Energy Ratchets

2.4.1 General Principles

The ability to perform work while consuming energy is one of the defining characteristics of both biological and artificial molecular machines. Translation of an energy input into a useful machinery output is far from trivial on the molecular scale, as microscopic reversibility[121] dictates that the transition state of every elementary step needed for the operation of the machinery is the same in both forwards and backwards direction, meaning that it is impossible to preferentially populate high energy states by thermodynamic means, making endergonic processes inefficient or unattainable.[122]

To overcome this limitation the endergonic process can be coupled to a secondary exergonic process, effectively transferring part of the energy gained from the exergonic process to the endergonic process. One example for this can be found in ATP photosynthesis, where the endergonic transformation of ADP to ATP is enabled by a light powered proton gradient across the thylakoid membrane of the chloroplasts.[123] Transport of the protons across the membrane is an exergonic process that serves as the energy source for the biological machine ATP synthase that uses this energy to drive the endergonic synthesis of ATP from ADP.[124]

A macroscopic example for this coupling of an energy consuming process with an energy delivering process can be found in an electric winch. It can lift a heavy object against the force of gravity, driven by rotation of an axle by an electrical motor that consumes electricity. The lifted object gains potential energy and could be considered “out-of-equilibrium” from its original state on the ground, that it would spontaneously fall back to if not interfered with. From the elevated state, it can release stored energy that could be harnessed to create macroscopically useful work. To stop the lifted object from immediately slipping back down, the reversibility of the lifting motion must be removed. This can be done by mechanically locking the rotation axle of the winch by incorporating a mechanical “ratchet” mechanism (**Figure 51**, **A**). This mechanism is typically composed of a gear with teeth, and a pivoting, spring-loaded finger that slips past the teeth when moving in the desired direction and engages the teeth and blocks movement when trying to move in the undesired direction, therefore removing the reversibility of the lifting process. In other words, a driving force could be applied either clockwise or anticlockwise to the rotational axle and the mechanical ratchet selects for one direction and allows only this input force to rotate the axle and drive the rotation only in the desired way.

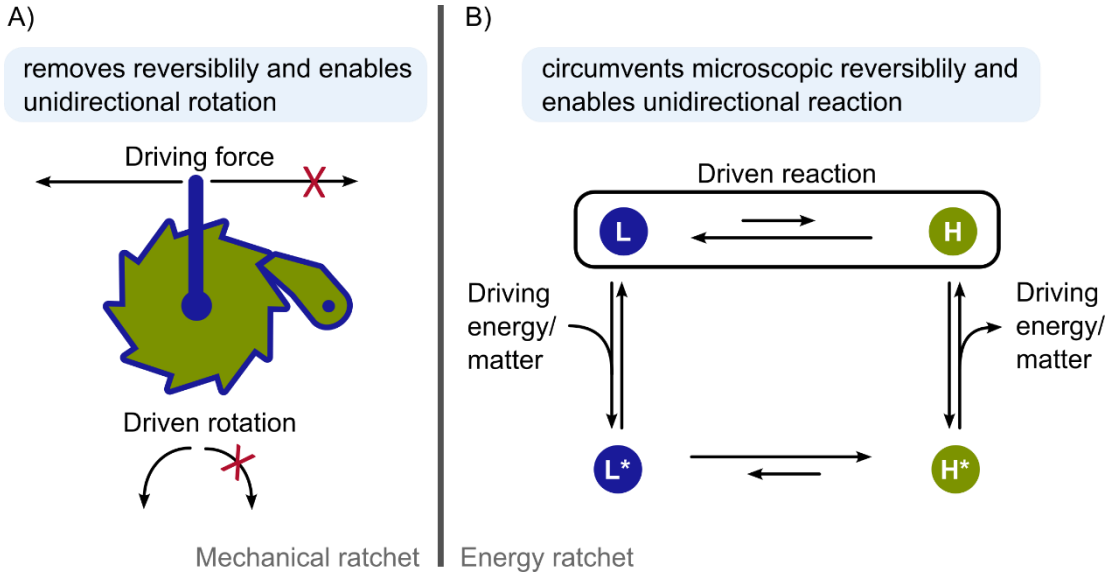

Figure 51. A) *A mechanical ratchet removes the reversibility of a rotational movement and enables unidirectional rotation.* ***B)*** *An energy ratchet circumvents microscopic reversibility and enables a unidirectional reaction of low-energy state* ***L*** *to a high-energy state* ***H*** *by coupling an exergonic process (driving reaction) with an endergonic process (driven reaction). This effectively transfers part of the energy of the driving reaction onto the system to bring it to an out-of-equilibrium state.*

Similarly, an energy ratchet is a reaction network that consumes energy to drive an equilibrium reaction between a low-energy state **L** and a high-energy state **H** unidirectionally, accumulating the high-energy state **H** by circumventing microscopic reversibility of the equilibrium by taking a detour over two related states **L*** and **H*** (**Figure 51**, **B**). While this cannot remove the microscopic reversibility of the **L** to **H** equilibrium reaction it can produce kinetically trapped or metastable states. The energy ratchet mechanism uses the exergonic reaction to enable the transformation of low energy state **L** to an activated state **L*** by consuming either energy directly or energy rich reactants ("fuel"[125]). The activated states **L*** and **H*** are on a different energy profile for their interconversion than the direct endergonic process **L** to **H** (**Figure 52**). In an energy ratchet, the energy difference ΔE_1 between the **L** and **H** states (**Figure 52**, **A**) is larger than the energy difference ΔE_2 between the activated states **L*** and **H*** (**Figure 52**, **B**). The equilibrium distribution of **L*** and **H*** is shifted towards **H*** compared to the **L**/**H** equilibrium (**Figure 52**, **C**). The reaction of **H*** to **H** completes the driving exergonic reaction and results in an overpopulation of the high energy **H** state (**Figure 52**, **D**)., thus using the exergonic reaction to drive the endergonic process.[126]

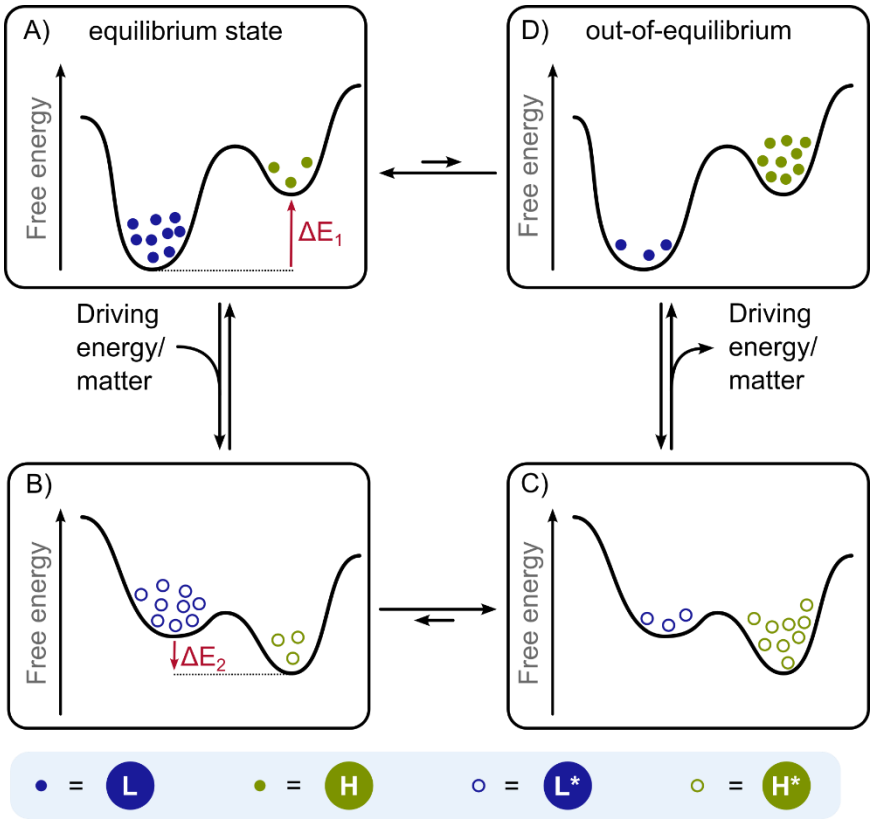

Figure 52. *Schematic representations of the free energy landscapes of an energy ratchet (see* ***Figure 51****) during its operation.* ***A)*** *The system starts in an equilibrium state.* ***B)*** *both components* ***L*** *and* ***H*** *are affected by an exergonic reaction ("driving energy/matter") and transformed into* ***L**** *and* ***H****. *The relative energy difference of* ***L****/***H**** *is much smaller than that of* ***L***/***H*** *($\Delta E_1 > 0 > \Delta E_2$).* ***C)*** *A new equilibrium state is reached where much more* ***H**** *is present relative to the amount of* ***H*** *in the equilibrium state.* ***D)*** *Dissipation of the driving energy/matter completes the cycle and produces an out-of-equilibrium state with a much higher* ***H*** *population than is the case for the equilibrium state.*

2.4.2 Light-driven Artificial Energy Ratchets

Energy ratchets consume energy during their operation. When driven by a chemical fuel, waste is produced. Contrary to biological systems that have evolved complex transport and regeneration processes, it typically accumulates in artificial systems.[126] This can be a problem that interferes with the operation of the energy ratchet as waste products have been found to autocatalytically decompose the fuel[127] or completely inhibit the desired reaction.[128] Therefore, light presents itself as an ideal energy source for energy ratchets, as the only waste it produces is heat. Furthermore, light can be used with excellent spatial and temporal resolution as it is not dependent on diffusion processes like chemical fuels. The energy ratchet mechanism offers the opportunity to use part of the energy of the photon absorbed during the photoswitching process to drive a thermodynamically unfavorable chemical transformation.[126]

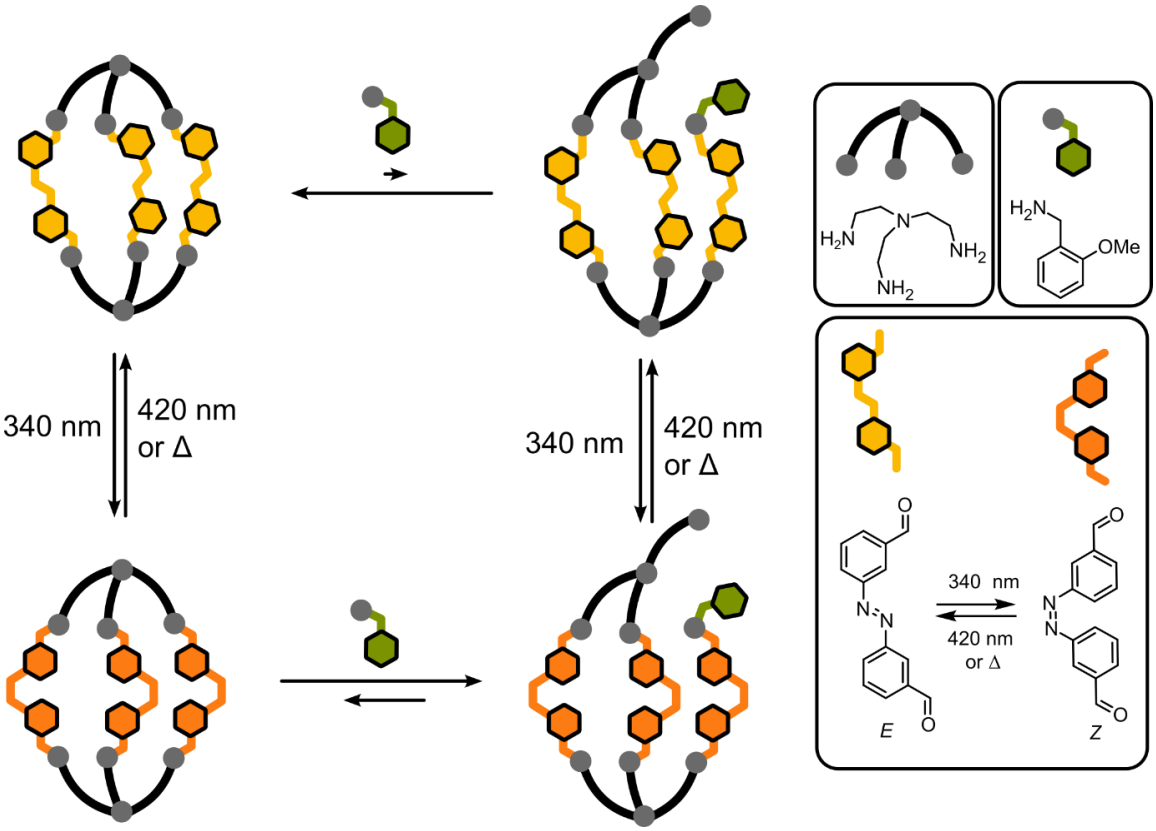

Figure 53. *Light-driven molecular ratchet based on a dynamic covalent organic capsule. Irradiation switches azobenzene moieties from their E ground state (yellow) into the metastable Z-state (orange). The conformational change induces strain, which drives an imine exchange reaction that leads to an open structure. Using blue light (λ = 420 nm) switches the azobenzene moieties back into their E-state, resulting in an energy rich kinetically trapped open structure.*[129]

In 2023, Feringa and coworkers published an example of a light-driven energy ratchet,[129] where the *E*/*Z* photoisomerization of an azobenzene moiety induces strain into a molecular capsule, therefore driving the hydrolysis of an imine (**Figure 53**). In their work, they used dialdehyde substituted azobenzene moieties that self-assemble into a triply stranded dynamic covalent cage in the presence of a triamine through reversible, but thermodynamically downhill, imine condensation reactions. Initially, the stable *E*-cage resists intermolecular imine exchange reactions with monoaldehydes, as it is stabilized by cooperativity effects.[89] However, upon UV-light irradiation, the azobenzene units undergo *E*/*Z* isomerization, resulting in the formation of strained *Z*-cage isomers. These *Z*-cage isomers are less stable since the geometry of the *Z*-azobenzenes induces strain into the cage structure. Thus, the *Z*-cage will spontaneously undergo imine exchange, opening the cage and alleviating strain. Subsequent blue light irradiation of the *Z*-open compound yields a high-energy, kinetically trapped *E*-open species, which cannot be directly obtained from the initial *E*-cage. The stable *E*-cage can be regenerated from the metastable *E*-open structure upon heating, which displaces the monoaldehyde back into solution. This cycle represents a light-driven energy ratchet that

translates the geometric changes observed during the azobenzene switching process into drastic changes to the energy profile of the imine condensation reaction, effectively using light energy to accumulate a metastable isomer and drive the system out of equilibrium.

2.4.3 Energy Ratchets and Information Ratchets

Another type of molecular ratcheting mechanism can be found in information ratchets.[126,130] The key difference between energy ratchets and information ratchets can be found in the driving force of the directionality of the chemical reaction network. Energy ratchets are only driven by the changed thermodynamic landscape and the changed population of **L*** and **H***. The transformation of **L*** to **H*** must be energetically downhill for the ratchet to operate (**Figure 54**, A).

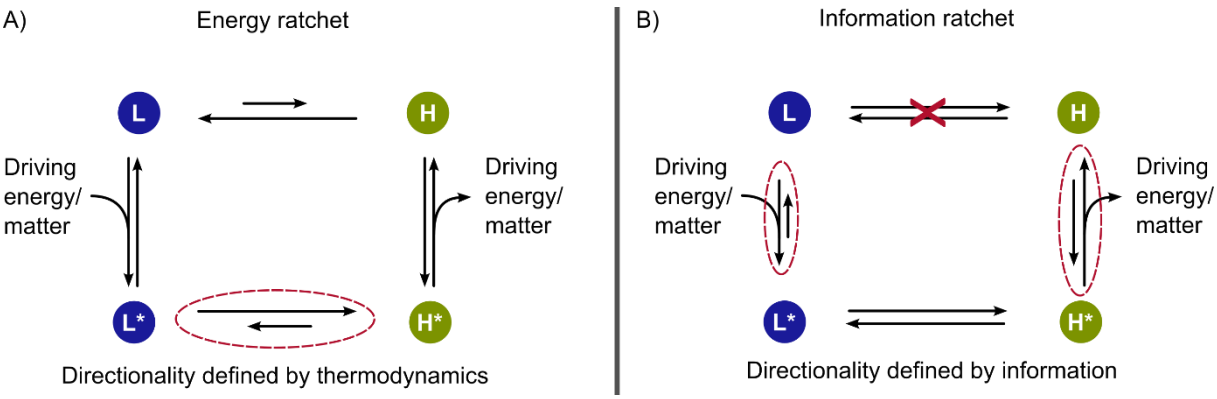

Figure 54. *Comparison of an energy ratchet (**A**) and an information ratchet (**B**) with the reactions that define the directionality marked in red. The directionality of an energy ratchet is thermodynamically defined by the energetically downhill reaction of **L*** to **H***. The directionality of an information ratchet is based upon relative kinetics of the **L*** to **L** and **H*** to **H** transformations and therefore the chemical selectivity that is defined by information carried in the substrates that induces a kinetic asymmetry.*

This is not a prerequisite for information ratchets, **L*** and **H*** only need to interconvert on the experiment timescale, but the relative energy and therefore the position of this equilibrium does not matter. Instead, the directionality is defined by the kinetic asymmetry of the reactions between **L** and **L*** and **H** and **H***, effectively making this a kinetically driven process akin to the kinetic resolution of racemic mixtures (**Figure 54**, B).

2.4.4 Light-Driven Information Ratchets

An example for a light-driven information ratchet can be found in a rotaxane system developed by the Leigh group (**Figure 55**).[131] This system consists of an axle with bulky stoppers at each

end, preventing the macrocycle from slipping off. The axle features two binding sites that are identical in binding strength, and a stilbene moiety that can switch between a bent *Z*-state and a linear *E*-state. The macrocycle cannot pass the *Z*-stilbene but can slip past the *E*-stilbene. Continuous irradiation results in a preferential population of the right binding site, driven by an information ratchet mechanism.

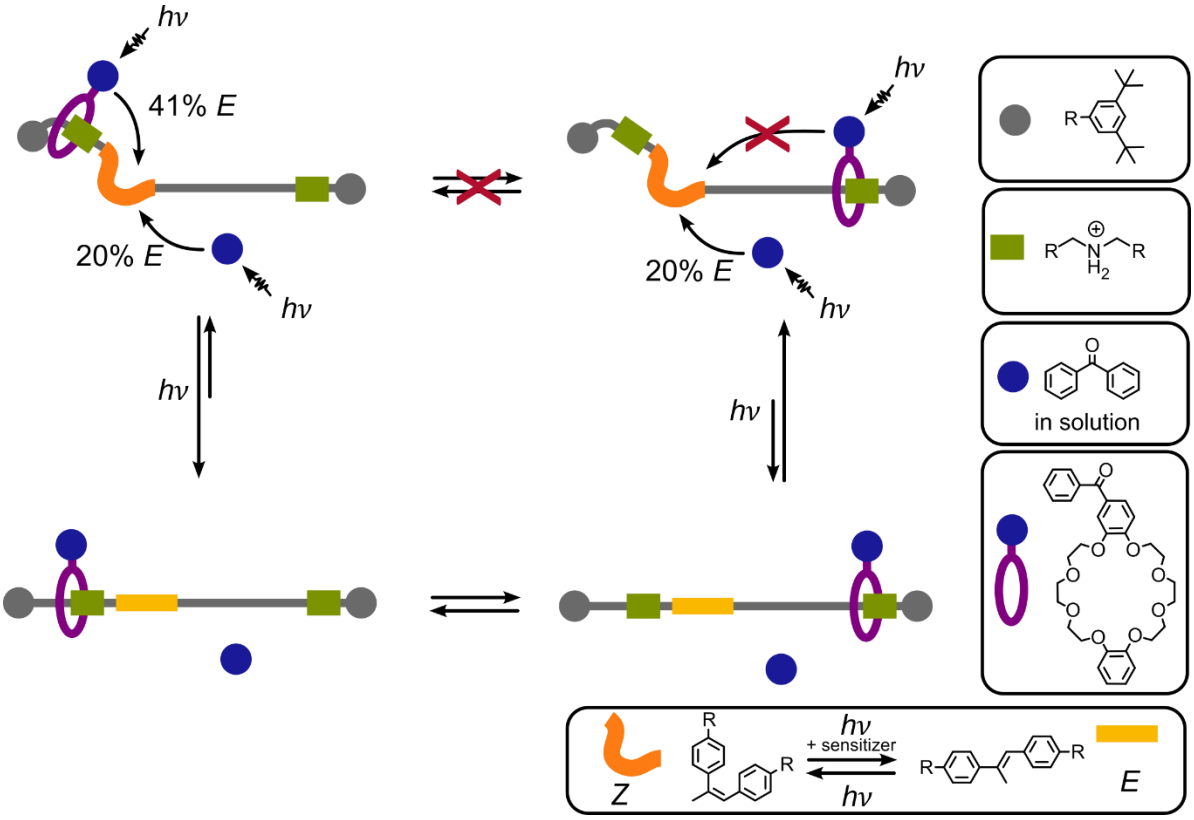

Figure 55. *Molecular information ratchet based on a rotaxane by the Leigh group. The axle has a bulky stopper on each end (grey), keeping the macrocycle (purple) on the axle. The axle contains two binding sites (green) that do not differ in binding strength. The axle contains a stilbene moiety (yellow/orange) that can be switched between the bent Z-state (orange) and the linear E-state (yellow). The macrocycle cannot slip past the Z-stilbene but can slip past the E-stilbene. Continuous irradiation will result in a preferential population of the right binding site, driven by an information ratchet mechanism. The directionality of the reaction cycle is defined by the distance of the photosensitizer on the macrocycle (purple) from the binding site. When it is bound to the left binding site, the stilbene moiety is much more likely to be in the passable E-state. When the macrocycle is bound to the right binding site, the stilbene unit is much more likely to be in the impassable Z-state. Therefore, the macrocycle will be much more likely to be found at the right binding site, despite no thermodynamic differences between the positions. Overall, this represents a directed molecular motion, which is a stark contrast to the random molecular movements caused by Brownian motion.*[131]

The kinetic asymmetry of the process and therefore its directionality is determined by the distance of the bound photosensitizer on the macrocycle from the binding site. When the macrocycle is bound to the left binding site, the stilbene moiety is more likely to be in the

passable *E*-state. When the macrocycle is bound to the right binding site, the stilbene unit is more likely to be in the impassable *Z*-state. As a result, the macrocycle is predominantly found at the right binding site, despite no thermodynamic difference between the left and right binding sites. This represents a directed molecular motion, which contrasts sharply with the random molecular movements caused by Brownian motion. It must be stressed that this directionality is not a result of physical contacts redirecting force but instead defined solely by kinetic factors.[132]

2.4.5 Molecular Ratchets and Molecular Machines

The two examples discussed previously highlight the potential of molecular ratchets in achieving temporal control over the behavior of molecules on a microscopic level. Information ratchets provide directionality to molecular movement by harnessing random thermal fluctuations, enabling the directional operation of molecular motors. The integration of molecular ratchets in larger chemical architectures such as gels[133] or metal-organic frameworks[134] allows for the creation of systems that produce useful (directed) work instead of dissipating energy randomly. Information ratchets enable the effective conversion of (photo)chemical energy into *useful* work, enabling tasks such as actively pumping molecules across phases[135–137] and reading stereochemical information encoded on a molecular thread, akin to how information is read from DNA strands.[138]

Besides the incorporation of information ratchet mechanisms, artificial molecular machines might benefit from the integration of energy ratchets to perform *useful* work. It has been postulated[2] that artificial molecular machines are missing crucial aspects commonly found in biological machines that enable them to perform *useful* work. These aspects include spatial alignment, directionality, compartmentalization, temporal and spatial control, and many more.[2] Similarly, energy ratchets have not yet been used to perform macroscopically *useful* work[130] and development of such systems is still in its infancy.[139] Energy ratchets provide a means of storing potential energy in the form of chemical energy. Like a compressed spring, the system can release the stored energy. Successfully harnessing this energy requires a complex chemical system that controls and directs the energy release and translates it into useful work.

A strategy towards *useful* molecular machines might be to combine aspects of molecular ratchets with the concepts of metal-organic cage chemistry, combining the chemical directionality of molecular ratchets with the precise spatial arrangement found within metal-organic cages and their cavities.

3 Research Objective

The research objective of this dissertation is to incorporate photoresponsive ligands into metal-organic cages, investigate how light can be used to access meta-stable states, and how these can be harnessed for function. This will require the following steps:

I. Suitable photoresponsive building blocks must be synthesized. They should show a large geometry change during switching while also exhibiting favorable switching properties like selective and reversible switching.

II. Methods for the photochemical characterization of photoswitches must be established and applied. These should be robust and efficient, as screening of numerous different building blocks will likely be required to find ideal candidates for the incorporation into metal-organic cages.

III. After an ideal photoresponsive building block was found, its synthetic route should be optimized and scaled up to ensure sufficient material can be obtained.

IV. A suitable metal-organic cage structure must be designed, synthesized, and fully characterized in its non-switched state.

V. The photoresponsive behavior of the metal-organic cage must be investigated and interpreted in the context of potential pathways towards meta-stable states.

VI. If a meta-stable state is successfully obtained, it should be thoroughly characterized and avenues for harnessing its innate energy to enable function should be explored.

4 Results and Discussion

4.1 Twelve-Membered Ring Photoswitches

This research project was published in Organic and Biomolecular Chemistry.[140] The full paper is reprinted in Appendix Section 7.1 with permission[1] from the Royal Society of Chemistry.

4.1.1 Bibliography

Title Twelve-membered ring photoswitches with excellent *Z* → *E* conversion under ambient light

Authors Ruben Falkenburg‡, Maximilian J. Notheis‡, Gregor Schnakenburg, Larissa K. S. von Krbek

‡*These authors contributed equally.*

Citation *Org. Biomol. Chem.* **2023**, *21*, 4993-4998.[140]
https://doi.org/10.1039/D3OB00413A

Abstract Incorporation of azobenzenes into macrocycles is an intriguing approach for fine tuning the photophysical properties of these photoswitches and tailoring them to specific applications. A versatile synthesis of macrocyclic azobenzenes has been developed that allows for facile modification of these photoswitches. One example shows high chemical stability, long half-life of its *Z*-isomers, quantitative *Z* → *E* conversion under white light, and excellent separation of excitation bands to address either the *E* or *Z*-state selectively. The near quantitative *Z* → *E* conversion under white light is a unique feature with an important impact on applications, in which the configuration under ambient light needs to be close to 100%.

Contribution I co-conceptualized the project and synthesized three cyclic azobenzenes (**I-2**, **I-3**, **I-4**). I co-developed HPLC and UV-vis methods to analyze photoresponsive properties of all compounds, performed data analysis and determined photostationary states and thermal half-lives of all compounds, grew crystals of **I-1** for X-ray crystallography, and visualized the data for the Supporting Information. Complete author contributions are published within the article.

[1] Royal Society of Chemistry allows the reproduction of full articles in the dissertation of an author without the need to request permission.

4.1.2 Project Conceptualization

Azobenzenes are popular photoswitches (see Chapter **2.1.2**) with applications in photopharmacology,[13,141–143] chemical sensing,[144,145] molecular logic gates,[146] smart materials,[147–149] and data storage.[150] The incorporation of azobenzenes into cyclic structures is an attractive way to improve photochemical properties by inducing ring strain and reducing conformational degrees of freedom. Especially diazocines have gained attention as their eight membered ring structure inverts the thermodynamic stability of the *E*- and *Z*-isomers (see Chapter **2.1.4**). While boasting better photochemical properties, diazocines exhibit a reduced geometry change between the two states (**Figure 56**, blue and red).

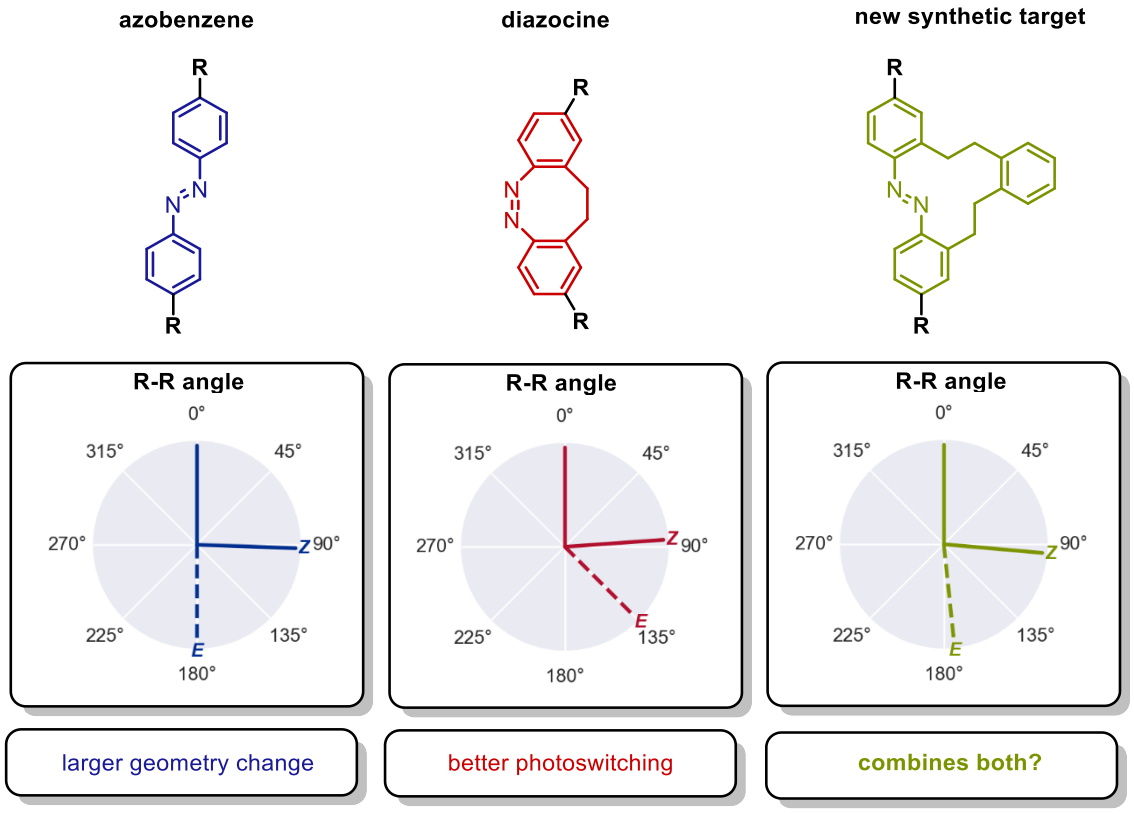

Figure 56. *Structures of azobenzene, diazocine, and the new synthetic target. The angle between the two R groups was measured in models optimized on GFN2-xTB level.*

This is disadvantageous when using them in photoresponsive structures since the smaller change in geometry of less than 50° will have a lesser effect on the overall structure and its properties. Increasing the ring size of a cyclic azobenzene from eight to twelve should result in a system that combines the large geometry change observed in azobenzenes (90°) with the reduced conformational freedom and improved photochemical properties found in bridged azobenzenes, therefore resulting in an ideal switch for future incorporation into self-assembled structures (**Figure 56**, green). A twelve membered ring oxygen bridged azobenzene has been

published by the Staubitz group in 2020.[151] In our project, we target an all-carbon derivative in hopes of further improving photochemical properties and chemical stability. In addition to immediate scientific insight, this project would allow us to gain valuable experience on the synthesis and investigation of photo-responsive molecules.

4.1.3 Project Results: Synthesis

We successfully developed a straightforward synthetic route to twelve-membered ring photoswitches inspired by the diazocine synthesis of Trauner.[49] The target compound **I-1** was obtained in three steps with an overall yield of 58% (**Figure 57**). The carbon skeleton was built using a Sonogashira cross coupling with subsequent reduction using Pd/C and hydrogen gas, furnishing the bis-aniline **I-C** in 87% yield over two steps. The third step, oxidative ring closure, proved to be difficult. Commonly used oxidants such as *m*CPBA[49] could not furnish the product, with either no reaction or complete oxidation to black tar being observed. Staubitz used MnO_2 for the synthesis of the oxygen containing twelve-membered ring,[151] but despite detailed investigations and utilizing a plethora of different MnO_2 sources and pre-treating procedures, this oxidant failed for the all-carbon derivative. We assume that the two oxygen atoms in the *ortho*-positions of the azo bridge are non-innocent in the cyclization step and might coordinate to MnO_2, therefore templating and enabling the cyclisation step for the oxygen containing twelve membered ring.

An extensive literature search revealed that lead(IV) acetate had been used in the past in oxidative aniline cyclizations.[152] This oxidant finally brought the breakthrough in our synthesis and when employed in *pseudo* high dilution conditions enabled the isolation of **I-1** in 67% yield. However, a large excess of lead(IV) acetate was needed. This is not ideal since lead(IV) acetate is a problematic reagent that is not just directly toxic, but also an extremely lipophilic form of lead.[153] Therefore, exposition could lead to an accumulation of lead in the body as it is readily absorbed. Despite all of this, usage of lead(IV) acetate was indispensable for the synthesis of **I-1**. A *para*-iodinated derivative **I-5** was obtained by iodination of bisaniline **I-C** using N-iodosuccinimide (NIS) to **I-D** and subsequent oxidative ring closure to **I-5**.

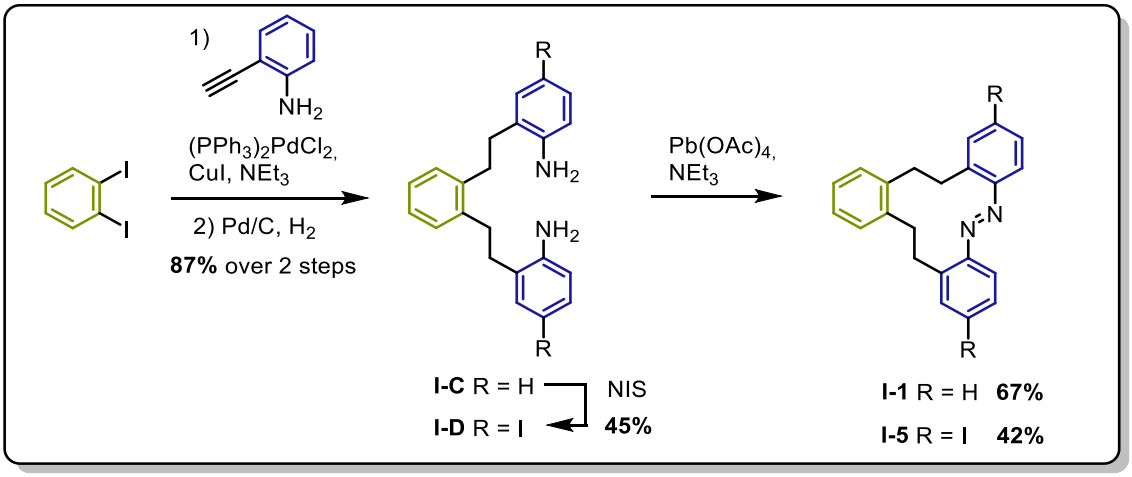

Figure 57. *Synthesis of all-carbon twelve membered ring photoswitch* ***I-1*** *and derivative* ***I-5****. NIS = N-iodosuccinimide*

To investigate the influence of substituents on the photochromic properties and investigate the structure-property relationship we synthesized a series of *ortho*-alkoxylated derivatives using conditions published by Thorn-Seshold in 2022[66] (**Figure 58**). Under ligand free conditions, palladium(II) acetate coordinates to the azo-bridge and can undergo *ortho*-C-H activation, forming a five membered palladacycle. In the presence of a strong oxidizing agent like (diacetoxyiodo)benzene(phenyl) iodine(III) diacetate (PIDA) and an alcohol the *ortho*-position is selectively alkoxylated. Using methanol and pentafluoroethanol, we obtained **I-2** and **I-3** in moderate yields. However, when using hexafluoro-isopropanol the only product isolated was acetate substituted **I-4**. While unexpected, its formation is easily rationalized considering that the reaction mixture contains an excess of acetate and that hexafluoro isopropanol is extremely electron deficient. This enables it to either behave like a leaving group or have such a low nucleophilicity that acetate can directly participate in the formation of **I-4** from the palladacycle.

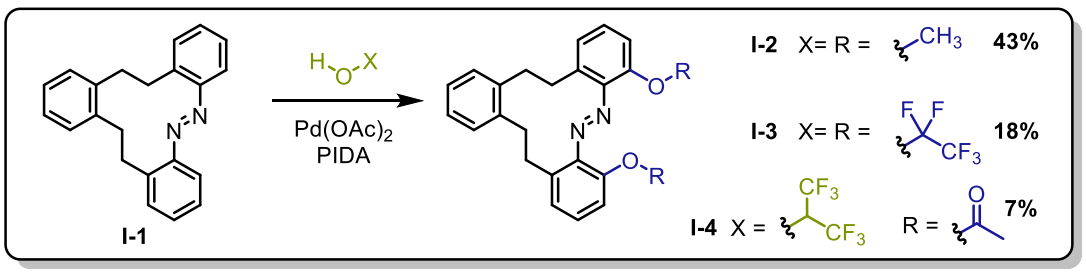

Figure 58. *Palladium catalyzed ortho-functionalization of* ***I-1****. PIDA = (diacetoxyiodo)benzene(phenyl) iodine(III) diacetate.*

Further derivatives with substituents in the *para*-positions were synthesized using palladium catalyzed cross coupling reactions starting from iodide bearing **I-5** (**Figure 59**). The incorporation of sulfur into photoactive molecules is often beneficial for their properties due to the lower energy differences between HOMO and LUMO orbitals in heavier atoms.[154] However, sulfur containing compounds are often catalysts poisons due to the formation of strong M-S bonds. Therefore, we applied a methodology published by Despras in 2022[154] that allowed us to successfully synthesize **I-6** in 86% yield. Additionally, we were interested in the effect of the size of the conjugated aromatic system on the photoswitching properties, since aromatic conjugation is broken in the *Z*-state. Therefore, we synthesized **I-7** which was obtained through a Suzuki Miyaura cross coupling reaction in quantitative yield.

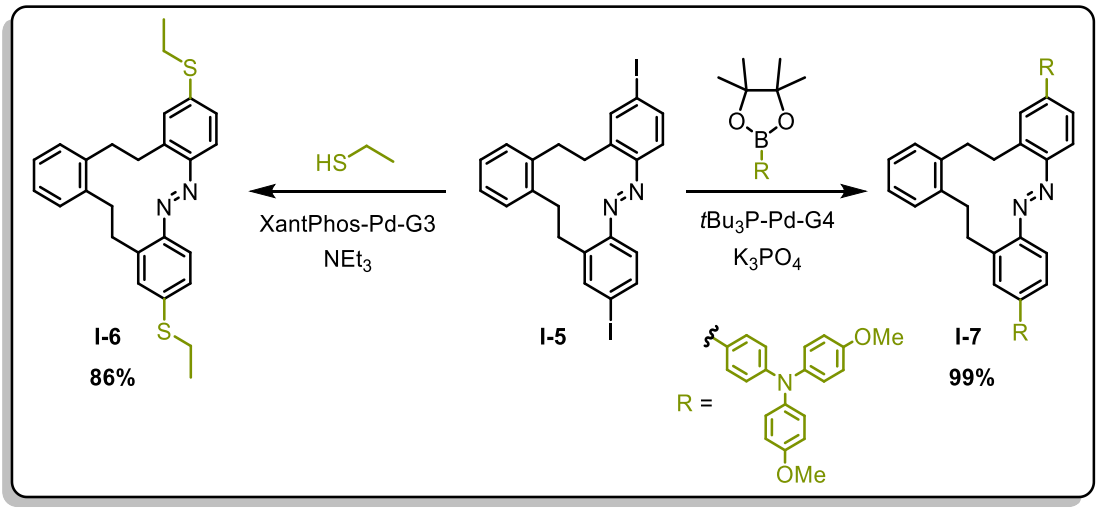

Figure 59. *Derivatization of* ***I-5*** *by palladium catalyzed cross coupling reactions.*

The thermodynamically most stable isomer of **I-1** could be unambiguously confirmed as its *E*-isomer using X-ray crystallography (**Figure 60**). As initially postulated, the azobenzene moiety in *E*-**1-I** closely resembles the *E*-isomer of unsubstituted azobenzene.

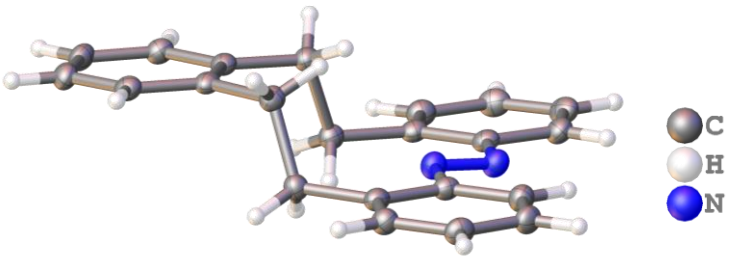

Figure 60. *Asymmetric unit of cyclic azobenzene* ***I-1*** *as observed in the crystal structure. Hydrogen atoms omitted for clarity. Displacement ellipsoids are drawn at 50% probability.*

4.1.4 Project Results: Photochemical Characterization

After having synthesized seven novel cyclic azobenzenes, we investigated their photochemical properties, initially focusing on the unsubstituted **I-1**. As discussed in detail in Chapter **2.1.1**, the photoresponsive behavior of a photoswitch is defined by the excitation wavelength (λ), the thermal half-life of the metastable state ($t_{1/2}$), and the amount of metastable isomer that can be accumulated at the photostationary state (PSS^{λ}).

First, we determined the wavelength dependent photochromic response with the goal of finding the best wavelength to switch the molecule to its metastable state and back to its thermodynamic ground state. The UV-vis spectrum of **I-1** under ambient conditions is identical to that of pure *E* **I-1** (**Figure 61**, A, blue line). It consists of an intense ππ* transition at λ = 327 nm and a barely detectable nπ* transition at λ = 457 nm. When irradiated with UV light (λ = 365 nm), the ππ* band drastically decreases in intensity while a new absorbance band appears at λ = 442 nm (**Figure 61**, A, black line). This is in line with the expected behavior of azobenzene photoswitches (see Chapter **2.1.2**) since aromatic conjugation is broken in the *Z*-state, resulting in a blue shifted ππ* band of lower intensity. Additionally, the nπ* band is typically more intense in the *Z*-state due to a stronger vibronic coupling, explaining the new band at λ = 442 nm. These observations are reflected in the spectrum of *Z* (**Figure 61**, A, green line). Surprisingly, only irradiation with λ = 365 nm had a significant effect on **I-1** and almost no change to the intensity of the ππ* band of *E* **I-1** (λ = 327 nm) was observed when irradiating with any other wavelength (**Figure 61**, B).

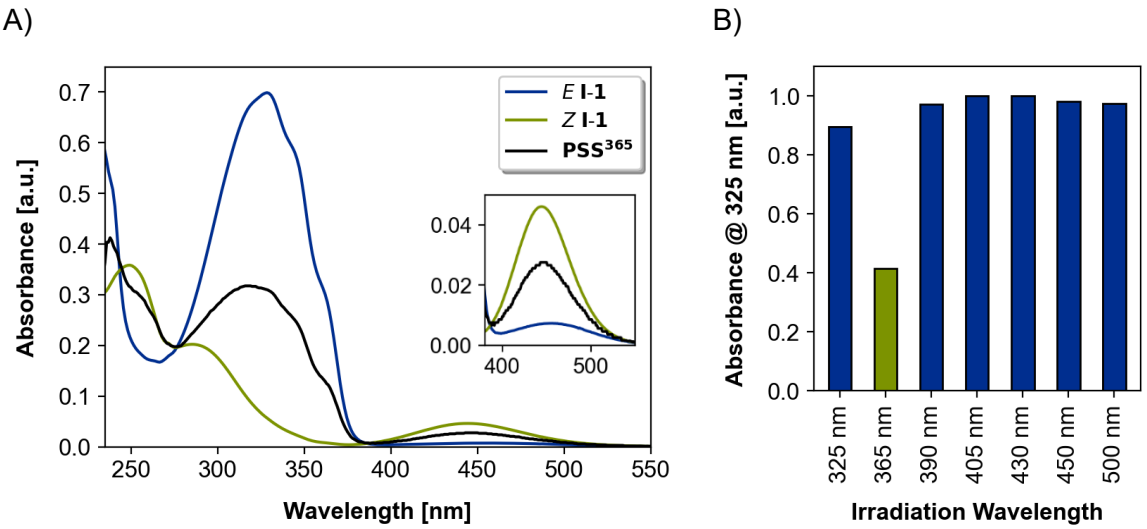

Figure 61. A) *UV-vis spectra of E* ***I-1*** *and Z* ***I-1*** *(obtained by HPLC) and the photostationary state under UV light (λ = 365 nm) irradiation (MeCN/MeOH 1:1 (v/v), 1 mM).* ***B)*** *Absorbance at λ = 325 nm after irradiation of* ***I-1*** *with light of different wavelengths (20 minutes each, 1 mM, DMF).*

In the second step we determined the thermal half-life of the metastable state using UV-vis spectroscopy. An irradiated sample of **I-1** was placed in the spectrometer and left in the dark while the time course of the absorbance at λ = 325 nm was measured. This was normalized and fitted with first-order kinetics, enabling the determination of the thermal half-life as 31 hours at 45°C (**Figure 62**, blue).

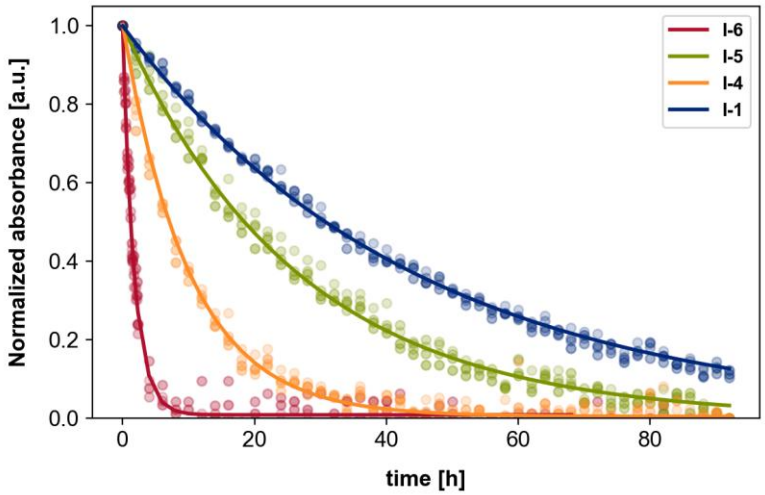

Figure 62. *Thermal relaxation of novel photoswitches as followed by UV-vis spectroscopy (45 °C, DMF, 1 mM) with four replicates of each substance.*

In the third step, we determined the PSS of irradiated samples using UV-vis spectroscopy, NMR spectroscopy, and HPLC chromatography. UV-vis and HPLC methods require

determination of isosbestic points in the UV-vis spectra during switching (**Figure 63**, A). At the isosbestic points, the molar extinction coefficients for both isomers of the switch are equal, and the absorbance remains unchanged during the switching process. This enables the determination of the photostationary state by integration of an HPLC chromatogram (**PSS^{HPLC}**) recorded at the wavelength of the isosbestic point (**Figure 63**, B). Additionally, this separation yields UV-vis spectra of pure stable and metastable isomer that can be used to fit the experimentally observed spectrum of the photostationary state (**PSS^{fit}**, **Figure 63**, C). The relative intensity of the two spectra is normalized to ensure intersection at the isosbestic point. Lastly, NMR spectroscopy enables the observation of separate signals for both states and integration can be used for PSS determination (**PSS^{NMR}**, **Figure 63**, D). All three methods gave mediocre photostationary states for **I-1** of around 55% *Z*-isomer under 365 nm irradiation.

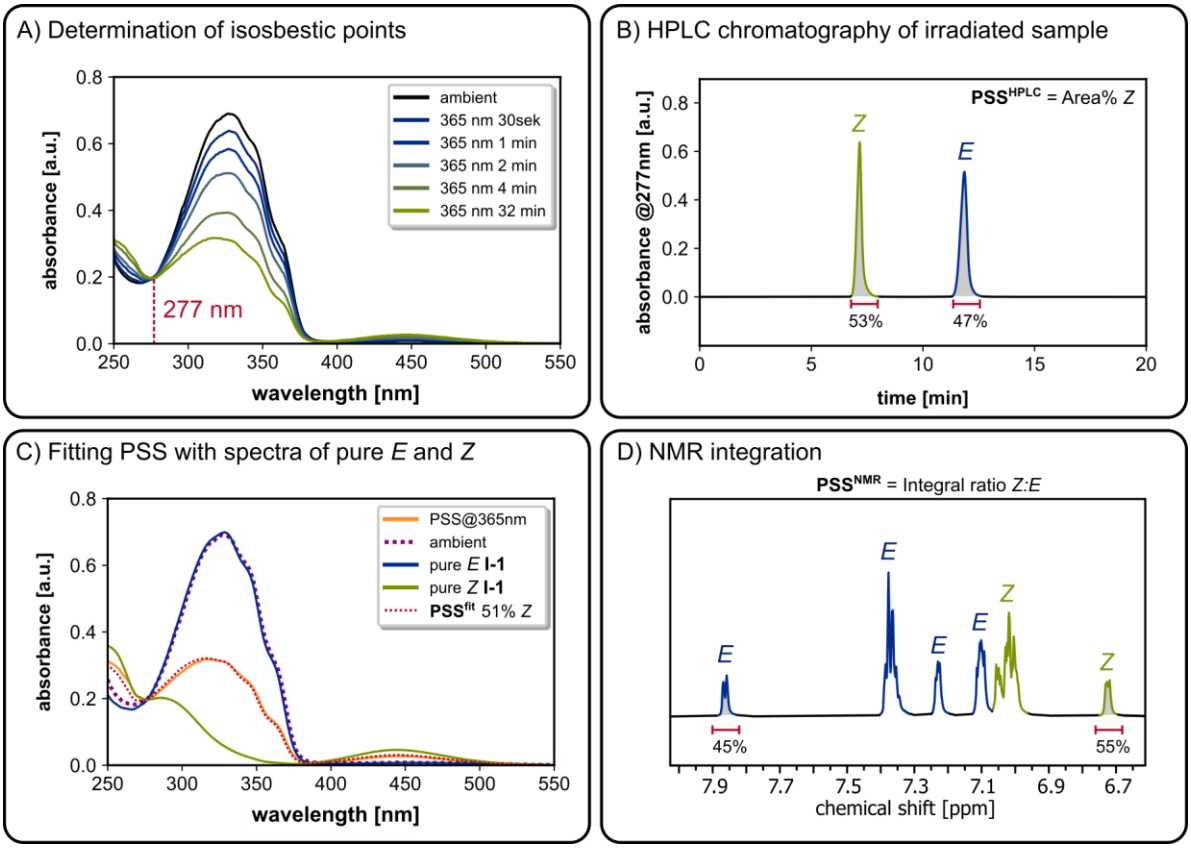

Figure 63. *Overview of analytical techniques used to determine photochemical properties.* ***A)*** *determination of isosbestic points of* ***I-1*** *by UV-vis spectroscopy of a sample during irradiation (MeCN/MeOH 1:1 (v/v), 1 mM).* ***B)*** *HPLC separation of an irradiated sample of* ***I-1*** *at the photostationary state. Recording the chromatogram at the wavelength of the isosbestic point allows determination of* ***PSS^{HPLC}*** *by integration.* ***C)*** *Fitting the UV-vis spectrum of an irradiated sample using the spectra of pure E* ***I-1*** *and Z* ***I-1*** *enables determination of* ***PSS^{fit}*** *(MeCN/MeOH 1:1 (v/v), 1 mM).* ***D)*** *^{1}H NMR spectroscopy of an irradiated sample enables direct determination of* ***PSS^{NMR}*** *by integration (700 MHz, CD_2Cl_2, 3 mM, 298 K).*

Extending the investigation of photochemical properties to the derivatives of **I-1** revealed that most derivatives showed significant changes in their UV-vis spectra upon irradiation. The results of our extensive characterization of the twelve-membered ring photoswitches are summarized in **Table 1**. As was previously discovered for diazocines (see Chapter **2.1.6**), the photostationary state in cyclic azobenzenes is not improved by adding substituents. Surprisingly, *ortho*-substitution had an adverse effect on photochromic properties with **I-2** not exhibiting any photoresponsive behavior. This is in stark contrast to azobenzenes where *ortho*-substitution with either electron donating[155] or withdrawing[37] groups improves photochemical properties (see Chapter **2.1.3**). Halide substitution in the *para*-position (**I-5**) had minimal effect on the photostationary state while thioether incorporation resulted in a slight decrease of the photostationary state (**I-6**). Increasing the size of the conjugated aromatic system (**I-7**) resulted in no photoswitching being observed, likely due to an increased energy difference between the two isomers brought on by the need to break a larger conjugated system to reach the *Z* state.

The parent system **I-1** showed an increased thermal half-live of 16 days at room temperature, a fivefold increase in thermal stability over azobenzene. Thermal half-lives of all photochromic compounds were determined at 45°C, where all derivatives showed faster thermal relaxation than **I-1**. Especially thioether substituted **I-6** showed a 25-fold decreased thermal stability, likely due to its +M effect decreasing the double bond character of the azo bride by enabling quinoid mesomeric structures. Additionally, we investigated the photostability and reversibility of photoswitches **I-1**, **I-4**, and **I-5**. Both **I-1** and **I-4** showed no changes in their absorbance over ten irradiation cycles, demonstrating their stability towards photodegradation. Only **I-5** showed a slight downwards trend, indicating that the iodine substituent resulted in photodegradation, likely by enabling homolytic bond cleavage and radical formation, leading to oxidative decomposition.

Table 1. *Summary of photochemical properties. Photostationary states were determined by fitting UV-vis spectra (MeCN/MeOH 1:1 (v/v), 1 mM) of the irradiated compounds with spectra of pure E-isomer and pure Z-isomer obtained from HPLC. Thermal half-life was determined by following the absorbance recovery of irradiated samples using UV-vis spectroscopy (45 °C, DMF, 1 mM).*

	PSS^{365} (% *Z*)	t½ [h] (45°C)
I-1	53%	30.6
I-3	14%	8.2
I-4	34%	7.1
I-5	54%	19
I-6	38%	1.23

4.1.5 Project Summary

We successfully synthesized, derivatized and characterized a novel photoswitch. Its ground state structure could be unambiguously confirmed as the planar macrocyclic *E*-state using X-ray crystallography. The switch reached moderate photostationary states in $E \rightarrow Z$ switching, but surprisingly $Z \rightarrow E$ switching is nearly quantitative under irradiation with visible light. This is not observed for most azobenzene derivatives and is useful for applications, where full deactivation is required to reach an off state. Complete back switching enables efficient data erasing in data storage applications and fully reversible binding in chemical sensors.

Ab initio models of the *E* state were in good agreement with the crystal structure, but photochromic properties were worse than expected. Therefore, we continued our search for a molecule with excellent photochromic properties and a large geometry change during switching which we intended to use in photoresponsive metal-organic structures.

4.1.6 New Insights

After this paper was published, a question remained in my mind: Why was the photostationary state for *E* → *Z* switching so bad? The UV-vis spectrum of **I-1** showed well separated *E*-$S_2\pi\pi^*$ and *Z*-$S_1n\pi^*$ transitions 115 nm apart from each other. Such a large band separation is essential for achieving high photostationary states by enabling selective excitation,[46,151,156] so additional factors seemed to be at play.

Comparing the spectrum of *E*-2,2′-dimethylazobenzene (**MeAzo**, **Figure 64**, green) and **I-1** (**Figure 64**, blue) helps to shine some light on the underlying factors and help explain the low photostationary state of **I-1**. Surprisingly, both compounds exhibit very similar spectra with almost identical molar extinction coefficients throughout the spectrum. The $S_2\pi\pi^*$ transition is redshifted by around 20 nm compared to unsubstituted azobenzene for both molecules, as would be expected for methyl/methylene substituents with a positive inductive effect. Therefore, it is safe to assume that the $S_0 \rightarrow S_2$ transition of **I-1** is not affected by the incorporation of the azo bridge into a cyclic system. As diazocines show, steric strain has a strong influence on absorbance spectra,[157] indicating that the C-N=N-C moiety in **I-1** is not geometrically constrained and the backbone is flexible, which is corroborated by the broad ethylene signals observed by ^{1}H NMR spectroscopy.

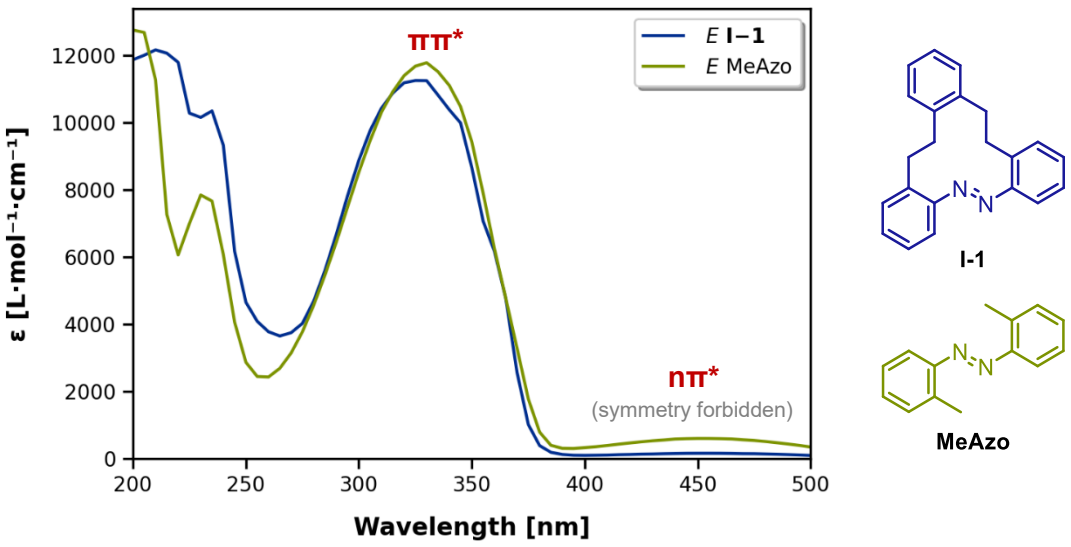

***Figure 64**. UV-vis spectra of **MeAzo** and **I-1** (MeCN, 0.1 mM, 25 °C).*

With identical molar extinction coefficients, both molecules absorb the same number of photons under identical conditions (concentration, temperature, light intensity, and cuvette path length). Consequently, excitation to the S_2 state is equally probable for **I-1** and **MeAzo**, so one might initially expect similar photoswitching behavior. **Figure 65** shows the time course

of the observed molar extinction coefficient at 365 nm during orthogonal 365 nm irradiation. **MeAzo** displays a much steeper decrease and reaches its photostationary state in under one minute, whereas **I-1** switches almost ten times more slowly. As discussed in Chapter **2.1.2**, azobenzene photoswitching proceeds via *E*-S_2 → *E*-S_1 → *Z*-S_0 relaxation. Although both compounds reach comparable initial populations of the *E*-S_2 state, the relaxation pathway in **I-1** preferentially returns to the *E*-S_0 ground state rather than producing *Z*-S_0. This preference is likely caused by additional vibrational relaxation pathways introduced by the flexible bridge in **I-1**. The *Z* isomer of both molecules shows negligible absorption at 365 nm, making significant *Z* → *E* back-switching under these irradiation conditions unlikely. Therefore, the only remaining option that can explain this observation is a low switching quantum yield in **I-1.**

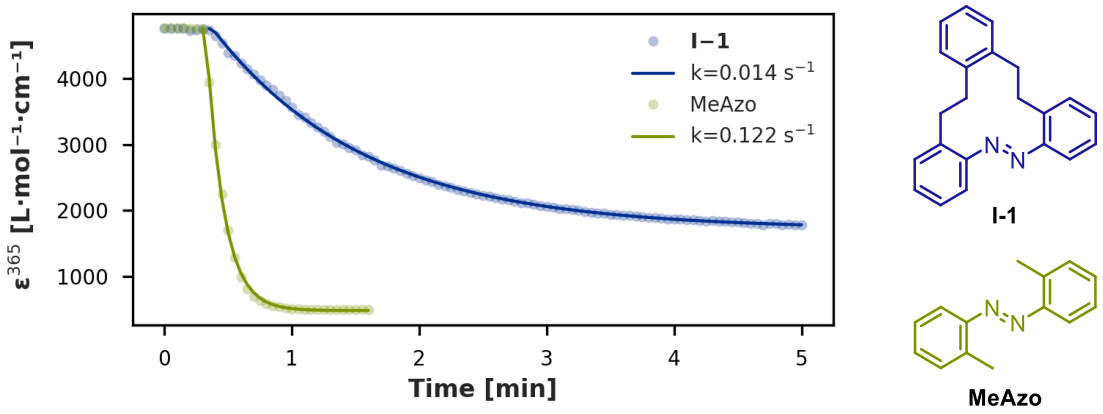

Figure 65. *Molar extinction coefficient at 365 nm of* ***MeAzo*** *and* ***I-1*** *as followed by UV-vis spectroscopy (MeCN, 0.1 mM, 25 °C). After 20 seconds, the samples were irradiated with a 365 nm LED.*

The switching process of azobenzene exhibits a quantum yield of Φ_{S2} = 5% to 15% following $S_2\pi\pi^*$ excitation.[30] Assuming a similar quantum yield for **MeAzo** would indicate that **I-1** exhibits a quantum yield of around 1%, making it an unusually inefficient *E* → *Z* photoswitch. While the $S_2\pi\pi^*$ transition remained unaffected by any constraints the bridge might have, a drastic decrease in molar extinction of the $S_1n\pi^*$ transition is observed in *E*-**I-1** (ε = 150 L mol^{-1} cm^{-1}) as compared to *E*-azobenzene (ε = 400 L mol^{-1} cm^{-1}).[30] The $S_1n\pi^*$ transition is symmetry-forbidden and only becomes weakly allowed through vibronic coupling,[158] indicating that the flexible bridging backbone results in decreased vibronic coupling. The decreased intensity of the *E*-$S_1n\pi^*$ transition enables near quantitative *Z* → *E* photoswitching in **I-1** under all wavelengths of visible light, as the much more intensive *Z*-$S_1n\pi^*$ transition is excited preferentially. Tuning the vibronic coupling of the $S_1n\pi^*$ transition through modulating ring strain enables this switch to show excellent *Z* → *E* switching, while on the flipside exhibiting mediocre *E* → *Z* switching.

4.2 2,8-Dihalogenated Diazocines

This research project was published in Synlett.[159] The full paper is reprinted in Appendix Section 7.2 with permission[2] from Thieme.

4.2.1 Bibliography

Title 2,8-Dihalogenated diazocines: versatile reactants for functionalised photoswitches

Authors Maximilian J. Notheis‡, Vigan Sahiti‡, Vivienne Prangenberg, Johannes S. Kruse, Larissa K. S. von Krbek*

‡ *These authors contributed equally*.

Citation *Synlett* **2025**, *36*, 1569-1573.[159] https://doi.org/10.1055/a-2567-1399

Abstract Diazocine photoswitches possess distinctive structural characteristics and remarkable photochemical properties, leading to their growing application in photopharmacology and smart materials. We report the synthesis of 2,8-pseudo-*para*-substituted diazocines with two bromo, two iodo, or a combination of both substituents, achieving effective scalability. Besides demonstrating good reactivity in Suzuki cross-coupling reactions, the substituted diazocines predominantly retain their good photochemical properties, rendering them valuable components for said applications.

Contribution I co-conceptualized the project and designed the complete synthetic route, including optimization of reaction conditions, upscaling, and establishing reliable purification of the isomeric mixtures using automated chromatography as the key step. I synthesized compounds **II-E**, **II-F**, **II-G**, **II-I**, **II-1**, and **II-3**, supervised optimization of Suzuki coupling conditions, developed USB-powered 3D-printed light sources for sample irradiation and implemented procedures for their usage, and performed quantum mechanical modeling of **II-1** and **II-B**. Complete author contributions are published within the article.

[2] The open-access article is licensed under a Creative Commons attribution license (CC BY 4.0).

4.2.2 Project Conceptualization

The inverted stability of the two isomers of diazocine switches makes them intriguing building blocks. Contrary to non-cyclic azobenzenes, the planar *E*-state is thermodynamically less stable than the bent *Z*-state (see Chapter **2.1.4**). Substitution in an asymmetric 2,8 substitution pattern gives rise to a photoswitch that is linear in its metastable state and bent in its thermodynamic ground state, maximizing the geometry change observed during switching (**Figure 66**). This makes it a very interesting candidate for the incorporation into photoresponsive metal-organic cages.

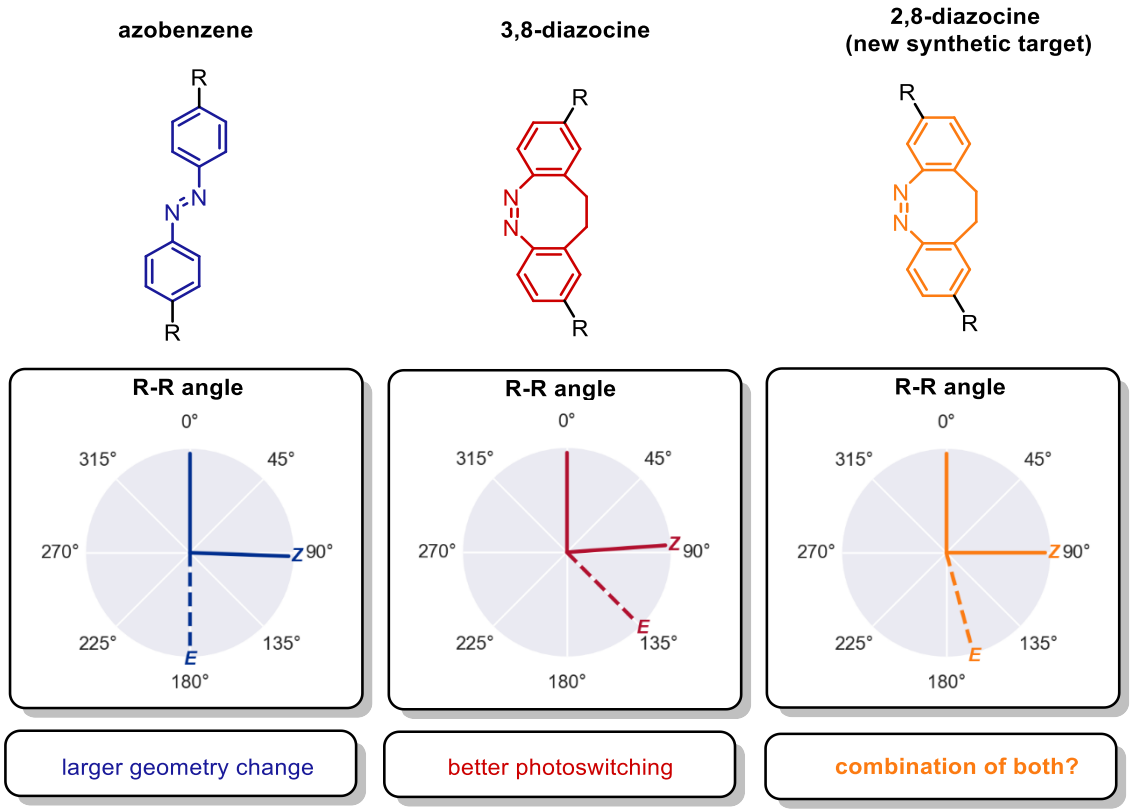

Figure 66. *Structures of azobenzene, 3,8-diazocine, and the new synthetic target 2,8-diazocine. The angle between the two R groups was measured in models optimized on GFN2-xTB level.*

Due to their asymmetric core 2,8-substituted diazocines are expected to form isomeric cages when bearing identical substituents in the 2- and 8- positions (see Chapter **2.2.4**). Therefore, it is desirable to synthesize a 2,8-substituted diazocine with mixed halogen substituents to enable subsequent regioselective cross coupling reactions to yield a 2,8-substituted diazocine with two different coordination moieties. Very few 2,8-substituted diazocines have been synthesized so far and none of their synthetic routes are suitable for the synthesis of 2,8-asymetrically dihalogenated diazocines.

4.2.3 Project Results: Synthesis

A series of iodinated and brominated 2,8-diazocines were synthesized in four steps, starting from dinitro precursor **II-D (Figure 67)**. In the first step **II-D** was halogenated in an S_EAr reaction utilizing *N*-halogensuccinimide (NXS) in concentrated sulfuric acid. These conditions allow the *meta*-selective halogenation of very electron poor aromatic systems. Howerver, due to the electronic decoupling of the two aromatic rings, a statistical mixture of molecules bearing no iodides, one iodide, and two iodides (one on each aromatic ring) was obtained in a ratio of roughly 1:2:1.

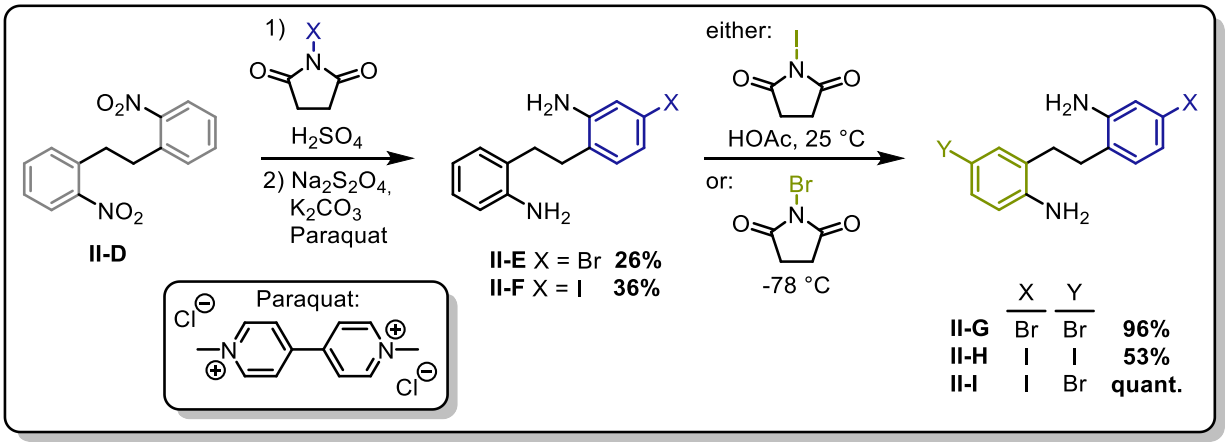

Figure 67. *Synthesis of asymetrically substituted dianiline precoursers* ***II-G****,* ***II-H****, and* ***II-I*** *from commercially available precoursor* ***II-D****.*

Due to the lower reactivity and greater steric demand of *N*-iodosuccinimide (NIS) compared to *N*-bromosuccinimide (NBS) it showed a greater selectivity for the desired *meta*-position (*para* of the methylene group) over the undesired *meta*-position (*ortho* to the methylene group). Although separation of the isomers was not possible at this stage, the mixture was used as-is in the next step, where it was reduced with sodium dithionite in a biphasic dichloromethane-water system using paraquat as an electron-phase-transfer catalyst. The reductive conditions had to be chosen carefully to avoid dehalogenation that was observed in the presence of transition metal ions. The dicationic form of paraquat is readily oxidized by nitrobenzenes to a radical species that is in turn readily reduced by the aqueous dithionite to reform the catalytically active dicationic form. This reaction furnished a crude mixture of iodinated bisanilines that could be separated by automated flash chromatography utilizing an MPLC system, enabling the isolation of monohalogenated **II-E** and **II-F** in 26% and 36% yield over two steps. The electronic character of the molecule changed drastically from electron poor to electron rich with the amine groups being strongly *ortho*/*para*-directing with an apparent preference for the *para*-position. This enabled the halogenation using NBS at -78°C obtain

dibromo bisaniline **II-G** in 96% yield and mixed iodo/bromo bisaniline **II-I** in quantitative yield. Using acetic acid activated NIS at room temperature enabled the isolation of diiodo bisaniline **II-H** in 53% yield. The bisanilines were subjected to oxidative cyclisation by slow addition of *meta*-chlorperbenzoic acid (*m*CPBA) to furnish 2,8-dibromo diazocine **II-1** in 61% yield, 2,8-diiodo diazocine **II-2** in 48% yield, and 2-iodo 8-bromo diazocine **II-3** in 63% yield (**Figure 68**).

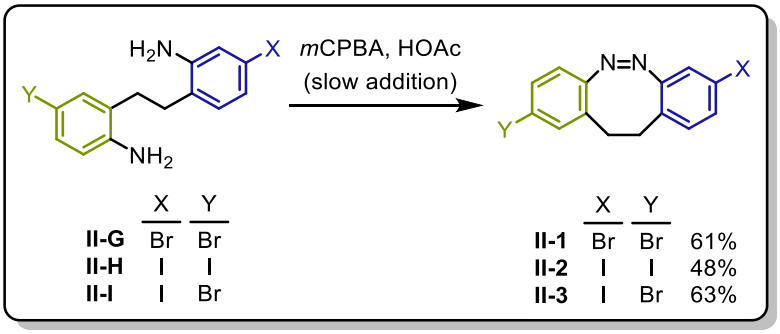

Figure 68. *Synthesis of 2,8-disubstituted diazocines* ***II-1****,* ***II-2****, and* ***II-3****.*

A series of boronic acids bearing a diverse set of substituents ranging from electron rich to electron poor were coupled with 2,8-diiodo diazocine **II-2** in a palladium catalyzed Suzuki Miyaura coupling to yield bis arylated diazocines **II-4**, **II-5**, **II-6**, and **II-7** (**Figure 69**). Additionally, bis arylated diazocines bearing two different substituents were obtained by consecutive Suzuki-Miyaura couplings on 2-iodo-8-bromo diazocine **II-3**. The first coupling was carried out at a lower temperature (45 °C) at which only the more reactive C-I bond was substituted with an electron rich aromatic ring to furnish **II-8**. A second coupling reaction with an electron poor aromatic ring was carried out at a higher temperature (100 °C) to enable coupling of the bromide to yield diazocine **II-9** bearing both an electron donating and an electron withdrawing substituent.

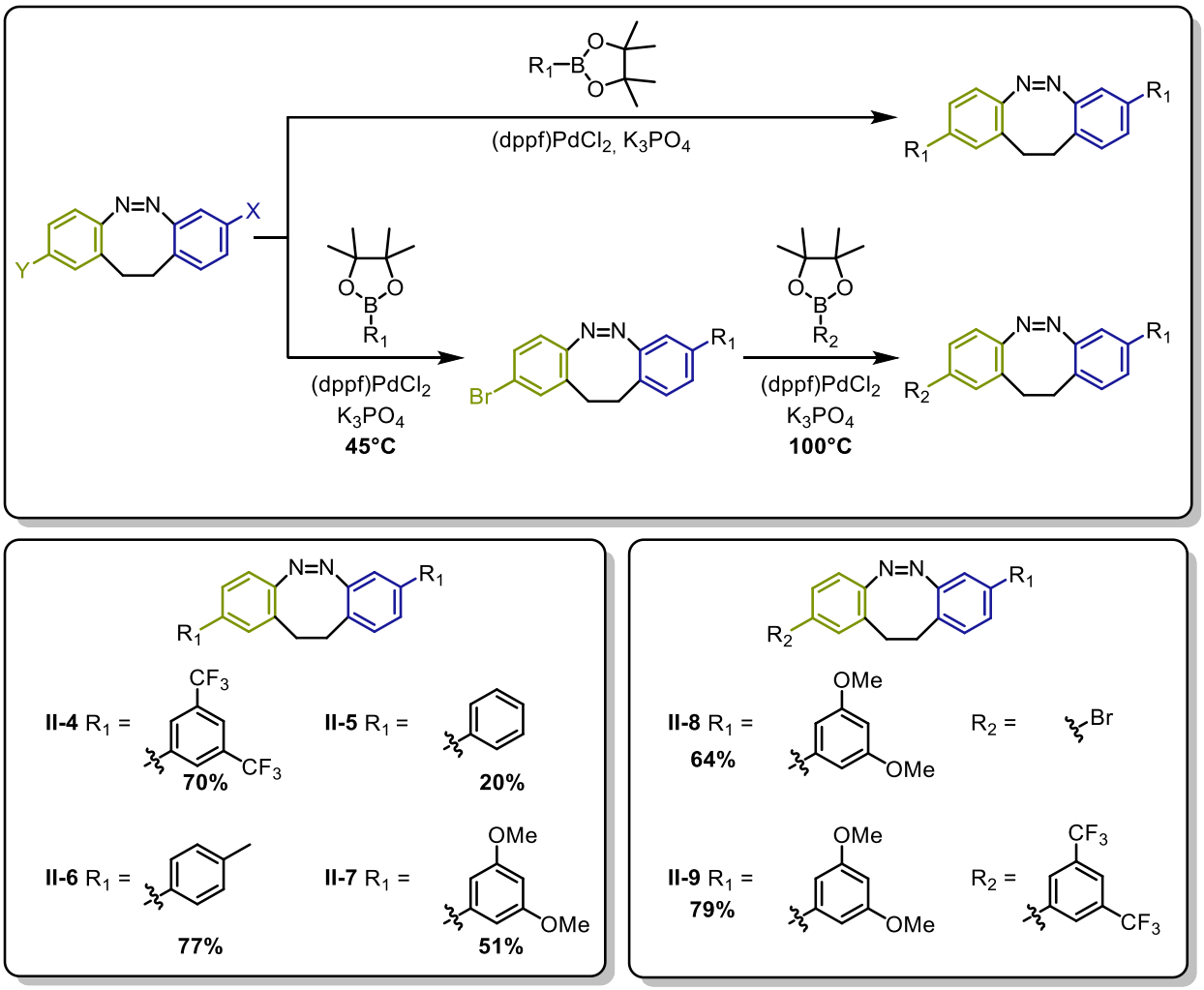

Figure 69. *Synthesis of 2,8-disubstituted diazocines with substituents of varying electronic properties through palladium catalyzed Suzuki Miyaura cross coupling reactions of dihalogenated diazocines.*

4.2.4 Project Results: Upscaling

To enable future research on asymmetrically disubstituted 2,8-diazocines the scalability of the synthesis of **II-3** was investigated (**Figure 70**). The statistical halogenation of **II-D** was independent of reaction scale and halogenation of 60 mmol of **II-D** was unproblematic, yielding 24 g of the isomer mixture. Problems were encountered during upscaling of the biphasic reduction step. Almost quantitative reduction was observed at small reaction scales. However, despite using a mechanical overhead stirrer the yield decreased drastically at larger reaction scales. We assume this reaction to be phase transfer limited. This is problematic for upscaling as the surface area of the phase boundary layer increases slower than the volume when moving to larger reaction vessels (r^2 vs. r^3). Although a drastic reduction in yield to just 10% was observed we were still able to obtain a sufficient amount of 2.4 g of bisaniline **II-F**. A multitude of monophasic reduction procedures failed to yield the desired product, so the

biphasic reduction step remains the only option. The low yield is partially offset by cheap and readily available starting materials. Separation of the halogenated bisaniline isomers was easily scalable by using a proportionally larger column size for the automated flash chromatography. The selective bromination of **II-F** was quantitative both at small and large reaction scales, enabling the isolation of 3.0 g of bisaniline **II-I**. The oxidative ring closure of **II-I** benefited from larger reactions scales. The larger volume of the oxidant solution potentially enables better control over the slow addition rate with an overall larger reaction volume helping to achieve and maintain pseudo high-dilution conditions. This allowed 1.5 grams of diazocine **II-3** to be isolated, representing a yield of 63%.

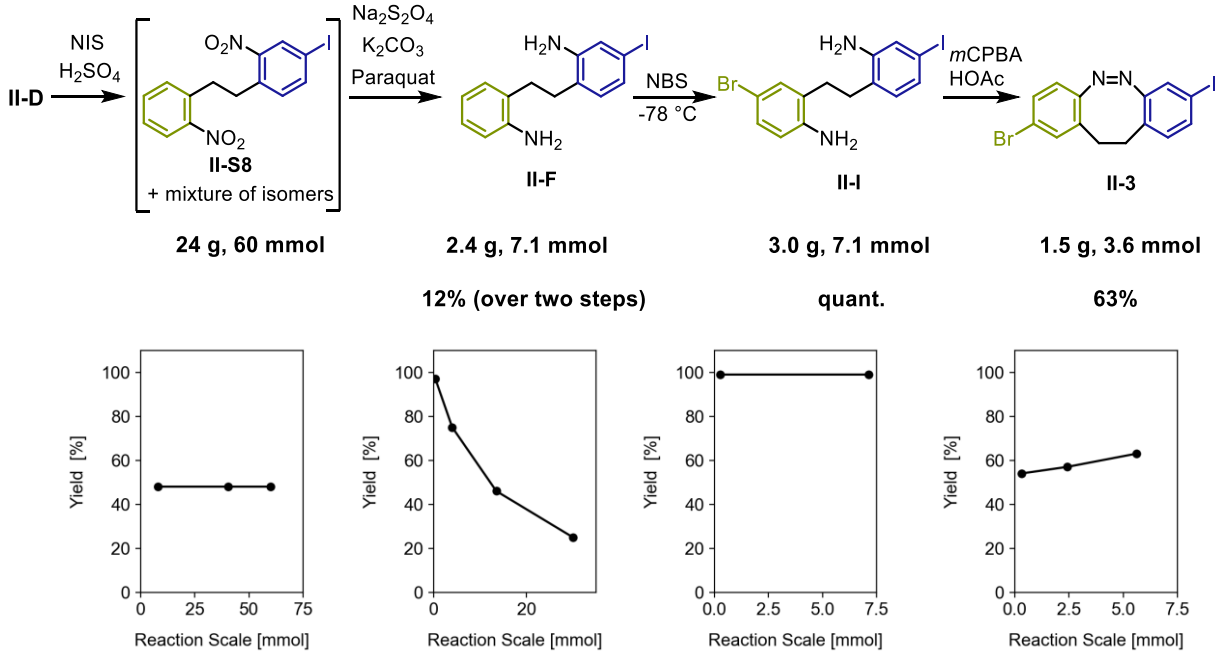

Figure 70. *Scalability of the synthetic route towards diazocine **II-3** visualized for each step by a yield vs scale plot.*

4.2.5 Project Results: Selective Suzuki-Miyaura Coupling

After having established a reliable and reproducible route to diazocine **II-3** we investigated conditions for the iodine selective Suzuki-Miyaura coupling step (**Figure 71**). We focused our investigation on finding the best ligand while leaving other factors such as the base, temperature, and reaction time unchanged. We tested a diverse set of ligands ranging from highly reactive bulky monophosphines and biarylphosphines to less reactive smaller monophosphines and chelating phosphine ligands. We used preformed palladium ligand complexes to ensure the correct palladium to ligand ratio and therefore optimal reactivity. Yields were determined using quantitative ^{1}H NMR spectroscopy with an internal standard and are listed in **Table 2**. The best selectivity was observed for dppf-$PdCl_2$ in which a less reactive

14 valence electron bisligated palladium is the catalytically active species, resulting in a slower but more selective reaction.[160]

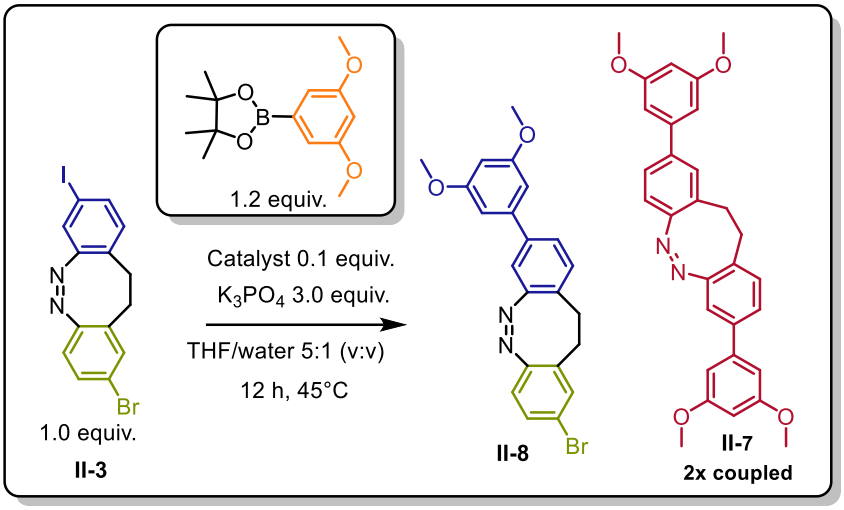

Figure 71. *Conditions for the screening of the selective Suzuki Miyaura cross coupling of diazocine* ***II-3*** *to yield* ***II-8*** *and structures of potential side products.*

Table 2. *Results of Suzuki Miyaura cross coupling of diazocine* ***II-3*** *utilizing different catalysts* ***Figure 71****. Yield determined by* ^{1}*H NMR spectroscopy and comparison with an internal standard.*

	dppf-$PdCl_2$	$(PPh_3)_2PdCl_2$	XPhos-Pd-G3	XantPhos-Pd-G3	tBu_3P-Pd-G4	SPhos-Pd-G3
Product II-8 [%]	**66**	**63**	**20**	**18**	**18**	**17**
2x coupled **II-7** [%]	4	15	8	6	0	4

4.2.6 Project Results: Photochemical Characterization

After having synthesized nine new diazocine derivatives we investigated their photochemical properties. Under ambient conditions, the UV-vis spectrum of diazocine **II-3** shows an absorbance band at λ = 400 nm, which is characteristic for the nπ* transition in *Z*-diazocines. The intensity of this band decreases drastically after irradiation with blue light (λ = 390 nm) and a new absorbance band at λ = 485 nm appears (**Figure 72**). This can be assigned to the the nπ* transition in an *E*-diazocine. All synthesized diazocines showed the same behavior with their respective absorbance bands being shifted by less than five nanometers.

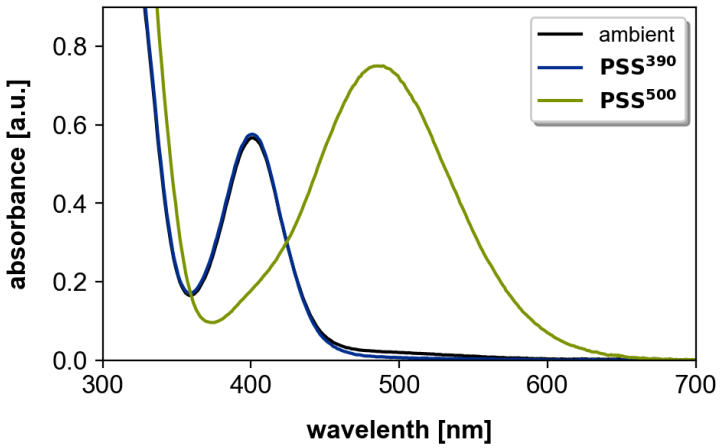

Figure 72. *UV-vis spectrum of diazocine* ***II-3*** *before irradiation and after irradiation with blue (λ = 390 nm) and green (λ = 500 nm) light (3 minutes each, 1 mM, CH_2Cl_2, 298 K).*

Photostationary states were determined using ^{1}H NMR spectroscopy of *ex-situ* irradiated samples and thermal half-lives were determined using UV-vis spectroscopy (**Table 3**). *Z* → *E* switching resulted in slightly reduced photostationary states (63-77% *E*) compared to the unsubstituted diazocine **II-A** (87% *E*). *E* → *Z* back switching remained nearly quantitative for all compounds. Thermal half-lives were decreased but remained in the range of multiple hours.

Table 3. *Summary of photostationary states at UV light (λ=385 nm) and green light (λ=505 nm) irradiation as determined by ^{1}H NMR as well as thermal half-lives at 25°C determined by UV-vis spectroscopy. All experiments carried out in dichloromethane.*

molecule	**PSS^{385}** [%] *E*	**PSS^{550}** [%] *Z*	**$t_{½}$** (298 K) [h]
II-A	87	>99	8
II-1	77	98	3.5
II-2	75	>99	3.2
II-3	76	>99	3.7
II-4	73	97	4.4
II-5	73	>99	3.7
II-6	66	97	3.7
II-7	67	99	1.4
II-8	72	>99	6.1
II-9	63	98	2.1

4.2.7 Project Summary

We established the reliable gram scale synthesis of previously inaccessible 2,8-dihalogenated diazocines and conditions for the selective Suzuki cross coupling reactions thereof. The excellent photoswitching properties of the diazocine core are largely retained when avoiding very electron rich substituents and push/pull substitution patterns. All substitution patterns reduce the thermal half-life.

We were successful in establishing a photoswitch that exhibits the desired geometry changes while upholding good photochromic properties, making this a promising structural motive for incorporation into photoresponsive metal-organic structures.

4.3 Light-Responsive Heterobimetallic Helicates

This research project was published in Angewandte Chemie International Edition.[161] The full paper is reprinted in Appendix Section 7.3 with permission[3] from John Wiley and Sons.

4.3.1 Bibliography

Title Light-Driven Ratchet Mechanism Accelerates Regioselective Metal-Cation Exchange in a Heterobimetallic Helicate

Authors Maximilian J. Notheis‡, Gregor Schnakenburg, Larissa K. S. von Krbek

Citation *Angew. Chem. Int. Ed.* ***2025****, e202508952.* *https://doi.org/10.1002/anie.202508952*

Abstract Molecular machines rely on their capacity to exploit non-equilibrium processes to perform work. However, the development of these non-equilibrium processes, such as molecular ratchets, is still in its early stages. Here, we report a diazocine-containing ligand (L) harbouring two distinct chelating coordination sites that can self-sort into dinuclear homo- and heterobimetallic helicates ($[Fe^{II}_2L](OTf)_4$, $[Co^{II}_2L](OTf)_4$, $[Zn^{II}_2L](OTf)_4$, $[Zn^{II}Fe^{II}L](OTf)_4$, $[Zn^{II}Co^{II}L](OTf)_4$) with precisely controlled metal cation distribution. The photoisomerisation of the helicates operates via a molecular ratchet mechanism, resulting in metastable diastereomers that shift the system from thermodynamic equilibrium. Continuous white-light irradiation autonomously drives this ratchet process, selectively enriching an out-of-equilibrium pseudo-mesocate structure. Crucially, the ratchet mechanism can significantly accelerate metal-cation exchange from the $[Zn^{II}_2L](OTf)_4$ helicate to the $[Zn^{II}Fe^{II}L](OTf)_4$ helicate. Thus, the system operates in a manner reminiscent of a “claw machine”, selectively seizing Fe^{II} ions when subjected to a precisely controllable external stimulus. These findings lay the foundation for creating adaptive and reconfigurable supramolecular structures that use non-equilibrium phenomena on a molecular level.

Contribution I conceptualized the project and carried out all experimental, computational, and analytical tasks (excluding X-ray crystallography). I analyzed, interpreted, and visualized all results, and wrote the Supporting Information and the first draft of the manuscript. Complete author contributions are published within the article.

[3] The open-access article is licensed under a Creative Commons attribution license (CC BY 4.0).

4.3.2 Project Conceptualization

After establishing reliable synthetic access to 2,8-diazocines (see previous Chapter) we intended to use this building block in photoresponsive metal-organic cages. However, the 2,8-diazocine core is asymmetric and could form multiple different heteroleptic cages with mixed ligand orientations. To solve this, two different metal binding moieties were incorporated to preorganize the ligand and eliminate other orientations. One of the binding moieties is a pyridine carboxaldehyde (**Figure 73**, green) that will form imine bonds with tris(2-aminoethyl)amine (TREN, **Figure 73**, red). This forms a covalently bound structure that is an excellent ligand for octahedral metal cations[162] and forces the 2,8-diazocines in a specific orientation. This preorganizes the secondary bipyridine coordination site (**Figure 73**, blue) and the structure is expected to form an M_2L helicate with two distinct metal binding sites, $\mathbf{M}^{\mathbf{TREN}}$ and $\mathbf{M}^{\mathbf{bipy}}$.

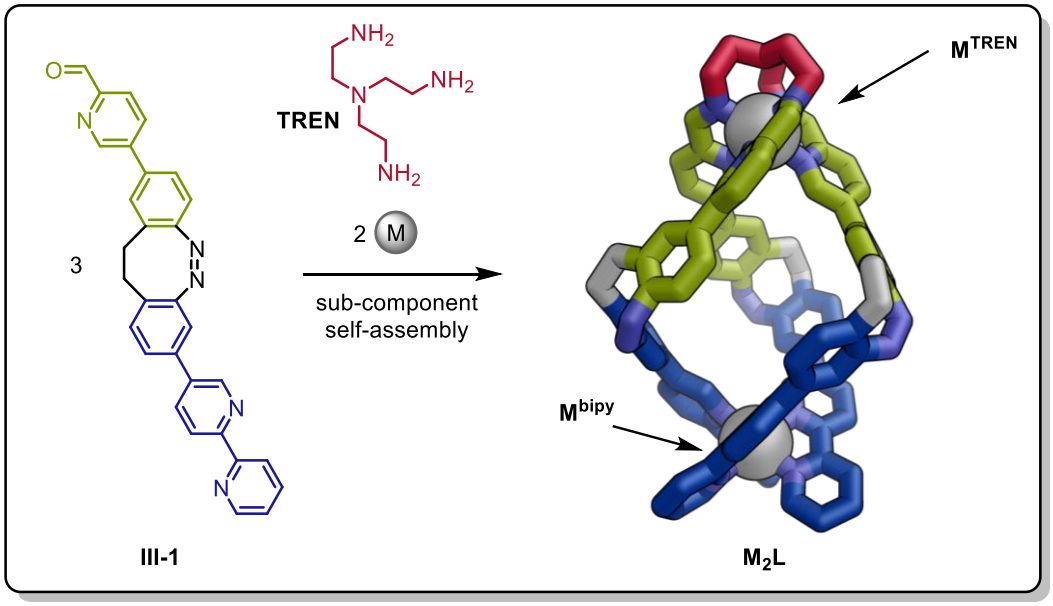

Figure 73. *Sub-component self-assembly of* ***M₂L*** *helicates from three equivalents of diazocine* ***III-1****, one equivalent of a trivalent amine (TREN) and two equivalents of an octahedral metal. The top metal site will be referred to as "****M^{TREN}****" while the bottom metal site will be referred to as "****M^{bipy}****".*

4.3.3 Project Results: Ligand Synthesis

The ligand was synthesized starting from 2-iodo-8-bromo diazocine **II-3** in two consecutive Suzuki couplings. This benefited greatly from previous work (see Chapter **4.1.6**) in which both the synthesis of **II-3** and conditions for the stepwise functionalization were established.[159] However, the inherent instability of pyridyl boronic acid pinacol esters caused by their autocatalytic hydrolysis[163] makes their use in cross coupling reactions difficult, especially in combination with halogenated diazocines where no product formation was

observed.[164] Usually, the solution for unstable boronic acids is the use of highly active catalysts,[165] but this was not possible here since those active catalysts had previously been shown to exhibit insufficient selectivity for the stepwise functionalization.[159] Therefore, we used the corresponding ethyl pinacol esters ("EPin") instead.[166] EPin boronic acid esters inhibit autocatalytic decomposition by sterically blocking access to the empty orbitals on the boron atom.[166] They are not active in Suzuki cross coupling reactions and need to hydrolyze to the boronic acid, which is active in the cross-coupling reaction. This hydrolysis is slow, resulting in a slow release of the reactive boronic acid. The catalyst will continuously undergo oxidative addition with the aryl halide, resulting in a relative excess of oxidative addition products in solution compared to the slowly released boronic acid, enabling trans-metallation to be much more likely than deborylation.[160] This strategy enabled the iodine selective cross-coupling of **III-S1** with **III-S3** to produce **III-S8** in a good yield of 69% (**Figure 74**). **III-S8** and **III-S6** were coupled in a second Suzuki coupling reaction at elevated temperatures to enable substitution of the less reactive bromine. Protection of the aldehyde as an acetal was necessary to avoid decomposition at the elevated temperatures. Due to the presence of pyridines and a strained ring system, the deprotection was tricky. Common conditions such as catalytic amounts of (Lewis) acids[167] failed due to quenching by the pyridines while using an excess of aqueous acids[97] resulted in complete decomposition of the strained diazocine core. However, using exactly three equivalents of a super-acid like HBF_4 will protonate the molecule, forming pyridinium salts that are active in the deprotection. This enabled the acetal deprotection when heated to more than 50°C but less than 60 °C, furnishing the pre-ligand **III-1** in 66% yield over two steps.

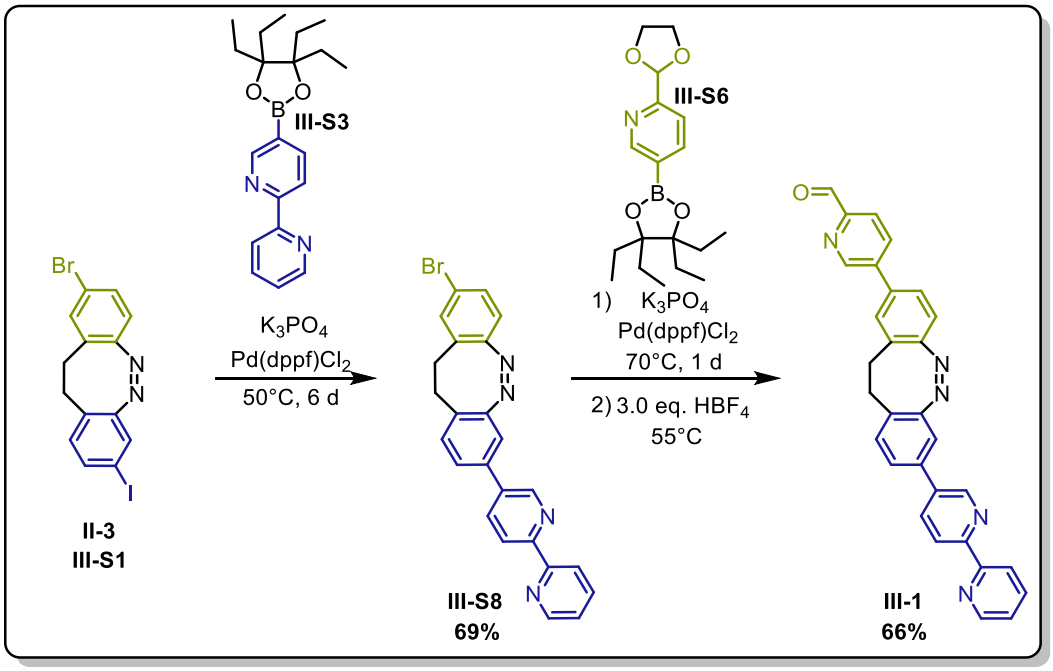

Figure 74. *Synthesis of pre-ligand* ***III-1*** *from 2-iodo-8-bromo diazocine* ***III-S1****.*

4.3.4 Project Results: One-Pot Synthesis of Self-Sorted Heterobimetallic Helicates

Pre-ligand **III-1** and triamine **TREN** were successfully used in a series of one-pot sub-component self-assembly reactions with metal salts, furnishing homometallic helicates Co_2**L**, Fe_2**L**, and Zn_2**L** as well as heterobimetallic helicates ZnFe**L**, ZnCo**L**, and CoFe**L** (**Figure 75**). Furthermore, a stepwise approach enabled the synthesis of tripodal complex Fe**L** and consecutive synthesis of heterobimetallic FeZn**L**. The identity of all complexes could be unambiguously confirmed by ESI^+ HRMS, NMR and UV-vis spectroscopy, as well as X-ray crystallography of Fe_2**L** and ZnFe**L.**

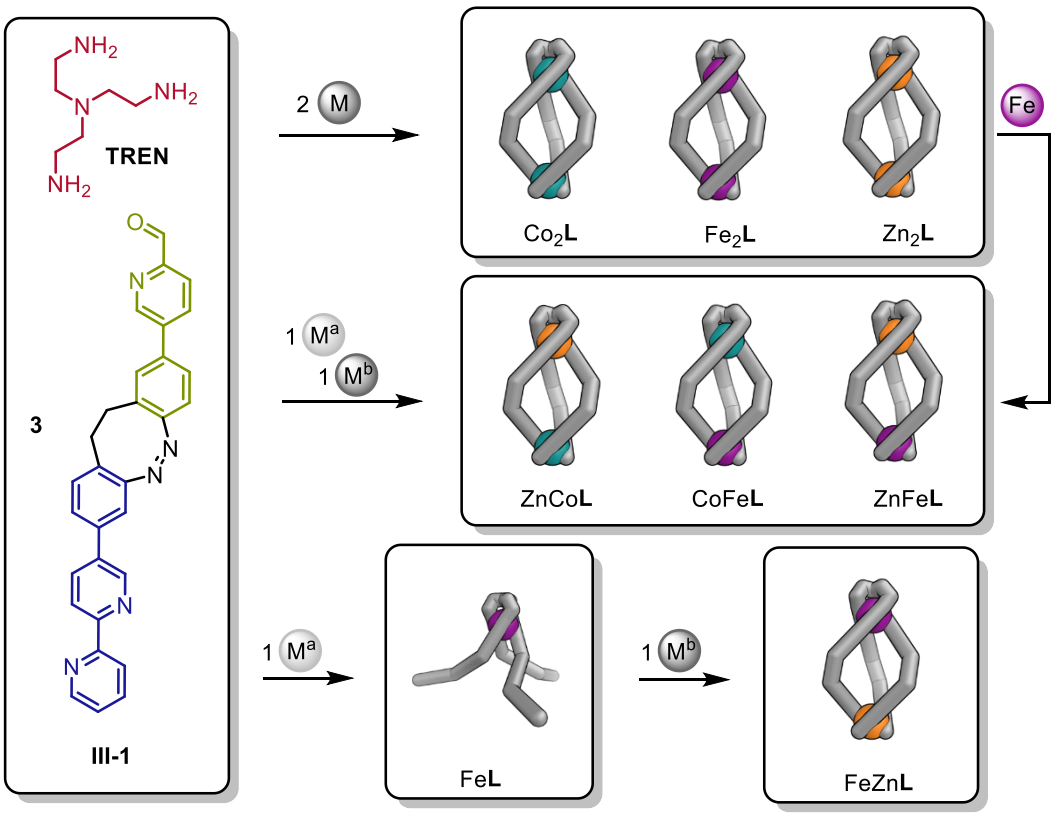

Figure 75. *Sub-component self-assembly of transition metal complexes using **III-1** and triamine **TREN**. Graphical representations of the complexes are stylized versions of geometries optimized on GFN2-xTB level.*[161]

The one-pot self-assembly of heterobimetallic helicates from a 1:1 mixture of the two metal cations was found to proceed with excellent selectivity. Quantitative self-sorting was observed for ZnCo**L** and ZnFe**L** helicates, whereas CoFe**L** was formed with slightly reduced selectivity under identical conditions. The selectivity of the self-sorting process that directs each of the two different metal cations into one of the two binding site is governed by the interplay between kinetic and thermodynamic parameters intrinsic to the metal centers. The metal ion exhibiting stronger metal-ligand binding affinity (Fe < Co < Zn)[168] preferentially occupies the bipyridine coordination site ($\mathbf{M}^{\mathbf{bipy}}$), while the metal ion with faster ligand exchange kinetics (Zn << Fe < Co)[169–171] is found in the hexadentate $\mathbf{M}^{\mathbf{TREN}}$. The mechanism of the self-sorting process was uncovered by *in-situ* UV-vis spectroscopy. Initially, both metals can bind to the bipyridines and form octahedral M(**III-1**)$_3$ complexes. In this step, both metals compete for the three equivalents of bipyridine moieties. Here, the metal with the greater binding affinity will displace the more labile metal and full conversion to free M^{weak} and bound M^{strong}(**III-1**)$_3$ is observed within minutes. This leaves the second metal (M^{weak}) to coordinated to the weaker binding pyridine carboxaldehydes and template the formation of $\mathbf{M}^{\mathbf{TREN}}$ around itself (**Figure 76**). $\mathbf{M}^{\mathbf{TREN}}$ formation was observed to occur on a timescale of multiple hours. The $\mathbf{M}^{\mathbf{bipy}}$ metal is not active in this process as it is effectively "trapped" in the bipyridine moiety by its relatively slower ligand exchange kinetics. Once $\mathbf{M}^{\mathbf{TREN}}$ has formed it is seemingly inert due the sixfold chelating ligand that results in extraordinarily slow metal exchange kinetics. Despite $\mathbf{M}^{\mathbf{TREN}}$ being thermodynamically favored over $\mathbf{M}^{\mathbf{bipy}}$ (as evidenced in Fe**L**, **Figure 75**), the metal that forms thermodynamically more stable bonds will be found in $\mathbf{M}^{\mathbf{bipy}}$.

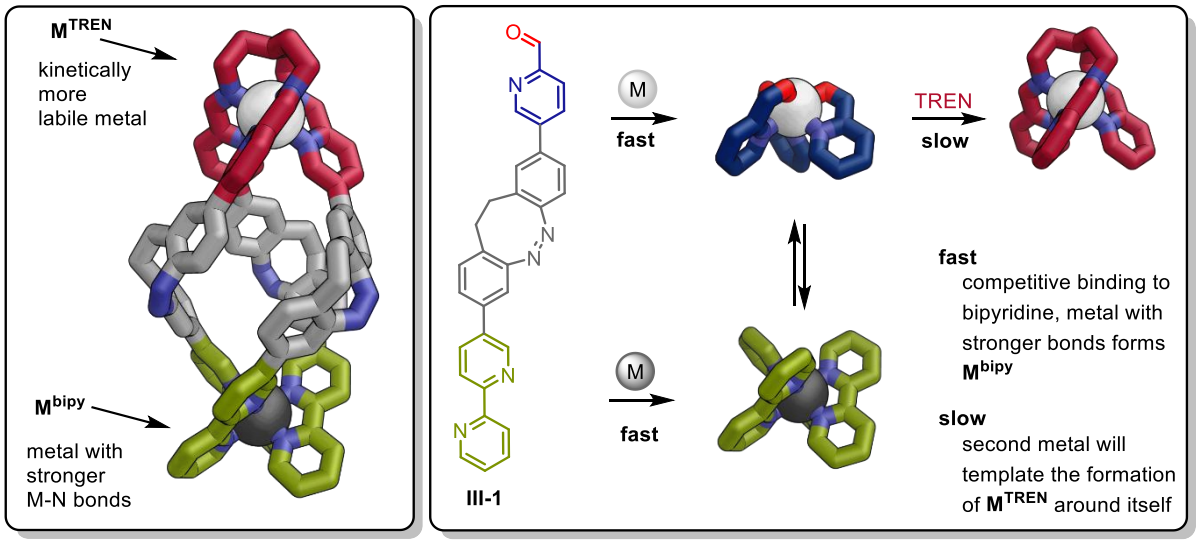

Figure 76. *Self-sorting of the heterobimetallic helicates is enabled by thermodynamic and kinetic effects. All structures are optimized on GFN2-xTB level.*[161]

Sixteen stereoisomers are possible for the triply stranded structure, enabled by the inherent axial chirality of the asymmetrically substituted diazocine core and the two octahedral metal centers. The isomers include four potential diazocine orientations (MMM, MMP, MPP, PPP) for each of the two potential octahedral chirality combinations (ΔΔ, ΔΛ) as well as enantiomers of those eight structures (**Figure 77**). Through diligent characterization using X-ray crystallography and {^{1}H,^{1}H} ROESY NMR spectroscopy we were able to determine the relative stereo information of all triply stranded complexes as a racemic mixture of the homochiral $M^{\Delta}M^{\Delta}\mathbf{L}^{(M,M,M)}$ helicate and its enantiomer.

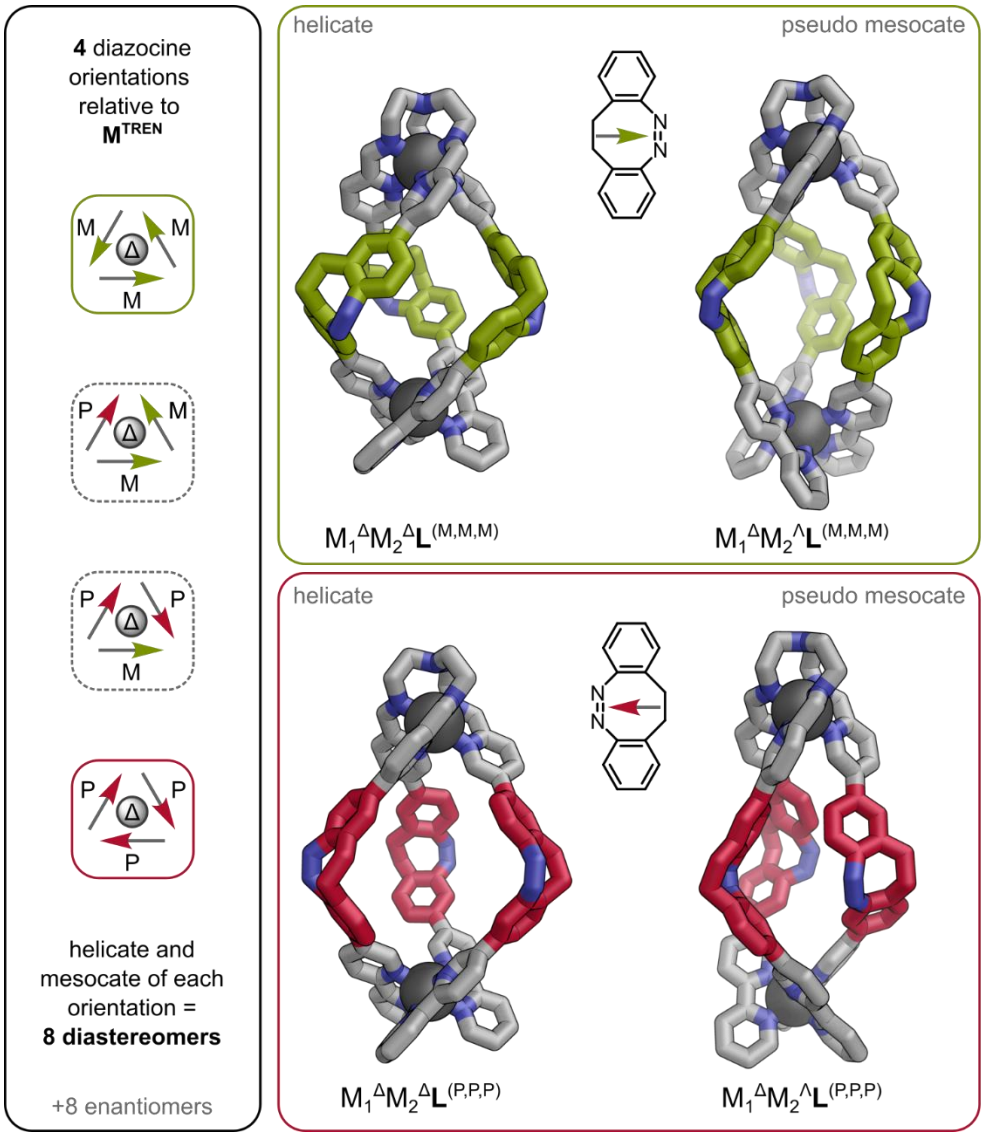

Figure 77. *Potential diastereomers and nomenclature of the diazocine stereoisomers in $M_2\mathbf{L}$. Four of the eight possible diastereomers are shown as an example. All structures are optimized on GFN2-xTB level.*[161]

4.3.5 Project Results: Photochemical Properties

The photochemical properties of the helicates were investigated using UV-vis, ^{1}H NMR spectroscopy, and ESI-MS. UV-vis spectroscopy showed that irradiation of ZnFe**L** with blue light (λ = 405 nm) switched the majority of diazocine units to the thermodynamically less stable *E*-isomer. The spectral differences before and after irradiation closely resembled those observed for the free diazocine subcomponent **III-1**, indicating that formation of the helicate does not significantly perturb the photochemical behavior of the diazocine chromophore. Corresponding ^{1}H NMR spectra of blue light irradiated ZnFe**L** showed numerous small and broadened signals (**Figure 78**, green) that sharpened upon cooling to 240 K, indicating a dynamic equilibrium between multiple conformers. We assume that photoswitching of *Z*-ZnFe**L** results in the formation of an *E*-ZnFe**L** helicate which in turn will readily isomerize to a complex mixture of constantly interconverting diastereomers termed i-*E*-ZnFe**L** (**Figure 79**, green box).

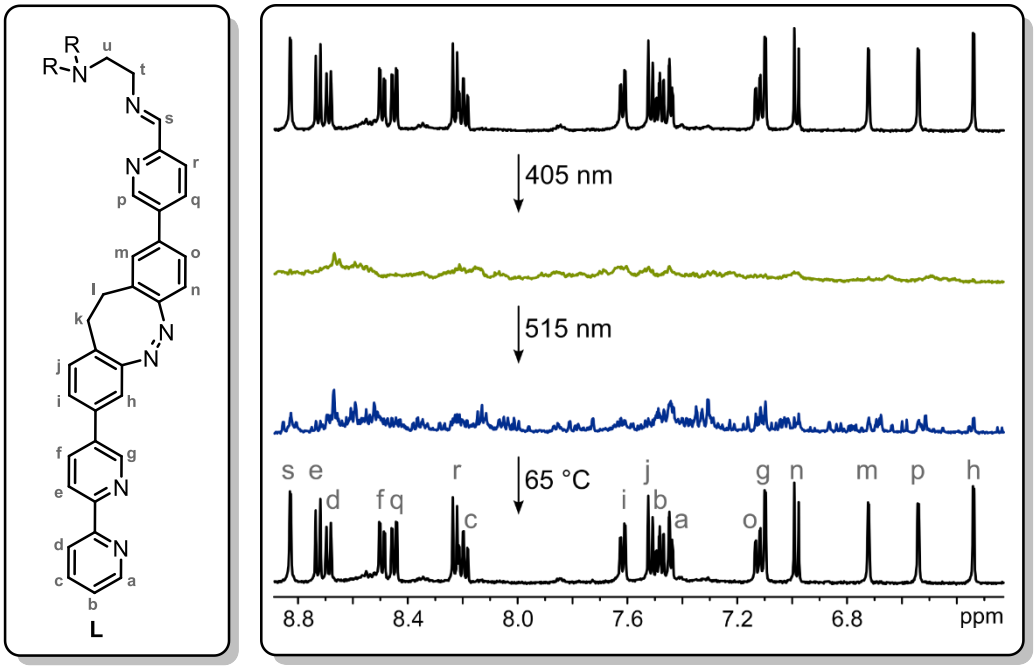

Figure 78. *^{1}H NMR spectra (500 MHz, CD_3CN) of ZnFe**L** under ambient conditions (298 K, black), after 405 nm light irradiation (1 min; 298 K, green), after 515 nm light irradiation (1 min, 298 K, blue), and after heating to 65 °C (5 h, 298 K, black).*

Subsequent irradiation of the i-*E*-ZnFe**L** state with longer wavelengths (λ = 500 nm, 515 nm, or white light) resulted in complete back-isomerization of the diazocines to their thermodynamically favored *Z*-state, as evidenced by UV-vis spectroscopy. The ^{1}H NMR spectrum exhibited a multitude of sharp signals (**Figure 78**, blue), most of which were distinct from the ground state of ZnFe**L**. We assume that returning the diazocines from their linear *E*-state to their bent *Z*-state drastically increases the energy barrier of the isomerization process, therefore “freezing out” the isomeric mixture as i-*Z*-ZnFe**L** (**Figure 79**, blue box). Heating this

state to 65 °C for 5 hours resulted in full recovery of the original NMR spectrum of *Z*-ZnFe**L** (**Figure 78**, black), indicating that photoswitching produced kinetically trapped states. ESI-MS analysis confirmed that the stoichiometry of the helicate remained unchanged throughout all states of the switching process, ruling out decomposition or formation of other structures. A similar behavior was observed for Zn_2**L**, with the only difference being that a lower temperature was needed to kinetically trap the isomerized states, indicating that the activation barrier for isomerization depends on the bond strength and kinetic lability of the metal in $\mathbf{M}^{bipy}$.

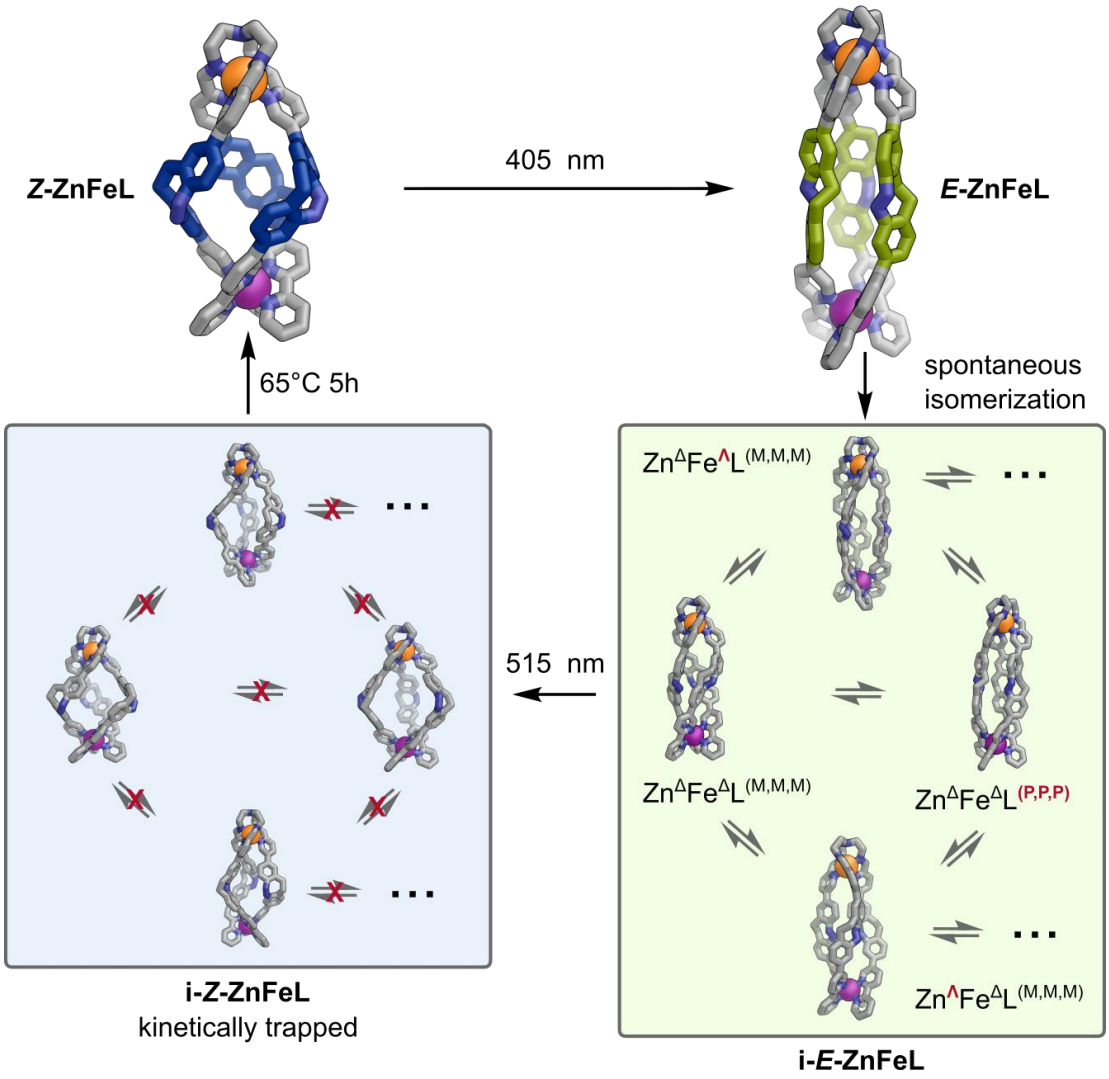

Figure 79. *Proposed processes during the photoswitching of ZnFe**L**. Rapid interconversion of isomers is possible in the E state (green box). When switching back to the Z state, the kinetic barrier for interconversion becomes much larger and the isomers become kinetically trapped, resulting in atropisomers. All structures are optimized on GFN2xTB level.*[161]

4.3.6 Project Results: Interpretation as an Energy Ratchet

The photoswitching behavior of the helicates is an energy ratchet (see Chapter **2.4**), wherein light energy is harnessed to drive the system into a high-energy, out-of-equilibrium state.

The system starts out in the thermodynamic equilibrium where population of the isomers is Boltzmann distributed according to their relative energy. The helicate exclusively exists as a racemic mixture of *Z*-Zn$^{\Delta}$Fe$^{\Delta}$**L**$^{(M,M,M)}$ (**Figure 80**, **A**). Irradiation of the helicate with blue light (λ = 405 nm) induces diazocine *Z*→*E* isomerization, significantly altering the energetic landscape of the system (**Figure 80**, **B**). Isomers i-*E*-ZnFeL are now the lowest energy isomers (**Figure 80**, $\Delta E_1 > \Delta E_2$). Drastically reduced activation barriers (**Figure 80**, $E_{A1} > E_{A2}$) enable the system to quickly reach a new Boltzmann distributed population with a large population of the i-*E*-ZnFeL isomers (**Figure 80**, **C**). Back-isomerization of the diazocines to the *Z* configuration restores the initial energy landscape. Due to the higher activation barrier, i-*Z*-ZnFeL isomers are kinetically trapped in a high energy state which would not be populated under thermal equilibrium conditions (**Figure 80**, **D**). Heating returns the system to the thermodynamic equilibrium by providing the activation energy needed to restore the Boltzmann distributed population of the isomers.

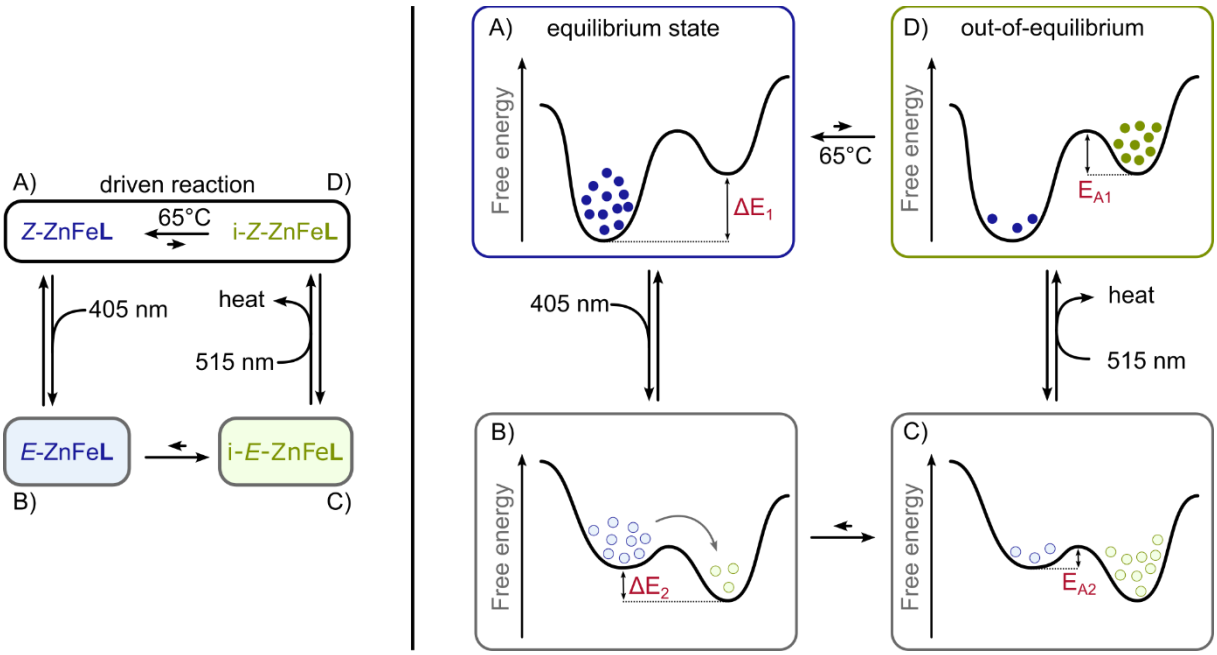

Figure 80. *Energy ratchet mechanism and schematic representation of the energy profiles during energy ratchet operation.*

White light irradiation of thermally equilibrated ZnFe**L** for one day resulted in the accumulation of a single new isomer (**Figure 81**). Just like the i-*Z*-ZnFe**L** isomers, this state is kinetically trapped and heating to 65°C will reform the initial state. Two dimensional {^{1}H,^{1}H} ROESY NMR allowed us to determine the relative stereo information of the new state as Zn$^{\Delta}$Fe$^{\wedge}$**L**^{MMM} and its enantiomer. Exposing ZnFe**L** to sunlight also accumulates this isomer, meaning that the system can absorb and store sunlight in the form of kinetically trapped high-energy isomers. Under white light irradiation, *E* → *Z* switching is very fast and a photostationary state of 99% *Z*-isomer is observed. However, this does not mean that *Z* → *E* switching is not occurring, it only implies that it is much slower. This slow *Z* → *E* switching is enough to operate the energy ratchet, accumulating metastable i-*Z*-ZnFe**L** isomers. Over the long time period of twenty-four hours, the mixture of metastable isomers undergoes what might be understood as a thermal annealing process, eliminating kinetically labile isomers and furnishing just the kinetically most stable isomer. Operating under continuous irradiation is an exceptional behavior as most energy ratchets require a chemist's intervention to toggle between two stimuli such as λ = 405 nm and then λ = 515 nm irradiation or sequential addition of reagents.[126] The extraordinary ability to operate under continuous irradiation makes this system an autonomously operating energy ratchet. It is remarkable that the ratchet mechanism amplifies a photostationary state of 1% *E*-isomer under white light into 70% of the new isomer being formed.

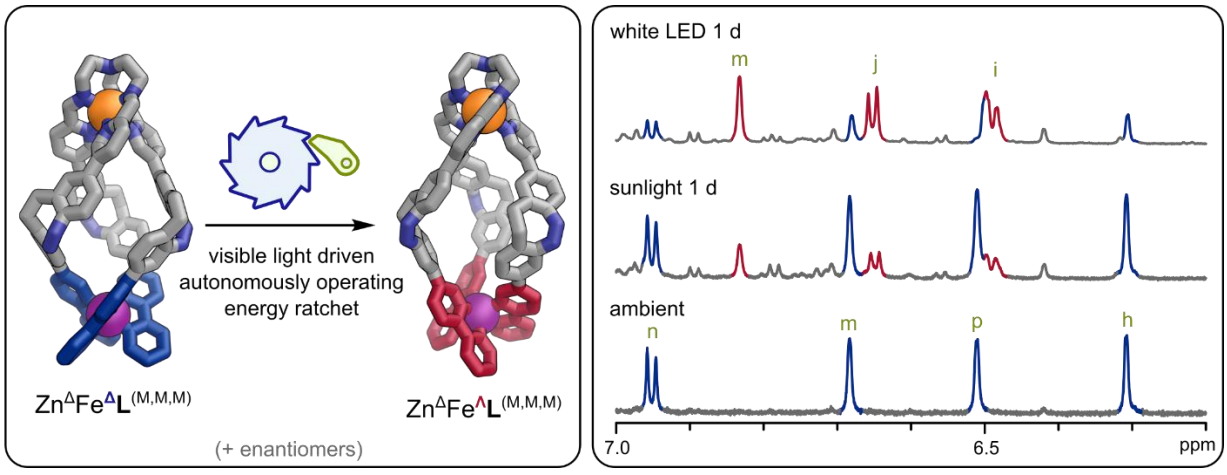

Figure 81. *Continuous white light irradiation powers the ratchet autonomously, leading to the formation of a mesocate (Z-Zn$^{\Delta}$Fe$^{\wedge}$**L**^{MMM}). ^{1}H NMR spectra (500 MHz, CD$_3$CN, 298 K) of ZnFe**L** under ambient conditions, after white light irradiation for 24 h, and after one day of sunlight. Signals corresponding to Z-Zn$^{\Delta}$Fe$^{\Delta}$**L**^{MMM} in blue, signals corresponding to Z-Zn$^{\Delta}$Fe$^{\wedge}$**L**^{MMM} in red. All structures are optimized on GFN2-xTB level.*[161]

The formation of high energy isomers accelerates processes that can harness the high energy isomers of the helicate. Therefore, we investigated the selective metal exchange reaction of Zn_2**L** to form ZnFe**L**. We used *in-situ* UV-vis spectroscopy, following the absorbance at λ = 550 nm where the **Fe^{bipy}** MLCT band appears (**Figure 82**). If the reaction is carried out in the dark, a slow background reaction is observed (**Figure 82**, black dotted line). Irradiation of the reaction mixture with λ = 405 nm light for one minute every 20 minutes resulted in an initial increase of the absorbance at λ = 550 nm due to the *E*-diazocine chromophore (**Figure 82**, red line). After this decayed with a thermal half-life of one minute a plateau was reached that was significantly higher than the background reaction. Each consecutive irradiation step increased this difference, indicating that each irradiation step resulted in an accelerated formation of ZnFe**L** that stopped once all chromophores were back in their *Z*-state. Continuous irradiation with λ = 405 nm light for 60 minutes enabled determination of the reaction rate (**Figure 82**, green dotted line) under irradiation and in the dark. This revealed a five-fold acceleration of the metal exchange rate enabled by the operation of the energy ratchet. The acceleration of the exchange process can be precisely controlled by targeted irradiation, giving the chemist spatial and temporal control over chemo selective iron(II) uptake in bulk solution, akin to an arcade claw machine that can be steered to selectively grab on the molecular scale (**Figure 83**).

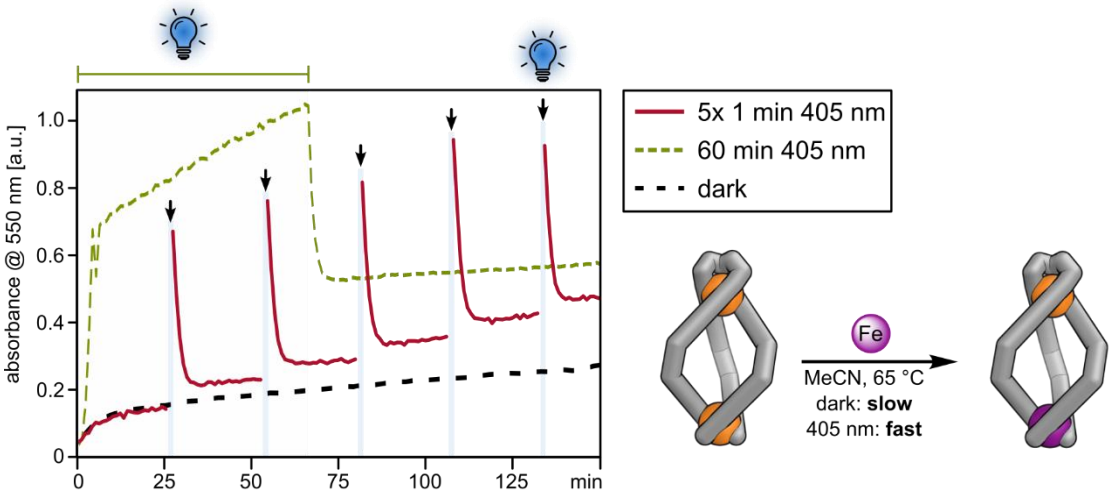

Figure 82. *In-situ UV-vis spectroscopy of the metal exchange reaction of Zn_2**L** to ZnFe**L** by mixing $Fe(OTf)_2$ (1.5 equiv.) and Zn_2**L** (CH_3CN, 0.06 mM, 65 °C). The reaction progress can be derived from the absorbance at λ = 550 nm that corresponds to the **Fe^{bipy}** MLCT band. Black dotted line: background reaction in the dark. Green dotted line: continuous irradiation with λ = 405 nm. Red line: irradiation with λ = 405 nm for one minute every 20 minutes. The steep increases of the absorbance correspond to the absorbance of the E-diazocine that decays with a thermal half-life of one minute.*

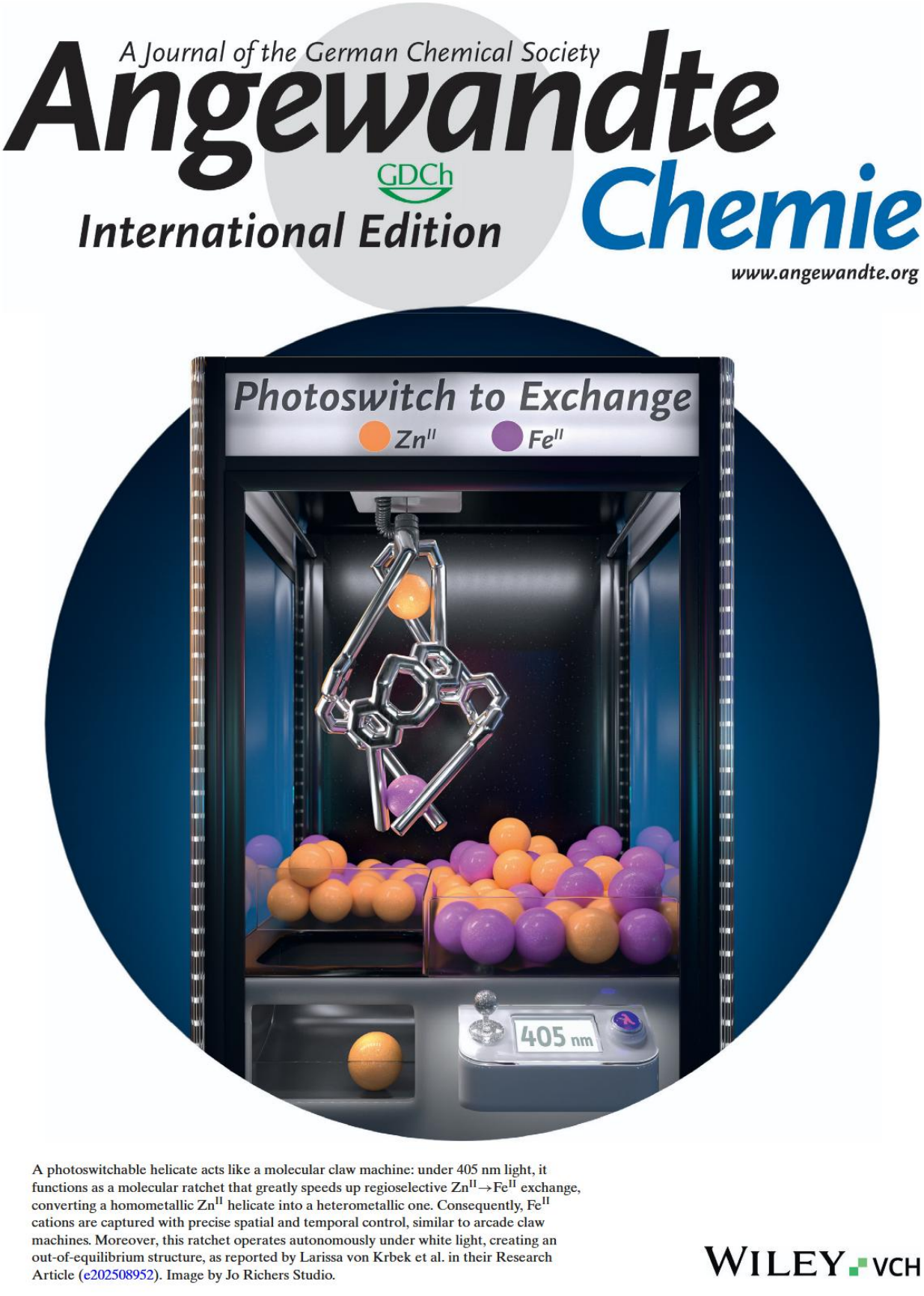

Figure 83. *Outside Back Cover: Light-Driven Ratchet Mechanism Accelerates Regioselective Metal-Cation Exchange in a Heterobimetallic Helicate.*[172] *Reprinted from Angewandte Chemie International Edition*[172] *with permission from John Wiley and Sons under license number 6106431263601.*

4.3.7 Project Summary

We synthesized a novel photoswitchable diazocine-based ligand **III-1** that forms a series of photo-responsive metallo-supramolecular bimetallic helicates in a one-pot sub-component self-assembly reaction. We achieved highly selective self-sorting of heterobimetallic ZnFe**L** and ZnCo**L** helicates with precise metal distribution through the interplay of bond strength and kinetic lability at the ligand coordination sites and the metal centers. During the self-sorting process, the $\mathbf{M}^{\mathbf{bipy}}$ coordination site is formed first and binds the metal with stronger N-M bonds, leaving the second metal to template the formation of $\mathbf{M}^{\mathbf{TREN}}$ around itself while the first metal stays trapped in the $\mathbf{M}^{\mathbf{bipy}}$ coordination site.

We showed that *Z*→*E* photoisomerization of the diazocines in Zn_2**L** and ZnFe**L** results in conformational changes while preserving the overall integrity of the helicate. The formation of these high-energy atropisomers is driven by a light-driven molecular energy ratchet mechanism that stores part of the light energy in the form of metastable isomers. Notably, the energy ratchet was also operating under continuous white light irradiation, making this a rare example of an autonomously operating energy ratchet. The metastable isomers contain a less stable $\mathbf{M}^{\mathbf{bipy}}$ site which enables light-controlled acceleration of metal-cation exchange from homobimetallic Zn_2**L** to heterobimetallic ZnFe**L**.

Our work expands the structural complexity and functionality of photoswitchable complexes and highlights the potential of light to drive supramolecular systems out of equilibrium, opening avenues for light-controlled molecular machines, stimuli-responsive catalysis, and smart materials with tunable energy storage and release properties.

5 Conclusion and Outlook

5.1 Insights Into Cyclic Azobenzenes

The first part of this thesis involved the synthesis of photoresponsive building blocks. Compared to azobenzene (**Figure 84**), the photoswitching properties of novel photoswitch **I-1** are defined by a mediocre photostationary state for $E \rightarrow Z$ switching, excellent $Z \rightarrow E$ switching that is nearly quantitative under visible light, and a much longer thermal half-life of 16 days.[140]

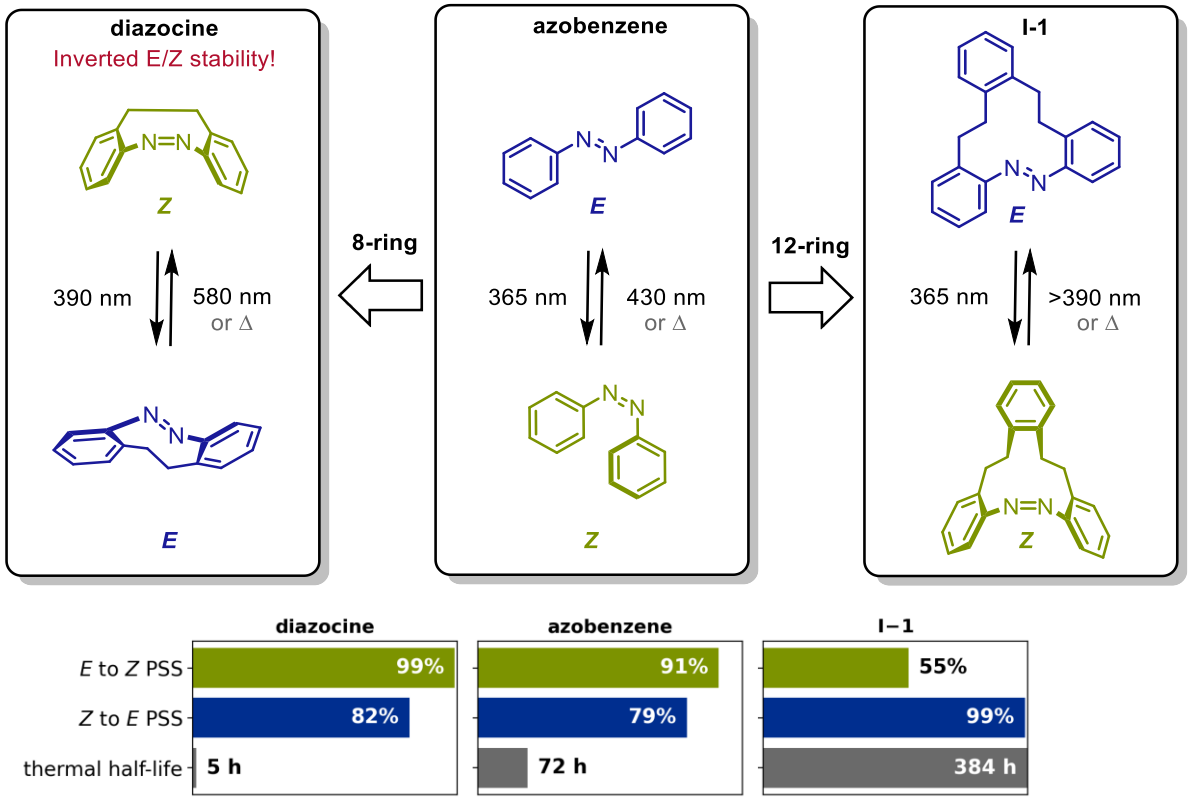

Figure 84. *Comparison of photoswitching properties of azobenzene with cyclic twelve and eight membered derivatives.*[46,140]

Diazocines contain an eight membered ring and show quantitative $E \rightarrow Z$ switching and drastically decreased thermal half-life. Interestingly, this is the opposite behavior as in twelve-membered **I-1**. These differences are a direct result of a flexible twelve-membered structure compared to a strained eight-membered ring. Comparing the UV-vis spectra of the three switches (**Figure 85**, *E*-isomers in blue, *Z*-isomers in green) reveals drastic changes in the relative intensity of the $S_1n\pi^*$ transitions.

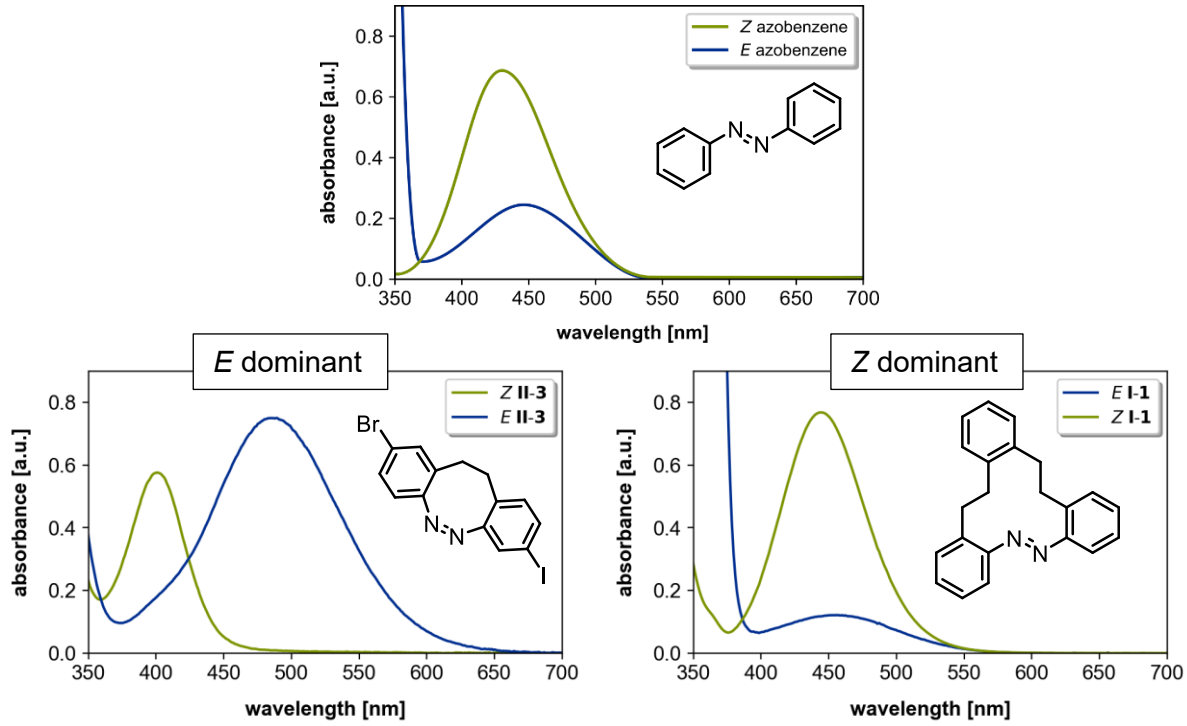

Figure 85. *Comparison of the spectra of the E and Z states of azobenzene,[23,24] twelve membered ring I-1[140] and eight membered ring II-3.[159] Note that the colors of the E and Z state of the diazocine are inverted from the rest of the thesis to facilitate comparability.*

Differences in ring strain and backbone flexibility can therefore result in excellent switching behavior, enabling quantitative *E* → *Z* switching in diazocines by drastically increased vibronic coupling in the *E*-S_1nππ* transition while on the other hand enabling quantitative *Z* → *E* switching due to drastically decreased vibronic coupling in the *E*-S_1nππ* transition of **I-1** (**Table 4**). Through comparison with 2,2'-dimethyl azobenzene (**MeAzo**), the reason for the mediocre *E* → *Z* switching in **I-1** was found to be a low quantum yield for the photoswitching process following *E*-S_2ππ* excitation. Despite nearly identical spectral profiles of the *E*-S_2ππ* transition in both **MeAzo** and **I-1**, it took much longer for **I-1** to reach a steady state under light irradiation, thus indicating that the flexible bridge enables nonproductive relaxation pathways that reduce quantum yield.

Table 4. *Comparison of selected diazocine and **I-1** photoswitching properties.*

Ring size	Ring strain	Relative intensity	outcome
8	high	*E*-S_1 > *Z*-S_1	quantitative *E* → *Z* switching
12	low	*E*-S_1 < *Z*-S_1	quantitative *Z* → *E* switching

5.2 Rapid Characterization of Photoswitches

An integral part of this thesis was the investigation of photoresponsive compounds. Initial implementations of characterization methods by HPLC or UV-vis spectroscopy had significant limitations such as relying on the determination of an isosbestic point.[140] This isosbestic point is highly sensitive to solvent, temperature, and concentration, thereby compromising the flexibility and accuracy of both methods. Although NMR spectroscopy allows direct observation and integration of both isomers, achieving sufficient irradiation to reach the PSS was challenging due to the curved glass of NMR tubes, which results in low photon flux within the solution.[140]

This issue was partially addressed through *in-situ* illuminated NMR spectroscopy (Chapter **4.1,**). For this method, a special quartz glass fiber where one end had been carefully exposed and filed rough was placed in a coaxial insert tube made from quartz glass that was then inserted into an NMR tube containing the sample (**Figure 86).**

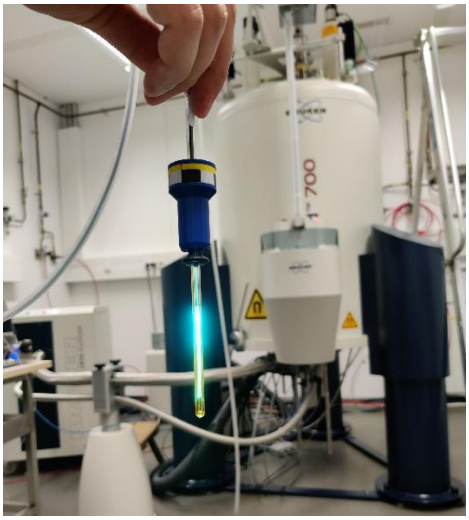

Figure 86. *NMR sample with quartz glass insert and optical fibre for in-situ illumination during NMR experiments.*

Using fiber coupled light sources enables direct irradiation while the sample is inside of the spectrometer. This allows for the direct observation of the photostationary state without having to stop irradiation, which is crucial for switches with fast thermal relaxation. Additionally, this enables measurement of *in-situ* kinetics of photochemical reactions. While this method has unique features that cannot be replicated by *ex-situ* illumination methods, it also exhibits a few drawbacks. Most importantly, the additional objects in the spectrometer perturb the homogeneity of the magnetic field, leading to automatic shimming algorithms failing and requiring an experienced NMR technician to manually shim the magnetic field. Still, the spectral

quality remains dramatically lowered which restricts the use of this system to the 700 MHz spectrometer. Additionally, preparing the experimental setup is tedious and time-consuming, limiting the number of samples that can be investigated per day to just two or three. With spectrometer time being a bottleneck for further investigations, an improved method for reliable NMR sample irradiation was needed.

Reliable irradiation of NMR samples without the drawbacks of *in-situ* illumination was finally enabled by developing 3D printed light sources for *ex-situ* illumination. These use commercial LED chips (**Figure 87**) and enabled an improved workflow that reduced the time for photochemical characterization drastically.[159]

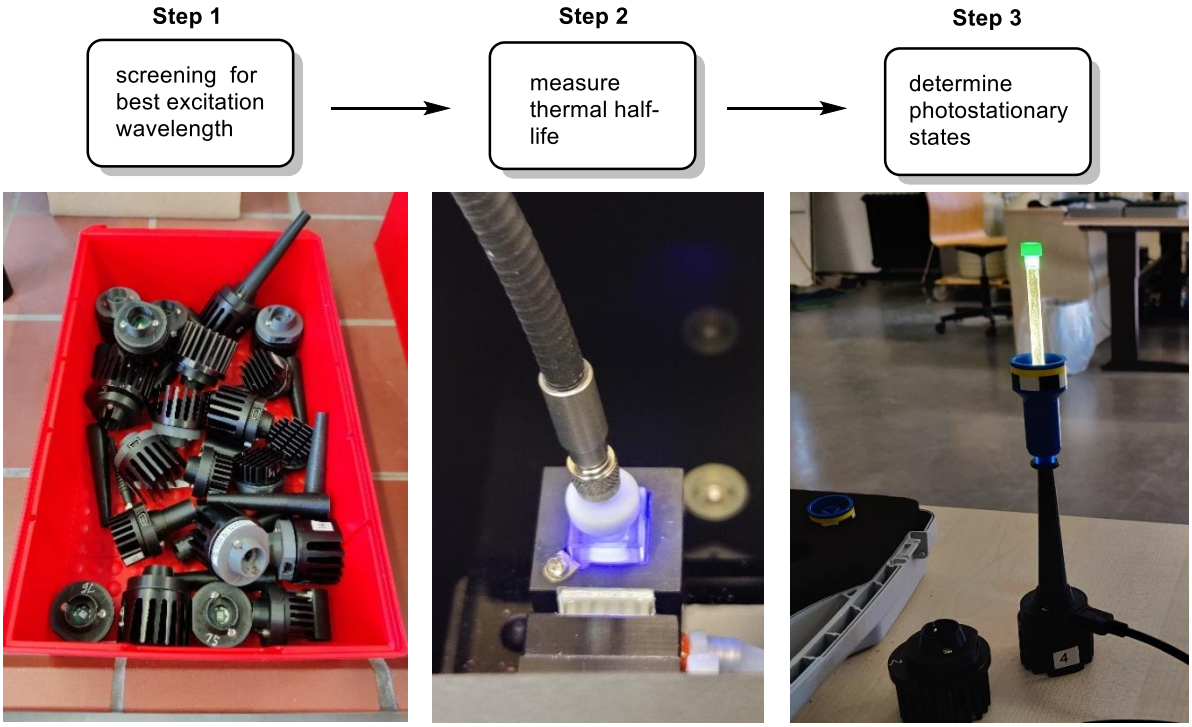

Figure 87. Left: *Stockpile of self-built light sources containing cheap commercial LED chips enable broader screening.* ***Middle:*** *A modified cuvette lid with a centrally drilled hole enables hassle-free recording of in-situ illuminated UV-vis spectra. The spectrometer is fitted with a Peltier element for heating and cooling which makes recording of spectra at specific temperatures trivial.* ***Right:*** *Portable, 5 V USB powered, 3D printed light sources suitable for ex-situ illumination of NMR tubes and 2 mL vials enable fast and flexible irradiation of samples.*

The new light sources can be powered by 5 V USB phone chargers/power banks. The light sources are designed in a way where the glass of the NMR tube is directly touching the LED chip, with the whole tube acting as a lightguide. Adapters for NMR tubes or 2 mL GC vials can be easily exchanged, enabling flexible usage and allowing samples to be irradiated everywhere, making *ex-situ* illuminated HPLC, NMR, and MS experiments trivial.[161] To demonstrate the effectiveness of these light sources, an NMR sample of red *E*-diazocine was irradiated with white light (**Figure 88**). Initially, the light shining through the tube appears red due to the intense absorbance at 500 nm of the *E*-diazocine. The red color fades within seconds and the light shining through appears white/yellow since *Z*-diazocine has a much weaker absorbance band at around 400 nm. This demonstrates the high photon flux that is generated in the solution inside of the NMR tube and just seconds of irradiation are sufficient to reach the PSS.

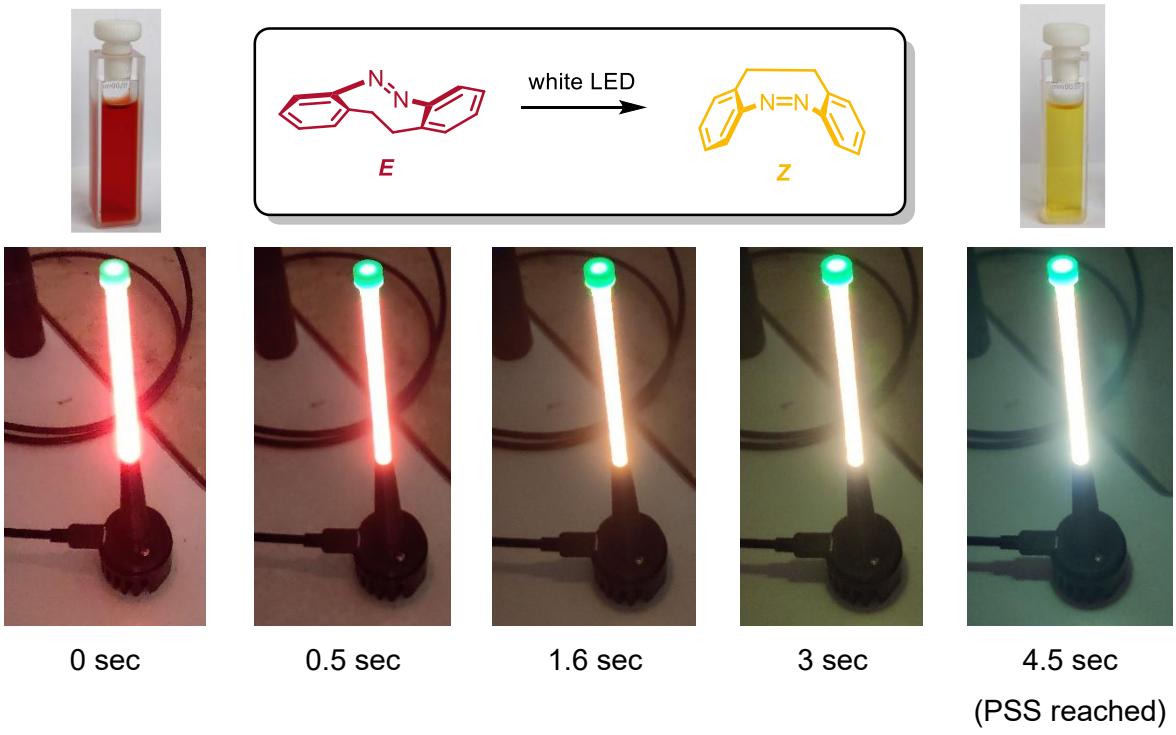

Figure 88. *Photochromic response of an E-diazocine sample in an NMR tube under white light irradiation using custom light source (MeCN, 1mM, frames extracted from a video).*

Ex-situ illumination has significant drawbacks for photoswitches with very fast thermal relaxation or when the photochemical process itself must be investigated. However, since all photoswitches herein are sufficiently stable with thermal half-lives of more than 30 minutes these new light sources resulted in a series of benefits (**Figure 89**). Compared to the fiber collimated light sources, the cost per light source was reduced by 98%, which facilitated testing across a much wider range of wavelengths. Custom 3D printed adapters enable reliable *ex-situ* irradiation of NMR samples with high photon flux, cutting irradiation times by at least 80% when compared to *in-situ* irradiation due to brighter LED chips being used. Additionally, compared to other *ex-situ* irradiation methods that are not suitable for NMR tubes this eliminates darkroom sample transfers. As a result of the flexible *ex-situ* illumination approach, total NMR instrument time required for photochemical characterization of a single compound fell by 94% compared with the slower and lower-quality *in-situ* illumination method.

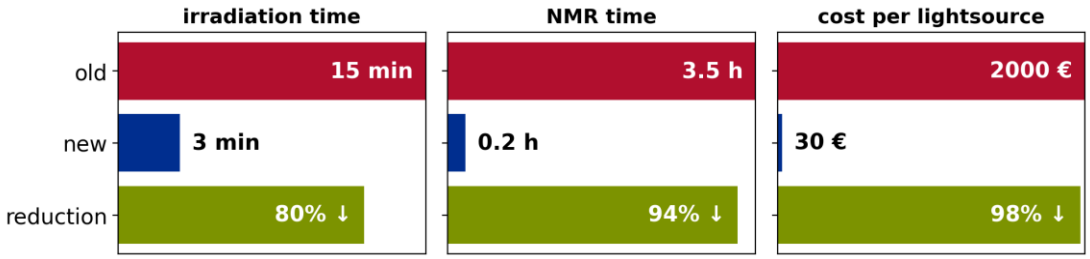

Figure 89. *Improvements for the characterization of photoswitchable molecules when using the newly developed LED sources for ex-situ illumination as compared to fiber coupled in-situ illumination.*

5.3 A Photoresponsive Ligand

Building on the experiences gained during synthesis and investigation of twelve-membered cyclic azobenzene **I-1**, we proceeded to target a 2,8-diazocine based photoresponsive ligand that combines reliable photoswitching with a pseudo-linear residue arrangement. Compared to symmetrically 2,9- or 3,9-disubstituted diazocines, the 2,8-substitution pattern provides a larger conformational change to be harnessed in driving self-assembled metal-organic architectures towards high-energy metastable states, while still maintaining the diazocines excellent photochemical properties.

The 2,8-dihalogenated diazocine was obtained from a four-step synthesis starting from an electron-deficient nitro precursor **II-D** (**Figure 90**). The sequence begins with a statistical, *meta*-selective iodination to introduce the first halide, followed by reduction of the resulting isomer mixture to a bis-aniline intermediate. At this stage, automated column chromatography is the critical step that allows highly reproducible isolation of the desymmetrized precursor. This chromatographic separation enables straightforward scale-up to a reaction scape of at

least 60 mmol (≈26 g) without loss of selectivity. Subsequent low-temperature bromination of the mono-iodinated bis-aniline proceeds quantitatively and controlled oxidative ring closure by slow addition of *m*CPBA furnishes the 2,8-dihalogenated diazocine **II-3**. Several alternative synthetic approaches were investigated, but proved unable to produce the asymmetric dihalogenated motif.

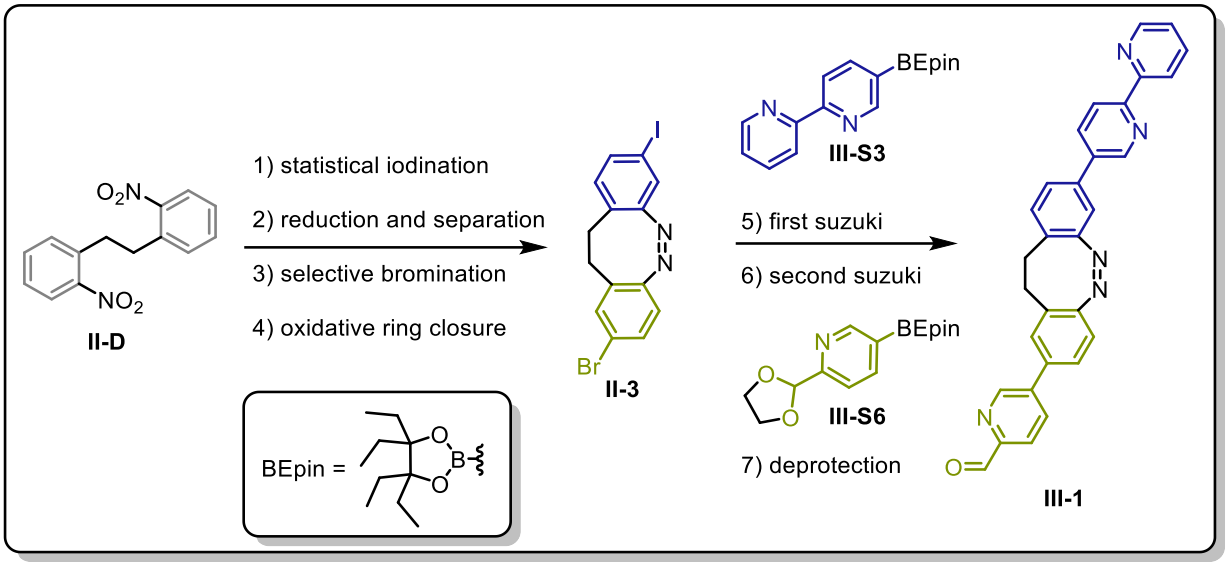

Figure 90. *Seven step synthesis of pre-ligand **III-1**. Conditions: 1) NIS, H_2SO_4. 2) $Na_2S_2O_4$, Na_2CO_3, paraquat. 3) NBS, -78 °C. 4) mCPBA, HOAc. 5) $(dppf)PdCl_2$, K_3PO_4, 50 °C. 6) $(dppf)PdCl_2$, K_3PO_4, 70 °C. 7) HBF_4.*

The 2,8-dihalogenated diazocine is a versatile building block for the divergent syntheses of a whole series of potential building blocks that share its large geometry changes during switching. Using two consecutive Suzuki couplings, the 2,8-dihalogenated diazocine **II-3** was transformed into preligand **III-1**. Suzuki couplings containing either halogenated diazocines[173] or heteroaryl boronic acids/esters[163] are documented to be challenging, even with an ideal coupling partner. Only one reference of a Suzuki coupling of both molecule types exists, resulting in a poor yield of 7-19%.[164] Diazocine halides are poor cross-coupling partners that show slow reactions while heteroaryl boronic acids quickly undergo autocatalytic decomposition. Therefore, the sensitive boronic acids were converted into ethyl pinacol (EPin) esters and a deliberately less reactive but highly selective catalyst system was selected to suppress side reactions. A slow-release strategy for the EPin boronate was applied where slow boronate hydrolysis matches the modest reactivity of the halide partner. These combined measures permitted reliable formation of the desired C-C bonds and following a deprotection reaction delivered preligand **III-1** in good and reproducible yields.

5.4 Diazocine Helicate - Heterobimetallic One-Pot Self-Sorting

After successfully establishing synthetic access to heteroleptic pre-ligand **III-1**, we used it to synthesize a series of self-assembled photoresponsive metal-organic helicates (**Figure 91**). Combining three equivalents of pre-ligand **III-1** with one equivalent of a trivalent amine (TREN) and two equivalents of either cobalt(II), iron(II), or zinc(II) triflate results in the formation of homometallic helicates Co_2**L**, Fe_2**L**, and Zn_2**L**. Pre-ligand **III-1** was deliberately designed with two different coordination sites, allowing for the formation of self-sorted heterobimetallic helicates ZnCo**L**, CoFe**L**, and ZnFe**L** when using one equivalent each of two different metal salts. This demonstrated how carefully designed heteroleptic ligand **III-1** used in a one-pot self-assembly reaction can deliver perfectly self-sorted (hetero)bimetallic helicates with excellent diastereo- and regioselectivity.

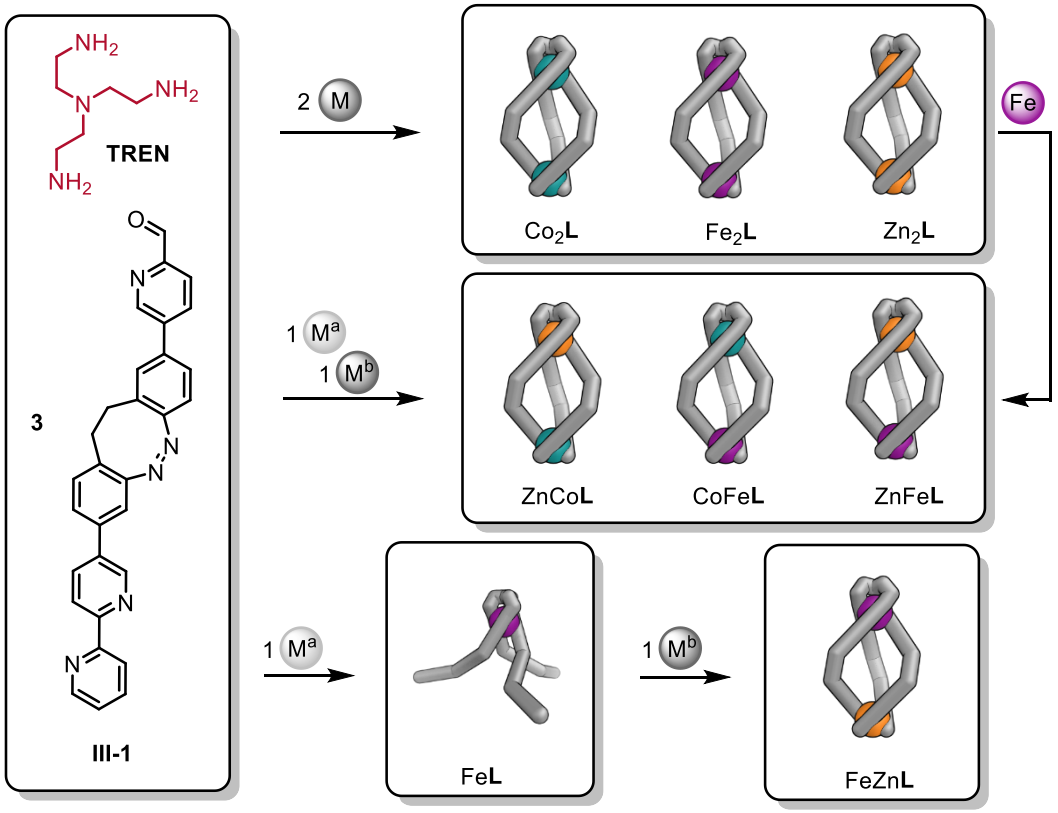

Figure 91. *Sub-component self-assembly of transition metal complexes using **III-1** and triamine **TREN**. Graphical representations of the complexes are stylized versions of geometries optimized on GFN2-xTB level.*[161]

Single crystal X-ray diffraction structures of Fe_2**L** and ZnFe**L** unambiguously confirmed the three-stranded helical structure (**Figure 92**). The solution structure was confirmed to be identical by ROESY NMR and UV-vis spectroscopy as well as ESI-HRMS. It must be noted, that the structure exists as a racemic mixture of enantiomers, but for better readability all

figures just show one of the two enantiomers. The “top” coordination site that is a product of the sub-component assembly was termed **M**$^{\mathbf{TREN}}$ while the “bottom” coordination site containing the bipyridine moieties was termed **M**$^{\mathbf{bipy}}$.

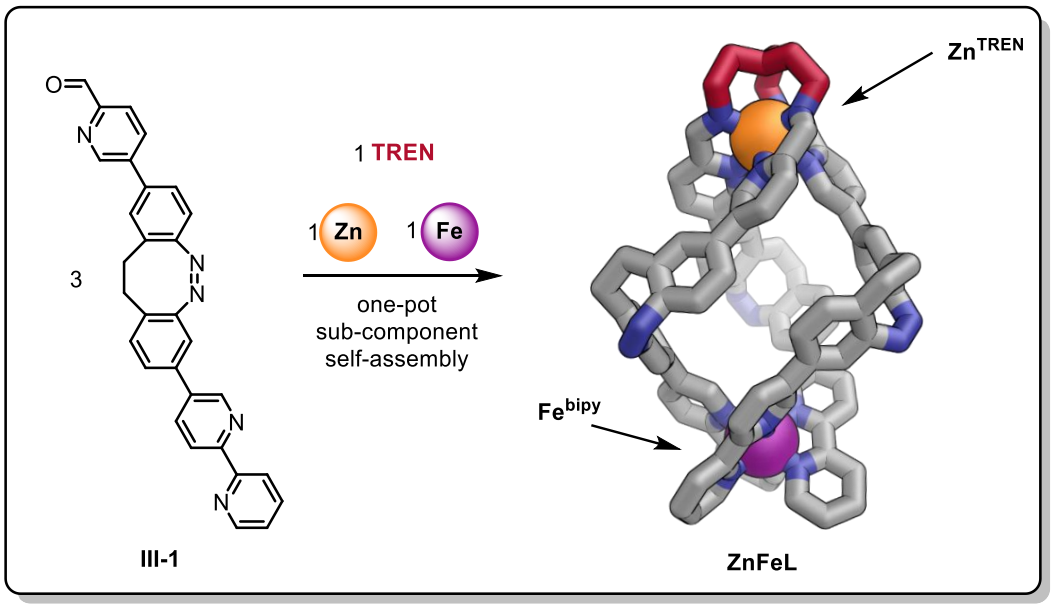

Figure 92. *One-pot sub-component self-assembly of self-sorted FeZn**L** helicates from three equivalents of diazocine **III-1**, one equivalent of a trivalent amine (TREN) and one equivalent of zinc(II) and iron(II) ions each (crystal structure, hydrogens and counter anions omitted for clarity).*

Heterobimetallic helicate ZnFe**L** could also be obtained by a metal exchange reaction of Zn_2**L** in the presence of Fe(II) ions. The **Zn**$^{\mathbf{bipy}}$ ion in the bipyridine coordination site is selectively replaced by Fe(II) to quantitatively yield ZnFe**L**. The helicate with the inverse metal distribution (FeZn**L**) could be accessed in a stepwise procedure. First, a self-assembly reaction with just one equivalent of Fe(II) predominantly forms monometallic Fe**L**, where the bipyridine moiety is empty and the Fe(II) ion is located only in the **M**$^{\mathbf{TREN}}$ position. Subsequent addition of Zn(II) triflate resulted in the formation of FeZn**L** as the major product, showcasing that all four potential distributions Zn_2**L**, ZnFe**L**, FeZn**L**, and Fe_2**L** are synthetically accessible and stable. This indicates that both coordination sites will readily bind both metal ions. Therefore, the observed selectivity is not due to metal selective binding sites, but instead a direct outcome of the assembly process.

In-situ UV-vis kinetic experiments provided mechanistic insight into the self-sorting process. Time-resolved absorption spectroscopy of the self-assembly process of Fe_2**L**, Fe**L**, and ZnFe**L** revealed drastically different timescales for the formation of the two binding sites. **M**$^{\mathbf{bipy}}$ formed in less than five minutes while **M**$^{\mathbf{TREN}}$ only formed over multiple hours. Initially, the metal cations compete for the bipyridine units of the pre-ligand, forming M(**III-1**)$_3$ complexes. If two different metals are present, the metal with the greater M-N bond strength (Fe>Co>Zn) will displace the

other metal. $\mathbf{M}^{\mathbf{bipy}}$ formation essentially sequesters the stronger binding metal from the $\mathbf{M}^{\mathbf{TREN}}$ formation process, as its Lewis acidity is decreased and its coordination sphere is saturated, meaning it will no longer catalyze the formation of the iminopyridines. This leaves the uncoordinated second metal to bind to the pyridine carboxaldehyde moieties where it will template the formation of $\mathbf{M}^{\mathbf{TREN}}$ around itself. Once $\mathbf{M}^{\mathbf{TREN}}$ is formed, it is kinetically inert, making metal exchange a slow process that takes months even at elevated temperatures. In addition to the differences in M-N bond strength (Fe>Co>Zn), the difference in ligand exchange kinetics (Co≈Fe>Zn) play a role in defining self-sorting results, as self-sorting is less efficient in CoFe**L** than in ZnFe**L** or ZnCo**L**. For the metal in $\mathbf{M}^{\mathbf{bipy}}$ to be effectively sequestered, it must show slower ligand exchange kinetics than the second metal, essentially being kinetically trapped.

In summary, the selective formation of (hetero)bimetallic helicates is enabled by three key concepts. Firstly, careful ligand design encoded the final structure in its building blocks, enabling a **one-pot** self-assembly reaction in which a complex network of reversible reactions form complementary interactions, allowing the system to reach its thermodynamic minimum and form only the most stable product where positive interactions are maximized. Secondly, to minimize synthetic effort, a **sub-component** self-assembly approach was used. This allowed the simultaneous formation of both covalent and coordinative bonds from simpler precursors during the self-assembly process. Thirdly, **self-sorting** of metal ions occurs during the assembly process based on their innate properties, directing them into separate, albeit very similar, coordination sites. This remarkable level of control in a complex single reaction step pushes the boundaries of fidelity previously reported for photoresponsive metal-organic assemblies and highlights how combining molecular switching motifs with designed coordination sites permits access to structurally complex assemblies.

5.5 Diazocine Helicate - Photoswitching and Energy Ratchet

The photoresponsive behavior of the helicates was found to involve a mechanism in which chromophore isomerization reversibly changes the helicate structure and its reactivity. Irradiation with blue light (405 nm) switches the diazocine units into their metastable *E*-isomer (**Figure 93**, step 1). This immediately enables rapid structural reorganization into a complex mixture of interconverting species, as indicated by a multitude of very broad, ill-defined signals in the NMR spectrum (**Figure 93**, step 2). Subsequent back-switching with green light (500 nm) returns the diazocine units into their stable *Z*-isomer. This halts the dynamic interconversion, kinetically trapping the isomers as a complex but well-resolved mixture, as indicated by many sharp NMR signals not part of the original structure (**Figure 93**, step 3). Heating the kinetically trapped mixture restores the initial helicate. The required temperature depends on the metal in the $\mathbf{M}^{\mathbf{bipy}}$ site (**Figure 93**, step 4). In $\mathbf{Fe}^{\mathbf{bipy}}$, full recovery of the initial structure requires several hours at 65 °C, whereas $\mathbf{Zn}^{\mathbf{bipy}}$ already shows full recovery after back switching at room temperature. This indicates that metal-bipyridine dissociation is a necessary step and determines the height of the energy barrier for the kinetically trapped isomers. The stoichiometry of all isomers remains unchanged throughout this reaction cycle, as confirmed by ESI MS. Therefore, we assume these isomers to be atropisomers that are differentiated by rotation around single bonds.

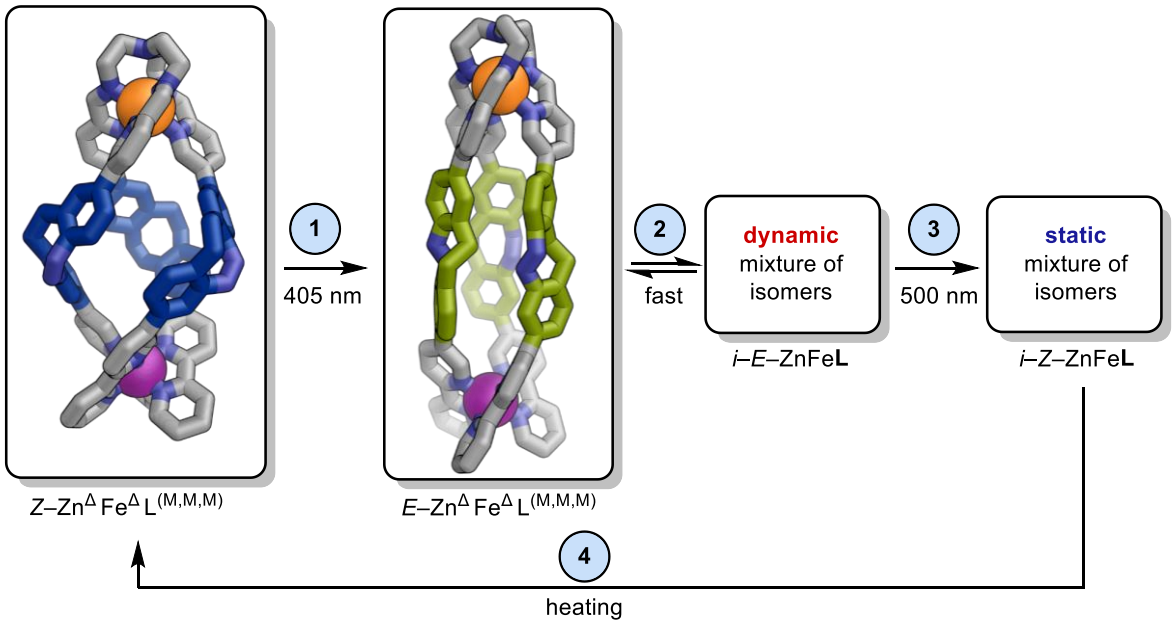

Figure 93. *Photoresponsive behavior of the ZnFe**L** helicate.*

The light-driven reaction sequence that forms kinetically trapped metastable structures is best described as an energy ratchet mechanism. In a fully equilibrated sample, only the

thermodynamic minimum structure *Z*-ZnFe**L** is present. It is impossible to form metastable isomers i-*Z*-ZnFe**L** by heating or cooling. This transformation is the endergonic reaction that is driven by the energy ratchet (**Figure 94**, step 4, small red arrow). The energy ratchet reaction network uses the exergonic relaxation of the exited state of the *Z*-diazocine to the ground state of the *E*-diazocine to transfer energy into the system, therefore completely altering the energy landscape of the ZnFe**L** to i-ZnFe**L** conversion (**Figure 94**, step 1, blue arrow). On this new energy surface, the transformation of ZnFe**L** to i-ZnFe**L** is energetically downhill and nearly barrierless, resulting in the spontaneous isomerization of *E*-ZnFe**L** to i-*E*-ZnFe**L** (**Figure 94**, step 2, blue arrow). Subsequent back switching with green light (500 nm) returns the energy surface to its original state, with metastable isomers i-*Z*-ZnFe**L** being kinetically trapped (**Figure 94**, step 3, blue arrow). The ratchet mechanism translates an input of light energy into an energetically uphill structural transformation, accumulating temporarily stable high energy isomers.

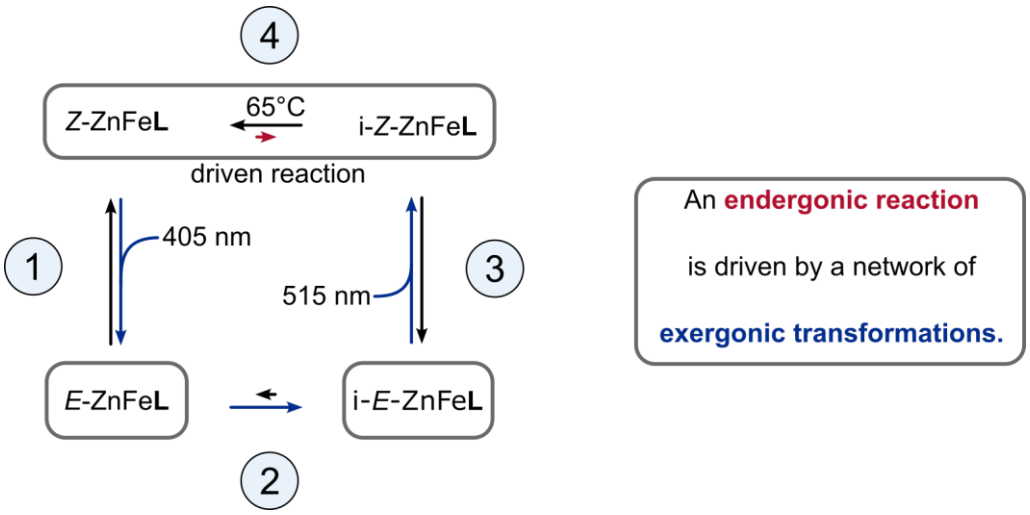

*Figure 94. Energy ratchet mechanism operating during photoswitching of ZnFe**L**. The endergonic transformation of the thermodynamically most stable isomer into meta-stable isomers is driven by a series of exergonic reactions. Part of the energy transferred during light irradiation is stored as chemical energy in the metastable products.*

Remarkably, continuous white light irradiation drives the energy ratchet autonomously without the need to switch between blue and green light. White light irradiation for 24 h accumulates a single long-lived isomer in which one of the metal centers has been inverted, resulting in a pseudo mesocate (**Figure 95**, left). White light predominantly induces $E \rightarrow Z$ switching, resulting in a photostationary state in **III-1** of 99% *Z*-isomer. However, due to a small but relevant overlap of white light with the $E \rightarrow Z$ transition, a small fraction of molecules is constantly switched to the *E*-isomer and quickly switched back to the *Z* isomer. Despite this low steady-state *E*-isomer population, the ultrafast dynamics of the helicate reconfiguration

allow the ratchet to operate under white light and accumulate metastable assemblies. During prolonged irradiation, a process occurs that could be understood as thermal annealing. It favors formation of only the kinetically most inert metastable structure. Two-dimensional ROESY NMR spectroscopy could unambiguously assign this structure as a diastereomer of the initial structure, where only the $\mathbf{M}^{\mathbf{bipy}}$ site is inverted (**Figure 95**, left). The assignment of this new structure as an atropisomer supports our hypothesis that the isomeric mixture obtained after switching consists of a series of rotational isomers.

The regioselective transformation of $Zn_2\mathbf{L}$ to ZnFe**L** allowed us to harness the dynamic formation of high-energy and presumably less stable isomers. We observed that irradiation increases the lability of the $\mathbf{M}^{\mathbf{bipy}}$ site and thereby accelerates metal exchange. Light therefore provides spatial and temporal control over a bulk solution process, allowing the chemist to trigger and localize the selective capture of Fe(II) by the helicate. This behavior is reminiscent of a claw machine one might find at an arcade that only grabs when and where the operator engages the control (**Figure 95**, right).

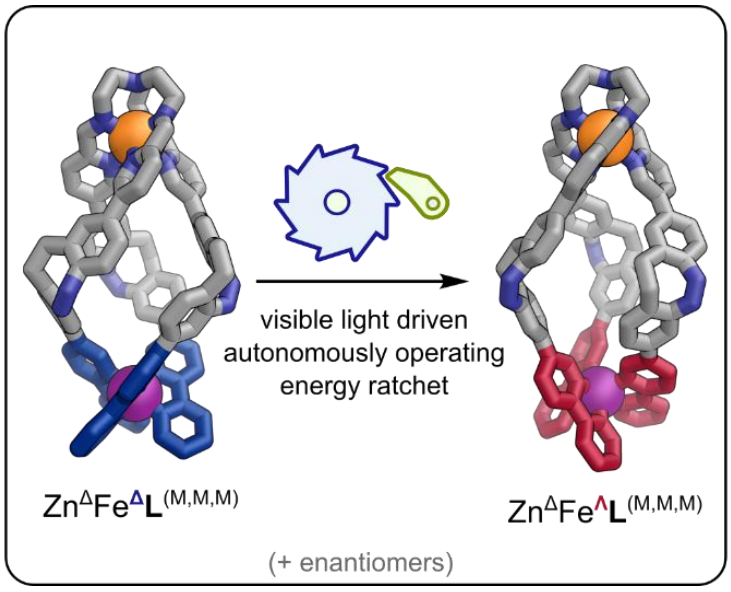

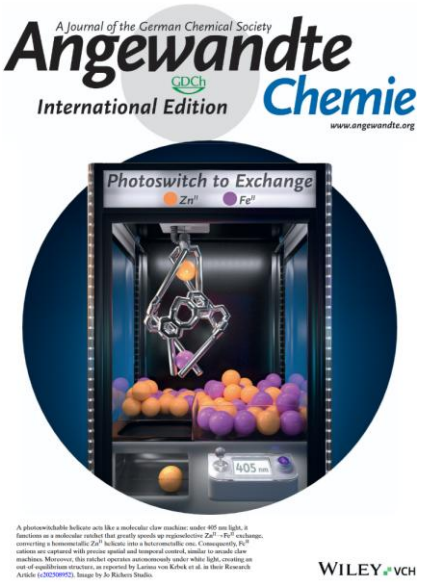

Figure 95. Right: *Continuous white light irradiation powers the ratchet autonomously, leading to the formation of a mesocate (Z-Zn^ΔFe^^**L**^MMM). All structures are optimized on GFN2xTB level.*[161] ***Left:*** *Outside Back Cover: Light-Driven Ratchet Mechanism Accelerates Regioselective Metal-Cation Exchange in a Heterobimetallic Helicate.*[172] *Reprinted from Angewandte Chemie International Editionwith permission from John Wiley and Sons under license number 6106431263601.*[172]

5.6 Outlook

In this work, a systems chemistry approach was applied to metal-organic cages by integrating an energy ratchet mechanism into a cage. The photoresponsive helicate described in this dissertation demonstrates that incorporating photoswitches into metal-organic assemblies is a successful and reliable pathway to out-of-equilibrium structures. Continuous operation of the energy ratchet mechanism under white light reversibly transforms the helicate into a pseudo-mesocate. Furthermore, light induced strain weakens coordinative bonds and allows the system to operate as a molecular claw machine, thus demonstrating how dynamic behavior enabled by the energy ratchet mechanism can be harnessed in molecular machines. This step towards increased complexity shows promising perspectives for further research.

One approach might be the incorporation of a chiral trivalent amine.[174] This would result in enantiomerically pure helicates[175] that could be transformed into enantiomerically pure pseudo-mesocates, thus enabling external control of properties like circular dichroism. Furthermore, a chiral trivalent amine might enable the use of circularly polarized light to turn the system from an energy ratchet to an information ratchet by enabling enantioselective photoswitching.[176]

A second approach might be the extension of the sub-component self-assembly approach using photoresponsive building blocks towards larger, more complex cage structures like bipyramids[177] or cubes.[84] Dynamic behavior in these structures will be more difficult to characterize, but the helicate presented herein gives a fundamental understanding of the behavior to be expected from these structures. Their larger cavities could enable remarkable host-guest behavior[84] that would be controlled by the energy ratchet mechanism, enabling enzyme-like properties such as controlled catalysis or molecular transport.

Beyond specific examples, this work shows that applying out-of-equilibrium systems chemistry enables new properties and behaviors in metal-organic cages. This combination is a solid stride towards bridging the gap between nanoscale molecular machines and the real-world macroscale *useful* work chemists would like them to produce.

6 Literature

[1] J. Lehn, “Supramolecular Chemistry—Scope and Perspectives Molecules, Supermolecules, and Molecular Devices (Nobel Lecture)” *Angew. Chem. Int. Ed. Engl.* **1988**, *27*, 89–112.

[2] I. Aprahamian, “The Future of Molecular Machines” *ACS Cent. Sci.* **2020**, *6*, 347–358.

[3] G. Ashkenasy, T. M. Hermans, S. Otto, A. F. Taylor, “Systems chemistry” *Chem. Soc. Rev.* **2017**, *46*, 2543–2554.

[4] J. Al-Bassam, F. Chang, “Regulation of microtubule dynamics by TOG-domain proteins XMAP215/Dis1 and CLASP” *Trends Cell Biol.* **2011**, *21*, 604–614.

[5] G. Wald, “Molecular Basis of Visual Excitation” *Science* **1968**, *162*, 230–239.

[6] P. D. Kiser, M. Golczak, K. Palczewski, “Chemistry of the Retinoid (Visual) Cycle” *Chem. Rev.* **2014**, *114*, 194–232.

[7] T. Gruhl, T. Weinert, M. J. Rodrigues, C. J. Milne, G. Ortolani, K. Nass, E. Nango, S. Sen, P. J. M. Johnson, C. Cirelli, A. Furrer, S. Mous, P. Skopintsev, D. James, F. Dworkowski, P. Båth, D. Kekilli, D. Ozerov, R. Tanaka, H. Glover, C. Bacellar, S. Brünle, C. M. Casadei, A. D. Diethelm, D. Gashi, G. Gotthard, R. Guixà-González, Y. Joti, V. Kabanova, G. Knopp, E. Lesca, P. Ma, I. Martiel, J. Mühle, S. Owada, F. Pamula, D. Sarabi, O. Tejero, C.-J. Tsai, N. Varma, A. Wach, S. Boutet, K. Tono, P. Nogly, X. Deupi, S. Iwata, R. Neutze, J. Standfuss, G. Schertler, V. Panneels, “Ultrafast structural changes direct the first molecular events of vision” *Nature* **2023**, *615*, 939–944.

[8] V. Y. Arshavsky, T. D. Lamb, E. N. P. Jr., “G PROTEINS AND PHOTOTRANSDUCTION” *Physiology* **2002**, *64*, 153–187.

[9] Z. Ashbridge, J. N. H. Reek, “The multifaceted roles of MnL2n cages in catalysis” *Nat. Synth.* **2024**, *3*, 1197–1207.

[10] E. Benchimol, J. Tessarolo, G. H. Clever, “Photoswitchable coordination cages” *Nat. Chem.* **2024**, *16*, 13–21.

[11] E. Benchimol, B.-N. T. Nguyen, T. K. Ronson, J. R. Nitschke, “Transformation networks of metal–organic cages controlled by chemical stimuli” *Chem. Soc. Rev.* **2022**, *51*, 5101–5135.

[12] J. Volarić, W. Szymanski, N. A. Simeth, B. L. Feringa, “Molecular photoswitches in aqueous environments” *Chem. Soc. Rev.* **2021**, *50*, 12377–12449.

[13] J. Ewert, L. Heintze, M. Jordà-Redondo, J.-S. von Glasenapp, S. Nonell, G. Bucher, C. Peifer, R. Herges, “Photoswitchable Diazocine-Based Estrogen Receptor Agonists: Stabilization of the Active Form inside the Receptor” *J. Am. Chem. Soc.* **2022**, *144*, 15059–15071.

[14] H. Qian, S. Pramanik, I. Aprahamian, “Photochromic Hydrazone Switches with Extremely Long Thermal Half-Lives” *J. Am. Chem. Soc.* **2017**, *139*, 9140–9143.

[15] G. S. HARTLEY, “The Cis-form of Azobenzene” *Nature* **1937**, *140*, 281–281.

[16] F. A. Jerca, V. V. Jerca, R. Hoogenboom, “Advances and opportunities in the exciting world of azobenzenes” *Nat. Rev. Chem.* **2022**, *6*, 51–69.

[17] Y. Ito, H. Ito, T. Matsuura, “Trans-cis photoisomerization of meta-(phenylazo)azobenzenes” *Tetrahedron Lett.* **1988**, *29*, 563–566.

[18] G. S. HARTLEY, “The Cis-form of Azobenzene” *Nature* **1937**, *140*, 281–281.

[19] X.-M. Liu, X.-Y. Jin, Z.-X. Zhang, J. Wang, F.-Q. Bai, “Theoretical study on the reaction mechanism of the thermal cis – trans isomerization of fluorine-substituted azobenzene derivatives” *RSC Adv.* **2018**, *8*, 11580–11588.

[20] M. Quick, A. L. Dobryakov, M. Gerecke, C. Richter, F. Berndt, I. N. Ioffe, A. A. Granovsky, R. Mahrwald, N. P. Ernsting, S. A. Kovalenko, “Photoisomerization Dynamics and Pathways of trans- and cis-Azobenzene in Solution from Broadband Femtosecond Spectroscopies and Calculations” *J. Phys. Chem. B* **2014**, *118*, 8756–8771.

[21] A. Nenov, R. Borrego-Varillas, A. Oriana, L. Ganzer, F. Segatta, I. Conti, J. Segarra-Marti, J. Omachi, M. Dapor, S. Taioli, C. Manzoni, S. Mukamel, G. Cerullo, M. Garavelli, “UV-Light-Induced Vibrational Coherences: The Key to Understand Kasha Rule Violation in trans-Azobenzene” *J. Phys. Chem. Lett.* **2018**, *9*, 1534–1541.

[22] M. Kasha, “Characterization of electronic transitions in complex molecules” *Discuss. Faraday Soc.* **1950**, *9*, 14–19.

[23] M. C. Brand, H. G. Trowell, M. J. Fuchter, R. L. Greenaway, “Incorporating Photoresponses into Porous Liquids” *Chem. A Eur. J.* **2024**, *30*, e202303593.

[24] Z. Zhang, D. Dong, T. Bösking, T. Dang, C. Liu, W. Sun, M. Xie, S. Hecht, T. Li, “Solar Azo-Switches for Effective E→Z Photoisomerization by Sunlight” *Angew. Chem. Int. Ed.* **2024**, *63*, e202404528.

[25] C. Nançoz, G. Licari, J. S. Beckwith, M. Soederberg, B. Dereka, A. Rosspeintner, O. Yushchenko, R. Letrun, S. Richert, B. Lang, E. Vauthey, “Influence of the hydrogen-bond interactions on the excited-state dynamics of a push–pull azobenzene dye: the case of Methyl Orange” *Phys. Chem. Chem. Phys.* **2018**, *20*, 7254–7264.

[26] I. Conti, M. Garavelli, G. Orlandi, “The Different Photoisomerization Efficiency of Azobenzene in the Lowest nπ* and ππ* Singlets: The Role of a Phantom State” *J. Am. Chem. Soc.* **2008**, *130*, 5216–5230.

[27] H. Satzger, C. Root, M. Braun, “Excited-State Dynamics of trans- and cis-Azobenzene after UV Excitation in the ππ* Band” *J. Phys. Chem. A* **2004**, *108*, 6265–6271.

[28] O. Laporte, W. F. Meggers, “Some Rules of Spectral Structure*” *J. Opt. Soc. Am.* **1925**, *11*, 459.

[29] J. Franck, E. G. Dymond, “Elementary processes of photochemical reactions” *Trans. Faraday Soc.* **1926**, *21*, 536–542.

[30] L. M. Obloy, P. Z. El-Khoury, A. N. Tarnovsky, “Excited-State-Selective Ultrafast Relaxation Dynamics and Photoisomerization of trans-4,4′-Azopyridine” *J. Phys. Chem. Lett.* **2022**, *13*, 10863–10870.

[31] H. Rau, E. Lueddecke, “On the rotation-inversion controversy on photoisomerization of azobenzenes. Experimental proof of inversion” *J. Am. Chem. Soc.* **1982**, *104*, 1616–1620.

[32] C. M. Stuart, R. R. Frontiera, R. A. Mathies, “Excited-State Structure and Dynamics of cis- and trans-Azobenzene from Resonance Raman Intensity Analysis” *J. Phys. Chem. A* **2007**, *111*, 12072–12080.

[33] J. Casellas, M. J. Bearpark, M. Reguero, “Excited-State Decay in the Photoisomerisation of Azobenzene: A New Balance between Mechanisms” *ChemPhysChem* **2016**, *17*, 3068–3079.

[34] H. M. D. Bandara, S. C. Burdette, “Photoisomerization in different classes of azobenzene” *Chem. Soc. Rev.* **2011**, *41*, 1809–1825.

[35] C. Slavov, C. Yang, L. Schweighauser, C. Boumrifak, A. Dreuw, H. A. Wegner, J. Wachtveitl, “Connectivity matters – ultrafast isomerization dynamics of bisazobenzene photoswitches” *Phys. Chem. Chem. Phys.* **2016**, *18*, 14795–14804.

[36] M. Gao, D. Kwaria, Y. Norikane, Y. Yue, “Visible-light-switchable azobenzenes: Molecular design, supramolecular systems, and applications” *Nat. Sci.* **2023**, *3*, DOI 10.1002/ntls.20220020.

[37] D. Bléger, J. Schwarz, A. M. Brouwer, S. Hecht, “o-Fluoroazobenzenes as Readily Synthesized Photoswitches Offering Nearly Quantitative Two-Way Isomerization with Visible Light” *J. Am. Chem. Soc.* **2012**, *134*, 20597–20600.

[38] C. E. Weston, R. D. Richardson, P. R. Haycock, A. J. P. White, M. J. Fuchter, “Arylazopyrazoles: Azoheteroarene Photoswitches Offering Quantitative Isomerization and Long Thermal Half-Lives” *J. Am. Chem. Soc.* **2014**, *136*, 11878–11881.

[39] Y. Yang, R. P. Hughes, I. Aprahamian, “Near-Infrared Light Activated Azo-BF2 Switches” *J. Am. Chem. Soc.* **2014**, *136*, 13190–13193.

[40] S. Crespi, N. A. Simeth, B. König, “Heteroaryl azo dyes as molecular photoswitches” *Nat. Rev. Chem.* **2019**, *3*, 133–146.

[41] H. Chen, W. Chen, Y. Lin, Y. Xie, S. H. Liu, J. Yin, “Visible and near-infrared light activated azo dyes” *Chin. Chem. Lett.* **2021**, *32*, 2359–2368.

[42] W. W. Paudler, A. G. Zeiler, “Diazocine chemistry. V. Synthesis and rearrangement of dibenzo[b,f][1,4]diazocine-6,11(5H,12H)-dione” *J. Org. Chem.* **1969**, *34*, 2138–2140.

[43] W. W. Paudler, A. G. Zeiler, “Diazocine chemistry. VI. Aromaticity of 5,6-dihydrodibenzo[b,f][1,2]diazocine” *J. Org. Chem.* **1969**, *34*, 3237–3239.

[44] F. Klockmann, C. Fangmann, E. Zender, T. Schanz, C. Catapano, A. Terfort, “Substituted Dibenzodiazocines: Rapid Synthesis and Photochemical Properties” *ACS Omega* **2021**, *6*, 18434–18441.

[45] M. H. Duval, “Recherches sur la benzidination” *Bull. Soc. Chim. Fr.* **1910**, 727–782.

[46] R. Siewertsen, H. Neumann, B. Buchheim-Stehn, R. Herges, C. Näther, F. Renth, F. Temps, “Highly Efficient Reversible Z−E Photoisomerization of a Bridged Azobenzene with Visible Light through Resolved S1(nπ*) Absorption Bands” *J. Am. Chem. Soc.* **2009**, *131*, 15594–15595.

[47] W. Moormann, T. Tellkamp, E. Stadler, F. Röhricht, C. Näther, R. Puttreddy, K. Rissanen, G. Gescheidt, R. Herges, “Efficient Conversion of Light to Chemical Energy: Directional, Chiral Photoswitches with Very High Quantum Yields” *Angew. Chem. Int. Ed.* **2020**, *59*, 15081–15086.

[48] H. Sell, C. Näther, R. Herges, “Amino-substituted diazocines as pincer-type photochromic switches” *Beilstein J. Org. Chem.* **2013**, *9*, 1–7.

[49] M. S. Maier, K. Hüll, M. Reynders, B. S. Matsuura, P. Leippe, T. Ko, L. Schäffer, D. Trauner, “Oxidative Approach Enables Efficient Access to Cyclic Azobenzenes” *J. Am. Chem. Soc.* **2019**, *141*, 17295–17304.

[50] S. Samanta, C. Qin, A. J. Lough, G. A. Woolley, “Bidirectional Photocontrol of Peptide Conformation with a Bridged Azobenzene Derivative” *Angew. Chem. Int. Ed.* **2012**, *51*, 6452–6455.

[51] P. Lentes, E. Stadler, F. Röhricht, A. Brahms, J. Gröbner, F. D. Sönnichsen, G. Gescheidt, R. Herges, “Nitrogen Bridged Diazocines: Photochromes Switching within the Near-Infrared Region with High Quantum Yields in Organic Solvents and in Water” *J. Am. Chem. Soc.* **2019**, *141*, 13592–13600.

[52] J. B. Trads, K. Hüll, B. S. Matsuura, L. Laprell, T. Fehrentz, N. Görldt, K. A. Kozek, C. D. Weaver, N. Klöcker, D. M. Barber, D. Trauner, “Sign Inversion in Photopharmacology: Incorporation of Cyclic Azobenzenes in Photoswitchable Potassium Channel Blockers and Openers” *Angew. Chem. Int. Ed.* **2019**, *58*, 15421–15428.

[53] W. Moormann, D. Langbehn, R. Herges, “Synthesis of functionalized diazocines for application as building blocks in photo- and mechanoresponsive materials” *Beilstein J. Org. Chem.* **2019**, *15*, 727–732.

[54] S. Li, K. Bamberg, Y. Lu, F. D. Sönnichsen, A. Staubitz, “Facile Synthesis of Light-Switchable Polymers with Diazocine Units in the Main Chain” *Polymers* **2023**, *15*, 1306.

[55] N. A. Vepřek, M. H. Cooper, L. Laprell, E. J.-N. Yang, S. Folkerts, R. Bao, M. Boczkowska, N. J. Palmer, R. Dominguez, T. G. Oertner, L. A. Pon, J. B. Zuchero, D. H. Trauner, “Optical Control of G-Actin with a Photoswitchable Latrunculin” *J. Am. Chem. Soc.* **2024**, *146*, 8895–8903.

[56] T. Zheng, J. Fu, Q. Xiong, X. Shen, B. Li, X. Zhao, Z. Yu, “Photo-regulated genetic encoding of dibenzo[c,g][1,2]diazocine on proteins via configuration switching” *Chem. Commun.* **2023**, *59*, 1201–1204.

[57] A. Businski, T. C. Ta, L. Unterriker, N. Gindullis, J. von Glasenapp, C. Näther, R. Herges, “Synthesis and Properties of Cyclic Imide Extended Diazocines: Tweezer-Like, Rigid Photoswitches With Large Switching Amplitudes” *Chem. A Eur. J.* **2025**, e202500435.

[58] T. Zheng, L. Tan, M. Lee, Y. Li, E. Sim, M. Lee, “Active Molecular Gripper as a Macrocycle Synthesizer” *J. Am. Chem. Soc.* **2024**, *146*, 25451–25455.

[59] L. Camerin, G. Maleeva, A. M. J. Gomila, I. Suárez-Pereira, C. Matera, D. Prischich, E. Opar, F. Riefolo, E. Berrocoso, P. Gorostiza, “Photoswitchable Carbamazepine Analogs for Non-Invasive Neuroinhibition In Vivo” *Angew. Chem. Int. Ed.* **2024**, *63*, e202403636.

[60] L. Qiang, H. Bai, X. Li, H. Yang, C. Gong, Q. Tang, “A Visible Light Responsive Smart Covalent Organic Framework with a Bridged Azobenzene Backbone” *Macromol. Rapid Commun.* **2024**, *45*, e2300506.

[61] H. Lee, J. Tessarolo, D. Langbehn, A. Baksi, R. Herges, G. H. Clever, “Light-Powered Dissipative Assembly of Diazocine Coordination Cages” *J. Am. Chem. Soc.* **2022**, *144*, 3099–3105.

[62] D. Hugenbusch, M. Lehr, J. von Glasenapp, A. J. McConnell, R. Herges, “Light-Controlled Destruction and Assembly: Switching between Two Differently Composed Cage-Type Complexes” *Angew. Chem. Int. Ed.* **2023**, *62*, e202212571.

[63] S. Li, N. Eleya, A. Staubitz, “Cross-Coupling Strategy for the Synthesis of Diazocines” *Org. Lett.* **2020**, *22*, 1624–1627.

[64] M. Hammerich, C. Schütt, C. Stähler, P. Lentes, F. Röhricht, R. Höppner, R. Herges, “Heterodiazocines: Synthesis and Photochromic Properties, Trans to Cis Switching within the Bio-optical Window” *J. Am. Chem. Soc.* **2016**, *138*, 13111–13114.

[65] C. Deo, N. Bogliotti, R. Métivier, P. Retailleau, J. Xie, “A Visible-Light-Triggered Conformational Diastereomer Photoswitch in a Bridged Azobenzene” *Chem. A Eur. J.* **2016**, *22*, 9092–9096.

[66] A. Müller-Deku, O. Thorn-Seshold, “Exhaustive Catalytic ortho-Alkoxylation of Azobenzenes: Flexible Access to Functionally Diverse Yellow-Light-Responsive Photoswitches” *J. Org. Chem.* **2022**, *87*, 16526–16531.

[67] W. Yuan, M. Wu, C. Qian, J. Guo, Y. Wu, T. He, H. Wei, X. Chen, D. Wang, J. Liu, Y. Zhao, S. Wang, J. Yang, Z. Zhang, Y. Chen, Y. Zhao, “π-Fused Diazocines with Controllable Photoswitching Properties as Molecular Tweezers” *CCS Chem.* **2024**, *6*, 2175–2185.

[68] W. Moormann, D. Langbehn, R. Herges, “Solvent-Free Synthesis of Diazocine” *Synthesis* **2017**, *49*, 3471–3475.

[69] Y. Yang, X. Jing, J. Zhang, F. Yang, C. Duan, “Modifying electron injection kinetics for selective photoreduction of nitroarenes into cyclic and asymmetric azo compounds” *Nat. Commun.* **2022**, *13*, 1940.

[70] Y. Liu, F. Li, D. Li, W. Dong, B. Jin, “Controllable synthesis of diazocine - investigation on electroreduction mechanism for intramolecular cyclization of 2,2′- dinitrodibenzyl in the presence of CO2” *J. Electroanal. Chem.* **2023**, *944*, 117644.

[71] C. J. Rybak, C. Fan, P. Sharma, C. Uyeda, “Dinickel-Catalyzed N=N Coupling Reactions for the Synthesis of Hindered Azoarenes” *J. Am. Chem. Soc.* **2024**, *146*, 29720–29727.

[72] M. Irie, T. Fukaminato, K. Matsuda, S. Kobatake, “Photochromism of Diarylethene Molecules and Crystals: Memories, Switches, and Actuators” *Chem. Rev.* **2014**, *114*, 12174–12277.

[73] D. Villarón, S. J. Wezenberg, “Stiff-Stilbene Photoswitches: From Fundamental Studies to Emergent Applications” *Angew. Chem. Int. Ed.* **2020**, *59*, 13192–13202.

[74] T. Kudernac, N. Ruangsupapichat, M. Parschau, B. Maciá, N. Katsonis, S. R. Harutyunyan, K.-H. Ernst, B. L. Feringa, “Electrically driven directional motion of a four-wheeled molecule on a metal surface” *Nature* **2011**, *479*, 208–211.

[75] T. R. Cook, P. J. Stang, “Recent Developments in the Preparation and Chemistry of Metallacycles and Metallacages via Coordination” *Chem. Rev.* **2015**, *115*, 7001–7045.

[76] R. K. Grötsch, J. Boekhoven, “Self-assembling Biomaterials” *Self-Assembling Biomaterials: Molecular Design, Characterization and Application in Biology and Medicine* **2018**, 235–250.

[77] B. Olenyuk, A. Fechtenkötter, P. J. Stang, “Molecular architecture of cyclic nanostructures: use of co-ordination chemistry in the building of supermolecules with predefined geometric shapes” *J. Chem. Soc., Dalton Trans.* **1998**, *0*, 1707–1728.

[78] M. Fujita, “Metal-directed self-assembly of two- and three-dimensional synthetic receptors” *Chem. Soc. Rev.* **1998**, *27*, 417–425.

[79] M. Fujita, K. Umemoto, M. Yoshizawa, N. Fujita, T. Kusukawa, K. Biradha, “Molecular paneling via coordination” *Chem. Commun.* **2001**, *0*, 509–518.

[80] D. L. Caulder, K. N. Raymond, “The rational design of high symmetry coordination clusters†” *J. Chem. Soc., Dalton Trans.* **1999**, *0*, 1185–1200.

[81] J. R. Nitschke, “Construction, Substitution, and Sorting of Metallo-organic Structures via Subcomponent Self-Assembly” *Acc. Chem. Res.* **2007**, *40*, 103–112.

[82] A. M. Castilla, N. Ousaka, R. A. Bilbeisi, E. Valeri, T. K. Ronson, J. R. Nitschke, “High-Fidelity Stereochemical Memory in a FeII 4L4 Tetrahedral Capsule” *J. Am. Chem. Soc.* **2013**, *135*, 17999–18006.

[83] C. R. K. Glasson, J. K. Clegg, J. C. McMurtrie, G. V. Meehan, L. F. Lindoy, C. A. Motti, B. Moubaraki, K. S. Murray, J. D. Cashion, “Unprecedented encapsulation of a [Fe III Cl 4] − anion in a cationic [Fe II 4 L 6] 8+ tetrahedral cage derived from 5,5‴-dimethyl-2,2′:5′,5″:2″,2‴-quaterpyridine” *Chem. Sci.* **2010**, *2*, 540–543.

[84] M. Hardy, J. Tessarolo, J. J. Holstein, N. Struch, N. Wagner, R. Weisbarth, M. Engeser, J. Beck, S. Horiuchi, G. H. Clever, A. Lützen, “A Family of Heterobimetallic Cubes Shows Spin-Crossover Behaviour Near Room Temperature” *Angew. Chem. Int. Ed.* **2021**, *60*, 22562–22569.

[85] W. Meng, B. Breiner, K. Rissanen, J. D. Thoburn, J. K. Clegg, J. R. Nitschke, “A Self-Assembled M8L6 Cubic Cage that Selectively Encapsulates Large Aromatic Guests” *Angew. Chem. Int. Ed.* **2011**, *50*, 3479–3483.

[86] M. Otte, P. F. Kuijpers, O. Troeppner, I. Ivanović-Burmazović, J. N. H. Reek, B. de Bruin, “Encapsulation of Metalloporphyrins in a Self-Assembled Cubic M8L6 Cage: A New Molecular Flask for Cobalt–Porphyrin-Catalysed Radical-Type Reactions” *Chem. A Eur. J.* **2013**, *19*, 10170–10178.

[87] R. Kramer, J. M. Lehn, A. Marquis-Rigault, “Self-recognition in helicate self-assembly: spontaneous formation of helical metal complexes from mixtures of ligands and metal ions.” *Proc. Natl. Acad. Sci.* **1993**, *90*, 5394–5398.

[88] G. Ercolani, “Assessment of Cooperativity in Self-Assembly” *J. Am. Chem. Soc.* **2003**, *125*, 16097–16103.

[89] L. K. S. von Krbek, C. A. Schalley, P. Thordarson, “Assessing cooperativity in supramolecular systems” *Chem. Soc. Rev.* **2017**, *46*, 2622–2637.

[90] A. M. Castilla, W. J. Ramsay, J. R. Nitschke, “Stereochemistry in Subcomponent Self-Assembly” *Acc. Chem. Res.* **2014**, *47*, 2063–2073.

[91] P. Mal, D. Schultz, K. Beyeh, K. Rissanen, J. R. Nitschke, “An Unlockable–Relockable Iron Cage by Subcomponent Self-Assembly” *Angew. Chem. Int. Ed.* **2008**, *47*, 8297–8301.

[92] S. Pullen, J. Tessarolo, G. H. Clever, “Increasing structural and functional complexity in self-assembled coordination cages” *Chem. Sci.* **2021**, *12*, 7269–7293.

[93] T. Abe, N. Sanada, K. Takeuchi, A. Okazawa, S. Hiraoka, “Assembly of Six Types of Heteroleptic Pd2L4 Cages under Kinetic Control” *J. Am. Chem. Soc.* **2023**, *145*, 28061–28074.

[94] K. Wu, E. Benchimol, A. Baksi, G. H. Clever, “Non-statistical assembly of multicomponent [Pd2ABCD] cages” *Nat. Chem.* **2024**, *16*, 584–591.

[95] M. Hardy, A. Lützen, “Better Together: Functional Heterobimetallic Macrocyclic and Cage-like Assemblies” *Chem. A Eur. J.* **2020**, *26*, 13332–13346.

[96] L. S. Lisboa, M. Riisom, H. J. Dunne, D. Preston, S. M. F. Jamieson, L. J. Wright, C. G. Hartinger, J. D. Crowley, “Hydrazone- and imine-containing [PdPtL 4] 4+ cages: a comparative study of the stability and host–guest chemistry” *Dalton Trans.* **2022**, *51*, 18438–18445.

[97] M. Hardy, N. Struch, F. Topić, G. Schnakenburg, K. Rissanen, A. Lützen, “Stepwise Construction of Heterobimetallic Cages by an Extended Molecular Library Approach” *Inorg. Chem.* **2018**, *57*, 3507–3515.

[98] P. Cecot, A. Walczak, G. Markiewicz, A. R. Stefankiewicz, “Gating the photoactivity of azobenzene-type ligands trapped within a dynamic system of an M 4 L 6 tetrahedral cage, an M 2 L 2 metallocycle and mononuclear ML n complexes” *Inorg. Chem. Front.* **2021**, *8*, 5195–5200.

[99] N. Yoshida, K. Ichikawa, “Synthesis and structure of a dinuclear zinc(ii) triple helix of an N,N-bis-bidentate Schiff base: new building blocks for the construction of helical structures” *Chem. Commun.* **1997**, *0*, 1091–1092.

[100] C. Bannwarth, S. Ehlert, S. Grimme, “GFN2-xTB—An Accurate and Broadly Parametrized Self-Consistent Tight-Binding Quantum Chemical Method with Multipole Electrostatics and Density-Dependent Dispersion Contributions” *J. Chem. Theory Comput.* **2019**, *15*, 1652–1671.

[101] A. Tarzia, K. E. Jelfs, “Unlocking the computational design of metal–organic cages” *Chem. Commun.* **2022**, *58*, 3717–3730.

[102] R. G. DiNardi, A. O. Douglas, R. Tian, J. R. Price, M. Tajik, W. A. Donald, J. E. Beves, “Visible-Light-Responsive Self-Assembled Complexes: Improved Photoswitching Properties by Metal Ion Coordination**” *Angew. Chem. (Int. Ed Engl.)* **2022**, *61*, e202205701.

[103] T. Murase, S. Sato, M. Fujita, “Switching the Interior Hydrophobicity of a Self-Assembled Spherical Complex through the Photoisomerization of Confined Azobenzene Chromophores” *Angew. Chem.* **2007**, *119*, 5225–5228.

[104] Y. Qin, L.-J. Chen, Y. Zhang, Y.-X. Hu, W.-L. Jiang, G.-Q. Yin, H. Tan, X. Li, L. Xu, H.-B. Yang, “Photoswitchable Förster resonance energy transfer (FRET) within a heterometallic Ir–Pt macrocycle” *Chem. Commun.* **2019**, *55*, 11119–11122.

[105] A. Ghosh, L. Slappendel, B.-N. T. Nguyen, L. K. S. von Krbek, T. K. Ronson, A. M. Castilla, J. R. Nitschke, “Light-Powered Reversible Guest Release and Uptake from Zn4L4 Capsules” *J. Am. Chem. Soc.* **2023**, *145*, 3828–3832.

[106] M. Han, R. Michel, B. He, Y. Chen, D. Stalke, M. John, G. H. Clever, “Light-Triggered Guest Uptake and Release by a Photochromic Coordination Cage” *Angew. Chem. Int. Ed.* **2013**, *52*, 1319–1323.

[107] C. Stuckhardt, D. Roke, W. Danowski, E. Otten, S. J. Wezenberg, B. L. Feringa, “A chiral self-sorting photoresponsive coordination cage based on overcrowded alkenes” *Beilstein J. Org. Chem.* **2019**, *15*, 2767–2773.

[108] A. D. W. Kennedy, R. G. DiNardi, L. L. Fillbrook, W. A. Donald, J. E. Beves, “Visible-Light Switching of Metallosupramolecular Assemblies**” *Chem. A Eur. J.* **2022**, *28*, e202104461.

[109] E. Nieland, J. Voss, B. M. Schmidt, “Photoresponsive Supramolecular Cages and Macrocycles” *ChemPlusChem* **2023**, *88*, e202300353.

[110] M. C. Brand, H. G. Trowell, J. T. Pegg, J. L. Greenfield, M. Odaybat, M. A. Little, P. R. Haycock, G. Avci, N. Rankin, M. J. Fuchter, K. E. Jelfs, A. I. Cooper, R. L. Greenaway, “Photoresponsive Organic Cages□Computationally Inspired Discovery of Azobenzene-Derived Organic Cages” *J. Am. Chem. Soc.* **2024**, *146*, 30332–30339.

[111] M. B. Tipping, L. P. Lara, A. B. Solea, L. K. S. von Krbek, M. D. Ward, “Photoswitching of Co(ii)-based coordination cages containing azobenzene backbones” *Chem. Sci.* **2024**, *15*, 8488–8499.

[112] M. Lohse, K. Nowosinski, N. L. Traulsen, A. J. Achazi, L. K. S. von Krbek, B. Paulus, C. A. Schalley, S. Hecht, “Gating the photochromism of an azobenzene by strong host–guest interactions in a divalent pseudo[2]rotaxane” *Chem. Commun.* **2015**, *51*, 9777–9780.

[113] J. Long, D. Kumar, C. Deo, P. Retailleau, G. V. Dubacheva, G. Royal, J. Xie, N. Bogliotti, “Photo-/Electroinduced Irreversible Isomerization of 2,2’-Azobispyridine Ligands in Arene Ruthenium(II) Complexes” *Chem. A Eur. J.* **2021**, *27*, 9563–9570.

[114] J. Long, L. Rocard, E. V. Elslande, P. Retailleau, J. Xie, N. Bogliotti, “Light-Promoted Basic Nitrogen Unmasking in Arene Ruthenium Complexes Derived from Z-Configured 2,2′-Azobispyridine” *Chem. A Eur. J.* **2023**, *29*, e202301301.

[115] P. Liao, B. W. Langloss, A. M. Johnson, E. R. Knudsen, F. S. Tham, R. R. Julian, R. J. Hooley, “Two-component control of guest binding in a self-assembled cage molecule” *Chem. Commun.* **2010**, *46*, 4932–4934.

[116] R. Li, M. Han, J. Tessarolo, J. J. Holstein, J. Lübben, B. Dittrich, C. Volkmann, M. Finze, C. Jenne, G. H. Clever, “Successive Photoswitching and Derivatization Effects in Photochromic Dithienylethene-Based Coordination Cages” *ChemPhotoChem* **2019**, *3*, 378–383.

[117] D. K. Chand, K. Biradha, M. Kawano, S. Sakamoto, K. Yamaguchi, M. Fujita, “Dynamic Self-Assembly of an M3L6 Molecular Triangle and an M4L8 Tetrahedron from Naked PdII Ions and Bis(3-pyridyl)-Substituted Arenes” *Chem. Asian J.* **2006**, *1*, 82–90.

[118] S. Sudan, F. Fadaei-Tirani, R. Scopelliti, K. E. Ebbert, G. H. Clever, K. Severin, “LiBF4-Induced Rearrangement and Desymmetrization of a Palladium-Ligand Assembly” *Angew. Chem. Int. Ed.* **2022**, *61*, e202201823.

[119] Y. Liu, T. Wang, W. Wang, “Photopharmacology and photoresponsive drug delivery” *Chem. Soc. Rev.* **2025**, *54*, 5792–5835.

[120] R. G. DiNardi, S. Rasheed, S. S. Capomolla, M. H. Chak, I. A. Middleton, L. K. Macreadie, J. P. Violi, W. A. Donald, P. J. Lusby, J. E. Beves, “Photoswitchable Catalysis by a Self-Assembled Molecular Cage” *J. Am. Chem. Soc.* **2024**, *146*, 21196–21202.

[121] R. D. Astumian, “Microscopic reversibility as the organizing principle of molecular machines” *Nat. Nanotechnol.* **2012**, *7*, 684–688.

[122] M. Kathan, S. Hecht, “Photoswitchable molecules as key ingredients to drive systems away from the global thermodynamic minimum” *Chem. Soc. Rev.* **2017**, *46*, 5536–5550.

[123] Y. Munekage, M. Hashimoto, C. Miyake, K.-I. Tomizawa, T. Endo, M. Tasaka, T. Shikanai, “Cyclic electron flow around photosystem I is essential for photosynthesis” *Nature* **2004**, *429*, 579–582.

[124] P. D. Boyer, “The binding change mechanism for ATP synthase — Some probabilities and possibilities” *Biochim. Biophys. Acta (BBA) - Bioenerg.* **1993**, *1140*, 215–250.

[125] I. Aprahamian, S. M. Goldup, “Non-equilibrium Steady States in Catalysis, Molecular Motors, and Supramolecular Materials: Why Networks and Language Matter” *J. Am. Chem. Soc.* **2023**, *145*, 14169–14183.

[126] T. Sangchai, S. A. Shehimy, E. Penocchio, G. Ragazzon, “Artificial Molecular Ratchets: Tools Enabling Endergonic Processes” *Angew. Chem. Int. Ed.* **2023**, *62*, e202309501.

[127] J. Boekhoven, W. E. Hendriksen, G. J. M. Koper, R. Eelkema, J. H. van Esch, “Transient assembly of active materials fueled by a chemical reaction” *Science* **2015**, *349*, 1075–1079.

[128] M. Tena-Solsona, B. Rieß, R. K. Grötsch, F. C. Löhrer, C. Wanzke, B. Käsdorf, A. R. Bausch, P. Müller-Buschbaum, O. Lieleg, J. Boekhoven, “Non-equilibrium dissipative supramolecular materials with a tunable lifetime” *Nat. Commun.* **2017**, *8*, 15895.

[129] M. Ovalle, M. Kathan, R. Toyoda, C. N. Stindt, S. Crespi, B. L. Feringa, “Light-Fueled Transformations of a Dynamic Cage-Based Molecular System” *Angew. Chem. Int. Ed.* **2023**, *62*, e202214495.

[130] S. Borsley, D. A. Leigh, B. M. W. Roberts, “Molecular Ratchets and Kinetic Asymmetry: Giving Chemistry Direction” *Angew. Chem. Int. Ed.* **2024**, *63*, e202400495.

[131] V. Serreli, C.-F. Lee, E. R. Kay, D. A. Leigh, “A molecular information ratchet” *Nature* **2007**, *445*, 523–527.

[132] R. D. Astumian, “Trajectory and Cycle-Based Thermodynamics and Kinetics of Molecular Machines: The Importance of Microscopic Reversibility” *Acc. Chem. Res.* **2018**, *51*, 2653–2661.

[133] J. T. Foy, Q. Li, A. Goujon, J.-R. Colard-Itté, G. Fuks, E. Moulin, O. Schiffmann, D. Dattler, D. P. Funeriu, N. Giuseppone, “Dual-light control of nanomachines that integrate motor and modulator subunits” *Nat. Nanotechnol.* **2017**, *12*, 540–545.

[134] W. Danowski, T. van Leeuwen, S. Abdolahzadeh, D. Roke, W. R. Browne, S. J. Wezenberg, B. L. Feringa, “Unidirectional rotary motion in a metal–organic framework” *Nat. Nanotechnol.* **2019**, *14*, 488–494.

[135] J. Pruchyathamkorn, B.-N. T. Nguyen, A. B. Grommet, M. Novoveska, T. K. Ronson, J. D. Thoburn, J. R. Nitschke, “Harnessing Maxwell’s demon to establish a macroscale concentration gradient” *Nat. Chem.* **2024**, *16*, 1558–1564.

[136] L. Feng, Y. Qiu, Q.-H. Guo, Z. Chen, J. S. W. Seale, K. He, H. Wu, Y. Feng, O. K. Farha, R. D. Astumian, J. F. Stoddart, “Active mechanisorption driven by pumping cassettes” *Science* **2021**, *374*, 1215–1221.

[137] B. Shao, H. Fu, I. Aprahamian, “A molecular anion pump” *Science* **2024**, *385*, 544–549.

[138] Y. Ren, R. Jamagne, D. J. Tetlow, D. A. Leigh, “A tape-reading molecular ratchet” *Nature* **2022**, *612*, 78–82.

[139] V. García-López, D. Liu, J. M. Tour, “Light-Activated Organic Molecular Motors and Their Applications” *Chem. Rev.* **2020**, *120*, 79–124.

[140] R. Falkenburg, M. J. Notheis, G. Schnakenburg, L. K. S. von Krbek, “Twelve-membered ring photoswitches with excellent Z → E conversion under ambient light” *Org. Biomol. Chem.* **2023**, *21*, 4993–4998.

[141] Q. Zhang, C. S. Kounde, M. Mondal, J. L. Greenfield, J. R. Baker, S. Kotelnikov, M. Ignatov, C. P. Tinworth, L. Zhang, D. Conole, E. D. Vita, D. Kozakov, A. McCluskey, J. D. Harling, M. J. Fuchter, E. W. Tate, “Light-mediated multi-target protein degradation using arylazopyrazole photoswitchable PROTACs (AP-PROTACs)” *Chem. Commun.* **2022**, *58*, 10933–10936.

[142] J. Broichhagen, J. A. Frank, D. Trauner, “A Roadmap to Success in Photopharmacology” *Acc. Chem. Res.* **2015**, *48*, 1947–1960.

[143] T. Ko, M. M. Oliveira, J. M. Alapin, J. Morstein, E. Klann, D. Trauner, “Optical Control of Translation with a Puromycin Photoswitch” *J. Am. Chem. Soc.* **2022**, *144*, 21494–21501.

[144] E. Wagner-Wysiecka, T. Rzymowski, M. Szarmach, Marina. S. Fonari, E. Luboch, “Functionalized azobenzocrown ethers as sensor materials—The synthesis and ion binding properties” *Sens. Actuators B: Chem.* **2013**, *177*, 913–923.

[145] J. P. V. der Berg, W. A. Velema, W. Szymanski, A. J. M. Driessen, B. L. Feringa, “Controlling the activity of quorum sensing autoinducers with light” *Chem. Sci.* **2015**, *6*, 3593–3598.

[146] Y. Chen, C. Li, X. Xu, M. Liu, Y. He, I. Murtaza, D. Zhang, C. Yao, Y. Wang, H. Meng, “Thermal and Optical Modulation of the Carrier Mobility in OTFTs Based on an Azo-anthracene Liquid Crystal Organic Semiconductor” *ACS Appl. Mater. Interfaces* **2017**, *9*, 7305–7314.

[147] A. Goulet-Hanssens, F. Eisenreich, S. Hecht, “Enlightening Materials with Photoswitches” *Adv. Mater.* **2020**, *32*, e1905966.

[148] G. Tyagi, J. L. Greenfield, B. E. Jones, W. N. Sharratt, K. Khan, D. Seddon, L. A. Malone, N. Cowieson, R. C. Evans, M. J. Fuchter, J. T. Cabral, “Light Responsiveness and Assembly of Arylazopyrazole-Based Surfactants in Neat and Mixed CTAB Micelles” **2022**, *2*, 2670–2677.

[149] Z. L. Pianowski, “Recent Implementations of Molecular Photoswitches into Smart Materials and Biological Systems” *Chem. A Eur. J.* **2019**, *25*, 5128–5144.

[150] T. Ikeda, O. Tsutsumi, “Optical Switching and Image Storage by Means of Azobenzene Liquid-Crystal Films” *Science* **1995**, *268*, 1873–1875.

[151] N. Eleya, S. Ghosh, E. Lork, A. Staubitz, “A new photo switchable azobenzene macrocycle without thermal relaxation at ambient temperature” *J. Mater. Chem. C* **2020**, *9*, 82–87.

[152] A. H. Heindl, J. Becker, H. A. Wegner, “Selective switching of multiple azobenzenes” *Chem. Sci.* **2019**, *10*, 7418–7425.

[153] K.-Y. Kim, K.-M. Lim, J.-H. Shin, J.-Y. Noh, J.-B. Ahn, D.-H. Lee, J.-H. Chung, “Effect of Lead(IV) Acetate on Procoagulant Activity in Human Red Blood Cells” *Toxicol. Res.* **2009**, *25*, 175–180.

[154] J. Berry, T. K. Lindhorst, G. Despras, “Sulfur and Azobenzenes, a Profitable Liaison: Straightforward Synthesis of Photoswitchable Thioglycosides with Tunable Properties” *Chem. A Eur. J.* **2022**, *28*, e202200354.

[155] M. J. Hansen, M. M. Lerch, W. Szymanski, B. L. Feringa, “Direct and Versatile Synthesis of Red-Shifted Azobenzenes” *Angew. Chem. Int. Ed.* **2016**, *55*, 13514–13518.

[156] D. Samanta, J. Gemen, Z. Chu, Y. Diskin-Posner, L. J. W. Shimon, R. Klajn, “Reversible photoswitching of encapsulated azobenzenes in water” *Proc. Natl. Acad. Sci.* **2018**, *115*, 9379–9384.

[157] R. Siewertsen, J. B. Schönborn, B. Hartke, F. Renth, F. Temps, “Superior Z → E and E → Z photoswitching dynamics of dihydrodibenzodiazocine , a bridged azobenzene , by S 1 (n π*) excitation at λ = 387 and 490 nm” *Phys. Chem. Chem. Phys.* **2011**, *13*, 1054–1063.

[158] M. Marcon, C. Haag, B. König, “Photoswitches beyond azobenzene: a beginner’s guide” *Beilstein J. Org. Chem.* **2025**, *21*, 1808–1853.

[159] M. J. Notheis, V. Sahiti, L. K. S. von Krbek, V. Prangenberg, J. S. Kruse, “2,8-Dihalogenated Diazocines: Versatile Reactants for Functionalized Photoswitches” *Synlett* **2025**, *36*, 1569–1573.

[160] J. W. Meringdal, D. Menche, “Suzuki–Miyaura (hetero-)aryl cross-coupling: recent findings and recommendations” *Chem. Soc. Rev.* **2025**, *54*, 5746–5765.

[161] M. J. Notheis, G. Schnakenburg, L. K. S. von Krbek, “Light-Driven Ratchet Mechanism Accelerates Regioselective Metal-Cation Exchange in a Heterobimetallic Helicate” *Angew. Chem. Int. Ed.* **2025**, e202508952.

[162] L. J. Wilson, N. J. Rose, “Geometrically specific multidentate ligands and their complexes. I. A nickel(II) complex of the potentially heptadentate Schiff base derived from 2,2’2’’-triaminotriethylamine and 2-pyridinecarboxaldehyde” *J. Am. Chem. Soc.* **1968**, *90*, 6041–6045.

[163] X. A. F. Cook, A. de Gombert, J. McKnight, L. R. E. Pantaine, M. C. Willis, “The 2-Pyridyl Problem: Challenging Nucleophiles in Cross-Coupling Arylations” *Angew. Chem. Int. Ed.* **2021**, *60*, 11068–11091.

[164] T. Brandt, P. Lentes, J. Rudtke, M. Hösgen, C. Näther, R. Herges, “Synthesis of N-acetyl diazocine derivatives via cross-coupling reaction” *Beilstein J. Org. Chem.* **2025**, *21*, 490–499.

[165] N. Kudo, M. Perseghini, G. C. Fu, “A Versatile Method for Suzuki Cross-Coupling Reactions of Nitrogen Heterocycles” *Angew. Chem. Int. Ed.* **2006**, *45*, 1282–1284.

[166] N. Oka, T. Yamada, H. Sajiki, S. Akai, T. Ikawa, “Aryl Boronic Esters Are Stable on Silica Gel and Reactive under Suzuki–Miyaura Coupling Conditions” *Org. Lett.* **2022**, *24*, 3510–3514.

[167] T. W. G. Ph.D.,, P. G. M. W. Ph.D., “Protective Groups in Organic Synthesis” **2023**, DOI 10.1002/0471220574.

[168] H. Nose, M. T. Rodgers, “Energy-Resolved Collision-Induced Dissociation Studies of 2,2′-Bipyridine Complexes of the Late First-Row Divalent Transition-Metal Cations: Determination of the Third-Sequential Binding Energies” *ChemPlusChem* **2013**, *78*, 1109–1123.

[169] L. Helm, A. E. Merbach, “Applications of advanced experimental techniques: high pressure NMR and computer simulations” *J. Chem. Soc., Dalton Trans.* **2002**, *0*, 633–641.

[170] L. Helm, A. E. Merbach, “The Periodic Table and Kinetics?” *Chim. Int. J. Chem.* **2019**, *73*, 179–184.

[171] D. T. Richens, *The Chemistry of Aqua Ions*, Wiley & Sons Ltd, **1997**.

[172] M. J. Notheis, G. Schnakenburg, L. K. S. von Krbek, “Outside Back Cover: Light-Driven Ratchet Mechanism Accelerates Regioselective Metal-Cation Exchange in a Heterobimetallic Helicate” *Angew. Chem. Int. Ed.* **2025**, DOI 10.1002/anie.202517049.

[173] M. Walther, W. Kipke, R. Renken, A. Staubitz, “Stille vs. Suzuki – cross-coupling for the functionalization of diazocines” *RSC Adv.* **2023**, *13*, 15805–15809.

[174] Y. Pei, K. Brade, E. Brulé, L. Hagberg, F. Lake,, C. Moberg, “A General Method for the Preparation of Chiral TREN Derivatives” *Eur. J. Org. Chem.* **2005**, *2005*, 2835–2840.

[175] C. Müller, K. Scholten, E. Engelage, C. Merten, “Synthesis and VCD Spectroscopic Characterization of a Series of Azacryptands from a Chiral Valine-Based Derivative of Tris(2-aminoethyl)amine (TREN)” *Chem. A Eur. J.* **2023**, *29*, e202302126.

[176] N. Tamaoki, M. Wada, “Dynamic Control of Racemization Rate through E − Z Photoisomerization of Azobenzene and Subsequent Partial Photoresolution under Circular Polarized Light” *J. Am. Chem. Soc.* **2006**, *128*, 6284–6285.

[177] M. Hardy, N. Struch, J. J. Holstein, G. Schnakenburg, N. Wagner, M. Engeser, J. Beck, G. H. Clever, A. Lützen, “Dynamic Complex-to-Complex Transformations of Heterobimetallic Systems Influence the Cage Structure or Spin State of Iron(II) Ions” *Angew. Chem. Int. Ed.* **2020**, *59*, 3195–3200.

7 Appendix

7.1 *Org. Biomol. Chem.* **2023**, *21*, 4993-4998.

Volume 21
Number 24
28 June 2023
Pages 4917-5130

Organic & Biomolecular Chemistry

rsc.li/obc

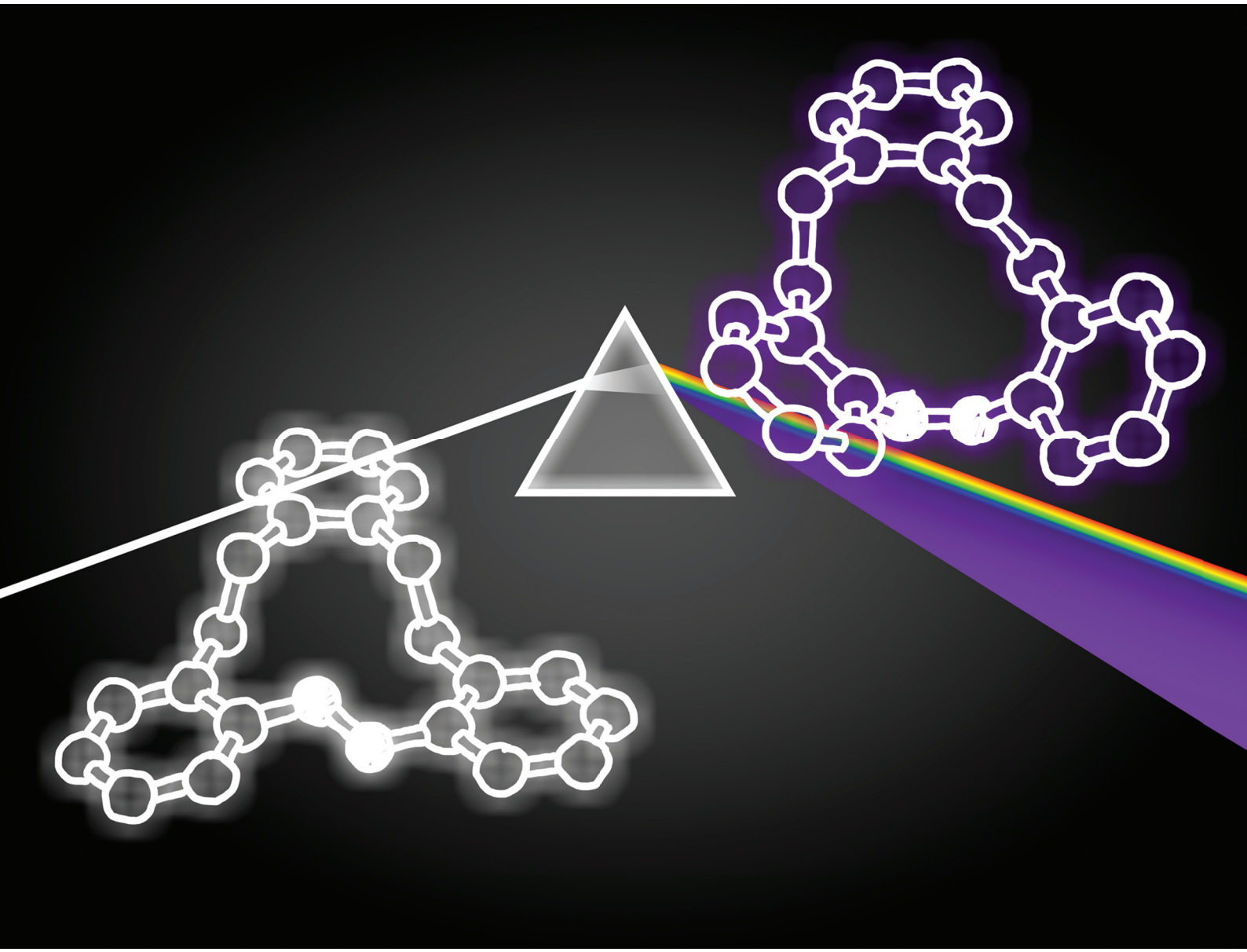

ISSN 1477-0520

ROYAL SOCIETY OF CHEMISTRY

PAPER

Larissa K. S. von Krbek *et al.*

Twelve-membered ring photoswitches with excellent $Z \rightarrow E$ conversion under ambient light

Organic & Biomolecular Chemistry

ROYAL SOCIETY OF CHEMISTRY

PAPER

Cite this: *Org. Biomol. Chem.*, 2023, **21**, 4993

Twelve-membered ring photoswitches with excellent $Z \rightarrow E$ conversion under ambient light†

Ruben Falkenburg, ‡[a] Maximilian J. Notheis, ‡[a] Gregor Schnakenburg [b] and Larissa K. S. von Krbek *[a]

Received 16th March 2023,
Accepted 31st March 2023

DOI: 10.1039/d3ob00413a

rsc.li/obc

Incorporation of azobenzenes into macrocycles is an intriguing approach for fine tuning the photophysical properties of these photoswitches and tailoring them to specific applications. A versatile synthesis of macrocyclic azobenzenes has been developed that allows for facile modification of these photoswitches. One example shows high chemical stability, long half-life of its *Z*-isomers, quantitative $Z \rightarrow E$ conversion under white light, and excellent separation of excitation bands to address either the *E* or *Z*-state selectively. The near quantitative $Z \rightarrow E$ conversion under white light is a unique feature with an important impact on applications, in which the configuration under ambient light needs to be close to 100%.

Introduction

The ability of photoswitchable molecules to address two distinct isomers of the same molecule by the non-invasive stimulus "light" opens numerous areas of potential application, including, but not limited to, chemical sensing,[1,2] smart materials,[3–5] data storage,[6] logic gates,[7] photopharmacology,[8–11] and life-like motion.[12] With the broad scope of potential applications arises the need for a wide variety of chemically stable photoswitches with distinct properties – such as excitation wavelength, the photostationary state (PSS) under irradiation and under ambient conditions, and thermal half-life $\tau_{\frac{1}{2}}$.[13]

Azobenzenes are amongst the most commonly used photoswitches, due to their high PSS, as well as high chemical and photochemical stability.[14,15] Azobenzene switches from the thermodynamically more stable *E*-isomer to the *Z*-isomer (63.7 kJ mol^{-1})[16] by excitation of the $E(\pi \rightarrow \pi^*)$ band under irradiation with 365 nm light with a PSS of 91%.[17] The *Z*-isomer switches back to the *E*-isomer either thermally or by exciting the $Z(n \rightarrow \pi^*)$ band *via* irradiation with visible light (>400 nm).[13,15] Good separation of the two excitation bands, thus, allows both isomers to be addressed precisely, which is crucial for applications such as data storage. However, even though the *E*-isomer is thermodynamically more stable, 21% of the *Z*-isomer is still present under ambient conditions due to photoswitching with white light.[17] Various substitution patterns with both electron withdrawing and donating substituents have been demonstrated to be effective at fine tuning the photophysical properties of an azobenzene switch.[18]

An intriguing approach incorporates an azo-bridge into cyclic molecules of various ring sizes,[2,19–23] resulting in extended thermal half-lives, improved band separations, and red shifted excitation wavelengths. Additionally, swapped thermal stability of the isomers is observed in the case of small ring sizes of seven (diazepines)[24] or eight atoms (diazocines).[25–27] These cyclic azobenzenes represent a small but fast-growing class of molecular switches. The eight-membered ring diazocines, whose photochemical properties have been investigated as early as 2009,[25] have recently been successfully applied in photopharmacology[10,11] and smart materials.[28] Comparison of the ethylene-bridged diazocine[25] with the oxamethylene-bridged diazocine[26] shows increased thermal half-life and photoconversion for the ethylene-bridged analogue. Recently, Staubitz and co-workers[19,20] developed a series of photoswitches, in which an azobenzene unit was incorporated into a medium-sized 12-membered ring in a four-step synthesis. Within the macrocycle, the *ortho*-positions of the azobenzene are bridged *via* a 1,2-phenylenebis(methylene)bis(oxa) moiety. The cyclic structure significantly extended the thermal half-life, improved the band separation, and allowed for selective switching of the macrocycle to its *Z*- (81%, 365 nm) and *E*-isomers (88%, 405 nm) in solution as well as in the solid state, which could prove to be useful for applications such as data storage and smart materials.

Inspired by this new bisoxa-12-membered ring motif, we wanted to prepare a new family of "all-carbon" bridged deriva-

[a]*Kekulé-Institut für Organische Chemie und Biochemie, Rheinische Friedrich-Wilhelms-Universität Bonn, Gerhard-Domagk-Str. 1, 53121 Bonn, Germany. E-mail: larissa.vonkrbek@uni-bonn.de*

[b]*Institut für Anorganische Chemie, Rheinische Friedrich-Wilhelms-Universität Bonn, Gerhard-Domagk-Str. 1, 53121 Bonn, Germany*

†Electronic supplementary information (ESI) available. CCDC 2248689. For ESI and crystallographic data in CIF or other electronic format see DOI: https://doi.org/10.1039/d3ob00413a

‡These authors contributed equally to this work.

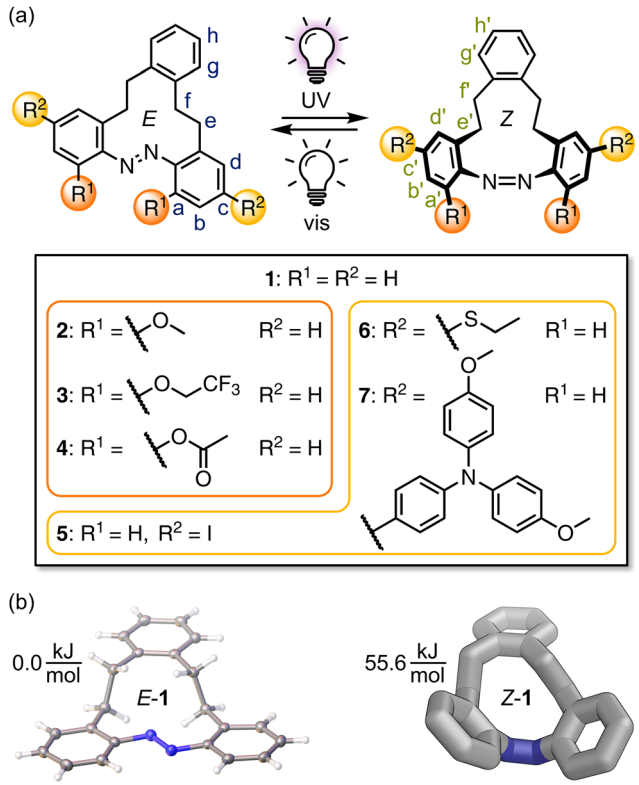

Fig. 1 (a) A variety of 12-membered ring photoswitches. (b) Crystal structure of *E*-**1** and the DFT-optimized§ structure of *Z*-**1** and their relative free energies $\Delta\Delta G$ in dichloromethane.

tives of these 12-membered cyclic photoswitches, thereby avoiding potentially reactive sites in the backbone. Furthermore, we wanted to investigate whether these "all-carbon" bridged derivatives show similarly improved properties as their analogues bearing smaller[23,24] ring sizes do. Therefore, we synthesised a variety of "all-carbon" bridged macrocyclic azobenzenes **1**–**7** (Fig. 1). The synthetic route to parent system **1** is modular and allows for facile substitution at both *ortho*- and *para*-positions to the azo-group, potentially allowing for easy fine-tuning of the photophysical properties as previously demonstrated for azobenzene-based photoswitches.[24–26,29,30]

Results and discussion

Synthesis of photoswitches

Photoswitch **1** was obtained in three steps with good to excellent yields and an overall yield of 58% (Scheme 1). Sonogashira cross coupling of commercially available 2-ethynylaniline (**A**) and 1,2-diodobenzene (**B**) with subsequent reduction of the newly formed ethynyl connections afforded diamine **C** in excellent yield. Successive oxidative azo-coupling of the aniline moieties with $Pb(OAc)_4$ under pseudo-high-dilution conditions to close the 12-membered ring yielded photoswitch **1** (67%). Although 67% is an excellent yield for a cyclic azo-coupling and $Pb(OAc)_4$ proved useful for the synthesis of cyclic azo-compounds before,[21,31] its high toxicity made us search for less harmful reagents to achieve the desired transformation. However, commonly used, less hazardous oxidants for azo-couplings such as Cu/O_2,[32] *tert*-butyl hypochlorite (*t*BuOCl),[33] MnO_2,[20] and *meta*-chloroperoxy benzoic acid (*m*CPBA)[27] resulted in no or only poor conversion (ESI, Table S2†).

With regard to azobenzenes[29,30,34] and azobenzene-based photoswitches,[26,27] various electron withdrawing or donating *ortho*- and *para*-substituents have been reported to influence their thermal stability, excitation wavelengths, and PSS quite significantly. Therefore, we synthesized six chemically diverse derivatives of **1** with electron withdrawing or donating substituents at the *ortho*- or *para*-position to the azo-bridge (Scheme 1). To introduce *ortho*-substituents, we used a recently reported method by Müller-Deku and Thorn-Seshold.[35] Dimethoxy derivative **2**, bis(trifluoroethoxy) derivative **3**, and diaceto derivative **4** were obtained *via* a simple Pd-catalysed *ortho*-alkoxylation reaction involving only one additional step and demonstrating the chemical stability of parent system **1**.

Our synthetic approach allowed for straightforward modification of the synthetic route to obtain diiodo photoswitch **5** with only one additional step (Scheme 1). Iodination of dianiline **C** to diiodide **D** using *N*-iodosuccinimide (NIS) and subsequent oxidative azo-coupling yielded the desired diiodated photoswitch **5**. **5** could then be subjected to different Pd-catalysed coupling reactions to provide thioether derivative **6** and bis(4-methoxyphenyl) phenylamine derivative **7**. All photoswitches were characterized and investigated by NMR and UV-vis spectroscopy as well as mass spectrometry (ESI, sections S2 and S3†).

Characterisation of photoswitches

To investigate the photoswitching behaviour of all seven derivatives, we irradiated solutions of **1**–**7** (1 mM, DMF) at seven different wavelengths between 325 and 500 nm (325, 365, 390, 405, 430, 450, and 500 nm; ESI, section S3.3†). While compounds **1**, **3**, **4**, **5**, and **6** showed significant changes in their UV-vis spectra after irradiation, almost no changes were observed for **2** and **7** for any excitation wavelength. Since tetra (*o*-methoxy)azobenzene[36] has excellent photoswitching abilities, dimethoxy derivative **2** not switching at any wavelength it was subjected to was highly unexpected.

Compounds **1**, **3**, **4**, and **5** could be switched using 365 nm light, while **6** showed partial switching over a broader spectral range (365–430 nm) with the most pronounced changes observed under irradiation with slightly red-shifted 405 nm light. With the ideal excitation wavelengths, λ_{ex}, determined, we investigated the photostationary states (PSS) of **1**, **3**, **4**, **5**, and **6** using HPLC,[35] NMR or UV-vis spectroscopy[35] (Fig. 2a; ESI, section S3†) as well as their thermal half-lives $\tau_{\frac{1}{2}}$ (Fig. 2b; ESI, section S3.4†).

§ DFT calculations were performed on a ωB97X-v def2-QZVPP level of theory for geometry optimization and with a rigid-rotor harmonic-oscillator approximation and a continuous solvation model (r2scan-3c and COSMO-RS) to calculate ΔG in dichloromethane (ESI, section S4†).

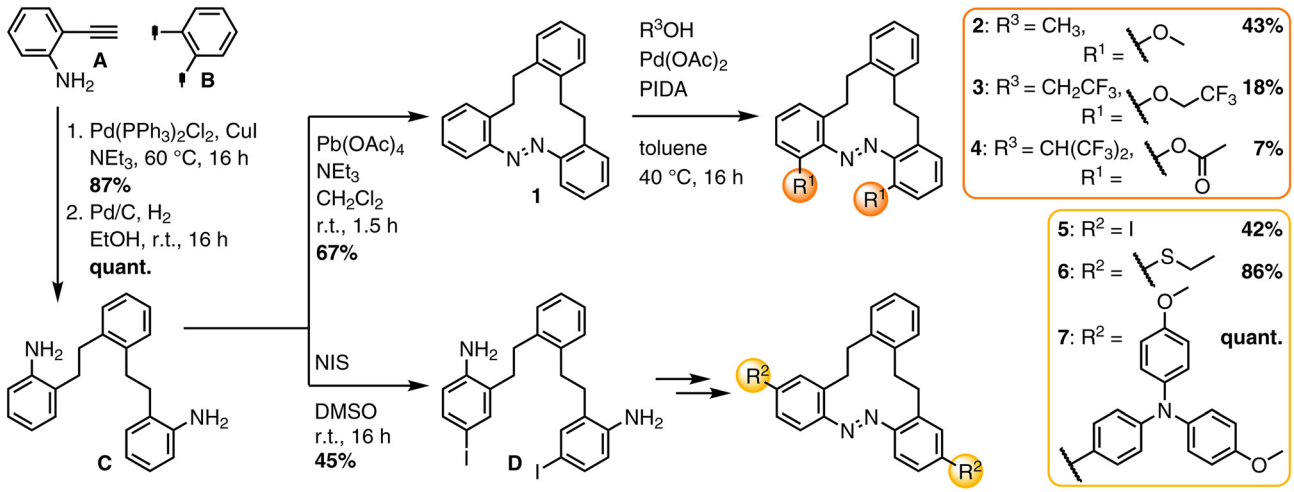

Scheme 1 Synthesis of a group of photoswitches (**1–7**), in which the azo-units are embedded in "all-carbon" 12-membered rings. Reaction conditions: **D** → **5**: $Pb(OAc)_4$, NEt_3, CH_2Cl_2, r.t., 1 h; **5** → **6**: ethanethiol, $Pd(PPh_3)_2Cl_2$, CuI, NEt_3, 60 °C, 16 h; **5** → **7**: 4-methoxy-*N*-(4-methoxyphenyl)-*n*-(4-(4,4,5,5-tetramethyl-1,3,2-dioxaborolan-2-yl)phenyl)aniline, $Pd(PPh_3)_2Cl_2$, CuI, NEt_3, 60 °C, 16 h.

(a)

	λ_{ex} [nm]	PSS [% Z]	$\tau_{1/2}$ [h]
1	365	53%*	30.6
2	–	n.d.	n.d.
3	365	14%*	8.20
4	365	34%*	7.10
5	365	54%$^+$	19.0
6	405	38%*	1.23
7	–	n.d.	n.d.

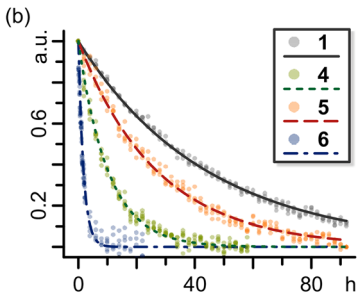

Fig. 2 (a) Excitation wavelengths λ_{ex}, PSS, and thermal half-lives $\tau_{\frac{1}{2}}$ of **1–7**. PSS were determined in CH_3CN by integration of HPLC traces (*) or ^1H NMR signals ($^+$), respectively. (b) Change in absorption $(A_t - A_\infty)\cdot(A_0 - A_\infty)^{-1}$ plotted over time t following thermal relaxation of **1** (grey), **4** (green), **5** (red), and **6** (blue) to provide their respective half-lives $\tau_{\frac{1}{2}}$ (45 °C, DMF, 1 mM, 4–6 replicates each).

In contrast to regular azobenzenes[29,30,36] and more in line with the behaviour of diazocines,[26,27] none of the investigated substitution patterns, irrespective of their electron donating or withdrawing nature, significantly increased the PSS compared to our parent photoswitch **1** (Fig. 2a; ESI, section S3†). Similar to the bisoxa-12-membered ring azobenzene,[19] thermal half-lives $\tau_{\frac{1}{2}}$ of all derivatives were reduced compared to parent system **1** (Fig. 2a and b; ESI, section S3.4†). Since parent compound **1** showed the most promising initial photophysical properties, we decided to investigate it in more detail.

UV-vis spectroscopic study of 1. The UV-vis spectrum of **1** (1 mM, CH_3CN/CH_3OH 1 : 1 (v/v)) showed a characteristic, strong absorption maximum at 327 nm, which we attributed to the π → π* transition, and a much weaker n → π*-band at 457 nm (Fig. 3a, orange dashed line), both indicative of an azobenzene photoswitch in its *E*-configuration.[14,20,22,29] Upon irradiation of **1** at 365 nm (12 min), the UV-vis spectrum showed a decrease and hypsochromic shift of the π → π* band to 291 nm, along with an increase and slight hypsochromic shift of the n → π* band to 442 nm (Fig. 3a, yellow line), characteristic for an azobenzene-based photoswitch[14,20,22,26,29] changing from its *E* to its *Z*-configuration. Interestingly, the absorption maxima λ_{max} for *E*(π → π*) = 327 nm and *Z*(n → π*) = 442 nm are well separated by 115 nm, which is crucial for achieving high selectivities in the photostationary states of a photoswitch.[20,25,37]

NMR spectroscopic study of 1. ^1H NMR spectroscopy further supported the interpretation of our UV-vis results. The ^1H NMR spectrum of photoswitch **1** under ambient light displayed one set of signals (Fig. 3b, top), indicating that **1** resides either entirely in its *E* or *Z*-configuration (*E*-**1** and *Z*-**1**, respectively) under ambient conditions. Aromatic signals of **1** were sharp, whereas the ethylene protons H_e and H_f gave a broad signal, which could be resolved into four sharp diastereotopic signals upon cooling to 243 K (ESI, Fig. S26†).

From the coalescence of the two proton signals H_e and H_f at room temperature, we infer the cyclic structure of **1** to be reasonably flexible to allow for the azo-moiety to be either in its *E* or *Z*-configuration within the macrocycle (*E*-**1** and *Z*-**1**, respectively). *In situ* irradiation[38] of *E*-**1** inside the NMR spectrometer with 365 nm light for 60 minutes resulted in the appearance of a second set of sharp signals (51% *Z*-**1**), which were all upfield shifted compared to the ones of *E*-**1** (Fig. 3b, middle). These upfield shifts are well in line with the chemical shift changes observed for the *E* → *Z* isomerisation of other azobenzene-based photoswitches.[20,22,26,29] Most prominently, the proton next to the azo-bridge (H_a) shifted by more than 2 ppm from δ_E = 7.86 ppm to δ_Z = 6.72 ppm and the diastereotopic ethylene protons H_e and H_f were well resolved in *Z*-**1** at room temperature. Irradiation with white light for 20 minutes restored the original set of signals (Fig. 3b, bottom).

Crystal structure and DFT-optimized structures of 1. To further support our assumption that **1** resides in its

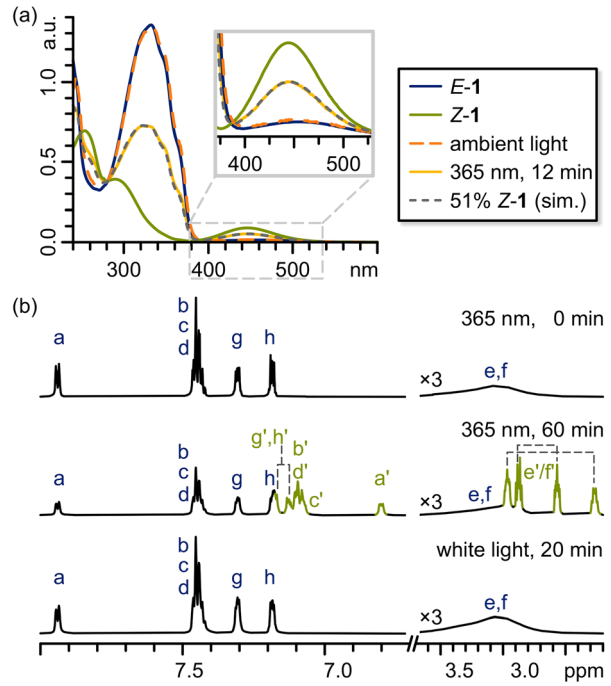

Fig. 3 (a) UV-vis spectra (CH_3CN/CH_3OH 1 : 1 (v/v))¶ of *E*-**1** (blue, normalized) and *Z*-**1** (green, normalized) as obtained after HPLC separation, **1** subjected to ambient light (orange, 1 mM), PSS of **1** after 12 min irradiation with 365 nm light (yellow, 1 mM), and the simulated spectrum of the PSS of **1** showing 51% *Z*-**1** (grey). (b) ^{1}H NMR (700 MHz, CD_2Cl_2,¶ 3 mM, 298 K) of **1** under ambient light and after *in situ* irradiation with 365 nm light (60 min, PSS 51% *Z*-**1**) or white light (20 min; top to bottom).

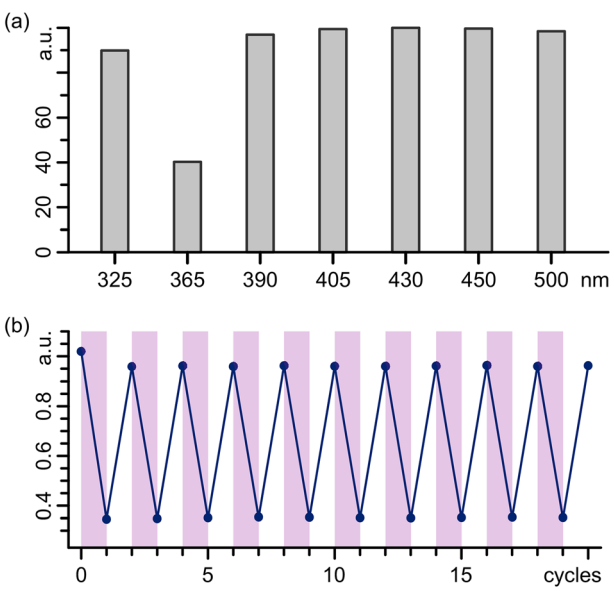

Fig. 4 (a) Absorption of **1** at 330 nm (1 mM, DMF¶) after irradiation with light of different wavelengths demonstrating *E*-**1** to be the favoured isomer under any wavelength except 365 nm. (b) Absorption of **1** at 330 nm (1 mM, DMF¶) after alternating irradiation with 365 nm and white light demonstrating reversible photoisomerization cycles of **1**.

E-configuration (*E*-**1**) in the ground state, we obtained single crystals of **1** suitable for X-ray analysis by slow solvent evaporation under ambient conditions. The resulting crystal structure shows **1** in its *E*-configuration (Fig. 1b; ESI, section S5†). This was further supported by the DFT-calculated§ relative Gibbs free energies for *E*-**1** and *Z*-**1** in dichloromethane (Fig. 1b; ESI, section S4†). As expected from the UV-vis spectrum under ambient light (Fig. 3a, dashed orange line), *E*-**1** is more stable than *Z*-**1** by 55.6 kJ mol^{-1} – a difference which is in the same order of magnitude as that of regular azobenzenes (63.7 kJ mol^{-1}).[16]

PSS and thermal stability of 1. A PSS of 53% *Z*-**1** for **1** in acetonitrile was determined *via* HPLC[35] and confirmed by ^{1}H NMR integration (55% in CD_3CN; ESI, section 3.4, Fig. S27, Table S3†). Simulating[35] the UV-vis spectrum of the PSS (Fig. 3a, grey dashed line; ESI, Fig. S36†) in acetonitrile/methanol 1 : 1 (v/v) resulted in a similar PSS value (51% *Z*-**1**), despite having a protic solvent in the mixture. The PSS of **1** in dimethylformamide and dichloromethane determined by ^{1}H NMR integration was only slightly increased (59%) or decreased (51%) compared to acetonitrile (53%), respectively. These small deviations were probably caused by the higher and lower polarities of dimethylformamide and dichloromethane, which would in turn be expected to stabilise and destabilise the more polar configurational isomer *Z*-**1**. Additionally, *Z*-**1** showed excellent thermal stability with a half-life $\tau_{\frac{1}{2}}$ of 35.6 hours at 45 °C in acetonitrile (ESI, Fig. S55†). Switching the solvent to the higher boiling dimethylformamide,¶ we could determine the half-life $\tau_{\frac{1}{2}}$ as 30.6 hours at 45 °C (Fig. 2b, grey line) and 16 days at ambient temperature (ESI, Fig. S56†), which exceeds the thermal half-life of regular azobenzene[14,29] more than five-fold (3 d at 25 °C). In line with our observations on the solvent dependence of **1**'s PSS, changing the solvent from acetonitrile to dimethylformamide did not seem to have a significant impact on the observed thermal half-life $\tau_{\frac{1}{2}}$.

Using HPLC, we determined that 99% of *E*-**1** was present under ambient light (ESI, Fig. S34†). Indeed, the photostationary state of **1** is close to that of 99% *E*-**1** under irradiation with any of our tested wavelengths between 325 and 500 nm, including 405 nm and ambient light (Fig. 4a; ESI, Fig. S31, S34 and S35†). Moreover, macrocyclic photoswitch **1** showed high cycling stability over 20 cycles switching from *E*-**1** to *Z*-**1** and back using 365 nm and white light, respectively, without significant photodegradation (Fig. 4b).

Even though the PSS of **1** at 365 nm is not particularly high compared to other azobenzene-based photoswitches, ranging

¶Regarding solvents: long-time UV-vis experiments required use of a high-boiling solvent (DMF), whereas HPLC required acetonitrile/methanol (1 : 1 (v/v)) as an eluent after irradiating the sample in acetonitrile. Hence, related UV-vis spectra were recorded in the same solvent for comparability. Therefore, the PSS determined by HPLC (CH_3CN) and simulation of the obtained UV-vis spectrum of the PSS (CH_3CN/CH_3OH, 1 : 1 (v/v)) cannot be directly compared. In ^{1}H NMR, dichloromethane was the solvent of choice for solubility analysis and to avoid the overlap of the compound signals with the solvent residual signal. However, ^{1}H NMR spectra of **1** and **5** were also recorded in deuterated acetonitrile to allow for the comparison of the PSS determined by HPLC and by NMR integration.

from 92% *Z* in azobenzene[17] to 81% *Z* in the previously reported bisoxa-12-membered ring,[20] **1**'s high cycling stability, thermal stability, and the fact that **1** switches back to its *E*-form almost quantitatively even upon irradiation with white light opens up a wide scope of applications in materials which require high structural order when used under ambient light.

Conclusion

In conclusion, we were able to develop a straightforward route to a variety of macrocyclic azobenzenes, which is easily adaptable and also demonstrates parent system **1**'s chemical stability. From all substitution patterns, **1** shows the most promising photoswitching behaviour with reversible photoinduced *E* → *Z* conversion and excellent band separation (115 nm) for precisely addressing one configuration over the other. Despite **1**'s PSS (53% *Z*-**1**) not being particularly high, it shows high thermal stability ($\tau_{\frac{1}{2}}$ = 30.6 h at 45 °C and 16 d at ambient temperature). Furthermore, to the best of our knowledge, an almost quantitative conversion to *E*-**1**, even under white light, is a unique feature with an important impact on applications, in which the configuration under ambient light needs to be close to 100%, such as smart materials. This almost complete *Z* → *E* conversion should also allow for efficient erasing of data in data storage applications and full reversibility of binding in chemical sensors.

Author contributions

M. J. N. and L. K. S. v. K. conceptualized the project and all authors were involved in collecting the details. R. F. and M. J. N. synthesized and investigated the compounds. R. F., M. J. N., and L. K. S. v. K. performed formal analysis. G. S. collected the crystallographic data as well as solved and refined the crystal structure. L. K. S. v. K. visualized the data for the manuscript and wrote the original draft. All authors contributed to reviewing and editing the final draft.

Conflicts of interest

There are no conflicts to declare.

Acknowledgements

This work is supported by the Fonds der Chemischen Industrie (FCI, Liebig Fellowship) and the German Research Foundation (DFG; Emmy Noether Programme, 446317932). M. J. N. thanks the FCI for a PhD Fellowship. R. F., M. J. N., and L. K. S. v. K. thank Dr O. Thorn-Seshold and B. Baumgartner for helpful discussions on the investigation of photoswitches. M. J. N. thanks M. Stahn for helpful discussions on DFT calculations. G. S. thanks Prof. Dr A. C. Filippou for providing X-ray infrastructure.

References

1 J. P. Van Der Berg, W. A. Velema, W. Szymanski, A. J. M. Driessen and B. L. Feringa, *Chem. Sci.*, 2015, **6**, 3593–3598.
2 E. Wagner-Wysiecka, T. Rzymowski, M. Szarmach, M. S. Fonari and E. Luboch, *Sens. Actuators, B*, 2013, **177**, 913–923.
3 A. Goulet-Hanssens, F. Eisenreich and S. Hecht, *Adv. Mater.*, 2020, **32**, 1905966.
4 G. Tyagi, J. L. Greenfield, B. E. Jones, W. N. Sharratt, K. Khan, D. Seddon, L. A. Malone, N. Cowieson, R. C. Evans, M. J. Fuchter and J. T. Cabral, *J. Am. Chem. Soc.*, 2022, **2**, 2670–2677.
5 Z. L. Pianowski, *Chem. – Eur. J.*, 2019, **25**, 5128–5144.
6 T. Ikeda and O. Tsutsumi, *Science*, 1995, **268**, 1873–1875.
7 Y. Chen, C. Li, X. Xu, M. Liu, Y. He, I. Murtaza, D. Zhang, C. Yao, Y. Wang and H. Meng, *ACS Appl. Mater. Interfaces*, 2017, **9**, 7305–7314.
8 Q. Zhang, C. S. Kounde, M. Mondal, J. L. Greenfield, J. R. Baker, S. Kotelnikov, M. Ignatov, C. P. Tinworth, L. Zhang, D. Conole, E. De Vita, D. Kozakov, A. McCluskey, J. D. Harling, M. J. Fuchter and E. W. Tate, *Chem. Commun.*, 2022, **58**, 10933–10936.
9 J. Broichhagen, J. A. Frank and D. Trauner, *Acc. Chem. Res.*, 2015, **48**, 1947–1960.
10 T. Ko, M. M. Oliveira, J. M. Alapin, J. Morstein, E. Klann and D. Trauner, *J. Am. Chem. Soc.*, 2022, **144**, 21494–21501.
11 J. Ewert, L. Heintze, M. Jordà-Redondo, J.-S. S. Von Glasenapp, S. Nonell, G. Bucher, C. Peifer and R. Herges, *J. Am. Chem. Soc.*, 2022, **144**, 15059–15071.
12 F. Lancia, A. Ryabchun and N. Katsonis, *Nat. Rev. Chem.*, 2019, **3**, 536–551.
13 C. Fedele, T. P. Ruoko, K. Kuntze, M. Virkki and A. Priimagi, *Photochem. Photobiol. Sci.*, 2022, **21**, 1719–1734.
14 S. Crespi, N. A. Simeth and B. König, *Nat. Rev. Chem.*, 2019, **3**, 133–146.
15 Z. Mahimwalla, K. G. Yager, J. I. Mamiya, A. Shishido, A. Priimagi and C. J. Barrett, *Polym. Bull.*, 2012, **69**, 967–1006.
16 J. Dokić, M. Gothe, J. Wirth, M. V. Peters, J. Schwarz, S. Hecht and P. Saalfrank, *J. Phys. Chem. A*, 2009, **113**, 6763–6773.
17 Y. Ito, H. Ito and T. Matsuura, *Tetrahedron Lett.*, 1988, **29**, 563–566.
18 A. Kerckhoffs, K. E. Christensen and M. J. Langton, *Chem. Sci.*, 2022, **13**, 11551–11559.
19 S. Ghosh, C. Eschen, N. Eleya and A. Staubitz, *J. Org. Chem.*, 2023, **88**(6), 3372–3377.
20 N. Eleya, S. Ghosh, E. Lork and A. Staubitz, *J. Mater. Chem. C*, 2021, **9**, 82–87.
21 A. H. Heindl, J. Becker and H. A. Wegner, *Chem. Sci.*, 2019, **10**, 7418–7425.
22 E. Wagner-Wysiecka, N. Łukasik, J. F. Biernat and E. Luboch, *J. Inclusion Phenom. Macrocyclic Chem.*, 2018, **90**, 189–257.
23 C. Slavov, C. Yang, L. Schweighauser, H. A. Wegner, A. Dreuw and J. Wachtveitl, *ChemPhysChem*, 2017, **18**, 2137–2141.

24 X. Shen, C. Zhang, F. Lan, Z. Su, Y. Zheng, T. Zheng, Q. Xiong, X. Xie, G. Du, X. Zhao, C. Hu, P. Deng and Z. Yu, *Angew. Chem., Int. Ed.*, 2022, **61**, e202209441.
25 R. Siewertsen, H. Neumann, B. Buchheim-Stehn, R. Herges, C. Näther, F. Renth and F. Temps, *J. Am. Chem. Soc.*, 2009, **131**, 15594–15595.
26 M. Hammerich, C. Schütt, C. Stähler, P. Lentes, F. Röhricht, R. Höppner and R. Herges, *J. Am. Chem. Soc.*, 2016, **138**, 13111–13114.
27 M. S. Maier, K. Hüll, M. Reynders, B. S. Matsuura, P. Leippe, T. Ko, L. Schäffer and D. Trauner, *J. Am. Chem. Soc.*, 2019, **141**, 17295–17304.
28 S. Li, K. Bamberg, Y. Lu, F. D. Sönnichsen and A. Staubitz, *Polymer*, 2023, **15**, 1306.
29 H. Chen, W. Chen, Y. Lin, Y. Xie, S. H. Liu and J. Yin, *Chin. Chem. Lett.*, 2021, **32**, 2359–2368.
30 D. Bléger, J. Schwarz, A. M. Brouwer and S. Hecht, *J. Am. Chem. Soc.*, 2012, **134**, 20597–20600.
31 H. Hilpert, L. Hoesch and A. S. Dreiding, *Helv. Chim. Acta*, 1985, **68**, 325–333.
32 J. Wang, J. He, C. Zhi, B. Luo, X. Li, Y. Pan, X. Cao and H. Gu, *RSC Adv.*, 2014, **4**, 16607–16611.
33 M. Benz, T. M. Klapotke, J. Stierstorfer and M. Voggenreiter, *J. Am. Chem. Soc.*, 2022, **144**, 6143–6147.
34 M. Kathan and S. Hecht, *Chem. Soc. Rev.*, 2017, **46**, 5536–5550.
35 A. Müller-Deku and O. Thorn-Seshold, *J. Org. Chem.*, 2022, **87**, 16526–16531.
36 M. J. Hansen, M. M. Lerch, W. Szymanski and B. L. Feringa, *Angew. Chem., Int. Ed.*, 2016, **55**, 13514–13518.
37 D. Samanta, J. Gemen, Z. Chu, Y. Diskin-Posner, L. J. W. Shimon and R. Klajn, *Proc. Natl. Acad. Sci. U. S. A.*, 2018, **115**, 9379–9384.
38 Y. Ji, D. A. DiRocco, J. Kind, C. M. Thiele, R. M. Gschwind and M. Reibarkh, *ChemPhotoChem*, 2019, **3**, 984–992.

Electronic Supplementary Information

for

A family of twelve-membered ring photoswitches with excellent *Z*→*E* conversion

Ruben Falkenburg,[‡a] Maximilian J. Notheis,[‡a] Gregor Schnakenburg [b] and Larissa K. S. von Krbek*[a]

a. Kekulé-Institut für Organische Chemie and Biochemie, Rheinische Friedrich-Wilhelms-Universität Bonn, Gerhard-Domagk-Str. 1, 53121 Bonn, Germany.
E-mail: larissa.vonkrbek@uni-bonn.de.

b. Institut für Anorganische Chemie, Rheinische Friedrich-Wilhelms-Universität Bonn, Gerhard-Domagk-Str. 1, 53121 Bonn

‡ These authors contributed equally.

Contents

1. General procedures

Reagents and materials. Commercial solvents and reagents were obtained from the following suppliers and used without further purification unless specified otherwise: Sigma Aldrich, Alfa Aesar, abcr, Acros Organics, BLD-Pharm, Fluorochem, Merck, TCI, Carbolution, Thermo Fisher Scientific.

Dry solvents (acetonitrile, tetrahydrofuran, methanol) were dried using a MP-SPS 800 (MBraun) drying apparatus. Solvents used for column chromatography were distilled at atmospheric pressure prior to use.

Schlenk techniques. All reactions using chemicals sensitive to air were carried out under argon using established Schlenk techniques. If chemicals were also sensitive to moisture, glassware was flame-dried prior to use.

Column chromatography. Column chromatography was carried out either using a puriFlash 5.020 (Interchim) flash chromatography machine with PuriFlash 15 µm Si HP (Interchim) flash cartridges or by hand using Silica gel ultra pure (Thermo scientific, 60 µm).

HPLC. Analytical HPLC runs were carried out on a Prominence Modular HPLC (Shimadzu) using a YMC-Pack Pro C18 (spherical, 3 µm) column with 0.5 mL min^{-1} flow rate of CH_3OH / CH_3CN (1:1 (v:v)) using the built-in UV-vis detector.

NMR spectroscopy. All NMR spectroscopic measurements were carried out using 300 MHz, 400 MHz, 500 MHz or 700 MHz spectrometers (Bruker Avance I 300, Bruker Avance I 400, Bruker Avance I 500, Bruker Avance III HD Prodigy 500, Bruker Avance III HD Ascend 700). ^{1}H and ^{13}C NMR spectra are referenced to the residual solvent peak for CD_3CN (^{1}H: 1.94 ppm, ^{13}C: 1.32 ppm), CD_2Cl_2 (^{1}H: 5.32 ppm, ^{13}C: 53.5 ppm) or $CDCl_3$ (^{1}H: 7.26 ppm, ^{13}C: 77.16 ppm). NMR signals are reported in terms of chemical shift (δ) in ppm, relative integral, multiplicity, coupling constants (in Hz) and assignment, in that order. The following abbreviations for multiplicity are used: s, singlet; d, doublet; t, triplet; qu, quartet; qn, quintet; m, multiplet; br, broad. Spectra were digitally processed (phase and baseline corrections, integration, peak analysis) using MestReNova 14.2.1 (Mestrelab) and TopSpin 4.05 (BrukerBioSpin) were used to evaluate and plot the data. All processing operations were manually checked to ensure that the processed spectra accurately represented the raw data.

Mass spectrometry. Mass spectra were acquired using an Orbitrap XL (Thermo Fischer Scientific) and evaluated and plotted using XCalibur 4.2 (Thermo Fischer Scientific).

UV-vis spectroscopy. UV-vis spectroscopy was carried out using a Clariostar Plus (BMG Labtech) plate reader utilizing a flash lamp style spectrometer.

Light sources. Illumination experiments were carried out using Prizmatrix fiber collimated LEDs.

Table S1. Light output of used LEDs.

λ [nm]	**310**	**325**	**365**	**390**	**405**	**430**	**450**	**500**	**590**	**660**	**white**
Output power (1 m optical fiber) [mW]	8.6	13	170	220	260	160	440	165	230	140	74

2. Synthetic procedures

2.1. 2,2'-(1,2-phenylenebis(ethyne-2,1-diyl))dianiline (S1)

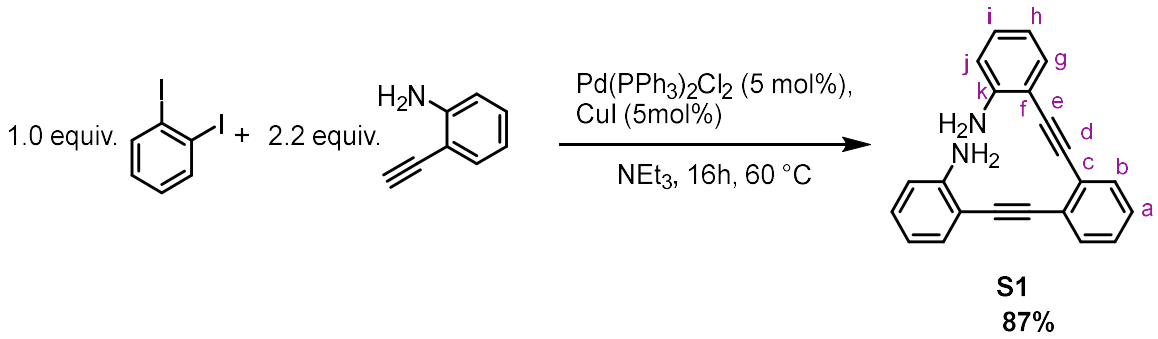

2,2'-(1,2-phenylenebis(ethyne-2,1-diyl))dianiline (**S1**) was synthesized after a modified literature procedure for analogous reactions.[1]

Triethylamine (15 mL) was deoxygenated by bubbling under a stream of Ar for 15 min. Bis(triphenylphosphine)palladium(II) dichloride (0.05 equiv., 27.8 mg, 39.7 µmol), copper iodide (0.05 equiv., 7.9 mg, 41.5 µmol), 1,2-diiodobenzene (1.00 equiv., 247 mg, 750 µmol), and 2-ethinylaniline (2.20 equiv., 220 mg, 1.88 mmol) were added to the triethylamine and the mixture deoxygenated a second time by bubbling under a stream of Argon for 20 min. The yellow reaction mixture was stirred at 60 °C for 16 h. Subsequently, the solution was allowed to cool to room temperature before purification. All volatiles were removed from the reaction mixture under reduced pressure on a rotary evaporator, the crude product was dissolved in dichloromethane, and filtered over a short silica plug (5 cm diameter, 5 cm height) with DCM to afford diamine **S1** as a brown oil (200 mg, 648 µmol, 87%).

$C_{22}H_{16}N_2$ 308.38 g mol^{-1}

R_F value (cyclohexane:ethyl acetate; (8:2 (v/v)) = 0.30.

^{1}H NMR (500 MHz, CD_2Cl_2, 298 K): δ_H [ppm] = 4.40 (s, 4H, NH_2), 6.74 – 6.67 (m, 4H, H-j,h), 7.19 – 7.13 (m, 2H, H-i), 7.39 – 7.31 (m, 4H, H-b,g), 7.57 – 7.64 (m, 2H, H-a).

^{13}C NMR (126 MHz, CD_2Cl_2,298 K): δ_C [ppm] = 90.47, 94.09, 107.39, 114.52, 117.93, 128.50, 130.54, 132.15, 132.43, 148.88.

HRMS (ESI$^+$-Orbitrap): *m*/*z* (relative intensity) = 309.1377 (100%, $[M+H]^+$, calcd 309.1386).

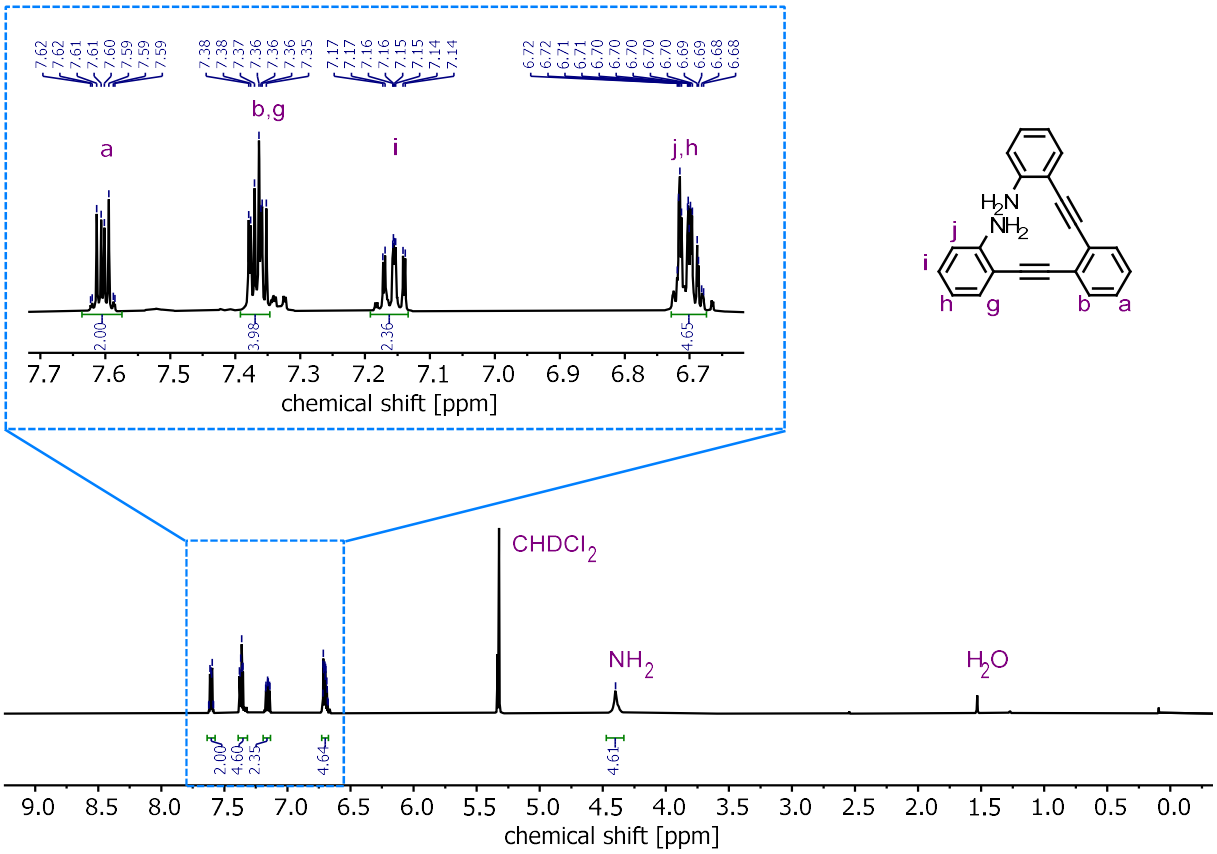

Figure S1. ^{1}H NMR spectrum (500 MHz, CD_2Cl_2, 298 K) of dianiline **S1**.

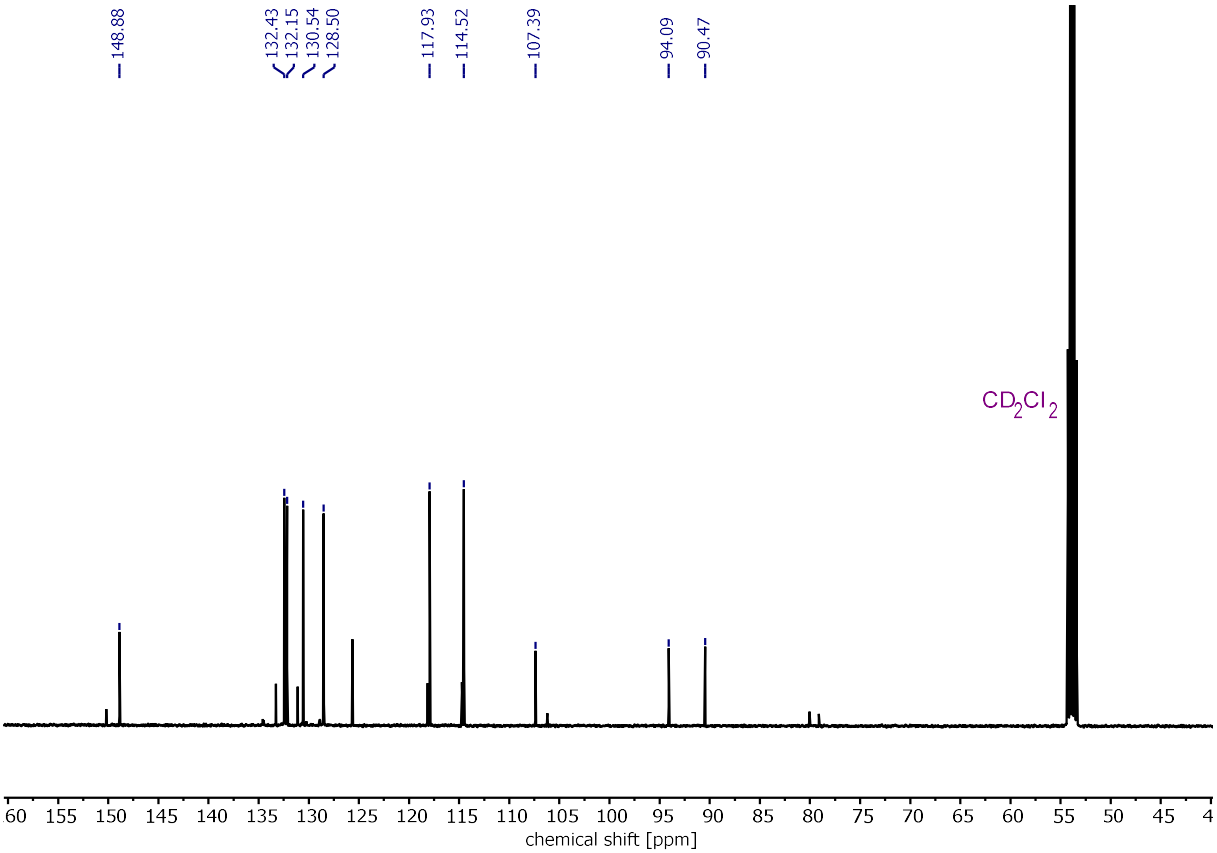

Figure S2. ^{13}C NMR spectrum (126 MHz, CD_2Cl_2, 298 K) of dianiline **S1**.

2.2. 2,2'-(1,2-phenylenebis(ethane-2,1-diyl))dianiline (C)

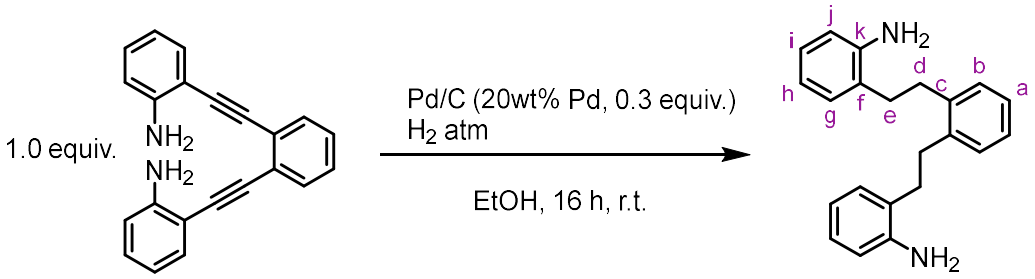

S1 **C** **quant.**

2,2'-(1,2-phenylenebis(ethane-2,1-diyl))dianiline (**C**) was synthesized after a modified literature procedure for analogous reactions.[1]

Diamine **ESI-1** (200 mg, 648 µmol, 1.0 equiv.) and Pd/C (20%^{wt} Pd, 100 mg, 189 µmol, 0.3 equiv.) were suspended in 25 mL ethanol. The reaction mixture was purged with hydrogen and stirred for 16 h under a hydrogen atmosphere. The volatiles were removed from the reaction mixture under reduced pressure at a rotary evaporator. The obtained crude product was dissolved in EtOAc (5 mL) filtered over a silica plug (5 cm diameter, 5 cm height) using EtOAc (150 mL). Removing the solvent from the obtained filtrate under reduced pressure on a rotary evaporator afforded diamine **C** as a brown oil (202 mg, 648 µmol, quant.).

$C_{22}H_{24}N_2$ 316.45 g mol^{-1}

R_F value (cyclohexane:ethyl acetate; 8:2 (v/v)) = 0.18.

^{1}H NMR (500 MHz, CD_2Cl_2, 298 K): δ_H [ppm] = 2.71 – 2.78 (m, 4H, H-e), 2.91 – 2.97 (m, 4H, H-d), 3.61 (s, 4H, NH_2), 6.67 (dd, J = 8.3, 1.3 Hz, 2H, H-j), 6.71 (td, J = 7.4, 1.2 Hz, 2H, H-h), 6.99 – 7.06 (m, 4H, H-g,i), 7.16 – 7.21 (m, 2H, H-a), 7.21 – 7.25 (m, 2H, H-b).

^{13}C NMR (126 MHz, CD_2Cl_2, 298 K): δ_C [ppm] = 27.33, 32.19, 33.41, 115.90, 118.99, 126.49, 126.69, 127.47, 129.67, 129.78, 140.24, 144.91.

HRMS (ESI$^+$-Orbitrap): *m/z* (relative intensity) = 317.2012 (100%, $[M+H]^+$, calcd 317.2012).

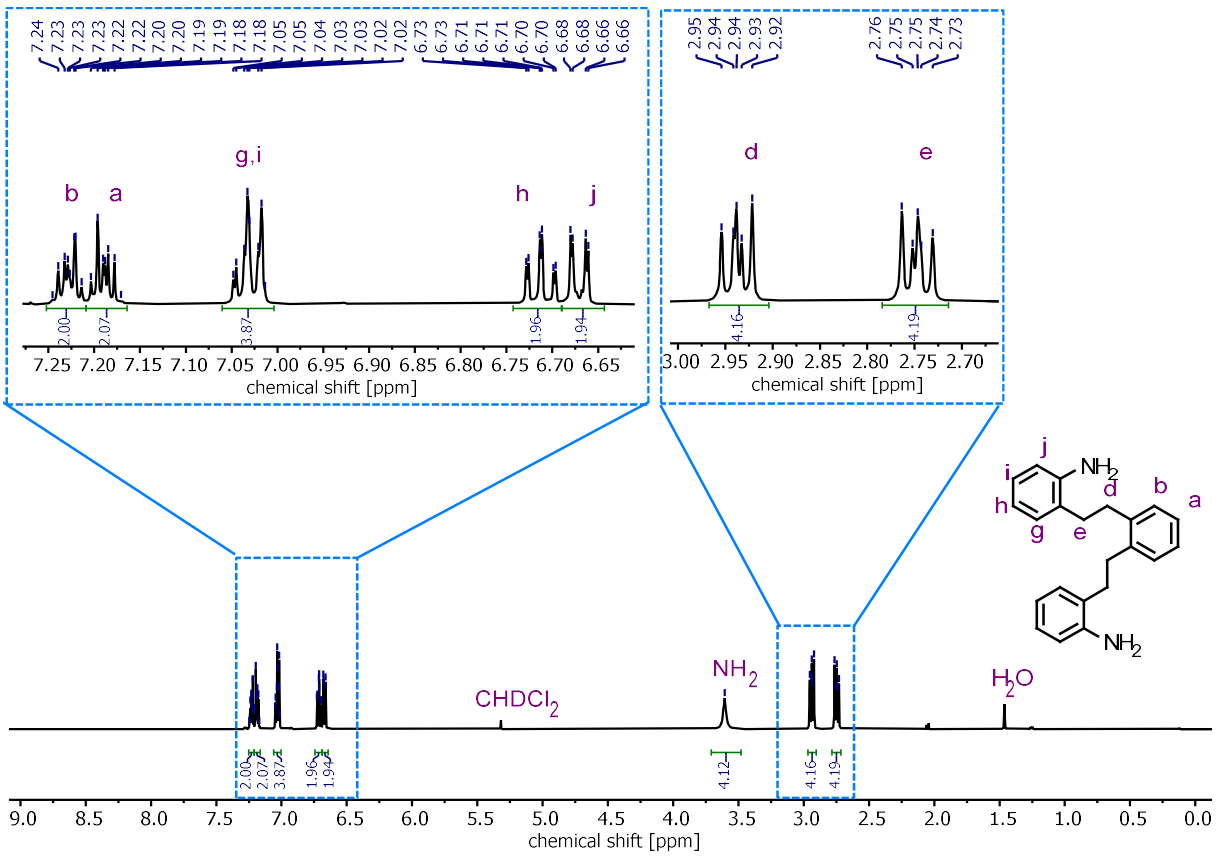

Figure S3. ^{1}H NMR spectrum (500 MHz, CD_2Cl_2, 298 K) of dianiline **C**.

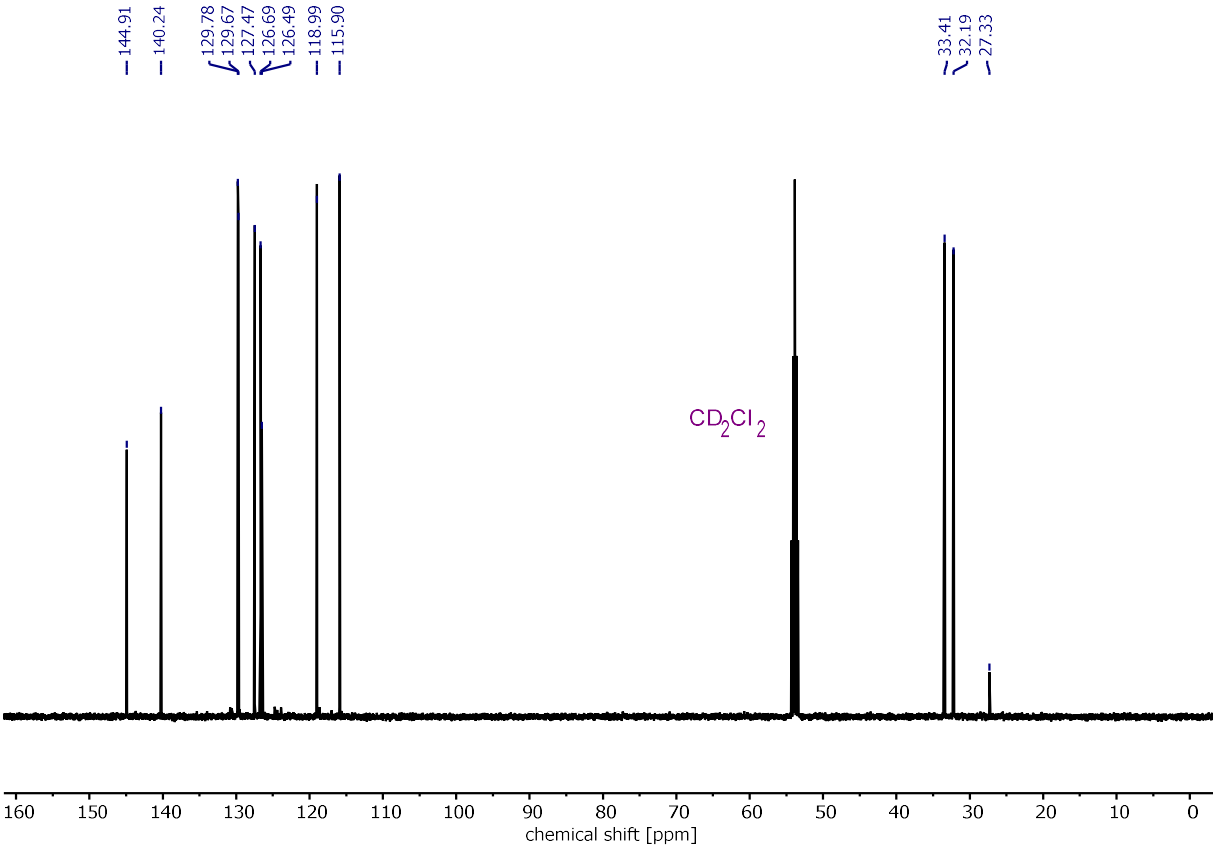

Figure S4. ^{13}C NMR spectrum (126 MHz, CD_2Cl_2, 298 K) of dianiline **C**.

2.3. 2,2'-(1,2-phenylenebis(ethane-2,1-diyl))bis(4-iodoaniline) (D)

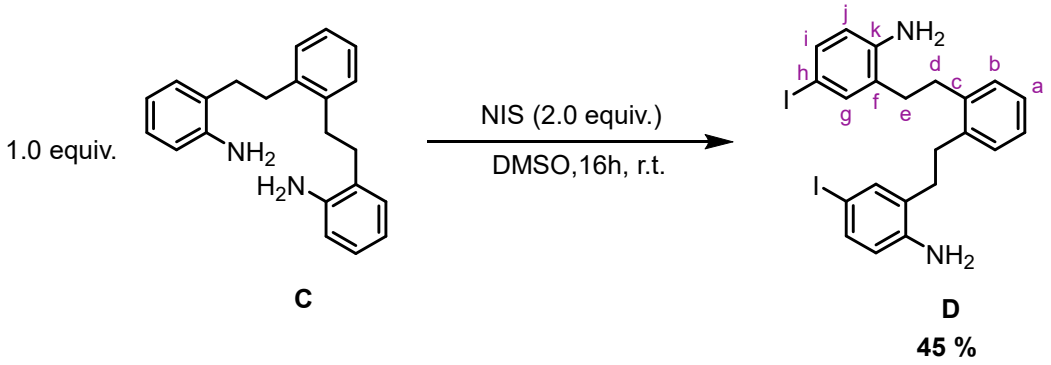

2,2'-(1,2-phenylenebis(ethane-2,1-diyl))bis(4-iodoaniline) (**D**) was synthesized after a modified literature procedure for analogous reactions.[1]

N-iodosuccinimide (524 mg, 2.33 mmol, 2.01 equiv.) was added to a solution of **C** (367 mg, 1.16 mmol, 1.0 equiv.) in DMSO (25 mL). After stirring for 16 h at room temperature, a water/saturated aqueous sodium chloride solution (4:1, 50 mL) was added to the reaction mixture and the resulting water/DMSO mixture extracted with dichloromethane (3×30 mL). The combined organic phases were dried over sodium sulfate. The solvent was removed under reduced pressure a rotary evaporator and the residue purified by column chromatography (0 to 30% ethyl acetate in cyclohexane) to afford the title compound **D** as a yellow oil (298 mg, 0.524 mmol, 45%).

$C_{22}H_{22}I_2N_2$ 568.24 g mol^{-1}

R_F value (cyclohexane:ethyl acetate; 8:2 (v/v)) = 0.15.

^{1}H NMR (500 MHz, CD_2Cl_2, 298 K): δ_H [ppm] = 2.60 – 2.70 (m, 4H, H-e), 2.80 – 2.90 (m, 4H, H-d), 3.64 (s, 4H, NH_2), 6.47 (dd, J = 7.9, 0.7 Hz, 2H, H-j), 7.18 (s, 4H, H-a,b), 7.24 – 7.32 (m, 4H, H-g,i).

^{13}C NMR (126 MHz, CD_2Cl_2, 298 K): δ_C [ppm] = 31.87, 33.05, 79.86, 118.03, 126.92, 129.16, 129.71, 136.11, 138.17, 139.75, 144.75.

HRMS (ESI$^+$-Orbitrap): *m*/*z* (relative intensity) = 568.9942 (100%, $[M+H]^+$, calcd 568.9945).

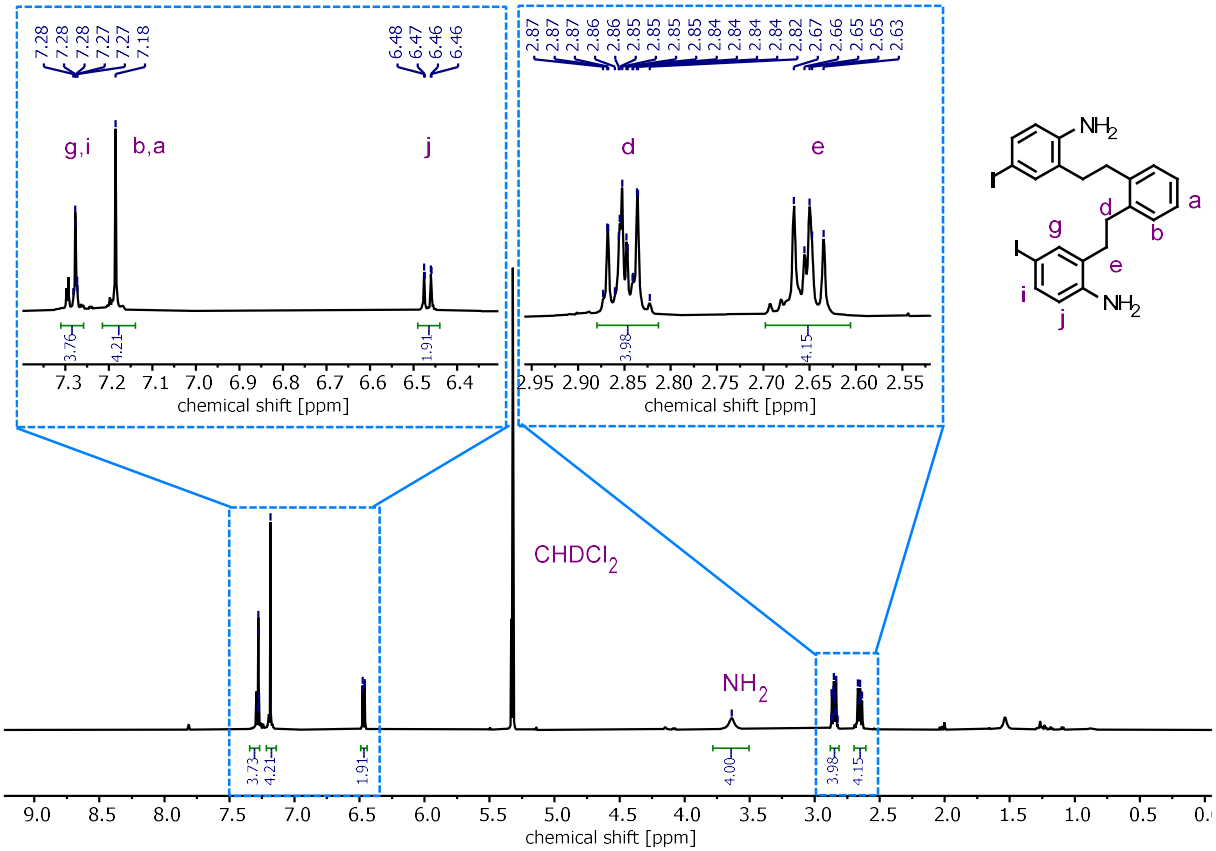

Figure S5. ^{1}H NMR spectrum (500 MHz, CD_2Cl_2, 298 K) of di*iodide* **D**.

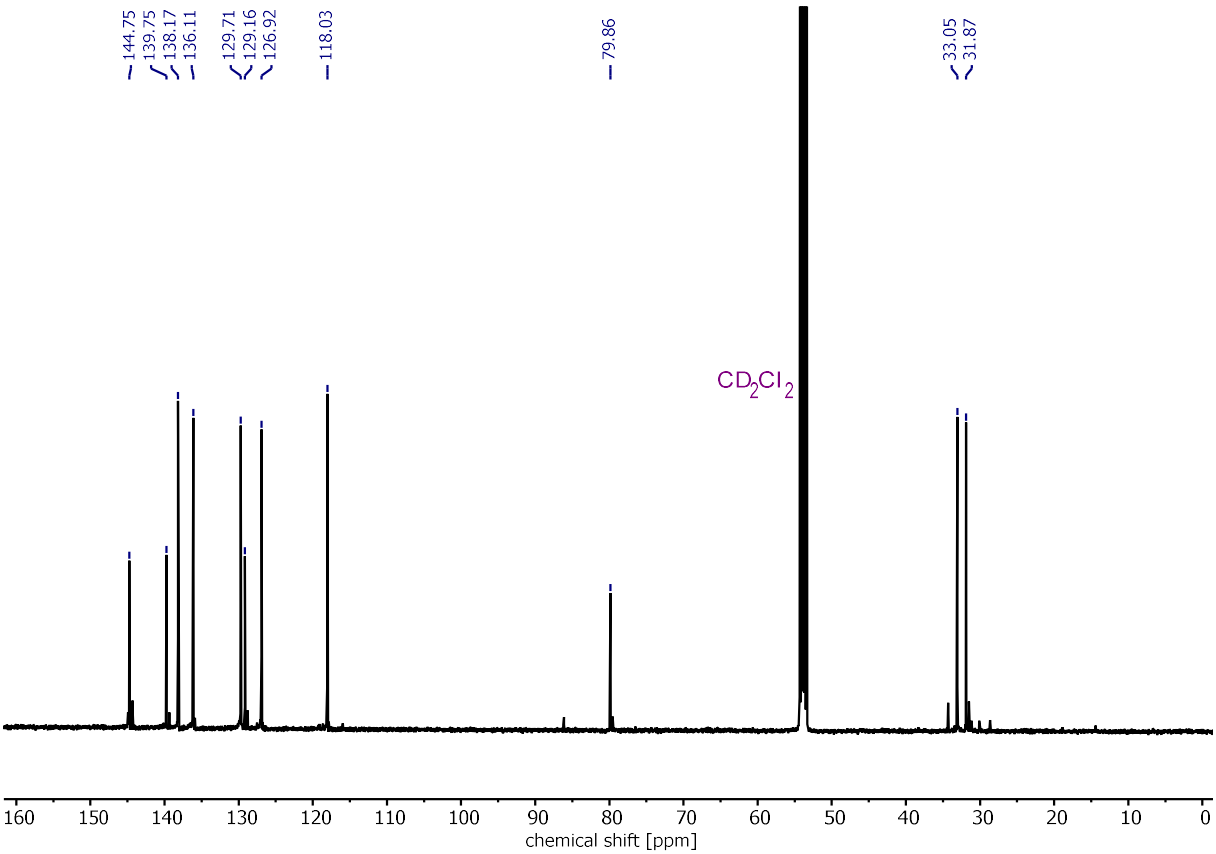

Figure S6. ^{13}C NMR spectrum (126 MHz, CD_2Cl_2, 298 K) of di*iodide* **D**.

2.4. (*E*)-11,12,17,18-tetrahydrotribenzo[*c*,*g*,*k*][1,2]diazacyclododecine (1)

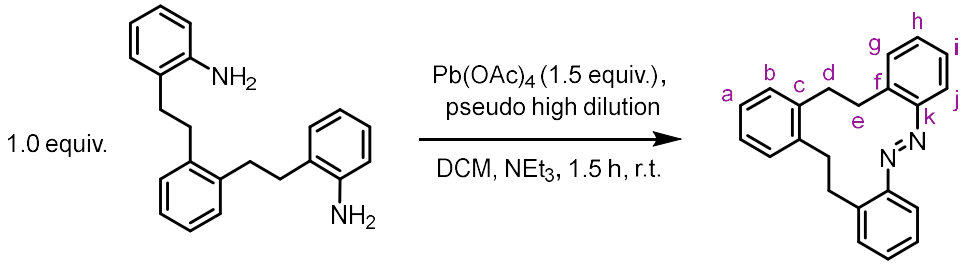

C **1**

67%

A three-necked flask was equipped with two 250 mL dropping funnels. One funnel was loaded with a solution of dianiline **C** (134 mg, 0.423 mmol, 1.00 equiv., 3 mmol/L) and TEA (1 mL) in DCM (140 mL) and the other dropping funnel was loaded with a solution of lead(IV) acetate (296 mg, 0.634 mmol, 1.50 equiv., 6 mmol/L) in DCM (100 mL). Both solutions were added dropwise into DCM (250 mL) within 50 min* at room temperature. After the addition was complete, the reaction mixture was stirred at room temperature for another 30 min. Afterwards the solvents were removed from the reaction mixture under reduced pressure on a rotary evaporator. The remaining residue was redissolved in cyclohexane and filtered over a silica plug (5 cm diameter, 5 cm height). The macrocyclic azobenzene **1** was obtained as an orange solid (89 mg, 0.285 mmol, 67%).

$C_{22}H_{20}N_2$ 312,42 g mol^{-1}

R_F value (cyclohexane:ethyl acetate; 8:2 (v/v)) = 0.67.

^{1}H NMR (500 MHz, CD_2Cl_2, 298 K) δ_H [ppm] = 2.75 – 3.69 (m, 8H, H-e,d), 7.16 – 7.21 (m, 2H, H-a), 7.28 – 7.33 (m, 2H, H-b), 7.40 – 7.50 (m, 6H, H-g,h,i), 7.92 – 7.96 (m, 2H, H-j).

^{13}C NMR (126 MHz, CD_2Cl_2, 298 K) δ_C [ppm] = 36.69 (C-d), 38.02 (C-e), 124.30 (C-j), 126.67 (C-a), 127.55 (C-g/h/i), 130.50 (C-f), 130.97 (C-b), 131.81 (C-g/h/i), 137.84 (C-g/h/i), 140.78 (C-c), 151.31 (C-l). Due to their overlap in the ^{1}H NMR spectrum C-g, C-h and C-i could not be distinguished.

HRMS (ESI$^+$-Orbitrap): m/z (relative intensity) = 313.1697 (100%, $[M+H]^+$, calcd 313.1699).

*The reaction is relatively robust. However, addition times between 10 and 50 minutes afforded the highest yields.

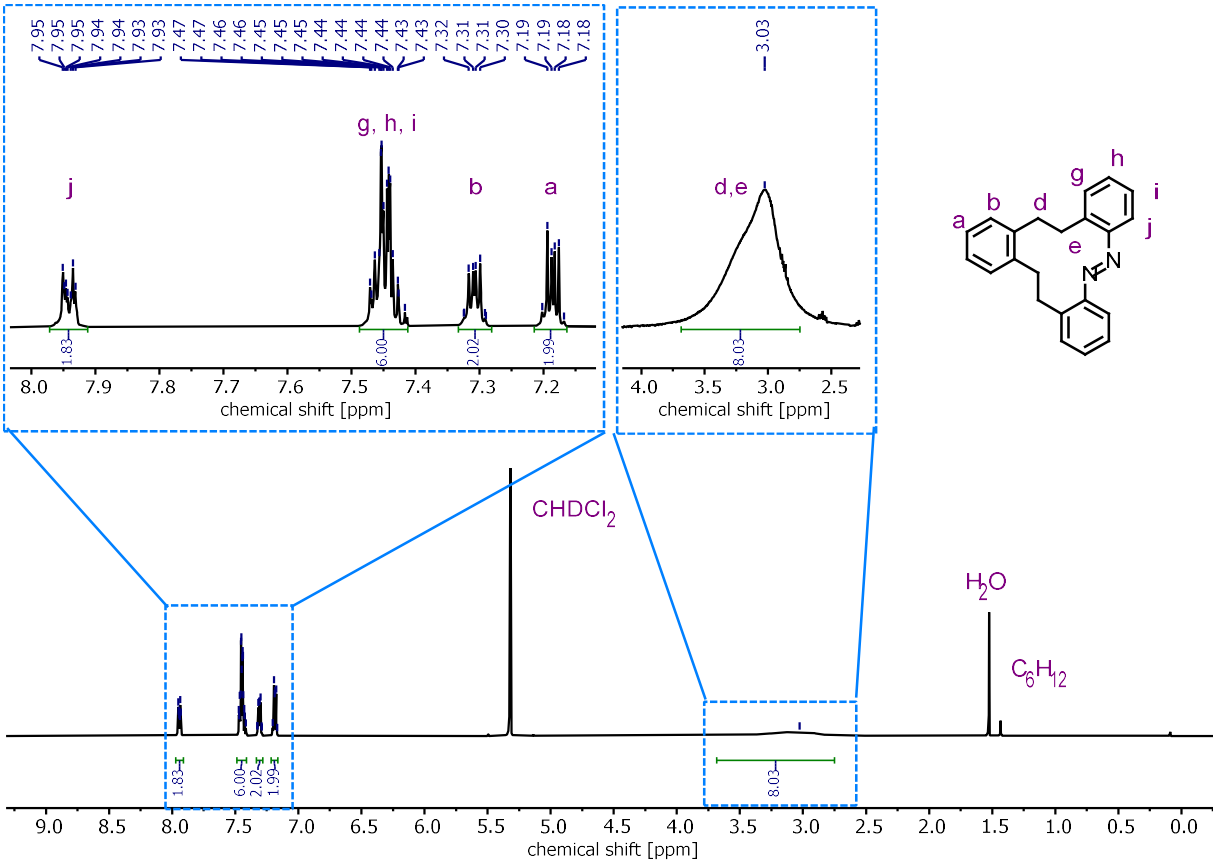

Figure S7. ^{1}H NMR spectrum (500 MHz, CD_2Cl_2, 298 K) of cyclic azobenzene **1**.

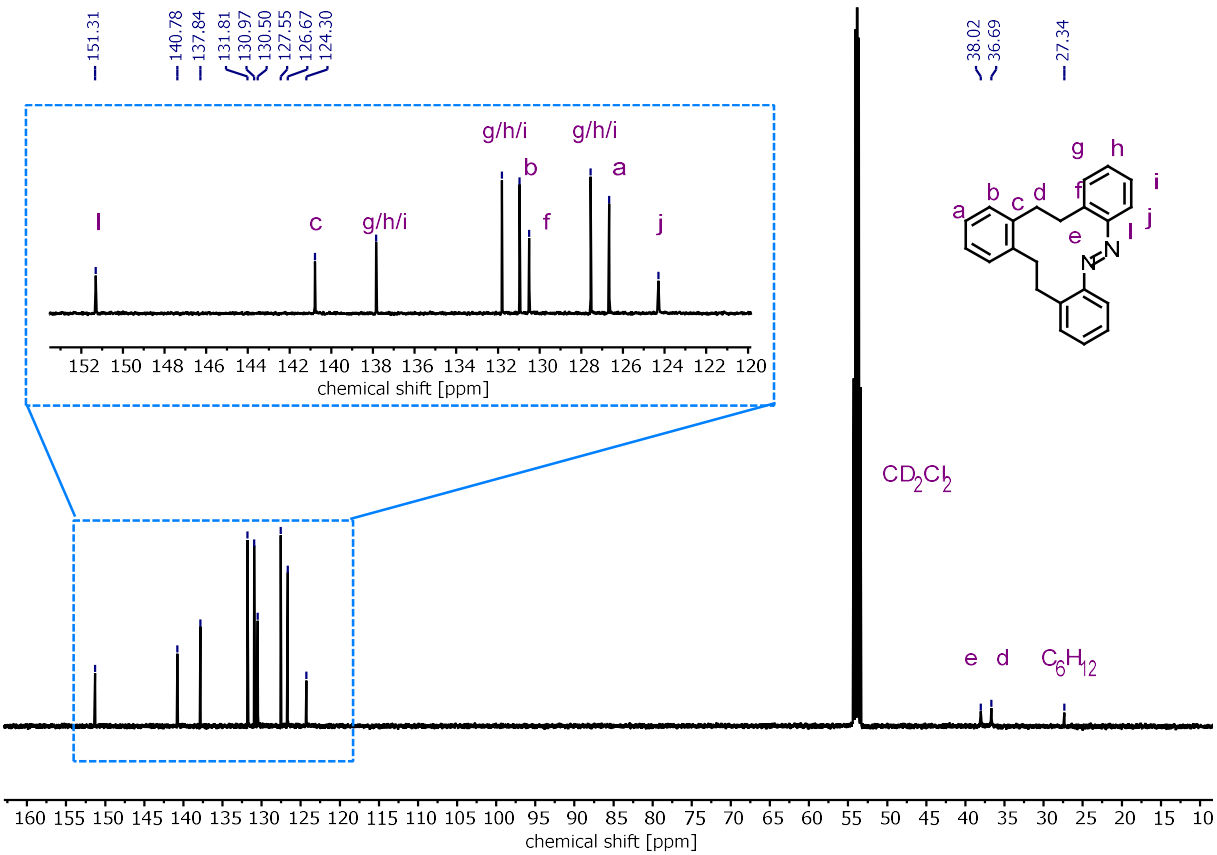

Figure S8. ^{13}C NMR spectrum (126 MHz, CD_2Cl_2, 298 K) of cyclic azobenzene **1**.

2.5. Unsuccessful attempts to synthesize 1

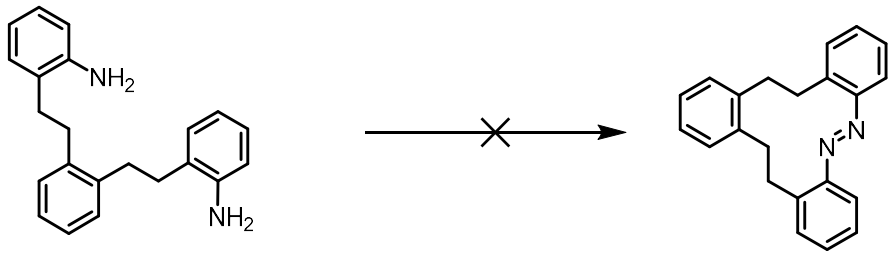

C 1

General procedure (a) for the oxidation of C

Dianiline **C** was dissolved in dry toluene (6 mL), the oxidant (2-6 equiv.) was added, and the suspension was heated to reflux for the indicated time. Then the reaction mixture was allowed to reach room temperature and was diluted with DCM (10 mL). The reaction mixture was filtered through celite. The filtrate was evaporated to dryness under reduced pressure, and the residue was chromatographed on silica gel with cyclohexane as eluent, to obtain the desired product.

General procedure (b) for the oxidation of C

A freshly prepared and titrated (0.57 – 0.62 M) solution of the oxidant (2.0 equiv.) in acetic acid was added to a solution of dianiline **C** in acetic acid/dichloromethane = 1/3 (6.25 mL) via a syringe pump within a period of **X** hours under rapid stirring. After the complete addition of the oxidant solution, the mixture was stirred for at least one more hour. The solvent was then removed under reduced pressure, the residue taken up in ethyl acetate (10 mL), and the ethyl acetate solution washed with saturated aqueous sodium hydrogen carbonate solution (2×5 mL), followed by saturated aqueous sodium chloride solution (5 mL). The organic layer was dried over sodium sulphate, the solvent was removed under reduced pressure, and the residue was purified by filtration over silica using cyclohaxene as eluent.

Table S2. Overview over the reaction conditions tested for the synthesis of **5**.

Oxidant	Reaction time	time for the addition of the oxidant	concentration of dianiline C [mol L^{-1}]	yield [%]	General procedure
Cu/O_2	4 h	-	0.5	0	a
Cu/O_2	16 h	-	0.5	0	a
Cu/air	4 h		0.5	0	a
Cu/air	16 h		0.5	0	a
tBuOCl	1 h	5 min	0.26	0	b
tBuOCl	4 h	3h 30 min	0.26	0	b
tBuOCl	16 h	15 h 30 min	0.26	0	b
MnO_2 dried at 80 °C	8 h	-	0.52	0	a
MnO_2 dried at 120 °C	8 h	-	0.52	0	a
MnO_2	8 h	-	0.52	0	a
mCPBA	16 h	12 h	0.18-0.36	3	b
mCPBA	24 h	23 h	0.36	3	b
mCPBA pseudo high dilution	48 h	48 h	0.13	8	b
mCPBA at 0 °C	16 h	15 h 30min	0.36	5	b
mCPBA at -78 °C	16 h	12 h	0.36	0	b
$Pb(OAc)_4$	1.5 h	30 min	0.85	67	-

2.6. General procedure for the ortho alkoxylation of cyclic azobenzene 1

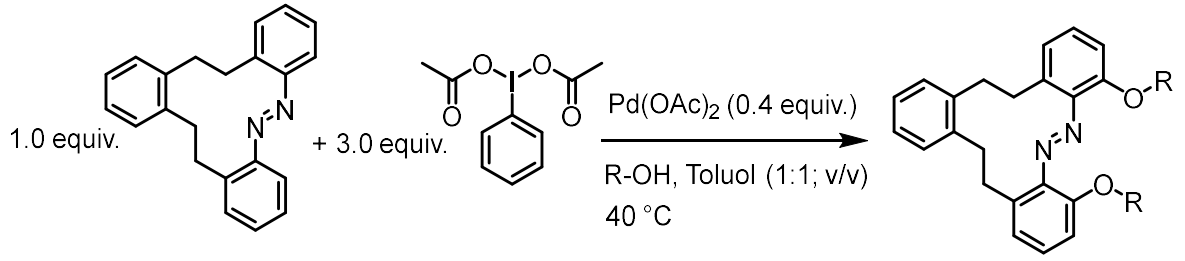

1

R=			
CH_3	**2**	**43%**
CH_2CF_3	**3**	**18%**
$OCOCH_3$	**4**	**7%**

Derivatives **2**, **3**, and **4** were synthesized following a literature procedure[2] for the ortho alkoxylation of noncyclic azobenzenes.

Cyclic azobenzene **1** (1.0 equiv.), (diacetoxyiodo)benzene(phenyl)iodine(III) diacetate (PIDA; 3.0 equiv.) and palladium(II) acetate (0.4 equiv.) were suspended in a mixture of toluene (10 mL/mmol), and the respective alcohol (10 mL/mmol, >100 equiv.). The reaction mixture was stirred at 40 °C for 16 hours. Subsequently, all volatiles were removed under reduced pressure on a rotary evaporator and the residue was subjected to column chromatography (silica gel, cyclohexane/ethyl acetate) to afford the desired product.

2.7. (*E*)-4,7-dimethoxy-11,12,17,18-tetrahydrotribenzo[*c*,*g*,*k*][1,2]diazacyclo-dodecine (2)

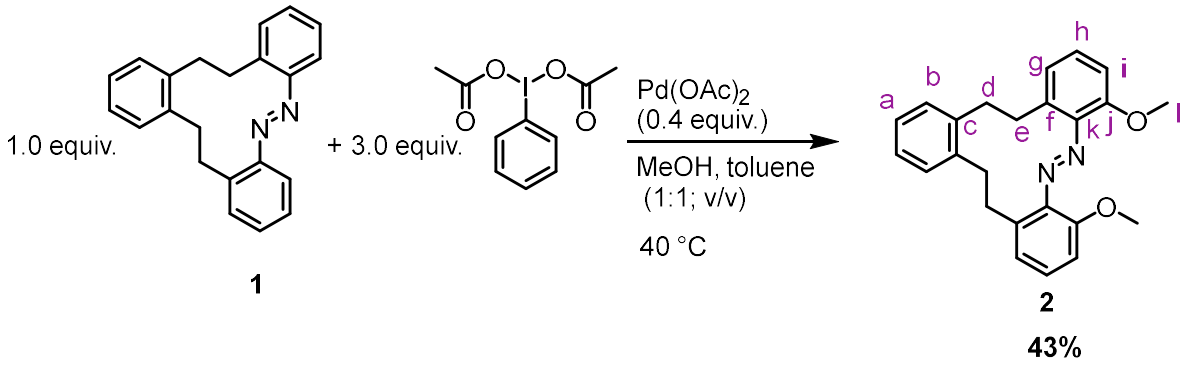

Dimethoxy derivative **2** was synthesized according to the general procedure for the ortho alkoxylation using **1** (25 mg, 0.08 mmol, 1.0 equiv.), PIDA (77 mg, 0.24 mmol, 3.0 equiv.), $Pd(OAc)_2$ (7 mg, 0.03 mmol, 0.4 equiv.), methanol (0.8 g, 24 mmol, 300 equiv.), and toluene (1.0 mL). Purification by column chromatography (silica gel, cyclohexane:ethyl acetate; 100:0 → 70:30 (v/v)) afforded dimethoxy derivative **2** as a yellow powder in 43% yield (13 mg, 0.03 mmol).

$C_{24}H_{24}N_2O_2$ 372.47 g mol^{-1}

R_F value (cyclohexane:ethyl acetate; 1:1 (v/v)) = 0.52

^{1}H NMR (500 MHz, $CDCl_3$, 298 K) δ_H [ppm] = 2.92 (s, 4H, H-d), 3.00 (s, 4H, H-e), 3.96 (s, 6H, H-l), 6.98 (dd, J = 8.2, 1.2 Hz, 2H, H-i), 7.01 (dd, J = 7.5, 1.2 Hz, 2H, H-g), 7.24 – 7.17 (m, 2H, H-a), 7.32 – 7.25 (m, 2H, H-b), 7.32 (dd, J = 8.1, 7.6 Hz, 2H, H-h).

^{13}C NMR (126 MHz, $CDCl_3$, 298 K) δ_C [ppm] = 20.71, 29.64, 36.10, 36.65, 77.49, 121.99, 126.48, 128.85, 130.15, 130.35, 137.37, 139.97, 143.78, 144.64, 169.22.

HRMS (ESI$^+$-Orbitrap) *m*/*z* (relative intensity) = 373.1905 (100%, $[M+H]^+$, calcd 373.1911), 395.172 (100%, $[M+Na]^+$, calcd 395.1730).

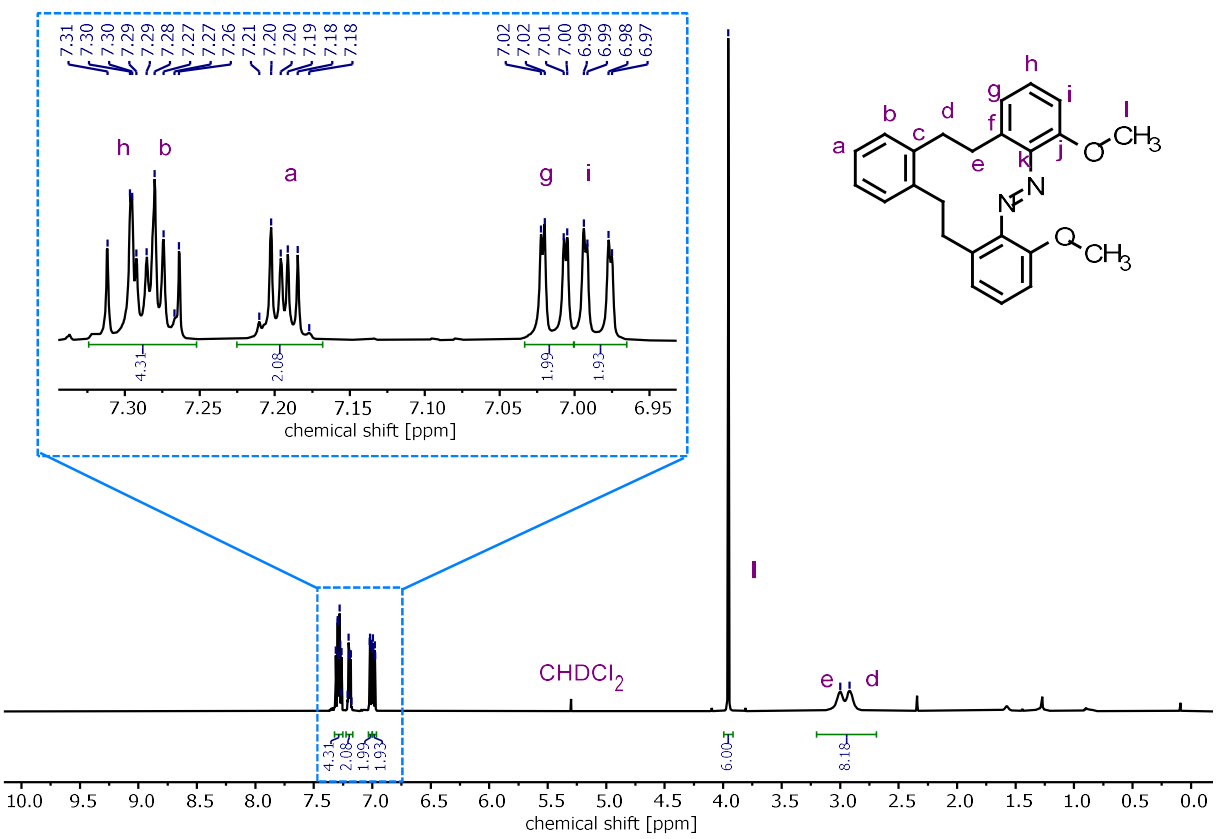

Figure S9. ^{1}H NMR spectrum (500 MHz, CD_2Cl_2, 298 K) of cyclic dimethoxy derivative **2**.

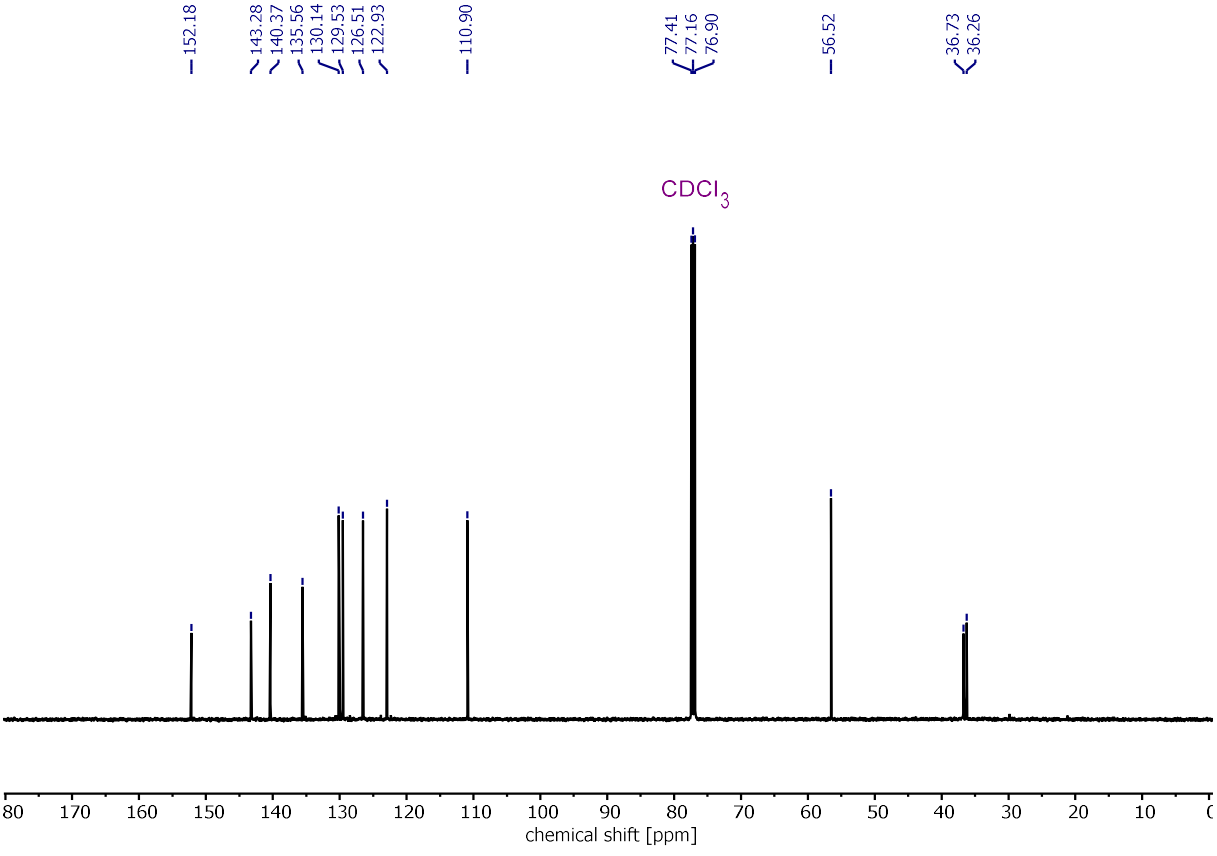

Figure S10. ^{13}C NMR spectrum (126 MHz, $CDCl_3$, 298 K) of cyclic dimethoxy derivative **2**.

2.8. (*E*)-4,7-bis(2,2,2-trifluoroethoxy)-11,12,17,18-tetrahydrotribenzo[*c*,*g*,*k*][1,2]-diazacyclododecine (3)

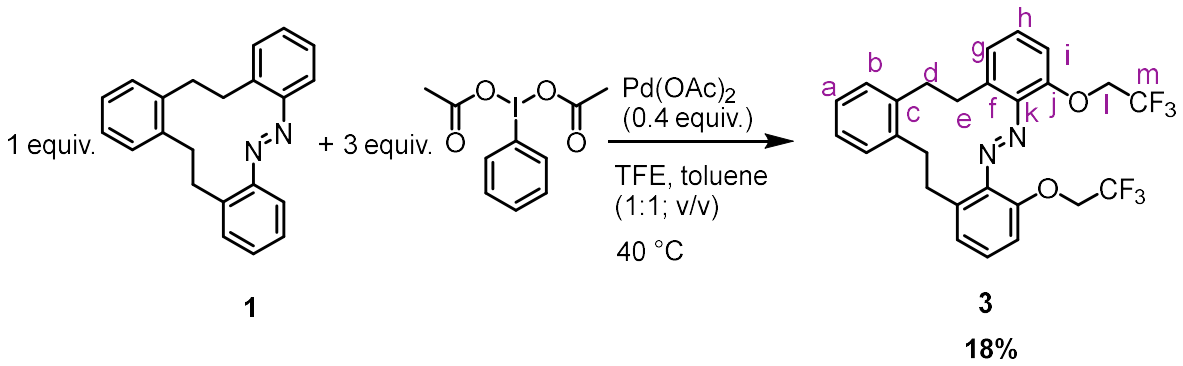

1 **3**

18%

Triflouroethanolether derivative **3** was synthesized according to the general procedure for the ortho alkoxylation using **1** (30 mg, 0.10 mmol, 1.0 equiv.), PIDA (93 mg, 0.30 mmol, 3.0 equiv.), $Pd(OAc)_2$ (9 mg, 0.04 mmol, 0.4 equiv.), triflourethanol (TFE; 1.4 g, 14 mmol, 140 equiv.), and toluene (1.0 mL). Purification by column chromatography (silica gel, cyclohexane: ethyl acetate; 100:0 → 70:30 (v/v)) afforded triflouroethanolether derivative **3** as an orange powder in 18% yield (9 mg, 0.02 mmol).

$C_{26}H_{22}F_6N_2O_2$ 508.46 g mol^{-1}

R_F (cyclohexane:ethyl acetate; 1:1 (v/v)) = 0.64

^{1}H NMR (500 MHz, CD_2Cl_2, 298 K) δ_H [ppm] = 2.94 (s, 4H, H-d), 3.05 (s, 4H, H-e), 4.47 (q, J = 8.6 Hz, 4H, H-l), 7.12 (dd, J = 8.2, 1.4 Hz, 2H, H-i), 7.14 – 7.20 (m, 2H, H-a), 7.18 (dd, J = 7.6, 1.4 Hz, 2H, H-g), 7.24 – 7.28 (m, 2H, H-b), 7.34 (dd, J = 8.2, 7.6 Hz, 2H, H-h).

^{13}C NMR (126 MHz, $CDCl_3$, 298 K) δ_C [ppm] = 36.40, 36.92, 69.19 (q, J = 35.6 Hz), 117.20, 123.83 (q, J = 278.9 Hz), 126.42, 126.70, 130.22, 130.42, 136.97, 140.05, 144.28, 151.41.

^{19}F NMR (471 MHz, $CDCl_3$, 298 K) δ_F [ppm] = –75.68 (t, J = 8.3 Hz).

HRMS (ESI^+-Orbitrap): m/z (relative intensity) = 509.1657 (100%, $[M+H]^+$, calcd 509.1658).

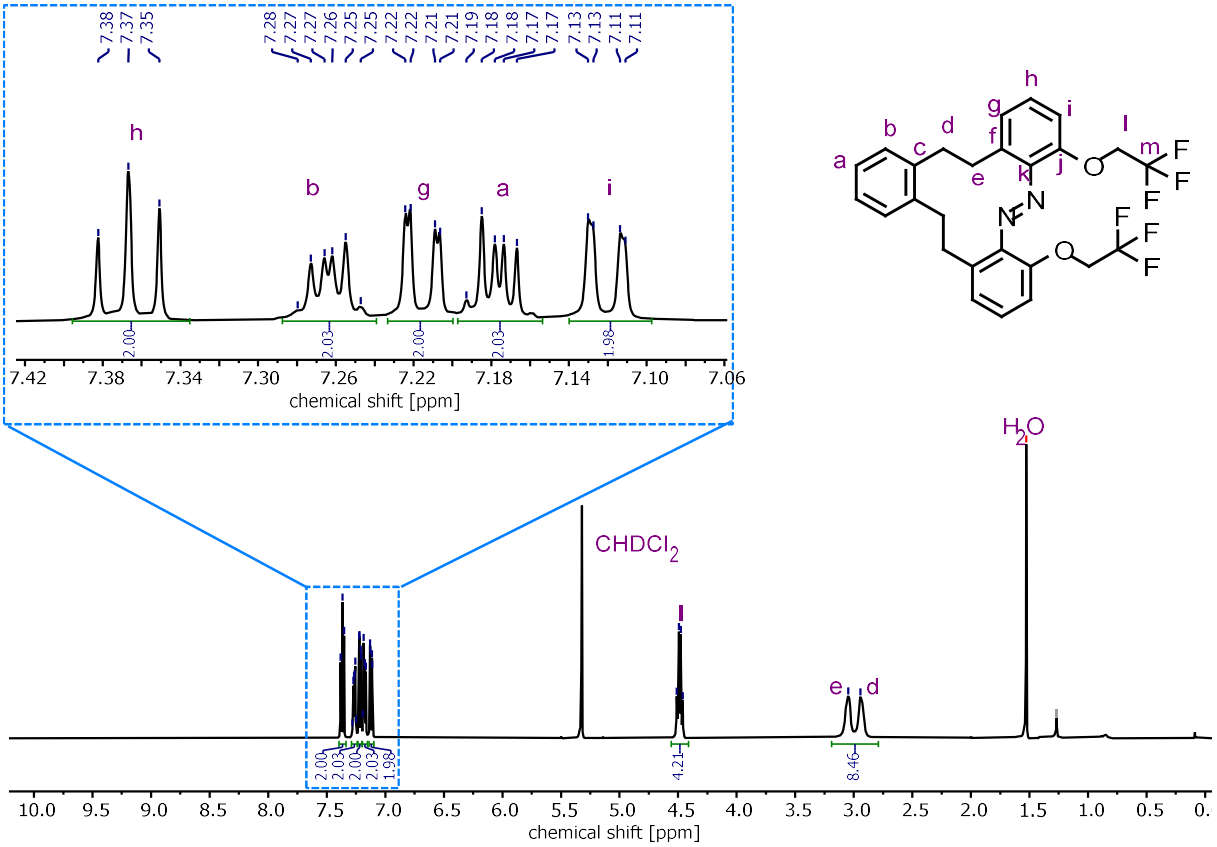

Figure S11. ^{1}H NMR spectrum (500 MHz, CD_2Cl_2, 298 K) of cyclic dimethoxy derivative **3**.

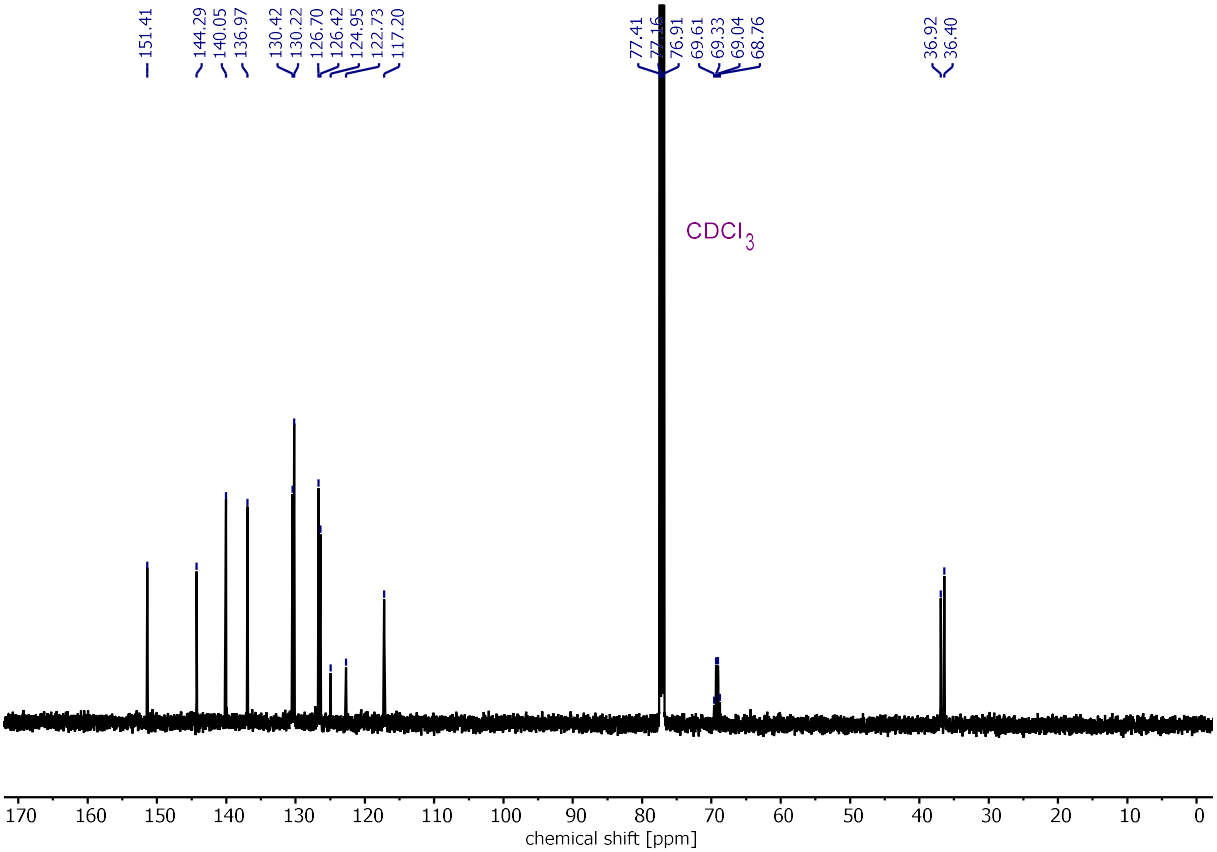

Figure S12. ^{13}C NMR spectrum (126 MHz, $CDCl_3$, 298 K) of cyclic dimethoxy derivative **3**.

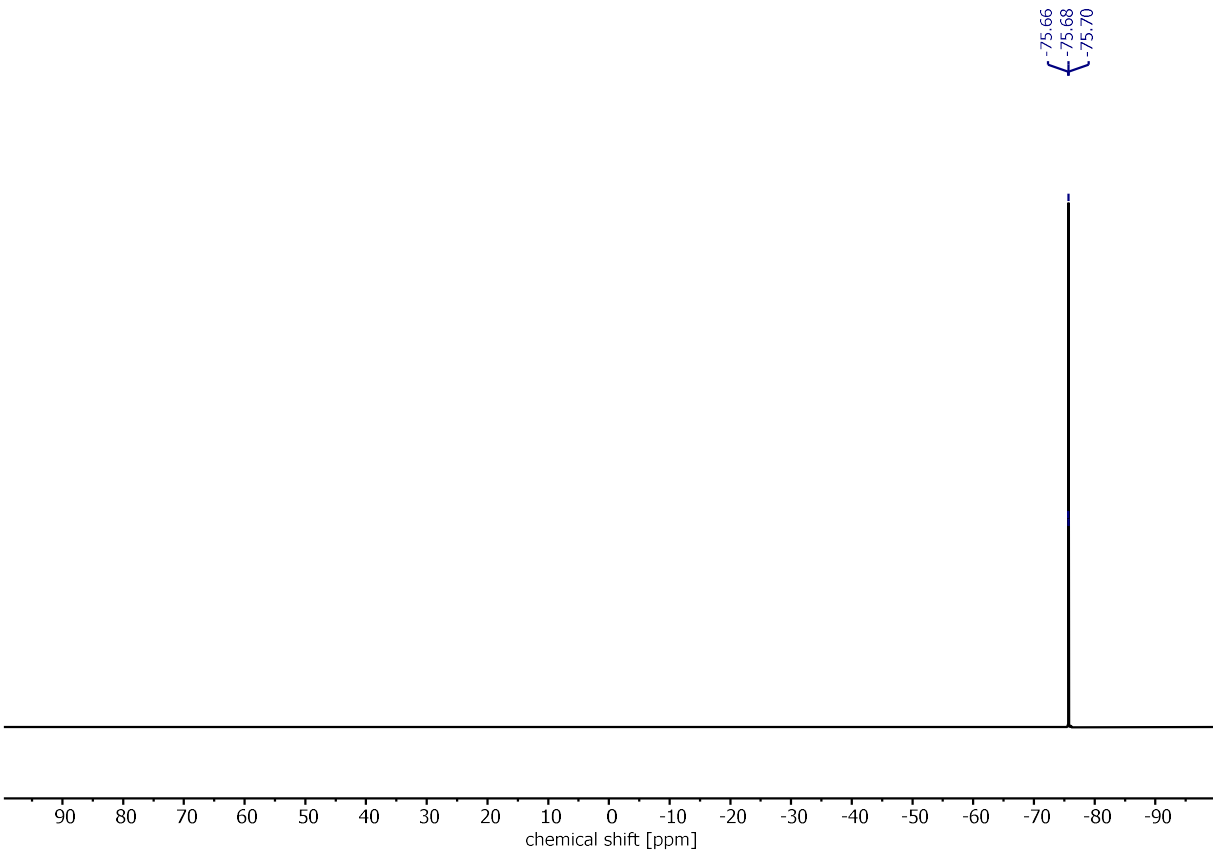

Figure S13. ^{19}F NMR spectrum (471 MHz, $CDCl_3$, 298 K) of cyclic dimethoxy derivative **3**.

2.9. (*E*)-11,12,17,18-tetrahydrotribenzo[*c*,*g*,*k*][1,2]diazacyclododecine-4,7-diyl diacetate (4)

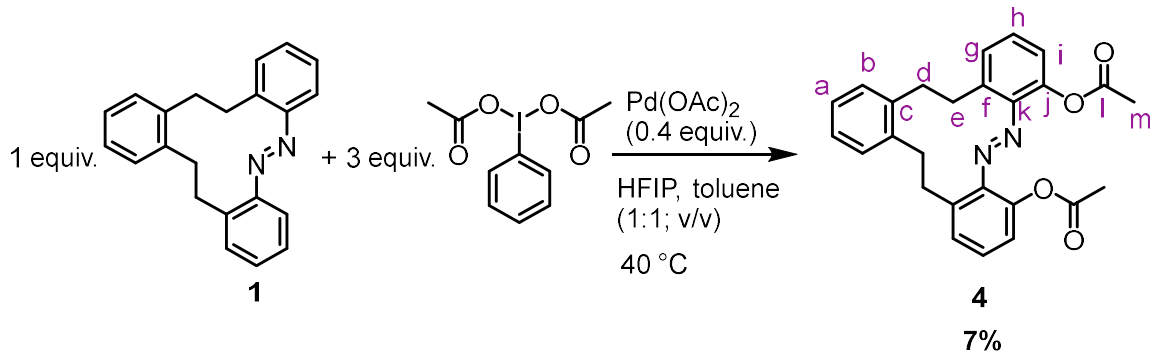

Acetylester derivative **4** was synthesized according to the general procedure for the ortho alkoxylation using **1** (30 mg, 0.10 mmol, 1.0 equiv.), PIDA (93 mg, 0.30 mmol, 3.0 equiv.), $Pd(OAc)_2$ (9 mg, 0.04 mmol, 0.4 equiv.), hexafluoroisopropanol (HFiP;1.6 g, 10 mmol, 100 equiv.), and toluene (1.0 mL). Purification by column chromatography (silica gel, cyclohexane: ethyl acetate; 100:0 → 70:30 (v/v)) afforded only one compound which was the acetylester derivative **4** as a red powder in 7% yield (4 mg, 0.01 mmol).

The desired product of this reaction was the HFiP ether derivative. However, the only compound that could be isolated from the reaction mixture was the acetylester derivative **4**. The reaction was carried out three times with the same result.

$C_{26}H_{24}N_2O_4$ 428.49 g mol^{-1}

R_F (cyclohexane: ethyl acetate; 1:1 (v/v)) = 0.62.

^{1}H NMR (500 MHz, CD_2Cl_2, 298 K) δ_H [ppm] = 2.33 (s, 6H, H-m), 2.98 (s, 4H, H-d), 3.08 (s, 4H, H-e), 7.09 (dd, *J* = 8.0, 1.5 Hz, 2H, H-i), 7.20 – 7.14 (m, 2H, H-a), 7.27 – 7.23 (m, 2H, H-b), 7.34 (dd, *J* = 7.7, 1.5 Hz, 2H, H-g), 7.41 (t, *J* = 7.8 Hz, 2H, H-h).

^{13}C NMR (126 MHz, CD_2Cl_2, 298 K) δ_C [ppm] = 20.71, 29.64, 36.10, 36.65, 77.49, 121.99, 126.48, 128.85, 130.15, 130.35, 137.37, 139.97, 143.78, 144.64, 169.22.

HRMS (ESI$^+$-Orbitrap) *m*/*z* (relative intensity) = 429.1809 (100%, $[M+H]^+$, calcd 429.1809), 387,170 (53%, $[M+H-Ac^-]^+$, calcd 387,1703).

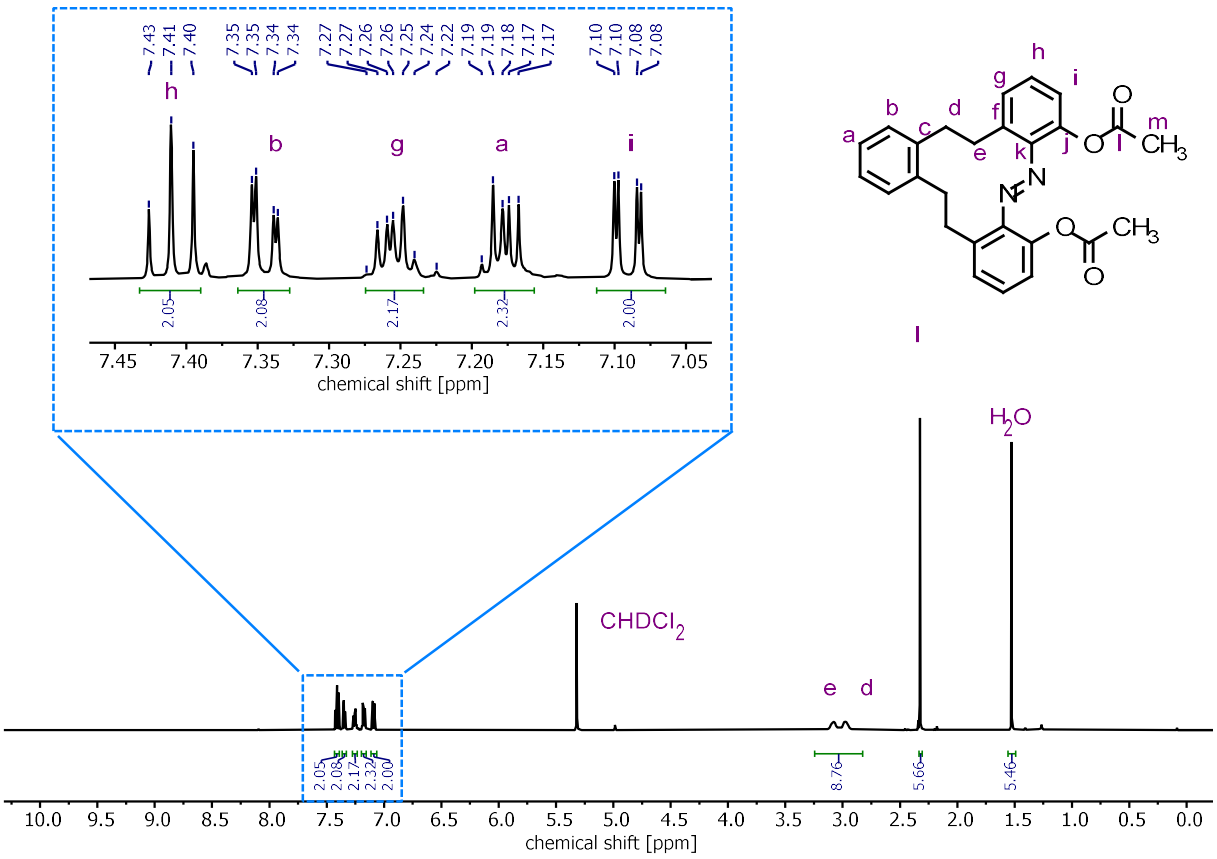

Figure S14. ^{1}H NMR spectrum (500 MHz, CD_2Cl_2, 298 K) of cyclic dimethoxy derivative **4**.

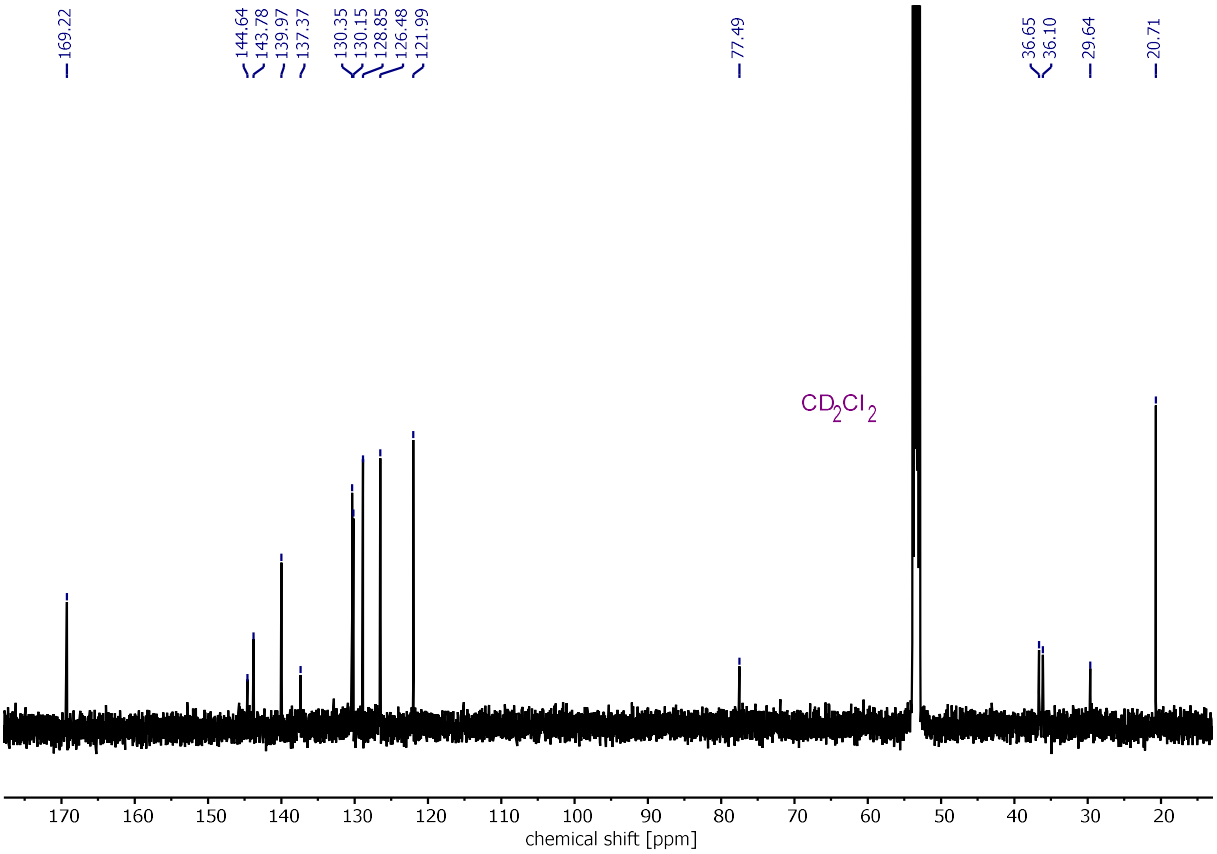

Figure S15. ^{13}C NMR spectrum (126 MHz, $CDCl_3$, 298 K) of cyclic dimethoxy derivative **3**.

2.10. (*E*)-2,9-diiodo-11,12,17,18-tetrahydrotribenzo[*c*,*g*,*k*][1,2]diazacyclododecine (5)

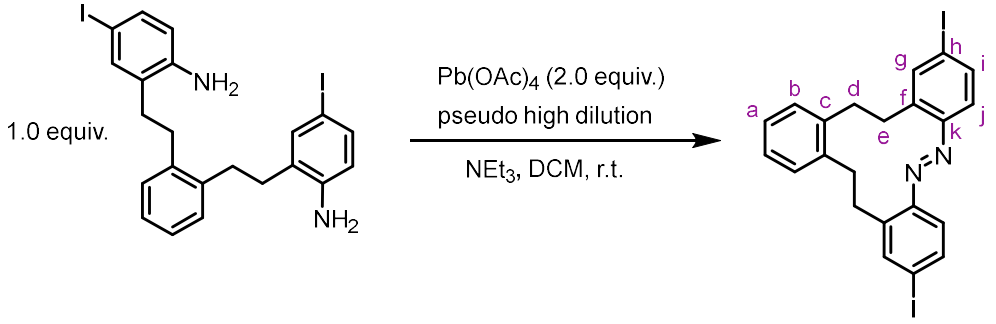

D **5** **42%**

A three-necked flask was equipped with two 250 mL dropping funnels. One funnel was loaded with a solution of diiodide **D** (100 mg, 0.316 mmol, 1.00 equiv., 3 mmol/L), and TEA (1 mL) in DCM (100 mL) and the other dropping funnel was loaded with a solution of lead(IV) acetate (280 mg, 0.632 mmol, 2.00 equiv., 6 mmol/L) in DCM (100 mL). Both solutions were added dropwise into DCM (250 mL) within 30 min. After complete addition, the solution was stirred at room temperature for 30 min. Afterwards the solution was concentrated under reduced pressure. The residue was filtered over a silica plug (5 cm diameter, 5 cm height) with cyclohexane. Diiodinated macrocyclic azobenzene **5** was obtained as an orange solid (66 mg, 116 µmol, 42%).

$C_{22}H_{18}I_2N_2$ 564.21 g mol^{-1}

R_F value (cyclohexane:ethyl acetate; 8:2 (v/v)) = 0.67

^{1}H NMR (500 MHz, CD_2Cl_2, 298 K): δ_H [ppm] = 2.57 – 3.60 (m, 6H, H-d,e), 7.16 – 7.22 (m, 2H, H-a), 7.24 – 7.31 (m, 2H, H-b), 7.66 (d, J = 8.3 Hz, 2H, H-j), 7.79 (dd, J = 8.4, 2.0 Hz, 2H, H-i), 7.84 (d, J = 2.0 Hz, 2H, H-g).

^{13}C NMR (126 MHz, CD_2Cl_2, 298 K): δ_C [ppm] = 36.27, 37.55, 97.94, 126.07, 126.84, 130.54, 136.88, 139.93, 140.25, 140.84, 150.49.

HRMS (ESI$^+$-Orbitrap): m/z (relative intensity) = 564.9632 (100%, $[M+H]^+$, calcd 564.9626).

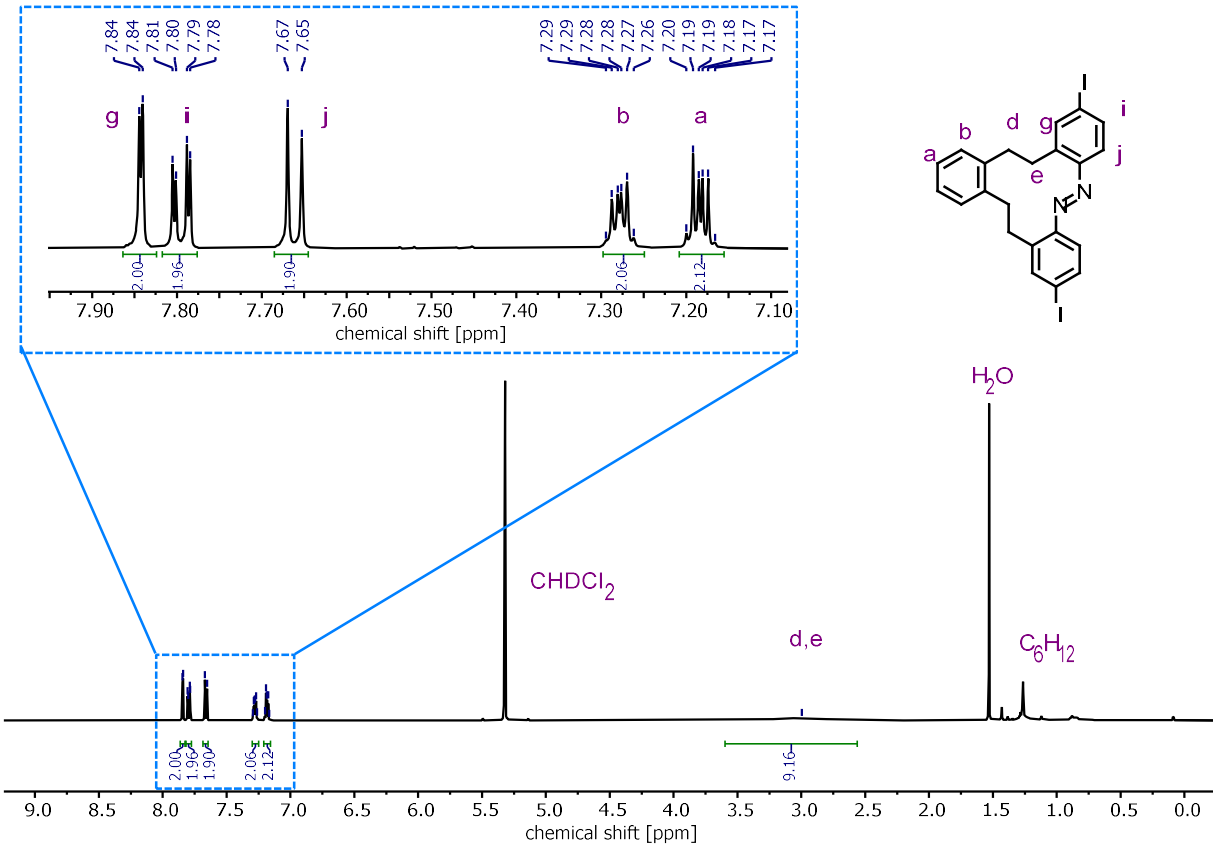

Figure S16. ^{1}H NMR spectrum (500 MHz, CD_2Cl_2, 298 K) of cyclic azobenzene **5**.

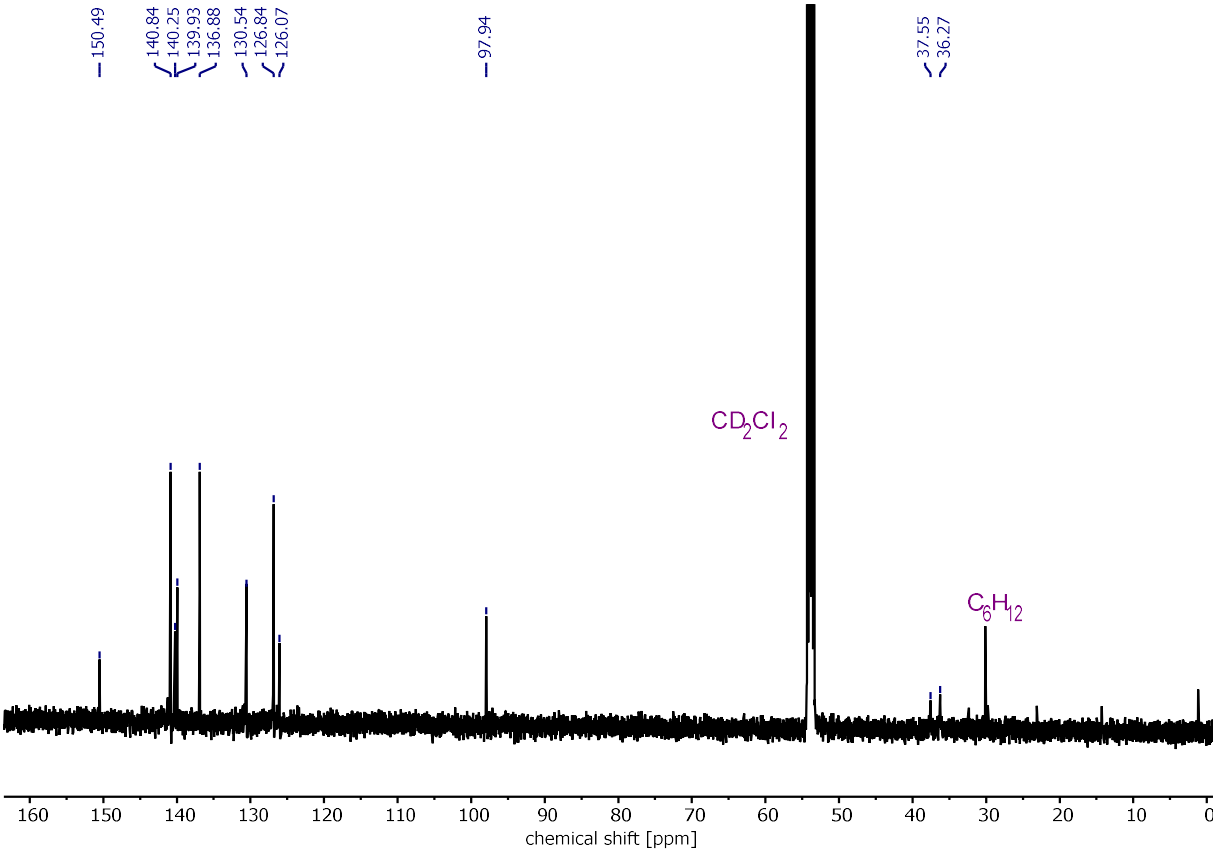

Figure S17. ^{13}C NMR spectrum (126 MHz, CD_2Cl_2, 298 K) of cyclic azobenzene **5**.

2.11. (*E*)-2,9-bis(ethylthio)-11,12,17,18-tetrahydrotribenzo[*c*,*g*,*k*][1,2]diazacyclo-dodecine (6)

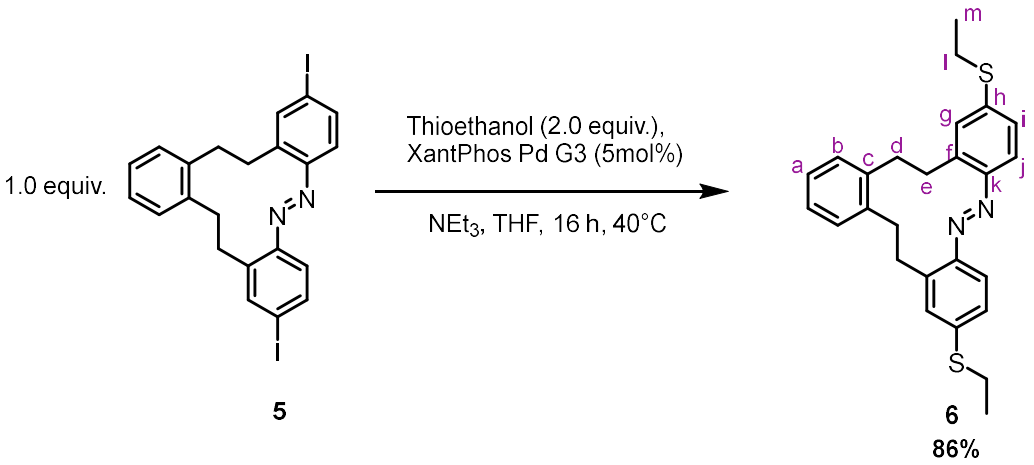

A flame dried schlenk flask was loaded with diiodinated macrocyclic azobenzene **5** (30.0 mg, 53.2 µmol, 1.00 equiv.), thioethanol (9.0 mg, 142 µmol 2.00 equiv.), and XantPhos Pd G3 (1.5 mg, 1.44 µmol, 0.02 equiv.) and vacuum was applied for 15 min. Meanwhile dry THF (10 mL) was degassed by bubbling Ar through. Then the flask was filled with a Ar atmosphere and the solvent was added, followed by dry NEt_3 (1 mL). The reaction was stirred at 40 °C for 16 h. After cooling to room temperature, the reaction mixture was diluted with EtOAc (10 mL), washed with aq. 1 M HCl (10 mL) and saturated aqueous NaCl solution (10 mL), and the aqueous phase was extracted with EtOAc (3x 50 mL). The combined organic layers were dried over $MgSO_4$, filtered, and concentrated in under reduced pressure at a rotary evaporator. Column chromatography (cyclohexane) afforded the desired compound **6** (20 mg, 53 µmol, 86%).

$C_{26}H_{28}N_2S_2$ 432.17 g mol^{-1}

R_F value (cyclohexane:ethyl acetate; 8:2 (v/v)) = 0.75

^{1}H NMR (400 MHz, CD_2Cl_2, 298 K) δ_H [ppm] = 1.41 (t, J = 7.4 Hz, 6H, H-l), 2.54 – 3.55 (m, 8H, H-d,e), 3.09 (q, J = 7.4 Hz, 4H, H-m), 7.15 – 7.22 (m, 2H, H-a), 7.25 – 7.35 (m, 6H, H-b,g,i), 7.88 (d, J = 8.9 Hz, 2H, H-j).

^{13}C NMR (126 MHz, CD_2Cl_2, 298 K) δ_C [ppm] = 8.78, 14.39, 26.91, 46.16, 124.93, 125.71, 126.66, 129.92, 130.49, 138.55, 140.66, 141.28, 148.63.

HRMS (ESI$^+$-Orbitrap): m/z (relative intensity) = 433.1764 (100%, $[M+H]^+$, calcd 433.1767).

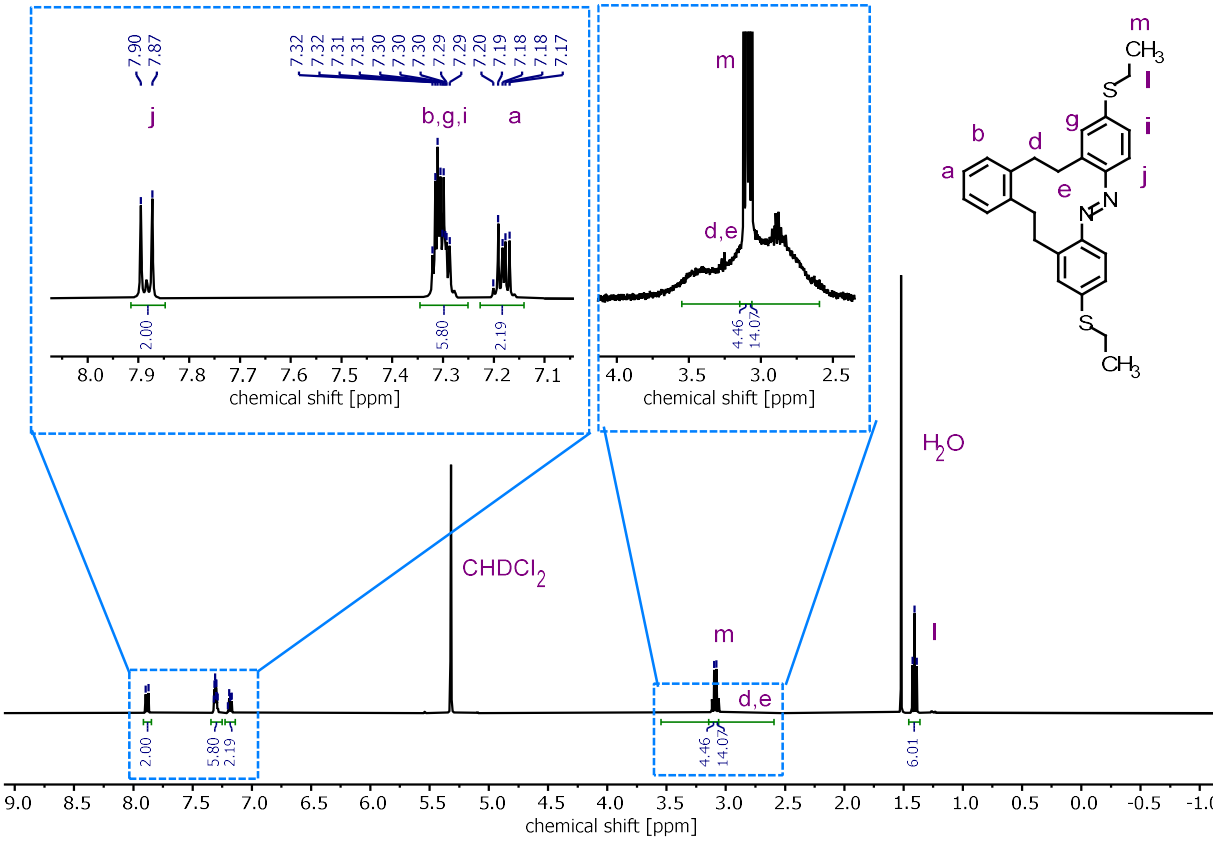

Figure S18. ^{1}H NMR spectrum (400 MHz, CD_2Cl_2, 298 K) of thioether derivative **6**.

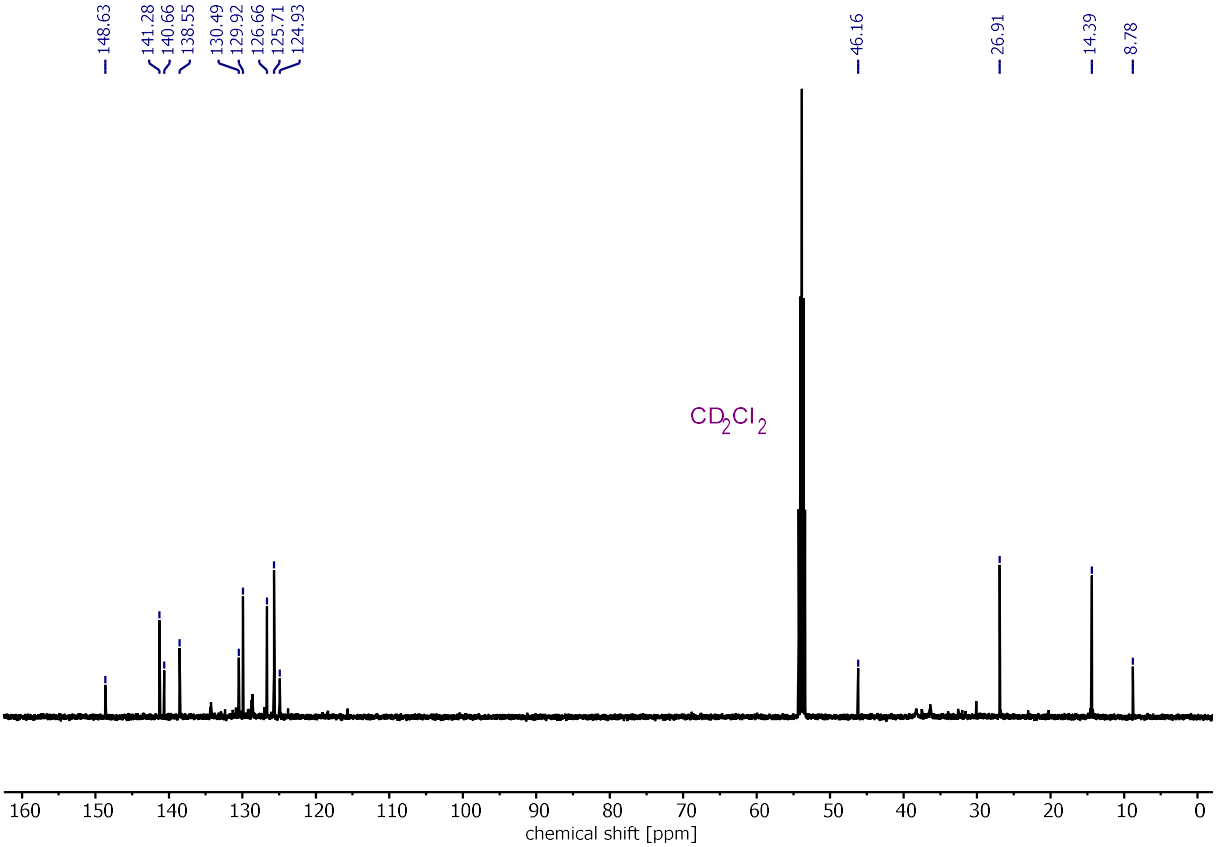

Figure S19. ^{13}C NMR spectrum (126 MHz, CD_2Cl_2, 298 K) of thioether derivative **6**.

2.12. (*E*)-4,4'-(11,12,17,18-tetrahydrotribenzo[*c*,*g*,*k*][1,2]diazacyclododecine-2,9-diyl)bis(N,N-bis(4-methoxyphenyl)aniline) (7)

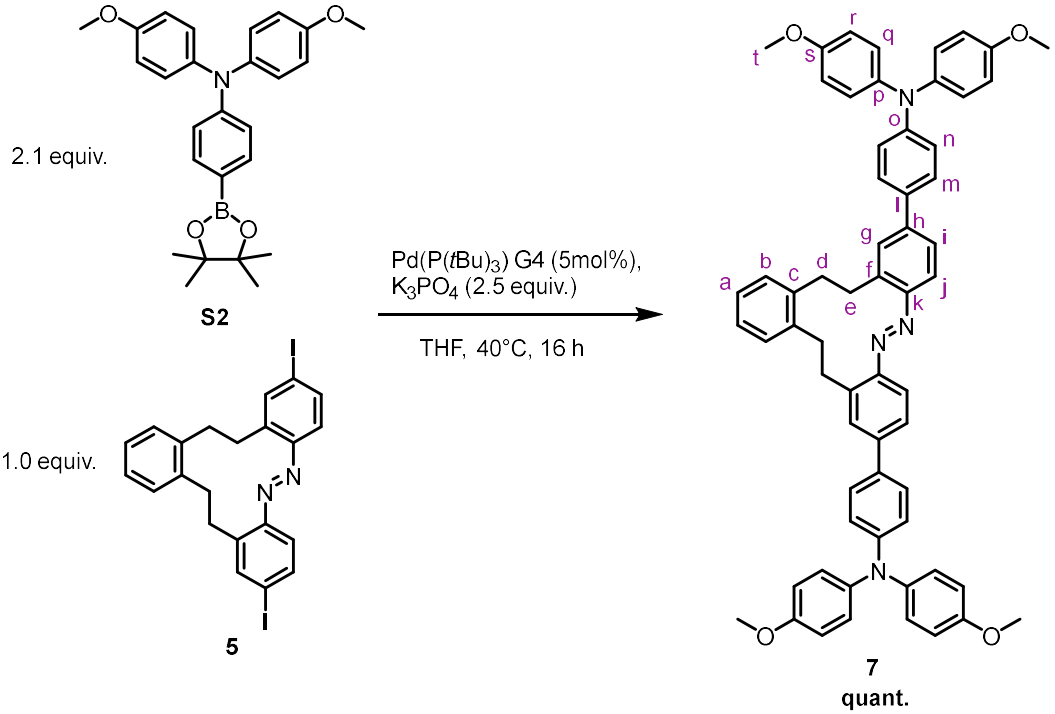

A flame dried Schlenk flask was loaded with diiodinated macrocyclic azobenzene **5** (24 mg, 42.54 µmol, 1.00 equiv.), boronic acid pinacolester **S2** (38.5 mg, 89.5 µmol, 2.10 equiv.), and Pd(P(tBu)$_3$) G4 (1.25 mg, 2.13 µmol, 0.05 equiv.) and vacuum was applied for 15 min. Meanwhile dry THF (10 mL) was degassed by bubbling Ar through. Then the flask was filled with a Ar atmosphere and the solvent was added, followed by K_3PO_4 (22.5 mg, 106 µmol, 2.50 equiv.). The reaction was stirred at the 40 °C for 16 h. After cooling to room temperature, the reaction mixture was diluted with EtOAc (10 mL), washed with aq. 1 M HCl (10 mL) and saturated aqueous NaCl solution (10 mL), and the aqueous phase was extracted with EtOAc (3x 50 mL). The combined organic layers were dried over MgSO4, filtered, and concentrated in under reduced pressure at a rotary evaporator. Column chromatography (cyclohexane:ethylactate:1:1) afforded the desired product **7** (39 mg, 42 µmol, quant.).

$C_{62}H_{54}N_4O_4$ 919.14 g mol^{-1}

R_F value (cyclohexane:ethyl acetate; 8:2 (v/v)) = 0.48

^{1}H NMR (700 MHz, CD_2Cl_2, 298 K) δ_H [ppm] = 3.81 (s, 12H, H-t), 6.87 – 6.89 (m, 8H, H-r), 6.99 – 7.01 (m, 4H, H-n), 7.10 – 7.12 (m, 8H, H-q), 7.17 – 7.20 (m, 2H, H-a), 7.33 (dd, J = 5.5, 3.4 Hz, 2H, H-b), 7.55 – 7.59 (m, 4H, H-m), 7.63 – 7.66 (m, 4H, H-g,i), 8.02 (d, J = 8.6 Hz, 2H, H-j).

^{13}C NMR (176 MHz, CD_2Cl_2, 298 K) δ_C [ppm] = 24.62, 26.91, 55.45, 108.48, 114.72, 118.72, 120.07, 124.71, 126.22, 126.43, 126.93, 127.48, 129.03, 131.32, 138.10, 140.54, 142.56, 148.90, 156.32.

HRMS (ESI$^+$-Orbitrap): *m*/*z* (relative intensity) = 918.4142 (100%, $[M+H]^+$, 918.4140).

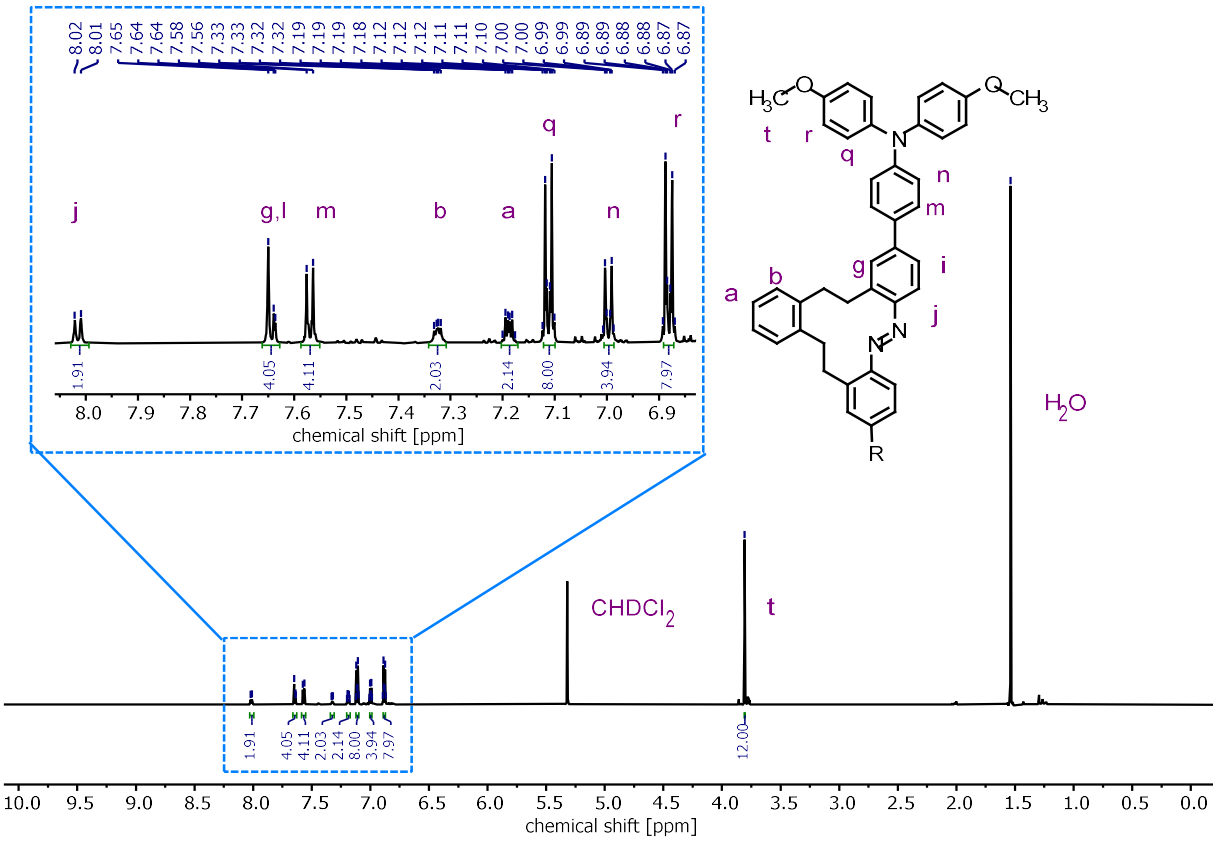

Figure S20. ^{1}H NMR spectrum (700 MHz, CD_2Cl_2, 298 K) of cyclic azobenzene **7**.

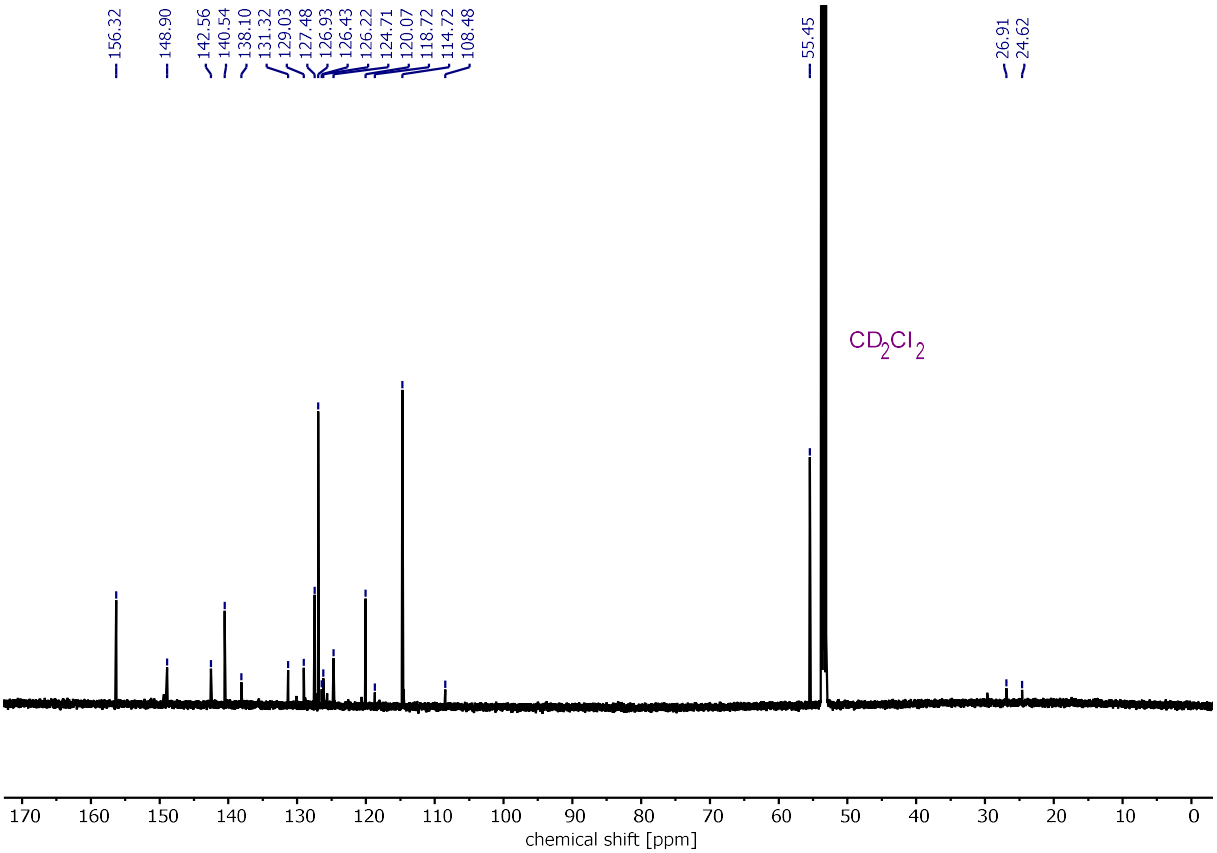

Figure S21. ^{13}C NMR spectrum (176 MHz, CD_2Cl_2, 298 K) of cyclic azobenzene **7**.

3. Photophysical characterization

3.1. General procedures for the illumination of different types of samples

Irradiation of single samples. Single samples in amberised vials or on 96-well plates were irradiated from a distance of 2 cm using a collimator that was connected to the respective light sources using a 60 cm long quartz glass fibre. The collimator gave a light spot with an approximate diameter of 4 cm.

Figure S22. Irradiation setup with a collimator connected to the fibre collimated light source showing an evenly irradiated circle with a diameter of 4 cm. Samples were placed 2 cm under the collimator.

Irradiation of 96-well plates. The filled 96-well plates (UV grade PP) were irradiated using a non-terminated optical fibre attached to a custom 3d printed box (136 mm × 146 mm × 96 mm) designed to achieve even and reproducible irradiation by placing the optical fibre exactly 13.0 cm above the centre of the well plate. Irradiation times to reach the PSS were usually longer with this setup since a larger area was illuminated. A quartz glass plate of appropriate dimensions was used as a lid for the 96-well plate, being fixed to the well plate using Teflon tape to reduce evaporation.

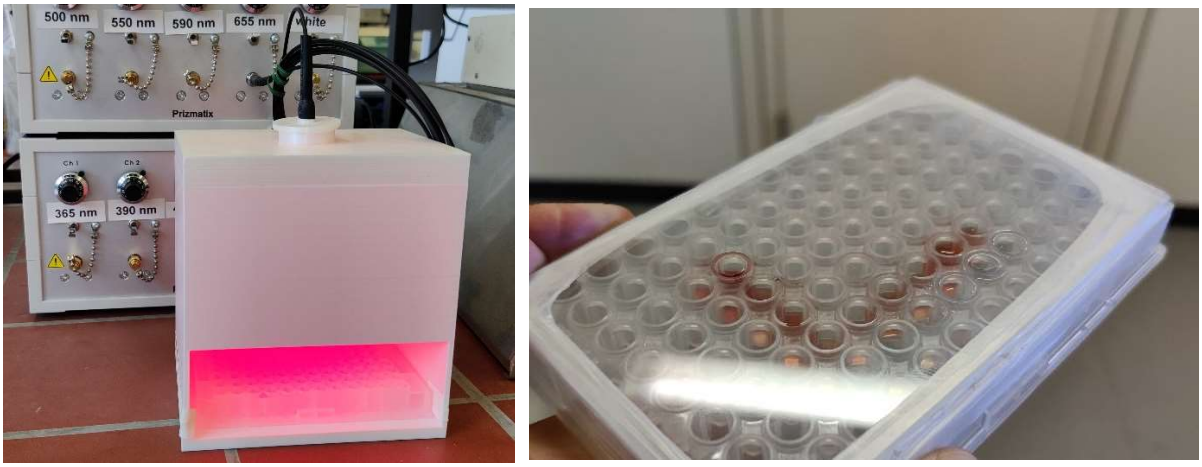

Figure S23. 3D printed chamber (136 mm × 146 mm × 96 mm) for even and reproducible irradiation of 96-well plates (left) and 96-well plate with quartz glass lid and Teflon tape seal (right).

3.2. NMR measurements of irradiated samples

***In-situ* illumination.** The NMR sample was fitted with an insert tube made from quartz glass and a quartz glass optical fibre was pushed down into the insert. The end of this fibre was non terminated, and the exposed surface had been roughened to ensure even and omnidirectional illumination. This construction was lowered into the NMR device using an aluminium rod to avoid damage to the fibre. The other end of the optical fibre was connected to the light source so the sample could be irradiated inside the spectrometer.[3]

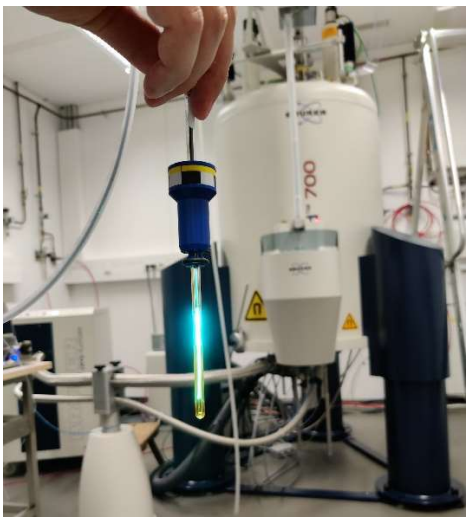

Figure S24. NMR sample with quartz glass insert and optical fibre for *in-situ* illumination during NMR experiments.

***Ex-situ* illumination.** The sample was irradiated in an amberised vial (2 mL volume) using the setup shown in **Figure S22**, transferred into an amberised NMR tube in a dark room, and shielded from ambient light by aluminium foil until placed in the NMR autosampler.[1,4]

Determination of the photo stationary state (PSS) by ^{1}H NMR spectroscopy. Two signals corresponding to the same proton were integrated. PSS^{NMR} corresponds to that integral ratio. Well separated and resolved signals were chosen to ensure the most accurate results. Usually, the signal of the proton in the ortho-position to the azo bridge was chosen.[1,4]

3.2.1. Cyclic azobenzene 1

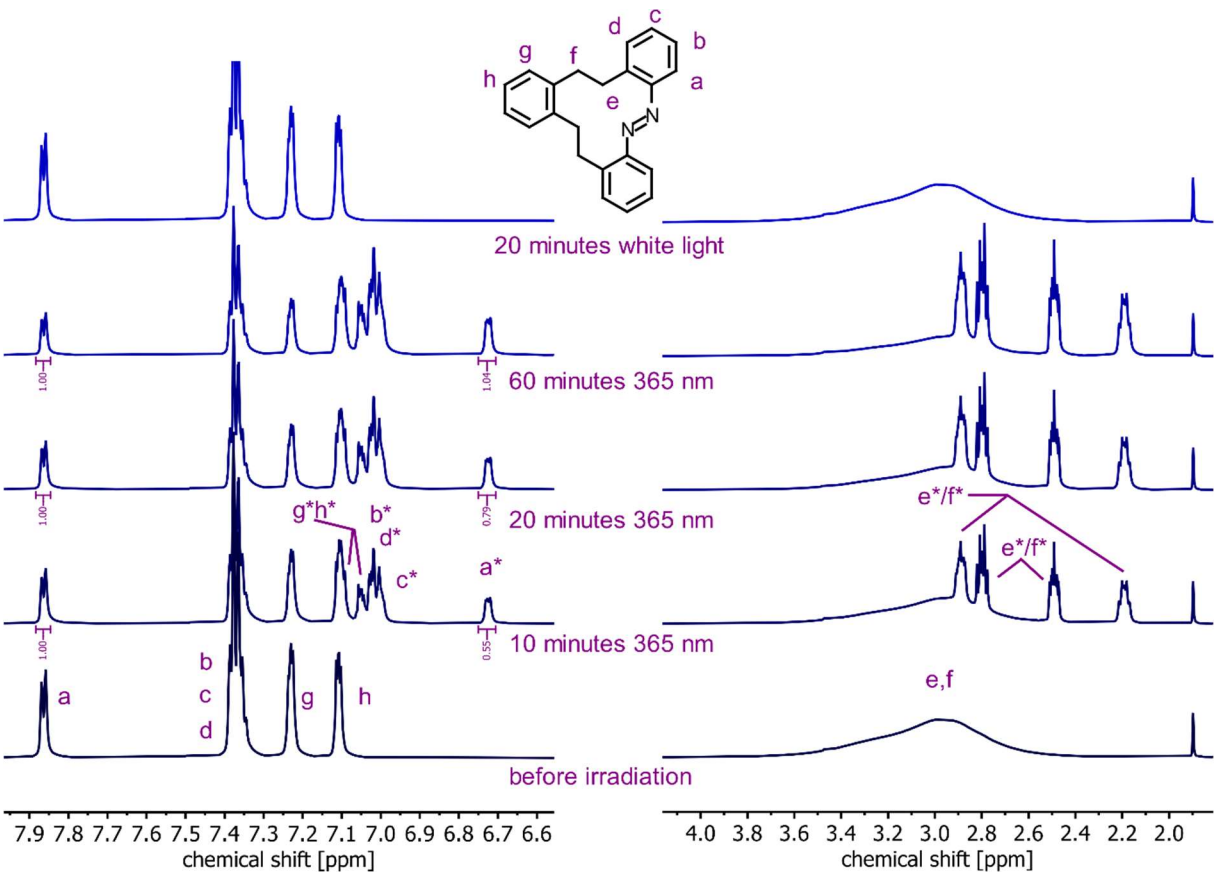

Figure S25. Partial ^{1}H NMR spectra (700 MHz, CD_2Cl_2, 3 mM, 298 K) of cyclic azobenzene **1** during *in-situ* illumination experiments. Integration of the ortho H_a signals gives 0% *Z*-**1** before irradiation and after irradiation with white light (20 min) and 34%, 42%, and 51% *Z*-**1** after irradiation with 365 nm light for 10, 20, and 60 min, respectively.

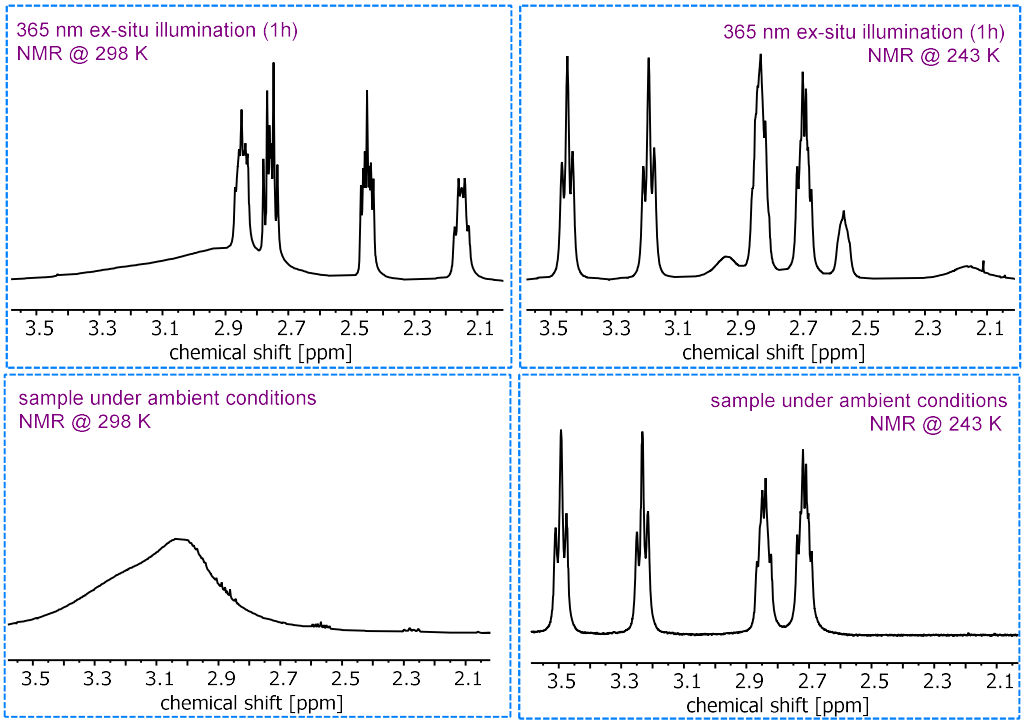

Figure S26. Partial ^{1}H NMR spectra (500 MHz, CD_2Cl_2) of cyclic azobenzene **1** showing H_e and H_f proton signals at 298 K (left) and 243 K (right) at ambient conditions (bottom) and after *ex-situ* illumination (365 nm, 60 min; top).

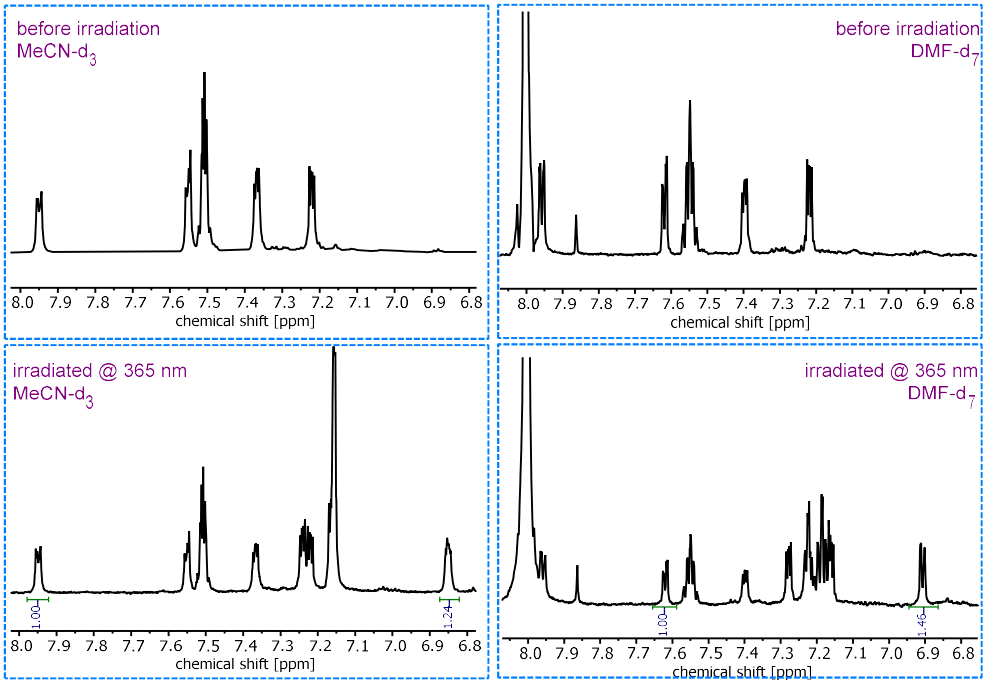

Figure S27. Partial ^{1}H NMR spectra (700 MHz, 298 K) in CD_3CN (left) and DMF-d_7 (right) of cyclic azobenzene **1** before (top) and after *ex-situ* illumination (365 nm, 60 min; bottom).

3.2.2. Diiodo cyclic azobenzene 5

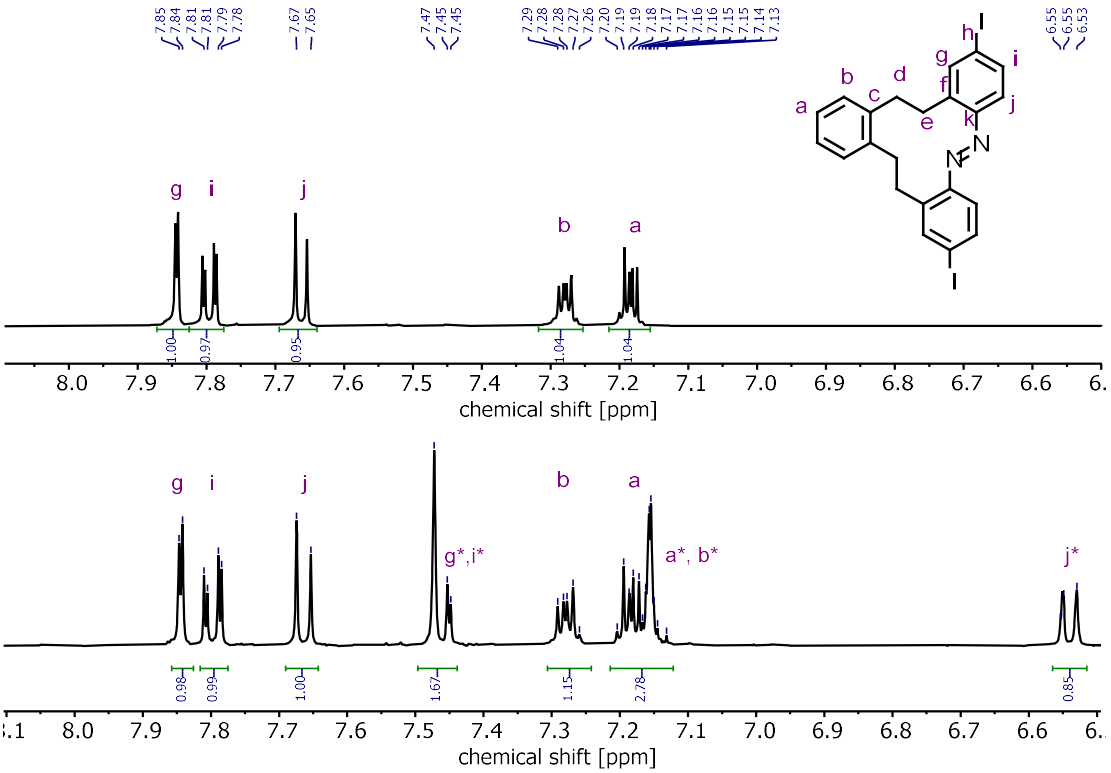

Figure S28. Partial ^{1}H NMR spectra (500 MHz, CD_2Cl_2, 298 K) of the aromatic region of **5** before (top) and after (bottom) *ex-situ* irradiation at 365 nm for 60 min. Integration of the signals H-g and H-g* gave a ratio of 45% *Z*-**5** in the sample.

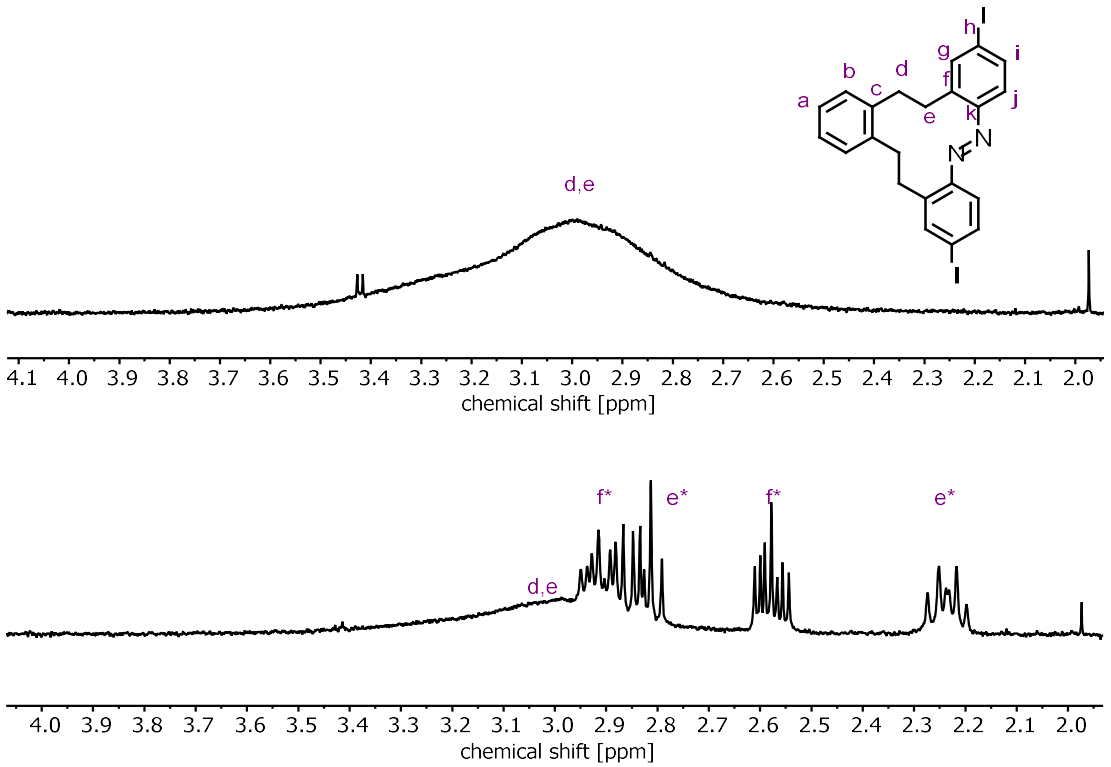

Figure S29. Partial ^{1}H NMR spectra (500 MHz, CD_2Cl_2, 298 K) of the aliphatic region of **5** before (top) and after (bottom) *ex-situ* irradiation at 365 nm for 60 minutes. The previously broad signals for H_d and H_e in *E*-**5** appear as four distinct, sharp diasterotopic signals for *Z*-**5**.

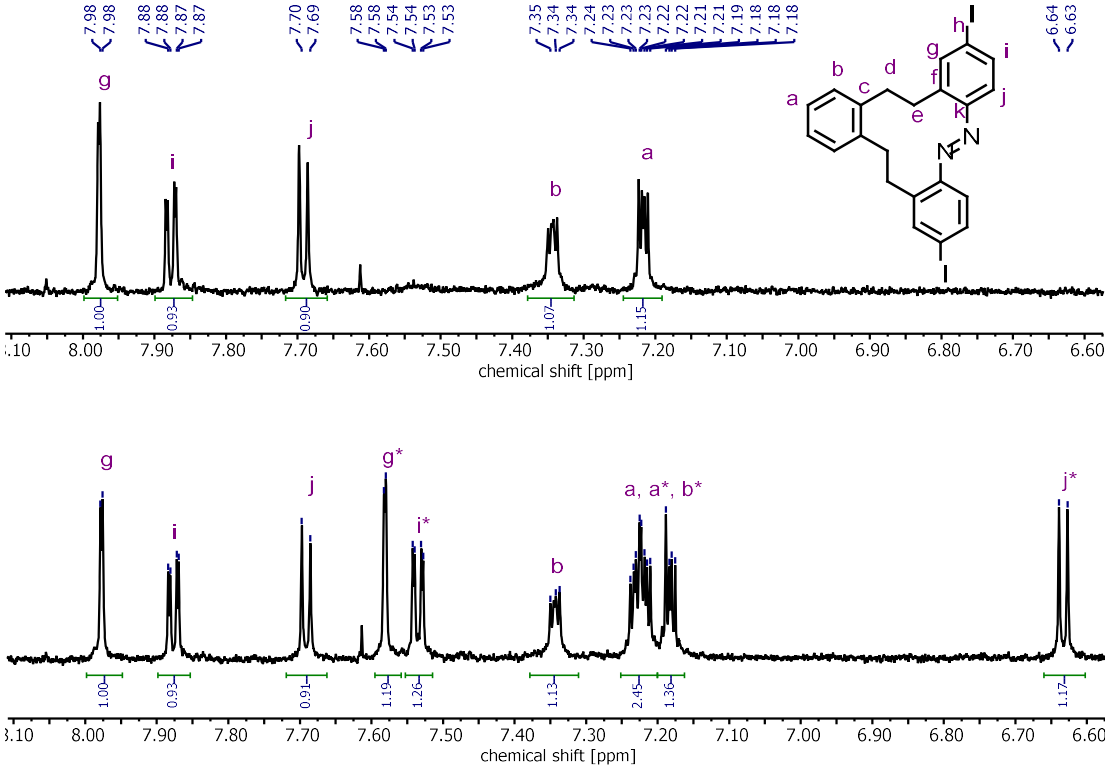

Figure S30. Partial ^{1}H NMR spectra (700 MHz, CD_3CN, 298 K) of the aromatic region of **5** before (top) and after (bottom) *ex-situ* irradiation at 365 nm for 45 min. Integration of the signals H-g and H-g* gave a ratio of 54% *Z*-**5** in the sample.

3.3. Determination of photostationary states (PSS) by HPLC and UV-vis spectroscopy

Method

Step 1 – determination of the optimal excitation wavelength. To determine the optimal excitation wavelength λ_{ex}, the sample was irradiated for 5 minutes using different wavelengths and UV-vis spectra were recorded using a flash-lamp spectrometer. The excitation wavelength that resulted in the largest change in the UV-vis spectrum was used for further experiments.

Step 2 – determination of isosbestic points. The sample was irradiated using the optimal excitation wavelength λ_{ex} in one of the illumination setups described in Section 3.1 and UV-vis spectra were recorded in regular time intervals. The resulting spectra were stacked to identify the isosbestic point(s).

Step 3 – HPLC run. The samples were irradiated inside an amberised vial using the setup shown in **Figure S22** until the PSS was reached and injected into the HPLC with the lights in the room turned off. Since a reverse phase column (C18) was used, the more polar *Z*-form is expected to be eluting first and the less polar *E*-form after that. The chromatogram was plotted using one of the isosbestic points as the detector wavelength since the extinction coefficients of *E* and *Z*-isomers are identical at those points. Area-integration of the chromatogram gives PSS^{HPLC} as determined by HPLC.[5]

Step 4 – Fit of PSS from UV-vis spectra. Due to the long half-lives of the compounds, UV-vis spectra of pure *E* and pure *Z*-isomers could be obtained from the HPLC runs using its internal UV-vis spectrometer. The absorbance of the *E*-isomer was scaled to be identical to the spectrum of a non-irradiated sample while the spectrum of the *Z*-isomer was scaled to intersect at the isosbestic point used in step 3. A UV-vis spectrum of the PSS obtained from the same sample (= exactly the same concentration) at the plate reader was fitted with a linear combination of the spectra of the *E* and *Z*-isomers to give the PSS^{Fit}.[5]

Table S3. Overview over the results of the determination of the photo stationary states for **1**, **3**, **4**, **5**, and **6**. The derivatives **2** and **7** showed almost no change upon irradiation and were therefore not investigated further.

Compound	**Isosbestic point**	**PSS^{HPLC}** (% *Z*) (CH_3CN)	**PSS^{Fit}** (% *Z*) (CH_3CN / CH_3OH 1:1 (v/v))	**PSS^{NMR}** (% *Z*)
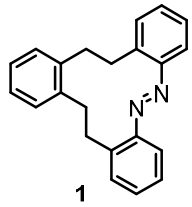 **1**	276 nm	53%	51%	55% (CD_3CN) 59% (DMF-d_7) 51% (CD_2Cl_2)
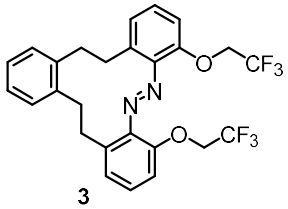 **3**	296 nm	14%	14%	
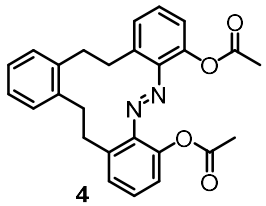 **4**	244 nm	34%	47%	
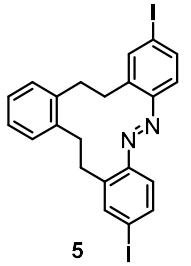 **5**	287 nm	*61%* (Chromatogram not clean)	65%	54% (CD_3CN) 45% (CD_2Cl_2)
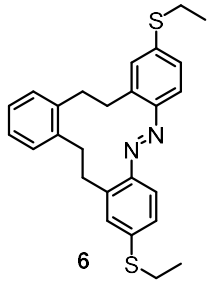 **6**	347 nm	38%	45%	

3.3.1. Cyclic azobenzene 1

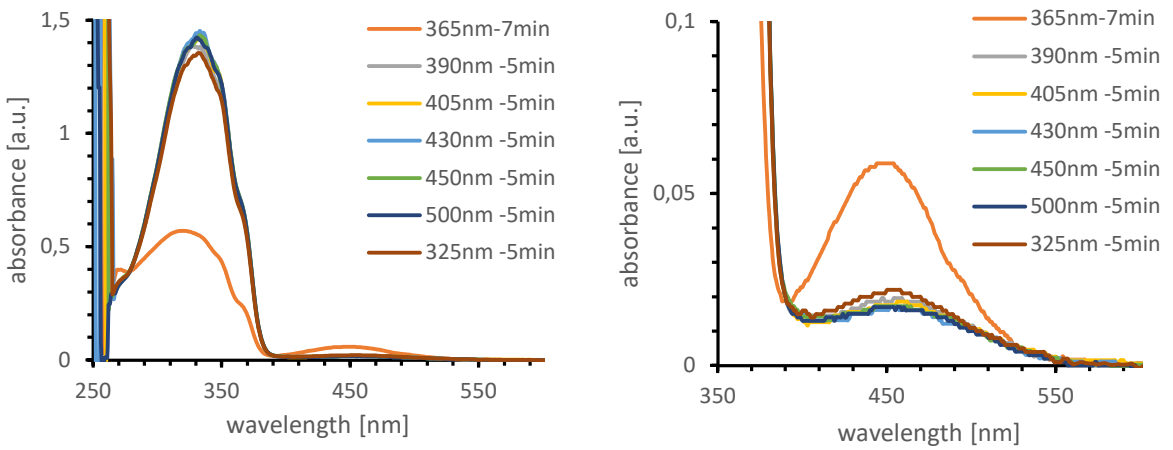

Figure S31. UV-vis spectra of **1** (DMF, 1 mM) after irradiation with different wavelengths (325, 365, 390, 405, 430, 450, and 500 nm, respectively) to determine the optimal excitation wavelength for photoswitching of **1**.

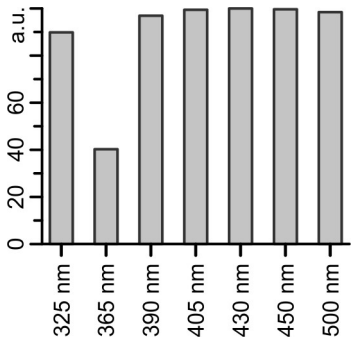

Figure S32. Absorptions of **1** at 330 nm (1 mM, DMF) after irradiations with light of different wavelengths demonstrating *E*-**1** to be the favoured isomer under any wavelength except 365 nm.

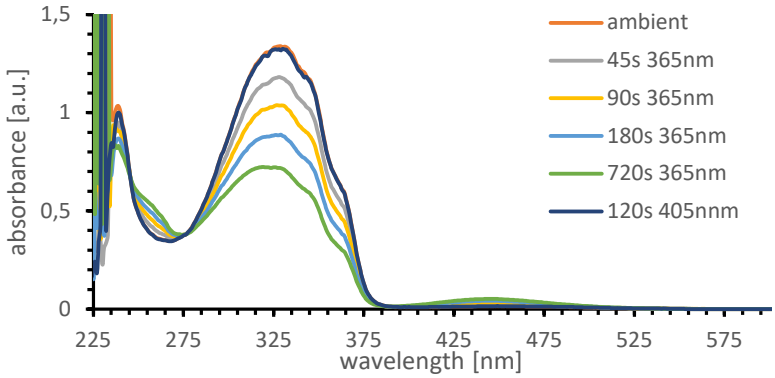

Figure S33. Irradiation of **1** (MeCN/MeOH 1:1 (v/v), 1 mM) with 365 nm light for different time intervals (45, 90, 120, 180, and 720 s, respectively) showing isosbestic points at 246 nm and 276 nm.

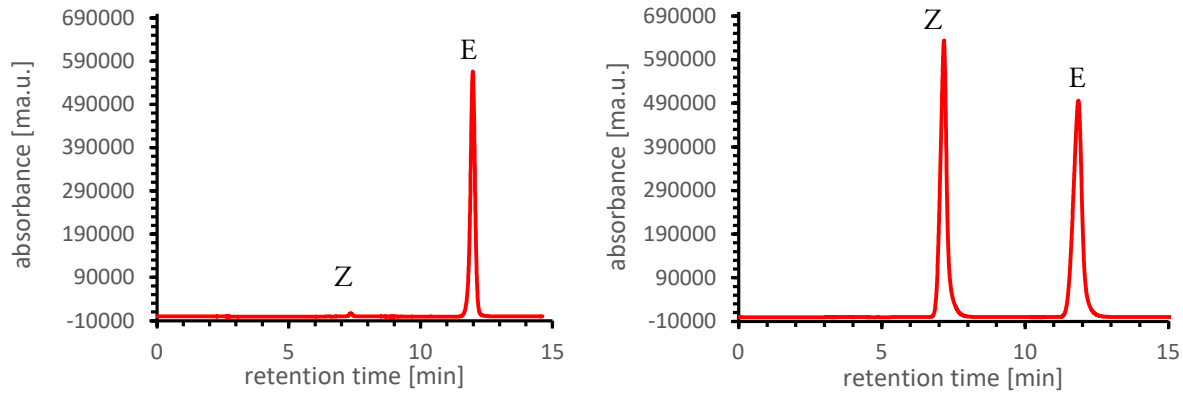

Figure S34. HPLC chromatogram (MeCN/MeOH 1:1 (v/v)) at 276.5 nm of **1** after standing on a sunny windowsill for 2 h showing 1% *Z*-**1** (left) and of the PSS^{365} of **1** (irradiated for 30 min @365nm, 1 mM in MeCN) showing 51% *Z*-**1** (right).

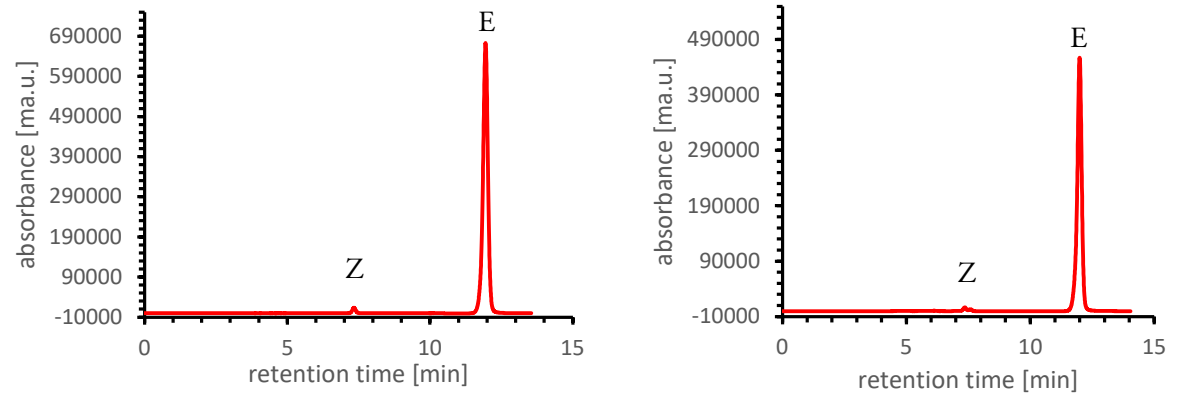

Figure S35. HPLC chromatogram (MeCN/MeOH 1:1 (v/v)) at 276.5 nm of the PSS^{405} of **1** (irradiated for 30 min @405nm, 1 mM in MeCN) showing 1% *Z*-**1**(left) and of the PSS^{450} of **1** (irradiated for 30 min @450nm, 1 mM, MeCN) showing 1% *Z*-**1**(right).

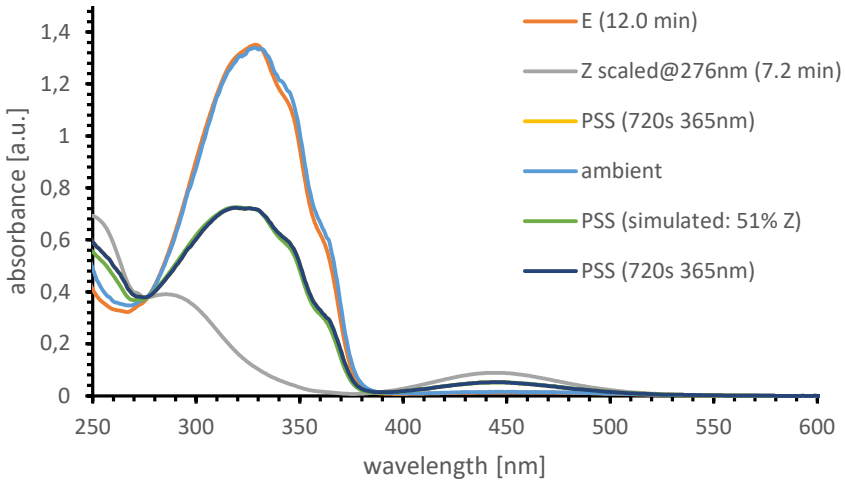

Figure S36. UV-vis spectra (CH_3CN/CH_3OH 1:1 (v/v)) of ***E*-1** (blue, normalized) and ***Z*-1** (green, normalized) as obtained after HPLC separation, **1** subjected to ambient light (orange, 1 mM), PSS of **1** after 12 min irradiation with 365 nm light (yellow, 1 mM), and the simulated spectrum of the PSS^{fit} of **1** showing 51% ***Z*-1** (grey).

3.3.2. Dimethoxy cyclic azobenzene 2

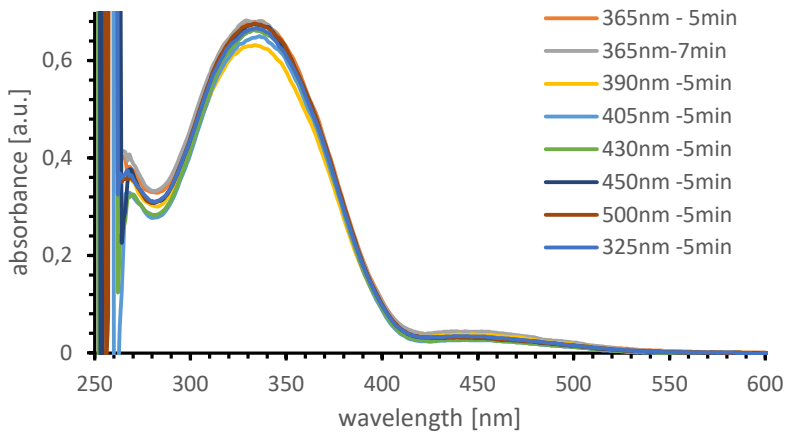

Figure S37. UV-vis spectra of **2** (DMF, 1 mM) after irradiation with different wavelengths (325, 365, 390, 405, 430, 450, and 500 nm, respectively) to determine the optimal excitation wavelength for photoswitching of **2**.

Compound **2** only showed slight changes in its absorption spectrum after irradiation at 390 nm and 405 nm. This shows that the excitation wavelength had been redshifted, but the difference before and after irradiation was rather small. This suggests a very low amount of *Z*-**2** being present. Due to this bad switching behaviour the photophysical properties of **2** were not investigated further.

3.3.3. Bis(trifluoroethoxy) cyclic azobenzene 3

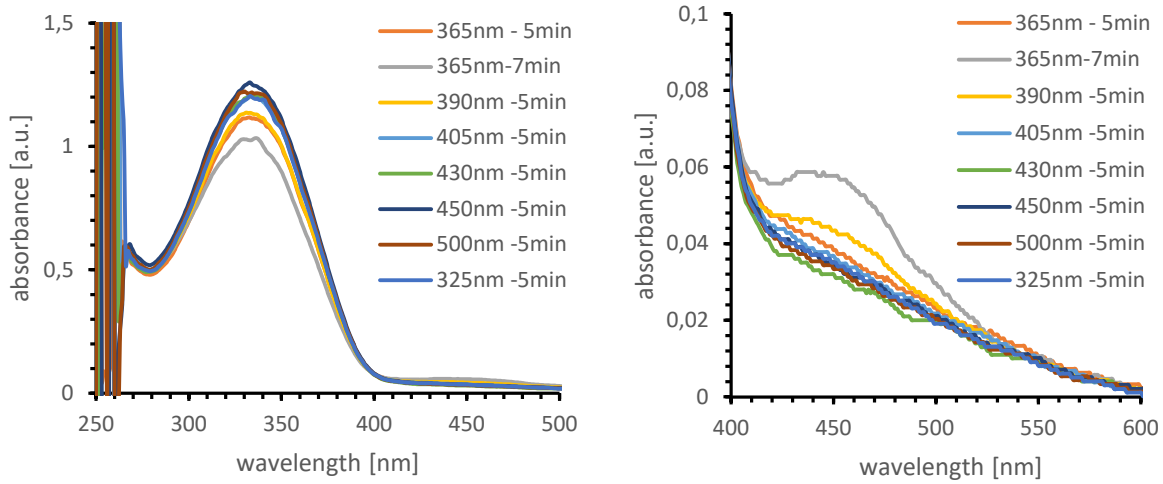

Figure S38. UV-vis spectra of **3** (DMF, 1 mM) after irradiation with different wavelengths (325, 365, 390, 405, 430, 450, and 500 nm, respectively) to determine the optimal excitation wavelength for photoswitching of **3**.

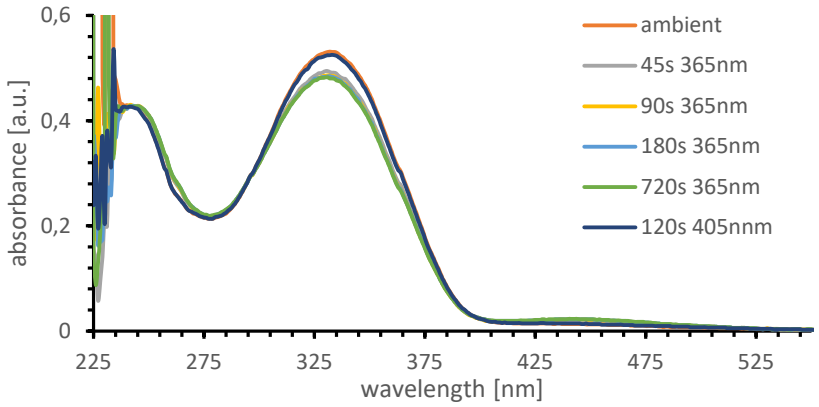

Figure S39. Irradiation of **3** (MeCN/MeOH 1:1 (v/v), 1 mM) with 365 nm light for different time intervals (45, 90, 120, 180, and 720 s, respectively) showing an isosbestic point at 296 nm.

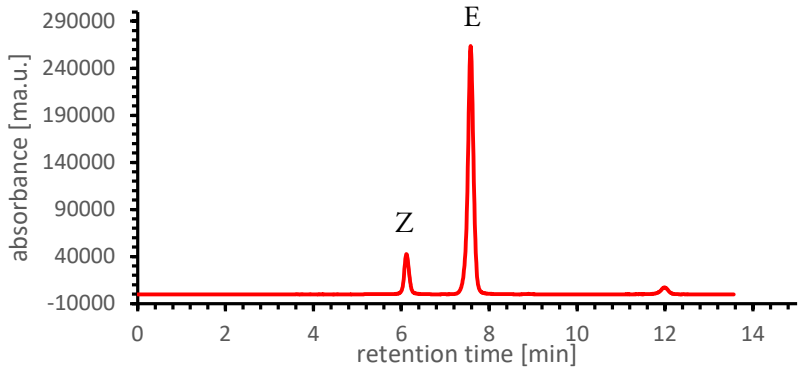

Figure S40. HPLC chromatogram (MeCN/MeOH 1:1 (v/v)) at 269.3 nm of the PSS^{365} of **3** (irradiated for 30 min @365nm, 1 mM in MeCN) showing 14% *Z*-**3**.

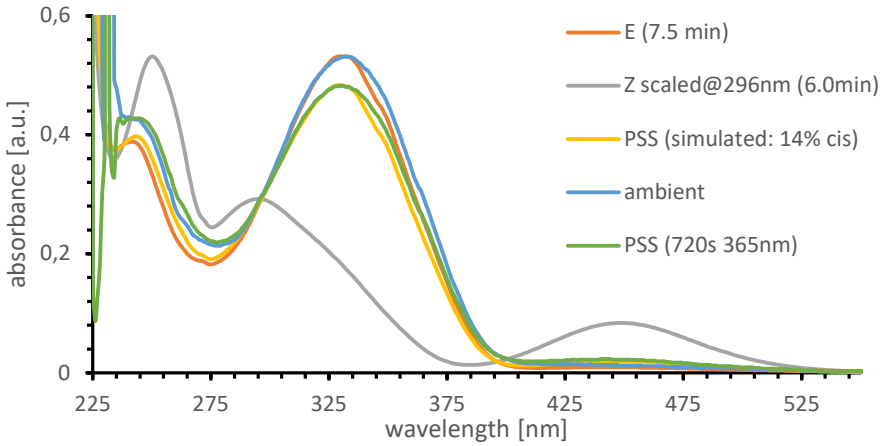

Figure S41. UV-vis spectra (CH_3CN/CH_3OH 1:1 (v/v)) of ***E*-3** (orange, normalized) and ***Z*-3** (yellow, normalized) as obtained after HPLC separation, **3** subjected to ambient light (blue,1 mM), PSS of **3** after 12 min irradiation with 365 nm light (green, 1 mM), and the simulated spectrum of the PSS^{fit} of **3** showing 14% ***Z*-3** (grey).

3.3.4. Diaceto cyclic azobenzene 4

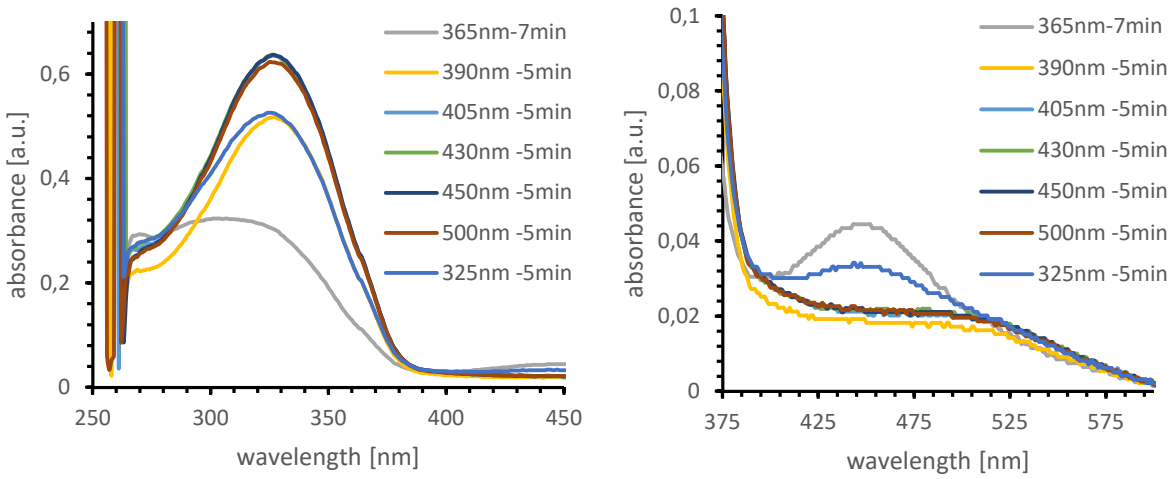

Figure S42. UV-vis spectra of **4** (DMF, 1 mM) after irradiation with different wavelengths (325, 365, 390, 405, 430, 450, and 500 nm, respectively) to determine the optimal excitation wavelength for photoswitching of **4**.

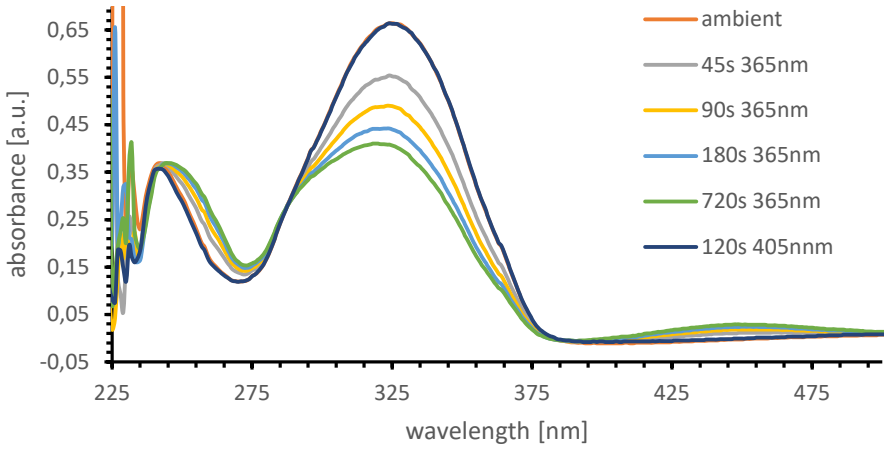

Figure S43. Irradiation of **4** (MeCN/MeOH 1:1 (v/v), 1 mM) with 365 nm light for different time intervals (45, 90, 120, 180, and 720 s, respectively) showing isosbestic points at 244 nm and 288 nm.

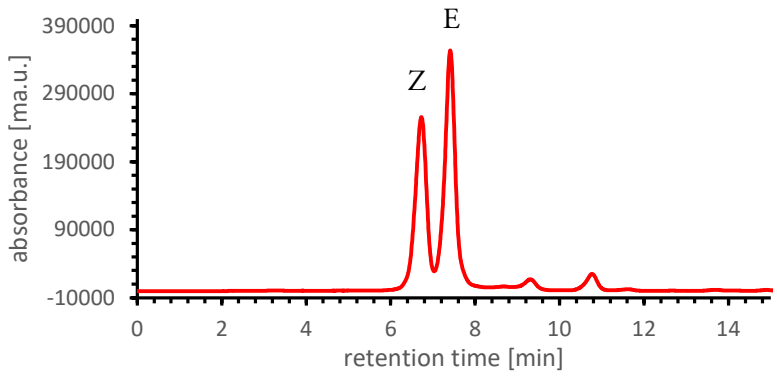

Figure S44. HPLC chromatogram (MeCN/MeOH 1:1 (v/v)) at 244.4 nm of the PSS^{365} of **4** (irradiated for 30 min @365nm, 1 mM in MeCN) showing 34% *Z*-**4**.

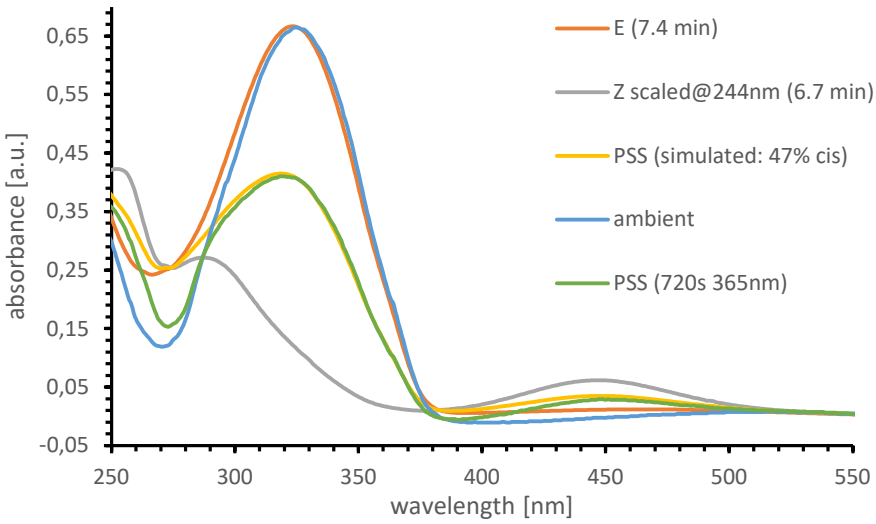

Figure S45. UV-vis spectra (CH_3CN/CH_3OH 1:1 (v/v)) of ***E*-4** (orange, normalized) and ***Z*-4** (grey, normalized) as obtained after HPLC separation, **4** subjected to ambient light (blue, 1 mM), PSS of **4** after 12 min irradiation with 365 nm light (green, 1 mM), and the simulated spectrum of the PSS^{fit} of **4** showing 47% ***Z*-4** (yellow).

3.3.5. Diiodo cyclic azobenzene 5

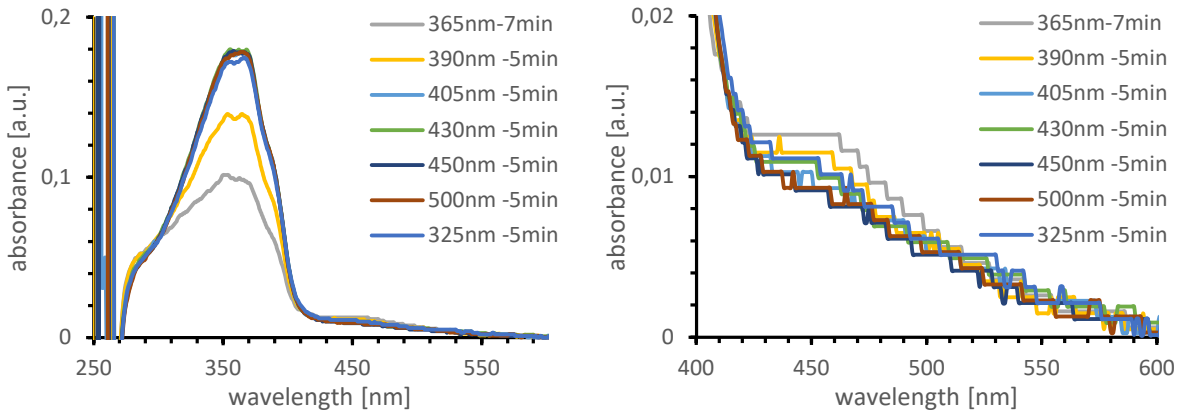

Figure S46. UV-vis spectra of **5** (DMF, 1 mM) after irradiation with different wavelengths (325, 365, 390, 405, 430, 450, and 500 nm, respectively) to determine the optimal excitation wavelength for photoswitching of **5**.

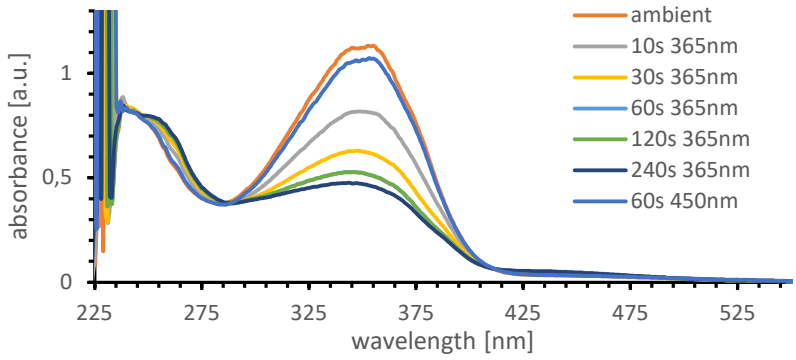

Figure S47. Irradiation of **5** (MeCN/MeOH 1:1 (v/v), 1 mM) with 365 nm light for different time intervals (45, 90, 120, 180, and 720 s, respectively) showing isosbestic points at 287 nm and 412 nm.

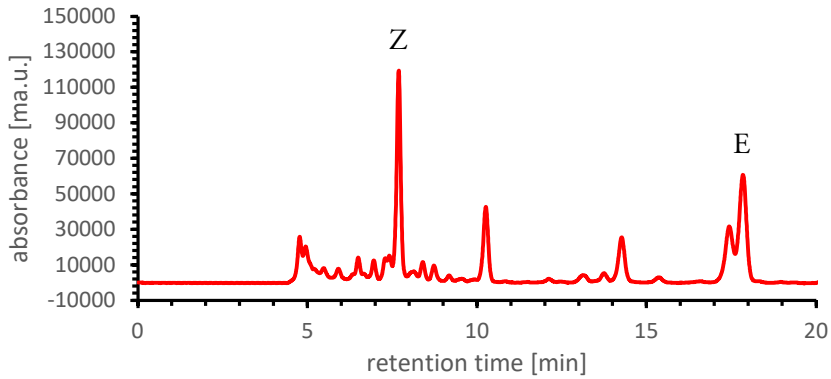

Figure S48. HPLC chromatogram (MeCN/MeOH 1:1 (v/v)) at 287.6 nm of the PSS^{365} of **5** (irradiated for 30 min @365nm, 1 mM in MeCN) showing 61% *Z*-**5**.

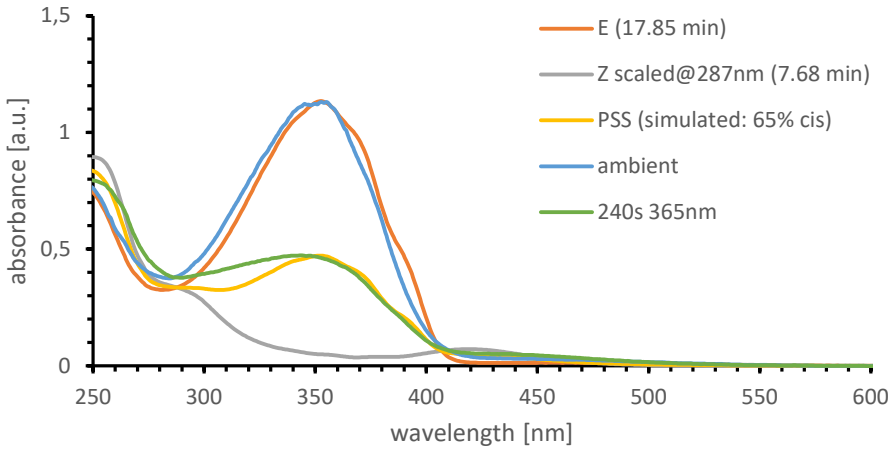

Figure S49. UV-vis spectra (CH_3CN/CH_3OH 1:1 (v/v)) of ***E*-5** (orange, normalized) and ***Z*-5** (grey, normalized) as obtained after HPLC separation, **5** subjected to ambient light (blue, 1 mM), PSS of **5** after 4 min irradiation with 365 nm light (green, 1 mM), and the simulated spectrum of the PSS^{fit} of **5** showing 65% ***Z*-5** (yellow).

The HPLC chromatogram showed multiple other peaks that could not be removed by repeated column chromatography and the resulting PSS^{HPLC} at 365 nm might therefore be inaccurate. Small contaminations by a strongly absorbing contamination might also affect PSS^{fit} resulting from the fitted UV-vis spectrum quite significantly. These contaminations were not visible in the ^{1}H NMR spectra. Therefore, an irradiated sample was investigated using ^{1}H NMR spectroscopy (see *ex-situ* irradiation in Section 3.2). Integration of the signals gave a ratio of 45% *Z*-**5** in the sample.

3.3.6. Thioether substituted cyclic azobenzene 6

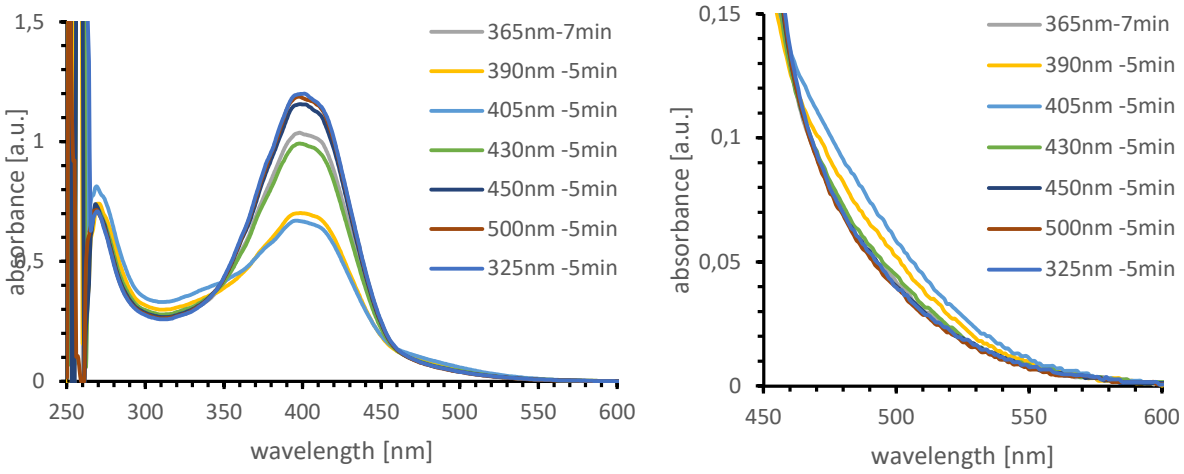

Figure S50. UV-vis spectra of **6** (DMF, 1 mM) after irradiation with different wavelengths (325, 365, 390, 405, 430, 450, and 500 nm, respectively) to determine the optimal excitation wavelength for photoswitching of **6**.

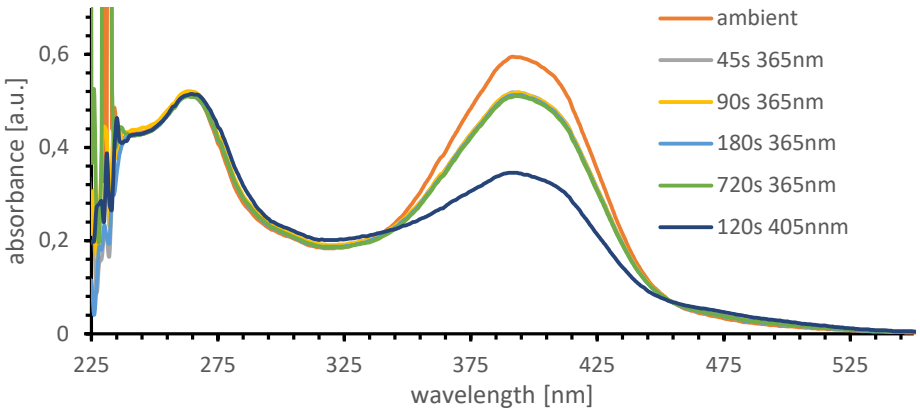

Figure S51. Irradiation of **6** (MeCN/MeOH 1:1 (v/v), 1 mM) with 365 nm light for different time intervals (45, 90, 120, 180, and 720 s, respectively) showing isosbestic points at 347 nm and 455 nm.

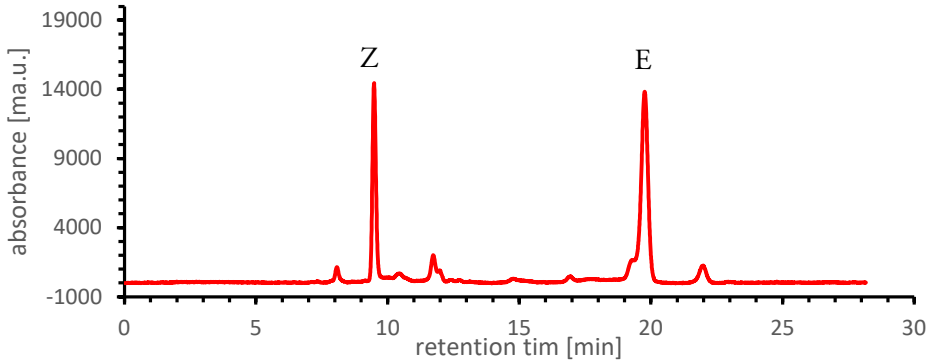

Figure S52. HPLC chromatogram (MeCN/MeOH 1:1 (v/v)) at 454.7 nm of the PSS^{405} of **6** (irradiated for 30 min @405nm, 1 mM in MeCN) showing 38% ***Z*-6**.

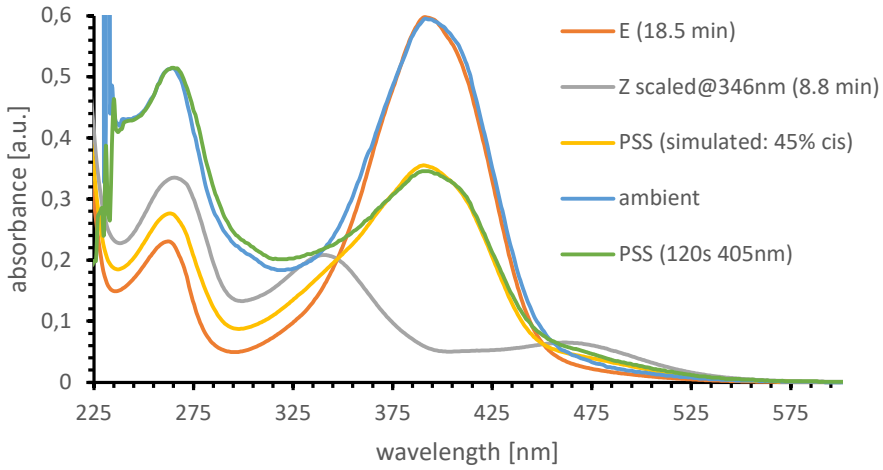

Figure S53. UV-vis spectra (CH_3CN/CH_3OH 1:1 (v/v)) of ***E*-6** (orange, normalized) and ***Z*-6** (grey, normalized) as obtained after HPLC separation, **6** subjected to ambient light (blue, 1 mM), PSS of **6** after 2 min irradiation with 405 nm light (green, 1 mM), and the simulated spectrum of the PSS^{fit} of **4** showing 45% ***Z*-6** (yellow).

3.3.7. bis(4-methoxyphenyl)phenylamine substituted cyclic azobenzene 7

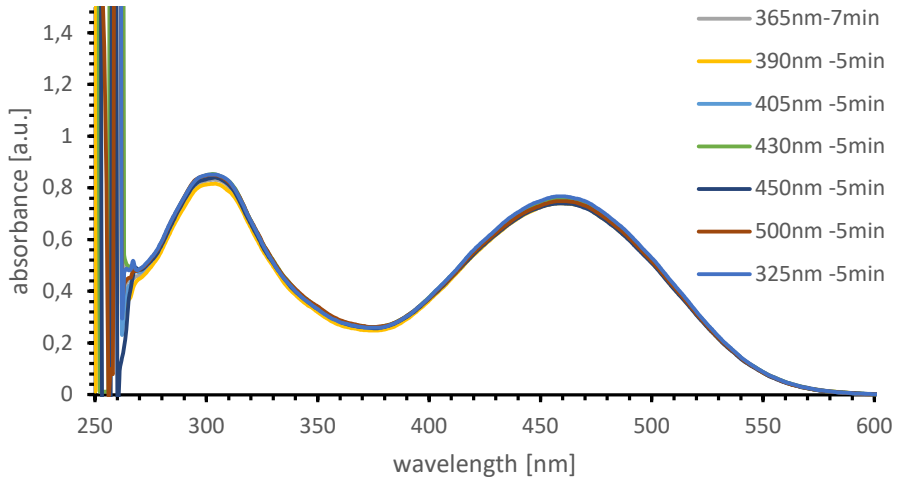

Figure S54. UV-vis spectra of **7** (DMF, 1 mM) after irradiation with different wavelengths (325, 365, 390, 405, 430, 450, and 500 nm, respectively) to determine the optimal excitation wavelength for photoswitching of **7**.

Compound 7 showed basically no changes in its absorption spectrum after irradiation at any wavelength. This suggests that either no *Z*-7 is being formed or thermal relaxation is extremely fast. Due to this bad switching behaviour, the photophysical properties of 7 were not investigated further.

3.4. Determination of thermal half-lives $\tau_{½}$ by UV-vis and ^{1}H NMR spectroscopy

General procedure for the NMR method

An NMR sample was prepared in CD_3CN and irradiated for 60 minutes in a brown glass vial that had been covered in aluminium foil using the 365 nm LED. In a dark room, the sample was transferred to an amberised NMR tube. The sample was placed inside of the spectrometer that had been heated to 45 °C and ^{1}H NMR spectra were recorded every 30 minutes for 72 h.

A well visible proton signal was chosen, and the corresponding signals in *Z*- and *E*-state integrated. The integrals were used to calculate the percentage of the excited *Z* isomer which was normalized and plotted against the time *t* and fitted using first order kinetics **(Equation S1)** to give rate constants *k* and the half-lives $\tau_{½} = \ln(2) \cdot k^{-1}$ (**Table S4**).

$$\%_t^{Z,\text{normalized}} = \frac{\%_t^Z - \%_\infty^Z}{\%_0^Z - \%_\infty^Z} = e^{-kt} \qquad \text{using:} \quad \%_x^Z = \frac{I_x^Z}{I_x^Z + I_x^E} \qquad \textbf{(S1)}$$

Table S4. Rate constants *k*, mean lifetimes $\tau = k^{-1}$, and half-lives $\tau_{½}$ obtained by thermal relaxation experiments of **1** using ^{1}H NMR (45 °C, CD_3CN, 50 mM).

	1
$\tau_{½}$ [h]	35.6
τ [h]	51.3
k [h^{-1}]	0.0195

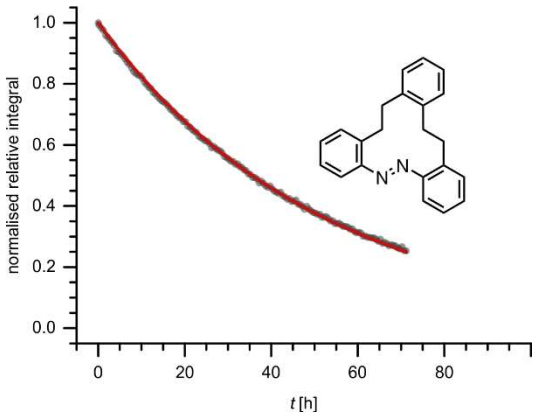

Figure S55. Thermal relaxation of **1** in CD_3CN (50 mmol L^{-1}) at 45 °C after irradiation at 365 nm for 60 minutes.

General procedure for the UV-vis method

First, a reference spectrum was taken of a 96-well plate containing multiple samples of each compound in DMF (1 mmol L^{-1}). The plate was then irradiated at 365nm for 40 minutes and placed in the plate reader that had been preheated to 45 °C. A UV-vis spectrum was measured every two hours.

One wavelength that showed significant changes in intensity was chosen for each compound. Using the spectra taken before irradiation this absorbance was normalized and plotted against the time t and fitted using first order kinetics **(Equation S2)** to give rate constants k and the half-lives $\tau_{½} = \ln(2) \cdot k^{-1}$ (**Table S5**).

$$A^{\text{normalized}} = \frac{A_t - A_\infty}{A_0 - A_\infty} = e^{-kt} \qquad \text{(S2)}$$

Table S5. Rate constants k, mean lifetimes $\tau = k^{-1}$, and half-lives $\tau_{½}$ obtained by thermal relaxation experiments of **1**, **3**, **4**, **5**, and **6** (45 °C, DMF, 1 mM) using UV-Vis. Relaxation of **1** was also investigated at ambient temperature (DMF, 1 mM). Multiple replicates were performed for each photoswitch as indicated. λ_{fit} indicates the wavelength at which the absorption was followed.

	1		**3**	**4**	**5**	**6**
λ_{fit} [nm]	330	330	330	330	360	400
replicates	4	4	6	6	4	5
$\tau_{½}$ [h]	30.6 (45 °C)	379 (ambient *T*)	8.2	7.1	19	1.23
τ [h]	44.2 (45 °C)	547 (ambient *T*)	11.8	10.2	27	1.77
k [h^{-1}]	0.0226 (45 °C)	0.0018 (ambient *T*)	0.0847	0.0980	0.0370	0.5650

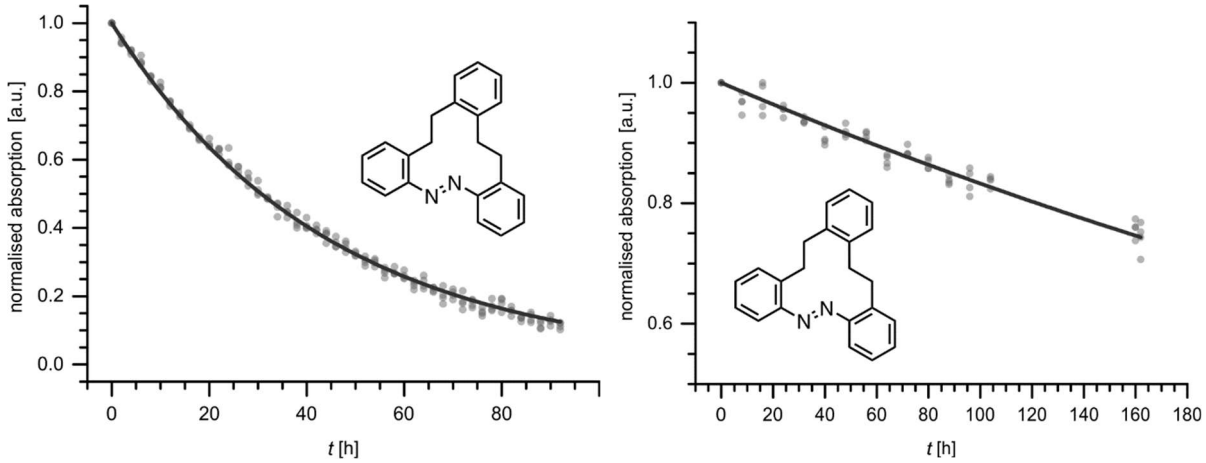

Figure S56. Thermal relaxation of **1** in DMF (1 mmol L^{-1}) at 45 °C (left) and ambient *T* (right) after irradiation at 365 nm for 40 minutes. Both graphs are a combination of four replicates.

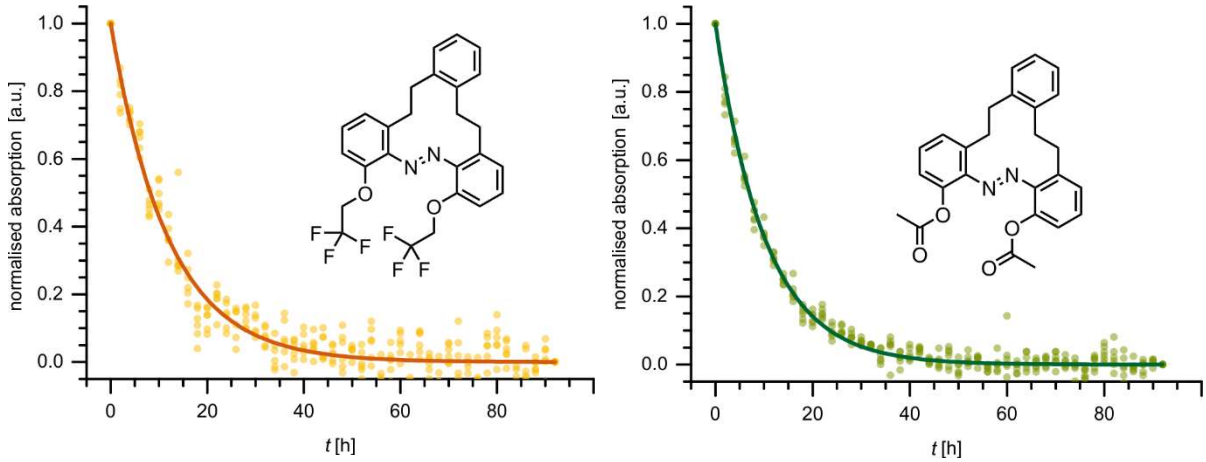

Figure S57. Thermal relaxation of **3** (left) and **4** (right) in DMF (1 mmol L^{-1}) at 45 °C after irradiation at 365 nm for 40 minutes. Both graphs are a combination of six replicates.

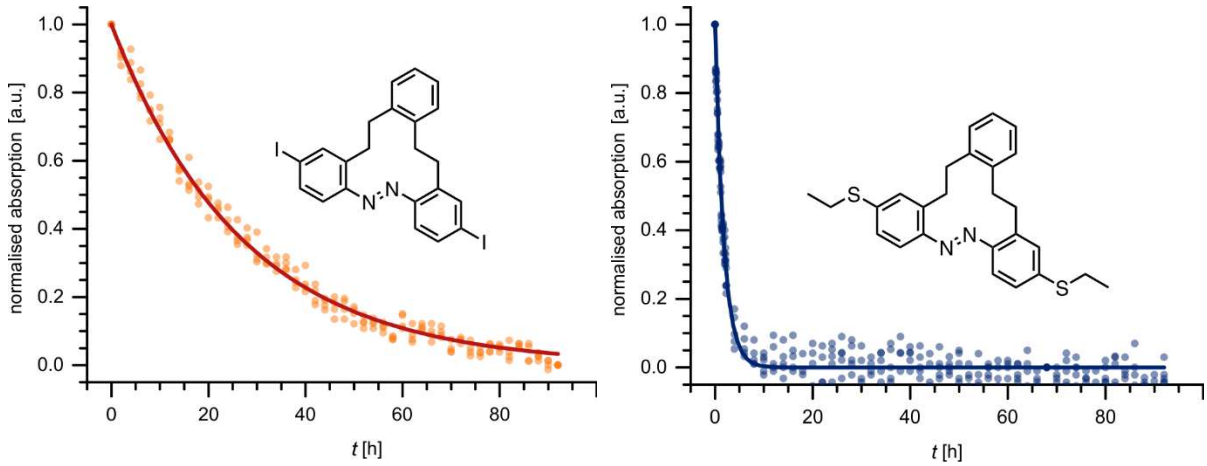

Figure S58. Thermal relaxation of **5** (left) and **6** (right) in DMF (1 mmol L^{-1}) at 45 °C after irradiation at 365 nm for 40 minutes. The left graph contains 4 replicates, and the right graph contains 5 replicates.

3.5. Reversibility of photoisomerization

Solutions of **1**, **4**, and **5** in DMF (1 mmol L^{-1}) were prepared in a 96-well plate and a reference UV-vis spectrum was measured. The sample was then irradiated for 15 minutes alternating between 365nm and white light. UV-vis spectra were recorded in between the irradiation steps and absorbances at 330 nm plotted against the number of cycles (**Figure S59**, **Figure S60**, and **Figure S61**). Compounds **1** and **4** showed no degradation over 20 cycles while slight degradation could be observed for **5**.

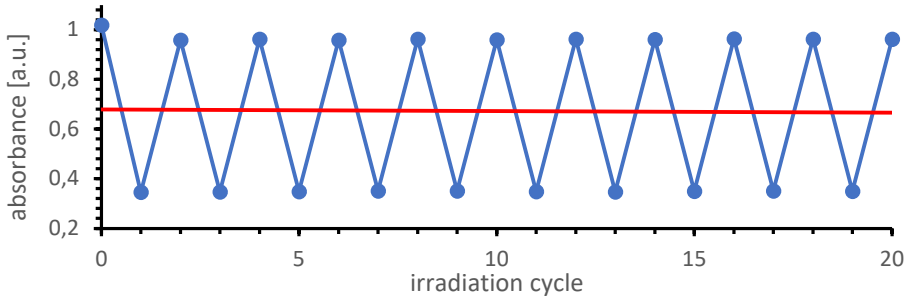

Figure S59. Absorbance at 330 nm with alternating irradiations at 365 nm and with white light demonstrating reversible photoisomerization cycles of compound **1** (1 mM, DMF).

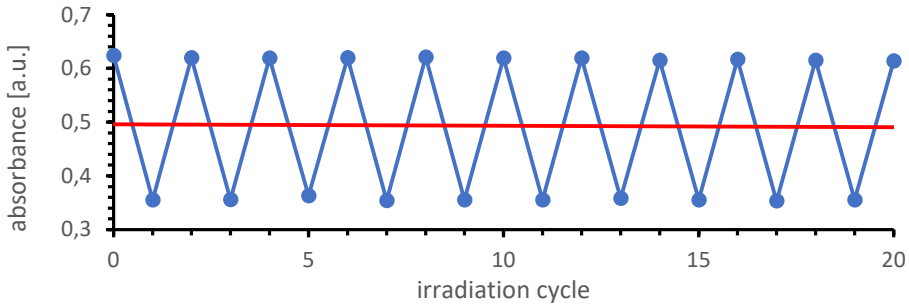

Figure S60. Absorbance at 330 nm with alternating irradiations at 365 nm and with white light demonstrating reversible photoisomerization cycles of compound **4** (1 mM, DMF).

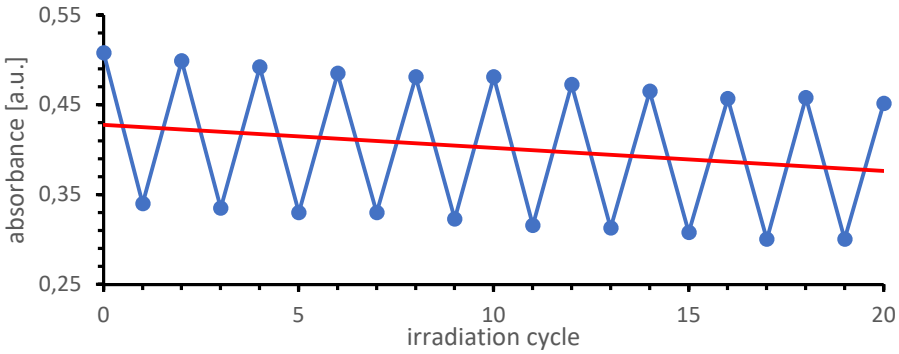

Figure S61. Absorbance at 330 nm with alternating irradiations at 365 nm and with white light showing slight photodegradation of compound **5** (1 mM, DMF) during the irradiation cycles.

4. Quantum chemical calculations

Geometries were optimized and energies calculated on DFT level using the range separated wb97x-v hybrid functional[6] on a def2-QZVP[7] level of theory using Orca 5.0.3. [8,9] The total energy was calculated using **Equation S2** with the gas phase energy at 0 K calculated by DFT (E^{0K}), the thermodynamic contribution dG^{T} and the solvation free energy corresponding to the change form gas phase to the solvent dG^{solv}.

$$dG^{total} = E^{0K} + dG^{T} + dG^{solv} \qquad \text{(S2)}$$

The thermodynamic contribution dG^{T} was calculated using a modified rigid-rotor harmonic-oscillator approach (mRRHO[10]) with frequencies calculated using the r2scan-3c composite method[11] and dG^{solv} was calculated using the conductor like screening model for realistic solvation (COSMO-RS).[12,13] The results of these calculations are presented in **Table S6**.

The resulting structures are shown in Figure S62 and additionally provided as separate xyz files.

Table S6. Results of quantum chemical calculations.

	E^{0K}	dG^{T}	dG^{solv} (DCM)	dG^{total}	ddG^{total} [kJ mol^{-1}]
Z-**1**	−959.97069	0.31869	−0.02712	−959.67912	0
E-**1**	−959.9934	0.31846	−0.02533	−959.70027	55.6

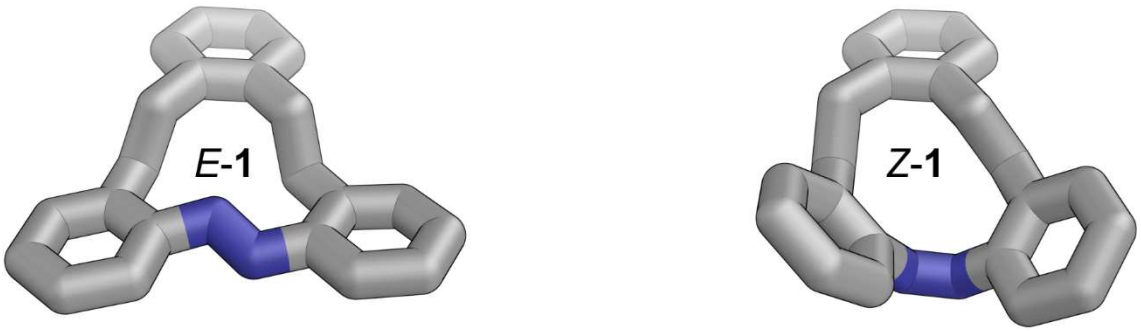

Figure S62. Optimized structures of *E*-1 and *Z*-1.

5. Crystal structure

Suitable clear orange plank-like single crystals of **E-1** were grown upon slow evaporation of its saturated solution in Dichloromethane at ca. 15 °C for about 4 weeks. The data collection was performed on a STOE Stadivari Eulerian 4-circle diffractometer using Cu-K_α radiation (λ = 1.54186 Å). The diffractometer was equipped with a low–temperature device (Cryostream 800er series, Oxford Cryosystems, 100(1) K). Intensities were measured by fine-slicing ω-scans and corrected for background, polarization and Lorentz effects. An absorption correction by scaling of reflection intensities with a subsequent spherical absorption correction was performed with STOE LANA programme.[14]

The structure was solved by intrinsing phasing methods[15] and refined anisotropically by the least-squares procedure implemented in the SHELX programme system.[16] The hydrogen atoms were included isotropically using the riding model on the bound carbon atoms.

The correct assignment of the absolute configuration was done via the Flack parameter[17] (Flack(x)=–0.02(12)) and by using Bayesian statistics on Bijvoet differences giving the a P2(true) and P3(true) probability of 1.000, the probability of racemic twinning with $0.5 \cdot 10^{-6}$, and the probability of the assignment of the wrong absolute structure with $0.2 \cdot 10^{-23}$.[18]

CCDC number 2248689 contains the supplementary crystallographic data for this paper, which can be obtained free of charge from the Cambridge Crystallographic Data Centre via http://www.ccdc.cam.ac.uk/data_request/cif.

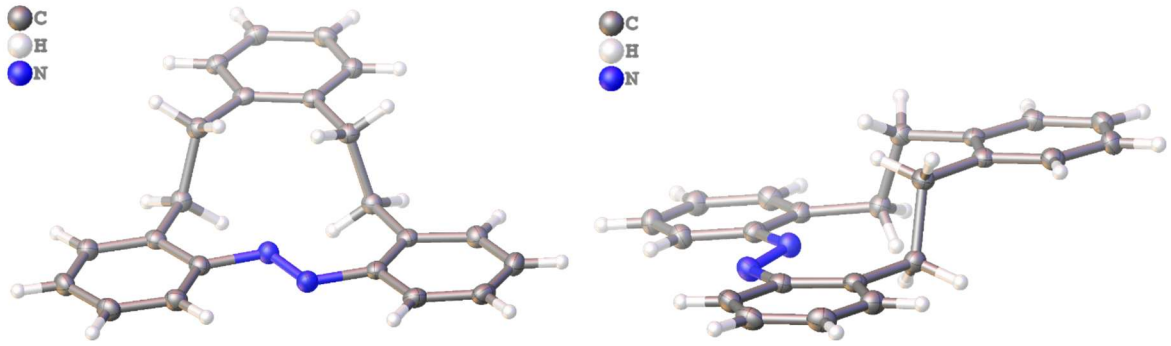

Figure S63. Asymmetric unit of cyclic azobenzene **1** as observed in the crystal structure, plotted from two different viewing angles. Hydrogen atoms omitted for clarity. Displacement ellipsoids are drawn at 50% probability.

Table S7. Crystal data and refinement parameters for cyclic azobenzene **1.**

Crystal Habitus	clear orange plank
Device Type	STOE STADIVARI
Empirical formula	$C_{22}H_{20}N_2$
Moiety formula	C22 H20 N2
Formula weight	312.40
Temperature/K	100.15
Crystal system	orthorhombic
Space group	$P2_12_12_1$
a/Å	4.96650(10)
b/Å	11.8329(2)
c/Å	27.6027(5)
α/°	90
β/°	90
γ/°	90
Volume/Å^3	1622.16(5)
Z	4
ρ_{calc}g/cm^3	1.279
μ/mm^{-1}	0.576
F(000)	664.0
Crystal size/mm^3	0.32 × 0.207 × 0.14
Absorption correction	multi-scan
Tmin; Tmax	0.6362; 0.6934
Radiation	CuKα (λ = 1.54186)
2Θ range for data collection/°	6.404 to 140.964°
Completeness to theta	1.000
Index ranges	-6 ≤ h ≤ 2, -13 ≤ k ≤ 14, -32 ≤ l ≤ 33
Reflections collected	65728
Independent reflections	3071 [R_{int} = 0.0211, R_{sigma} = 0.0056]
Data/restraints/parameters	3071/0/218
Goodness-of-fit on F^2	1.050
Final R indexes [I>=2σ (I)]	R_1 = 0.0249, wR_2 = 0.0641
Final R indexes [all data]	R_1 = 0.0251, wR_2 = 0.0643
Largest diff. peak/hole / e Å^{-3}	0.18/-0.12
Flack parameter	-0.02(12)

6. References

1 M. S. Maier, K. Hüll, M. Reynders, B. S. Matsuura, P. Leippe, T. Ko, L. Schäffer and D. Trauner, *J. Am. Chem. Soc.*, 2019, **141**, 17295–17304.

2 A. Müller-deku and O. Thorn-seshold, *ChemRxiv*, 2022, **20**, 1–6.

3 C. Feldmeier, H. Bartling, E. Riedle and R. M. Gschwind, *J. Magn. Reson.*, 2013, **232**, 39–44.

4 S. Ghosh, C. Eschen, N. Eleya and A. Staubitz, *J. Org. Chem.*, , DOI:10.1021/acs.joc.2c00549.

5 L. Gao, J. C. M. Meiring, Y. Kraus, M. Wranik, T. Weinert, S. D. Pritzl, R. Bingham, E. Ntouliou, K. I. Jansen, N. Olieric, J. Standfuss, L. C. Kapitein, T. Lohmüller, J. Ahlfeld, A. Akhmanova, M. O. Steinmetz and O. Thorn-Seshold, *Cell Chem. Biol.*, 2021, **28**, 228-241.e6.

6 N. Mardirossian and M. Head-Gordon, *Phys. Chem. Chem. Phys.*, 2014, **16**, 9904–9924.

7 F. Weigend and R. Ahlrichs, *Phys. Chem. Chem. Phys.*, 2005, **7**, 3297–3305.

8 F. Neese, *WIREs Comput. Mol. Sci.*, 2012, **2**, 73–78.

9 F. Neese, *Wiley Interdiscip. Rev. Comput. Mol. Sci.*, 2022, **12**, 1–15.

10 S. Grimme, *Chem. - A Eur. J.*, 2012, **18**, 9955–9964.

11 S. Grimme, A. Hansen, S. Ehlert and J. M. Mewes, *J. Chem. Phys.*, , DOI:10.1063/5.0040021.

12 A. Klamt, V. Jonas, T. Bürger and J. C. W. Lohrenz, *J. Phys. Chem. A*, 1998, **102**, 5074–5085.

13 A. Klamt, *J. Phys. Chem.*, 1995, **99**, 2224–2235.

14 X-Area LANA 2.7.9.0 (STOE&Cie, **2022**.)

15 G. M. Sheldrick, *Acta Crystallogr. Sect. A Found. Adv.*, 2015, **71**, 3–8.

16 G. M. Sheldrick, *Acta Crystallogr. Sect. C Struct. Chem.*, 2015, **71**, 3–8.

17 H. D. Flack, *Acta Crystallogr. Sect. A Found. Crystallogr.*, 1983, **39**, 876–881.

18 R. W. W. Hooft, L. H. Straver and A. L. Spek, *J. Appl. Crystallogr.*, 2008, **41**, 96–103.

7.2 *Synlett* **2025**, *36*, 1569-1573.

2,8-Dihalogenated Diazocines: Versatile Reactants for Functionalized Photoswitches

Maximilian J. Notheis◊
Vigan Sahiti◊
Vivienne Prangenberg
Johannes S. Kruse
Larissa K. S. von Krbek*

Kekulé-Institut für Organische Chemie and Biochemie, Rheinische Friedrich-Wilhelms-Universität Bonn, Gerhard-Domagk-Str. 1, 53121 Bonn, Germany
larissa.vonkrbek@uni-bonn.de

◊ These authors contributed equally

Published as part of the Cluster Supramolecular Catalysis and Molecular Switches

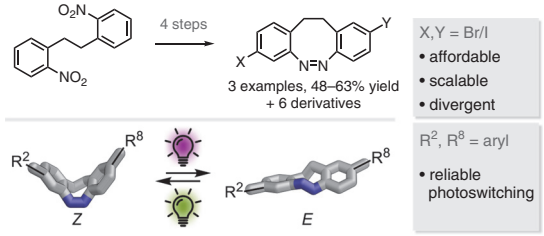

Received: 25.02.2025
Accepted after revision: 21.03.2025
Published online: 26.03.2025 (Accepted Manuscript), 12.05.2025 (Version of Record)
DOI: 10.1055/a-2567-1399; Art ID: ST-2025-02-0095-L

Crowd-Reviewed

Abstract Diazocine photoswitches possess distinctive structural characteristics and remarkable photochemical properties, leading to their growing application in photopharmacology and smart materials. We report the synthesis of 2,8-pseudo-*para*-substituted diazocines with two bromo, two iodo, or a combination of both substituents, achieving effective scalability. Besides demonstrating good reactivity in Suzuki cross-coupling reactions, the substituted diazocines predominantly retain their good photochemical properties, rendering them valuable components for said applications.

Key words photoswitches, diazocines, cross-coupling, gram-scale synthesis, photophysical properties

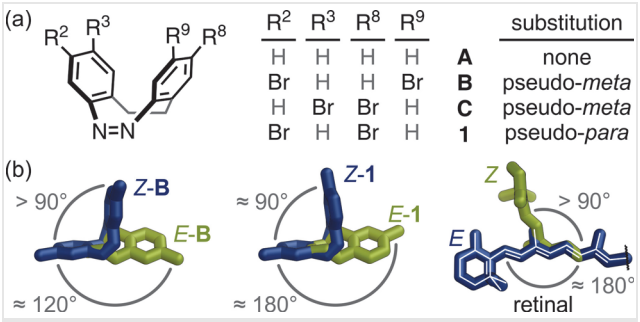

Figure 1 (a) Reported examples of pseudo-*meta*-dibromo diazocines (**B** and **C**)[2,6] and our pseudo-*para*-dibromo diazocine **1**. (b) A structural comparison of the *E*- and *Z*-isomers of **B**, **1**, and retinal, respectively, illustrating the unique near-180° angle between the two substituents in *E*-**1** [thermodynamically stable isomers: blue; metastable isomers: green. GFN2-xTB[13] structures (diazocines: Supplementary Information, Section S8) and crystal structures[14,15] (retinal)]

Ethylene-bridged azobenzene derivatives, termed diazocines, exhibit remarkable photoconversion between the thermodynamically stable U-shaped *Z*-isomer and the pseudo-planar metastable *E*-isomer (Figure 1), achieving photostationary states up to 92% (*E*),[1] and excellent quantum yields ranging from 70 to 90%.[2] The distinctive features of diazocines, combined with their ability to undergo visible-light photoswitching, have sparked significant interest in potential applications such as photodynamic therapy,[3–6] molecular imaging,[7] optical data storage,[8] and photoresponsive polymers.[7–12]

A diverse range of potential applications calls for various diazocine substitution patterns focusing on their ability to participate in efficient late-stage functionalizations, for example, in cross-coupling reactions.[2,4] Pseudo-*meta* substitutions in the 2,9- and 3,8-positions are the most common substitution patterns in diazocines (Figure 1a, **B** and **C**).[3,7–9,12] Conversely, pseudo-*para* substitution at the 2,8-positions of diazocines (**1**) remains uncommon, primarily because of synthetic difficulties arising from the asymmetric substitution pattern. This is despite a significantly greater change in distance and angle between the two substituents during photoisomerization (from 90° to 180°) compared with their pseudo-*meta* analogues (from 90° to 120°; Figure 1b), which is typically advantageous for many applications of photoswitches. This considerable change in the angle of the substituents is akin to the structural differences between *E*- and *Z*-retinal, which Nature employs in rhodopsin to efficiently convert light into a chemical signal in the eye (Figure 1b; right). For the employment of diazocines in various cross-coupling reactions, introducing halide substituents, preferentially bromides and iodides, is essential. However, this remains a challenge for 2,8-pseudo-*para*-substituted diazocines.[2,4]

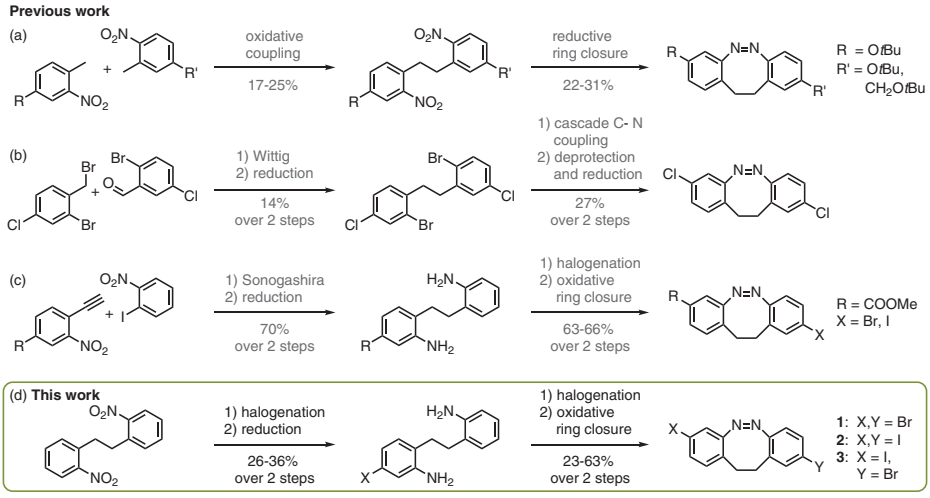

Scheme 1 Previous syntheses of 2,8-disubstituted diazocines by (a) Herges and co-workers,[3] (b) Staubitz and co-workers,[18] and (c) Trauner and co-workers.[2] (d) Our approach.

Several 2,8-pseudo-*para*-substituted diazocines have been synthesized from asymmetrically substituted ethylene-bridged precursors by a ring-closing step that involves reducing dinitro derivatives,[3,16] the oxidation of dianiline compounds,[2,17] or a cross-coupling strategy involving a diiodide precursor[18] [Scheme 1; see also the Supporting Information (SI), Section S7]. This asymmetric ethylene-bridged precursor had previously been obtained by three different strategies. The first strategy involved statistical coupling of two nitrotoluene derivatives to form an isomeric mixture of the corresponding 2,2′-dinitrodibenzyl derivative,[3] separation of which was nontrivial, particularly when halide substituents were involved. The diazocine was formed through reductive ring closure. In the second strategy, a Wittig reaction was followed by double-bond reduction and a bromine-to-iodine halide exchange to permit diazocine formation through a cross-coupling strategy.[18] Because halide substituents are essential for forming the diazocine, this approach cannot yield diazocines with bromide or iodide substituents. Thirdly, a Sonogashira cross-coupling reaction followed by the reduction of the triple bond with hydrogen and Pd on charcoal gave a monosubstituted asymmetric precursor. A second substituent was selectively introduced onto the ethylene-bridged dianiline precursor, which subsequently underwent oxidative ring closure to yield the diazocine.[2] The initial substituent had to remain unaffected by the reduction conditions, which ruled out iodo and bromo substituents. Given the challenges posed by these synthetic routes for bromo and iodo substituents, alternative pathways needed to be explored for 2,8-pseudo-*para*-halide-substituted diazocines.

Here, we report the synthesis of 2,8-pseudo-*para*-substituted diazocines with two bromo, two iodo, or a combination of the two substituents (**1**, **2**, and **3**, respectively) by harnessing the different regioselectivities of electron-deficient 2,2′-dinitrodibenzyl and electron-rich 2,2′-diaminodibenzyl toward aromatic halogenations (Scheme 2). Subsequently, we demonstrated the ability of diiodo diazocine **2** to undergo Suzuki cross-coupling reactions, introducing a diverse range of aryl substituents with various electronic properties (ranging from electron-rich to electron-deficient) onto the diazocine scaffold. The bromo iodo diazocine **3** was successfully used to sequentially introduce two distinct substituents featuring opposing electronic characteristics: one electron-rich and the other electron-deficient. The photophysical properties of all the diazocine derivatives were examined.

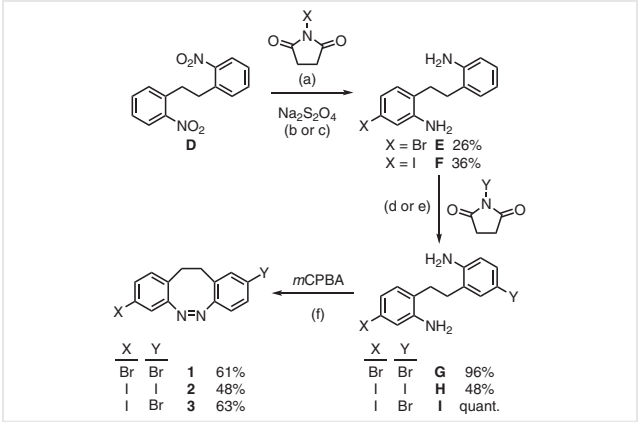

Scheme 2 Synthesis of 2,8-pseudo-*para*-halogenated diazocines **1**, **2**, and **3** from commercially available 2,2′-dinitrodibenzyl (**D**). *Reaction conditions*: (a) NBS or NIS (1.1 equiv), concd H_2SO_4, r.t., 1 d or 1 h, **D** (1.84 or 40.0 mmol, respectively); (b) $Na_2S_2O_4$ (8 equiv), 1:1 (v/v) 1,4-dioxane–water, 120 °C, 3 h; (c) $Na_2S_2O_4$ (24 equiv), K_2CO_3 (30 equiv), paraquat (10 mol%), 1:1 (v/v) CH_2Cl_2–water, 40 °C, 4 d; (d) NBS (1.0 equiv), 1:1 (v/v) CH_2Cl_2, –78 °C, 1 h, **E** (0.12 mmol); (e) NIS (1.0 equiv), 9:1 (v/v) CH_2Cl_2–HOAc, r.t., 2 h, **F** (2.61 mmol); (f) *m*CPBA (2.0 equiv, slow addition), 3:1 (v/v) CH_2Cl_2–HOAc, r.t., 1 d, 0.24–11.2 mmol.

2,8-Pseudo-*para*-halide-substituted diazocines **1**, **2**, and **3** were each synthesized in four steps from commercially available 1,2-bis(2-nitrophenyl)ethane (**D**; Scheme 2). Due to the almost complete electronic decoupling of the two nitrophenyl rings, a selective halogenation of just one of the rings is not possible. Consequently, **D** underwent halogenation with one equivalent of the appropriate *N*-halosuccinimide (NBS or NIS, respectively) in a statistical reaction. This process gave a mixture of nonhalogenated, monohalogenated, and dihalogenated 1,2-bis(2-nitrophenyl)ethanes in approximately a 1:2:1 ratio, which limited the expected yield to a maximum of around 50%. ^{1}H NMR spectroscopy showed that 52% of the desired isomer **S8** was formed by using NIS. In contrast, the use of NBS resulted in a lower 34% yield of the desired isomer **S1**, because single bromination occurred in both the desired 4-position and the undesired 6-position (SI; Section S3.1). At this stage, separating the isomeric mixture of halogenated dinitro compounds was complex, so it was directly reduced by using sodium dithionite, achieving moderate yields over the two steps.

The reduction conditions varied for the monohalogenated 1,2-bis(2-aminophenyl)ethanes **E** and **F**. Using a 1,4-dioxane–water solvent mixture, sodium dithionite reduction provided good yields of the monobrominated dianiline **E**, achieving a yield of 76% based on the ^{1}H NMR yield of its nitro counterpart **S1**. In contrast, monoiodinated dianiline **F** only resulted in a yield of 10% (based on the ^{1}H NMR yield of **S8**; SI, Sections S2.2). We therefore carried out the sodium dithionite reduction of monoiodinated **F** in a biphasic dichloromethane–water mixture using paraquat as an electron-phase-transfer catalyst, achieving a 93% yield (SI, Section S3.2). Isolating dianilines **E** and **F** from their isomers posed challenges; however, their amino groups exhibit increased affinity for silica, aiding this process. Whereas manual column chromatography for purification remained difficult, employing an automated medium-pressure liquid chromatography system gave fast and highly reproducible results (SI, Section S5).

Once the monohalogenated dianilines **E** and **F** had been obtained, they were subjected to a second halogenation step using NBS or NIS. This step resulted in selective halogenation at the *para*-position relative to the amino group on the less substituted aromatic ring, producing good to excellent yields of the dihalogenated dianilines **G**, **H**, and **I** (akin to the method used by Trauner and co-workers)[2] (SI, Sections S2.3–S2.5). In this second halogenation step, the selectivities for NBS and NIS were reversed compared with the first halogenation step. The greater reactivity of NBS facilitated near-quantitative formation of **G** and **I** at –78 °C. In contrast, the less reactive NIS required acid activation at room temperature for adequate conversion, which notably diminished the selectivity toward **H** to 53%. Oxidative ring closure using *meta*-chloroperoxybenzoic acid[2] (*m*CPBA) of dianilines **G**, **H**, and **I** afforded the corresponding 2,8-pseudo-*para*-halogenated diazocines **1**, **2**, and **3** in good yields.

Our synthetic approach is readily scalable, as was demonstrated by a gram-scale synthesis of the bromo iodo diazocine **3** (SI, Section S4). Although scaling up the halogenation and oxidation steps was straightforward, the biphasic reduction exhibited lower yields at larger scales (93% at 0.4 mmol, 36% at 8 mmol, 12% at 60 mmol). We consider this decreased yield in the initial synthetic step acceptable because of the cheap and easily accessible reagents that are used.

2,8-Pseudo-*para*-halogenated diazocines **1**, **2**, and **3** are excellent platforms for potential functionalization by, for example, C–C,[19–22] C–N,[2,23] or C–S[24] cross-coupling reactions. To demonstrate the exceptional ease with which diazocines **1**, **2**, and **3** can be functionalized through cross-coupling reactions, we subjected diiodo diazocine **2** to Suzuki cross-coupling reactions with various arylboronic acid pinacol esters, thereby incorporating electron-rich or electron-deficient substituents onto the diazocine framework (Scheme 3a). Diazocines **4**–**7**, which incorporate two 3,5-bis(trifluoromethyl)phenyl, two phenyl, two tolyl, and two 3,5-dimethoxyphenyl substituents, respectively, were obtained in moderate to good yields. Crucially, the bromo iodo diazocine **3** permits the highly selective sequential introduction of two different substituents onto the diazocine scaffold, yielding the asymmetrically substituted diazocine **9** (Scheme 3b), which features both an electron-rich and an electron-deficient substituent on one photoswitch.

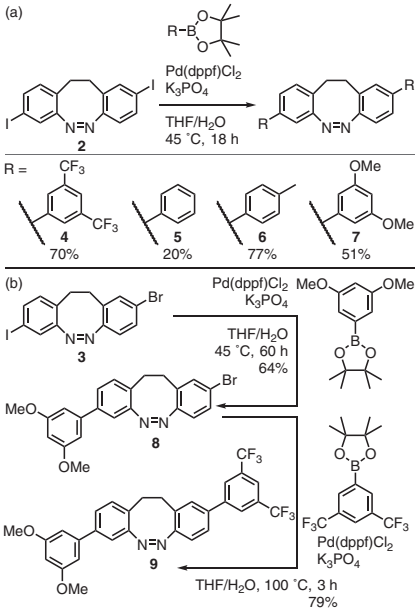

Scheme 3 (a) A range of 2,8-pseudo-*para* aryl-substituted diazocines can be obtained from diiodo diazocine **2** through Suzuki cross-coupling reactions. (b) The substituents vary from electron-rich to electron-deficient (left to right). Bromo iodo diazocine **3** permits the selective introduction of two distinct substituents, for example, one electron-rich and one electron-deficient substituent (**9**).

$Pd(dppf)Cl_2$ served as a catalyst for all the cross-coupling reactions, as it demonstrated the highest selectivity in producing the brominated (3,5-dimethoxy)phenyldiazocine **8** at 45 °C (SI, Section S3.3).

The photochemical and photophysical properties of diazocines **1**–**9** were investigated by UV-vis spectroscopy [thermal half-lives ($\tau_{½}$)] and ^{1}H NMR spectroscopy [photostationary states (PSS)] in dichloromethane (Table 1). *Z*→*E* and *E*→*Z* isomerizations were achieved by irradiating the respective n–π* bands [$\lambda_{max}(Z) \approx 400$ nm; $\lambda_{max}(E) \approx 490$ nm]. Illuminating diazocines **1**–**9** with 385 nm light for four to five minutes at NMR concentrations induced *Z*→*E* conversion, resulting in photostationary states of between 63 and 77%. *E*→*Z* isomerization occurred quantitatively under 505 nm light irradiation for one to two minutes or through thermal relaxation, with thermal half-lives ($\tau_{½}$) of between 1.4 and 6.1 hours (3.5 h on average). These values are notably lower than those of parent diazocine **A** ($\tau_{½}$ = 8.0 h), a frequent finding for disubstituted diazocines.[2] The photostationary states of the substituted diazocines varied from 63 to 77%. Dibromo, diiodo, and bromo iodo diazocines **1**, **2**, and **3** showed photostationary states that were as much as 14% lower than that of the parent diazocine **A**. Diazocines **4**–**9** interestingly showed a minor influence of the electron-rich or electron-deficient nature of their substituents on the photostationary states depending on their electronic conjugation with the diazocine phenyl groups. The most significant observed decrease in the photostationary state (14%) was seen with asymmetrically substituted diazocine **9** (compared to **4**), which contained both an electron-deficient and an electron-rich substituent. Although this decline is not negligible, previous observations[2] indicated a 48% reduction in photostationary states when moving from two electron-deficient substituents to a pairing of one electron-rich and one electron-deficient substituent. Thus, the electronic characteristics of the phenyl substituents have a noticeable, albeit relatively small, effect on the thermal half-lives and photostationary states of the diazocines.

We believe that the torsion between the diazocine phenyls and the phenyl substituents interferes with the electronic conjugation between the electron-withdrawing or -donating groups and the azo-group thereby minimizing the impact of these substituents on the photophysical properties. This is particularly clear when comparing the excellent n–π* band separation in diazocines **1**, **4**, and **7** with that in the parent system **A** (Figure 2), which shows minimal sensitivity to variations in the substituents. Therefore, the biphenyl connection presents a viable alternative for introducing methylene or ethylene groups[9,25] to achieve electronic decoupling between diazocines and their substituents.

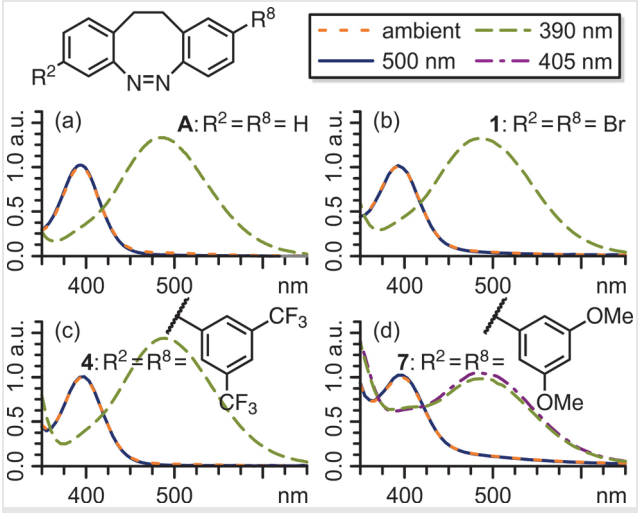

Figure 2 Normalized UV-vis absorption spectra (CH_2Cl_2, 0.8–1.6 mM, 298 K) of diazocines (a) **A**, (b) **1**, (c) **4**, and (d) **7** under ambient light (orange) and in their respective PSS after 390 nm and 500 nm light irradiation (blue and green, respectively; 405 nm for **7**, purple).

Table 1 Photostationary States (PSS at 385 and 505 nm, 298 K), Absorption Maxima (λ_{max}), and Half-Lives ($\tau_{½}$; 298 K) as Determined by ^{1}H NMR (PSS) and UV-vis Spectroscopy (λ_{max}, $\tau_{½}$) in CH_2Cl_2

Molecule	PSS_{385} (% *E*)	PSS_{505} (% *Z*)	$\lambda_{max}(Z)$ (nm)	$\lambda_{max}(E)$ (nm)	$\tau_{½}$ (298 K) (h)
A	87	99	401	490	8.0
1	77	98	400	485	3.5
2	75	>99	400	485	3.2
3	76	>99	400	485	3.7
4	73	97	405	490	4.4
5	73	>99	405	490	3.7
6	66	97	405	490	3.7
7	67	99	405	490	1.4
8	72	>99	400	485	6.1
9	63	98	405	490	2.1

In conclusion, nine asymmetrically pseudo-*para*-substituted diazocines **1**–**9** have been synthesized and characterized. The synthesis of dihalogenated diazocines **1**–**3** was achieved in four simple steps that use affordable readily available reagents, and can be scaled up to a minimum of 40 mmol. Various aryl substituents were introduced onto diiodo diazocine **2** to give diazocines **4**–**7**, showcasing its effective reactivity in cross-coupling reactions. Asymmetric substitution to give diazocines **8** and **9** was selectively accomplished by using the bromo iodo diazocine **3**. Although electronic conjugation exists between the aryl substituents and the diazocine cores, the influence of these substituents' electron-donating or electron-withdrawing characteristics on the photophysical properties of the photoswitches was minimal. The significant structural change that occurs during *Z*→*E* isomerization, along with a decreased reliance on substituent effects for photophysical properties, their

ease of synthesis, and their extensive potential for functionalisation through C–X coupling reactions make dihalogenated diazocines **1**–**3** important future building blocks for photoresponsive polymers used in smart materials, photodynamic therapy, molecular imaging, and optical data storage.

Conflict of Interest

The authors declare no conflict of interest.

Author contributions

M.J.N. and L.K.S.v.K. conceptualized the project and all authors were involved in developing the details. M.J.N., V.S., V.P., and J.S.K synthesized and investigated the compounds. Formal analysis was performed by M.J.N. and V.S. L.K.S.v.K. visualized the data for the manuscript and wrote the original draft. All authors contributed to reviewing and editing the final draft.

Funding Information

This work was supported by the Fonds der Chemischen Industrie (Liebig Fellowship) and the German Research Foundation (DFG; Emmy Noether Programme, 446317932). M.J.N. and V.S. thank the FCI and Avicenna-Studienwerk, respectively, for their Ph.D. scholarships.

Supporting Information

Supporting information for this article is available online at https://doi.org/10.1055/a-2567-1399.

References and Notes

(1) Siewertsen, R.; Neumann, H.; Buchheim-Stehn, B.; Herges, R.; Näther, C.; Renth, F.; Temps, F. *J. Am. Chem. Soc.* **2009**, *131*, 15594.
(2) Maier, M. S.; Hüll, K.; Reynders, M.; Matsuura, B. S.; Leippe, P.; Ko, T.; Schäffer, L.; Trauner, D. *J. Am. Chem. Soc.* **2019**, *141*, 17295.
(3) Ewert, J.; Heintze, L.; Jordà-Redondo, M.; von Glasenapp, J.-S.; Nonell, S.; Bucher, G.; Peifer, C.; Herges, R. *J. Am. Chem. Soc.* **2022**, *144*, 15059.
(4) Heintze, L.; Schmidt, D.; Rodat, T.; Witt, L.; Ewert, J.; Kriegs, M.; Herges, R.; Peifer, C. *Int. J. Mol. Sci.* **2020**, *21*, 8961.
(5) López-Cano, M.; Scortichini, M.; Tosh, D. K.; Salmaso, V.; Ko, T.; Salort, G.; Filgaira, I.; Soler, C.; Trauner, D.; Hernando, J.; Jacobson, K. A.; Ciruela, F. *J. Am. Chem. Soc.* **2025**, *147*, 874.
(6) Cabré, G.; Garrido-Charles, A.; González-Lafont, A.; Moormann, W.; Langbehn, D.; Egea, D.; Lluch, J. M.; Herges, R.; Alibés, R.; Busqué, F.; Gorostiza, P.; Hernando, J. *Org. Lett.* **2019**, *21*, 3780.
(7) Li, S.; Han, G.; Zhang, W. *Macromolecules* **2018**, *51*, 4290.
(8) Burk, M. H.; Langbehn, D.; Hernández Rodríguez, G.; Reichstein, W.; Drewes, J.; Schröder, S.; Rehders, S.; Strunskus, T.; Herges, R.; Faupel, F. *ACS Appl. Polym. Mater.* **2021**, *3*, 1445.
(9) Li, S.; Bamberg, K.; Lu, Y.; Sönnichsen, F. D.; Staubitz, A. *Polymers* **2023**, *15*, 1306.
(10) Burk, M. H.; Schröder, S.; Moormann, W.; Langbehn, D.; Strunskus, T.; Rehders, S.; Herges, R.; Faupel, F. *Macromolecules* **2020**, *53*, 1164.
(11) Wang, Y.; Yuan, Y.; Zhang, S.; Chen, L.; Chen, Y. *Chin. J. Chem.* **2024**, *42*, 3278.
(12) Li, S.; Colaco, R.; Staubitz, A. *ACS Appl. Polym. Mater.* **2022**, *4*, 6825.
(13) Bannwarth, C.; Ehlert, S.; Grimme, S. *J. Chem. Theory Comput.* **2019**, *15*, 1652.
(14) Okada, T.; Sugihara, M.; Bondar, A.-N.; Elstner, M.; Entel, P.; Buss, V. *J. Mol. Biol.* **2004**, *342*, 571.
(15) Choe, H.-W.; Kim, Y. J.; Park, J. H.; Morizumi, T.; Pai, E. F.; Krauß, N.; Hofmann, K. P.; Scheerer, P.; Ernst, O. P. *Nature* **2011**, *471*, 651.
(16) Löw, R.; Rusch, T.; Röhricht, F.; Magnussen, O.; Herges, R. *Beilstein J. Org. Chem.* **2019**, *15*, 1485.
(17) Bastien, G.; Severa, L.; Škuta, M.; Santos Hurtado, C.; Rybáček, J.; Šolínová, V.; Císařová, I.; Kašička, V.; Kaleta, J. *Chem. Eur. J.* **2024**, *30*, e202401889.
(18) Li, S.; Eleya, N.; Staubitz, A. *Org. Lett.* **2020**, *22*, 1624.
(19) Hugenbusch, D.; Lehr, M.; von Glasenapp, J.-S.; McConnell, A. J.; Herges, R. *Angew. Chem. Int. Ed.* **2023**, *62*, e202212571.
(20) Zheng, T.; Tan, L.; Lee, M.; Li, Y.; Sim, E.; Lee, M. *J. Am. Chem. Soc.* **2024**, *146*, 25451.
(21) Schultzke, S.; Walther, M.; Staubitz, A. *Molecules* **2021**, *26*, 3916.
(22) Lee, H.; Tessarolo, J.; Langbehn, D.; Baksi, A.; Herges, R.; Clever, G. H. *J. Am. Chem. Soc.* **2022**, *144*, 3099.
(23) Deng, J.; Wu, X.; Guo, G.; Zhao, X.; Yu, Z. *Org. Biomol. Chem.* **2020**, *18*, 5602.
(24) Berry, J.; Lindhorst, T. K.; Despras, G. *Chem. Eur. J.* **2022**, *28*, e202200354.
(25) Moormann, W.; Langbehn, D.; Herges, R. *Beilstein J. Org. Chem.* **2019**, *15*, 727.
(26) **2-Bromo-8-iodo-11,12-dihydrodibenzo[*c*,*g*][1,2]diazocine (3)**
A solution of *m*CPBA (75%, 2.58 g, 11.22 mmol, 2.00 equiv) in glacial HOAc (~0.6 M) was added to a solution of bromo iodo dianiline **I** (2.34 g, 5.61 mmol, 1.00 equiv) in 1:3 glacial HOAc–CH_2Cl_2 (60 mL) over 24 hours using a syringe pump. The mixture was then stirred for 18 h at r.t., then neutralized with sat. aq $NaHCO_3$. The organic layer was separated, washed with sat. aq $NaHCO_3$ (25 mL) and sat. aq NaCl (25 mL), dried ($MgSO_4$), and concentrated by rotary evaporation. The residue was purified by column chromatography [silica gel, cyclohexane–EtOAc (100:0 to 70:30 over 15 column volumes)] to give a yellow solid; yield: 1.47 g (63%, 3.56 mmol). R_f = 0.56 (cyclohexane–EtOAc, 8:2).
^{1}H NMR (500 MHz, CD_2Cl_2): δ = 2.64–2.96 (m, 4 H, H-7, H-8), 6.74 (d, *J* = 8.3 Hz, 1 H, H-11), 6.78 (d, *J* = 8.1 Hz, 1 H, H-5), 7.16 (d, *J* = 1.8, 1 H, H-2), 7.18 (d, *J* = 2.1 Hz, 1 H, H-14), 7.31 (dd, *J* = 8.4 Hz, 2.1, 1 H, H-12), 7.39 (dd, *J* = 8.1, 1.8 Hz, 1 H, H-4). ^{13}C NMR (126 MHz, CD_2Cl_2): δ = 31.0 (C-7), 31.1 (C-8), 90.9 (C-3), 120.3 (C-13), 120.6 (C-11), 127.2 (C-2), 127.7 (C-6), 129.9 (C-12), 130.2 (C-9), 131.6 (C-15), 132.4 (C-14), 136.1 (C-4), 154.1 (C-10), 156.2 (C-1). HRMS (ESI$^+$ Orbitrap): *m*/*z* [M + H]$^+$ calcd for $C_{14}H_{15}BrIN_2$ = 412.9145; found: 412.9138.

Synlett

Accounts and Rapid Communications in Chemical Synthesis

Supporting Information
for DOI: 10.1055/a-2567-1399

Georg Thieme Verlag KG, Oswald-Hesse-Straße 50, 70469 Stuttgart, Germany

Thieme

Supporting Information

for

2,8-Dihalogenated diazocines: versatile reactants for functionalized photoswitches

Maximilian J. Notheis,[a,‡] Vigan Sahiti,[a,‡] Vivienne Prangenberg,[a] Johannes S. Kruse,[a] Larissa K. S. von Krbek[a,*]

[a] Kekulé-Institut für Organische Chemie and Biochemie, Rheinische Friedrich-Wilhelms-Universität Bonn, Gerhard-Domagk-Str. 1, 53121 Bonn, Germany.
E-mail: larissa.vonkrbek@uni-bonn.de.

‡ These authors contributed equally.

Content

S1. General procedures

Reagents and materials. Commercial solvents and reagents were obtained from the following suppliers and used without further purification unless specified otherwise: Sigma Aldrich, Alfa Aesar, abcr, Acros Organics, BLD-Pharm, Fluorochem, Merck, TCI, Carbolution, Thermo Fisher Scientific.

Schlenk techniques. All reactions using chemicals sensitive to air were carried out under argon using established Schlenk techniques. If chemicals were also sensitive to moisture, glassware was heat-dried prior to use.

Column chromatography. Column chromatography was carried out either using a puriFlash 5.020 (Interchim) flash chromatography machine with PuriFlash 15 µm Si HP (Interchim) flash cartridges or by hand using Silica gel ultra pure (Thermo scientific, 60 µm).

NMR spectroscopy. All NMR spectroscopic measurements were carried out using 300 MHz, 400 MHz, 500 MHz or 700 MHz spectrometers (Bruker Avance I 300, Bruker Avance I 400, Bruker Avance I 500, Bruker Avance III HD Prodigy 500, Bruker Avance III HD Ascend 700). ^{1}H and ^{13}C NMR spectra are referenced to the residual solvent peak (CD_2Cl_2: ^{1}H: 5.32 ppm, ^{13}C: 53.5 ppm). NMR signals are reported in terms of chemical shift (δ) in ppm, relative integral, multiplicity, coupling constants (in Hz) and assignment, in that order. The following abbreviations for multiplicity are used: s, singlet; d, doublet; t, triplet; qu, quartet; qn, quintet; m, multiplet; br, broad. Spectra were digitally processed (phase and baseline corrections, integration, peak analysis) using MestReNova 14.2.1 (Mestrelab). All processing operations were manually checked to ensure that the processed spectra accurately represented the raw data.

Mass spectrometry. Mass spectra were acquired using an Orbitrap XL (Thermo Fischer Scientific) and a MAT 95 XL (Thermo Finnigan).

UV-vis spectroscopy. UV-vis spectroscopy was carried out using a Cary 60 (Agilent) with a temperature-controlled sample holder and plotted using Spectragryph 8.0.[1]

Light sources. *In situ* illumination experiments (UV-vis) were carried out using Prizmatrix FC5-LED Multi channel fibre collimated LED sources.

Table S1. Light output of fibre coupled LEDs.

λ [nm]	**365**	**390**	**405**	**430**	**450**	**500**	**590**	**660**	**white**
Output power [mW] (1 m optical fibre)	170	220	260	160	440	165	230	140	74

Ex situ illumination (NMR) was carried out using portable self-built light sources incorporating commercial LED chips.

Table S2. Light output of other LEDs.

λ [nm]	**385**	**405**	**505**
Manufacturer	Nichia	Nichia	Nichia
Type	NVSU233B(T) – U385	NVSU233B(T) - U405	NCSE219BT-V1
Light output (as specified by manufacturer)	1.7 W	1.4 W	1.2 W

Geometry optimisation for 3D structure modelling. The three-dimensional representations of 2,9-, 3,8-, and 2,8-substituted diazocines were modelled and pre-optimized using Avogardo[2] (Version 1.2.0) on UFF[3] level before final geometry optimisations were performed on GFN2-xTB[4] level (Version 6.7.1pre) and the resulting structures visualized using PyMol[5] (Version 3.1.0a OpenSource).

S2. Synthetic procedures

S2.1. 2-(2-Aminophenethyl)-5-bromoaniline (**E**)

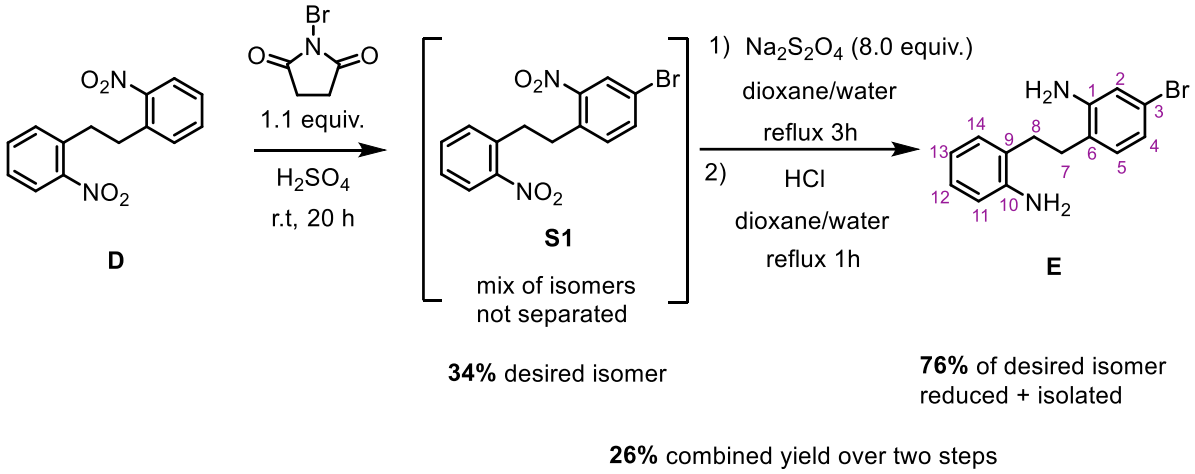

The halogenation was carried out following a modified procedure for the halogenation of electron-deficient aromatics[6] and the reduction following a modified procedure for the reduction of nitro aromatics using sodium dithionite as a reductant and paraquat dichloride as a phase transfer catalyst.[7]

1,2-Bis(2-nitrophenyl)ethane (**D**; 500mg, 1.84 mmol, 1.00 equiv.) was suspended in conc. sulfuric acid (95%, approx. 10 mL g^{-1}, 40 equiv.) and the suspension was sonicated for 2 minutes. Then, *N*-bromosuccinimide (NBS, 0.36 g, 2.02 mmol, 1.10 equiv.) was added portion-wise over 15 minutes, and the reaction mixture was stirred at room temperature for 20 hours. The mixture was poured into ice water (1 L) to precipitate the organics. The precipitate was filtered and washed thoroughly with water. The precipitate contained 34 mol% of desired product **S1** as well as other isomers (Figure S1; ratio determined by ^{1}H NMR). The solid was used without any further purification for the next step.

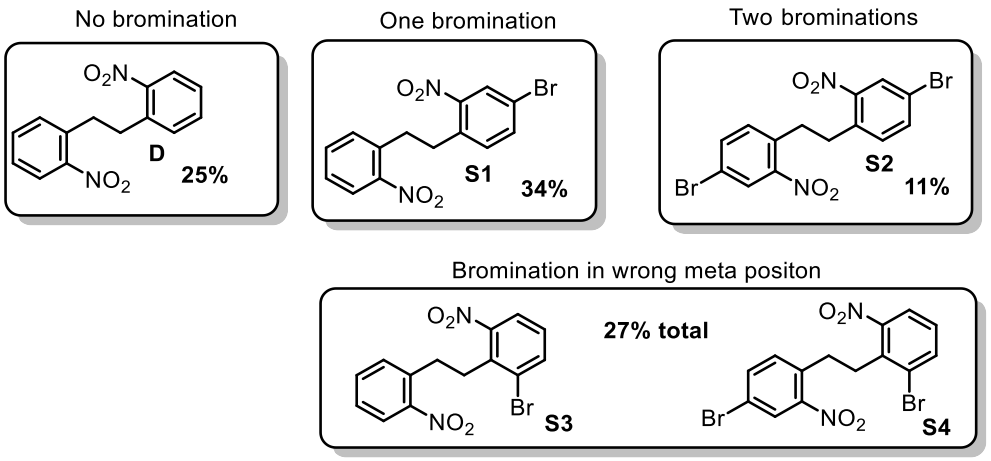

Figure S1. Different isomers obtained in the bromination and their different ratios as determined by ^{1}H NMR.

The second step was carried out using a product mixture from an unoptimized bromination procedure that contained less of the desired isomer **S1** (11% instead of 36%) as a sufficiently large amount of dibromo diazocin **1** had already been synthesized when the optimizations were done.

A mixture of brominated dinitro compounds (1.83 mmol, 1.00 equiv.) containing 11% of desired isomer **S1** (0.20 mmol) was dissolved in 50 mL dioxane and a solution of sodium dithionite (2.55 g, 14.7 mmol, 8.00 equiv.) in water (50 mL) was added. The mixture was refluxed for three hours and cooled to room temperature. Then, concentrated hydrochloric acid (5.0 mL) and water (5.0 mL) were added and the mixture was refluxed for another hour. The reaction mixture was poured into ice water (1 L) and the resulting mixture was brought to a basic pH by adding an excess of saturated aqueous sodium carbonate solution. The mixture was extracted with ethyl acetate (3 × 150 mL). The combined organic phases were washed with saturated aqueous sodium chloride solution (1 × 15 mL) and all volatiles were removed by rotary evaporation. The residue was subjected to column chromatography (silica gel, dichloromethane/(ethyl acetate + 5% triethylamine) 100:0 → 70:30 (v/v) over 10 column volumes), which afforded monobrominated dianiline **E** as a yellow oil (45 mg, 0.15 mmol). This corresponds to a 76% yield based on the content of the desired isomer in the isomer mixture.

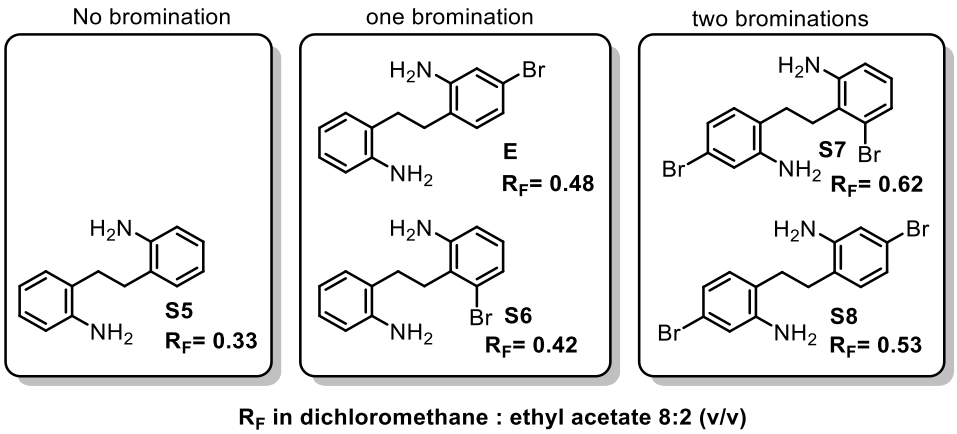

Figure S2. Different isomers produced by the reduction and their retention factors (silica, dichloromethane: ethyl acetate 8:2 (v/v)).

$C_{14}H_{11}BrN_2$ 291.19 g mol^{-1}

R_F value (cyclohexane/ethyl acetate 8:2 (v/v)) = 0.48.

^{1}H NMR (500 MHz, CD_2Cl_2, 298 K) δ [ppm] = 2.68 – 2.80 (m, 4H, H-7, H-8), 3.66 (s, 2H, NH_2), 3.73 (s, 2H, NH_2), 6.64 – 6.73 (m, 2H, H-11, H-13), 6.76 – 6.83 (m, 2H, H-2, H-4), 6.86 – 6.92 (m, 1H, H-5), 6.95 – 7.07 (m, 2H, H-14, H-12).

^{13}C NMR (126 MHz, CD_2Cl_2, 298 K) δ [ppm] = 30.6 (C-7), 31.0 (C-8), 116.1 (C-11), 118.3 (C-2), 119.2 (C-13), 120.6 (C-3), 121.6 (C-4), 125.5 (C-6), 126.3 (C-9), 127.7 (C-12), 129.9 (C-14), 131.4 (C-5), 144.9 (C-1), 146.6 (C-10).

HRMS (EI$^+$) m/z = 290.0411 ([M-H]$^{+\bullet}$, calcd 290.0413).

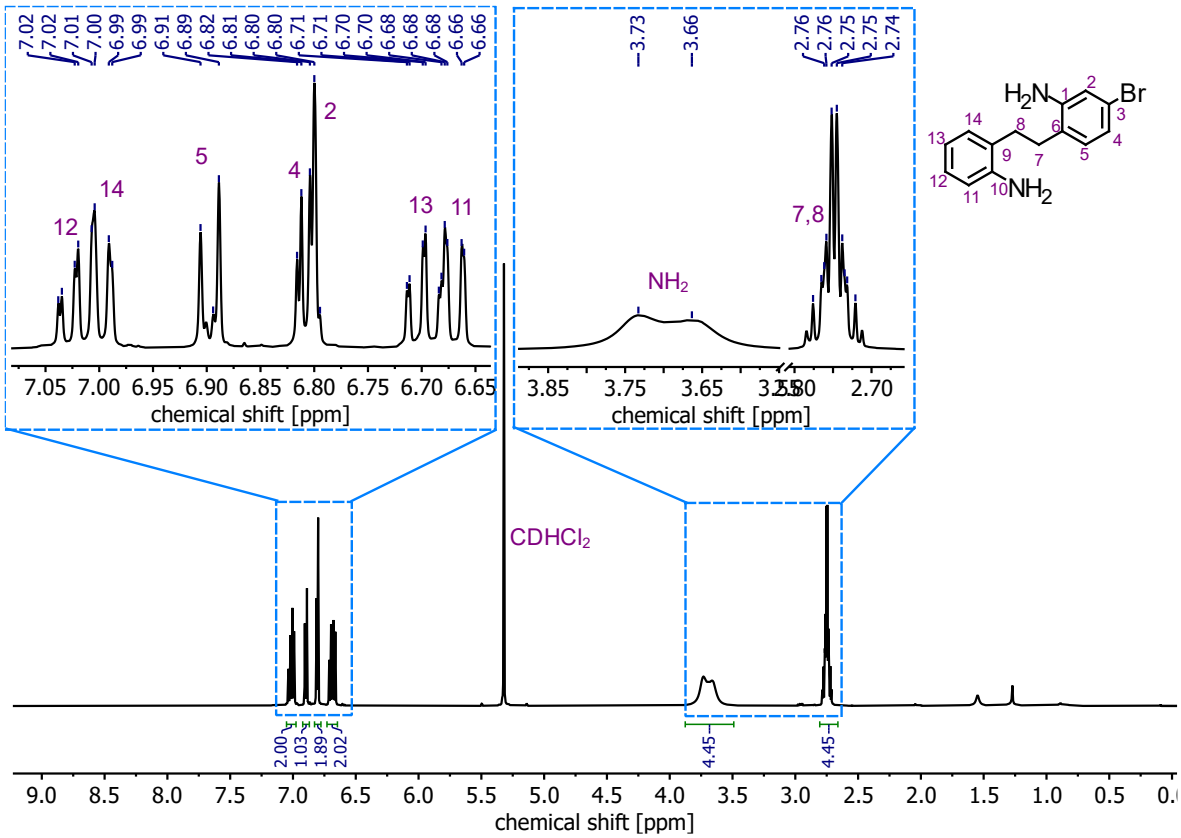

Figure S3. ^{1}H NMR (500 MHz, CD_2Cl_2, 298 K) of **E**.

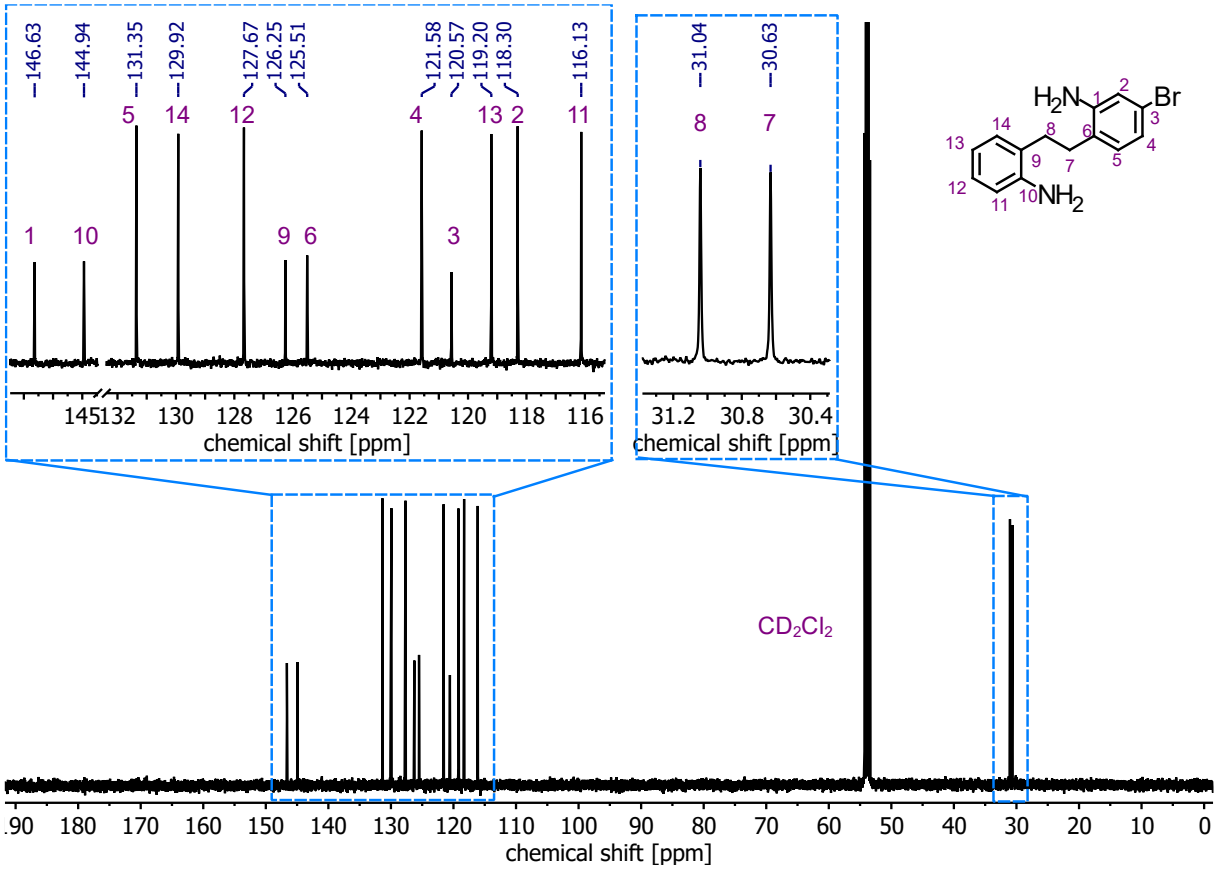

Figure S4. ^{13}C NMR (126 MHz, CD_2Cl_2, 298 K) of **E**.

S2.2. 2-(2-Aminophenethyl)-5-iodoaniline (**F**)

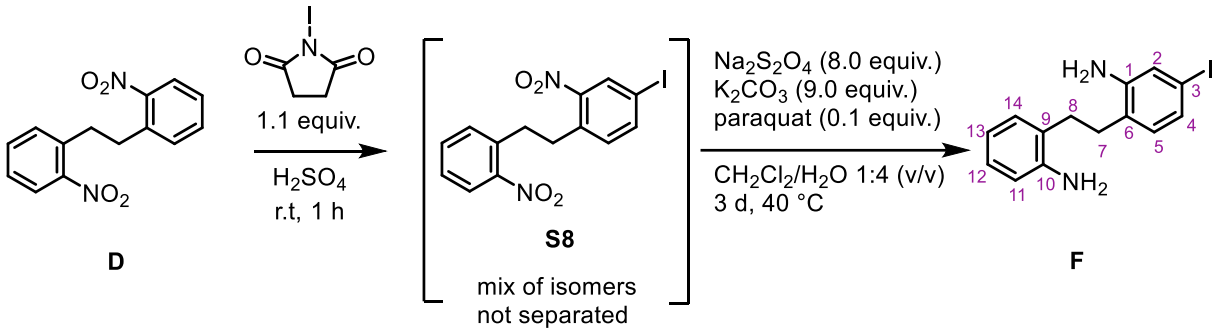

The halogenation was carried out following a procedure for the halogenation of electron-deficient aromatics[6] and the reduction following a modified procedure for the reduction of nitro aromatics using sodium dithionite as reductant and paraquat dichloride as a phase-transfer catalyst.[7]

1,2-Bis(2-nitrophenyl)ethane (**D**; 10.90 g, 40.0 mmol, 1.00 equiv.) was suspended in sulfuric acid (95%, approx. 10 mL g^{-1}, 50 equiv.). The suspension was sonicated for two minutes, then stirred at room temperature for 30 minutes. To the dark brown solution, *N*-iodosuccinimide (NIS) (9.90 g, 44.0 mmol, 1.10 equiv.) was added portion-wise over 12 minutes. After stirring the mixture at room temperature for 1 h, the now light brown suspension was poured on ice, and the remaining NIS was quenched by adding saturated aqueous sodium sulfite solution (200 mL). The precipitate was filtered off using a glass frit and the residue was washed thoroughly with water. The beige solid was suspended in acetone and sodium sulfite (approx. 50 mg) was added to the suspension to quench any traces of iodine, which got trapped within the organic material and were not quenched in the previous step. All volatiles were removed on a rotary evaporator to afford a mixture of different iodination products as a beige powder (16.0 g, "100%", containing 48% of desired isomer **S8**, Figure S5). This mixture was used without further purification in the next reaction step.

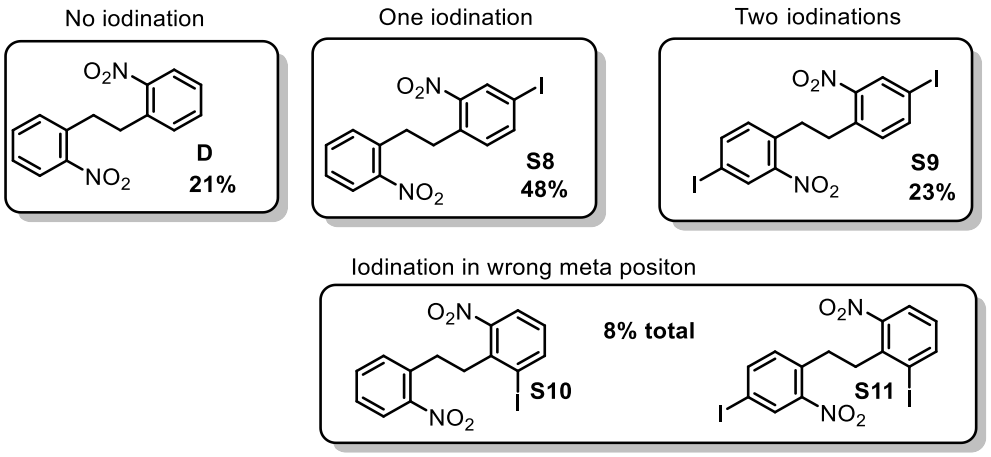

Figure S5. Different isomers obtained in the iodination and their different ratios as determined by ^{1}H NMR.

Under an argon atmosphere, a mixture of brominated dinitro compounds (3.00 g, 7.53 mmol, 1.00 equiv.) containing 49% of the desired isomer **S8** (3.69 mmol) was dissolved in dichloromethane (200 mL). A solution of sodium dithionite (10.49 g, 60.28 mmol, 8.00 equiv.) and K_2CO_3 (9.37 g, 67.81 mmol, 9.00 equiv.) in water (approx. 1 M, 150 mL), as well as *N*,*N*′-dimethyl-4,4′-bipyridinium dichloride (paraquat, 0.19 g, 0.75 mmol, 0.10 equiv.), were added. The addition of paraquat dichloride turned both phases a deep purple to deep blue colour. The biphasic mixture was refluxed until both phases were colourless (2-4 days). During this time, the organic phase gradually changed colour from blue to light green after 1 day, light yellow after 2 days, and orange after 3 days. The phases were separated, and the aqueous layer was extracted using dichloromethane (3 × 300 mL). The combined organic layers were dried over sodium sulfate and all volatiles were removed on a rotary evaporator. The residue was subjected to column chromatography (silica gel, dichloromethane/(ethyl acetate + 5% triethylamine) 100:0 → 80:20 (v/v) over 10 column volumes) to afford a mixture enriched with product **F** (Figure S6). A second chromatographic separation using the same method afforded the mono-iodinated dianiline **F** as a yellow oil (0.91 g, 2.69 mmol). This represents a yield of 75% based on the content of desired isomer **S8** and a combined yield of 36% over two steps.

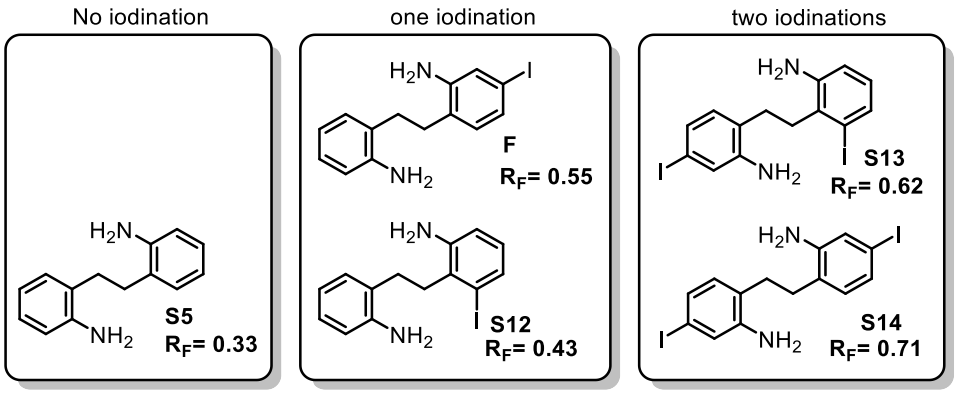

Figure S6. Different isomers produced by the reduction and their retention factors (silica, dichloromethane: ethyl acetate 8:2 (v/v)).

Table S3. Overview of yield vs. reaction scale for the synthesis of **F**.

	Small scale	**Medium scale**	**Large scale**
Starting material **D**	3 g, 8 mmol	11 g, 27 mmol	24 g, 60 mmol
Yield	36%	22%	12%

$C_{14}H_{15}IN_2$ 338.19 g mol^{-1}

R_F value (dichloromethane/ethyl acetate 8:2 (v/v) = 0.55

^{1}H NMR (499 MHz, CD_2Cl_2) δ [ppm] = 2.73 – 2.84 (m, 4H, H-7, H-8), 3.69 (s, 4H, NH_2), 6.72 (dd, *J*=7.8, 1.2, 1H, H-11), 6.76 (td, *J*=7.4, 1.3, 1H, H-13), 6.81 (d, *J*=7.8, 1H, H-5), 7.03 – 7.11 (m, 4H, H-2, H-4, H-12, H-14).

^{13}C NMR (126 MHz, CD_2Cl_2) δ [ppm] = 30.3 (C-8), 30.6 (C-7), 91.6 (C-3), 115.7 (C-11), 118.8 (C-13), 123.9 (C-2), 125.8 (C-6), 125.9 (C-9), 127.3 (C-4), 127.4 (C-12), 129.5 (C-14), 131.2 (C-5), 144.5 (C-10), 146.3 (C-1).

HRMS (ESI$^+$ Orbitrap): m/z = 339.0352 ([M+H]$^+$, calcd 339.0353).

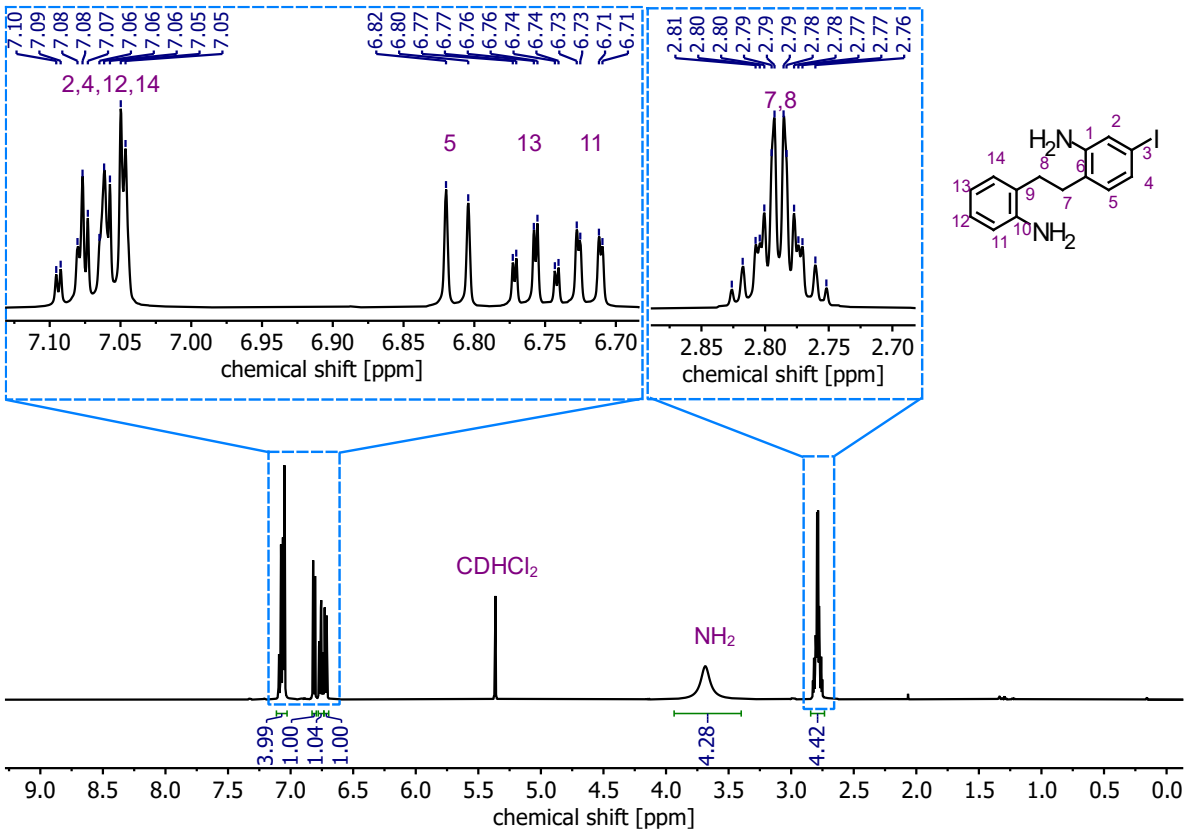

Figure S7. ^{1}H NMR (700 MHz, CD_2Cl_2, 298 K) of **F**.

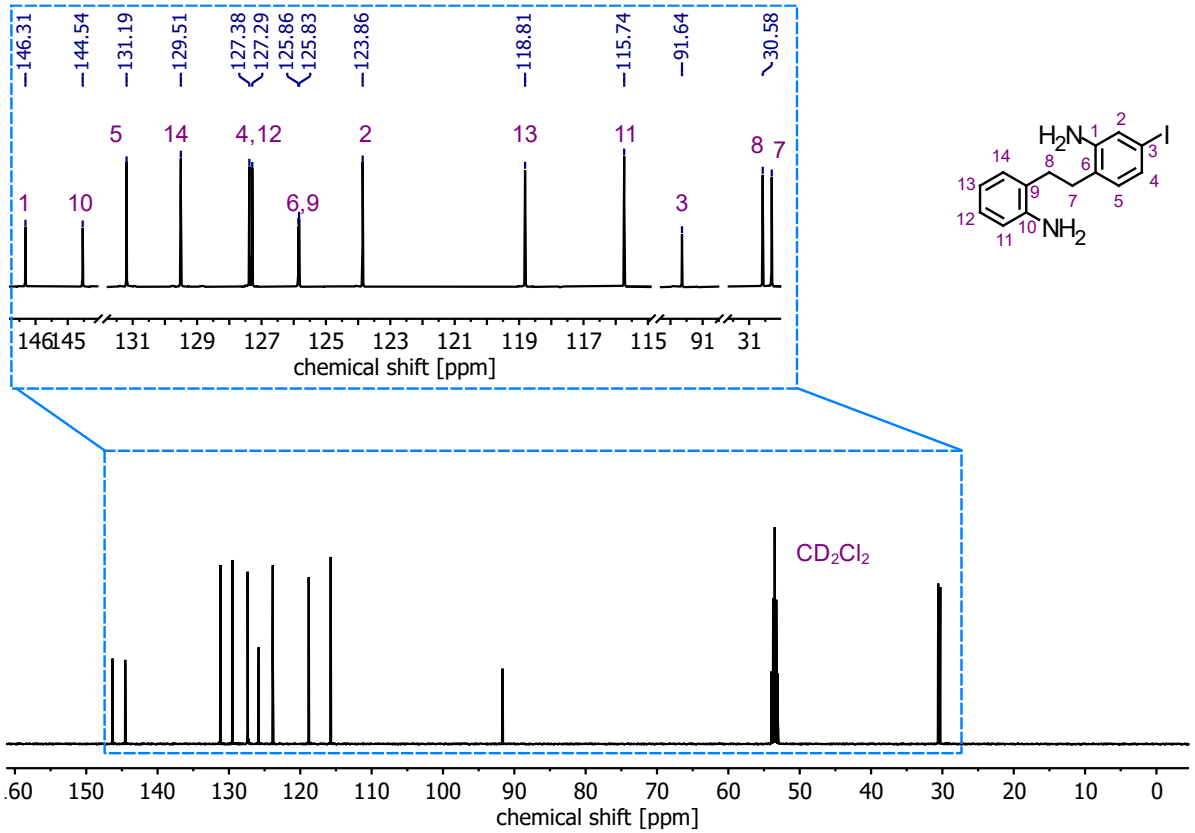

Figure S8. ^{13}C NMR (176 MHz, CD_2Cl_2, 298 K) of **F**.

S2.3. 2-(2-Amino-4-bromophenethyl)-4-bromoaniline (G)

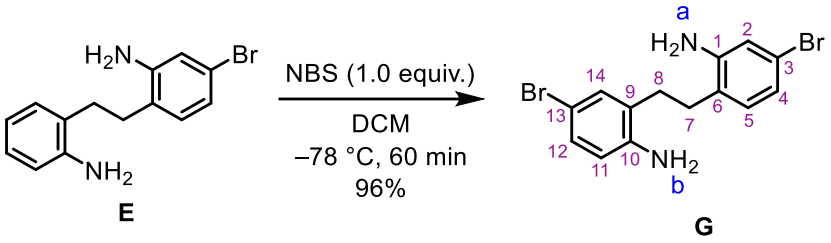

Bromo dianiline **E** (35 mg, 0.12 mmol, 1.00 equiv.) was dissolved in dichloromethane (approx. 25 mM, 2 mL) and cooled to −78°C under an argon atmosphere. A solution of NBS (21 mg, 0.12 mmol, 1.00 equiv.) in dichloromethane (approx. 10 mM, 5 mL) was added dropwise over 5 minutes. The cooling bath was removed, and the reaction mixture was stirred for another 60 minutes. All volatiles were removed using reduced pressure and the residue was subjected to column chromatography (silica gel, dichloromethane/(ethyl acetate +5% triethylamine) 100:0 → 70:30 (v/v) over 10 column volumes) to afford dibromo dianiline **G** as a brown oil (43 mg, 0.12 mmol, 96%).

$C_{14}H_{10}Br_2N_2$ g mol^{-1} 370.09 g/mol

R_F value (cyclohexane/ethyl acetate 8:2 (v/v)) = 0.48.

^{1}H NMR (500 MHz, CD_2Cl_2) δ [ppm] = 2.71 (s, 4H, H-7, H-8), 3.69 (s, 2H, NH_2-b), 3.78 (s, 2H, NH_2-a), 6.56 (d, J = 8.3 Hz, 1H, H-11), 6.79 – 6.83 (m, 2H, H-4, H-2), 6.87 (d, J = 8.0 Hz, 1H, H-5), 7.10 – 7.16 (m, 2H, H-12, H-14).

^{13}C NMR (126 MHz, CD_2Cl_2) δ [ppm] = 30.47 (C-8), 30.6 (C-7), 110.5 (C-13), 117.6 (C-11), 118.4 (C-4), 120.8 (C-3), 121.7 (C-2), 125.0 (C-6), 128.5 (C-9), 130.2 (C-12), 131.3 (C-5), 132.2 (C-14), 144.2 (C-10), 146.5 (C-1).

HRMS (EI$^+$) m/z = 367.9517 ([M-H]$^{+\bullet}$, calcd 367.9518).

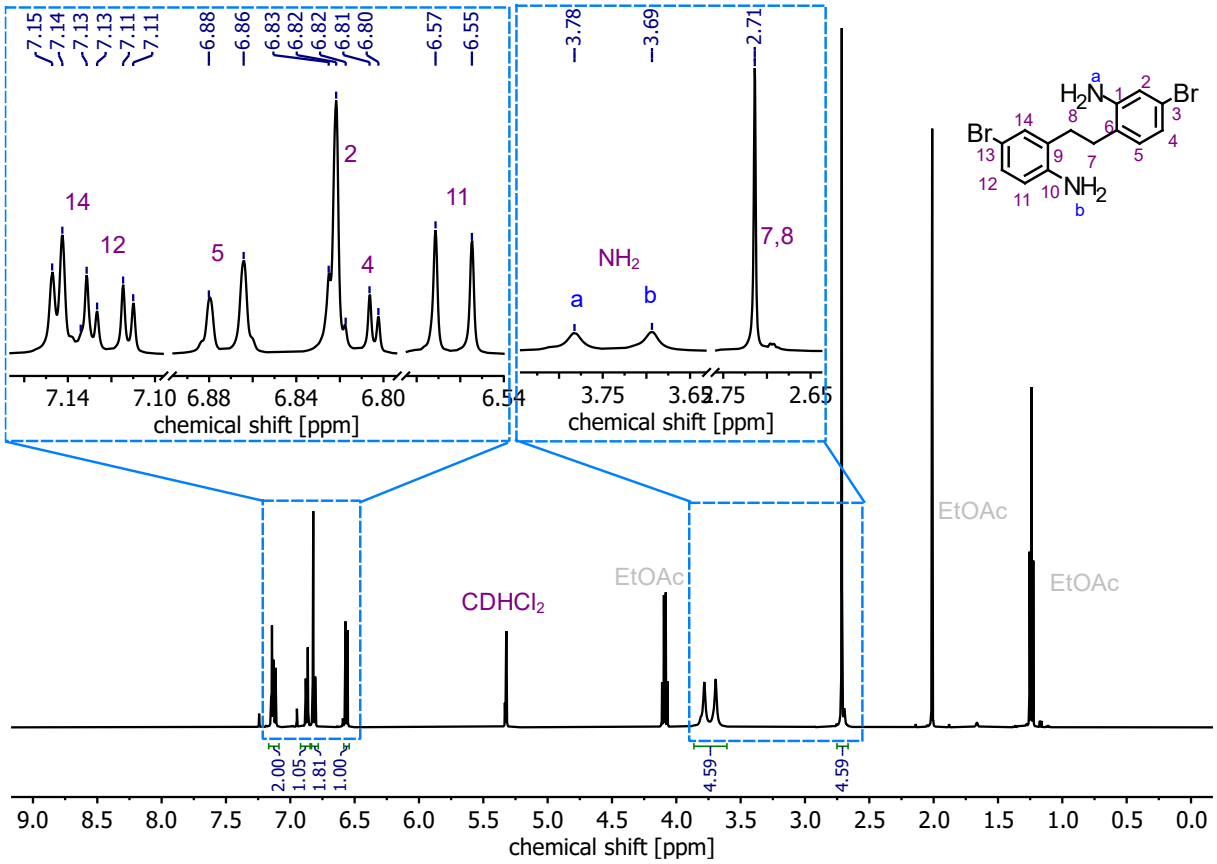

Figure S9. ^{1}H NMR (500 MHz, CD_2Cl_2, 298 K) of **G**.

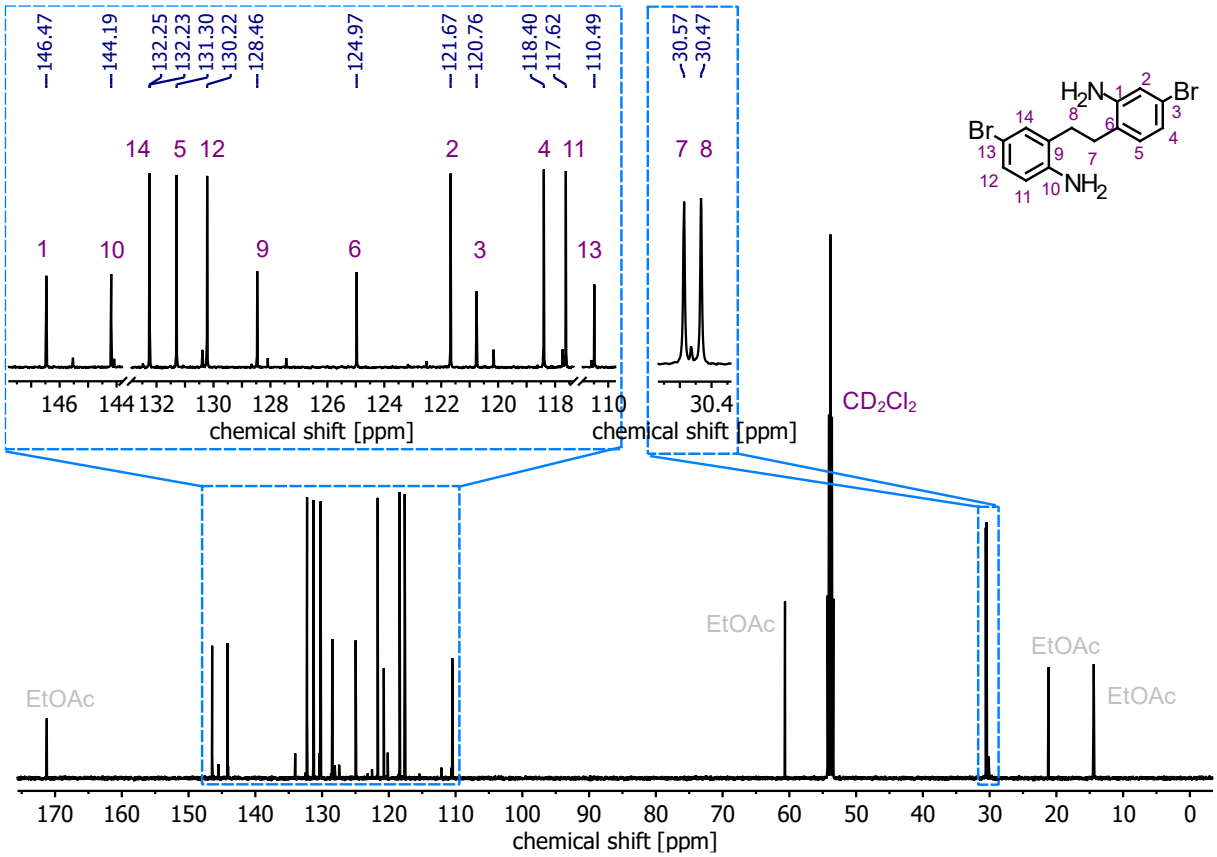

Figure S10. ^{13}C NMR (126 MHz, CD_2Cl_2, 298 K) of **G**.

S2.4. 2-(2-Amino-4-iodophenethyl)-4-iodoaniline (**H**)

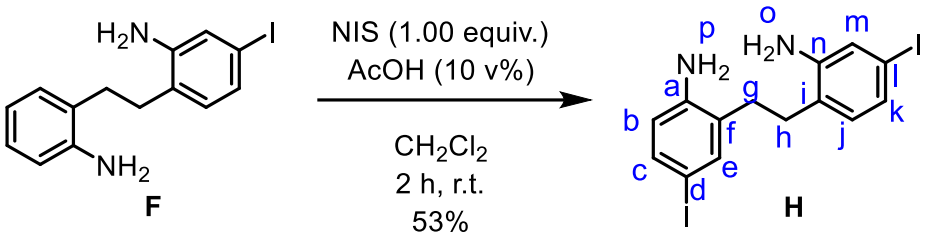

A solution of monoiodo dianiline **F** (882.3 mg, 2.61 mmol, 25 mM, 1.00 equiv.) in dichloromethane (105 mL) was acidified with glacial acetic acid (35 ml) and subsequently purged with argon. A violet-coloured solution of *N*-iodosuccinimide (NIS; 451.3 mg, 2.61 mmol, 1.00 equiv.) in dichloromethane (260 mL) was added dropwise to the substrate solution over the duration of 10 minutes and the was mixture stirred for 2 hours, during which it quickly turned dark orange. The solvent was removed under reduced pressure on a rotary evaporator and the crude product was subjected to column chromatography (silica gel, dichloromethane/(ethyl acetate + 5% triethylamine) 100:0 → 70:30 (v/v) over 10 column volumes) to afford diiodo dianiline **H** as a brown oil in 53% yield (556.8 mg, 120.0 mmol).

$C_{14}H_{14}I_2N_2$ 464.09 g mol^{-1}

R_F value (dichloromethane/ethyl acetate 4:1 (v/v) = 0.74

^{1}H NMR (700 MHz, CD_2Cl_2, 298 K): δ [ppm] = 2.69 (s, 4H, H-g,h), 2.79 (s, 4H, H-o,p), 6.46 (d, *J* = 8.3 Hz, 1H, H-b), 6.73 (d, *J* = 7.8 Hz, 1H, H-j), 7.02 (dd, *J* = 7.8 Hz, *J* = 1.8 Hz, 1H, H-k), 7.03 (d, *J* = 1.7 Hz, 1H, H-m), 7.29 (dd, *J* = 8.3 Hz, *J* = 2.1 Hz, 1H, H-c), 7,31 (d, *J* = 2.1 Hz, 1H, H-e).

^{13}C NMR (126 MHz, CD_2Cl_2, 298 K): δ [ppm] = 30.0 (C-g/h), 30.2 (C-g/h), 79.5 (C-d), 91.8 (C-l), 117.8 (C-b), 124.0 (C-m), 125.4 (C-i), 127.5 (C-k), 128.6 (C-j), 131.0 (C-f), 135.8 (C-c), 137.7 (C-e), 144.4 (C-n), 146.1 (C-a).

HRMS (ESI$^+$ Orbitrap): *m/z* (relative intensity) = 464.9325 (100%, $[M+H]^+$, calcd 464.9325), 338.028 (20%, $[M+H-I]^+$, calcd 338.0280).

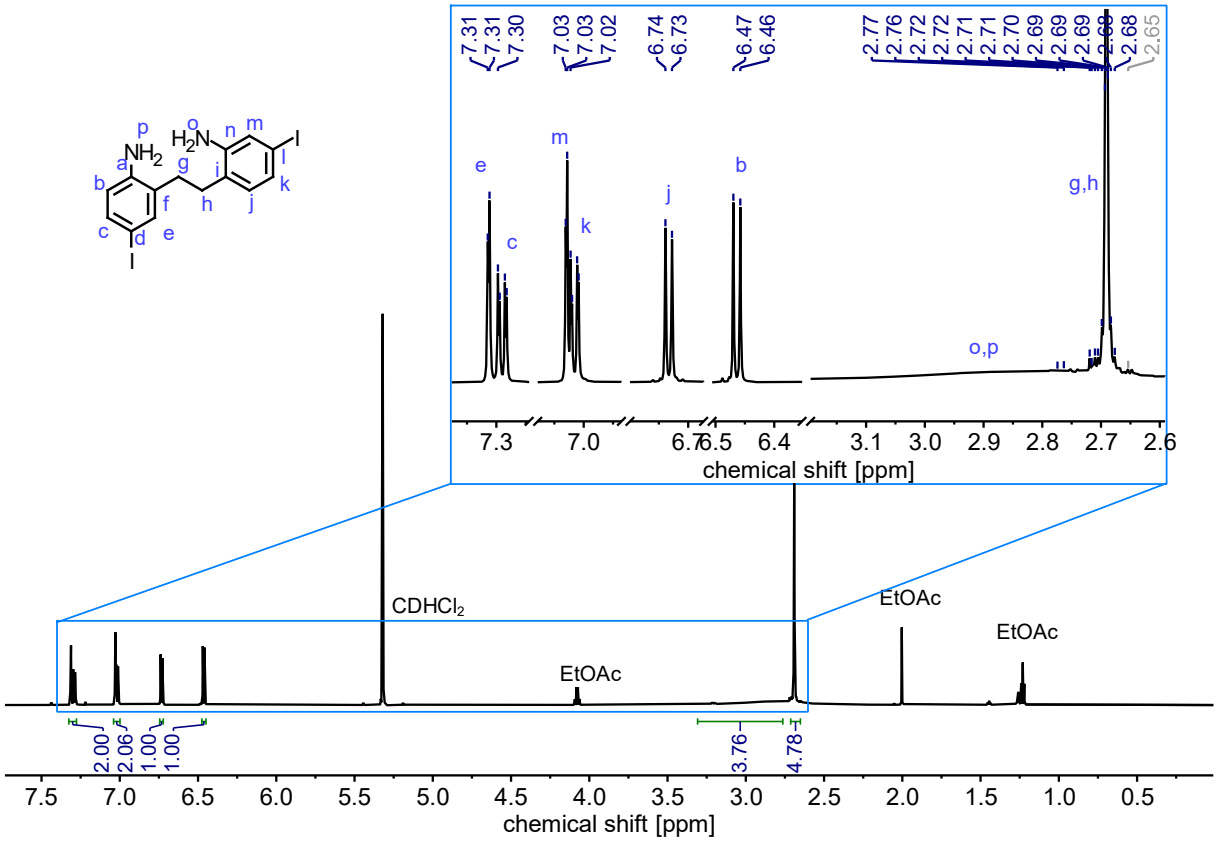

Figure S11. ^{1}H NMR (700 MHz, CD_2Cl_2, 298 K) of **H**.

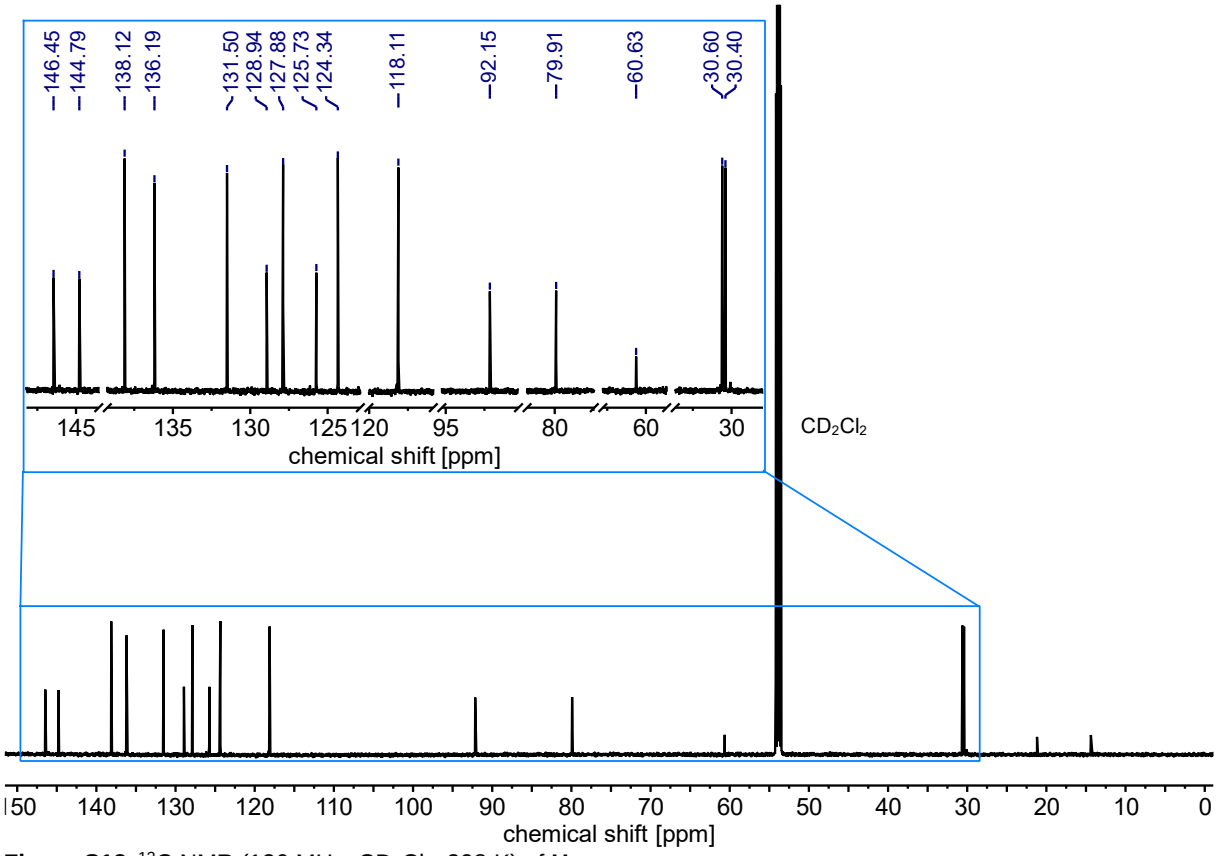

Figure S12. ^{13}C NMR (126 MHz, CD_2Cl_2, 298 K) of **H**.

S2.5. 2-(2-Amino-4-iodophenethyl)-4-bromoaniline (**I**)

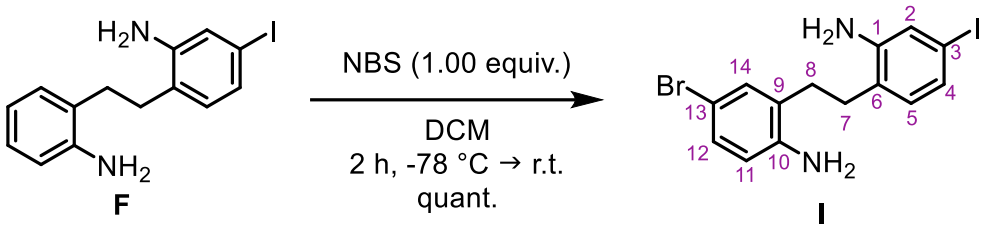

A solution of 2-(2-aminophenethyl)-5-iodoaniline (**F**) (90.0 mg, 266.1 µmol, 25.0 mM, 1.00 equiv.) in dichloromethane (11 mL) and a solution of *N*-bromosuccinimide (NBS; 47.4 mg, 266.1 µmol, 10.0 mM, 1.00 equiv.) in dichloromethane (27 mL) were purged with argon. At −78 °C, the NBS solution was added dropwise to the substrate solution over 10 minutes. After addition, the cooling bath was removed and the reaction mixture stirred for two hours, allowing it to warm to room temperature. The solvent was removed under reduced pressure on a rotary evaporator and the crude product was purified by column chromatography (silica gel, dichloromethane/(ethyl acetate + 5% triethylamine) 100:0 → 70:30 (v/v) over 10 column volumes), giving rise to bromo-iodo dianiline **I** as a brown oil in quantitative yield (111.4 mg, 267.0 µmol).

$C_{14}H_{14}BrIN_2$ 417.09 g mol^{-1}

R_F value (cyclohexane/ethyl acetate 8:2 (v/v)) = 0.63.

^{1}H NMR (500 MHz, CD_2Cl_2) δ [ppm] = 2.63 (s, 4H, H-7, H-8), 3.60 (s, 4H, NH_2), 6.48 (d, *J*=8.4, 1H, H-11), 6.65 (d, *J*=7.8, 1H, H-5), 6.91 – 6.97 (m, 2H, H-2, H-4), 7.01 – 7.08 (m, 2H, H-12, H-14).

^{13}C NMR (126 MHz, CD_2Cl_2) δ [ppm] = 30.1 (C-7, C-8), 91.7 (C-3), 110.1 (C-13), 117.2 (C-11), 123.9 (C-2), 125.3 (C-6), 127.5 (C-4), 128.0 (C-9), 129.8 (C-12), 131.1 (C-5), 131.8 (C-14), 143.7 (C-10), 146.1 (C-1).

HRMS (ESI$^+$ Orbitrap): *m/z* (relative intensity) = 416.9456 ([M+H]$^+$, calcd 416.9458).

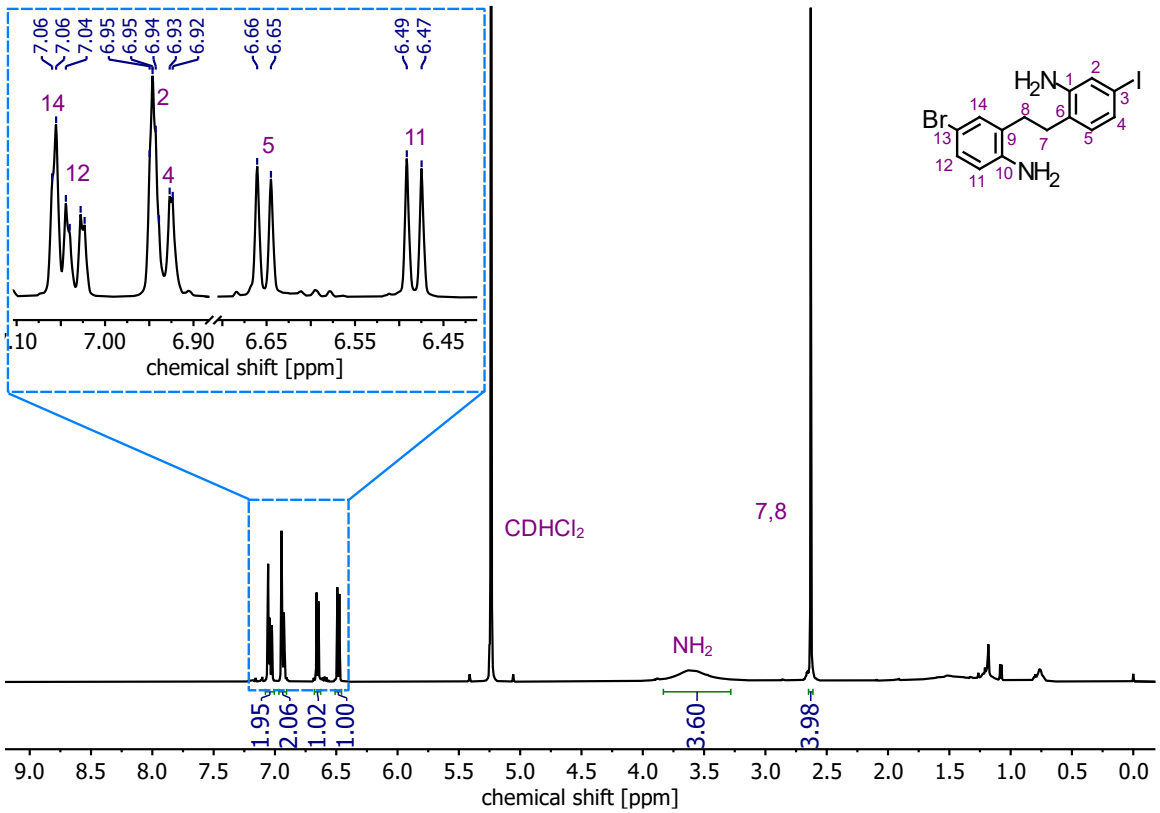

Figure S13. ^{1}H NMR (500 MHz, CD_2Cl_2, 298 K) of **I**.

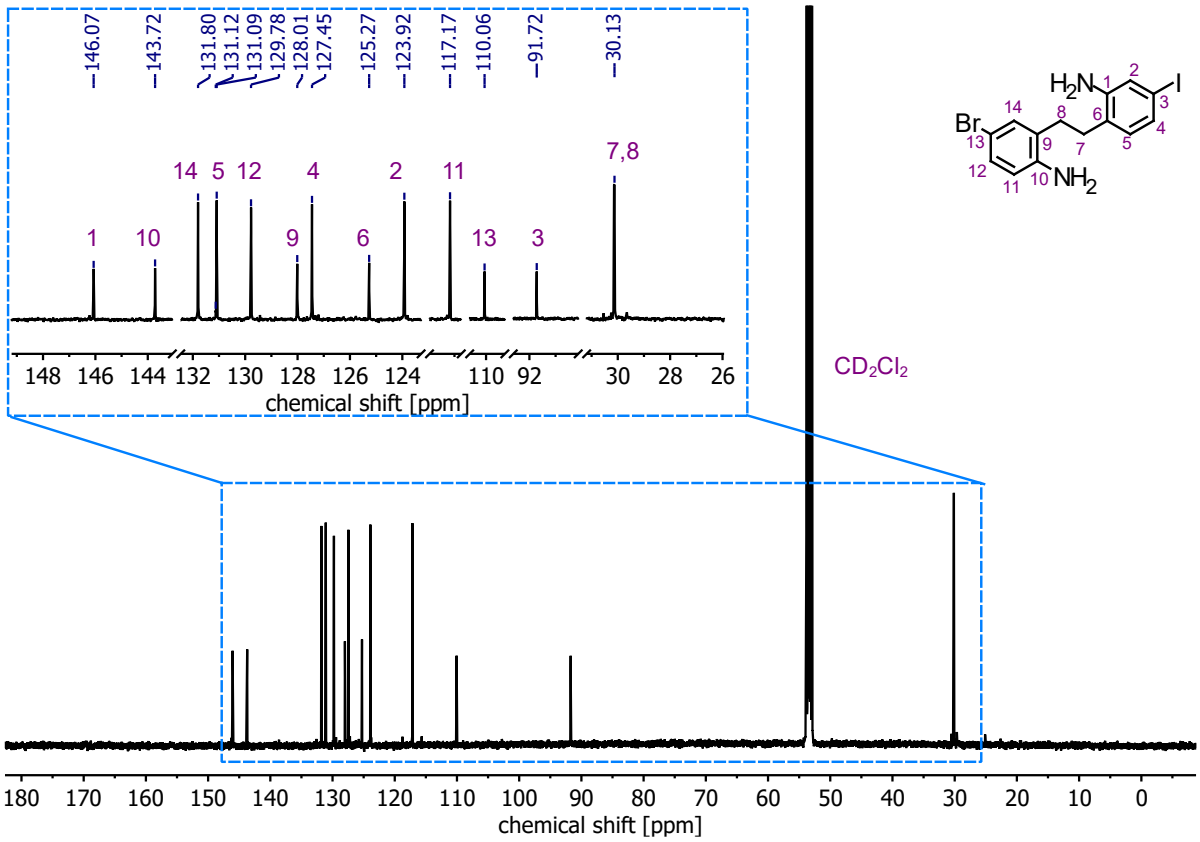

Figure S14. ^{13}C NMR (126 MHz, CD_2Cl_2, 298 K) of **I**.

S2.6. (*Z*)-2,8-Dibromo-11,12-dihydrodibenzo[c,g][1,2]diazocine (**1**)

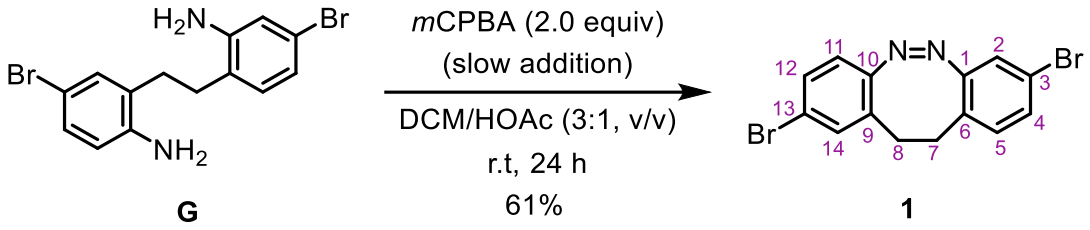

G **1**

Compound **1** was synthesized following the procedure for the oxidative formation of diazocines.[8]

A solution of *m*CPBA (80%, 52 mg, 0.24 mmol, 2.00 equiv.) in glacial acetic acid (0.6 mL, approx. 0.6 M) was added to a solution of dibromo dianiline **G** (45 mg, 0.12 mmol, 1.00 equiv.) in a mixture of acetic acid and dichloromethane (1:3 (v/v), 10 mL) using a syringe pump at room temperature over 24 hours. Following the completion of the addition, the reaction mixture was stirred for at least one hour at room temperature, after which the reaction mixture was neutralized using saturated aqueous sodium hydrogen carbonate solution. The organic layer was separated and the organic phase was washed with saturated aqueous solutions of sodium bicarbonate (25 mL) and sodium chloride (20 mL).. After drying the organic phase over magnesium sulfate, all volatiles were removed by rotary evaporation. The residue was subjected to column chromatography (silica gel, cyclohexane/ethyl acetate 100:0 → 70:30 (v/v) over 15 column volumes) to afford dibromo diazocine **1** as a yellow solid in 61% yield (27 mg, 0.07 mmol).

$C_{14}H_{10}Br_2N_2$ 366.06 g mol^{-1}

R_F value (cyclohexane/ethyl acetate 9:1 (v/v)) = 0.38.

^{1}H NMR (500 MHz, $CDCl_3$) δ [ppm] = 2.64 – 2.98 (m, 4H, H-7, H-8), 6.73 (d, *J*=8.4, 1H, H-11), 6.86 (d, *J*=8.2, 1H, H-5), 6.97 (d, *J*=2.0, 1H, H-2), 7.13 (d, *J*=2.0, 1H, H-14), 7.16 (dd, *J*=8.2, 2.0, 1H, H-4), 7.28 (dd, *J*=8.4, 2.0, 1H, H-12).

^{13}C NMR (126 MHz, CD_2Cl_2) δ [ppm] = 31.1 (C-7), 31.4 (C-8), 120.4 (C-3), 120.8 (C-9), 120.8 (C-11), 121.8 (C-2), 126.9 (C-13), 130.1 (C-6), 130.2 (C-12), 130.5 (C-4), 131.4 (C-5), 132.6 (C-14), 154.1 (C-10), 156.2 (C-1).

HRMS (ESI$^+$ Orbitrap): m/z = 364.9280 ([M+H]$^+$, calcd 364.9284).

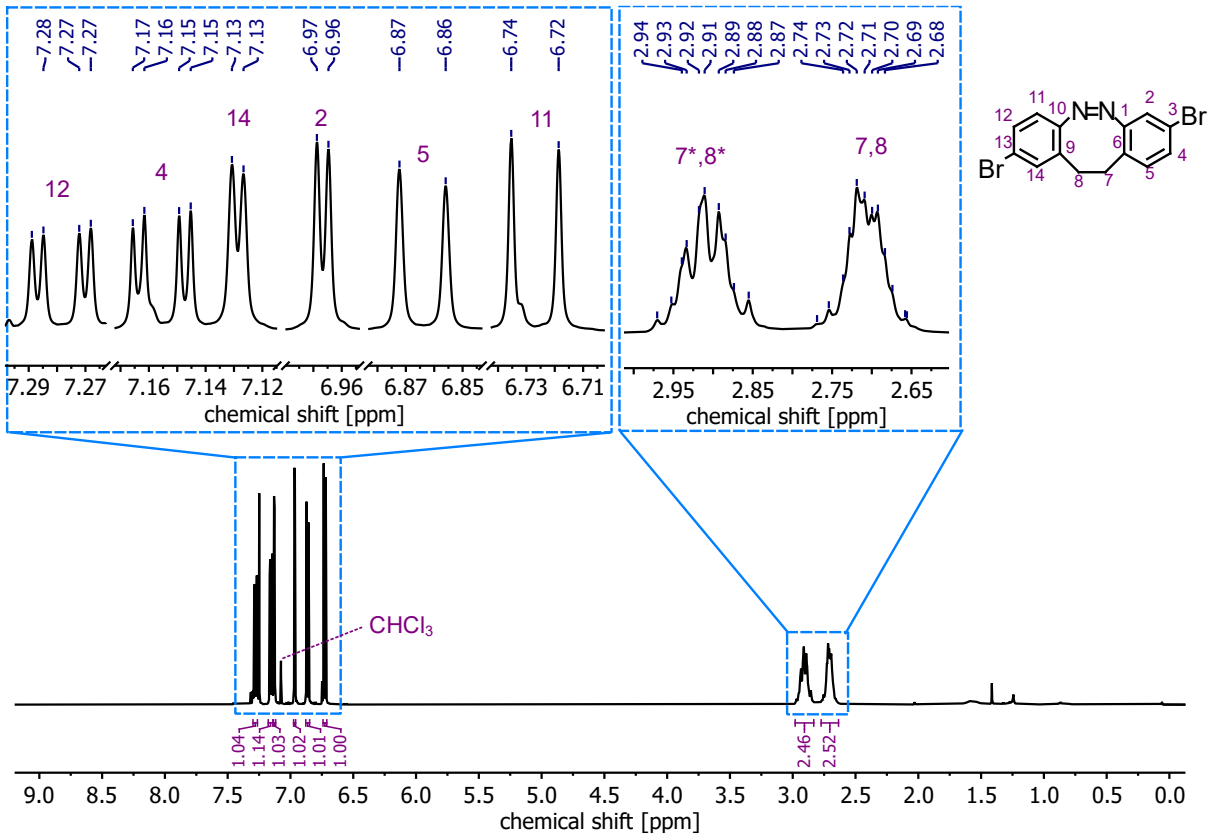

Figure S15. ^{1}H NMR (500 MHz, $CDCl_3$, 298 K) of **1**.

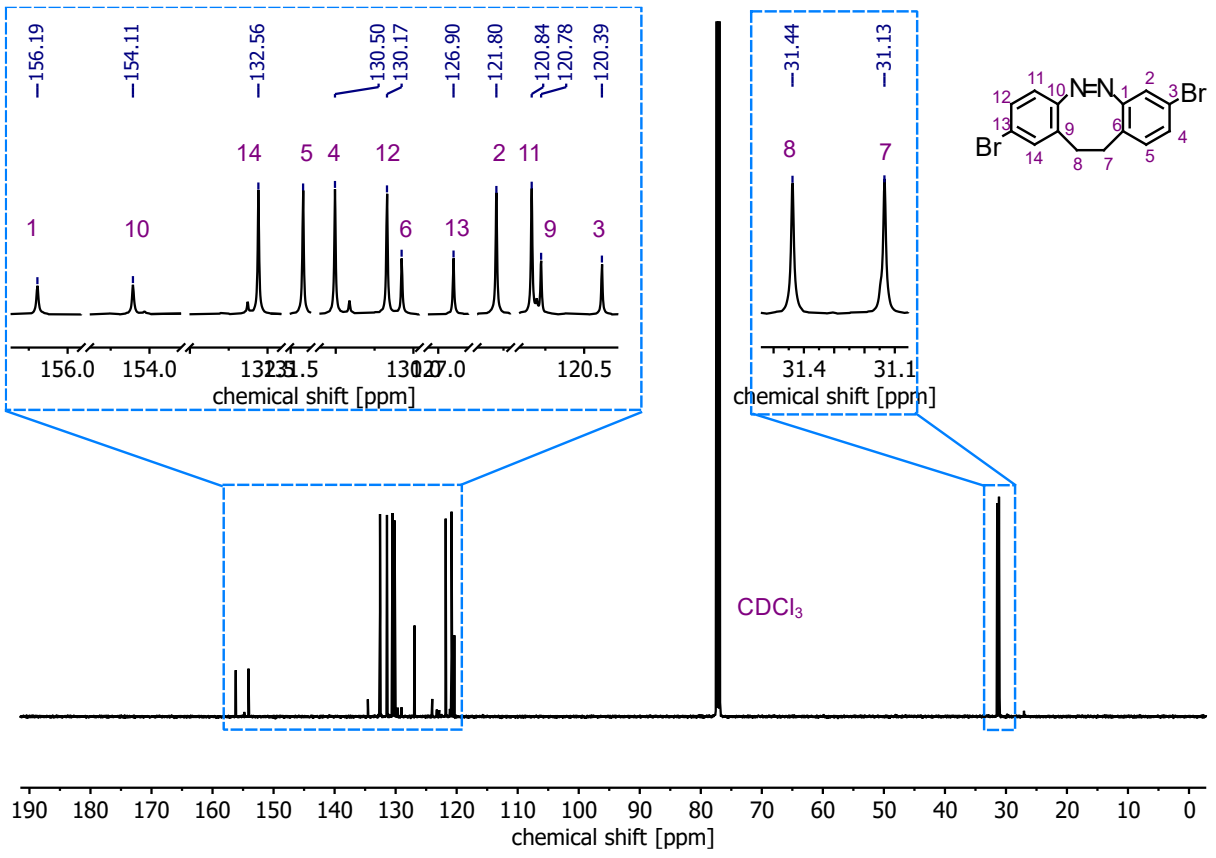

Figure S16. ^{13}C NMR (126 MHz, CD_2Cl_2, 298 K) of **1**.

S2.7. (*Z*)-2,8-Diiodo-11,12-dihydrodibenzo[c,g][1,2]diazocine (**2**)

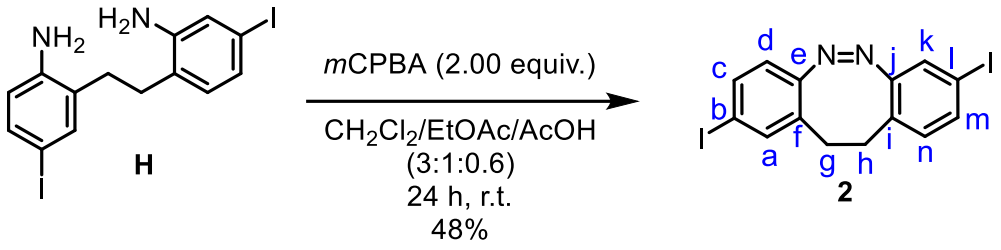

Compound **2** was synthesized following the procedure for the oxidative formation of diazocines.[8]

An Argon-purged solution of *m*CPBA (80%, 310.1 mg, 1.8 mmol, 2.00 equiv.) in glacial acetic acid (0.6 mL, approx. 0.6 M) was added to an Argon-purged solution of diiodo dianiline **H** (417.0 mg, 898.5 µmol, 1.00 equiv.) in a mixture of dichloromethane and ethylacetate (3:1 (v/v), 20 mL) using a syringe pump (rate of 0.25 mL/hour) at room temperature over 6 hours. Following the completion of the addition, the reaction mixture was stirred for 18 hours at room temperature, gradually turning dark brown. A saturated aqueous sodium bicarbonate solution (20 mL) was subsequently added to the reaction mixture to neutralize the acetic acid. The phases were separated and the organic phase was washed with saturated aqueous solutions of sodium bicarbonate (25 mL) and sodium chloride (20 mL). The combined organic layers were dried over anhydrous magnesium sulfate and filtered. All volatiles were removed from the filtrate under reduced pressure on a rotary evaporator. The oily residue was subjected to column chromatography (silica gel, cyclohexane/ethyl acetate 4:1) to afford diiodo diazocine **2** as a yellow solid in 48% yield (198.4 mg, 431.3 µmol).

$C_{14}H_{10}I_2N_2$ 460.06 g mol^{-1}

R_F value (cyclohexane/ethyl acetate 4:1 (v/v) = 0.50

^{1}H NMR (500 MHz, CD_2Cl_2, 298 K): δ [ppm] = 2.64 – 2.79 (m, 2H, H-g/h), 2.80 – 2.95 (m, 2H, H-g/h), 6.61 (d, *J* = 8.2 Hz, 1H, H-d), 6.78 (d, J = 8.1 Hz, 1H, H-n), 7.17 (d, *J* = 1.8 Hz, 1H, H-a), 7.38 (d, *J* = 1.8 Hz, 1H, H-k), 7.39 (dd, *J* = 7.2, 1.9 Hz, 1H, H-m), 7.51 (dd, *J* = 8.2, 1.8 Hz, 1H, H-c).

^{13}C NMR (126 MHz, CD_2Cl_2, 298 K): δ [ppm] = 31.5 (C-g/h), 31.5 (C-g/h), 91.3 (C-l), 92.3 (C-b), 121.1 (C-d), 127.7 (C-a), 128.2 (C-i), 130.8 (C-f), 132.0 (C-n), 136.3 (C-c), 136.6 (C-m), 138.9 (C-k), 155.3 (C-e), 156.8 (C-j).

HRMS (EI^+): *m/z* (relative intensity) = 460.899 (100%, $[M+H]^+$, calcd 460.9012), 333.995 (95%, $[M+H-I]^+$, calcd 333.9967).

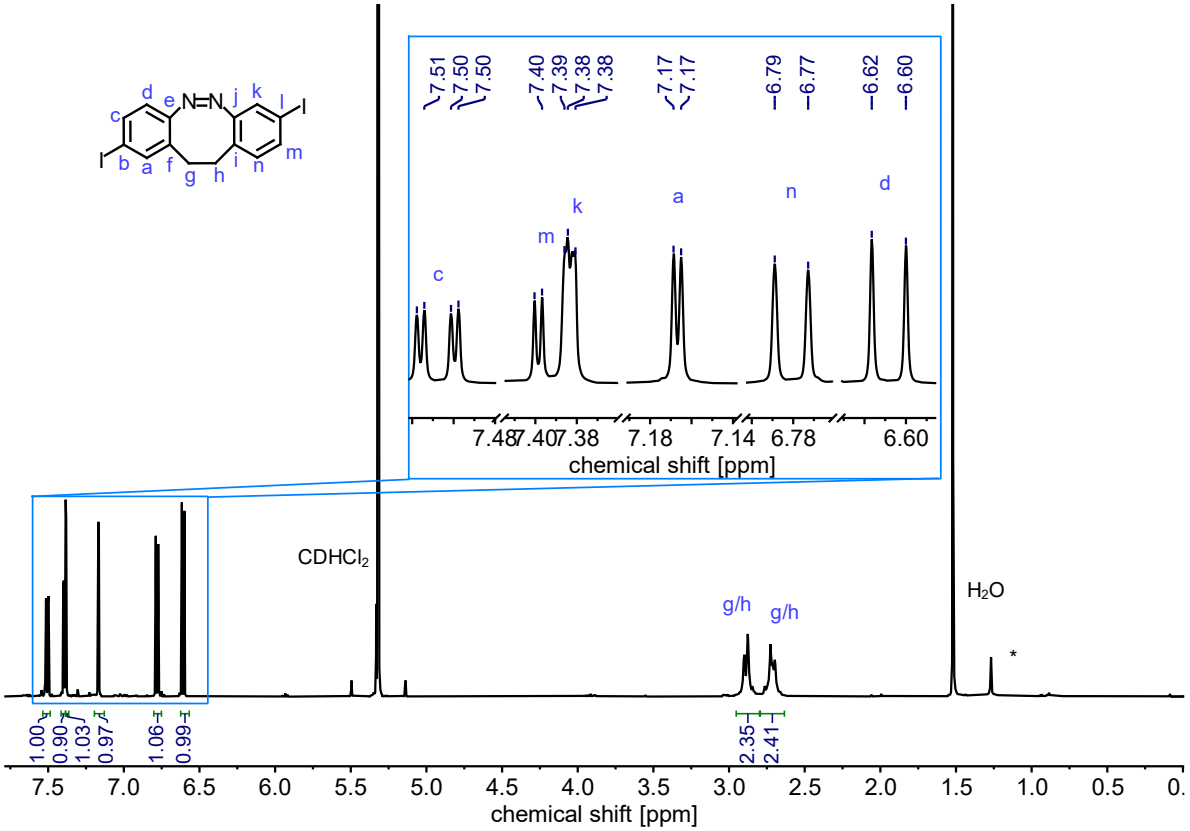

Figure S17. ^{1}H NMR (500 MHz, CD_2Cl_2, 298 K) of **2**.

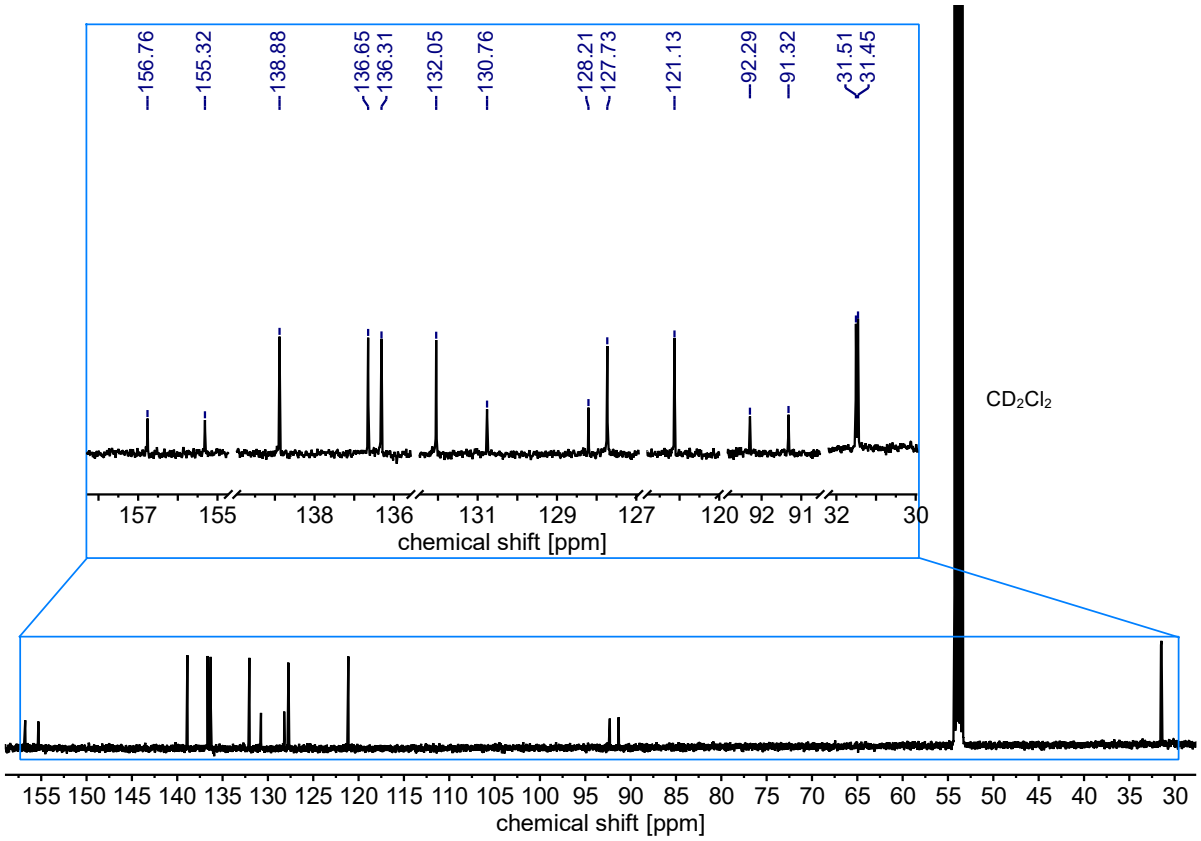

Figure S18. ^{13}C NMR (126 MHz, CD_2Cl_2, 298 K) of **2**.

S2.8. (*Z*)-2-Bromo-8-iodo-11,12-dihydrodibenzo[c,g][1,2]diazocine (**3**)

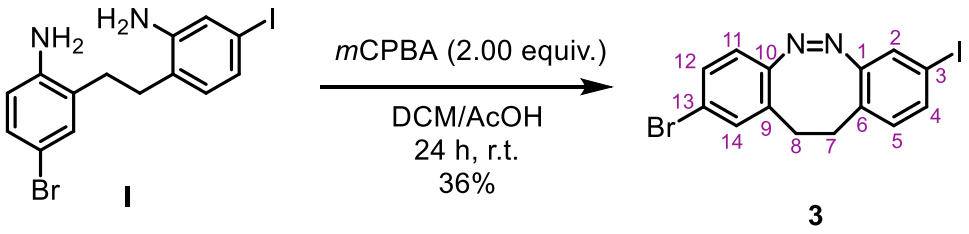

Compound **3** was synthesized following the procedure for the oxidative formation of diazocines.[8]

A solution of *m*CPBA (75%, 2.58 g, 11.22 mmol, 2.00 equiv.) in glacial acetic acid (approx. 0.6 M) was added to a solution of bromo-iodo dianiline **I** (2.34 g, 5.61 mmol, 1.00 equiv.) in a mixture of glacial acetic acid and dichloromethane (1:3 (v/v), 60 mL) using a syringe pump over 24 hours. Following the completion of the addition, the reaction mixture was stirred for 18 hours at room temperature, after which the reaction mixture was neutralized using saturated aqueous sodium hydrogen carbonate solution. The organic layer was separated and washed with saturated aqueous solutions of sodium hydrogen carbonate (25 mL) and sodium chloride (25 mL). After drying the organic phase over magnesium sulfate, all volatiles were removed by rotary evaporation. The residue was subjected to column chromatography (silica gel, cyclohexane/ethyl acetate 100:0 → 70:30 (v/v) over 15 column volumes) to afford the product as a yellow solid in 63% yield (1.47 g, 3.56 mmol).

$C_{14}H_{10}BrIN_2$ 413.06 g mol^{-1}

R_F value (cyclohexane/ethyl acetate 8:2 (v/v)) = 0.56.

^{1}H NMR (500 MHz, CD_2Cl_2) δ [ppm] = 2.64 – 2.96 (m, 4H, H-7, H-8), 6.74 (d, *J* = 8.3 Hz, 1H, H-11), 6.78 (d, *J* = 8.1 Hz, 1H, H-5), 7.16 (d, *J* =1.8, 1H, H-2), 7.18 (d, *J* = 2.1 Hz, 1H, H-14), 7.31 (dd, *J* = 8.4 Hz, 2.1, 1H, H-12), 7.39 (dd, *J* = 8.1, 1.8 Hz, 1H, H-4).

^{13}C NMR (126 MHz, CD_2Cl_2) δ [ppm] = 31.0 (C-7), 31.1 (C-8), 90.9 (C-3), 120.3 (C-13), 120.6 (C-11), 127.2 (C-2), 127.7 (C-6), 129.9 (C-12), 130.2 (C-9), 131.6 (C-15), 132.4 (C-14), 136.1 (C-4), 154.1 (C-10), 156.2 (C-1).

HRMS (ESI$^+$ Orbitrap): *m*/*z* = 412.9138 ([M+H]$^+$, calcd 412.9145).

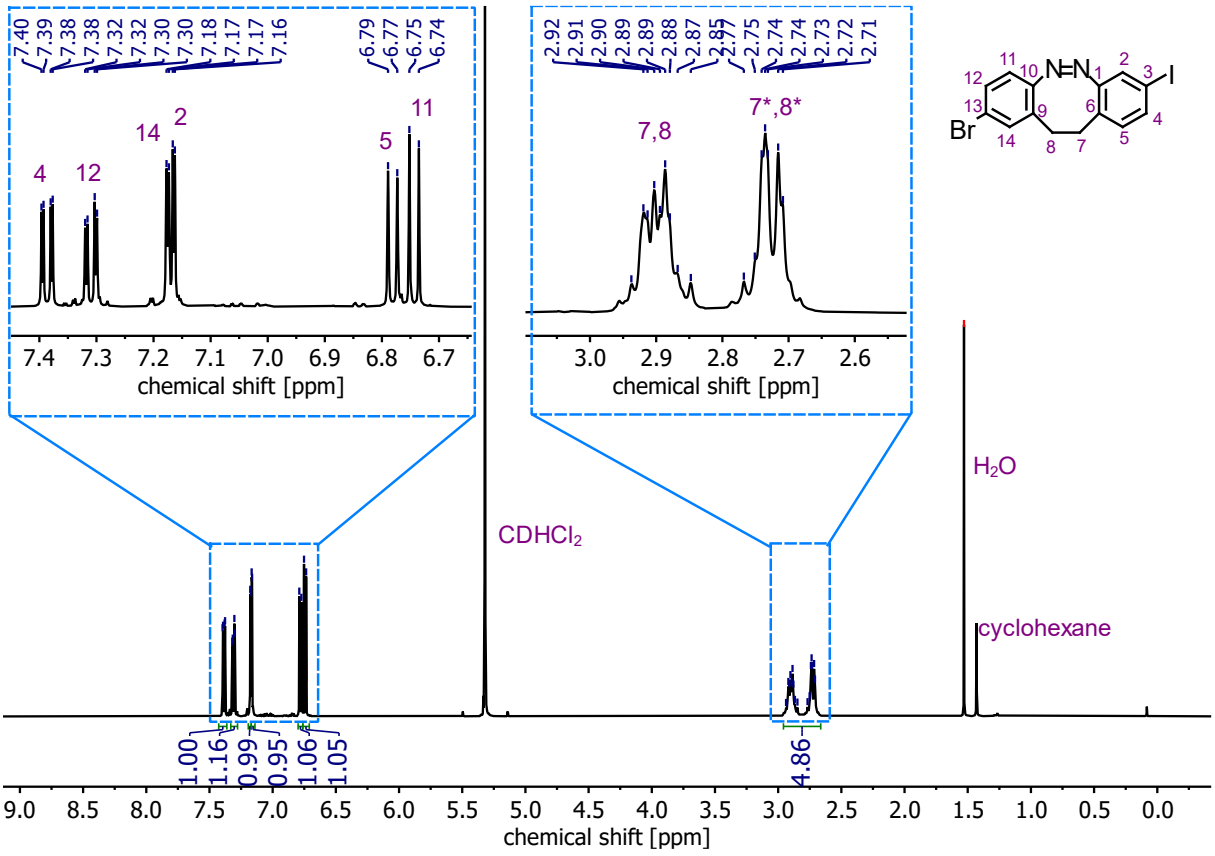

Figure S19. ^{1}H NMR (500 MHz, CD_2Cl_2, 298 K) of **3**.

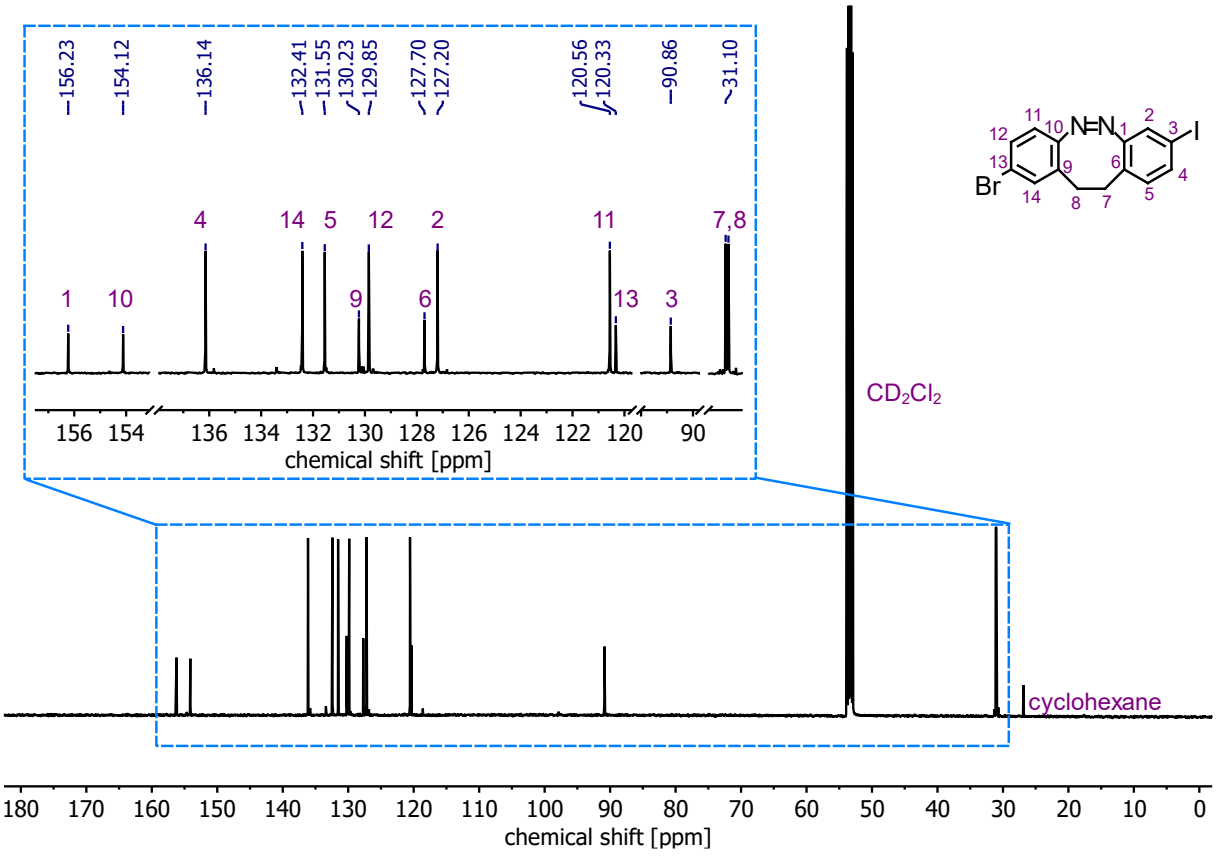

Figure S20. ^{13}C NMR (126 MHz, CD_2Cl_2, 298 K) of **3**.

S2.9. (*Z*)-2,8-Bis(3,5-bis(trifluoromethyl)phenyl)-11,12-dihydrodibenzo-[c,g][1,2]-diazocine (**4**)

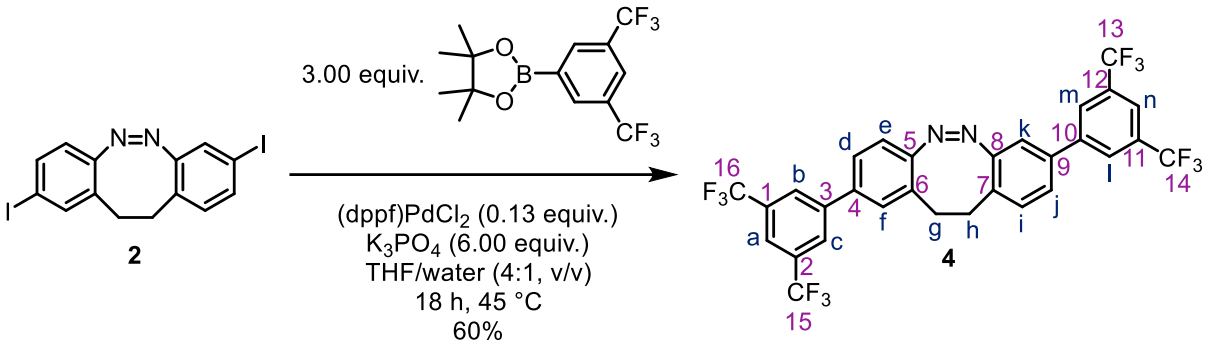

Diiodo diazocine **2** (54.1 mg, 117.6 µmol, 1.00 equiv.), 2-(3,5-bis(trifluoromethyl)-phenyl)-4,4,5,5-tetramethyl-1,3,2-dioxaborolane (120.0 mg, 352.8 µmol, 3.00 equiv.), potassium phosphate (149.8 mg, 705.6 µmol, 6.00 equiv.), and Pd(dppf)Cl_2 (11.0 mg, 15.0 µmol, 0.13 equiv.) were added into a screwcap vial. Under an argon atmosphere, the solids were suspended in tetrahydrofuran/water (4:1 (v/v), 5 mL) and the vial was closed. The suspension was stirred at 45 °C for 18 hours. All volatiles were removed by rotary evaporation. The oily residue was subjected to column chromatography (silica gel, cyclohexane/ethyl acetate 19:1 (v/v) over 8 column volumes) to afford bis(trifluoromethyl)phenyl) diazocine **4** as a yellow solid in 60% yield (44.4 mg, 70.2 µmol).

$C_{30}H_{16}F_{12}N_2$ 632.45 g mol^{-1}

R_F value (cyclohexane/ethyl acetate 19:1 (v/v)) = 0.23

^{1}H NMR (400 MHz, CD_2Cl_2, 298 K) δ [ppm] = 2.87 – 3.00 (m, 2H, H-g/h), 3.04 – 3.15 (m, 2H, H-g/h), 7.04 (d, *J* = 8.2 Hz, 1H, e), 7.17 (d, *J* = 2.0 Hz, 1H, H-k), 7.20 (d, *J* = 8.0 Hz, 1H, H-i), 7.33 (d, *J* = 2.0 Hz, 1H, H-f), 7.35 (dd, *J* = 7.9, 2.0 Hz, 1H, H-j), 7.45 (dd, *J* = 8.1, 2.0 Hz, 1H, H-d), 7.83 – 7.88 (m, 1H, H-a/n), 7.86 – 7.88 (m, 1H, H-H-a/n), 7.97 (d, *J* = 1.7 Hz, 2H, H-b,c/l,m), 7.98 (d, *J* = 1.7 Hz, 2H, H-b,c/l,m).

^{13}C NMR (126 MHz, CD_2Cl_2, 298 K) δ [ppm] = 31.9 (C-g/h), 32.1 (C-g/h), 118.0 (C-k), 120.4 (C-e), 121.5 (C-a/n), 121.6, 121.6, 121.7 (C-a/n), 122.8, 125.0, 126.2 (C-d/f), 126.3 (C-d/f), 127.6 (C-b,c,l,m), 129.1 (C-j), 129.5, 129.7, 131.5 (C-i), 132.3, 132.3, 132.5, 132.6, 137.3, 137.4, 142.3, 142.6, 156.2, 156.6.

C-1, C-2, C-3, C-4, C-5, C-6, C-7, C-8, C-9, C-10, C-11, C-12, C-13, C-14, C-15, C-16 could not be assigned unambiguously.

HRMS (EI^+): m/z (relative intensity) = 632.1108 (30%, $[M]^+$, calcd 632.1121) 604.0 (100%, $[M\text{-}N_2]^+$, calcd 604.1060), 391.1 (30%, $[M\text{-}C_{10}H_7F_6]^+$, calcd 391.0670).

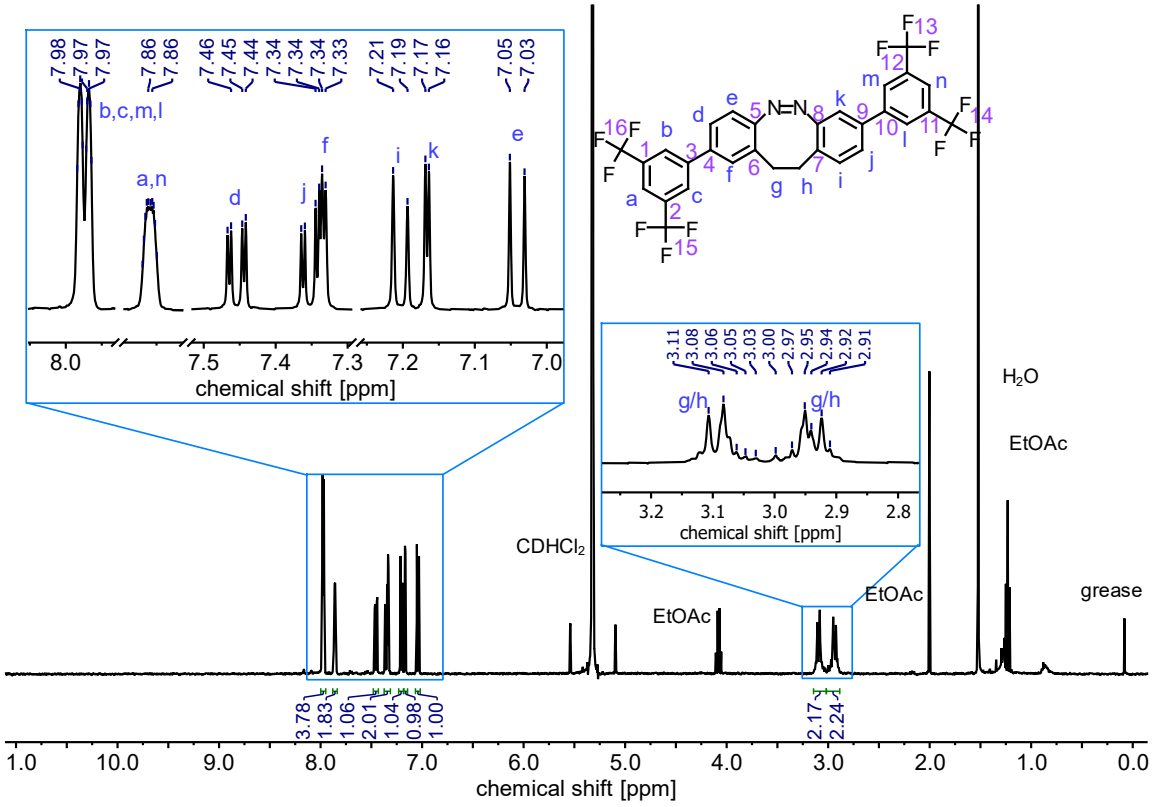

Figure S21. ^{1}H NMR (400 MHz, CD_2Cl_2, 298 K) of **4**.

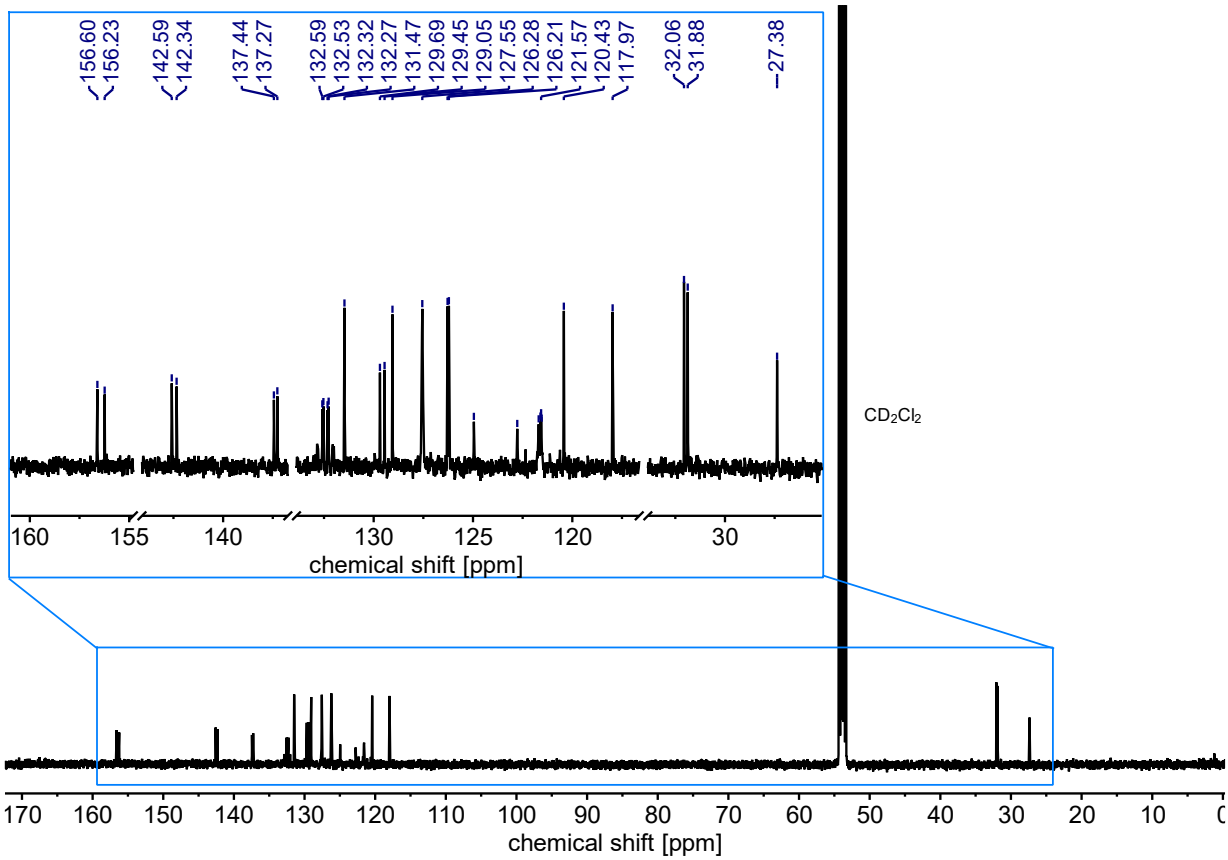

Figure S22. ^{13}C NMR (126 MHz, CD_2Cl_2, 298 K) of **4**.

S2.10. (*Z*)-2,8-Diphenyl-11,12-dihydrodibenzo[c,g][1,2]diazocine (**5**)

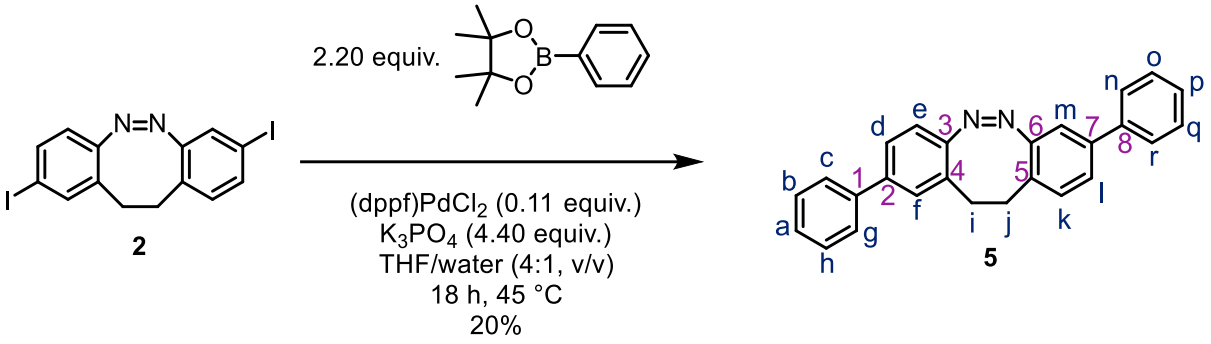

Diiodo-diazocine **2** (73.6 mg, 160.0 µmol, 1.00 equiv.), 4,4,5,5-tetramethyl-2-phenyl-1,3,2-dioxaborolane (91.9 mg, 352.8 µmol, 2.23 equiv.), potassium phosphate (149.5 mg, 1034.9 µmol, 4.41 equiv.), and $Pd(dppf)Cl_2$ (12.9 mg, 17.8 µmol, 0.11 equiv.) were added into a screwcap vial. Under an argon atmosphere, the solids were suspended in tetrahydrofuran/water (4:1 (v/v), 5 mL) and the vial was closed. The suspension was stirred at 45 °C for 18 hours. All volatiles were removed by rotary evaporation. The residue was subjected to column chromatography (silica gel, cyclohexane:dicholoromethane 1:1 (v/v)) to afford diphenyl diazocine **5** as a yellow solid in 20% yield** (11.5 mg, 31.9 µmol).

*

$C_{26}H_{20}N_2$ 360.46 g mol^{-1}

R_F value (cyclohexane/dichloromethane 1:1 (v/v)) = 0.26

^{1}H NMR (500 MHz, CD_2Cl_2, 298 K) δ [ppm] = 2.87 – 2.94 (m, 2H, H-i/j) 3.02 - 3.06 (m, 2H, H-i/j), 6.95 (d, *J* = 8.2 Hz, 1 H, H-e), 7.11 (d, *J* = 8.6 Hz, 1H, H-k), 7.13 (d, 1H, H-m), 7.30 – 7.34 (m, 4H, H-a,d,l,p), 7.38 – 7.42 (m, 5H, H-b,h,f,o,q), 7.51 – 7.54 (m, 4H, H-c,g,n,r).

^{13}C NMR (126 MHz, CD_2Cl_2, 298 K) δ [ppm] = 31.9 (C-i/j), 32.3 (C-i/j), 117.7 (C-m), 120.0 (C-e), 125.8, 126.0, 127.2, 127.2, 127.7, 127.9, 128.0, 128.7, 129.1, 129.2, 129.2, 130.8 (C-k), 140.1, 140.1, 140.3, 140.4, 155.2, 156.4.

* The low isolated yield results from insufficient separability between product and side products by column chromatography.

C-a, C-b, C-c, C-d, C-f, C-g, C-h, C-l, C-n, C-o, C-p, C-q, C-r, C-1, C-2, C-3, C-4, C-5, C-6, C-7, C-8 could not be assigned unambiguously.

HRMS (EI^+): *m/z* (relative intensity) = 360.1618 (70%, $[M]^+$, calcd 360,1625), 332.2 (100%, $[M\text{-}N_2]^+$, calcd 332.1565), 317.1 (30%, $[M\text{-}C_3H_7]^+$, calcd 317.1079), 241,1 (50%, $[M\text{-}C_9H_{11}]^+$, calcd 241.0766), 182.1 (50%, $[M\text{-}C_{12}H_{10}]^+$, calcd 182.0844).

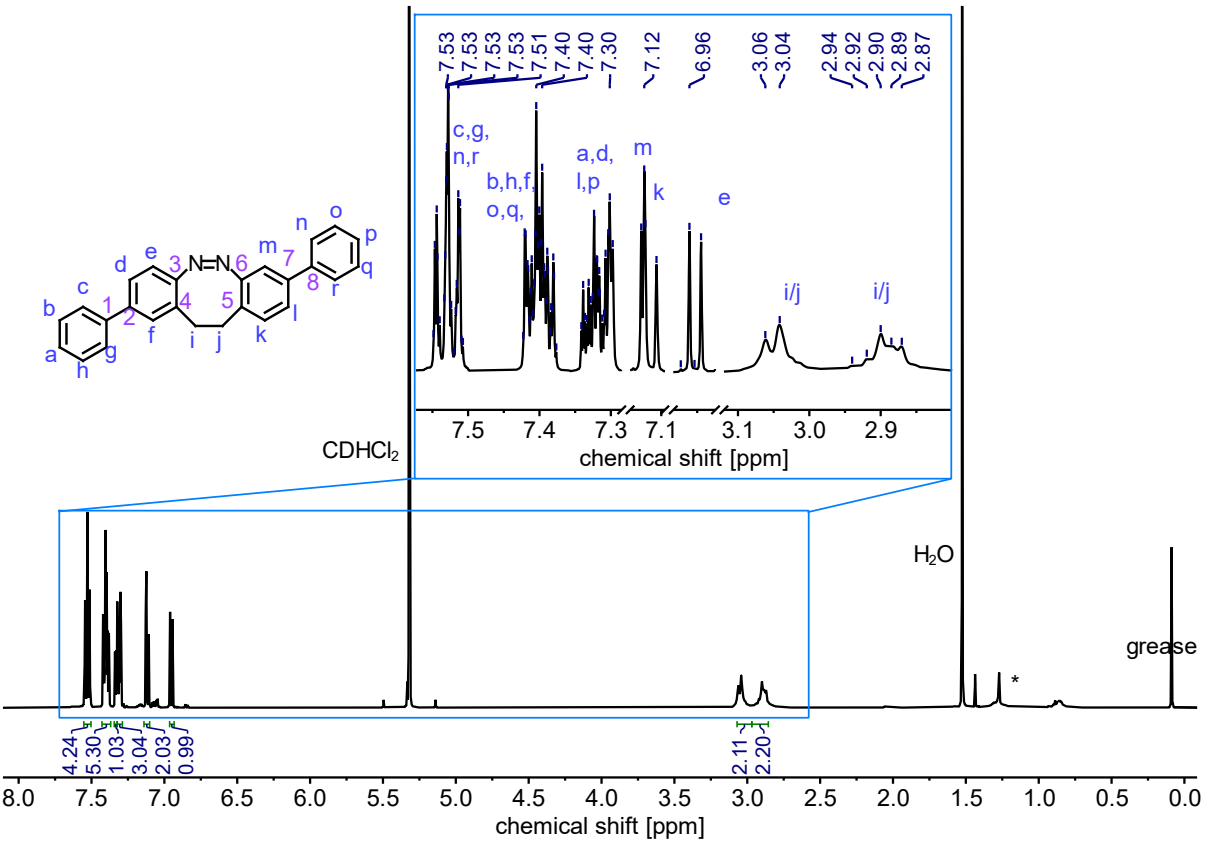

Figure S23. ^{1}H NMR (500 MHz, CD_2Cl_2, 298 K) of **5**. The asterisk indicates a signal caused by H grease, a contamination introduced from the used syringes and solvents.

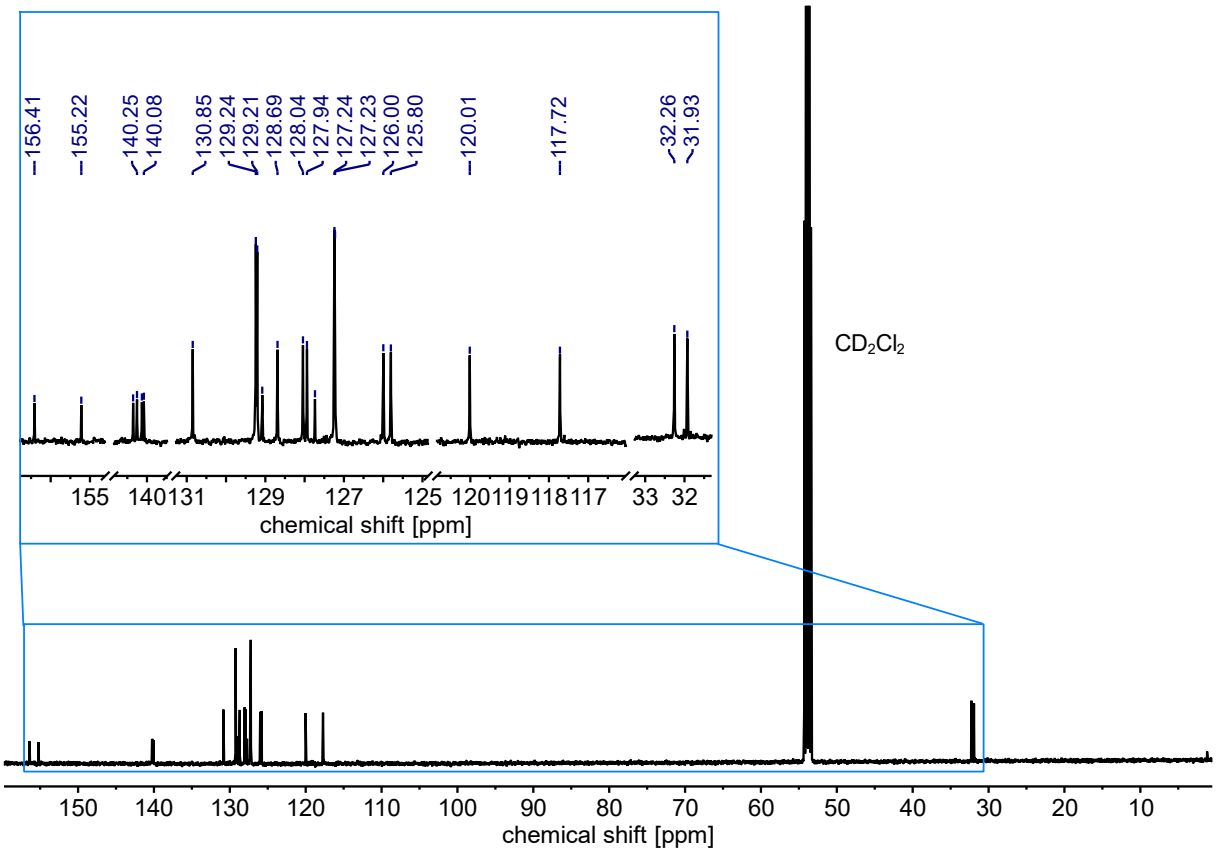

Figure S24. ^{13}C NMR (126 MHz, CD_2Cl_2, 298 K) of **5**.

S2.11. (*Z*)-2,8-Di-p-tolyl-11,12-dihydrodibenzo[c,g][1,2]diazocine (**6**)

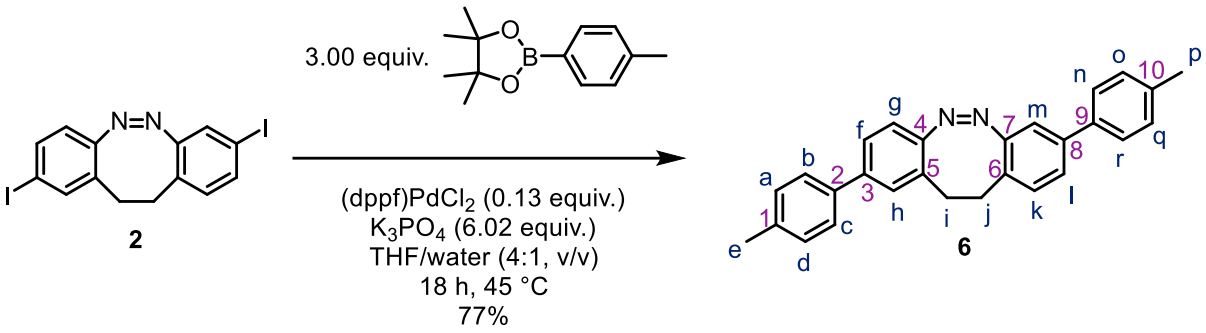

Diiodo diazocine **2** (55.0 mg, 119.6 µmol, 1.00 equiv.), 4,4,5,5-tetramethyl-2-(*p*-tolyl)-1,3,2-dioxaborolane (78.2 mg, 358.7 µmol, 3.00 equiv.), potassium phosphate (152.5 mg, 717.9 µmol, 6.02 equiv.), and Pd(dppf)Cl_2 (11.0 mg, 15.0 µmol, 0.13 equiv.) were added into a screwcap vial. Under an argon atmosphere, the solids were suspended in tetrahydrofuran/water (4:1 (v/v), 5 mL) and the vial was closed. The suspension was stirred at 45 °C for 18 hours. All volatiles were removed by rotary evaporation. The residue was subjected to column chromatography (silica gel, cyclohexane/dichloromethane 1:1 (v/v)) to afford ditoluyl diazocine **6** as a yellow solid in 77% yield (35.6 mg, 91.6 µmol).

$C_{28}H_{24}N_2$ 388.51 g mol^{-1}

R_F value (cyclohexan/dichloromethane 3:2 (v/v)) = 0.13

^{1}H NMR (500 MHz, CD_2Cl_2, 298 K) δ [ppm] = 2.36 (s, 6H, H-e,p), 2.82 – 2.93 (m, 2H, H-i/j), 2.97 - 3.08 (m, 2H, H-i/j), 6.93 (d, *J* = 8.1 Hz, 1H, H-g), 7.06 – 7.12 (m, 2H, H-k,m), 7.19 - 7.23 (m, 4H, H-a,d,o,q), 7.27 (d, *J* = 1.9 Hz, 1H, H-h), 7.29 (dd, *J* = 7.9 Hz, *J* = 2.0 Hz, 1H, H-l), 7.39 (dd, J = 7.9 Hz, J = 1.9 Hz, 1H, H-f), 7.40-7.45 (m, 4H, H-b,c,n,r).

^{13}C NMR (126 MHz, CD_2Cl_2, 298 K) δ [ppm] = 21.2 (C-e,p), 31.9 (C-i,j), 32.3 (C-i,j), 117.5 (C-m), 120.0 (C-g), 125.5 (C-l), 125.7 (C-f), 127.0 (C-r,n), 127.0 (C-b,c), 127.4 (C-6), 128.4 (C-5), 129.0 (C-h), 129.9 (C-a,d), 129.9 (C-o,q), 130.8 (C-k), 137.2 (C-4), 137.4 (C-7), 137.9 (C-2), 138.0 (C-9), 140.0 (C-3), 140.2 (C-8), 155.0 (C-1), 156.4 (C-10).

HRMS (ESI$^+$ Orbitrap): *m/z* (relative intensity) = 389.2009 (100%, $[M+H]^+$, calcd 389.2018), 299.154 (15%, $[M-C_7H_5+H]^+$, calcd 299.1548).

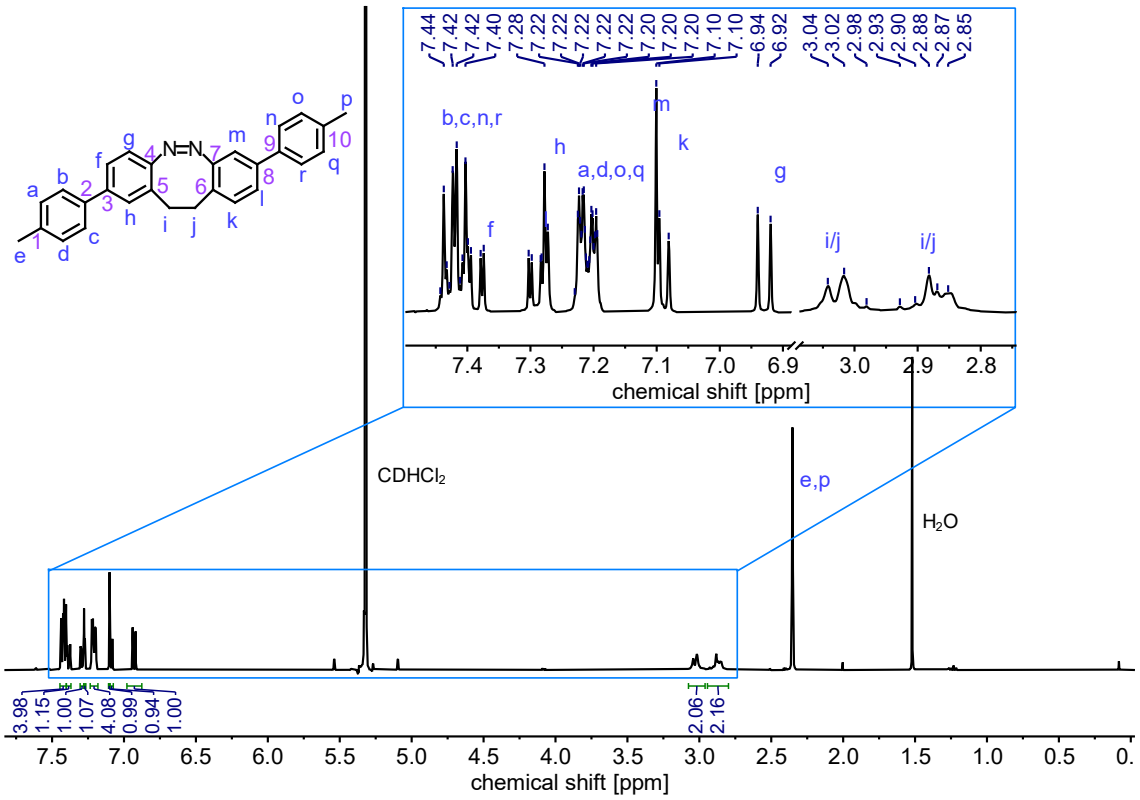

Figure S25. ^{1}H NMR (400 MHz, CD_2Cl_2, 298 K) of **6**.

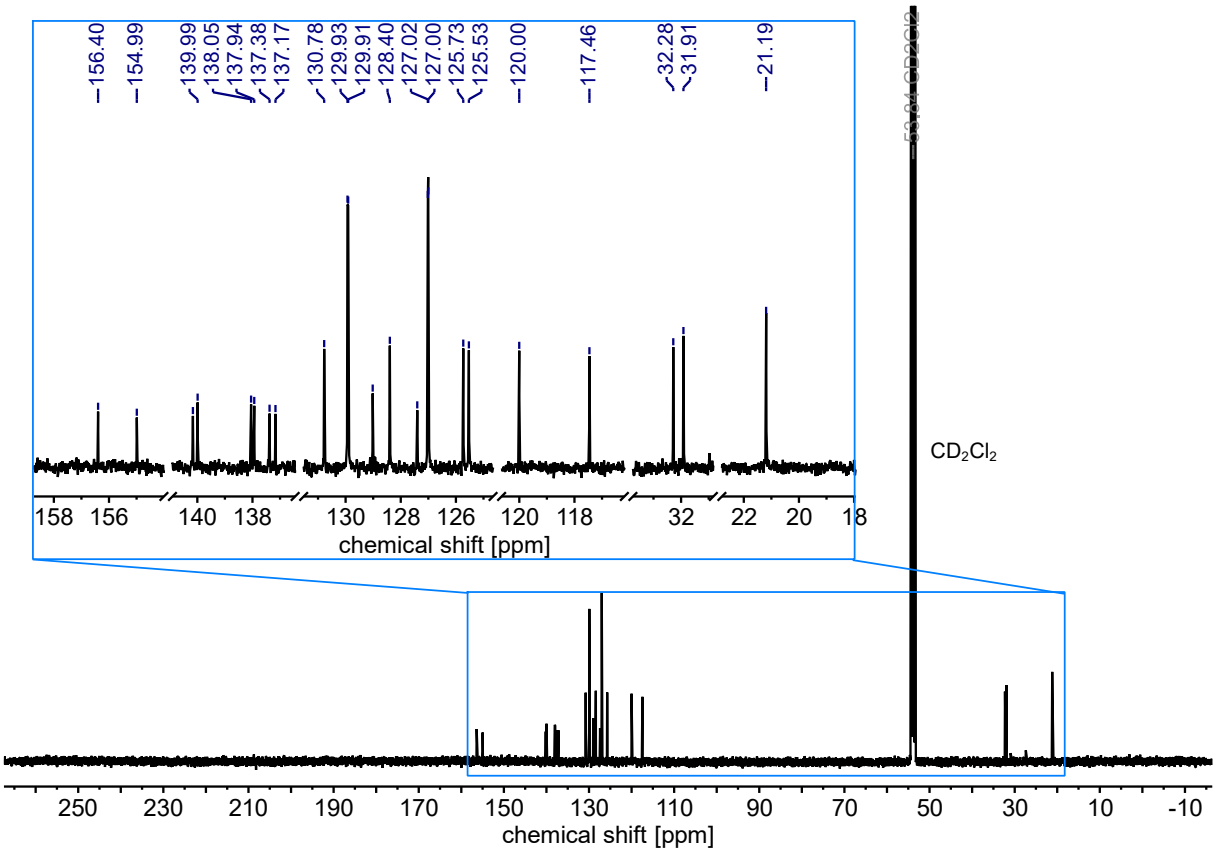

Figure S26. ^{13}C NMR (126 MHz, CD_2Cl_2, 298 K) of **6**.

S2.12. (*Z*)-2,8-Bis(3,5-dimethoxyphenyl)-11,12-dihydrodibenzo[c,g][1,2]-diazocine (**7**)

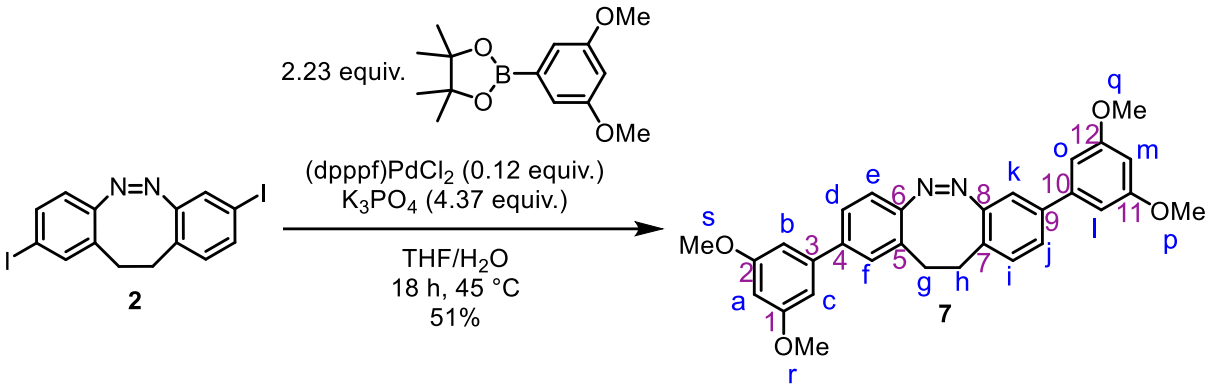

Diiodo-diazocine **2** (79.4 mg, 172.6 µmol, 1.00 equiv.), 2-(3,5-dimethoxyphenyl)-4,4,5,5-tetramethyl-1,3,2-dioxaborolane (123.3 mg, 384.9 µmol, 2.23 equiv.), potassium phosphate (160.1 mg, 754.2 µmol, 4.37 equiv.), and Pd(dppf)Cl_2 (15.2 mg, 20.7 µmol, 0.12 equiv.) were added into a screwcap vial. Under an argon atmosphere, the solids were suspended in tetrahydrofuran/water (4:1 (v/v), 5 mL) and the vial was closed. The suspension was stirred at 45 °C for 18 hours. All volatiles were removed by rotary evaporation. The oily residue was subjected to column chromatography (silica gel, cyclohexane/ethyl acetate 100:0 → 3:1 (v/v) over 8 column volumes) to afford bis(3,5-dimethoxyphenyl) diazocine **7** as a yellow solid in 51% yield (42.3 mg, 88.0 µmol).

$C_{30}H_{28}N_2O_4$ 480.56 g mol^{-1}

R_F value (cyclohexane/ethyl acetate 7:3 (v/v)) = 0.28

^{1}H NMR (500 MHz, CD_2Cl_2, 298 K) δ [ppm] = 2.82 – 2.94 (m, 2H, H-g/h), 2.96 – 3.08 (m, 2H, H-g/h), 3.80 (s, 6H, H-p,q/r,s), 3.80 (s, 6H, H-p,q/r,s), 6.43 (t, *J* = 2.3 Hz, 1H, H-a/m), 6.43 (t, *J* = 2.2 Hz, 1H, H-a/m), 6.64 (d, *J* = 2.3 Hz, 2H, H-b,c/l,o), 6.66 (d, *J* = 2.3 Hz, 2H, H-b,c/l,o), 6.94 (d, *J* = 8.1 Hz, 1H, H-e), 7.10 (d, *J* = 7.6 Hz, 1H, H-i), 7.11 (d, *J* = 1.6 Hz, 1H, H-k), 7.28 (d, *J* = 1.9 Hz, 1H, H-f), 7.30 (dd, *J* = 7.9, 2.0 Hz, 1H, H-j), 7.39 (dd, *J* = 8.2, 1.9 Hz, 1H, H-d).

^{13}C NMR (126 MHz, CD_2Cl_2, 298 K) δ [ppm] = 31.9 (C-g/h), 32.2 (C-g/h), 55.8 (C-p,q/r,s), 55.8 (C-p,q/r,s), 99.9 (C-a/m), 100.0 (C-a/m), 105.5 (C- b,c/l,o), 105.5 (C-b,c/l,o), 117.8 (C-i), 119.9 (C-e), 125.9 (C-d), 126.1 (C-j), 128.0 (C-3/10), 128.8 (C-f), 129.0 (C-3/10), 130.8 (C-k), 140.0 (C-5/6), 140.2 (C-5/6), 142.2 (C-7/8), 142.5 (C-7/8), 155.4 (C-4), 156.3 (C-9), 161.7 (C-1,2/11,12), 161.7 (C-1,2/11,12).

HRMS (EI^+): m/z (relative intensity) = 481.2122 (100%, $[M+H]^+$, calcd 481.2127), 394.0 (85%, $[M-CO]^+$, calcd 394.0681), 314.1 (65%, $[M-C_6H_5O_2+H]^+$, calcd 314.0419).

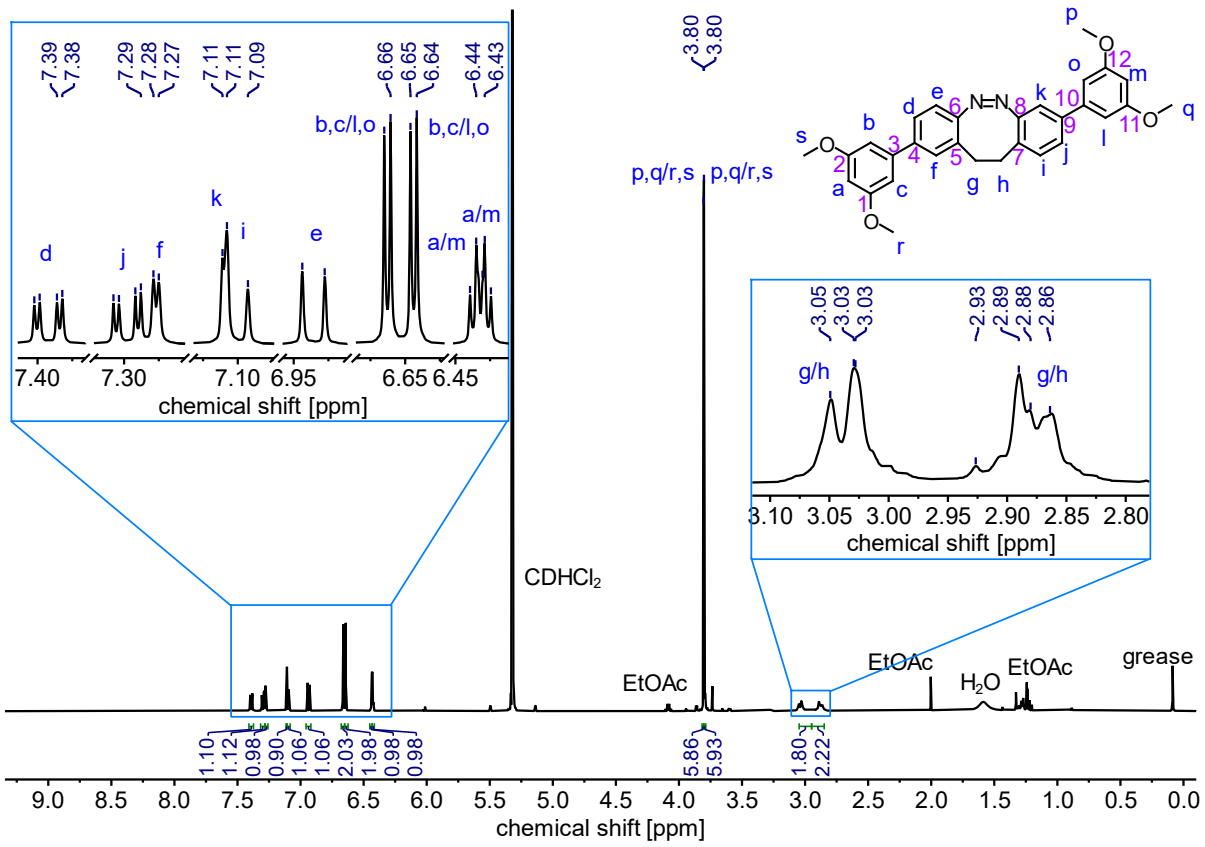

Figure S27. ^{1}H NMR (500 MHz, CD_2Cl_2, 298 K) of **7**.

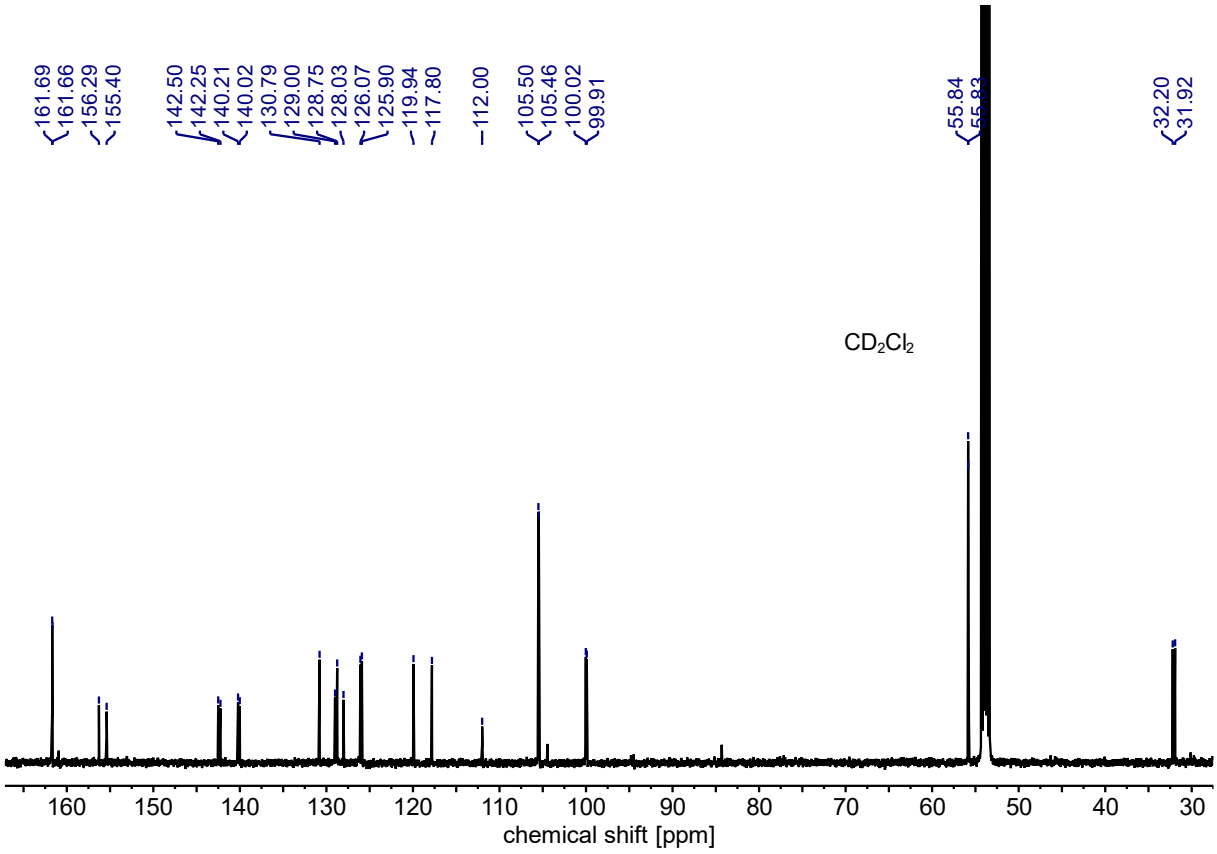

Figure S28. ^{13}C NMR (126 MHz, CD_2Cl_2, 298 K) of **7**.

S2.13. (*Z*)-2-Bromo-8-(3,5-dimethoxyphenyl)-11,12-dihydrodibenzo[c,g]- [1,2]diazocine (**8**)

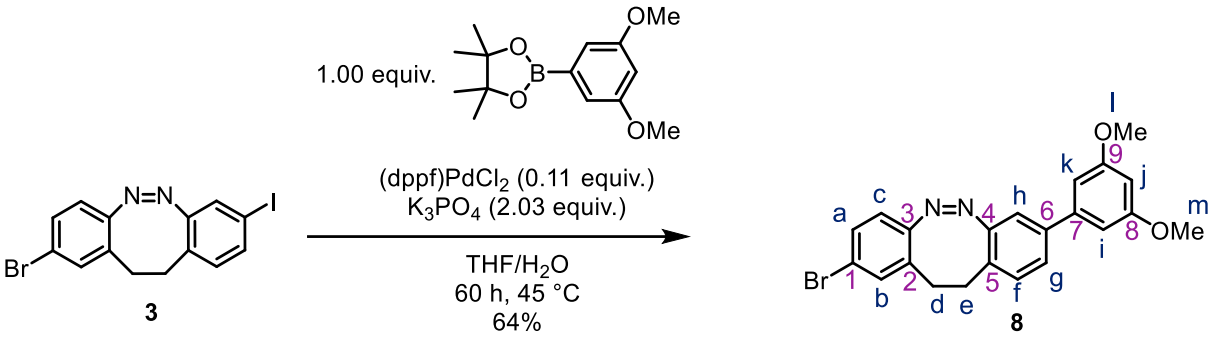

Bromo/iodo diazocine **3** (56.7 mg, 137.3 µmol, 1.00 equiv.), 2-(3,5-dimethoxyphenyl)-4,4,5,5-tetramethyl-1,3,2-dioxaborolane (36.3 mg, 137.3 µmol, 1.00 equiv.), potassium phosphate (59.2 mg, 278.7 µmol, 2.03 equiv.), and Pd(dppf)Cl_2 (11.1mg, 15.1 µmol, 0.11 equiv.) were added into a screwcap vial. Under an argon atmosphere, the solids were suspended in tetrahydrofuran/water (4:1 (v/v), 5 mL) and the vial was closed. The suspension was stirred at 45 °C for 60 hours. All volatiles were removed by rotary evaporation. The oily residue was subjected to column chromatography (silica gel, cyclohexane/ethyl acetate 100:0 → 70:30 (v/v) over 8 column volumes) to afford bromo/3,5-dimethoxyphenyl diazocine **8** as a yellow solid in 64% yield (37.2 mg, 87.9 µmol).

$C_{22}H_{19}BrN_2O_2$ 423.31 g mol^{-1}

R_F value (cyclohexane/ethyl acetate 4:1 (v/v)) = 0.30

^{1}H NMR (500 MHz, CD_2Cl_2, 298 K) δ [ppm] = 2.71 – 2.86 (m, 2H, H-d/e), 2.89 – 3.06 (m, 2H, H-d/e), 3.81 (s, 6H, H-l,m), 6.44 (t, *J* = 2.2 Hz, 1H, H-j), 6.65 (d, *J* = 2.3 Hz, 2H, H-k,l), 6.75 (d, *J* = 8.4 Hz, 1H, H-c), 7.07 (d, *J* = 1.8 Hz, 1H, H-h), 7.08 (d, *J* = 7.9 Hz, 1H, H-f), 7.21 (d, *J* = 2.0 Hz, 1H, H-b), 7.28 (dd, *J* = 8.4, 2.1 Hz, 1H, H-a), 7.31 (dd, *J* = 8.0, 2.0 Hz, 1H, H-g).

^{13}C NMR (126 MHz, CD_2Cl_2, 298 K) δ [ppm] = 31.7 (C-d/e), 31.8 (C-d/e), 55.8 (C-l,m), 100.0 (C-j), 105.5 (C-k,i), 117.6 (C-h), 120.6 (C-2), 121.1 (C-c), 126.2 (C-g), 127.6 (C-7), 130.2 (C-a), 130.8 (C-f), 131.1 (C-3), 132.8 (C-b), 140.2 (C-5), 142.2 (C-6), 154.9 (C-1), 156.1 (C-4), 161.7 (C-8,9).

HRMS (EI^+): *m/z* (relative intensity) = 422.0631 (100%, $[M+H]^+$, calcd 422.0630), 394.0 (85%, $[M–CO]^+$, calcd 394.0681), 314.1 (65%, $[M–C_6H_5O_2+H]^+$, calcd 314.0419).

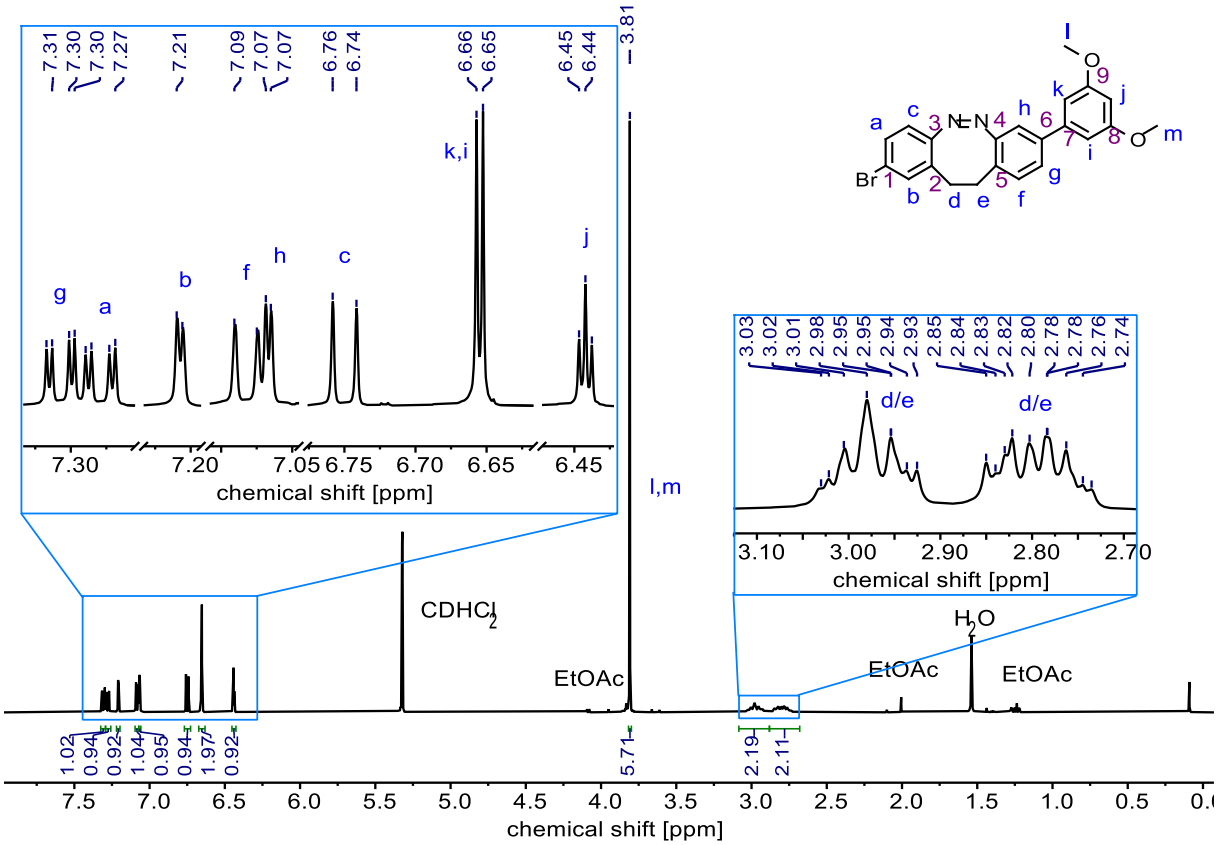

Figure S29. ^{1}H NMR (500 MHz, CD_2Cl_2, 298 K) of **8**.

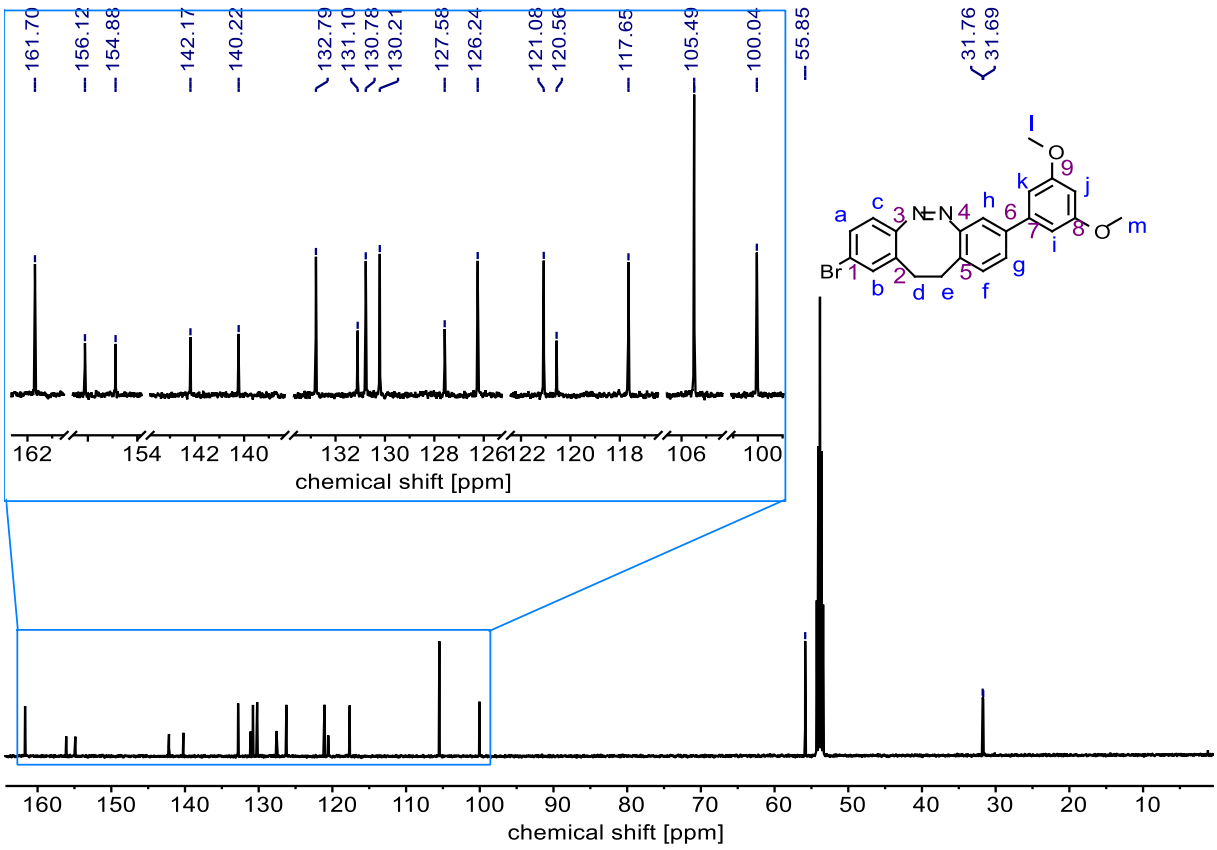

Figure S30. ^{13}C NMR (126 MHz, CD_2Cl_2, 298 K) of **8**.

S2.14. (*Z*)-2-(3,5-Bis(trifluoromethyl)phenyl)-8-(3,5-dimethoxyphenyl)-11,12-dihydrodibenzo[c,g][1,2]diazocine (**9**)

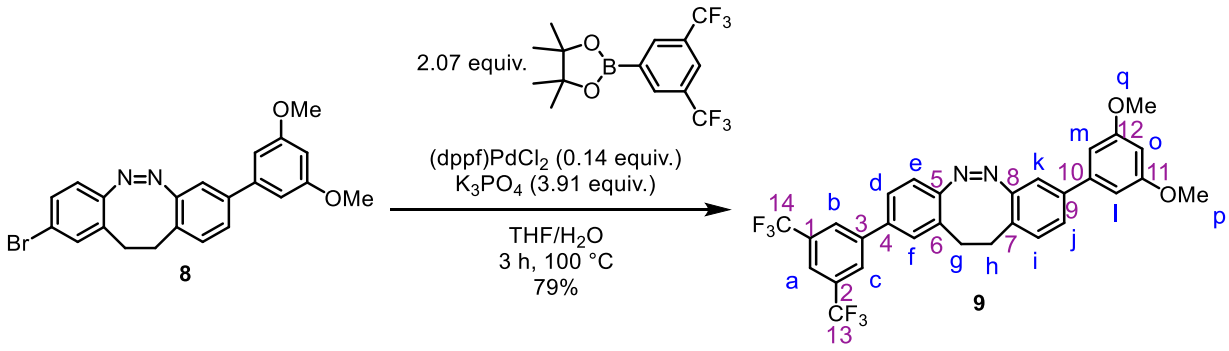

Bromo/3,5-dimethoxyphenyl diazocine **8** (28.0 mg, 66.2 µmol, 1.00 equiv.), 2-(3,5-bis(trifluoromethyl)phenyl)-4,4,5,5-tetramethyl-1,3,2-dioxaboro-lane (46.6 mg, 136.9 µmol, 2.07 equiv.), potassium phosphate (54.9 mg, 258.6 µmol, 3.91 equiv.), and Pd(dppf)Cl_2 (6.8 mg, 9.3 µmol, 0.14 equiv.) were added into a screwcap vial. Under an argon atmosphere, the solids were suspended in tetrahydrofuran/water (4:1 (v/v), 5 mL) and the vial was closed. The suspension was stirred at 100 °C for 3 hours. All volatiles were removed by rotary evaporation. The residue was subjected to column chromatography (silica gel, cyclohexane/ethyl acetate 100:0 → 70:30 (v/v) over 8 column volumes) to afford 3,5-dimethoxyphenyl/3,5-bis(trifluoromethyl)phenyl diazocine **9** as a yellow solid in 79% yield (29.0 mg, 52.3 µmol).

$C_{30}H_{22}F_6N_2O_2$ 556.5084 g mol^{-1}

R_F value (cyclohexane/ethyl acetate 4:1 (v/v)) = 0.26

^{1}H NMR (500 MHz, CD_2Cl_2, 298 K) δ [ppm] = 2.83 – 2.95 (m, 2H, H-g/h), 3.02 – 3.11 (m, 2H, H-g/h), 3.80 (s, 4H, H-p,q), 6.43 (t, *J* = 2.3 Hz, 1H, H-o), 6.65 (d, *J* = 2.3 Hz, 1H, H-l,m), 7.02 (d, *J* = 8.2 Hz, 1H, H-e), 7.10 (d, *J* = 8.0 Hz, 1H, H-i), 7.12 (d, *J* = 1.9 Hz, 1H, H-k), 7.30 (dd, *J* = 7.9, 2.0 Hz, 1H, H-j), 7.33 (d, *J* = 2.0 Hz, 1H, H-f), 7.45 (dd, *J* = 8.1, 2.0 Hz, 1H, H-d), 7.85 (dt, *J* = 1.5, 0.8 Hz, 1H, H-a), 7.95 – 8.00 (m, 2H, H-b,c).

^{13}C NMR (126 MHz, CD_2Cl_2, 298 K) δ [ppm] = 31.7 (C-g/h), 32.1 (C-g/h), 55.8 (C-p,q), 99.8 (C-o), 105.3 (C-l,m), 117.6 (C-k), 120.3 (C-e), 121.4 (C-a), 122.7, 124.9, 126.0 (C-d/j), 126.1 (C-d/j), 127.5 (C-b,c), 127.7, 129.0 (C-f), 129.8, 130.8 (C-i), 132.1,

132.4, 137.2 (C-3), 140.0 (C-10), 142.0 (C-9), 142.5 (C-4), 156.2, 156.2, 161.6 (C-11,12).

C-1, C-2, C-5, C-6, C-7, C-8, C-13, C-14 could not be assigned unambiguously.

HRMS (ESI$^+$ Orbitrap): m/z (relative intensity) = 557.1651 (15%, $[M+H]^+$, calcd 557.1658), 111.020, (100%, $[M-C_{23}H_{18}F_6N_2O_2+Na]^+$, calcd 111.0211).

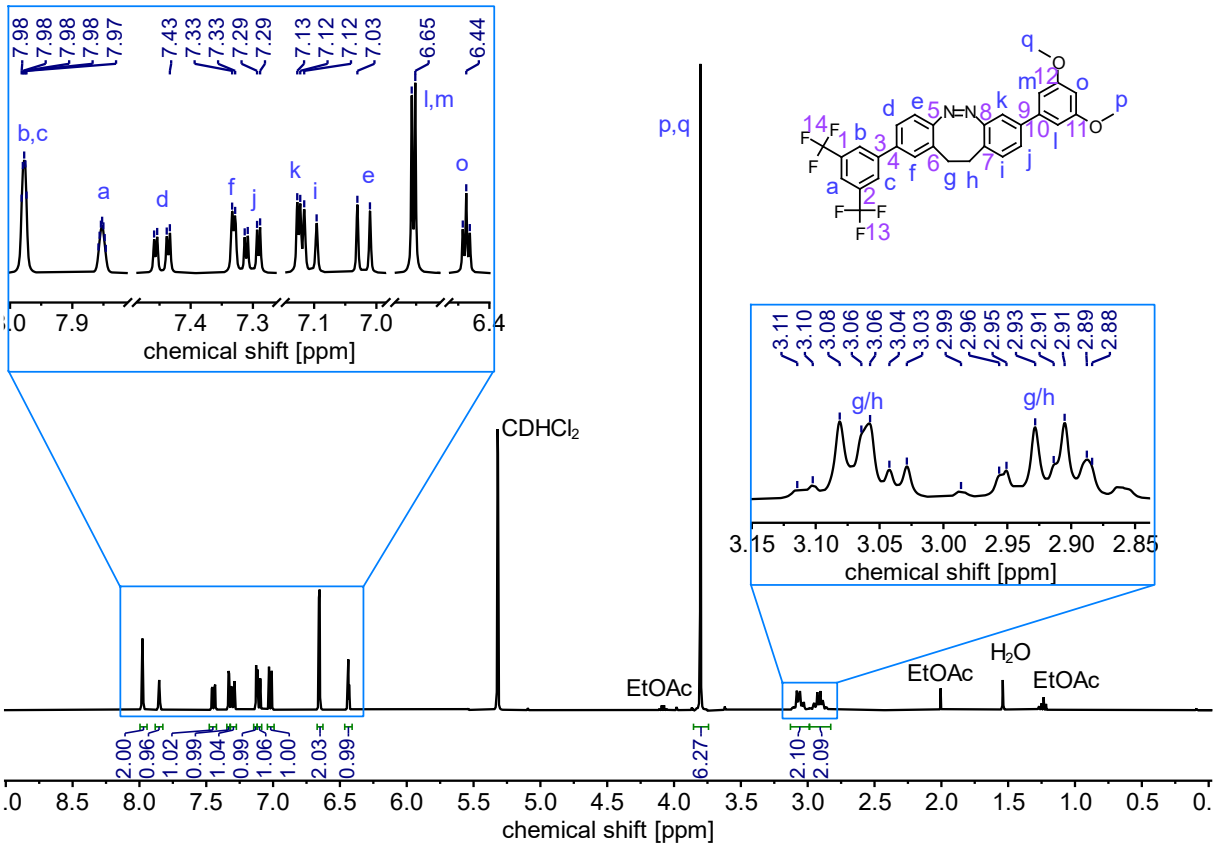

Figure S31. ^{1}H NMR (500 MHz, CD_2Cl_2, 298 K) of **9**.

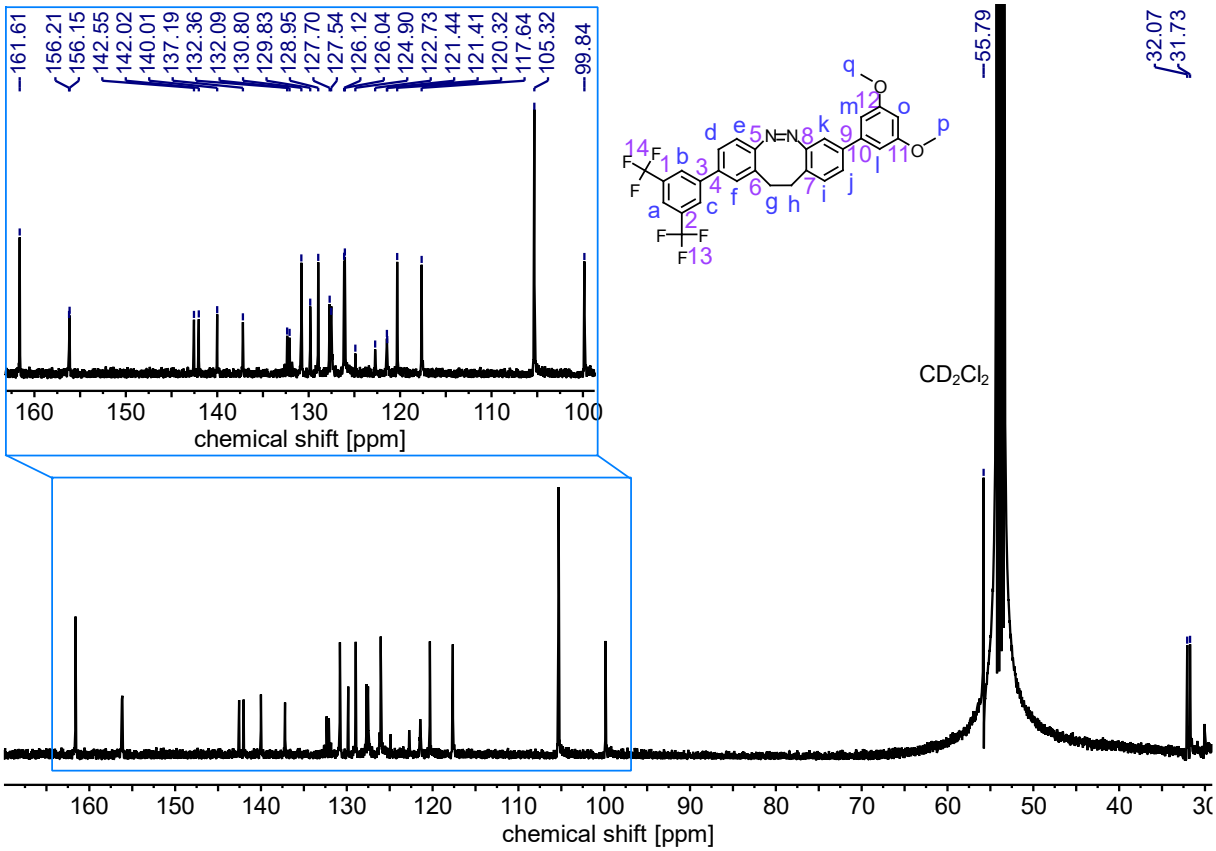

Figure S32. ^{13}C NMR (126 MHz, CD_2Cl_2, 298 K) of **9**.

S3. Screenings for reaction conditions

S3.1. Screening for 2,2'-dinitrodibenzyl (**D**) halogenation conditions

Screening for suitable reactions for the bromination of 2,2'-dinitrodibenzyl (D). Reactions were conducted in accordance with the procedure outlined in Section S2.1. Specific reaction conditions are detailed in Table S4. The bromination exhibits low selectivity for the desired meta-position (**S1**), with bromination occurring in the non-desired meta-position (**S3**) being unavoidable across all tested conditions.

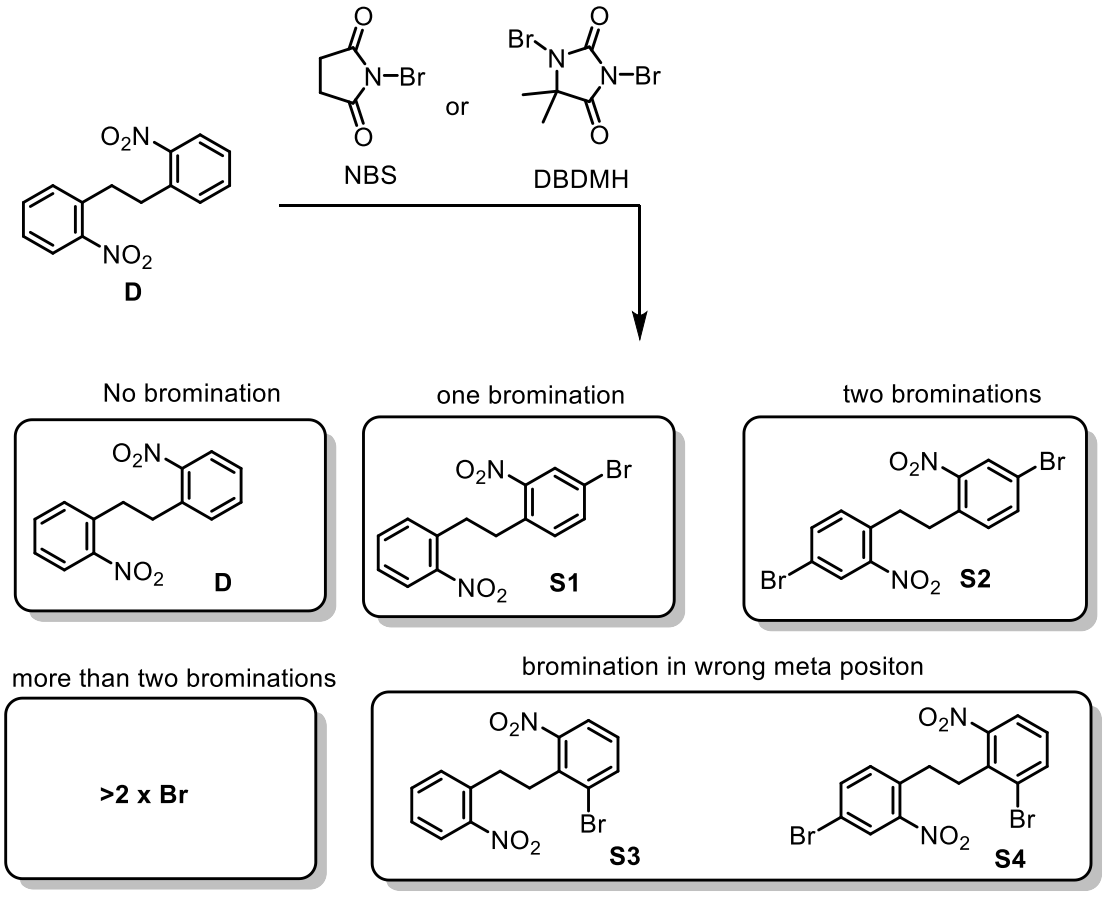

Figure S33. Bromination of **D** with either NBS (*N*-bromosuccinimide) or DBDMH (1,3-Dibromo-5,5-Dimethylhydantoin), resulting in mixtures of isomers.

Table S4. Identifying appropriate reaction conditions for the bromination of 2,2'-dinitrodibenzyl (**D**, Figure S33). Alterations to standard procedure #1 are highlighted in *italics*.

#	Conditions	Desired isomer S1	Isomer distribution
1	1.10 equiv. NBS H_2SO_4 r.t., 1 d	34%	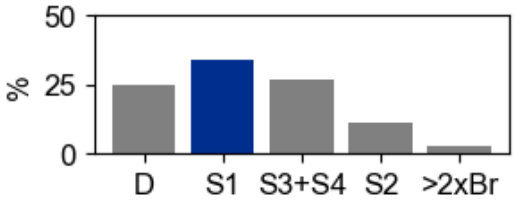
2	1.10 equiv. NBS H_2SO_4 r.t., *1 h*	11%	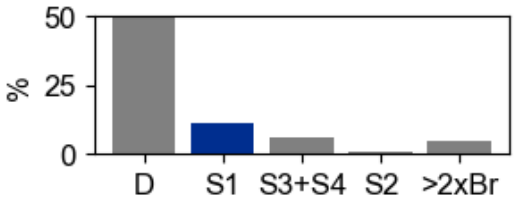
3	1.10 equiv. NBS *1.10 equiv. HOTf* *HOAc* r.t., *3 d*	3%	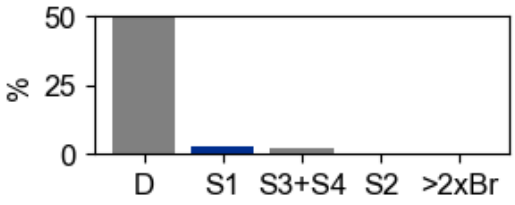
4	*0.45 equiv. DBDMH* H_2SO_4 r.t., 1 d	29%	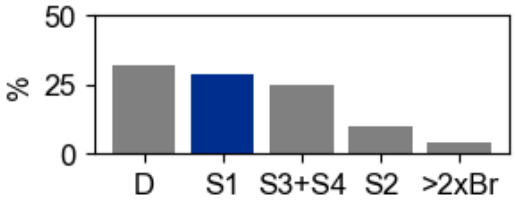
5	*0.50 equiv. DBDMH* H_2SO_4 r.t., *3 d*	25%	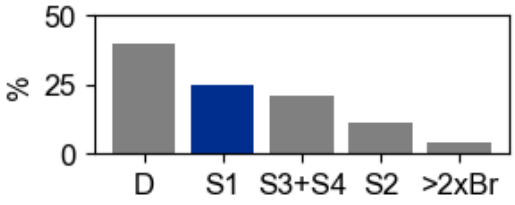
6	*0.75 equiv. DBDMH* H_2SO_4 r.t., *3 d*	27%	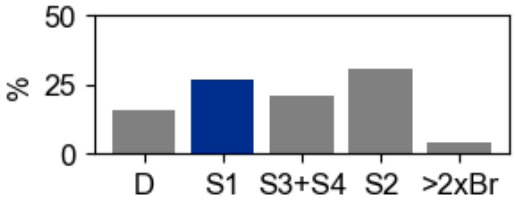

#	Reaction conditions	Desired isomer S1	Isomer distribution
7	*1.00 equiv. DBDMH* H_2SO_4 r.t., *3 d*	17%	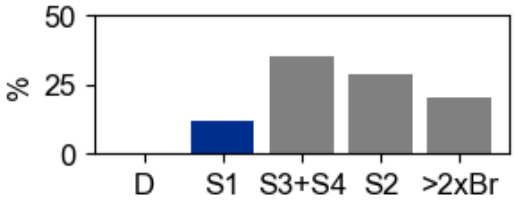
8	*1.00 equiv. DBDMH* *HOAc/H_2SO_4 10:1 (v/v)* r.t., *3 d*	10%	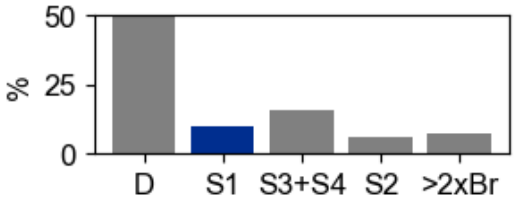
9	*1.00 equiv. DBDMH* *MeCN/H_2SO_4 10:1 (v/v)* r.t., *3 d*	19%	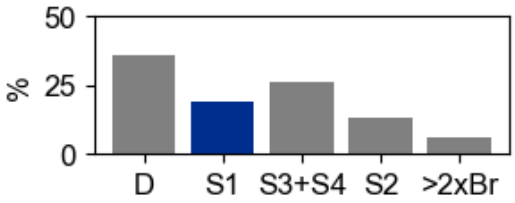
10	*1.00 equiv. DBDMH* *HOAc* r.t., *3 d*	0%	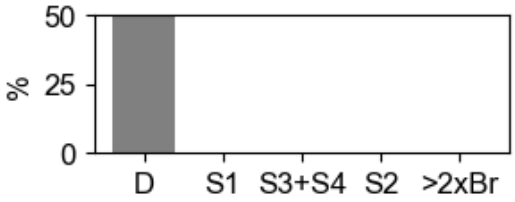

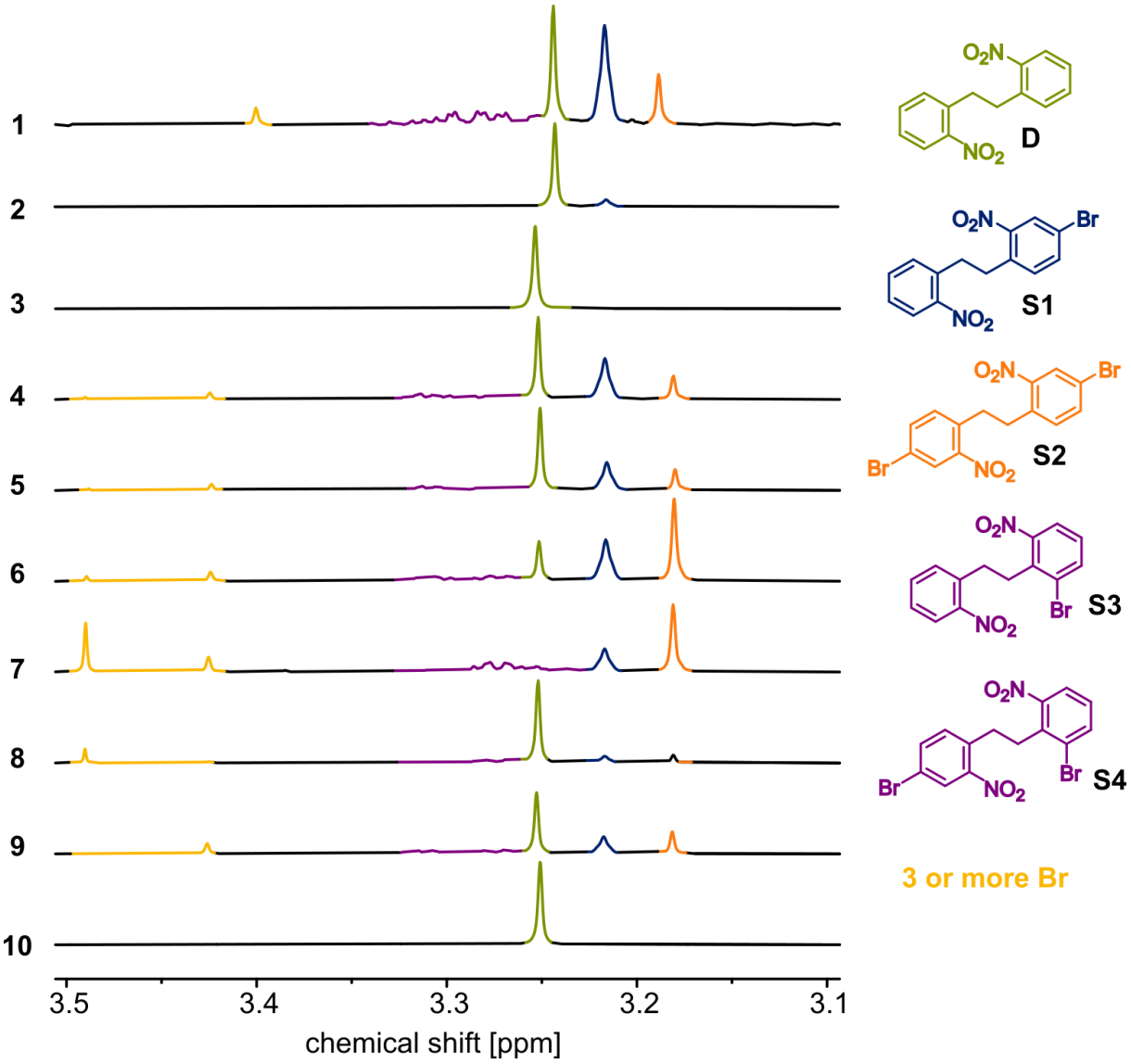

Figure S34. Partial ^{1}H NMR spectra (400 MHz, 298 K) of crude product mixtures of brominations #1−#10 (#1,#2: CD_2Cl_2; #4−#10: CD_3Cl; Table S4).

Screening for suitable reactions for the iodination of 2,2'-dinitrodibenzyl (D). Reactions were conducted following the procedure outlined in Section S2.2. Specific reaction conditions are detailed in Table S5. When compared to the bromination, the iodination shows notably enhanced selectivity for the preferred *meta* position (product **S8**), which meets the statistically anticipated 50%. This improvement is probably attributed to steric hindrance created by the larger iodine atom.

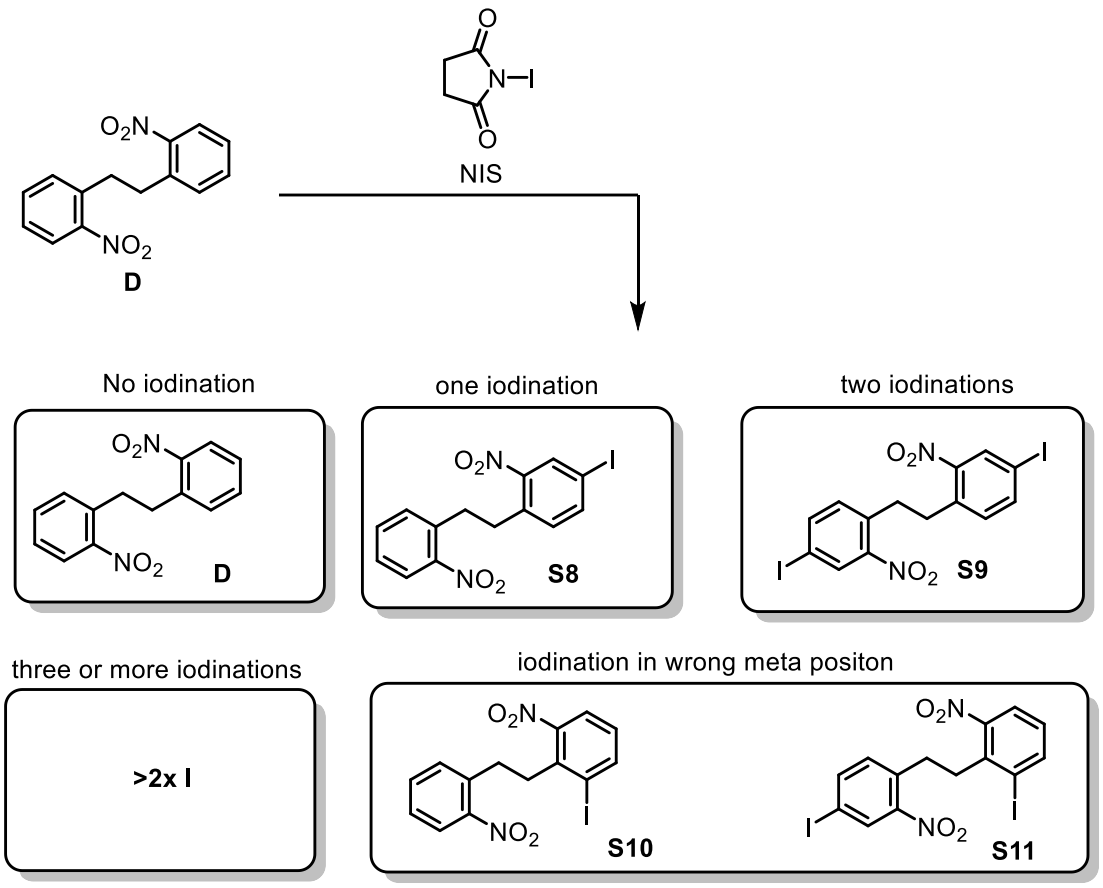

Figure S35. Iodination of **D** with NIS (*N*-iodosuccinimide), resulting in mixtures of isomers.

Table S5. Identifying appropriate reaction conditions for the iodination of 2,2'-dinitrodibenzyl (**D**, Figure S35). Alterations to standard procedure #1 are highlighted in *italics*.

#	Reaction conditions	Desired isomer S8	Isomer distribution
1	1.30 equiv. NIS H_2SO_4 r.t., 1 d	**52%**	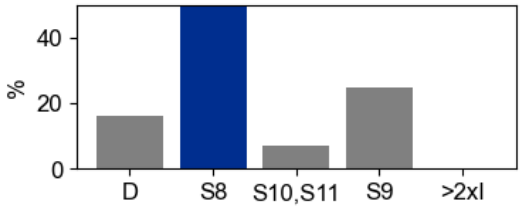
2	*1.10 equiv.* NIS H_2SO_4 r.t., 1 d	**48%**	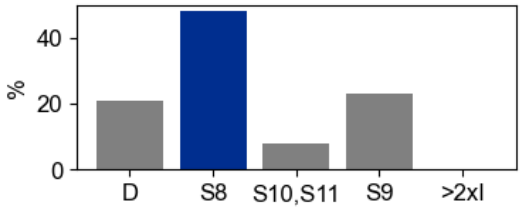

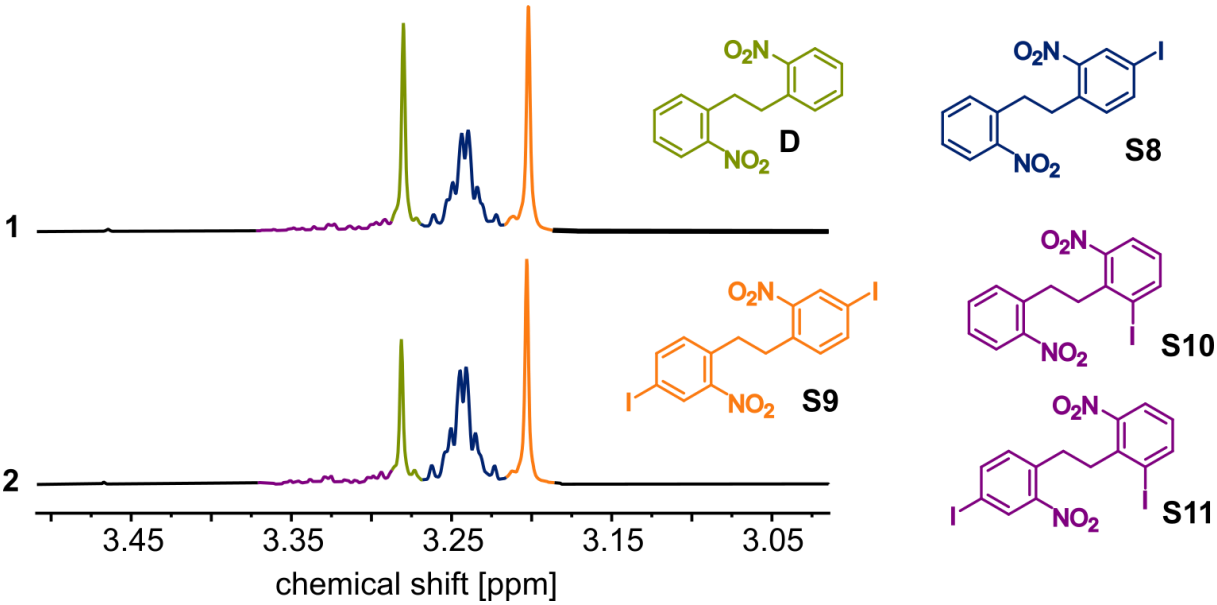

Figure S36. Partial ^{1}H NMR speactra (400 MHz, CD_2Cl_2, 298 K) of crude product mixtures of iodinations **1** and **2** (Table S5).

S3.2. Screening for nitroaryl reduction conditions

Screening for suitable reaction conditions for the reduction of dinitrobibenzyl **D** using sodium dithionite (Scheme S1) were carried out using 100 mg of **D** and the respective amounts of reagents as indicated in Table S6.

All solids were added to a screw cap vial and dichloromethane (4 mL) and water (4 mL) were added before the mixtures were stirred at the indicated temperatures for 12 hours. Due to the large difference in R_f values between **D** and **S5**, the reaction success was investigated using thin-layer chromatography (silica, dichrolomethane/ethyl acetate 4:1 (v/v), Figure S37). Excellent conversion of the nitro compound was observed for conditions #1, #4, and #9. Using paraquat as a phase transfer catalyst (Reaction conditions #4), resulted in clean conversion and no notably side products by TLC. Hence, the organic phase was separated, all volatiles removed on a rotary evaporator, and the residue investigated by ^{1}H NMR (Figure S38). This showed clean conversion to the product with only traces of the starting material remaining (7%) for reaction conditions #4.

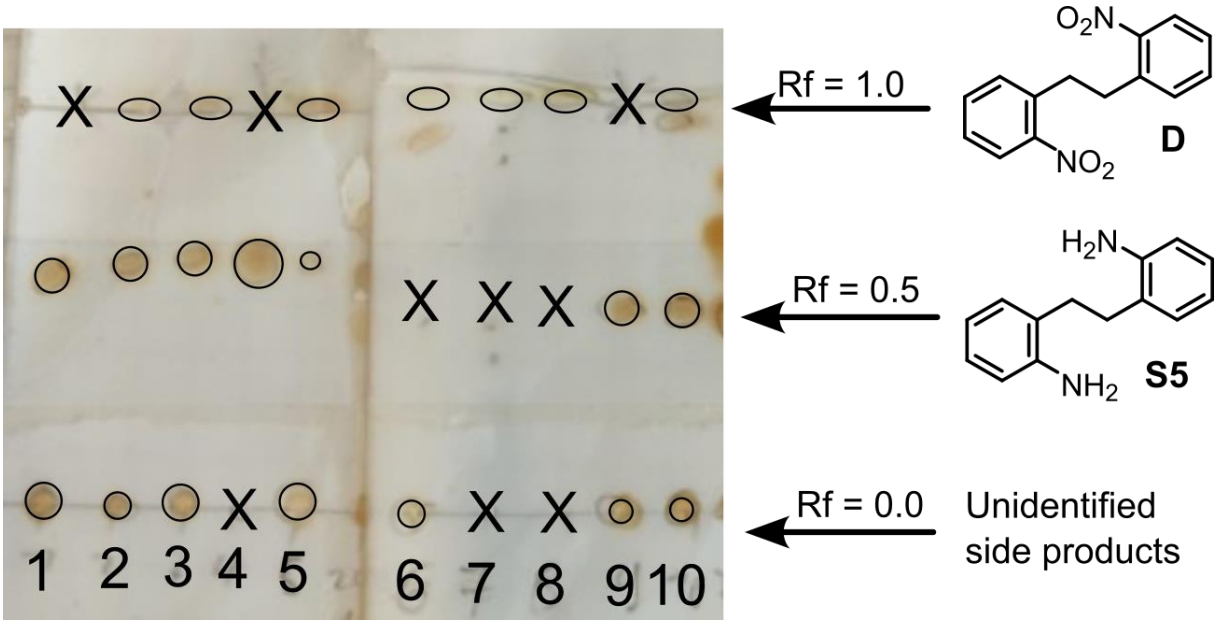

Figure S37. TLCs (silica, dichloromethane/ethyl acetate 4:1 (v/v)) of reactions #1−#10 for the reduction of **D** using sodium dithionite (Scheme S1, Table S6). Positions where no spot could be observed on the TLC are marked with an "X".

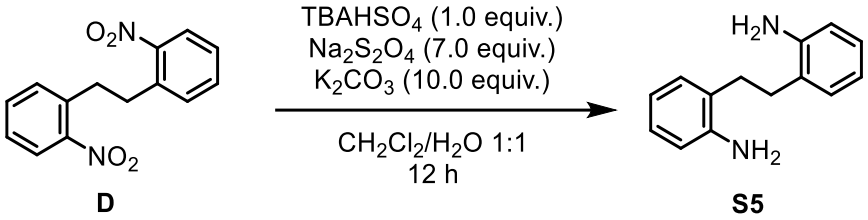

D **S5**

Scheme S1. Reduction of **D** using sodium dithionite. Reaction conditions are reported in Table S6.

Table S6. Identifying appropriate reaction conditions for the reduction of 2,2'-dinitrodibenzyl (**D**) using sodium dithionite (Scheme S1). Formation of **S5** and completeness of conversion were followed by TLC.

#	Deviation from standard conditions (Scheme S1)	Formation of S5	Complete Conversion
1	2.0 equiv. $TBAHSO_4$ 21 equiv. $Na_2S_2O_4$ 30 equiv. K_2CO_3	Yes	Yes
2	0.1 equiv. $TBAHSO_4$	Yes	No
3	none	Yes	No
4	0.1 equiv. Paraquat instead of $TBAHSO_4$	Yes	Yes
5	No K_2CO_3	Yes	No
6	1.0 equiv. HOAc instead of K_2CO_3	No	No
7	No phase transfer catalyst	No	No
8	No phase transfer catalyst No K_2CO_3	No	No
9	1.0 equiv. TBABr instead of $TBAHSO_4$	Yes	Yes
10	Temperature = 40°C	Yes	No

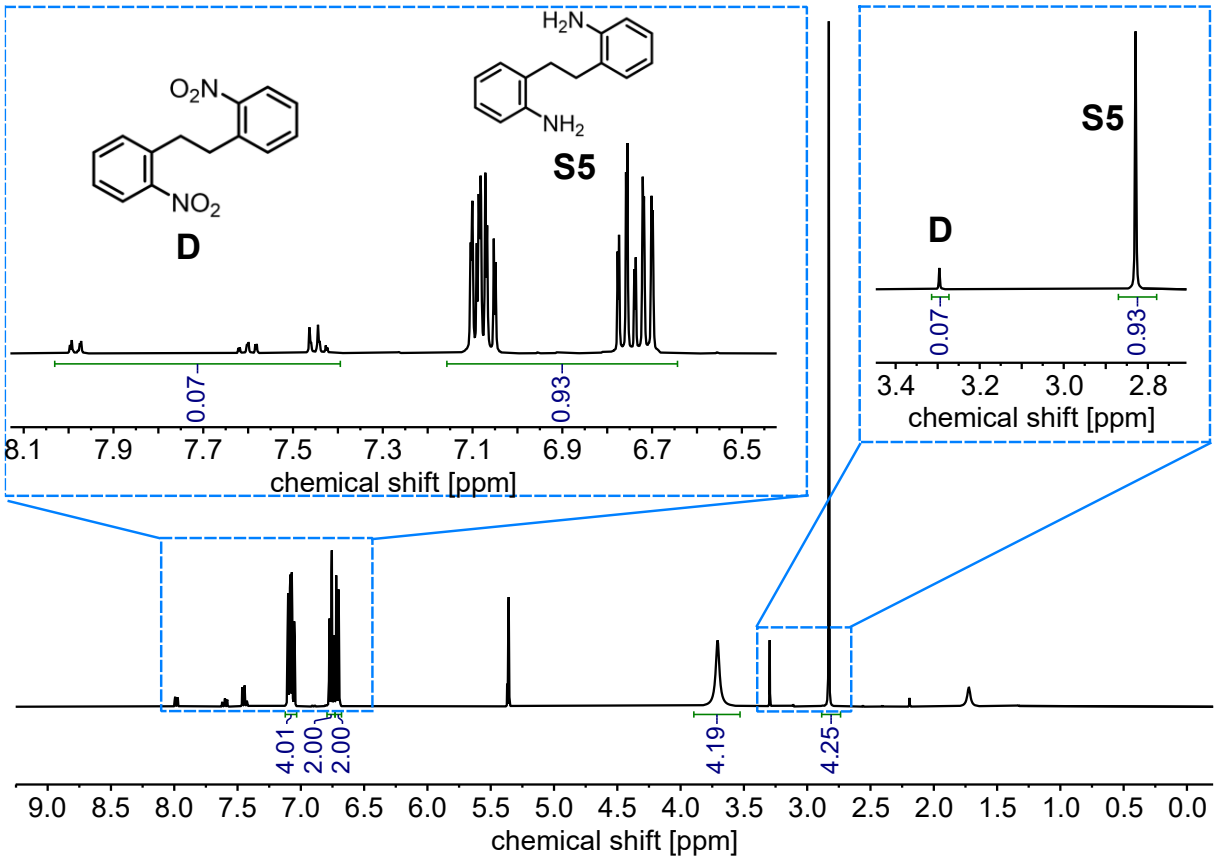

Figure S38. ^{1}H NMR spectrum (400 MHz, CD_2Cl_2, 298 K) of crude product mixture of reduction conditions #4 (Table S6).

S3.3. Screening for Suzuki cross-coupling catalysts

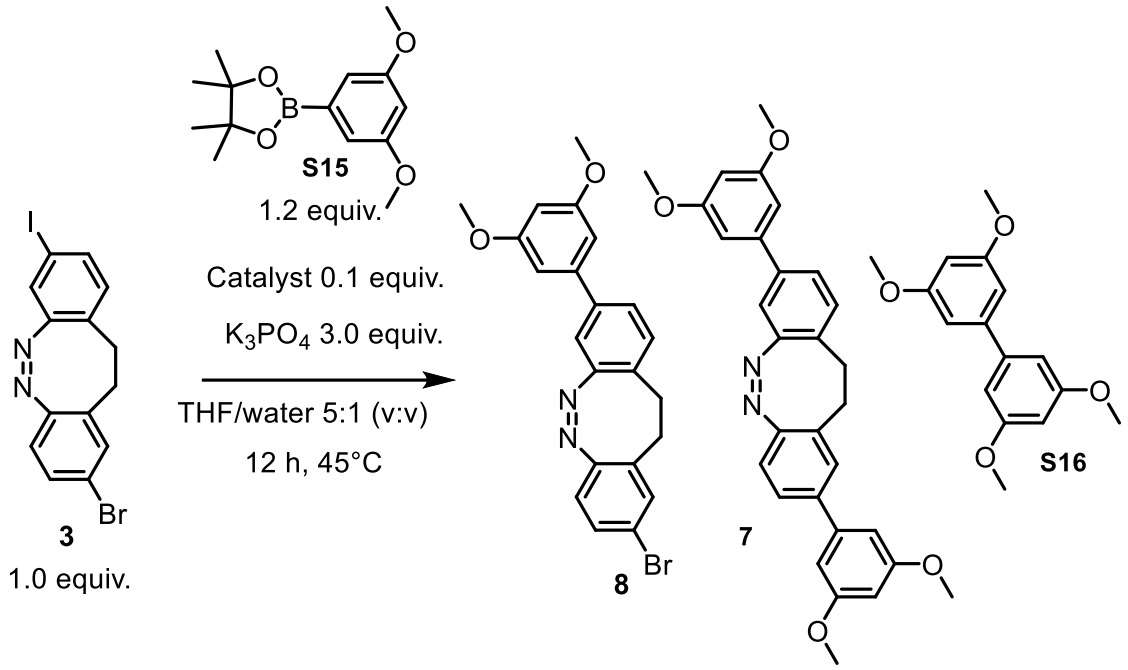

Figure S39. Screenings of suitable Suzuki cross-coupling catalysts for the selective asymmetric coupling of diazocine **3** with potential side products indicated. Reaction conditions are reported in Table S7.

Reaction mixtures for the screenings of suitable Suzuki cross-coupling catalysts (Figure S37) for the halogen selective coupling of diazocine **3** were prepared in a glove box, using diazocine **3** (10.0 mg, 24 µmol, 1.00 equiv.), dimethoxyphenyl boronic acid pinacol ester (7.7 mg, 29 µmol, 1.20 equiv.), and the respective catalyst (2.4 µmol, 0.10 equiv.). The reaction mixtures were taken out of the glove box and stirred at 45°C for 12 hours. Reaction conditions and their outcomes are detailed in Table S7. After the reaction was complete, water (5 mL) was added to each reaction vessel and the mixtures were extracted using ethyl acetate (3 × 5 mL). The organic phases were collected in pointed bottom flasks and all volatiles were removed by rotary evaporation.

To each of these flasks, 0.1 mL of a stock solution of 4-nitro-2,3,5,6-tetrachlorobenzene in deuterated dichloromethane (internal standard, 40.2 mmol mL^{-1}, 10.5 mg mL^{-1}) was added. The yellow solutions were transferred to NMR tubes. To ensure complete transfer, the flasks were rinsed with deuterated dichloromethane (3 × 0.15 mL), and these rinsing solutions were added to the respective NMR tubes. ^1H Q-NMRs were measured using a relaxation delay of D_1 =

30 ms. Integration of the internal standard was used to quantify the reaction products.

The weigh-ins for **3** had small deviations of 10.0±0.7 mg with the individual values noted for each of the six reaction vessels and the other reactants being scaled accordingly. The component percentages were scaled to the actual amount of starting material used (Table S7, right most column).

Internal standard:

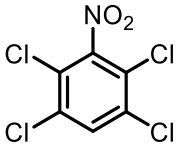

Table S7. Outcomes of the selective Suzuki cross-coupling on bromo/iodo diazocine **3** with different catalysts used (Figure S37). Relative yields determined by ^{1}H NMR are listed for all possible products and starting material **3**.

Catalyst	3 [%]	S15 [%]	8 [%]	7 [%]	S16 [%]	Scale [mg]
***t*Bu$_3$P-G4**	21	0	18	0	31	9.3
XPhos-G3	27	6	20	8	23	10.1
SPhos-G3	16	6	17	4	22	9.9
XantPhos-G3	22	35	18	6	3	10.4
DPPF-PdCl$_2$	0	0	66	4	2	10.0
(PPh$_3$)$_2$PdCl$_2$	4	0	63	15	3	9.7

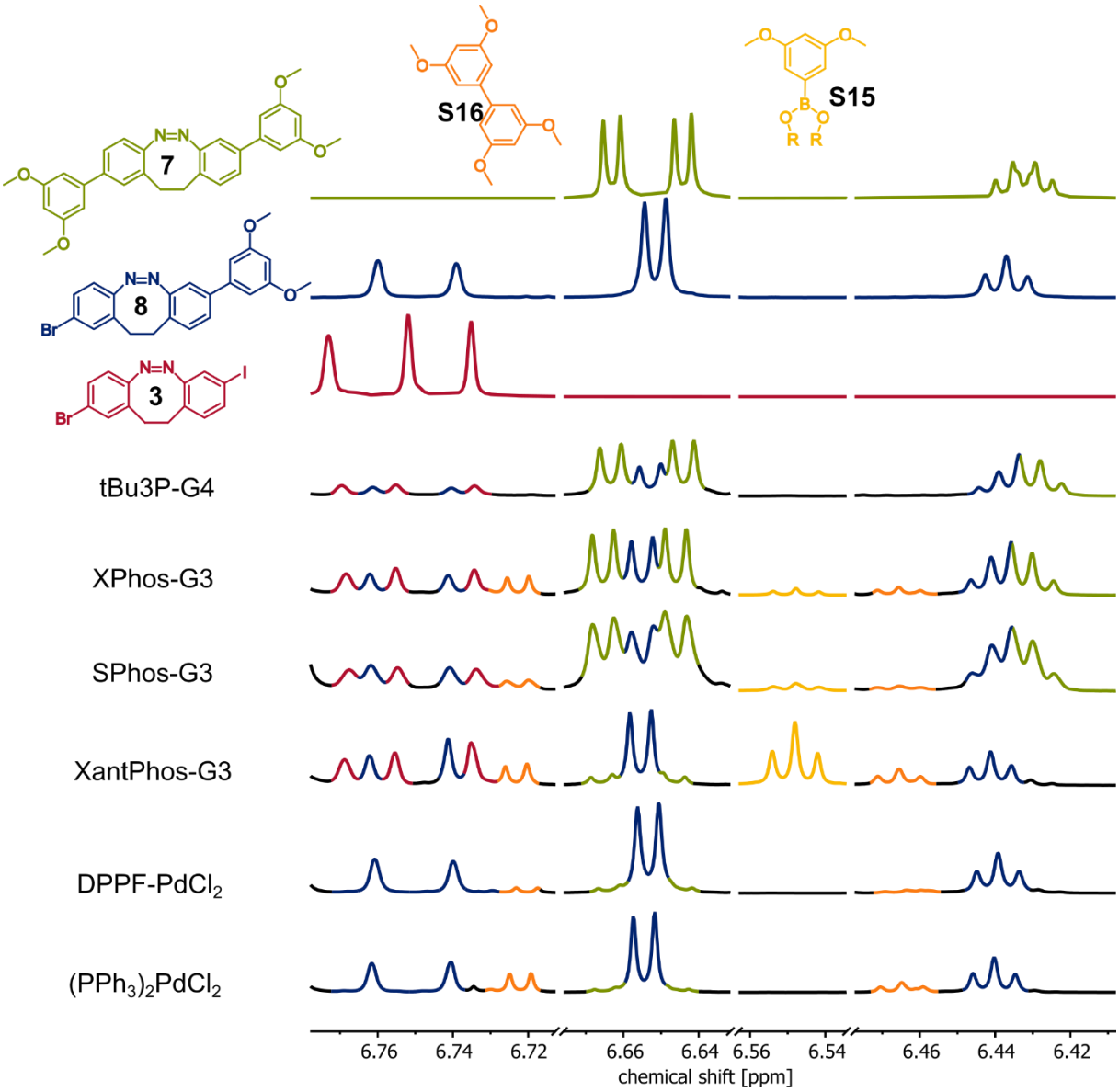

Figure S40. Partial ^{1}H Q-NMR spectra (400 MHz, CD_2Cl_2, 298 K) of reference compounds **7**, **8**, and **3**, as well as screening results (Table S7, top to bottom).

S4. Upscaling effects for the synthesis of bromo/iodo diazocine **3**

To evaluate the ease with which the synthetic route for the synthesis of asymmetric bromo-iodo diazocine can be scaled up, we compared the yields of reactions at different scales.

S4.1. Iodiation of 2,2'-dinitrodibenzyl (**D**)

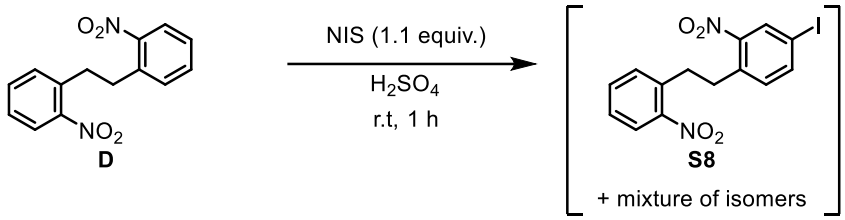

Iodination reactions of 2,2'-dinitrodibenzyl (**D**) were conducted as described in Section S2.2 at 8.1 mmol, 40.4 mmol, and 60.0 mmol scales with respect to starting material **D**. The yield (i.e., formation of the desired isomer **S8**) of this reaction remains notably consistent when increasing the reaction scale, making it unproblematic for scale-up (Figure S41).

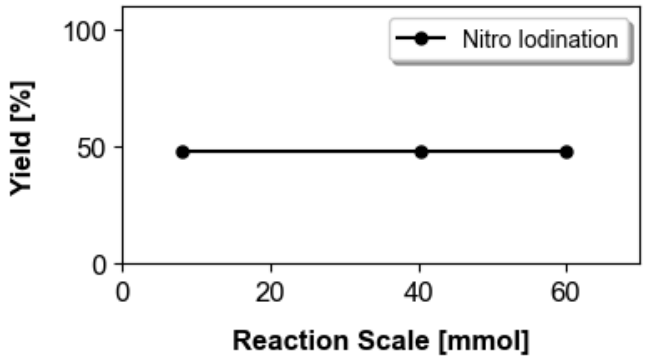

Figure S41. Plot of reaction scale in mmol against the isolated yield. Every data point represents an experimentally determined yield of desired isomer **S8**.

S4.2. Reduction of iodo-dinitrodibenzyl isomers

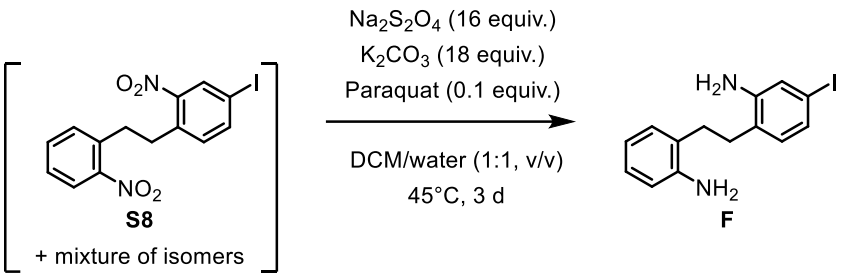

The reductions of the iodo-dinitro compound **S8** and its isomers were performed as described in Section S2.2 at 0.4 mmol, 4.0 mmol, 13.5 mmol, and 25 mmol scales concerning the isomeric mixture. The yield (based on the reduction and isolation of the desired isomer **S8**) decreased significantly as the scale increased (Figure S42), which is not uncommon in biphasic reactions. Therefore, this reduction step is the limiting factor when scaling up the synthetic route.

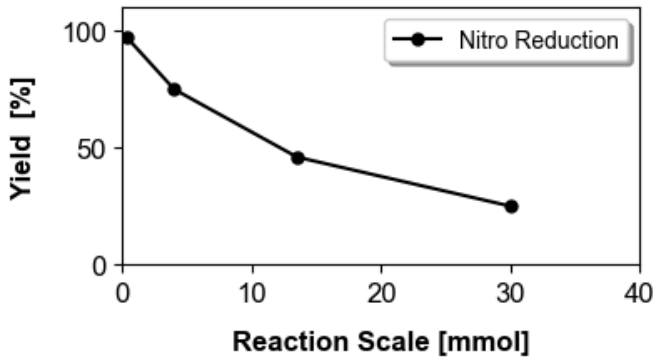

Figure S42. Plot of reaction scale in mmol against the isolated yield. Every data point represents an experimentally determined yield for desired isomer **F** with respect to its nitro precursor **S8**.

S4.3. Halogenation of iodo-diaminodibenzyl **F**

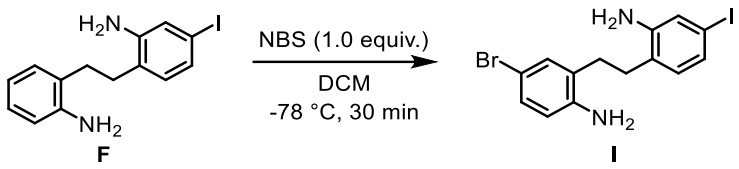

The halogenation reactions of iodo-diaminodibenzyl **F** were carried out as described in Section S2.5 at 0.3 mmol and 7.1 mmol scales concerning starting material **F**. The yield remained quantitative as the scale of the reaction increased (Figure S43). Larger scales may require a prolonged NBS addition period to ensure that the reaction mixture remains cold and that the reaction is selective. Nonetheless, this step poses no issues for the scale-up.

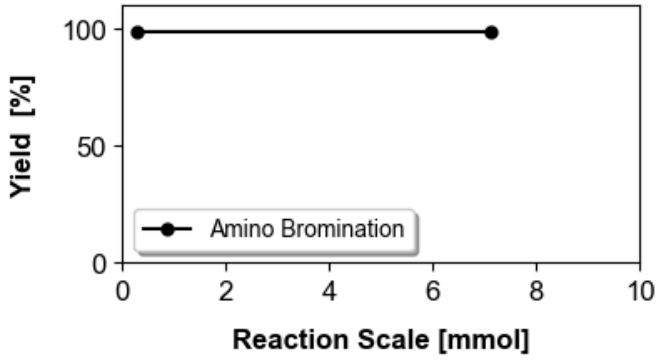

Figure S43. Plot of reaction scale in mmol against the isolated yield. Every data point represents an experimentally determined yield of **I**.

S4.4. Oxidative ring-closure

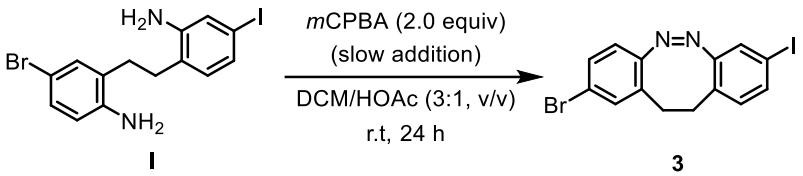

I **3**

The oxidative cyclisation reactions of bromo-iodo diaminodibenzyl **I** were conducted as described in Section S2.8 at 0.3 mmol, 2.4 mmol, and 5.6 mmol scales concerning starting material **I**. The yield slightly increased for larger scales (Figure S44), as the increased volumes may aid in maintaining a constant oxidant addition rate. This reaction appears to benefit from the scale-up.

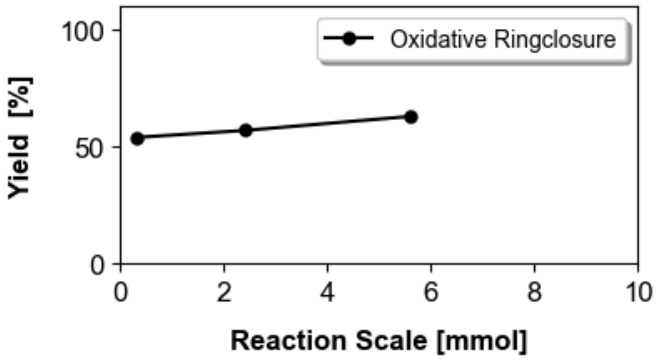

Figure S44. Plot of reaction scale in mmol against the isolated yield. Every data point represents an experimentally determined yield for **3**.

S5. Details on the chromatographic separation of dianiline isomers

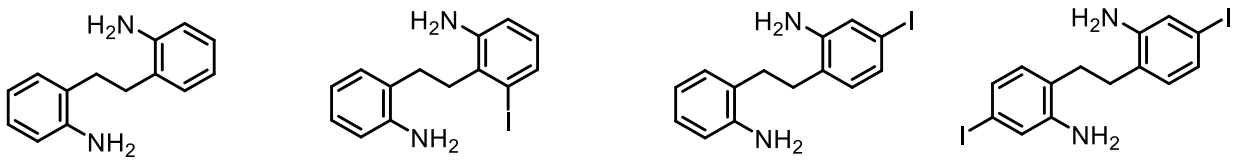

Figure S45. Isomers contained in the mixture, which were separated in the following example.

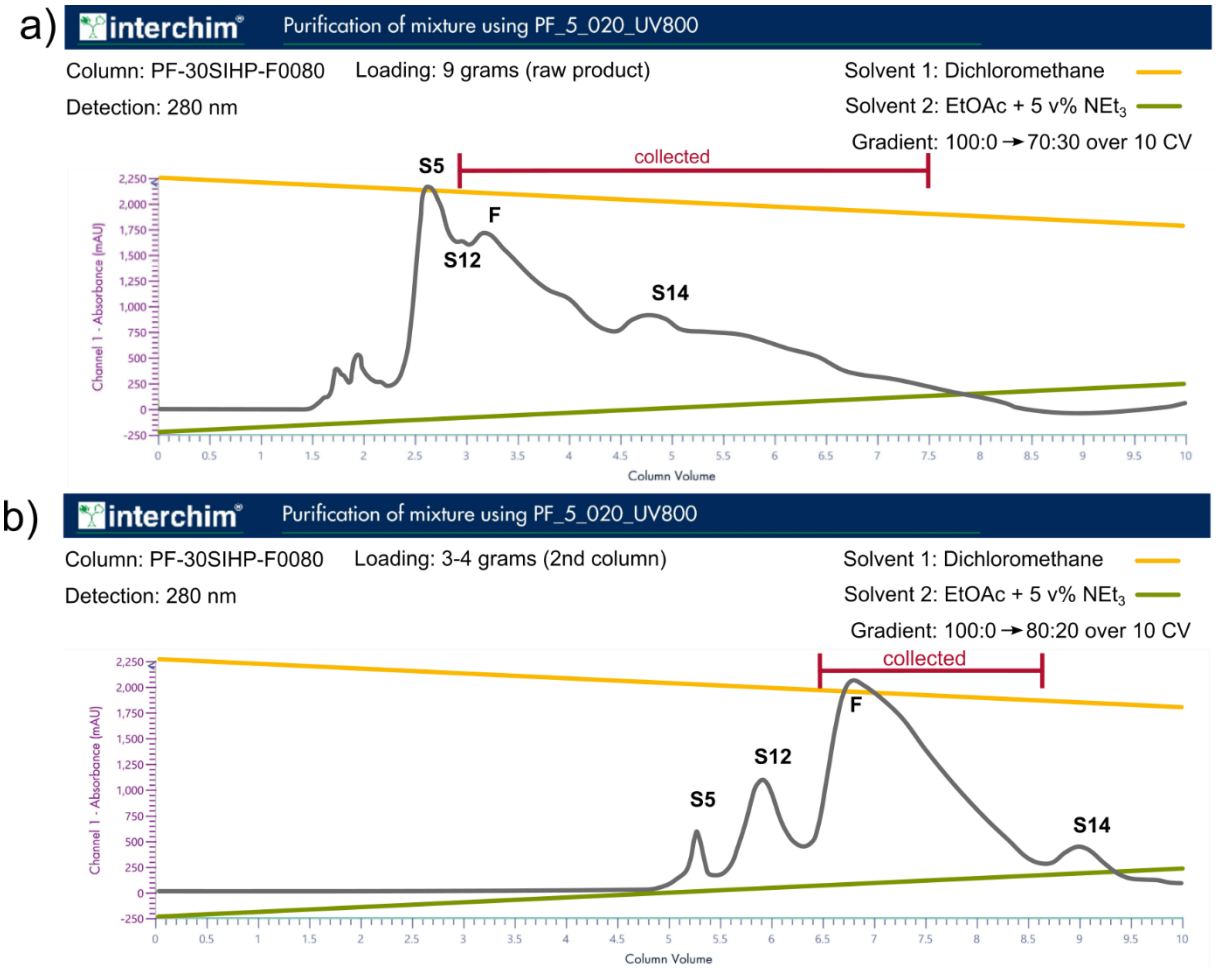

Figure S46. a) Chromatogramm (280 nm) for the automated chromatographic separation of the diaminodibenzyl mixture (**Figure S45**) All fractions showing the product TLC spot were collected and subjected to a second round of separation. b) Chromatogramm (280 nm) for the second run of automated chromatographic separation of mixture of dianilines. A total of 2.0 g (21.8% yield, 5.91 mmol) of dianiline **F** were isolated.

S6. Photochemical characterization

S6.1. General procedures for the Illumination of different types of samples

***In situ* illumination (UV-vis).** Samples were irradiated perpendicularly to the measurement axis within the UV-vis spectrometer using optical fibres connected to an LED light source (see Section S1. General Procedures). To facilitate the irradiation of the cuvettes perpendicularly to the spectrometer's measurement axis, a hole matching the diameter of the quartz glass fibre was drilled at the centre of the Teflon stopper used to seal the UV-vis cuvettes. This configuration enabled the connection of an optical fibre to the cuvette, allowing the irradiation of the samples from above.

Figure S47. Pictures of the *in-situ* illumination setup showing fibre collimated LED-sources connected to the cuvette with open (left) and closed measurement chamber (right).

***Ex-situ* illumination (NMR).** Portable, in-house built light sources fitted with custom 3D-printed adapters were used to irradiate NMR samples. After the irradiation was completed, the samples were promptly subjected to measurement.

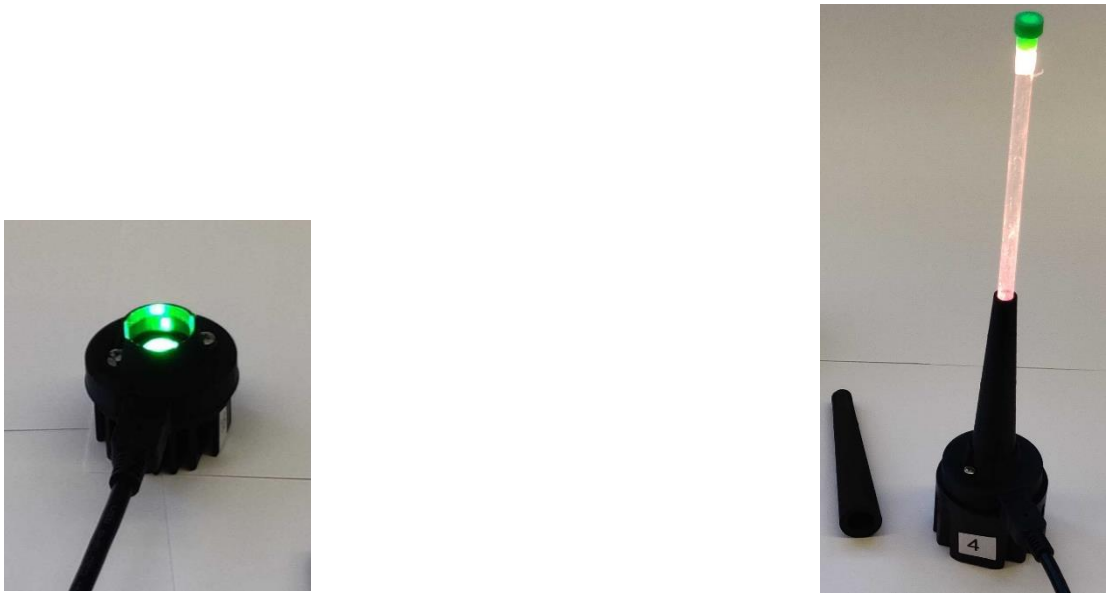

Figure S48. Pictures of the *ex-situ* illumination setup with USB-powered built-in-house light sources using commercial LED chips with 3D printed adaptors for 5 mm NMR-tubes.

Determination of the photostationary state (PSS). The photostationary states of the photoswitches were determined using ^{1}H NMR spectroscopy. For this purpose, two signals corresponding to the same proton were integrated and the PSS were calculated based on the resulting integral ratios. To ensure the highest accuracy, well-separated and clearly resolved signals were selected for analysis as recommended in the literature.[8,9]

S6.2. Photoswitching (UV-vis)

S6.2.1. Diazocine **A**

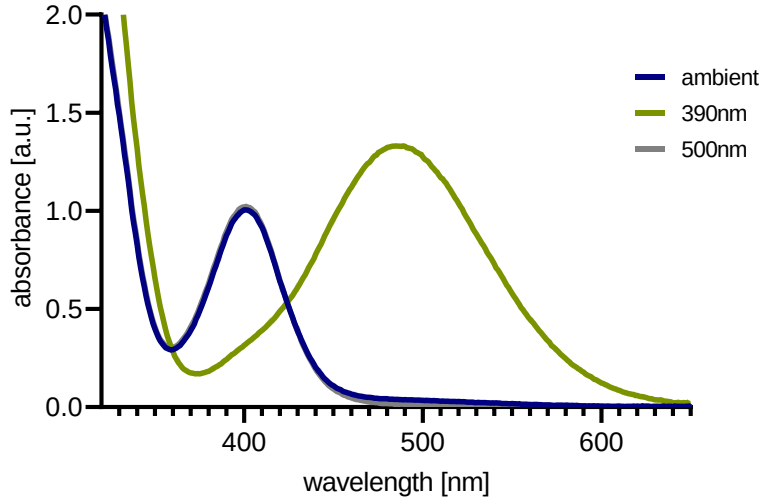

Figure S49. UV-vis spectra of diazocine **A** (0.8 mM, CH_2Cl_2, 25 °C)after irradiation with different wavelengths (390 nm: 1 min and 500 nm: 1 min).

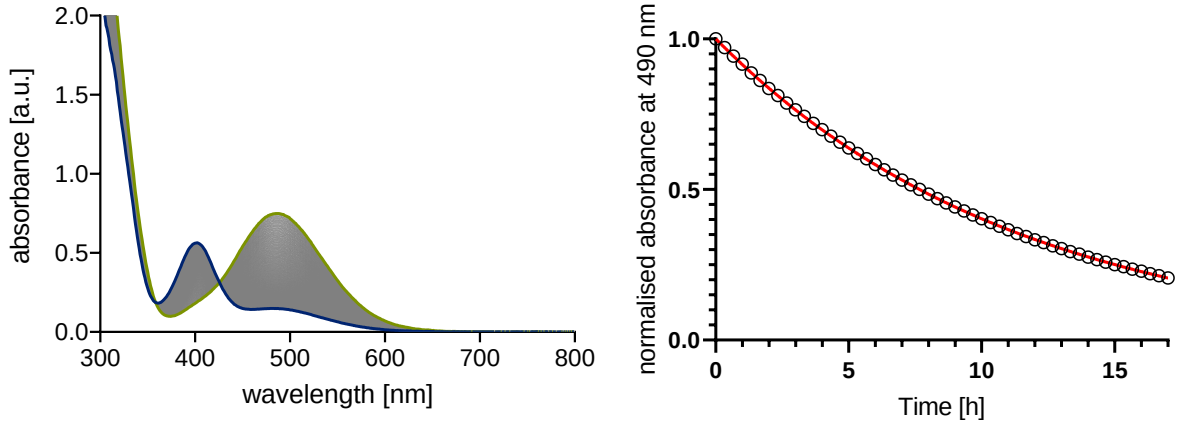

Figure S50. Thermal relaxation of diazocine **A** (0.8 mM, CH_2Cl_2, 25 °C). Left: UV-vis spectra of **A** measured every 5 minutes in the dark after irradiating with 390 nm. Right: Change in absorption $(A_t - A_\infty) \cdot (A_0 - A_\infty)^{-1}$ plotted over time *t* following thermal relaxation of **A** to provide its half-live $\tau_{½}$ = 8.0 h.

S6.2.2. Dibromo diazocine **1**

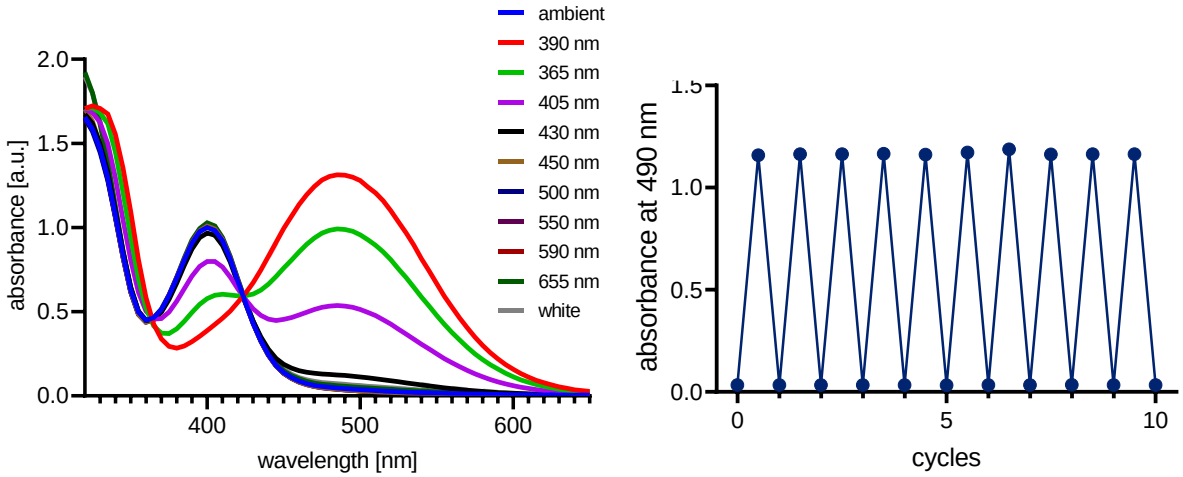

Figure S51. Left: UV-vis spectra of dibromo diazocine **1** (1.3 mM, CH_2Cl_2, 25 °C) after irradiation with different wavelengths (365−430 nm: 1 min; 450 nm−655 nm and white light: 20 s). Right: Absorption of dibromo diazocine **1** (1.3 mM, CH_2Cl_2, 25 °C) at 490 nm after alternating irradiations with 390 nm (1 min) and 500 nm light (20 s, right).

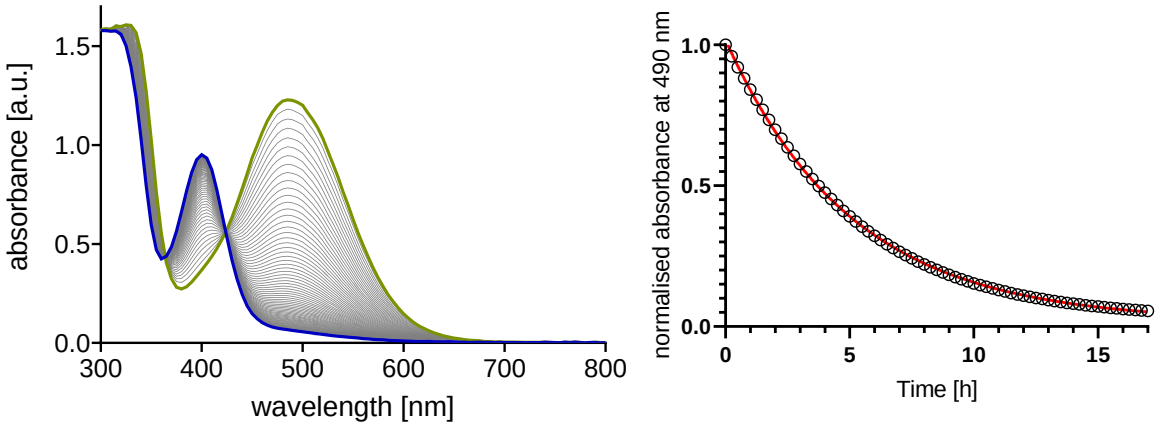

Figure S52. Thermal relaxation of dibromo diazocine **1** (1.2 mM, CH_2Cl_2, 25 °C). Left: UV-vis spectra of **1** measured every 15 minutes in the dark after irradiating with 390 nm. Right: Change in absorption $(A_t - A_\infty) \cdot (A_0 - A_\infty)^{-1}$ plotted over time *t* following thermal relaxation of 1 to provide its half-live $\tau_{½}$ = 3.5 h.

S6.2.3. Diiodo diazocine **2**

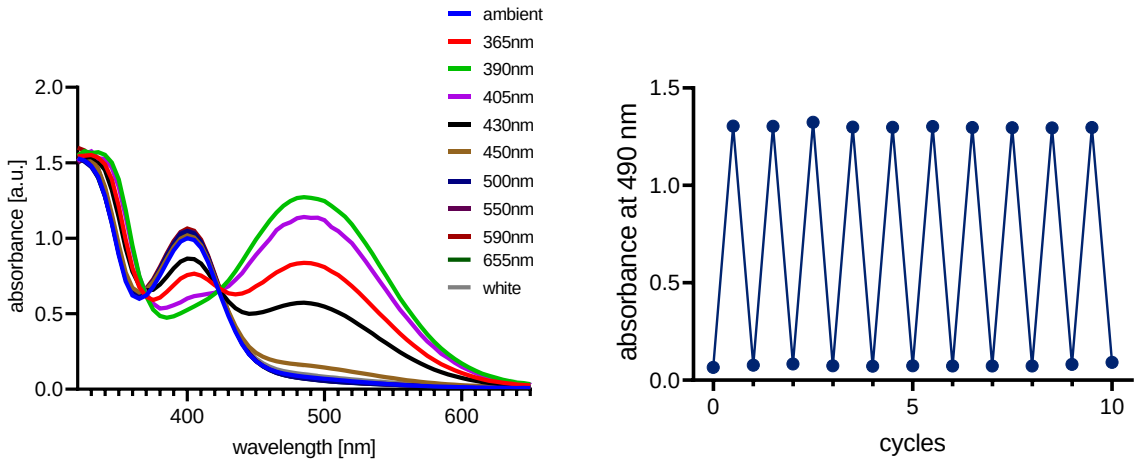

Figure S53. Left: UV-vis spectra of diiodo diazocine **2** (1.5 mM, CH_2Cl_2, 25 °C) after irradiation with different wavelengths (365−430 nm: 1 min; 450 nm−655 nm and white light: 20 s). Right: Absorption of **2** (1.5 mM, CH_2Cl_2, 25 °C) at 490 nm after alternating irradiations with 390 nm (1 min) and 500 nm light (20 s, right).

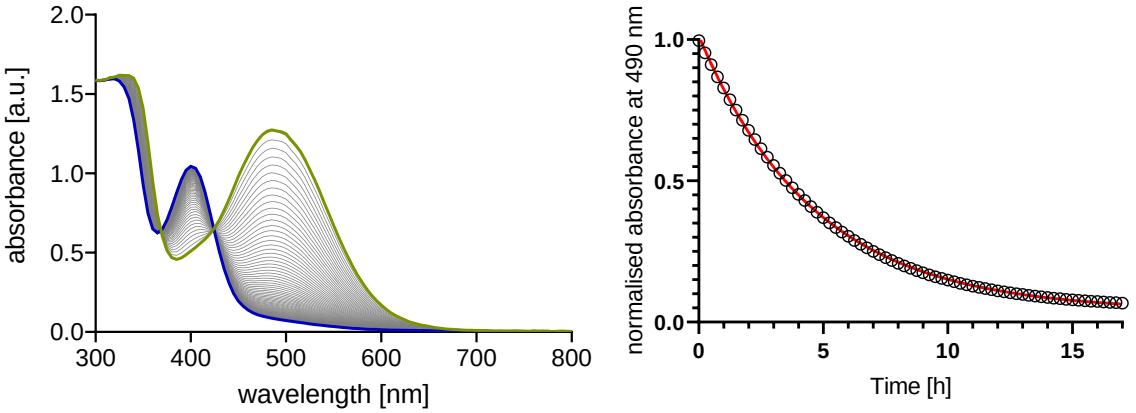

Figure S54. Thermal relaxation of diiodo diazocine **2** (1.5 mM, CH_2Cl_2, 25 °C). Left: UV-vis spectra of **2** measured every 15 minutes in the dark after irradiating with 390 nm light. Right: Change in absorption $(A_t - A_\infty) \cdot (A_0 - A_\infty)^{-1}$ plotted over time t following thermal relaxation of **2** to provide its half-live $\tau_{½}$ = 3.2 h.

S6.2.4. Bromo/iodo diazocine **3**

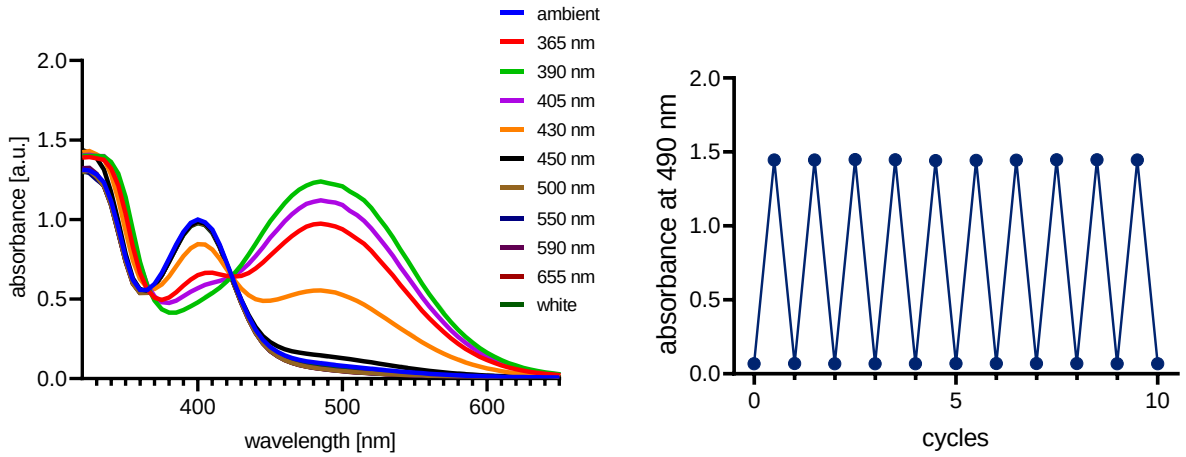

Figure S55. Left: UV-vis spectra of bromo/iodo diazocine **3** (1.3 mM, CH_2Cl_2, 25 °C) after irradiation with different wavelengths (365−430 nm: 1 min; 450 nm−655 nm and white light: 20 s). Right: Absorption of bromo/iodo diazocine **3** (1.3 mM, CH_2Cl_2, 25 °C) at 490 nm after alternating irradiations with 390 nm (1 min) and 500 nm light (20 s, right).

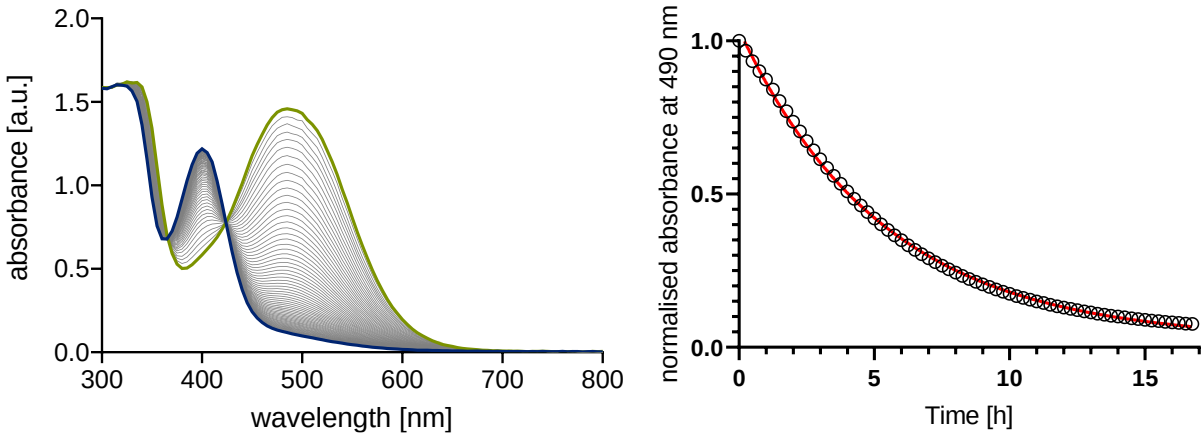

Figure S56. Thermal relaxation of bromo/iodo diazocine **3** (1.3 mM, CH_2Cl_2, 25 °C). Left: UV-vis spectra of **3** measured every 15 minutes in the dark after irradiating with 390 nm. Right: Change in absorption $(A_t - A_\infty) \cdot (A_0 - A_\infty)^{-1}$ plotted over time t following thermal relaxation of **3** to provide its half-live $\tau_{½}$ = 3.7 h.

S6.2.5. Bis(trifluoromethyl)phenyl) diazocine **4**

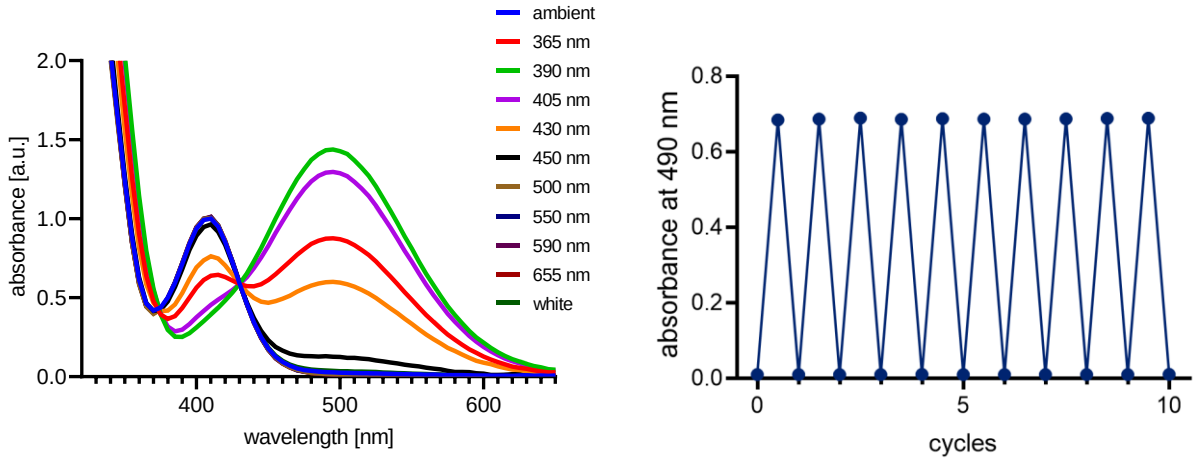

Figure S57. Left: UV-vis spectra of bis(trifluoromethyl)phenyl) diazocine **4** (1.0 mM, CH_2Cl_2, 25 °C) after irradiation with different wavelengths (365−430 nm: 1 min; 450 nm−655 nm and white light: 20 s). Right: Absorption of bis(trifluoromethyl)phenyl) diazocine **4** (1.0 mM, CH_2Cl_2, 25 °C) at 490 nm after alternating irradiations with 390 nm (1 min) and 500 nm light (20 s, right).

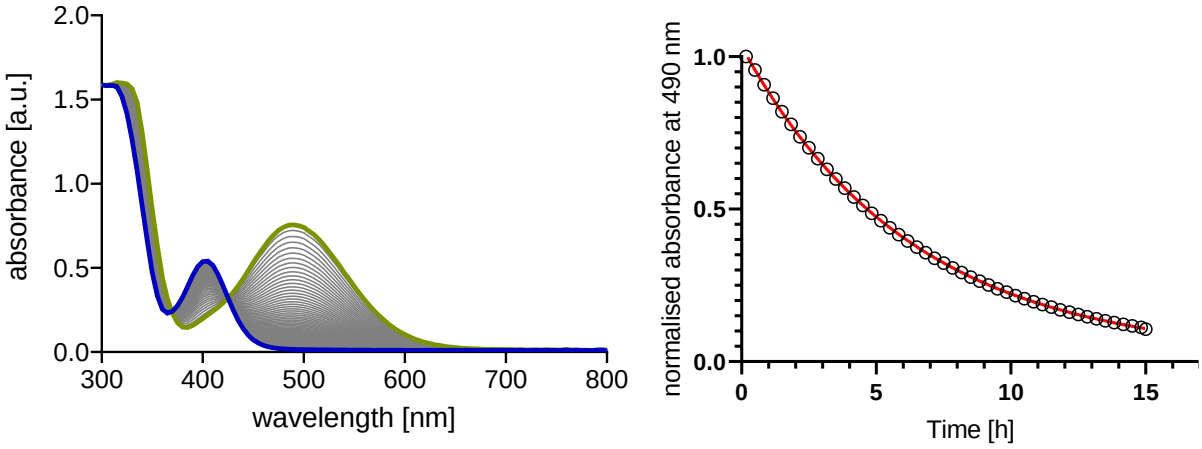

Figure S58. Thermal relaxation of bis(trifluoromethyl)phenyl) diazocine **4** (1.0 mM, CH_2Cl_2, 25 °C). Left: UV-vis spectra of **4** measured every 15 minutes in the dark after irradiating with 390 nm. Right: Change in absorption $(A_t - A_\infty) \cdot (A_0 - A_\infty)^{-1}$ plotted over time t following thermal relaxation of **4** to provide its half-live $\tau_{½}$ = 4.4 h.

S6.2.6. Diphenyl diazocine **5**

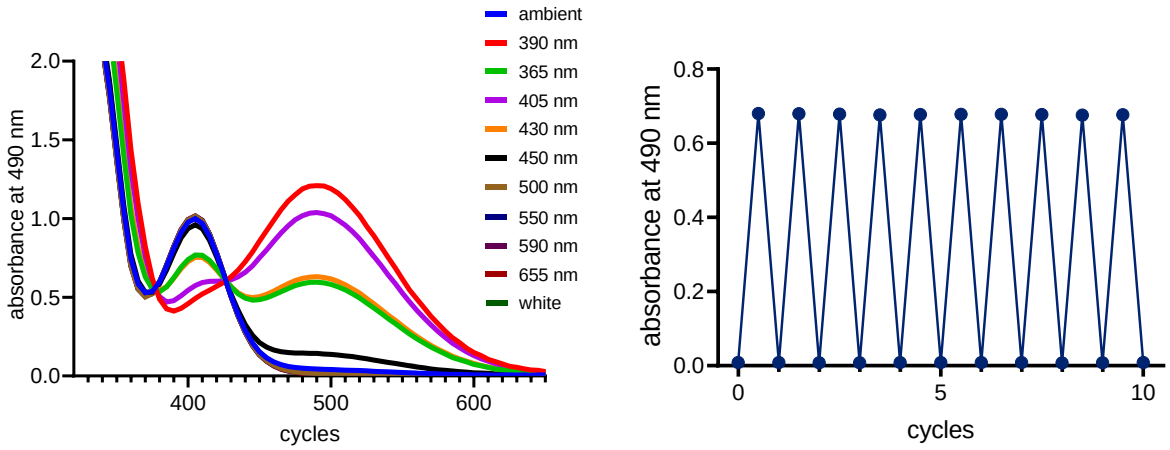

Figure S59. Left: UV-vis spectra of diphenyl diazocine **5** (1.0 mM, CH_2Cl_2, 25 °C) after irradiation with different wavelengths (365−430 nm: 1 min; 450 nm−655 nm and white light: 20 s). Right: Absorption of diphenyl diazocine **5** (1.0 mM, CH_2Cl_2, 25 °C) at 490 nm after alternating irradiations with 390 nm (1 min) and 500 nm light (20 s, right).

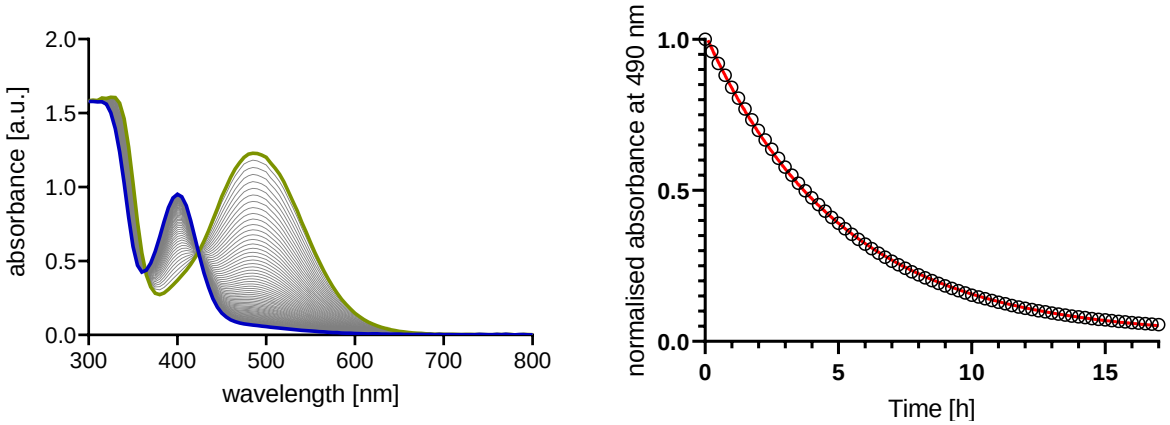

Figure S60. Thermal relaxation of diphenyl diazocine **5** (1 mM, CH_2Cl_2, 25 °C). Left: UV-vis spectra of **5** measured every 15 minutes in the dark after irradiating with 390 nm. Right: Change in absorption $(A_t - A_\infty) \cdot (A_0 - A_\infty)^{-1}$ plotted over time *t* following thermal relaxation of **5** to provide its half-live $\tau_{½}$ = 3.7 h.

S6.2.7. Ditoluyl diazocine **6**

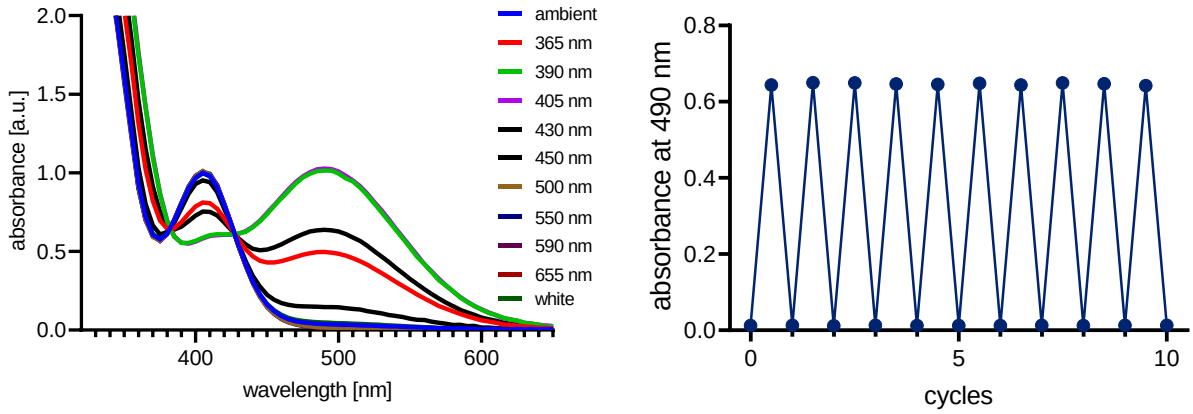

Figure S61. Left: UV-vis spectra of ditoluyl diazocine **6** (0.8 mM, CH_2Cl_2, 25 °C) after irradiation with different wavelengths (365−430 nm: 1 min; 450 nm−655 nm and white light: 20 s). Right: Absorption of ditoluyl diazocine **6** (0.8 mM, CH_2Cl_2, 25 °C) at 490 nm after alternating irradiations with 390 nm (1 min) and 500 nm light (20 s, right).

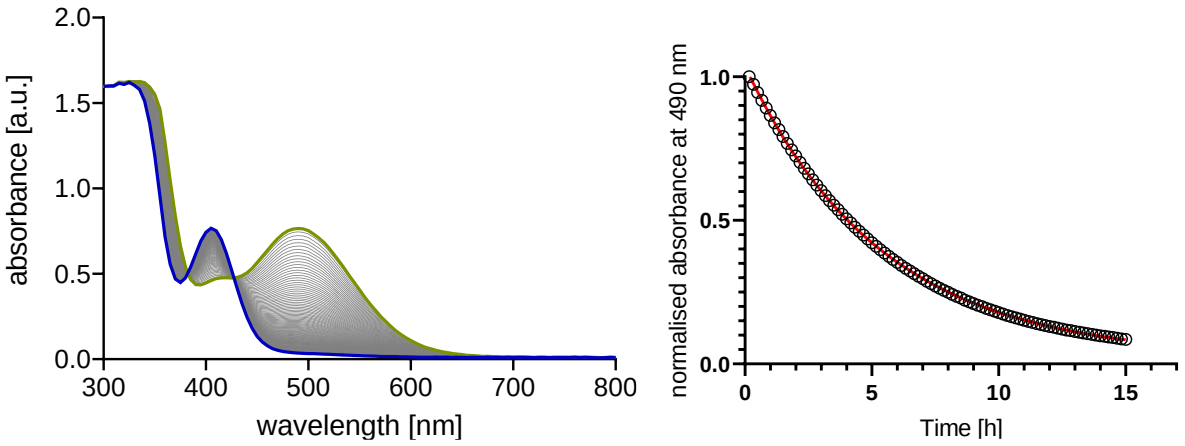

Figure S62. Thermal relaxation of ditoluyl diazocine **6** (0.8 mM, CH_2Cl_2, 25 °C). Left: UV-vis spectra of **6** measured every 15 minutes in the dark after irradiating with 390 nm. Right: Change in absorption $(A_t - A_\infty) \cdot (A_0 - A_\infty)^{-1}$ plotted over time *t* following thermal relaxation of **6** to provide its half-live $\tau_{½}$ = 3.7 h.

S6.2.8. Bis(3,5-dimethoxyphenyl) diazocine **7**

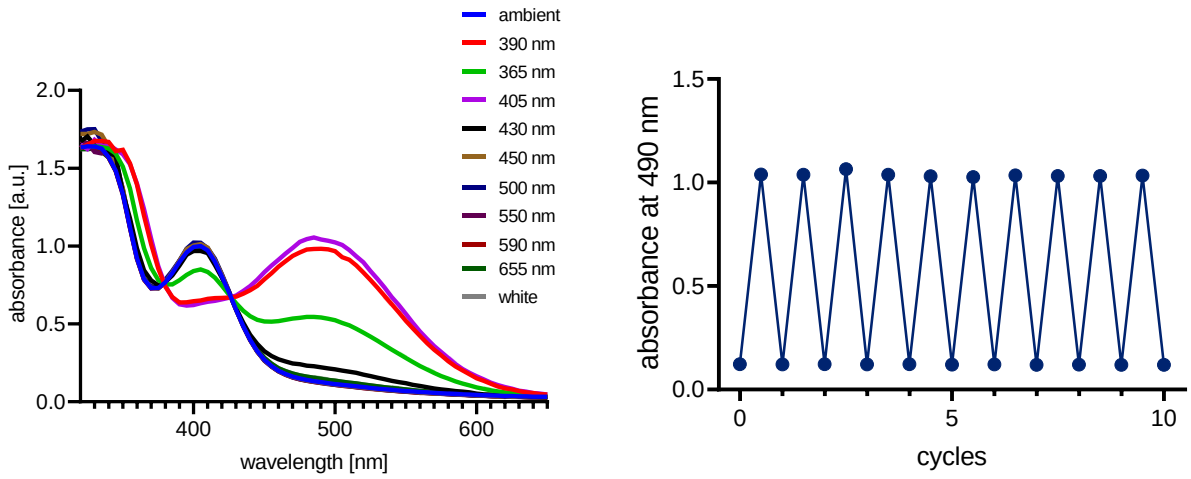

Figure S63. Left: UV-vis spectra of bis(3,5-dimethoxyphenyl) diazocine **7** (1 mM, CH_2Cl_2, 25 °C) after irradiation with different wavelengths (365−430 nm: 1 min; 450 nm−655 nm and white light: 20 s). Right: Absorption of bis(3,5-dimethoxyphenyl) diazocine **7** (1 mM, CH_2Cl_2, 25 °C) at 490 nm after alternating irradiations with 390 nm (1 min) and 500 nm light (20 s, right).

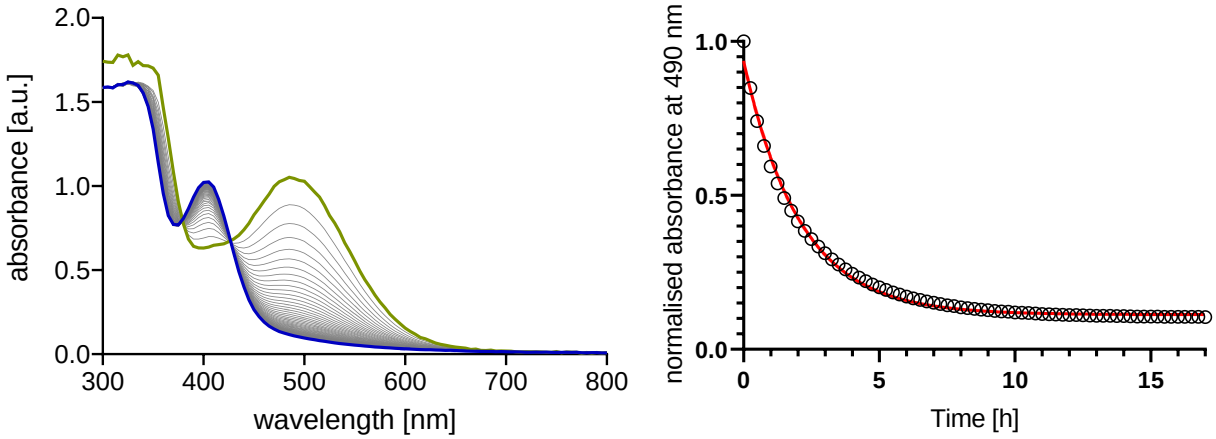

Figure S64. Thermal relaxation of bis(3,5-dimethoxyphenyl) diazocine **7** (1 mM, CH_2Cl_2, 25 °C). Left: UV-vis spectra of **7** measured every 15 minutes in the dark after irradiating with 390 nm. Right: Change in absorption $(A_t - A_\infty) \cdot (A_0 - A_\infty)^{-1}$ plotted over time t following thermal relaxation of **7** to provide its half-live $\tau_{1/2}$ = 1.4 h.

S6.2.9. Bromo/3,5-dimethoxyphenyl diazocine **8**

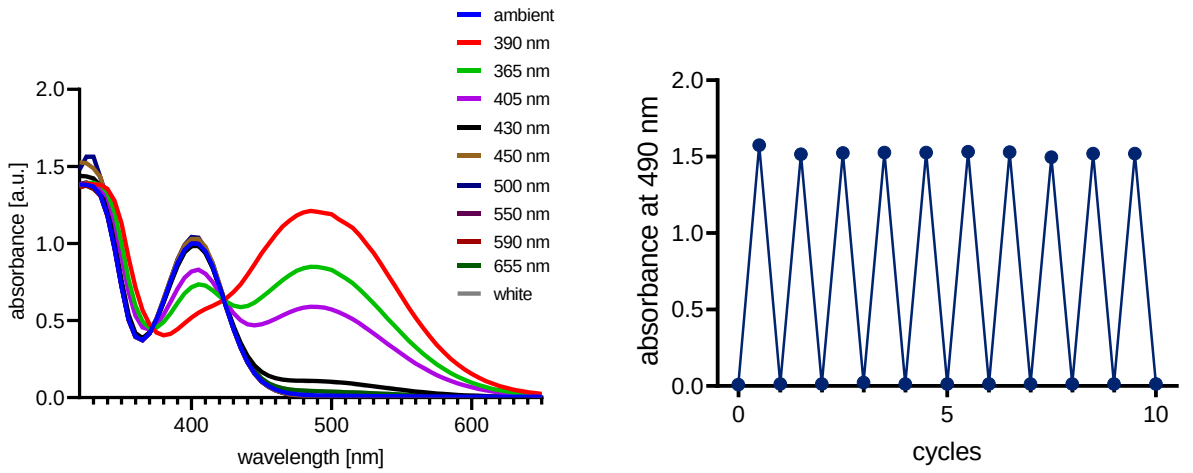

Figure S65. Left: UV-vis spectra of bromo/3,5-dimethoxyphenyl diazocine **8** (1.3 mM, CH_2Cl_2, 25 °C) after irradiation with different wavelengths (365−430 nm: 1 min; 450 nm−655 nm and white light: 20 s). Right: Absorption of **8** (1.3 mM, CH_2Cl_2, 25 °C) at 490 nm after alternating irradiations with 390 nm (1 min) and 500 nm light (20 s, right).

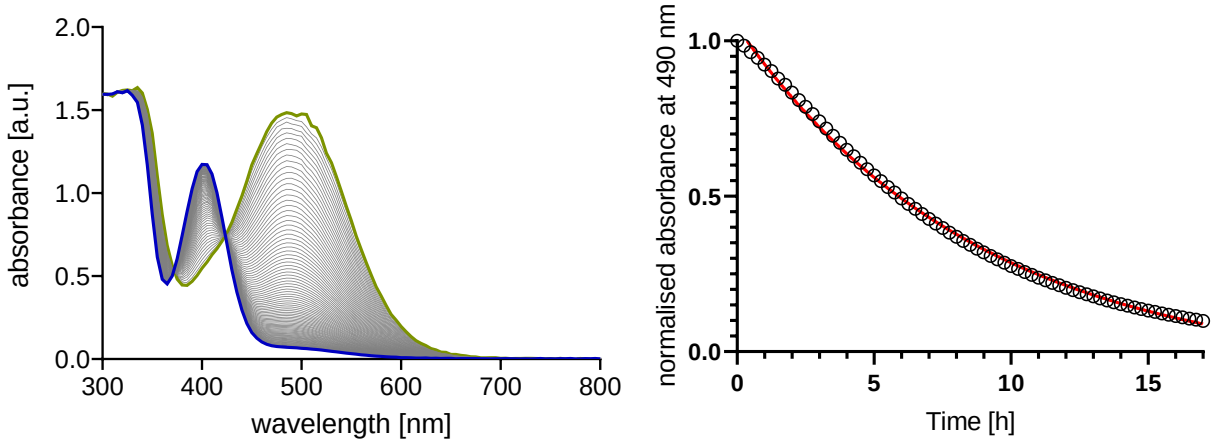

Figure S66. Thermal relaxation of bromo/3,5-dimethoxyphenyl diazocine **8** (1.3 mM, CH_2Cl_2, 25 °C). Left: UV-vis spectra of **8** measured every 15 minutes in the dark after irradiating with 390 nm. Right: Change in absorption $(A_t - A_\infty) \cdot (A_0 - A_\infty)^{-1}$ plotted over time t following thermal relaxation of **8** to provide its half-live $\tau_{½}$ = 6.1 h.

S6.2.10. 3,5-Dimethoxyphenyl/3,5-bis(trifluoromethyl)phenyl diazocine **9**

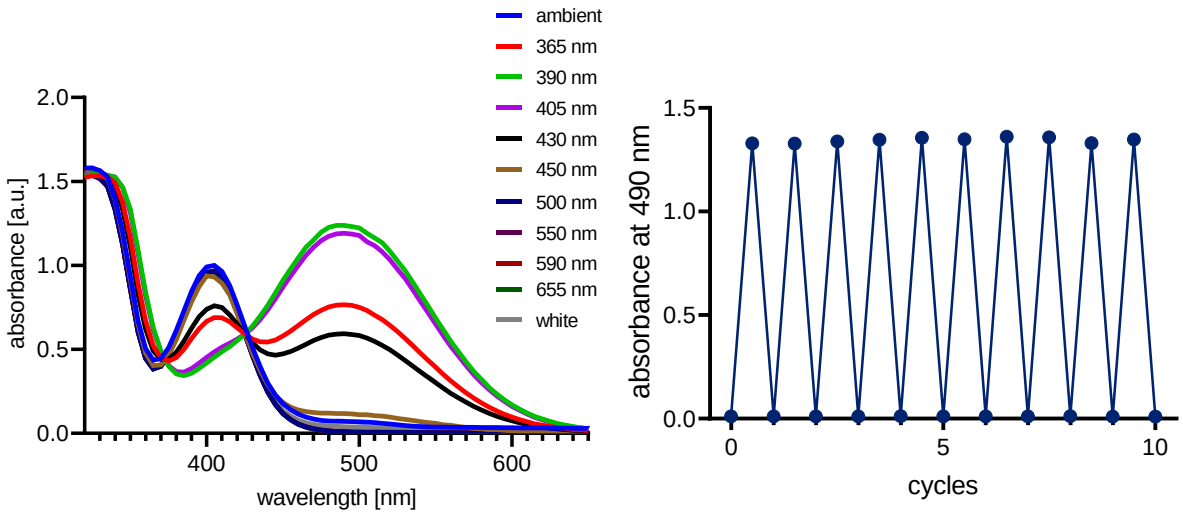

Figure S67. Left: UV-vis spectra of 3,5-dimethoxyphenyl/3,5-bis(trifluoromethyl)phenyl diazocine **9** (1.0 mM, CH_2Cl_2, 25 °C) after irradiation with different wavelengths (365−430 nm: 1 min; 450 nm−655 nm and white light: 20 s). Right: Absorption of **9** (1.0 mM, CH_2Cl_2, 25 °C) at 490 nm after alternating irradiations with 390 nm (1 min) and 500 nm light (20 s, right).

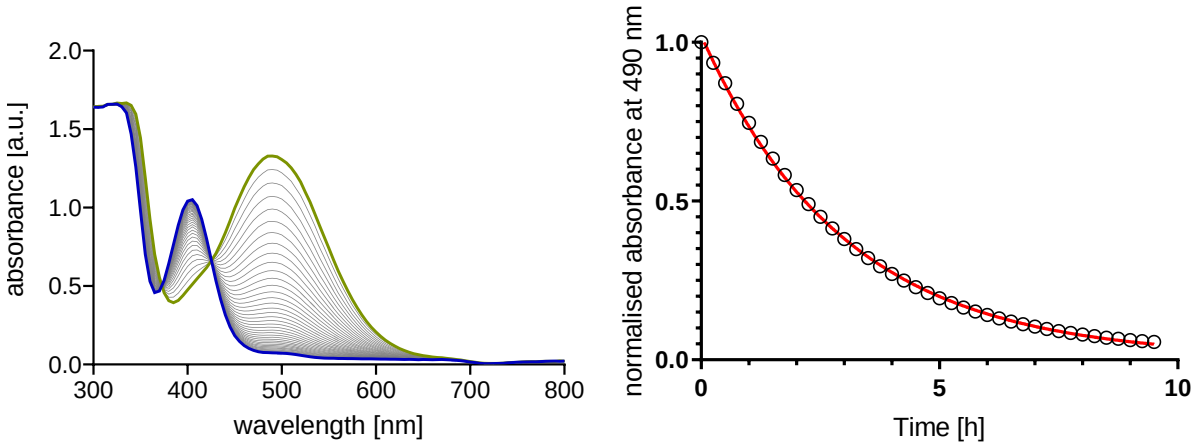

Figure S68. Thermal relaxation of 3,5-dimethoxyphenyl/3,5-bis(trifluoromethyl)phenyl diazocine **9** (1 mM, CH_2Cl_2, 25 °C). Left: UV-vis spectra of **9** measured every 15 minutes in the dark after irradiating with 390 nm. Right: Change in absorption $(A_t - A_\infty) \cdot (A_0 - A_\infty)^{-1}$ plotted over time t following thermal relaxation of **9** to provide its half-live $\tau_{½}$ = 2.1 h.

S6.3. Photoswitching (^{1}H NMR)

S6.3.1. Diazocine **A**

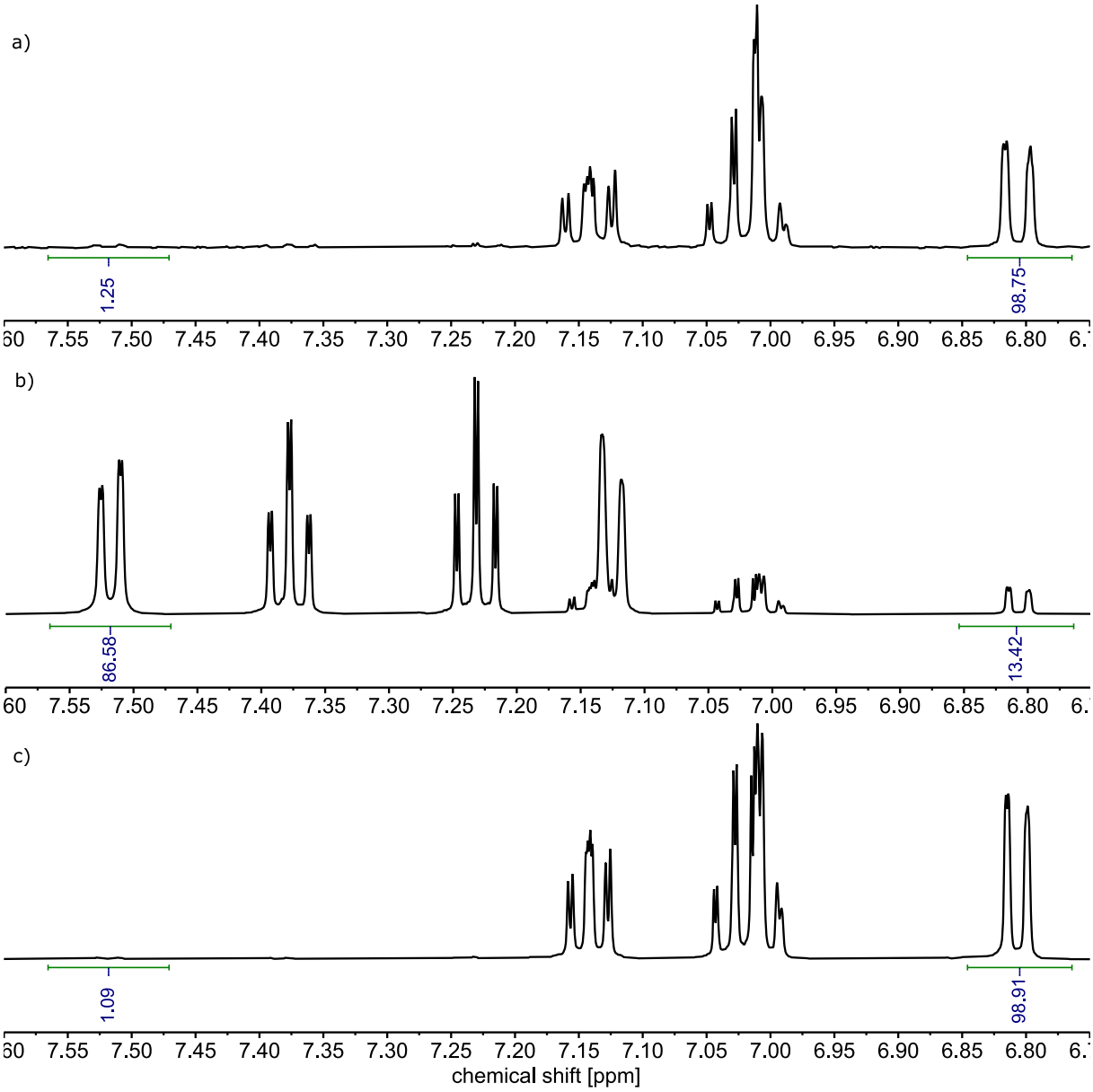

Figure S1. ^{1}H NMR (700 MHz, CD_2Cl_2, 3 mM, 298 K) of **A** (a) under ambient light, (b) after irradiation with 385 nm light (4 min, PSS 87% *E*-**A**) and (c) after irradiation with 505 nm light (2 min, PSS 99% *Z*-**A**).

S6.3.2. Dibromo diazocine **1**

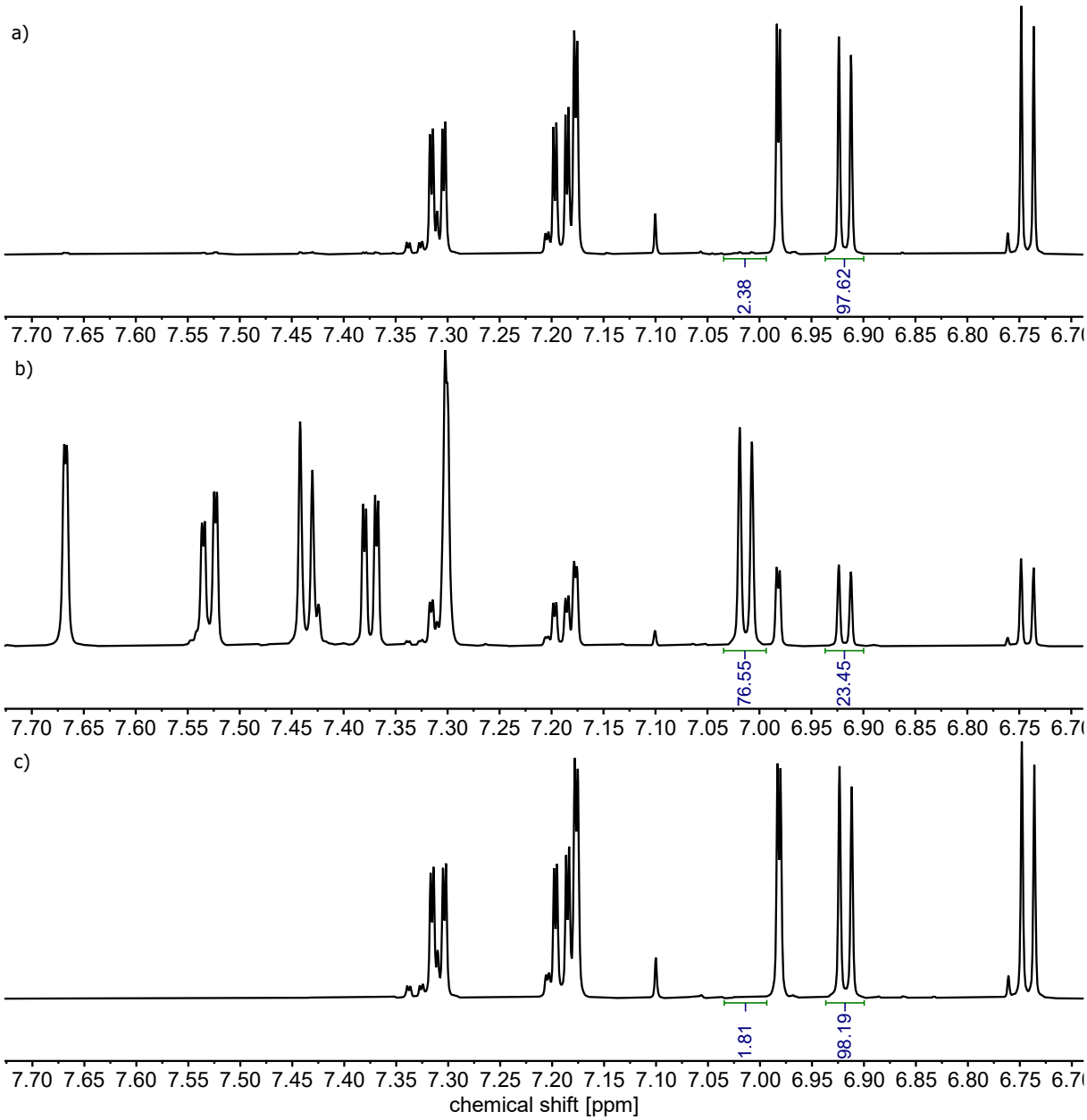

Figure S69. ^{1}H NMR (700 MHz, CD_2Cl_2, 3 mM, 298 K) of dibromo diazocine **1** (a) under ambient light, (b) after irradiation with 385 nm light (4 min, PSS 77% *E*-**1**) and (c) after irradiation with 505 nm light (2 min, PSS >98% *Z*-**1**).

S6.3.3. Diiodo diazocine **2**

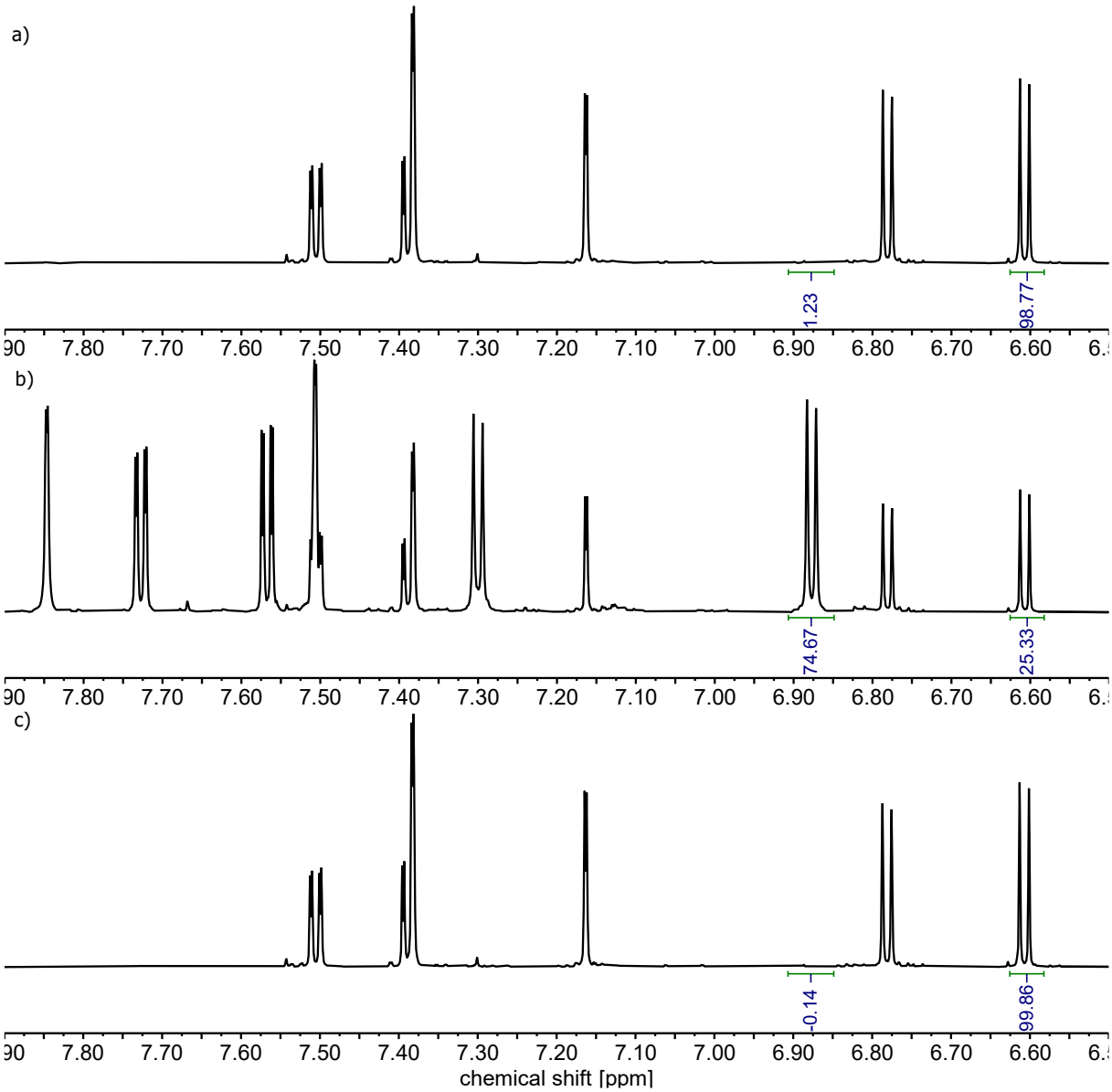

Figure S70. ^{1}H NMR (700 MHz, CD_2Cl_2, 3 mM, 298 K) of diiodo diazocine **2** (a) under ambient light, (b) after irradiation with 385 nm light (4 min, PSS 75% *E*-**2**) and (c) after irradiation with 505 nm light (2 min, PSS >99% *Z*-**2**).

S6.3.4. Bromo/iodo diazocine **3**

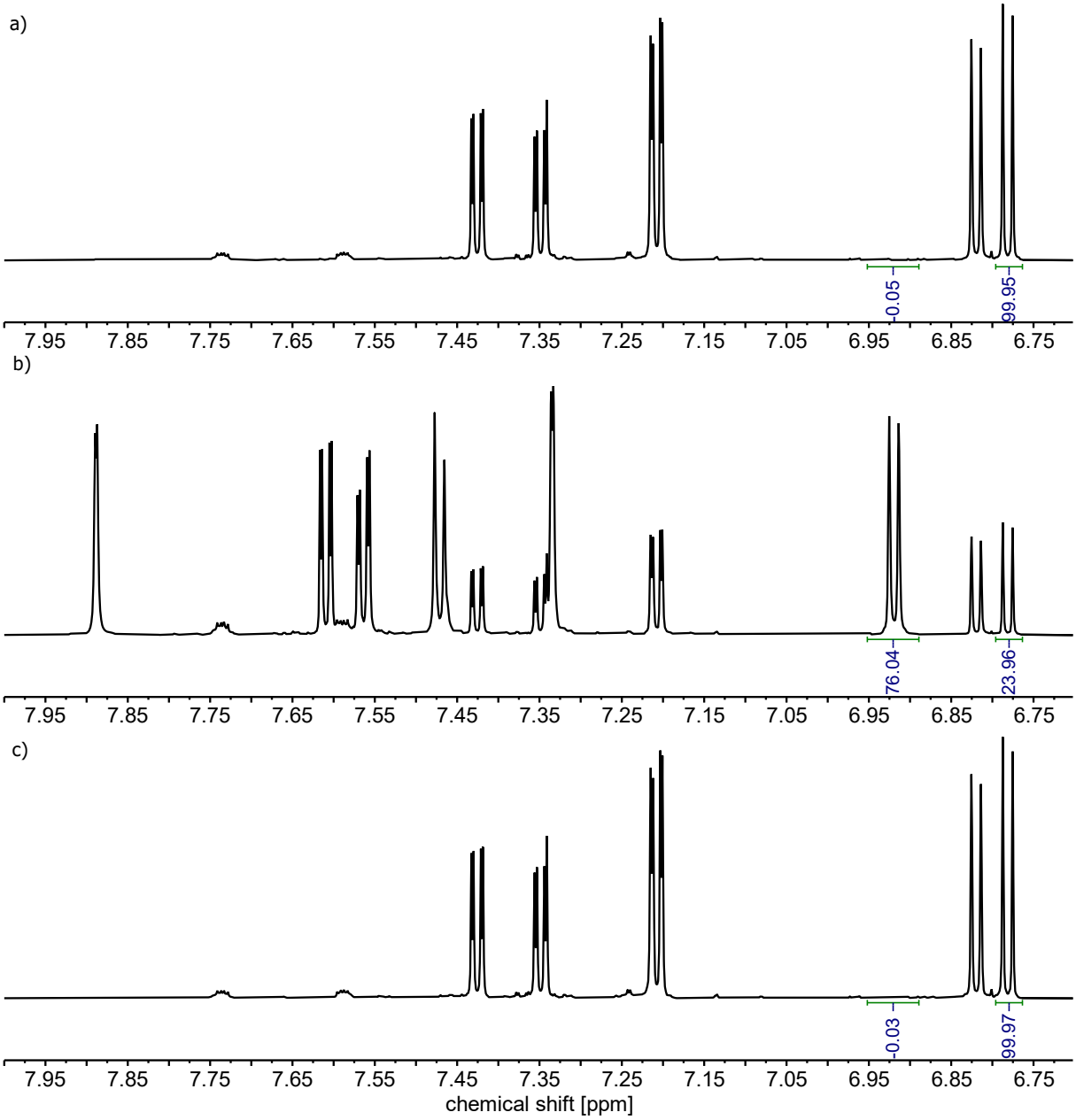

Figure S71. ^{1}H NMR (700 MHz, CD_2Cl_2, 3 mM, 298 K) of bromo/iodo diazocine **3** (a) under ambient light, (b) after irradiation with 385 nm light (4 min, PSS 76% *E*-**3**) and (c) after irradiation with 505 nm light (2 min, PSS >99% *Z*-**3**).

S6.3.5. Bis(trifluoromethyl)phenyl) diazocine **4**

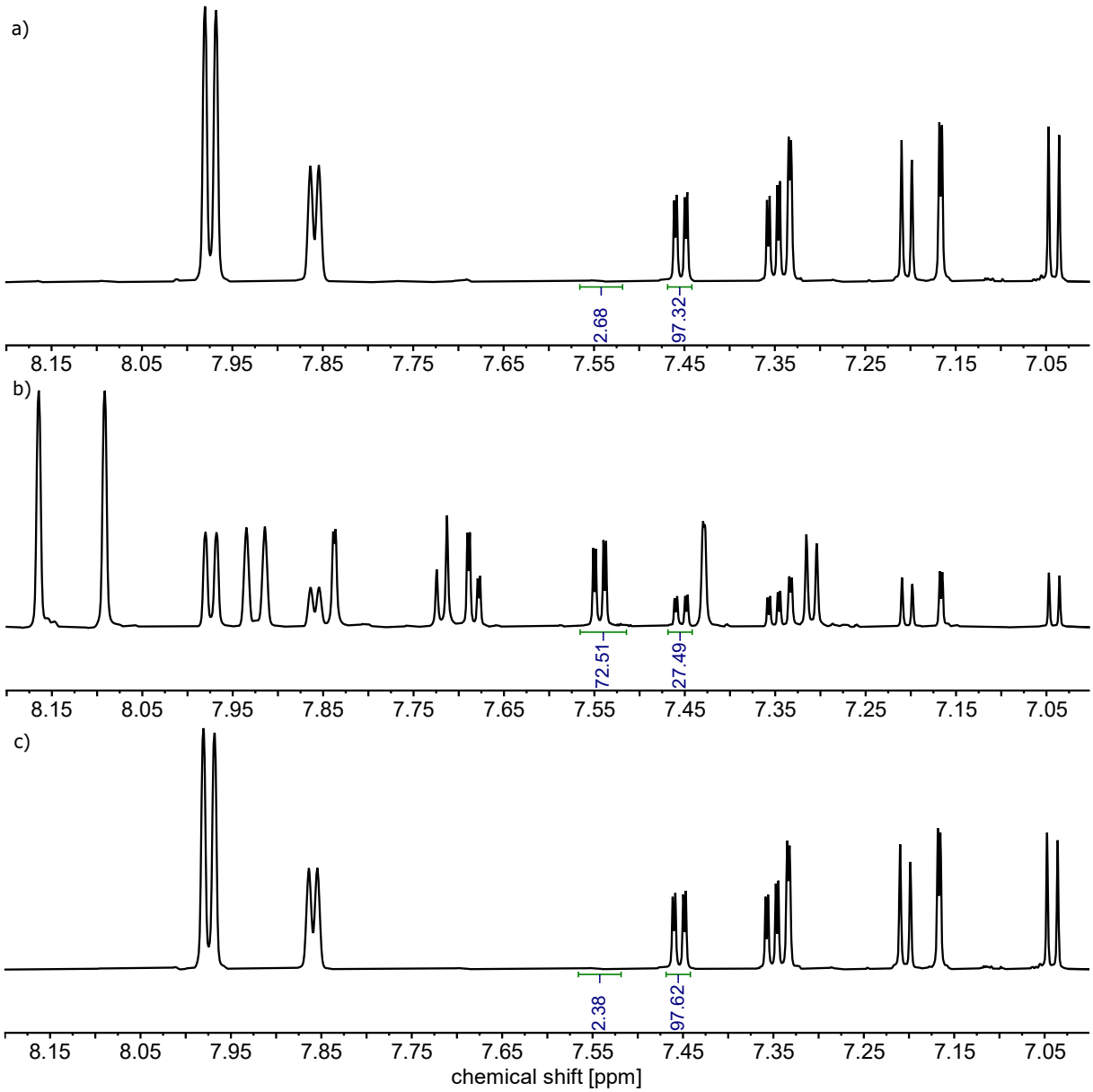

Figure S72. ^{1}H NMR (700 MHz, CD_2Cl_2, 3 mM, 298 K) of bis(trifluoromethyl)phenyl) diazocine **4** (a) under ambient light, (b) after irradiation with 385 nm light (4 min, PSS 73% *E*-**4**) and (c) after irradiation with 505 nm light (2 min, PSS 97% *Z*-**4**).

S6.3.6. Diphenyl diazocine **5**

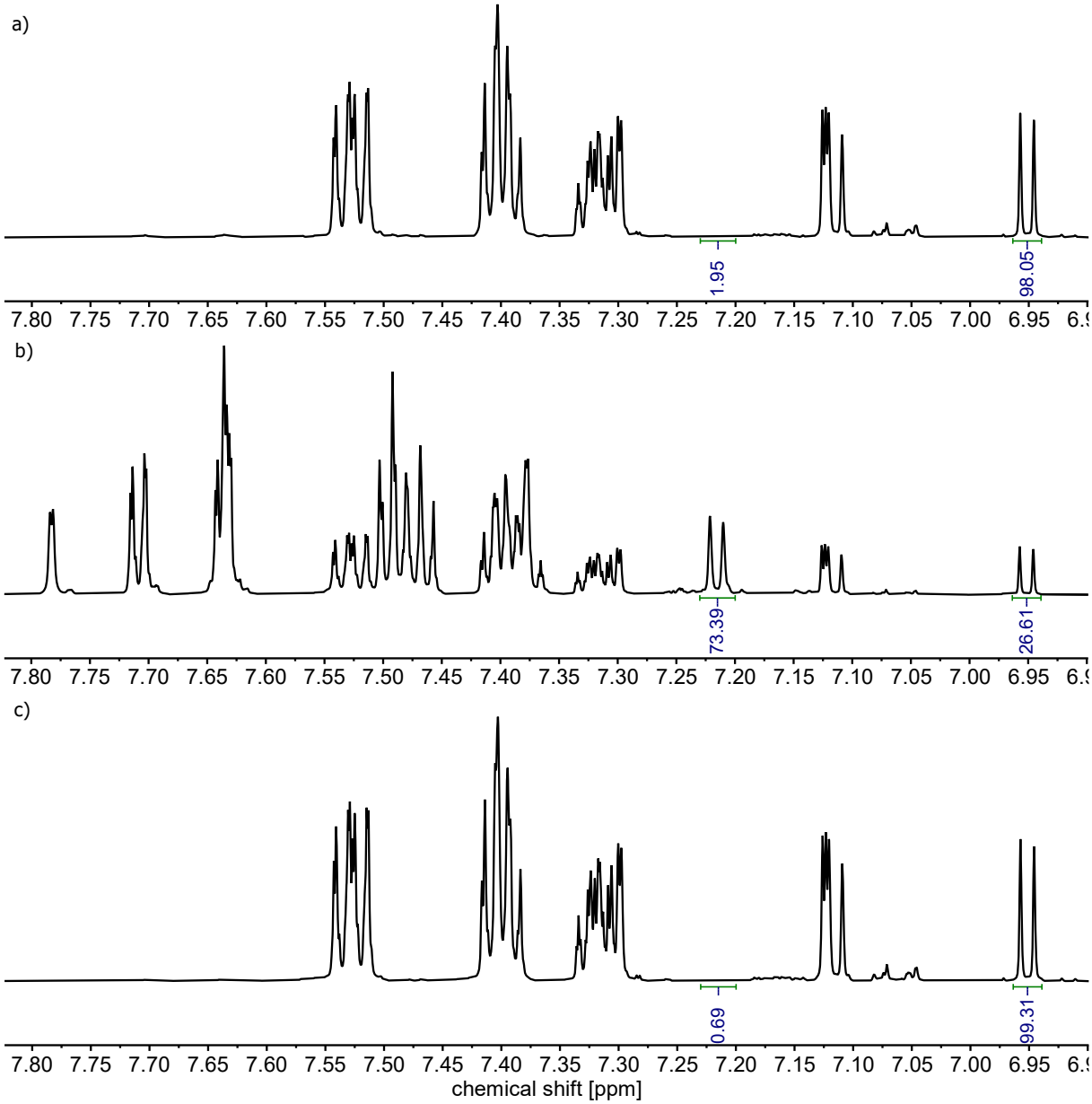

Figure S73. ^{1}H NMR (700 MHz, CD_2Cl_2, 3 mM, 298 K) of diphenyl diazocine **5** (a) under ambient light, (b) after irradiation with 385 nm light (4 min, PSS 73% *E*-**5**) and (c) after irradiation with 505 nm light (2 min, PSS >99% *Z*-**5**).

S6.3.7. Ditoluyl diazocine **6**

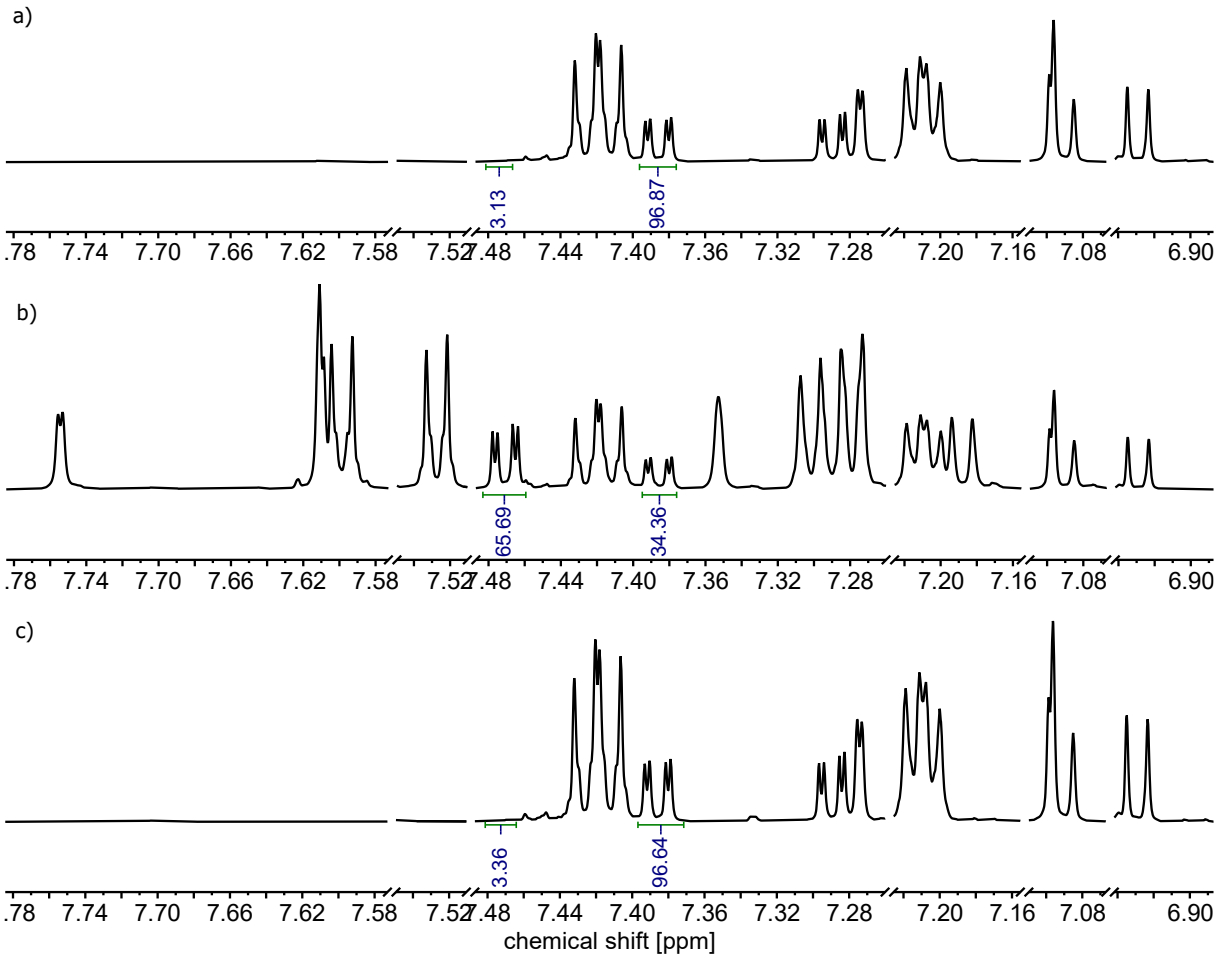

Figure S74. ^{1}H NMR (700 MHz, CD_2Cl_2, 3 mM, 298 K) of ditoluyl diazocine **6** (a) under ambient light, (b) after irradiation with 385 nm light (4 min, PSS 66% *E*-**6**) and (c) after irradiation with 550 nm light (1 min, PSS 97% *Z*-**6**).

S6.3.8. Bis(3,5-dimethoxyphenyl) diazocine **7**

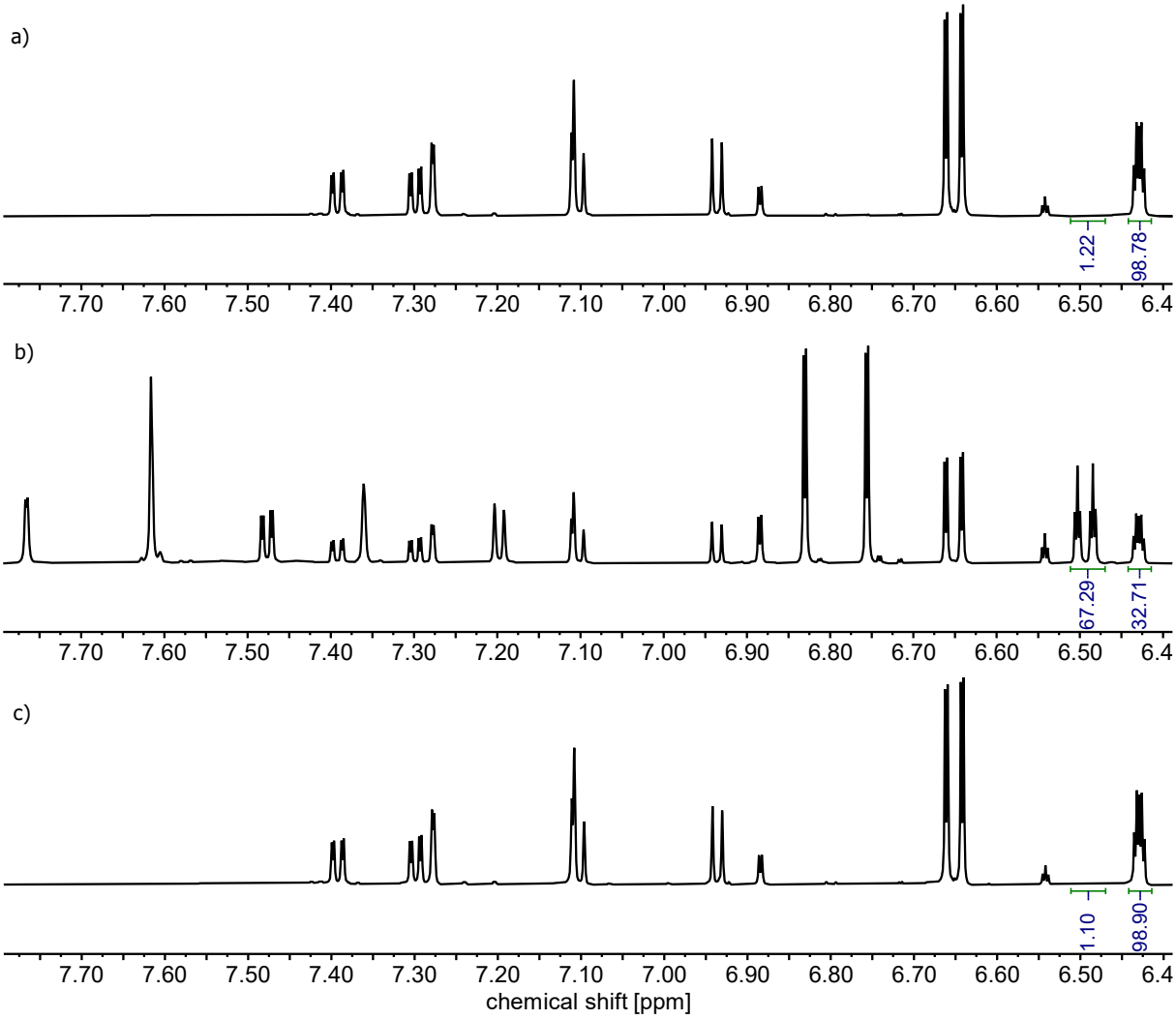

Figure S75. ^{1}H NMR (700 MHz, CD_2Cl_2, 3 mM, 298 K) of bis(3,5-dimethoxyphenyl) diazocine **7** (a) under ambient light, (b) after irradiation with 385 nm light (4 min, PSS 67% *E*-**7**) and (c) after irradiation with 505 nm light (1 min, PSS 99% *Z*-**7**).

S6.3.9. Bromo/3,5-dimethoxyphenyl diazocine **8**

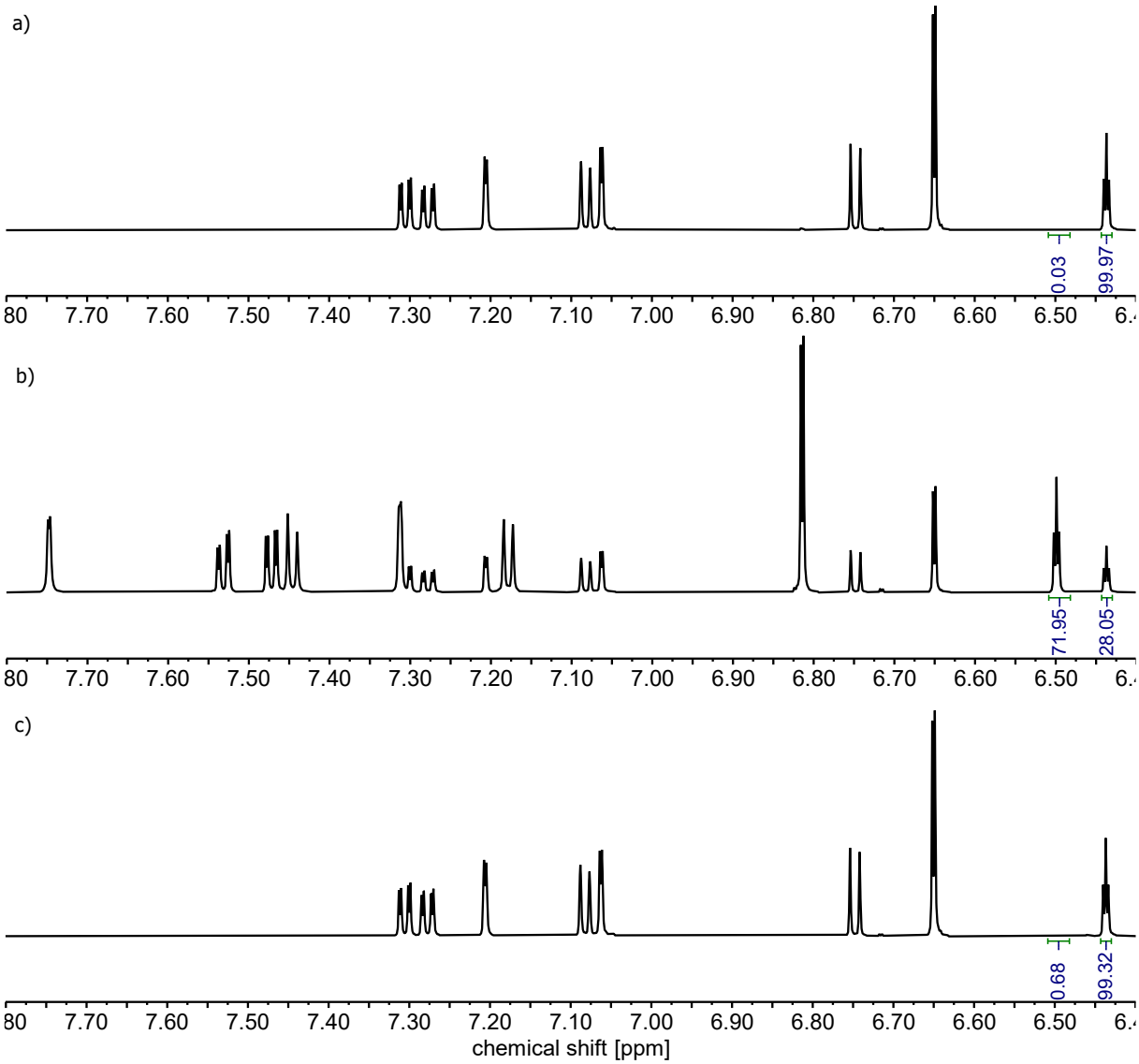

Figure S76. ^{1}H NMR (700 MHz, CD_2Cl_2, 3 mM, 298 K) of bromo/3,5-dimethoxyphenyl diazocine **8** (a) under ambient light, (b) after irradiation with 385 nm light (4 min, PSS 72% *E*-**8**) and (c) after irradiation with 505 nm light (1 min, PSS >99% *Z*-**8**).

S6.3.10. 3,5-Dimethoxyphenyl/3,5-bis(trifluoromethyl)phenyl diazocine **9**

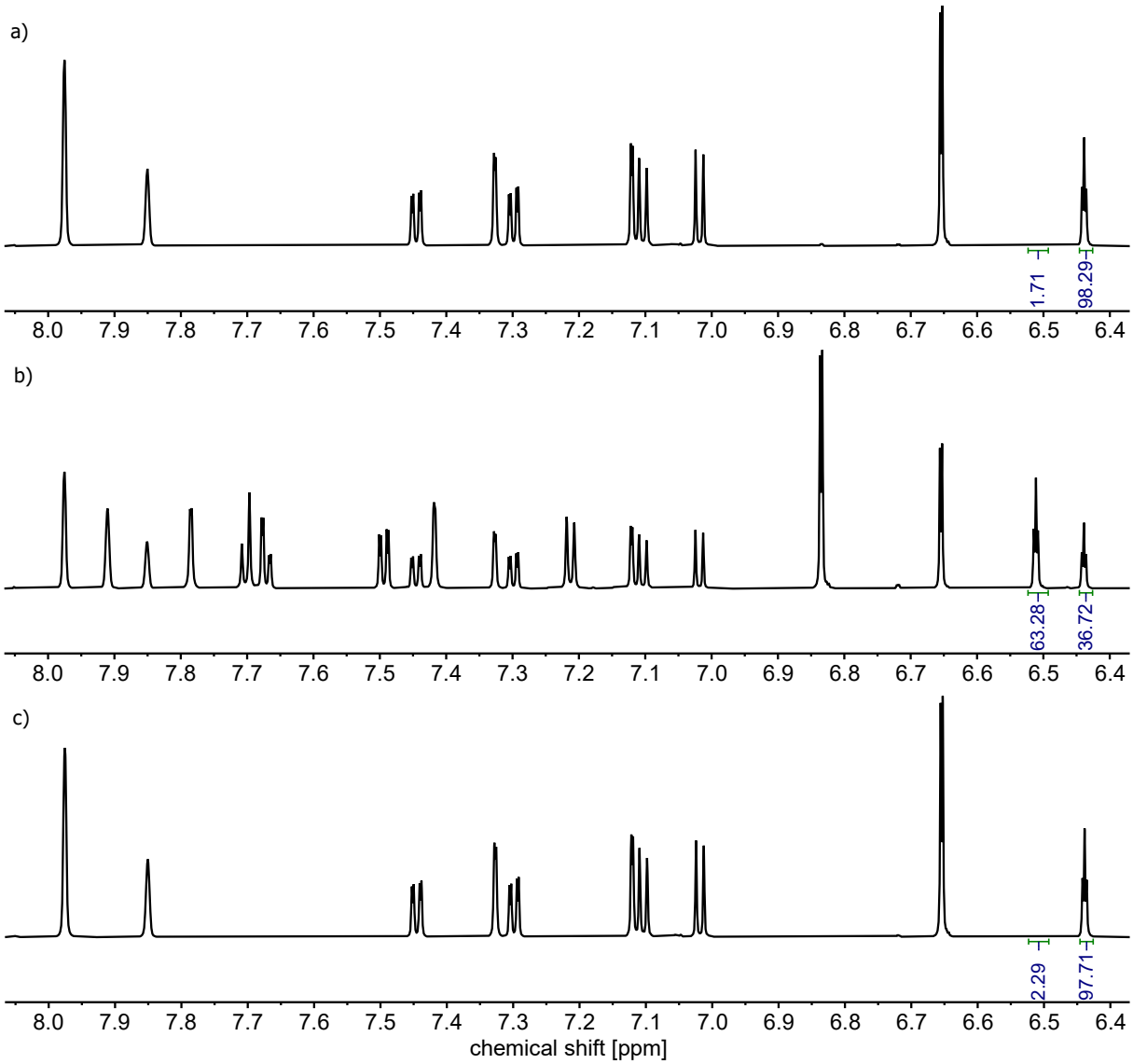

Figure S77. ^{1}H NMR (700 MHz, CD_2Cl_2, 3 mM, 298 K) of 3,5-dimethoxyphenyl/3,5-bis(trifluoromethyl)phenyl diazocine **9** (a) under ambient light, (b) after irradiation with 385 nm light (4 min, PSS 63% *E*-**9**) and (c) after irradiation with 505 nm light (4 min, PSS 98% *Z*-**9**).

S7. Overview of literature synthesis of 2,8-disubstituted diazocines

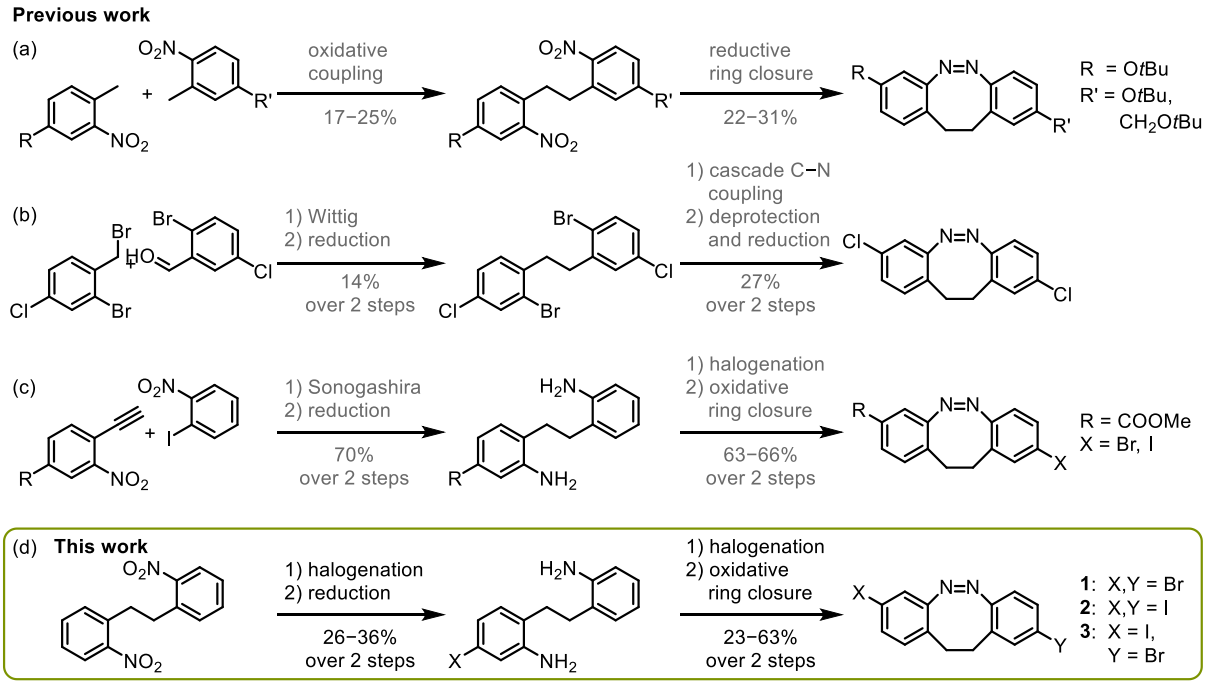

Scheme S2. Previous syntheses of 2,8-disubstituted diazocines by (a) Herges and coworkers,[10] (b) Staubitz and coworkers,[11] (c) Trauner and coworkers,[8] and (d) our approach.

For employing diazocines in various cross-coupling reactions, introducing halide substituents, preferentially bromides and iodides, is essential.

2,8-Pseudo-*para* substituted diazocines have been synthesised from asymmetrically substituted ethylene-bridged precursors in a ring-closing step either by reducing dinitro derivatives, the oxidation of dianiline compounds or a cross-coupling strategy involving a diiodide precursor.

Herges and coworkers[10] reported the statistical coupling of two nitrotoluene derivatives to the corresponding 2,2'-dinitrodibenzyl derivative, which then underwent reductive ring closure to form the 2,8-pseudo-*para* substituted diazocine (Scheme S2a). This strategy relies on the separation of a mixture of disubstituted 2,2'-dinitrodibenzyl derivatives, which is non-trivial for halide substituents.

Staubitz and coworkers[11] produced their asymmetric precursor through a Wittig reaction (Scheme S2b). After reducing the double bond, a halide exchange from

bromide to iodide facilitated diazocine formation using the cross-coupling, meaning that this strategy cannot produce bromide or iodide substituted diazocines.

Trauner and coworkers[8] employed a Sonogashira cross-coupling reaction to synthesize the asymmetric precursor (Scheme S2c). Following the reduction of the nitro groups and triple bond using hydrogen and Pd on charcoal, a second substituent was selectively introduced onto the less substituted aniline moiety. Both aniline moieties subsequently underwent intramolecular oxidative ring closure to form the 2,8-pseudo-*para* substituted diazocine. The substituent in the 8-position needs to be unaffected by the strongly reducing conditions during alkyne reduction, which renders this strategy unable to generate diazocines with bromide or iodide substituents in the meta position.

Therefore, we wanted to explore alternative pathways for the synthesis of 2,8-pseudo-*para* halide-substituted diazocines (Scheme S2d).

S8. Computational structures

S8.1. *Z*-**1**

28

energy: -49.045387798361 gnorm: 0.000248217481 xtb: 6.7.1pre (5071a88)

Br	6.20182403361178	3.19912706496400	3.89580926274751
Br	14.44166473587468	-0.34826034079914	2.76055325336970
H	13.10253273746766	-0.07401541910325	5.38886088488901
H	8.64841971052548	4.74208269759477	4.38890505463335
C	7.75360497347157	2.89609436224400	4.95706152890740
C	7.85412994483157	1.73824952914817	5.71199414445242
C	8.98273765697064	1.55390768733202	6.47598707493172
C	10.03684419844519	2.47821650125562	6.46568515592539
C	9.92494269974694	3.65439211582953	5.71223307900217
C	10.90666402337184	4.79876110409241	5.69587127758399
C	12.36861386862841	4.47348468429523	6.02591067171936
C	12.87367669784311	3.31637927170177	5.21466399751370
C	13.49782213934795	3.49657785700102	3.99071225654863
C	13.95483721746939	2.42083674257407	3.25074092830226
C	13.80834778985898	1.14233862012728	3.76438173816326
C	13.21611195403810	0.92241809126318	4.99161035201077
C	12.72318567732224	2.01132673208983	5.70406567538753
N	12.21164584739668	1.82075742607750	6.98378577406508
N	11.07458214256395	2.10355588338734	7.32230740526176
C	8.76038779443915	3.83949715723308	4.97133448786353
H	7.06352543591777	1.00500771876876	5.70847506740208
H	9.09175388403006	0.66622057220844	7.08026914008276
H	10.55293454306566	5.55566361026315	6.40412325188976
H	10.87092602019459	5.24649601840199	4.69949146144050
H	12.96797370168829	5.35977292876530	5.80974575888632
H	12.46746428752937	4.25626690612238	7.09181202496379
H	13.62104997121528	4.49749479096689	3.60386610371436
H	14.42434631313468	2.57169968619495	2.29166318834251

S8.2. *E*-**1**

28

energy: -49.025842208260 gnorm: 0.000814227833 xtb: 6.7.1pre (5071a88)

C	7.79870796204181	2.58268131305958	-0.95974335923072
H	9.59398243550264	5.90493947668709	-3.50908160030019
C	8.51612182260076	3.07657763511197	0.11661475022811
C	9.66247473673123	3.80600817691516	-0.12249592024326
C	10.10852793011378	4.00816559605078	-1.42748580893294
C	9.36727442865821	3.50992352984448	-2.53019780973610
C	9.79922074409472	3.78513722302546	-3.95638171878097
C	10.02576931220891	5.28263223477072	-4.29814105228104
C	11.47256842311404	5.67561117741714	-4.51448963043024
C	11.89335831923298	6.26355768395357	-5.69051218008391
C	13.22245103107696	6.60185786709452	-5.90713487153751
C	14.15314684081753	6.31647373751240	-4.92442183338267
C	13.79036640179900	5.70749115115645	-3.73904893968160
C	12.44989565155688	5.40347556632867	-3.52113370429119
N	11.99738568986733	4.58203915516373	-2.53825130168220
N	11.07483712277383	4.90556981824420	-1.76998105770036
C	8.20719461652335	2.80959019105777	-2.26707317965188
H	8.18102326258529	2.89650018906866	1.12583249627703
H	10.24469051124222	4.19585417156467	0.69736144595597
H	10.70882936562835	3.21923166279605	-4.17566040406206
H	9.02017648755116	3.39414456272568	-4.61230685947316
H	9.48385091597267	5.51653930380501	-5.21552987487685
H	11.16896515185125	6.47419592992118	-6.46357377144096
H	13.52502273024479	7.07314444817642	-6.82819826618096
H	14.51950724704210	5.49469239436450	-2.97371890343952
H	7.61362055707443	2.42662527108953	-3.08375843486378
Br	6.20929738639937	1.58009214554005	-0.64891416466820
Br	15.98248291569442	6.76453838755458	-5.21038404550883

S8.3. *Z*-**B**

28

energy: -49.045709271374 gnorm: 0.000374452514 xtb: 6.7.1pre (5071a88)

Br	6.29326684274759	3.20841864058137	3.75763452345332
Br	14.32017916920464	-0.41619261069088	2.79361049821099
H	12.91474506111781	0.30317730280900	7.52786837820670
H	8.87425942054738	4.61055353791309	4.01799643723687
C	7.73223578983357	3.09087985271820	5.00118453300268
C	7.64823328961690	2.19718151251272	6.05726478930487
C	8.69145223966174	2.12077390788668	6.95644121561758
C	9.82947180192155	2.90381189336849	6.77598561320124
C	9.90243204148107	3.81979914580848	5.71672695428974
C	11.11316980117161	4.69488261193464	5.57297374585393
C	12.19894205058971	4.02749342294783	4.71973550473636
C	12.57020333038588	2.60784664731382	5.06562754178761
C	13.13772825098749	1.85642359605255	4.03984687078844
C	13.58361626601785	0.56726353162456	4.24826749395483
C	13.51135003252322	-0.01464174464770	5.50392947563653
C	12.98210850234715	0.72412827284859	6.53625523448916
C	12.47934644027596	2.01673751136957	6.33284506440231
N	11.99833116912751	2.58793135759251	7.51381859876551
N	10.83718901524592	2.89242911986895	7.73360555701821
C	8.83721016295995	3.90766388255341	4.83686213752122
H	6.77623911055391	1.57347613730300	6.17607001750416
H	8.65165740819818	1.43257685232759	7.78626926772274
H	11.51482997134570	4.93801396215837	6.55926990908775
H	10.83142827237547	5.63109525783152	5.08785874428814
H	11.87197724709659	4.03641652500168	3.67711084909543
H	13.10695665734630	4.63705067259410	4.77973888741777
H	13.22327220275498	2.29348321398900	3.05594574214677
H	13.86935845256449	-1.01823401357107	5.66966641525940

S8.4. *E*-**B**

28

energy: -49.026277402954 gnorm: 0.000464785855 xtb: 6.7.1pre (5071a88)

C	2.90446094313596	8.52870144154836	-1.51204166406041
H	7.36128038559037	9.04602401993647	-2.22802582850835
Br	12.42415670661294	6.64963949585587	-4.25486258188252
C	3.19220863159535	8.24126956083071	-0.18868022559616
C	4.43761946051971	7.74178114296002	0.13263855171300
C	5.37671811077509	7.49699469509565	-0.86777899166694
C	5.08423249296250	7.80263620471649	-2.22277576823768
C	6.12594152703864	7.61465237253819	-3.30674701787503
C	7.48048188115153	8.32553629272293	-3.04203747018999
C	8.63690620432246	7.39839578567616	-2.72813598372488
C	9.79256699164204	7.42551724103084	-3.48150607164064
C	10.83562900137820	6.55070182656481	-3.20814877637929
C	10.73892596737931	5.60601205779909	-2.20077657152707
C	9.58107637200594	5.54027003981549	-1.45315034541700
C	8.54073156543546	6.43762906914299	-1.68759221755128
N	7.28284073023329	6.30078577004297	-1.18859674099073
N	6.69423065181240	7.24877182035735	-0.63790744282179
C	3.84283712640537	8.32893670958199	-2.51581636241540
H	2.45420114811798	8.40935860664754	0.57975143961490
H	4.68465449965123	7.50272801263957	1.15486955324063
H	6.29911038311312	6.54622520391124	-3.46287074025286
H	5.70464703333674	8.00407684607121	-4.23448657054273
H	7.75267626112549	8.89670171102278	-3.93058438704605
H	9.89181389133278	8.13712095893448	-4.28764440247501
H	9.48308054198180	4.81849408423361	-0.65781252791509
H	3.59393577179215	8.58265901096643	-3.53550324882607
Br	1.19266899417462	9.22640975044116	-1.97182143106659
H	11.55589672537753	4.92913026891559	-2.00641617595893

S9. Author contributions

M.J.N. and L.K.S.v.K. conceptualized the project and all authors were involved in developing the details. M.J.N., V.S., V.P., and J.S.K synthesized and investigated the compounds. Formal analysis was performed by M.J.N. and V.S.

L.K.S.v.K. visualized the data for the manuscript and wrote the original draft. All authors contributed to reviewing and editing the final draft.

S10. Literature

(1) Menges, F. *Spectragryph - optical spectroscopy software, Version 8.0*.

(2) Hanwell, M. D.; Curtis, D. E.; Lonie, D. C.; Vandermeersch, T.; Zurek, E.; Hutchison, G. R. J. *Cheminformatics* **2012**, *4*, 17.

(3) Rappe, A. K.; Casewit, C. J.; Colwell, K. S.; Goddard, W. A.; Skiff, W. M. *J. Am. Chem. Soc.* **1992**, *114*, 10024.

(4) Bannwarth, C.; Ehlert, S.; Grimme, S. J. *Chem. Theory Comput.* **2019**, *15*, 1652.

(5) Schrödinger, L. *The PyMOL Molecular Graphics System, Version~1.8*.

(6) Chaikovskii, V. K.; Filimonov, V. D.; Skorokhodov, V. I.; Ogorodnikov, V. D. *Russ. J. Org. Chem.* **2007**, *43*, 1278.

(7) Park, K. K.; Oh, C. H.; Joung, W. K. *Tetrahedron Lett.* **1993**, *34*, 7445.

(8) Maier, M. S.; Hüll, K.; Reynders, M.; Matsuura, B. S.; Leippe, P.; Ko, T.; Schäffer, L.; Trauner, D. *J. Am. Chem. Soc.* **2019**, *141*, 17295.

(9) Ghosh, S.; Eschen, C.; Eleya, N.; Staubitz, A. *J. Org. Chem.* **2022**, *88*, 3372.

(10) Ewert, J.; Heintze, L.; Jordà-Redondo, M.; Glasenapp, J.-S. von; Nonell, S.; Bucher, G.; Peifer, C.; Herges, R. *J. Am. Chem. Soc.* **2022**, *144*, 15059.

(11) Li, S.; Eleya, N.; Staubitz, A. *Org. Lett.* **2020**, *22*, 1624.

7.3 *Angew. Chem. Int. Ed.* **2025**, e202508952.

How to cite: *Angew. Chem. Int. Ed.* **2025**, e202508952
doi.org/10.1002/anie.202508952

Molecular Ratchets **Hot Paper**

Light-Driven Ratchet Mechanism Accelerates Regioselective Metal-Cation Exchange in a Heterobimetallic Helicate

*Maximilian J. Notheis, Gregor Schnakenburg, and Larissa K. S. von Krbek**

Abstract: Molecular machines rely on their capacity to exploit non-equilibrium processes to perform work. However, the development of these non-equilibrium processes, such as molecular ratchets, is still in its early stages. Here, we report a diazocine-containing ligand (**L**) harbouring two distinct chelating coordination sites that can self-sort into dinuclear homo- and heterobimetallic helicates ($[Fe^{II}_2\mathbf{L}](OTf)_4$, $[Co^{II}_2\mathbf{L}](OTf)_4$, $[Zn^{II}_2\mathbf{L}](OTf)_4$, $[Zn^{II}Fe^{II}\mathbf{L}](OTf)_4$, $[Zn^{II}Co^{II}\mathbf{L}](OTf)_4$) with precisely controlled metal cation distribution. The photoisomerisation of the helicates operates via a molecular ratchet mechanism, resulting in metastable diastereomers that shift the system from thermodynamic equilibrium. Continuous white-light irradiation autonomously drives this ratchet process, selectively enriching an out-of-equilibrium pseudo-mesocate structure. Crucially, the ratchet mechanism can significantly accelerate metal-cation exchange from the $[Zn^{II}_2\mathbf{L}](OTf)_4$ helicate to the $[Zn^{II}Fe^{II}\mathbf{L}](OTf)_4$ helicate. Thus, the system operates in a manner reminiscent of a "claw machine", selectively seizing Fe^{II} ions when subjected to a precisely controllable external stimulus. These findings lay the foundation for creating adaptive and reconfigurable supramolecular structures that use non-equilibrium phenomena on a molecular level.

Introduction

Harnessing endergonic reactions is crucial for operating molecular machinery and creating adaptive materials.[1] A prime example of harnessing endergonic reactions is photosynthesis, which captures light energy to create a proton gradient.[2] This gradient powers ATP synthase,[3] converting ADP into ATP through an endergonic reaction. In essence, photosynthesis acts as a molecular ratchet,[1,4] coupling an exergonic proton transport process with an endergonic reaction within a multi-step chemical reaction cycle.

Molecular ratchets function unidirectionally and bypass microscopic reversibility,[5] allowing them to access out-of-equilibrium states. Chemical stimuli or light can activate molecular ratchets,[6,7] with light being a notably appealing option due to its unique benefits: light generates no chemical waste and allows for precise spatial and temporal control.[8]

To effectively harness light in artificial molecular ratchets, precisely aligning the photoresponsive building blocks, such as azobenzenes,[9–13] diazocines,[14–16] crowded alkenes[17,18] or dithienylethanes (DTE),[19,20] can enhance the switching effect. A key method for organising several photoresponsive building blocks within one structure is through the self-assembly of supramolecular organic or metal-organic capsules.[8,21,22] Recently, Feringa, Kathan and colleagues[11] reported a supramolecular organic capsule that functions as a molecular ratchet, using photoisomerisation and imine exchange to form a kinetically trapped, out-of-equilibrium open capsule. In another study, Clever, Herges and co-workers[14] introduced a diazocine-containing ligand that preferentially formed an out-of-equilibrium $Pd^{II}_2L_4$ lantern when exposed to light in the presence of Pd^{II} cations and disassembled in darkness.

Improving the structural complexity of metallo-supramolecular capsules by integrating various ligands or metal cations into heteroleptic[23,24] or heterometallic[25] structures, or by incorporating asymmetric ligands,[26–28] may broaden their utility in guest binding and supramolecular catalysis, thus achieving the molecular recognition and catalytic regulation akin to that seen in biological host–guest systems.[29] Heterometallic structures are known for their improved magnetic[30] and photophysical properties,[31] along with enhanced redox[32] and catalytic activity[33] compared to their homometallic counterparts. However, accurately self-sorting various metal cations and ligands into heterobimetallic structures presents a substantial challenge, particularly when using metal cations that prefer similar ligand environments. A stepwise synthesis is commonly used,[34–43] starting with the assembly of one kinetically inert metal–ligand corner, followed by forming the rest of the structure using the pre-assembled building block or metal cation exchange. While

[*] M. J. Notheis, Dr. L. K. S. von Krbek
Kekulé-Institut für Organische Chemie and Biochemie, Rheinische Friedrich-Wilhelms-Universität Bonn, Gerhard-Domagk-Str. 1 53121, Bonn, Germany
E-mail: larissa.vonkrbek@uni-bonn.de

Dr. G. Schnakenburg
Institut für Anorganische Chemie, Rheinische Friedrich-Wilhelms-Universität Bonn, Gerhard-Domagk-Str. 1 53121, Bonn, Germany

Additional supporting information can be found online in the Supporting Information section

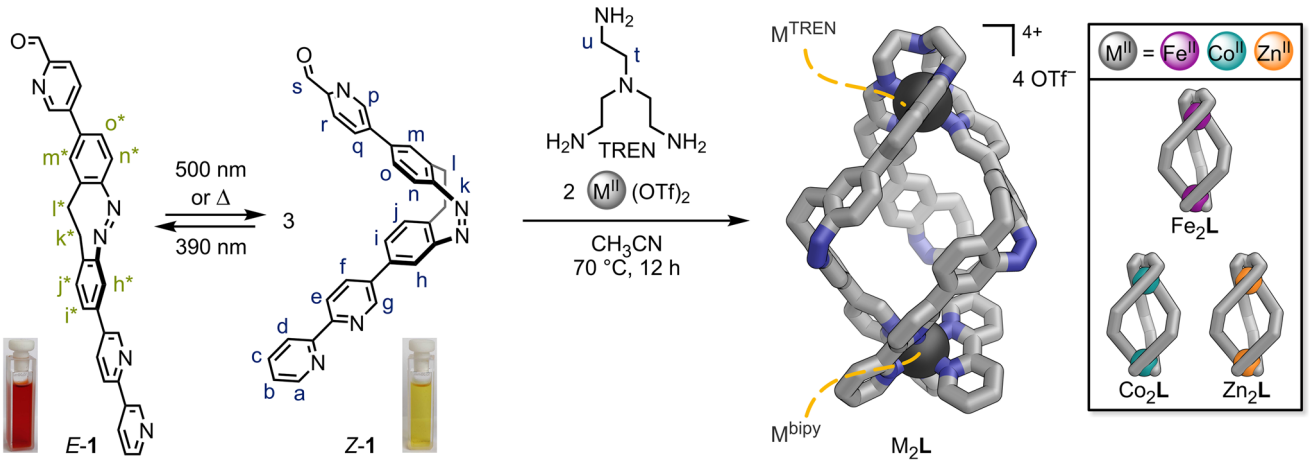

Scheme 1. Left: Photoswitching between the two isomers of **1** and their photochromism in acetonitrile. Right: Subcomponent self-assembly of *Z*-**1**, TREN and $M(OTf)_2$ yielding M_2**L** (GFN2-xTB optimised structure: hydrogens and counterions omitted for clarity; C: grey, N: blue, M^{II} (dark grey) = Fe^{II}, Co^{II}, Zn^{II}). Insert: Helicate structures obtained by self-assembly (Fe_2**L**, Co_2**L**, Zn_2**L**).

this approach tends to be effective, it involves two steps, requiring more synthetic effort than homometallic metallo-supramolecular one-pot self-assembly. A small number of one-pot self-assembly examples of heterobimetallic cages have been reported,[25,35,44–47] employing the two distinct coordination geometries of two different metal cations.

Here, we present a diazocine-based ligand (**L**) that self-assembles into various metallo-supramolecular M^{II}_2**L** helicates in the presence of different metal(II) cations (Zn^{II}, Fe^{II}, and Co^{II}). The ligand features two chemically distinct coordination sites, allowing the formation of both homo- and heterobimetallic helicates (Fe^{II}_2**L**, Co^{II}_2**L**, Zn^{II}_2**L**, $Zn^{II}Fe^{II}$**L**, $Fe^{II}Zn^{II}$**L**, and $Zn^{II}Co^{II}$**L**) with precise metal distribution achieved through one-pot self-sorting, sequential metal addition or metal exchange. Crucially, the reversible photoisomerisation of diazocines in **L** induces structural changes in the M^{II}_2**L** helicate, thereby shifting the assemblies away from the thermodynamic minimum, akin to a molecular ratchet. Continuous exposure to white light autonomously drives this molecular ratchet, leading to the formation of a single high-energy isomer with notable selectivity. Furthermore, we used this light-driven molecular ratchet to facilitate the dynamic and selective exchange of metal cations, transforming the homometallic Zn_2**L** helicate into a heterobimetallic ZnFe**L** helicate.

Results and Discussion

Synthesis and Photoswitching of Ligand L

Photoresponsive subcomponent **1** was synthesised from 2-bromo-8-iodo-11,12-dihydrodibenzo[c,g][1,2]diazocine[48] (Scheme S1 and Section S2) via two successive, selective, and high-yielding cross-coupling reactions with ethyl pinacol boronic acid esters[49] 5-(4,4,5,5-tetraethyl-1,3,2-dioxaborolan-2-yl)-2,2′-bipyridine (**S3**) and 2-(1,3-dioxolan-2-yl)-5-(4,4,5,5-tetraethyl-1,3,2-dioxaborolan-2-yl)pyridine (**S6**).

At ambient conditions, subcomponent **1** primarily exists as its thermodynamically stable *Z*-isomer (99% *Z*-**1**). When exposed to 390 nm light, a second set of signals associated with *E*-**1** emerged in the ^{1}H NMR spectrum, reaching a photostationary state of 72% *E*-**1** and resulting in a colour change of the solution from yellow to red (Scheme 1, left; Section S7.4). *E*→*Z* isomerisation (>99% *Z*-**1**) took place under white light or 500 nm light irradiation and through thermal relaxation, exhibiting a half-life of 165 min at 25 °C in acetonitrile (20 μM; Section S7.3.1). The photoswitching of subcomponent **1** is rapid and completely reversible, usually taking less than a minute of irradiation in either direction (20 μM–2 mM in CH_3CN, 0.1–0.2 mW light power). The asymmetric 2,8-substitution pattern at the central diazocine unit in subcomponent **1** enables a significant structural change from a 90° to a 180° angle between the two metal-binding moieties upon photoswitching (Scheme 1, left; Figure S67). Employing two distinct metal-binding moieties generates directionality within asymmetric subcomponent **1**. Dynamic covalent tethering of **1**'s pyridine carboxaldehydes into TREN tri-pyridylimines fixes subcomponent **1**'s orientation, leading to regioselective helicate self-assembly, as previously demonstrated[26] in related systems.

Synthesis of Homometallic Helicates

Homometallic, triple-stranded helicates Fe_2**L**, Co_2**L**, and Zn_2**L** were obtained from the self-assembly of pyridine carboxaldehyde **1** (1 equiv.), tris(2-aminoethyl)amine (TREN, 1 equiv.), and the corresponding metal(II) trifluoromethanesulfonates (triflate or $^-$OTf, 2 equiv.), $Fe(OTf)_2$, $Co(OTf)_2$, and $Zn(OTf)_2$, respectively (Scheme 1, right). Fe_2**L**, Co_2**L**, and Zn_2**L** were characterised by mass spectrometry, NMR spectroscopy, and UV–vis spectroscopy (Sections S3 and S7.3).

Fe_2**L** crystallised in the triclinic space group P1 (Figure 1a; Section S6.2). Triple-stranded ligand **L** connects two homochiral metal centres, forming a dinuclear helicate structure with distorted C_3 symmetry. All *Z*-diazocine units maintain

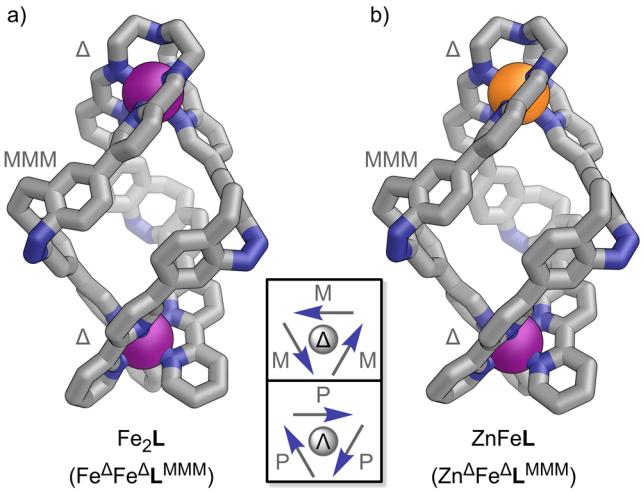

Figure 1. Crystal structures of a) homometallic helicate Fe_2**L** and b) heterobimetallic helicate ZnFe**L** (C: grey, N: blue, Fe: purple, Zn: orange). Disorder, solvent of crystallisation, and anions are omitted for clarity. Insert: Schematic representation of the helicates clarifying *nomenclature* (looking along the M^{TREN}–M^{bipy} axis; metal cations: grey circles; diazocine units: arrows): Δ/Λ: right-/lefthanded helicity of the metal cation ligand environment; P/M: diazocine azo-nitrogens pointing clockwise/anti-clockwise (see also Section S6.1).

the same orientation within ligand **L**, with their helical configuration ($\mathbf{L}^{MMM}$) opposing the helicity of the metal centres ($Fe^{\Delta\Delta}$, Figure 1a; Sections S6.1 and S6.2). The self-assembly of dinucelar homometallic helicate Fe_2**L** exhibits remarkable diastereoselectivity, resulting in the formation of only one pair of enantiomers: $Fe^{\Delta}Fe^{\Delta}\mathbf{L}^{MMM}$ and $Fe^{\Lambda}Fe^{\Lambda}\mathbf{L}^{PPP}$.

The high-resolution electrospray ionisation (ESI) mass spectrum of Fe_2**L** showed a sequence of signals corresponding to the species $[Fe_2\mathbf{L} - n\text{OTf}]^{n+}$ (n = 1, 2, 3, and 4), confirming the stoichiometry of Fe_2**L** in the gas phase (Figures 2a and S24). ^{1}H NMR spectroscopy indicated a C_3 symmetric structure with diasterotopic signals for the TREN ethylene groups, as expected for the chiral coordination pocket (Figures 2b and S19). Proton signals of H-p, H-s, H-u′, and H-t′ close to the TREN tri-pyridylimine metal corner (Fe^{TREN}) are significantly broadened with half-widths of 30 to 50 Hz and are only visible in highly concentrated samples (Figure S19). ^{1}H,^{1}H ROESY spectroscopy revealed close interproton contacts between diazocine protons H-h and H-m with bipyridine proton H-g and pyridylimine proton H-p, respectively, confirming that the same racemic diastereomer of Fe_2**L**, namely $Fe^{\Delta}Fe^{\Delta}\mathbf{L}^{MMM}$, together with its enantiomer $Fe^{\Lambda}Fe^{\Lambda}\mathbf{L}^{PPP}$, is present in both solution and the solid state (Figure S56 and Section S6.4.1). The UV–vis spectrum of Fe_2**L** displays a diazocine n–π* absorption band at 405 nm, along with three bands in the visible range that are characteristic of Fe^{II} MLCT transitions (λ = 497, 539, and 599 nm; Figure 3a). By synthesising model compounds for the two unique metal binding sites in Fe_2**L**—$Fe(bipy)_3(OTf)_2$ and Fe(TREN tri-pyridylimine)$(OTf)_2$ (short: $Fe(bipy)_3$ and Fe(TRENpy), respectively)—and comparing their UV–vis spectra to that of Fe_2**L** (Figure 3b), we assigned the three MLCT transition bands to the two distinct coordination sites in Fe_2**L**. The two lower-wavelength bands are attributed to the MLCT transition of one Fe^{II} coordinated by three bipyridines (Fe^{bipy}, λ_{bipy} = 497 and 539 nm). The second Fe^{II} coordinated by the TREN tri-pyridylimine coordination pocket (Fe^{TREN}) causes the much weaker higher-wavelength band at λ_{TREN} = 599 nm. These findings align well with comparable Fe^{II} complexes documented in the literature.[50,51]

Characterisation of homometallic helicates Co_2**L** and Zn_2**L** by mass spectrometry and NMR spectroscopy indicated the formation of similar structures to Fe_2**L** (Figures 2 and 3; Sections S3.3, S3.4 and S6.4.2).

The ^{1}H NMR spectrum of Co_2**L** is characteristically dispersed over a range of nearly 200 ppm (Figure S26), due to the paramagnetism of Co^{II}, which precludes further assignments of the signals. The UV–vis spectrum of Co_2**L** shows an MLCT absorption band at $\lambda \approx 350$ nm and an almost unchanged diazocine n–π* absorption band (405 nm; Figure S72).

The ^{1}H NMR spectrum of Zn_2**L** showed signal shifts similar to but clearly distinct from Fe_2**L** (Figure 2b). UV–vis spectroscopy of Zn_2**L** revealed an almost unchanged diazocine n–π* absorption band around 405 nm compared to subcomponent **1**, with no MLCT transition observed in the visible range (Figures 3a and S70).

The characteristic proton shifts of H-h, H-m, H-p, H-t, and H-u of Fe_2**L** and Zn_2**L** in ^{1}H NMR (Figure 2b), as well as the three characteristic MLCT bands of Fe^{bipy} and Fe^{TREN} in UV–vis (Figure 3a), allow for detailed elucidation of Fe^{II} and Zn^{II} distribution between the two coordination sites of ligand **L**, enabling us to analyse heterobimetallic helicates precisely.

Synthesis of Heterobimetallic Helicates

Ligand **L** features two coordination sites that are chemically, kinetically, and thermodynamically distinct: a TREN tri-pyridylimine and a bipyridine. The sixfold chelation of the TREN tri-pyridylimine coordination pocket (M^{TREN}) is kinetically more inert and potentially thermodynamically preferred over the three twofold chelating bipyridines (M^{bipy}) due to an enhanced chelate effect similar to that of a cryptand. The greater stability of TREN tri-pyridylimine coordination sites, compared to three individual pyridylimines, has been used in previous applications for subcomponent exchange and cage stabilisation.[52,53] Considering kinetics, the bipyridine binding site (M^{bipy}) should be accessible first, as the TREN tris-pyridylimine coordination pocket (M^{TREN}) has not yet formed via metal-mediated imine-bond formation. Thus, employing ligand **L** alongside two different metal cations, with one forming thermodynamically more stable M–N bonds[54] and exhibiting slower ligand exchange kinetics,[55–57] should result in the selective assembly of heterobimetallic helicates. Potential combinations of metal cations that favour an octahedral coordination sphere include Fe^{II} and Zn^{II} or Co^{II} and Zn^{II}.

Using the greater stability and kinetic inertness of the TREN tri-pyridylimine binding pocket (M^{TREN}), we attempted the consecutive assembly of a heterobimetallic helicate by mixing pyridine carboxaldehyde **1** (3 equiv.), TREN (1 equiv.), and $Fe(OTf)_2$ (1 equiv.) to form mononuclear complex Fe**L** with Fe^{II} in the TREN tris-pyridylimine

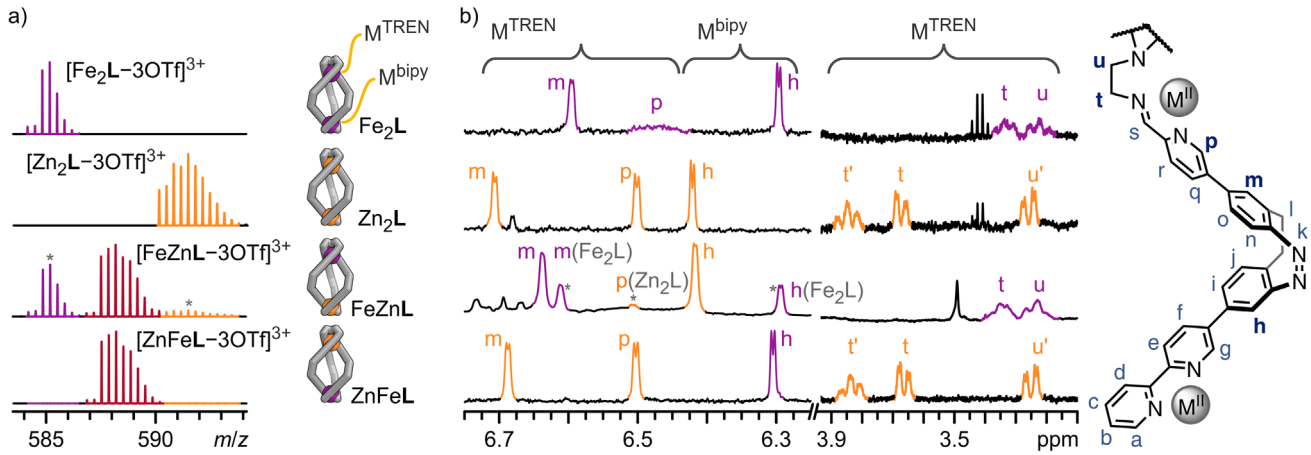

Figure 2. Analytical data of Fe_2**L**, Zn_2**L**, FeZn**L**, and ZnFe**L** (top to bottom). a) Partial high-resolution ESI$^+$ mass spectra (CH_3CN) showing the respective [MM'**L**–3OTf]$^{3+}$ isotope patterns. b) Partial ^{1}H NMR spectra (500 MHz, CH_3CN, 298 K) showing characteristic proton signals of the M^{TREN} and M^{bipy} coordination sites, respectively. Asterisks denote signals from Zn_2**L** and Fe_2**L**, respectively, indicating reduced selectivity in the stepwise formation of FeZn**L**. The spectra of Fe_2**L** and Zn_2**L** exhibit residual diethyl ether signals, as completely drying the sample under high vacuum led to decomposition. Right: Partial chemical structure of ligand **L**.

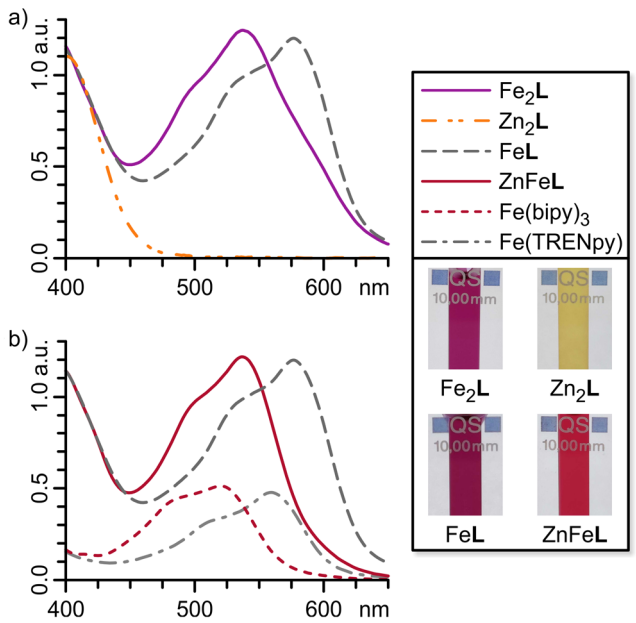

Figure 3. UV–vis spectra (0.03 mM, CH_3CN) of a) Fe_2**L**, Zn_2**L**, and Fe^{TREN}**L** as well as b) Fe^{TREN}**L**, ZnFe**L**, $Fe(bipy)_3$, and Fe(TRENpy). Insert: Photocromism of Fe_2**L**, Zn_2**L**, Fe^{TREN}**L**, and ZnFe**L**.

binding pocket (Fe^{TREN}**L**, Figure 4a). Subsequently, $Zn(OTf)_2$ (1 equiv.) was added to Fe**L** to allow formation of a heterobimetallic helicate with Fe^{II} remaining in the TREN tris-pyridylimine binding pocket (Fe^{TREN}) and Zn^{II} coordinating to the three bipyridine units (Zn^{bipy}), which we refer to as FeZn**L** (short for $Fe^{TREN}Zn^{bipy}$**L**). High-resolution ESI mass spectrometry confirmed the formation of an [Fe + **L**] species following the first reaction step, with minor amounts of Fe_2**L** also detected. After the second reaction step, an [Fe + Zn + **L**] species was generated, with some Fe_2**L** still present alongside newly formed Zn_2**L** (Figures 2a and S31). The presence of both Fe_2**L** and Zn_2**L**, alongside the desired FeZn**L**, suggests that the formation of Fe_2**L** is thermodynamically more favourable than the formation of Fe**L**, which results in unreacted or partially reacted TREN and **1** remaining in the reaction mixture. After the addition of $Zn(OTf)_2$, the unreacted or partially reacted ligand subcomponents, TREN and **1**, form Zn_2**L**.

The ^{1}H NMR spectrum of FeZn**L** confirmed the formation of a heterobimetallic helicate after the second reaction step (Figures 2b and S30). The chemical shifts of protons near the TREN tris-pyridylimine binding pocket, specifically diazocine proton H-m, pyridylimine proton H-p, and ethylene protons H-t and H-u, are comparable to the chemical shifts of their Fe_2**L** counterparts. In contrast, the chemical shift of diazocine proton H-h, which is close to the bipy unit, is nearly identical to that of its Zn_2**L** counterpart, indicating an $Fe^{TREN}Zn^{bipy}$**L** structure. As indicated by the ESI mass spectrum, ^{1}H NMR spectroscopy also suggested the formation of dinuclear homometallic Fe_2**L** and Zn_2**L** (25% and 10%, respectively, Figure 2b; Section S3.7). The higher proportion of Fe_2**L** compared to Zn_2**L** is likely due to an excess of $Fe(OTf)_2$ (approximately 10%) present during the formation of Fe**L**. As described above, distinct MLCT absorption bands for Fe^{II}, coordinated by three bipyridine units (Fe^{bipy}) or a TREN tris-pyridylimine binding pocket (Fe^{TREN}), facilitated further structural conformation of Fe**L** and FeZn**L** using UV-vis spectroscopy (Figures 3 and S32). The UV–vis spectra of Fe^{TREN}**L** and the reference compound Fe(TRENpy) are nearly identical, suggesting the presence of an Fe^{TREN} coordination sphere in Fe^{TREN}**L**. The UV–vis spectrum of FeZn**L** reveals a secondary band associated with the additional MLCT transition observed in the contaminant Fe_2**L**. Still, it displays a major band that is identical to the one found in Fe^{TREN}**L**. The difference in absorption bands between Fe^{bipy} and Fe^{TREN} is readily visible to the naked eye, as the bipyridine-containing Fe^{II} complexes exhibit a vibrant red colour, whereas their pyridylimine counterparts present a deep purple hue (Figure 3, insert). The kinetics of

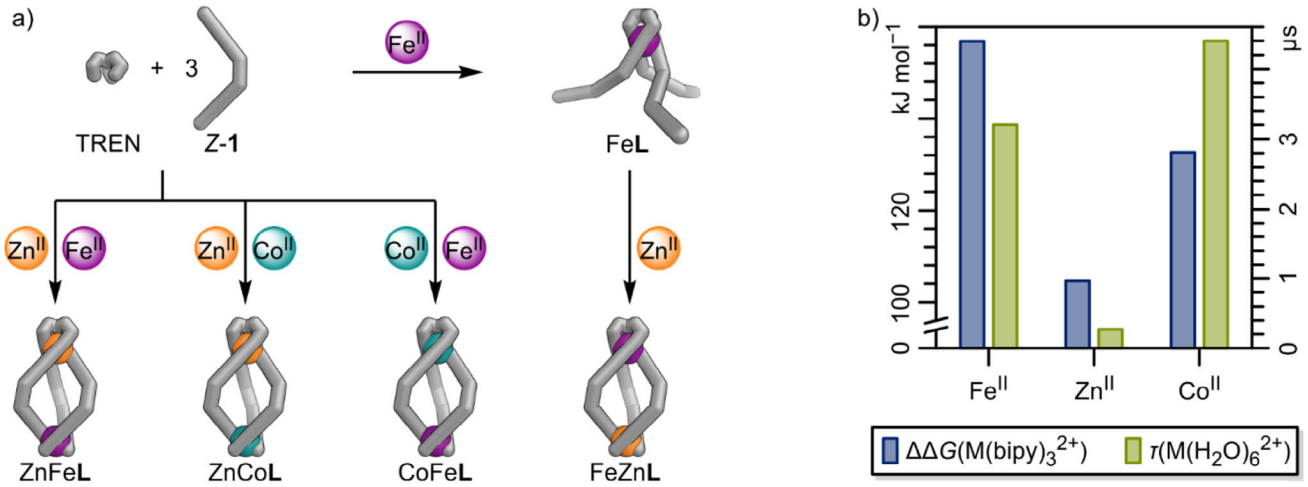

Figure 4. a) Stepwise self-assembly of heterobimetallic helicate FeZn**L** from TREN and *Z*-**1** and metal-cation self-sorting upon self-assembly of ZnFe**L**, ZnCo**L**, and CoFe**L**. Reaction conditions: CH_3CN, 70 °C, 12 h. b) Overview of thermodynamic and kinetic differences of Fe^{II}, Zn^{II} and Co^{II} complexes. Blue: Gibbs free energies[54] of the dissociation of one bipyridine ligand in $M(bipy)_3$. Green: mean lifetimes of coordinated water in $M(H_2O)_6^{2+}$ in water.[55–57]

Fe^{TREN}**L** complex formation were further investigated using UV–vis spectroscopy (Section S5), which indicated the nearly immediate formation of an Fe^{bipy}**1**$_3$ complex, in which Fe^{II} is coordinated by three bipy units, as evidenced by the appearance of the characteristic Fe^{bipy}-MLCT absorption band. Over a few hours, the Fe^{bipy}-MLCT absorption band transformed into an Fe^{TREN}-MLCT absorption band, thus indicating the successful formation of Fe^{TREN}**L**. The progress of the reaction can also be observed with the naked eye: the reaction solution turns a distinctive Fe^{bipy}-red colour within minutes and then gradually changes to a deep violet shade, characteristic of Fe^{TREN}, indicating the sequential formation of Fe^{bipy}**1**$_3$ and Fe^{TREN}**L**. Therefore, we conclude that Fe^{bipy}**1**$_3$ is kinetically favoured, whereas Fe^{TREN}**L** is potentially thermodynamically more stable but also kinetically more inert, thus confirming our assumption that the TREN tris-pyridylimine coordination pocket should be the more stable binding site.

After confirming our assumption regarding the kinetic and thermodynamic coordination behaviours of aldehyde **1** and ligand **L**, we aimed to harness these properties to achieve heterobimetallic social self-sorting using Fe^{II}, Zn^{II}, and Co^{II}. Given that Fe^{II} and Zn^{II} show the most significant difference in thermodynamic and kinetic stabilities (Figure 4b), we initially sought to form a self-sorted ZnFe**L** heterobimetallic helicate (short for $Zn^{TREN}Fe^{bipy}$**L**) from a mixture of pyridine carboxaldehyde **1** (3 equiv.), TREN (1 equiv.), $Fe(OTf)_2$ (1 equiv.), and $Zn(OTf)_2$ (1 equiv.) in acetonitrile (Figure 4a). The self-assembly of Fe^{TREN}**L** indicated that the M^{bipy} coordination site would form before the M^{TREN} binding site because it is readily accessible. In contrast, the M^{TREN} coordination site must be formed through three metal-mediated imine condensation reactions, which occur on a significantly slower timescale. Consequently, we anticipated that both Fe^{II} and Zn^{II} would first coordinate to the bipy units of **1**, with Fe^{II} gradually replacing the thermodynamically less stable Zn^{II} ($\Delta\Delta G^{Fe,Zn}(M(bipy)_3^{2+}) = 52.2$ kJ mol^{-1})[54] at all coordination sites, resulting in the formation of Fe^{bipy}**1**$_3$. Once all Fe^{II} is coordinated to bipy (Fe^{bipy}), only Zn^{II} should remain to facilitate the formation of TREN tri-pyridylimine, thereby selectively installing Zn^{II} in the M^{TREN} coordination pocket to produce ZnFe**L** (short for $Zn^{TREN}Fe^{bipy}$**L**). ZnFe**L** crystallised in the triclinic space group P1 (Figure 1b; Section S6.2). The solid-state structure confirmed the expected Zn^{TREN}-Fe^{bipy} metal distribution in a triple-stranded helicate structure almost identical to that of Fe_2**L** (Figure 1a; Section S6.2). High-resolution ESI mass spectrometry confirmed the formation of a [Zn + Fe + **L**] heterobimetallic helicate (Figures 2a and S38). ^{1}H NMR spectroscopy indicated the expected regioselectivity of the self-sorted helicate ZnFe**L** ($Zn^{TREN}Fe^{bipy}$**L**), as evidenced by the characteristic proton signal shifts of protons H-h, H-m, H-p, H-t, and H-u corresponding to Zn^{TREN} and Fe^{bipy} coordination (Figure 2b). Furthermore, ^{1}H,^{1}H ROESY NMR spectroscopy confirmed the retention of the solid-state structure in solution (Section S6.4.1). UV–vis spectroscopy revealed a characteristic Fe^{bipy}-MLCT absorption band ($\lambda_{bipy} = 537$ nm), whereas no Fe^{TREN}-MLCT absorption band ($\lambda_{TREN} \approx 580$ nm) was detected, further supporting the successful self-sorting within ZnFe**L** (Figures 3b and S76).

The investigation of the kinetics of ZnFe**L** complex formation via UV–vis spectroscopy further corroborated our proposed assembly mechanism for ZnFe**L** (Section S5). An Fe^{bipy}-MLCT absorption band ($\lambda_{bipy} = 540$ nm) quickly appeared, with no further changes to the spectra, indicating that Fe^{II} remained in the bipy binding site, thereby enabling the selective formation of TREN tri-pyridylimine around Zn^{II}. These findings suggest that this self-sorting into ZnFe**L** is, indeed, a delicate interplay between ligand association and formation kinetics as well as metal-coordination thermodynamics. Prolonged heating of ZnFe**L** (65 °C, 2 months) in the presence of 3.0 equiv. Fe^{II} led to the formation of 6% Fe_2**L**, demonstrating the kinetic inertness of the ZnFe**L** structure and the Zn^{TREN} coordination site while indicating

that Fe_2**L** might be thermodynamically favoured over ZnFe**L** (Section S9.4).

To support our hypothesis that heterobimetallic helicate self-sorting occurs due to a delicate interplay between metal–ligand stability and exchange kinetics, we attempted the synthesis of two additional heterobimetallic helicates using Zn^{II}/Co^{II} and Co^{II}/Fe^{II} mixtures. In these mixtures, both the differences in thermodynamic metal–ligand stability and in metal–ligand exchange kinetics are gradually reduced. While the difference in metal–ligand exchange kinetics between Zn^{II} and Co^{II} is comparable to that of the Zn^{II}/Fe^{II} pair,[55–57] the difference in M^{bipy}-association energy between $Co(bipy)_3^{2+}$ and $Zn(bipy)_3^{2+}$ is approximately half as high as that between $Fe(bipy)_3^{2+}$ and $Zn(bipy)_3^{2+}$ ($\Delta\Delta G^{Fe,Zn}(M(bipy)_3^{2+}) = 52.2$ kJ mol^{-1} and $\Delta\Delta G^{Co,Zn}(M(bipy)_3^{2+}) = 28.0$ kJ mol^{-1}, respectively; Figure 4b).[54] Therefore, helicate self-assembly from a mixture of Zn^{II} and Co^{II} should indicate whether the difference in thermodynamics or kinetics of the metal cations has a more significant impact on successful self-sorting. For Co^{II} and Fe^{II}, both the difference in M^{bipy}-association energy between $Co(bipy)_3^{2+}$ and $Fe(bipy)_3^{2+}$ and the difference in metal–ligand exchange kinetics are small.[54–57] Consequently, if our hypothesis was correct, we expected poor self-sorting, if any.

In the case of the one-pot heterobimetallic helicate assembly involving Zn^{II}, Co^{II}, **1**, and TREN (Figure 4a), both ^{1}H NMR spectroscopy and ESI mass spectrometry indicated selective self-sorting into the ZnCo**L** ($Zn^{TREN}Co^{bipy}$**L**) helicate (SI,Section S4.1.2). ESI mass spectrometry revealed a singular set of peaks for $[Zn + Co + \mathbf{L} + n\text{OTf}]^{(4-n)+}$ ($n = 0$, 1, 2), and the wide-sweep ^{1}H NMR spectrum displayed only signals reminiscent of those in $Co(bipy)_3(OTf)_2$, with none reminiscent of a Co^{II}-TREN tri-pyridylimine coordination.

Helicate assembly in the presence of Co^{II} and Fe^{II}, however, resulted in a mixture of CoFe**L** ($Co^{TREN}Fe^{bipy}$**L**, approx. 60%–70%), Fe_2**L** (approx. 15%) and Co_2**L** helicates (approx. 15%). The composition of the helicate mixture was tentatively estimated using ESI mass spectrometry, NMR, and UV–vis spectroscopy (Sections S4.3 and S4.4). The paramagnetic nature of Co^{II} hindered the determination of accurate values.

The attempted heterobimetallic self-sorting experiments with Zn^{II}/Co^{II} and Co^{II}/Fe^{II} indicate that self-sorting still occurs with a reduced difference in metal–ligand bond strength. However, self-sorting is significantly less efficient if both the binding energy difference and the difference in ligand exchange kinetics are diminished, as seen in the Co^{II}/Fe^{II} pair. Remarkably, Co^{II} can occupy both ligand **L**'s coordination sites, depending on the other metal cation present in the self-sorting process. These results further support our proposed self-sorting mechanism into heterobimetallic helicates (Scheme S54):

I. Both metal cations form M^{bipy}-complexes with three equivalents of subcomponent **1**, respectively.
II. Because of the disparity in metal–ligand binding energies ($Fe^{II} > Co^{II} > Zn^{II}$), the more stable metal cation replaces the weaker in the M^{bipy} complexes and gets sequestered by the M^{bipy} coordination sphere.

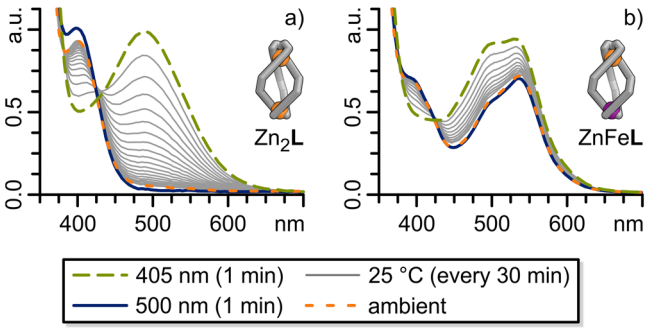

Figure 5. UV–vis spectra (0.03 mM, CH_3CN, 25 °C) under ambient light and after 405 and 500 nm light irradiation, respectively, as well as thermal relaxation after 405 nm light irradiation for a) Zn_2**L** and b) ZnFe**L**.

III. "Trapping" the more stable cation in the M^{bipy} coordination sphere allows the thermodynamically less stable metal cation to facilitate the formation of the TREN tri-pyridylimine binding pocket M^{TREN}, thereby completing the self-sorted heterobimetallic helicate.

Photoswitching of Zn_2L

After demonstrating the ability of ligand **L** to form either dinuclear homometallic helicates or even heterobimetallic ones via the effective self-sorting of two different metal cations, we investigated the effects of switching the photochromic diazocine units within the helicates.

Irradiation of an acetonitrile solution of Zn_2**L** with visible light (405 nm, 25 °C, 1 mM) resulted in a colour change from yellow to red, along with the disappearance of the 405 nm absorption band and the emergence of an intense absorption band at 490 nm in the UV–vis spectrum (Figure 5a). The changes in the UV–vis spectrum are nearly identical to those observed for aldehyde **1** (Figure S80), suggesting an equally efficient $Z \rightarrow E$ conversion in Zn_2**L** helicate as in free aldehyde **1** upon irradiation with 405 nm light. High-resolution ESI mass spectrometry demonstrates that the Zn_2**L** composition remains intact following irradiation with 405 nm light (Figure S99). Additionally, ^{1}H DOSY NMR spectroscopy indicated that the diffusion coefficients—and, therefore, the solvodynamic diameters—of the structures before and after 405 nm light irradiation differ only slightly (Figure 6b, bottom). In the ^{1}H NMR spectrum, irradiation of Zn_2**L** with 405 nm light results in the disappearance of nearly all previously sharp and well-defined signals, leaving only ill-defined and broad signals, apart from the signals of the ethylene groups H-t and H-u. Moreover, no signals for the free ligand **L** or free aldehyde **1** were detected, indicating that at least the Zn^{TREN} binding pocket remained intact following irradiation (Figure 6b, green, 2nd from top). The intact Zn^{TREN} binding pocket, along with high-resolution ESI mass spectrometry confirming the retention of the Zn_2**L** composition, ^{1}H DOSY NMR spectroscopy suggesting a structure of a similar solvodynamic diameter, and UV–vis

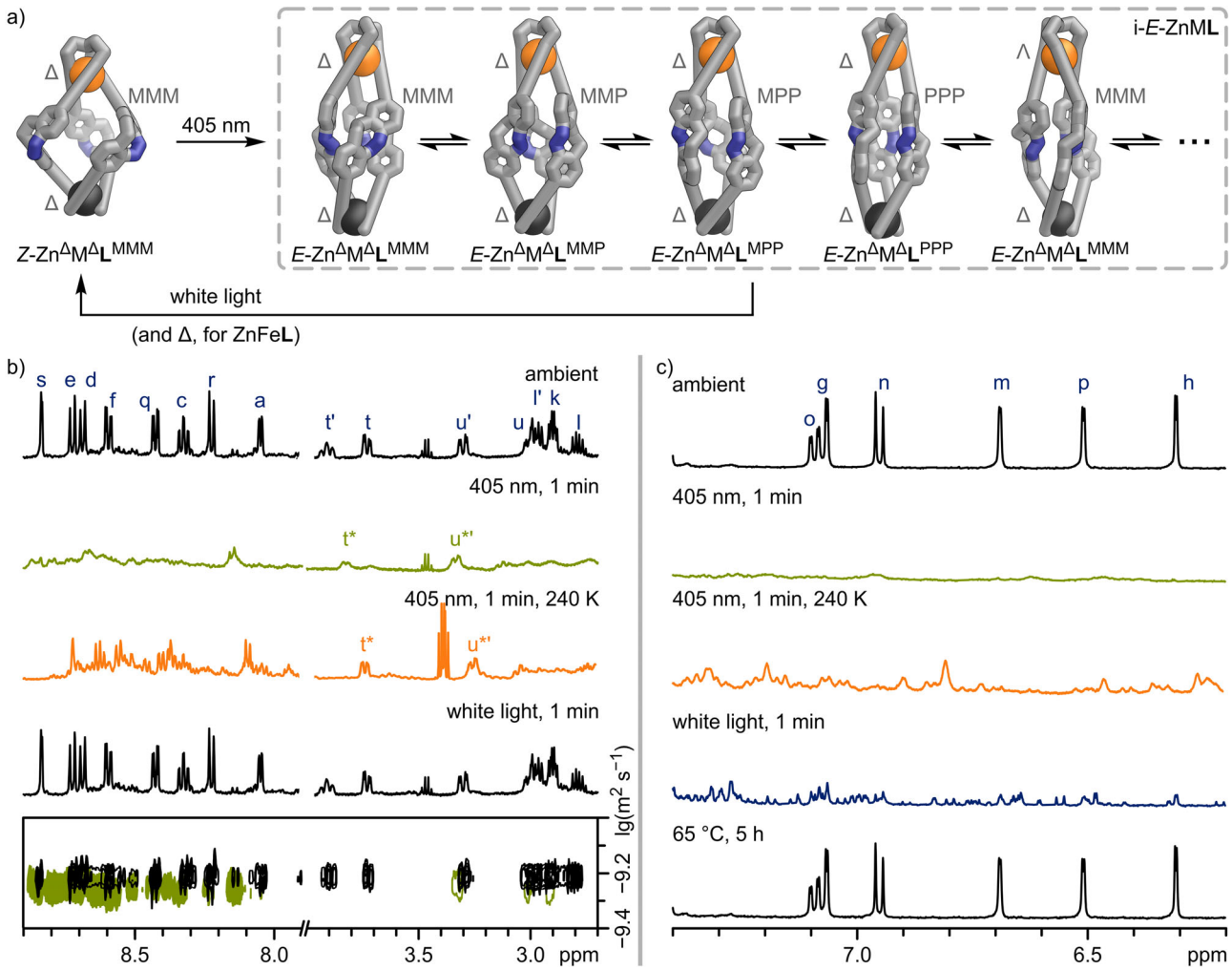

Figure 6. Photoswitching of Zn_2**L** and ZnFe**L** (ZnM**L**; stylised representations of GFN2-xTB optimised structures). a) Photoisomerisation of *Z*-ZnM**L** to a mixture of possible *E*-ZnM**L** diastereomers (i-*E*-ZnM**L**). *Nomenclature* (looking along the M^{TREN}–M^{bipy} axis) Δ/Λ: right-/lefthanded helicity of the metal cation ligand environment; P/M: diazocine nitrogens pointing clockwise/anti-clockwise. i: mixture of isomers of the same composition and ligand configuration (*E*/*Z*), i.e., i-*E*-ZnM**L** represents all states in the grey dashed box. b) ^{1}H NMR spectra (500 MHz, CD_3CN) of Zn_2**L** under ambient conditions (298 K, black), after 405 nm light irradiation (1 min; 298 K (green) and 240 K (orange), respectively), after white light irradiation (1 min, 298 K, black), and ^{1}H DOSY NMR spectrum before and after 405 nm light irradiation (black and green, respectively, 298 K; top to bottom). c) ^{1}H NMR spectra (500 MHz, CD_3CN) of ZnFe**L** under ambient conditions (298 K, black), after 405 nm light irradiation (1 min; 298 K (green) and 240 K (orange), respectively), after white light irradiation (1 min, 298 K, blue), and after heating to 65 °C (5 h, 298 K, black; top to bottom).

spectroscopy demonstrating successful switching of the diazocine units, might indicate the formation of an *E*,*E*,*E*-Zn_2**L** structure (abbreviated as *E*-Zn_2**L**, Figure 6a). Although switching should occur in a stepwise manner, we tentatively assume structures in which only some of the diazocines are switched, namely *E*,*E*,*Z*-Zn_2**L** and *E*,*Z*,*Z*-Zn_2**L**, to be unlikely, as literature precedence[14,18,58,59] of cages containing photochromic units in their ligand backbone suggests that switching is a highly cooperative process, with intermediates only observed at extremely low temperatures.[60] The first switching event causes the most significant structural change, potentially accelerating the subsequent switching of other photochromic units within the same structure to relieve strains caused by previous isomerisation events.

The observed broad ^{1}H NMR signals after 405 nm irradiation of Zn_2**L** (Figure 6b, green, 2nd from top) indicate structural transformations, which are on intermediate exchange on the NMR timescale. We tentatively assume these to be hindered rotations of the diazocine moieties within the arms of the ligands or isomerisation of the helicate to a pseudo-mesocate. In *E*,*E*,*E*-Zn_2**L**, the three "arms" of ligand **L** adopt a pseudo-linear configuration, enabling rotation of the diazocine moieties (i-*E*-Zn_2**L**, Figure 6a, right; Figure S102).

Rotation of the diazocine moieties would give rise to four potential constantly interconverting rotamers with the diazocine units pointing with their azo-nitrogens either in a clockwise ($\mathbf{L}^{PPP}$) or counterclockwise direction ($\mathbf{L}^{MMM}$) in the helicate or even mixtures of both ($\mathbf{L}^{PPM}$ or $\mathbf{L}^{MMP}$; Figure 6a). Additionally, due to steric strains within *E*-Zn_2**L**, we anticipate that both Zn^{II} corners in *E*-Zn_2**L** will be significantly weaker than those in *Z*-Zn_2**L**, potentially promoting

isomerisation between helicate and pseudo-mesocate or even facilitating metal exchange.

To test our hypothesis regarding the interconversion of rotamers and helicate-to-pseudo-mesocate leading to the broad signals in the ^{1}H NMR spectrum after 405 nm irradiation of *Z*-Zn_2**L**, we performed low-temperature ^{1}H NMR spectroscopy (240 K) on the same sample (Figure 6b, orange, 3rd from top; Figure S97). The resulting spectrum reveals a multitude of sharp signals, indicating a plethora of chemical environments and isomeric structures, which do not interconvert at this temperature. This observation supports our hypothesis that multiple interconverting diastereomers (i-*E*-Zn_2**L**) are responsible for the broad signals observed at 298 K. Irradiation of i-*E*-Zn_2**L** with either 500 nm or white light reverses the process almost instantly, indicating that Zn_2**L** switching is completely reversible at ambient temperature (Figure 6b, black, 4th from top). However, at 240 K, irradiation of i-*E*-Zn_2**L** with white light does not lead to the clean formation of *Z*-Zn_2**L** but rather a multitude of sharp signals that indicate the formation of multiple isomers (Figure S97). Therefore, we tentatively assume that irradiation with white light causes all diazocine moieties to switch back into their *Z* states, with each i-*E*-Zn_2**L** helicate or pseudo-mesocate rotamer isomerising to its corresponding i-*Z*-Zn_2**L** helicate or pseudo-mesocate atropisomer. These atropisomers cannot interconvert without breaking at least one pair of Zn^{II}-bipy coordinative bonds. At 240 K, the abundance of atropisomers results in numerous sharp ^{1}H NMR signals (Figure S97). At room temperature, the Zn^{II}-bipy coordinative bond readily dissociates, allowing the atropisomers to converge to the most stable *Z*-Zn_2**L** structure (Figure S97). Thus, the isomerisation process *Z*-Zn_2**L**→*E*-Zn_2**L**→*Z*-Zn_2**L** is influenced by the kinetic lability of the metal cation within the bipy pocket of **L**. To further explore the intricate *Z*-Zn_2**L**→*E*-Zn_2**L**→*Z*-Zn_2**L** switching mechanism and support our hypothesis, we investigated switching in ZnFe**L**, which contains a kinetically more stable Fe^{II} in the bipy binding site of **L** (Fe^{bipy}) and should, thus, hinder isomerisation of the atropisomers (i-*Z*-ZnFe**L**) to the thermodynamically preferred structure (*Z*-$Zn^{\Delta}Fe^{\Delta}$**L**^{MMM}).

Photoswitching of ZnFeL: A Molecular Energy Ratchet

Similar to Zn_2**L**, the irradiation of ZnFe**L** with 405 nm light resulted in a ^{1}H NMR spectrum featuring broad signals, while ^{1}H DOSY NMR spectroscopy and high-resolution ESI mass spectrometry indicated the formation of a species with the same composition and a similar size to *Z*-ZnFe**L**, which we denote as i-*E*-ZnFe**L** (Figure 6; Sections S7.4 and S7.5). The UV–vis spectra of *Z*-ZnFe**L** and *E*-ZnFe**L** showed nearly the same differences as those between *Z*-Zn_2**L** and *E*-Zn_2**L**, as well as *Z*-**1** and *E*-**1**, with the MLCT absorption band remaining unchanged (Figure 5b; Figure S80). This suggests that photoswitching remains efficient, even in the presence of the Fe^{bipy} MLCT absorption band, and that both Fe^{TREN} and Fe^{bipy} coordination are preserved. As with i-*E*-Zn_2**L**, the observed broad ^{1}H NMR signals for i-*E*-ZnFe**L** sharpened when cooled to 240 K (Figure 6c, orange, 3rd from top), indicating that diazocine rotation and helicate→pseudo-mesocate isomerisation caused the broadened signals at room temperature.

As envisioned, irradiating i-*E*-ZnFe**L** with white light resulted in a complex ^{1}H NMR spectrum featuring multiple signal sets (Figure 6c, blue, 4th from top). This signal pattern is similar to that of i-*E*-Zn_2**L** following 405 nm and white light irradiation at 240 K, prompting us to label it i-*Z*-ZnFe**L** (Scheme 2; Figure S98). We can reform the thermodynamically stable *Z*-ZnFe**L** by heating i-*Z*-ZnFe**L** at 65 °C for five hours (Figure 6c, black, 5th from top). The formation of kinetically trapped states after 405 nm and white light irradiation at room temperature was also observed for Fe_2**L** (Figure S84), supporting our hypothesis that the dissociation of bipyridine units in the M^{bipy} coordination site is the rate-determining step for the kinetically trapped states to revert to the thermodynamically favoured *Z*-$M^{\Delta}M^{\Delta}$**L**^{MMM} (*Z*-$Zn^{\Delta}Zn^{\Delta}$**L**^{MMM}, *Z*-$Zn^{\Delta}Fe^{\Delta}$**L**^{MMM}, and *Z*-$Fe^{\Delta}Fe^{\Delta}$**L**^{MMM}, respectively). The stronger metal–ligand bond of Fe^{II} compared to Zn^{II} leads to a higher barrier for the dissociation of metal–bipyridine coordination, creating a more effective kinetic trap. This elevated barrier is evident in the temperature needed for the various helicate and pseudo-mesocate atropisomers (i-*Z*-Zn_2**L**, i-*Z*-ZnFe**L**, and i-*Z*-Fe_2**L**) to return to their initial thermodynamically favoured states *Z*-$M^{\Delta}M^{\Delta}$**L**^{MMM} (*Z*-$Zn^{\Delta}Zn^{\Delta}$**L**^{MMM}, *Z*-$Zn^{\Delta}Fe^{\Delta}$**L**^{MMM}, and *Z*-$Fe^{\Delta}Fe^{\Delta}$**L**^{MMM}, respectively), which rises from room temperature for i-*Z*-Zn_2**L** to 65 °C for i-*Z*-ZnFe**L** and i-*Z*-Fe_2**L**.

We examined the kinetically trapped intermediates during the switching cycle of ZnFe**L** through in situ illuminated ^{1}H NMR spectroscopy (Section S7.4.3). Although the variety of signals hindered a thorough kinetic analysis, our findings indicate that irradiating ZnFe**L** with 405 nm light produces a mixture of at least two distinct species. This implies that the structural alterations induced by 405 nm light irradiation result in a distribution of conformational and possibly isomeric (helicate and pseudo-mesocate) states. The notable asymmetry in these i-*E*-ZnFe**L** states is evident in the intricate ^{1}H NMR spectrum.

From these findings, we conclude that photoswitchable helicate ZnFe**L** functions as a light-driven molecular energy ratchet (Scheme 2):

I. Irradiation of ZnFe**L** with 405 nm light causes all diazocine units within the structure to isomerise to their *E*-configurations, forming symmetric *E*-ZnFe**L** (*E*-$Zn^{\Delta}Fe^{\Delta}$**L**^{MMM}).
II. In *E*-ZnFe**L**, the diazocines can now rotate, albeit slowly, resulting in four rotamers (*E*-$Zn^{\Delta}Fe^{\Delta}$**L**^{MMM}, *E*-$Zn^{\Delta}Fe^{\Delta}$**L**^{PMM}, *E*-$Zn^{\Delta}Fe^{\Delta}$**L**^{PPM}, *E*-$Zn^{\Delta}Fe^{\Delta}$**L**^{PPP}; Figure 6a; Section S7.6). *E*-ZnFe**L** is sterically strained with weakened coordinative bonds around the Zn^{TREN} and Fe^{bipy} corners, which allows for helicate→pseudo-mesocate isomerisation, giving rise to four pseudo-mesocate rotamers (*E*-$Zn^{\Lambda}Fe^{\Delta}$**L**^{MMM} etc.; Sections S6.3 and S8). Rotamer and pseudo-mesocate formation from symmetric *E*-$Zn^{\Delta}Fe^{\Delta}$**L**^{MMM} to i-*E*-ZnFe**L** occurs rapidly, indicating low energy differences and activation barriers between the states.

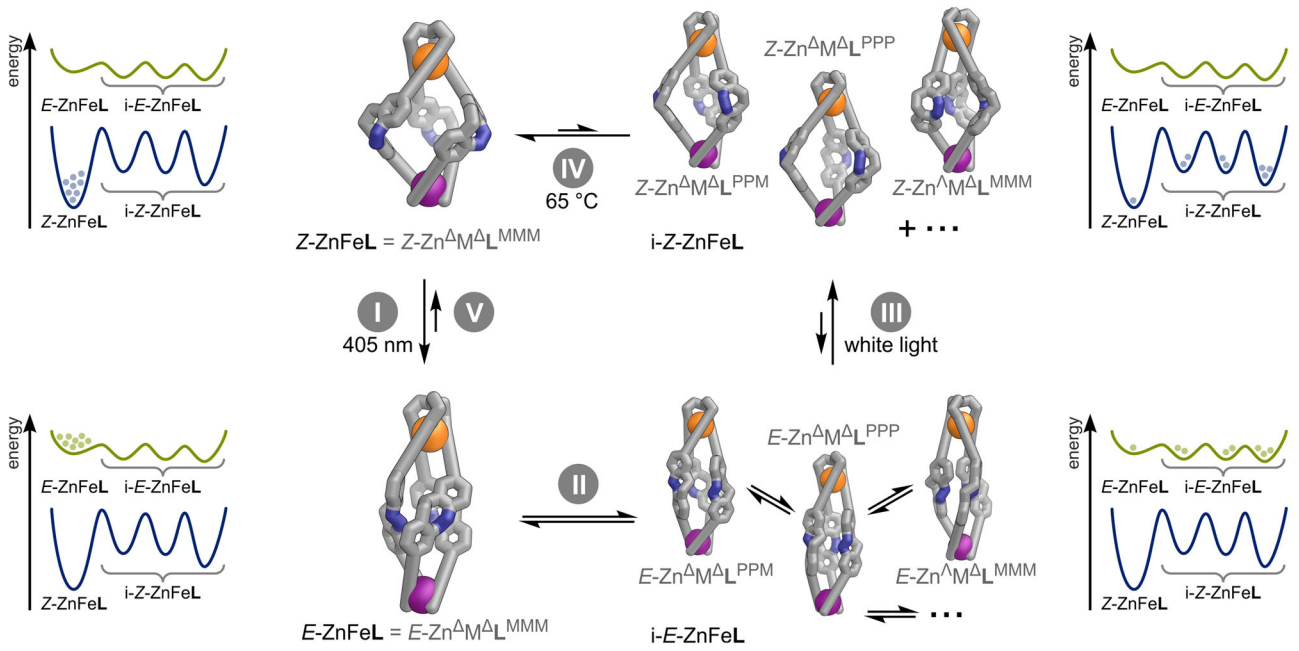

Scheme 2. Chemical reaction network and schematic potential energy surfaces related to the formation of high-energy diastereomers i-*Z*-ZnFe**L**, facilitated by a molecular ratchet mechanism driven by consecutive 405 nm and white light irradiation (stylised representations of GFN2-xTB optimised structures). (I) *Z*→*E* photoisomerisation of *Z*-ZnFe**L** to *E*-ZnFe**L**. (II) Isomerisation of *E*-ZnFe**L** via rotation of the diazocine moieties or helicity flipping of a metal vertex. (III) *E*→*Z* photoisomerization of different i-*E*-ZnFe**L** diastereomers, which are now kinetically trapped in their high-energy states. (IV) Thermal relaxation from i-*Z*-ZnFe**L** isomers to *Z*-ZnFe**L**.

III. Irradiating the isomeric mixture i-*E*-ZnFe**L** with 500 nm or white light causes all diazocine units within the supramolecular structures to isomerise to their *Z*-configurations, trapping the respective helicates, pseudo-mesocates, and their rotamers (i-*Z*-ZnFe**L**).
IV. Due to the kinetic inertness of Fe^{II}, i-*Z*-ZnFe**L** represent kinetically trapped states that can revert to the thermodynamically favoured *Z*-$Zn^{\Delta}Fe^{\Delta}\mathbf{L}^{MMM}$ by partial Fe^{bipy} coordination site dissociation at 65 °C, thus closing the reaction cycle.

Trapping the respective i-*E*-ZnFe**L** in their current isomeric forms through photoswitching provides a potential direct pathway from symmetric *E*-$Zn^{\Delta}Fe^{\Delta}\mathbf{L}^{MMM}$ to ground state *Z*-$Zn^{\Delta}Fe^{\Delta}\mathbf{L}^{MMM}$ (Scheme 2, process V).

In the case of Zn_2**L**, i-*Z*-Zn_2**L** are kinetically trapped at low temperatures (Figure 6b), demonstrating that the same processes operate during the irradiation of Zn_2**L**.

Since most molecules follow the reaction cycle unidirectionally (Scheme 2, processes I–IV), the photoswitching of ZnFe**L** acts as a light-driven molecular energy ratchet: 405 nm light irradiation drives the thermodynamically stable *Z*-ZnFe**L** helicate into metastable *E*-ZnFe**L** helicates, which can readily access various conformers and stereoisomers (i-*E*-ZnFe**L**). Under white light irradiation, these i-*E*-ZnFe**L** states relax swiftly into their corresponding kinetically trapped i-*Z*-ZnFe**L** isomers. These higher-energy kinetically trapped isomers (i-*Z*-ZnFe**L**) cannot readily return to the initial thermodynamically stable state (*Z*-ZnFe**L**) due to the required rotation of the diazocine units being only possible through partial Fe^{bipy} coordination-site dissociation. Thus, the system captures light energy to convert the more stable isomer (*Z*-ZnFe**L**) into less stable, kinetically trapped isomers (i-*Z*-ZnFe**L**). This transformation leads to the occupancy of higher-energy states, storing some of the absorbed light energy as strained or unfavourable molecular conformations.

An Autonomously Operating Molecular Ratchet Under White Light Irradiation

Remarkably, this molecular energy ratchet can operate autonomously when exposed to white light, even though the photostationary state under such light is less than 1% *E*-diazocine. Constant white light irradiation accumulates one specific structure (70% after 24 h; Figure 7). Using ^{1}H NMR and $^{1}H,^{1}H$ ROESY NMR spectroscopy, we unambiguously determined the structure as the *Z*-$Zn^{\Lambda}Fe^{\Delta}\mathbf{L}^{MMM}$ pseudo-mesocate (and its enantiomer). The observed proton–proton contacts between ligand **L**'s pyridine and diazocine phenyl rings (H-f↔H-h, H-g↔H-i, H-m↔H-p, H-o↔H-q) correspond to the ligand conformation within the *Z*-$Zn^{\Lambda}Fe^{\Delta}\mathbf{L}^{MMM}$ pseudo-mesocate (for further details see Section S8). Although a photostationary state below 1% *E*-diazocine enables efficient *E*→*Z* isomerisation on a macroscopic level, diazocine moieties and, consequently, ZnFe**L**, continually isomerise at a microscopic level. Given the properties of the molecular ratchet, a minimal quantity of *E*-ZnFe**L** effectively propels the reaction cycle. Similar to a mechanical ratchet, each light-triggered cycle advances the system by selectively confining it in energetically less favourable but kinetically stable states (i-*Z*-ZnFe**L**). Under continuous irradiation, the system converges into

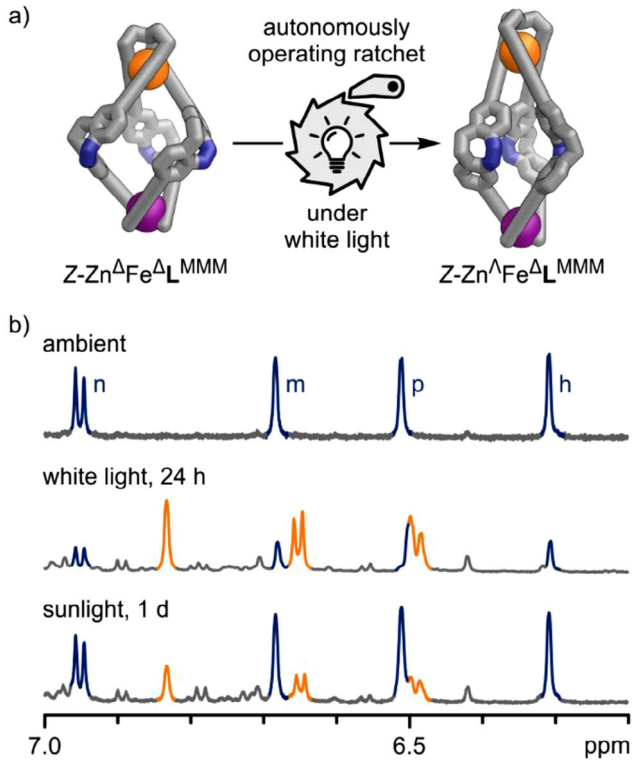

Figure 7. a) Continuous exposure to white light powers the ratchet autonomously, leading to the formation of a particular mesocate structure. (*Z*-Zn$^{\Lambda}$Fe$^{\Delta}$**L**^{MMM}, as a racemate; stylised representations of GFN2-xTB optimised structures). b) ^{1}H NMR spectra (500 MHz, CD_3CN, 298 K) of parent structure *Z*-Zn$^{\Delta}$Fe$^{\Delta}$**L**^{MMM} under ambient conditions, after white light irradiation for 24 h, and after exposing the parent structure *Z*-Zn$^{\Delta}$Fe$^{\Delta}$**L**^{MMM} to sunlight for one winter day (top to bottom). In all spectra post-irradiation, parent helicate *Z*-Zn$^{\Delta}$Fe$^{\Delta}$**L**^{MMM} (blue) and mesocate *Z*-Zn$^{\Lambda}$Fe$^{\Delta}$**L**^{MMM} (orange) could be identified.

the most stable high-energy configuration, identified as *Z*-Zn$^{\Lambda}$Fe$^{\Delta}$**L**^{MMM}. This conversion into *Z*-Zn$^{\Lambda}$Fe$^{\Delta}$**L**^{MMM} could occur via two pathways:

(i) Photochemical $Z \rightarrow E$ isomerisation of a *Z*-ZnFe**L** to an *E*-ZnFe**L** isomer, which subsequently isomerises into the corresponding *E*-Zn$^{\Lambda}$Fe$^{\Delta}$**L**^{MMM} pseudo-mesocate. $E \rightarrow Z$ isomerisation then yields *Z*-Zn$^{\Lambda}$Fe$^{\Delta}$**L**^{MMM}.

(ii) Slow thermal relaxation of less favourable high-energy i-*Z*-ZnFe**L** isomers to relatively more favourable pseudo-mesocate *Z*-Zn$^{\Lambda}$Fe$^{\Delta}$**L**^{MMM}.

Kinetic studies on the thermal relaxation of the i-*Z*-ZnFe**L** mixture, obtained via subsequent 405 nm and white light irradiation, support the thermal relaxation pathway (ii). The time-dependent ^{1}H NMR spectra revealed that various components of this mixture were interconverting, with none of the involved species returning to the initial ground state of *Z*-ZnFe**L** (*Z*-Zn$^{\Delta}$Fe$^{\Delta}$**L**^{MMM}; Section S7.4.4). Thermal conversion of pseudo-mesocate *Z*-Zn$^{\Lambda}$Fe$^{\Delta}$**L**^{MMM} into the overall thermodynamically more stable *Z*-Zn$^{\Delta}$Fe$^{\Delta}$**L**^{MMM} helicate occurred at room temperature, exhibiting a half-life of several days (Figure S115).

Curiously, the molecular ratchet functions in sunlight as well. When a sample of *Z*-Zn$^{\Delta}$Fe$^{\Delta}$**L**^{MMM} helicate is placed by a window for one winter day, it transforms into a mixture

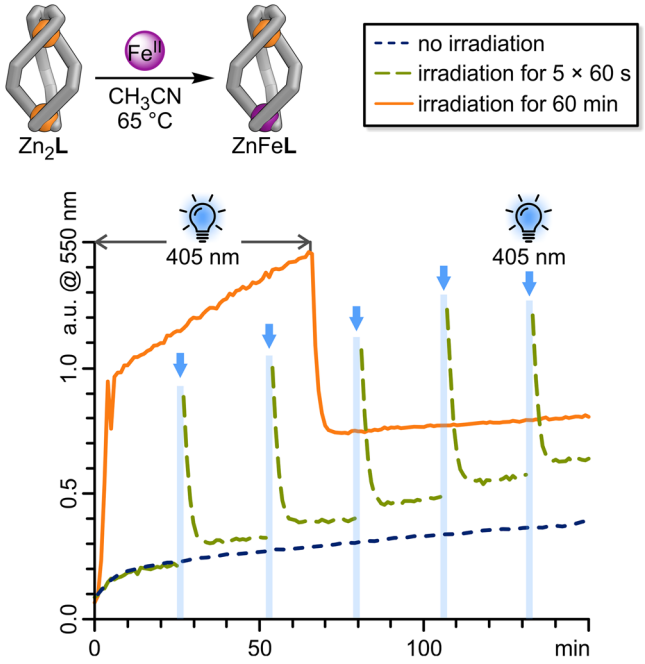

Figure 8. Zn^{II}→Fe^{II} exchange transforming Zn_2**L** into ZnFe**L** by mixing $Fe(OTf)_2$ (1.5 equiv.) and Zn_2L at 65 °C. The reaction progress was monitored by following the Fe^{bipy} MLCT absorption band at 550 nm via UV–vis spectroscopy (CH_3CN, 0.06 mM, 65 °C). Blue dotted line: background reaction without irradiation. Green dashed line: The sample was irradiated with 405 nm light for 60 s five times, as indicated by the blue arrows. Orange solid line: The sample was irradiated for the first 60 min of the measurement as indicated by grey arrows.

enriched with pseudo-mesocate *Z*-Zn$^{\Lambda}$Fe$^{\Delta}$**L**^{MMM} (Figure 7b, bottom). However, this process is less efficient compared to using a white LED. Therefore, the molecular ratchet is capable of converting light into chemical energy and can even retain that energy for a limited duration.

Metal Exchange

As mentioned earlier, ligand **L** contains two coordination sites with distinct kinetic stabilities, which we have shown to be essential for self-sorting of heterobimetallic helicates. To take advantage of the differences in kinetic inertness between the two binding sites, we performed a selective metal-cation exchange in the M^{bipy}-coordination site, transforming Zn_2**L** into ZnFe**L** via Zn^{II}→Fe^{II} exchange (Figure 8, top). Specifically, treating an acetonitrile solution of Zn_2**L** with $Fe(OTf)_2$ (1.5 equiv.) at 65 °C led to the formation of ZnFe**L**, confirmed by ^{1}H NMR, UV-vis spectroscopy, and ESI mass spectrometry (Section S9). Kinetic studies using ^{1}H NMR spectroscopy (Section S9.3) indicated that the Zn^{II}→Fe^{II} exchange does not follow apparent first-order kinetics. Rather, Zn_2**L** is rapidly consumed, resulting in both the intended product ZnFe**L** and a non-productive intermediate. This resting state is subsequently converted into the product ZnFe**L** via Zn_2**L** as an intermediate.

Given that the helicate molecular ratchet is accumulating high-energy structures (i-*E*-ZnFe**L**), in which the M^{bipy}

coordination site is likely weakened, we aimed to examine whether we could use this unidirectional reaction cycle (Scheme 2) to expedite the $Zn^{II} \rightarrow Fe^{II}$ cation exchange within Zn_2**L**, resulting in the formation of ZnFe**L**. To evaluate this hypothesis, $Fe(OTf)_2$ (1.5 equiv.) was added to an acetonitrile solution of Zn_2**L** at 65 °C, and the mixture was illuminated with 405 nm light for 60 seconds every 25 min. Since ZnFe**L** shows a distinct Fe^{bipy} MLCT transition band at 550 nm, which correlates with the number of Fe—N bonds formed and which Zn_2**L** entirely lacks (Figure 5), this reaction can also be monitored in situ using UV–vis spectroscopy (Figure 8). Note that *E*-diazocines exhibit strong absorption at 550 nm (Figure S68), and this will influence the absorption band at 550 nm during irradiation, continuing until the diazocine thermally returns to its *Z*-form. The thermal relaxation of the *E*-diazocine moieties to their *Z*-configurations occurs rapidly at 65 °C ($\tau_{\frac{1}{2}}(65\ °C) = 72$ s), achieving complete conversion within less than 10 min. In the dark, the Zn_2**L**→ZnFe**L** background reaction (Figure 8, blue dotted line) shows a rapid initial rise in conversion before stabilising to a nearly linear reaction rate after about 12 min. Irradiating the Zn_2**L**→ZnFe**L** reaction mixture with 405 nm light outside the UV–vis spectrometer results in a significant increase in absorption at 550 nm (Figure 8, green dashed line), primarily attributed to the absorption of the *E*-diazocine units. However, the observed increase in 550 nm absorption approximately 10 min after irradiation can be solely attributed to an increased Fe^{bipy} absorption, which reflects the Zn_2**L**→ZnFe**L** conversion. Four subsequent irradiations of the reaction mixture with 405 nm light further accelerate the conversion of Zn_2**L** to ZnFe**L**, resulting in nearly double the amount of ZnFe**L** produced compared to the background reaction after 150 min. The increased conversion of Zn^{bipy} to Fe^{bipy} after five 60-s light irradiations of the ZnFe**L**-$Fe(OTf)_2$ reaction mixture reinforces our hypothesis that the molecular ratchet can help promote this exchange.

Notably, the $Zn^{bipy} \rightarrow Fe^{bipy}$ exchange could also be accelerated under constant irradiation (60 min; Figure 8, orange solid line). Once the *E*-diazocine moieties have reached their photostationary states, their absorption remains constant under continuous irradiation. Consequently, the significant fivefold steeper increase in absorption observed between minutes 10 and 60, compared to the background reaction, can be solely ascribed to an accelerated exchange from Zn^{bipy} to Fe^{bipy}.

We believe that the molecular energy ratchet mechanism is vital for enabling the metal-cation exchange process. By populating higher-energy states and enriching non-ideal conformers, the photoswitching process effectively destabilises the coordination sphere around the metal centres, thereby accelerating the $Zn^{bipy} \rightarrow Fe^{bipy}$ exchange process. The ability to control this process through light irradiation offers a powerful tool for modulating kinetics in complex systems.

Conclusion

To summarise, we have created a unique photoswitchable diazocine-based ligand **L**, which self-assembles into a range of photo-responsive metallo-supramolecular bimetallic helicates. The subtle balance between bond strength and kinetic lability at both the ligand coordination sites and the metal cations enabled us to form dinuclear heterobimetallic Zn^{II}-Fe^{II} and Zn^{II}-Co^{II} helicates with precise metal distribution through one-pot self-sorting reactions. We believe that this self-sorting primarily involves a kinetic selection process regarding ligand **L**'s binding sites, meaning that the M^{bipy} coordination site is formed first. Additionally, it entails a thermodynamic selection for the metal cations, where the more thermodynamically stable Fe**1**$_3$ (or Co**1**$_3$) complex is favoured over the less stable Zn**1**$_3$.

Importantly, we discovered that $Z \rightarrow E$ photoisomerisation of the diazo units in the metallo-supramolecular Zn_2**L** and ZnFe**L** helicates initiates various conformational and stereochemical changes, all while preserving the overall constitutional integrity of the complexes. These conformers become trapped in higher energy isomers and atropisomers following $E \rightarrow Z$ isomerisation. We interpret the system as a molecular energy ratchet, capable of temporarily storing light energy by populating these energy-rich isomers. The molecular ratchet could autonomously function under continuous white light exposure, efficiently converting light energy into chemical energy within a high-energy *Z*-ZnFe**L** pseudo-mesocate.

The higher-energy *E*-isomers formed under light irradiation exhibit a more labile M^{bipy} coordination sphere, allowing the molecular ratchet to operate as a light-controlled accelerator for the highly selective metal-cation exchange process from homobimetallic Zn_2**L** to heterobimetallic ZnFe**L** helicate.

Our work enhances the structural complexity and functionality of photoswitchable complexes, highlighting the potential of using light to drive supramolecular systems out of equilibrium. This could open up new paths for developing light-controlled molecular machines, stimuli-responsive catalysis, and photo-responsive building blocks for smart materials, potentially with customised energy storage and release characteristics.

Supporting Information

The authors have cited additional references within the Supporting Information.[61–82]

Author Contributions

M. J. N.: Synthesis; characterisation; photoswitching studies; analysis of kinetics; calculations of molecular models; and project conception. G. S.: X-ray crystallography. L. K. S. v. K.: Project conception and supervision.

Acknowledgements

This work was supported by the Fonds der Chemischen Industrie (FCI, Liebig Fellowship) and the German Research

Foundation (DFG; Emmy Noether Programme, 446317932). M.J.N. thanks the FCI for a Ph.D. Fellowship and U. Weynand and Dr. S. Nozinovic for support with NMR measurements. M.J.N. and L.K.S.v.K. thank Dr B.M.W. Roberts for the helpful discussions regarding the fitting of kinetic data. G.S. thanks Prof. Dr. A.C. Filippou for providing X-ray infrastructure.

Open access funding enabled and organized by Projekt DEAL.

Conflict of Interests

The authors declare no conflict of interest.

Data Availability Statement

The data that support the findings of this study are available in the supplementary material of this article. Deposition numbers 2442413 (for Fe_2**L**) and 2442414 (for ZnFe**L**) contain the supplementary crystallographic data for this paper. These data are provided free of charge by the joint Cambridge Crystallographic Data Centre and Fachinformationszentrum Karlsruhe Access Structures service (http://www.ccdc.cam.ac.uk/structures).

Keywords: Heterometallic complexes · Molecular ratchet · Out-of-equilibrium · Self-assembly · Self-sorting

[1] T. Sangchai, S. A. Shehimy, E. Penocchio, G. Ragazzon, *Angew. Chem. Int. Ed.* **2023**, *62*, e202309501.
[2] Y. Munekage, M. Hashimoto, C. Miyake, K.-I. Tomizawa, T. Endo, M. Tasaka, T. Shikanai, *Nature* **2004**, *429*, 579–582.
[3] P. D. Boyer, *Biochim. Biophys. Acta, Bioenerg.* **1993**, *1140*, 215–250.
[4] S. Borsley, D. A. Leigh, B. M. W. Roberts, *Angew. Chem. Int. Ed.* **2024**, *63*, e202400495.
[5] R. D. Astumian, *Nat. Nanotechnol.* **2012**, *7*, 684–688.
[6] V. Balzani, M. Clemente-León, A. Credi, B. Ferrer, M. Venturi, A. H. Flood, J. F. Stoddart, *Proc. Natl. Acad. Sci. USA* **2006**, *103*, 1178–1183.
[7] L. Greb, J.-M. Lehn, *J. Am. Chem. Soc.* **2014**, *136*, 13114–13117.
[8] E. Benchimol, J. Tessarolo, G. H. Clever, *Nat. Chem.* **2024**, *16*, 13–21.
[9] R. G. DiNardi, A. O. Douglas, R. Tian, J. R. Price, M. Tajik, W. A. Donald, J. E. Beves, *Angew. Chem. Int. Ed.* **2022**, *61*, e202205701.
[10] R. G. DiNardi, S. Rasheed, S. S. Capomolla, M. H. Chak, I. A. Middleton, L. K. Macreadie, J. P. Violi, W. A. Donald, P. J. Lusby, J. E. Beves, *J. Am. Chem. Soc.* **2024**, *146*, 21196–21202.
[11] M. Ovalle, M. Kathan, R. Toyoda, C. N. Stindt, S. Crespi, B. L. Feringa, *Angew. Chem. Int. Ed.* **2023**, *62*, e202214495.
[12] R. I. Petrikat, J. Hornbogen, M. J. P. Schmitt, E. Resmann, C. Wiedemann, N. I. Dilmen, H. Schneider, A. M. Pick, C. Riehn, R. Diller, S. Becker, *Chem. A Eur. J.* **2024**, *30*, e202400205.
[13] J. Gemen, J. R. Church, T.-P. Ruoko, N. Durandin, M. J. Białek, M. Weißenfels, M. Feller, M. Kazes, M. Odaybat, V. A. Borin, R. Kalepu, Y. Diskin-Posner, D. Oron, M. J. Fuchter, A. Priimagi, I. Schapiro, R. Klajn, *Science* **2023**, *381*, 1357–1363.
[14] H. Lee, J. Tessarolo, D. Langbehn, A. Baksi, R. Herges, G. H. Clever, *J. Am. Chem. Soc.* **2022**, *144*, 3099–3105.
[15] D. Hugenbusch, M. Lehr, J. von Glasenapp, A. J. McConnell, R. Herges, *Angew. Chem. Int. Ed.* **2023**, *62*, e202212571.
[16] R. Siewertsen, H. Neumann, B. Buchheim-Stehn, R. Herges, C. Näther, F. Renth, F. Temps, *J. Am. Chem. Soc.* **2009**, *131*, 15594–15595.
[17] D. Villarón, S. J. Wezenberg, *Angew. Chem. Int. Ed.* **2020**, *59*, 13192–13202.
[18] C. Stuckhardt, D. Roke, W. Danowski, E. Otten, S. J. Wezenberg, B. L. Feringa, *Beilstein J. Org. Chem.* **2019**, *15*, 2767–2773.
[19] M. Irie, T. Fukaminato, K. Matsuda, S. Kobatake, *Chem. Rev.* **2014**, *114*, 12174–12277.
[20] M. Han, R. Michel, B. He, Y. Chen, D. Stalke, M. John, G. H. Clever, *Angew. Chem. Int. Ed.* **2013**, *52*, 1319–1323.
[21] E. Nieland, J. Voss, B. M. Schmidt, *ChemPlusChem* **2023**, *88*, e202300353.
[22] M. C. Brand, H. G. Trowell, J. T. Pegg, J. L. Greenfield, M. Odaybat, M. A. Little, P. R. Haycock, G. Avci, N. Rankin, M. J. Fuchter, K. E. Jelfs, A. I. Cooper, R. L. Greenaway, *J. Am. Chem. Soc.* **2024**, *146*, 30332–30339.
[23] T. Abe, N. Sanada, K. Takeuchi, A. Okazawa, S. Hiraoka, *J. Am. Chem. Soc.* **2023**, *145*, 28061–28074.
[24] S. Pullen, J. Tessarolo, G. H. Clever, *Chem. Sci.* **2021**, *12*, 7269–7293.
[25] M. Hardy, A. Lützen, *Chem. A Eur. J.* **2020**, *26*, 13332–13346.
[26] L. L. K. Taylor, R. Andrews, A. C. Y. Sung, I. J. Vitorica-Yrezabal, I. A. Riddell, *Chem. Commun.* **2022**, *58*, 12301–12304.
[27] J. E. M. Lewis, James. D. Crowley, *ChemPlusChem* **2020**, *85*, 815–827.
[28] J. A. Gome, Z. T. Avery, N. R. Lawson, O. G. Stansfield, J. D. Evans, M. G. Gardiner, T. U. Connell, D. Preston, *Angew. Chem. Int. Ed.* **2025**, *64*, e202503473.
[29] Z. Ashbridge, J. N. H. Reek, *Nat. Synth.* **2024**, *3*, 1197–1207.
[30] Y. Yang, Y. Wu, J.-H. Jia, X.-Y. Zheng, Q. Zhang, K.-C. Xiong, Z.-M. Zhang, Q.-M. Wang, *Cryst. Growth Des.* **2018**, *18*, 4555–4561.
[31] Z. Wang, L.-P. Zhou, T.-H. Zhao, L.-X. Cai, X.-Q. Guo, P.-F. Duan, Q.-F. Sun, *Inorg. Chem.* **2018**, *57*, 7982–7992.
[32] C. Schouwey, M. Papmeyer, R. Scopelliti, K. Severin, *Dalton Trans.* **2014**, *44*, 2252–2258.
[33] M. Otte, P. F. Kuijpers, O. Troeppner, I. Ivanović-Burmazović, J. N. H. Reek, B. de Bruin, *Chem. A Eur. J.* **2013**, *19*, 10170–10178.
[34] L. S. Lisboa, M. Riisom, H. J. Dunne, D. Preston, S. M. F. Jamieson, L. J. Wright, C. G. Hartinger, J. D. Crowley, *Dalton Trans.* **2022**, *51*, 18438–18445.
[35] V. Singh, M. G. Robb, S. Brooker, *Dalton Trans.* **2025**, *54*, 3165–3173.
[36] A. C. Pearcy, L. S. Lisboa, D. Preston, N. B. Page, T. Lawrence, L. J. Wright, C. G. Hartinger, J. D. Crowley, *Chem. Sci.* **2023**, *14*, 8615–8623.
[37] N. Eren, F. Fadaei-Tirani, K. Severin, *Inorg. Chem. Front.* **2024**, *11*, 3263–3269.
[38] H. Min, A. R. Craze, T. Taira, M. J. Wallis, M. M. Bhadbhade, R. Tian, D. J. Fanna, R. Wuhrer, S. Hayami, J. K. Clegg, C. E. Marjo, L. F. Lindoy, F. Li, *Chemistry* **2022**, *4*, 535–547.
[39] J. P. Carpenter, T. K. Ronson, F. J. Rizzuto, T. Héliot, P. Grice, J. R. Nitschke, *J. Am. Chem. Soc.* **2022**, *144*, 8467–8473.
[40] L. S. Lisboa, D. Preston, C. J. McAdam, L. J. Wright, C. G. Hartinger, J. D. Crowley, *Angew. Chem. Int. Ed.* **2022**, *61*, e202201700.
[41] H. B. Gearing, M. Cziferszky, T. Söhnel, L. J. Wright, J. D. Crowley, C. G. Hartinger, *Chem. Sci.* **2025**, *16*, 7294–7301.
[42] H. Ube, K. Endo, H. Sato, M. Shionoya, *J. Am. Chem. Soc.* **2019**, *141*, 10384–10389.
[43] J. Park, Y.-P. Chen, Z. Perry, J.-R. Li, H.-C. Zhou, *J. Am. Chem. Soc.* **2014**, *136*, 16895–16901.

[44] D. R. Turner, S. Thoonen, S. E. Walker, D. L. Marshall, T. M. Fulloon, S. Brandon, A. I. McKay, M. J. Paterson, K. M. Mullen, J. D. Crowley, K. L. Tuck, *Angew. Chem. Int. Ed.* **2025**, *64*, e202506064.
[45] D. Yang, J. L. Greenfield, T. K. Ronson, L. K. S. von Krbek, L. Yu, J. R. Nitschke, *J. Am. Chem. Soc.* **2020**, *142*, 19856–19861.
[46] S. Sudan, F. Fadaei-Tirani, K. Severin, *Chem. Commun.* **2023**, *59*, 8258–8261.
[47] D. Preston, J. J. Sutton, K. C. Gordon, J. D. Crowley, *Angew. Chem. Int. Ed.* **2018**, *57*, 8659–8663.
[48] M. J. Notheis, V. Sahiti, V. Prangenberg, J. S. Kruse, L. von Krbek, *Synlett* **2025**, *36*, https://doi.org/10.1055/a-2567-1399.
[49] N. Oka, T. Yamada, H. Sajiki, S. Akai, T. Ikawa, *Org. Lett.* **2022**, *24*, 3510–3514.
[50] L. Schmid, P. Chábera, I. Rüter, A. Prescimone, F. Meyer, A. Yartsev, P. Persson, O. S. Wenger, *Inorg. Chem.* **2022**, *61*, 15853–15863.
[51] A. M. McDaniel, A. K. Rappé, M. P. Shores, *Inorg. Chem.* **2012**, *51*, 12493–12502.
[52] E. G. Percástegui, J. Mosquera, T. K. Ronson, A. J. Plajer, M. Kieffer, J. R. Nitschke, *Chem. Sci.* **2019**, *10*, 2006–2018.
[53] A. M. Castilla, N. Ousaka, R. A. Bilbeisi, E. Valeri, T. K. Ronson, J. R. Nitschke, *J. Am. Chem. Soc.* **2013**, *135*, 17999–18006.
[54] H. Nose, M. T. Rodgers, *ChemPlusChem* **2013**, *78*, 1109–1123.
[55] D. T. Richens, *The Chemistry of Aqua Ions*, Wiley & Sons Ltd, Hoboken, **1997**.
[56] L. Helm, A. E. Merbach, *J. Chem. Soc. Dalton Trans.* **2002**, *0*, 633–641.
[57] L. Helm, A. E. Merbach, *Chim. Int. J. Chem.* **2019**, *73*, 179.
[58] R. Li, M. Han, J. Tessarolo, J. J. Holstein, J. Lübben, B. Dittrich, C. Volkmann, M. Finze, C. Jenne, G. H. Clever, *ChemPhotoChem* **2019**, *3*, 378–383.
[59] M. B. Tipping, L. Pruñonosa Lara, A. B. Solea, L. K. S. von Krbek, M. D. Ward, *Chem. Sci.* **2024**, *15*, 8488–8499.
[60] R.-J. Li, Julian. J. Holstein, W. G. Hiller, J. Andréasson, G. H. Clever, *J. Am. Chem. Soc.* **2019**, *141*, 2097–2103.
[61] M. Kieffer, B. S. Pilgrim, T. K. Ronson, D. A. Roberts, M. Aleksanyan, J. R. Nitschke, *J. Am. Chem. Soc.* **2016**, *138*, 6813–6821.
[62] D. A. Roberts, B. S. Pilgrim, J. D. Cooper, T. K. Ronson, S. Zarra, J. R. Nitschke, *J. Am. Chem. Soc.* **2015**, *137*, 10068–10071.
[63] X-Area LANA 2.7.9.0 (STOE&Cie, **2022**).
[64] G. M. Sheldrick, *Acta Crystallogr. Sect. A: Found. Crystallogr.* **2015**, *71*, 3–8.
[65] G. M. Sheldrick, *Acta Crystallogr. Sect. C: Struct. Chem.* **2015**, *71*, 3–8.
[66] A. L. Spek, *Acta Crystallogr. Sect. C* **2015**, *71*, 9–18.
[67] L. Turcani, A. Tarzia, F. T. Szczypiński, K. E. Jelfs, *J. Chem. Phys.* **2021**, *154*, 214102.
[68] L. Turcani, A. Tarzia, *Stk*, https://github.com/lukasturcani/stk (Accessed 01.11.2024).
[69] A. Tarzia, K. E. Jelfs, *Chem. Commun.* **2022**, *58*, 3717–3730.
[70] M. D. Hanwell, D. E. Curtis, D. C. Lonie, T. Vandermeersch, E. Zurek, G. R. Hutchison, *J. Cheminformatics* **2012**, *4*, 17.
[71] A. K. Rappe, C. J. Casewit, K. S. Colwell, W. A. Goddard, W. M. Skiff, *J. Am. Chem. Soc.* **1992**, *114*, 10024–10035.
[72] P. Pracht, S. Grimme, C. Bannwarth, F. Bohle, S. Ehlert, G. Feldmann, J. Gorges, M. Müller, T. Neudecker, C. Plett, S. Spicher, P. Steinbach, P. A. Wesołowski, F. Zeller, *J. Chem. Phys.* **2024**, *160*, 114110.
[73] S. Spicher, S. Grimme, *Angew. Chem. Int. Ed.* **2020**, *59*, 15665–15673.
[74] C. Bannwarth, S. Ehlert, S. Grimme, *J. Chem. Theory Comput.* **2019**, *15*, 1652–1671.
[75] S. Ehlert, M. Stahn, S. Spicher, S. Grimme, *J. Chem. Theory Comput.* **2021**, *17*, 4250–4261.
[76] L. Schrödinger, *The PyMOL Molecular Graphics System*, Version 3.1.0a0 Open-Source, **2025**.
[77] A. Tarzia, W. Shan, V. Posligua, C. J. T. Cox, L. Male, B. D. Egleston, R. L. Greenaway, K. E. Jelfs, J. E. M. Lewis, *Chem. A Eur. J.* **2025**, *31*, e202403336.
[78] C. Feldmeier, H. Bartling, E. Riedle, R. M. Gschwind, *J. Magn. Reson.* **2013**, *232*, 39–44.
[79] Y. Ji, D. A. DiRocco, J. Kind, C. M. Thiele, R. M. Gschwind, M. Reibarkh, *ChemPhotoChem* **2019**, *3*, 984–992.
[80] S. Ghosh, C. Eschen, N. Eleya, A. Staubitz, *J. Org. Chem.* **2023**, *88*, 3372–3377.
[81] M. S. Maier, K. Hüll, M. Reynders, B. S. Matsuura, P. Leippe, T. Ko, L. Schäffer, D. Trauner, *J. Am. Chem. Soc.* **2019**, *141*, 17295–17304.
[82] S. Hoops, S. Sahle, R. Gauges, C. Lee, J. Pahle, N. Simus, M. Singhal, L. Xu, P. Mendes, U. Kummer, *Bioinformatics* **2006**, *22*, 3067–3074.

Manuscript received: April 23, 2025
Revised manuscript received: May 22, 2025
Accepted manuscript online: June 02, 2025
Version of record online: ■■, ■■

Research Article

Molecular Ratchets

M. J. Notheis, G. Schnakenburg, L. K. S. von Krbek* — **e202508952**

Light-Driven Ratchet Mechanism Accelerates Regioselective Metal-Cation Exchange in a Heterobimetallic Helicate

Photoswitchable homo- and heterobimetallic helicates form with high diastereo- and regioselectivity via single-step self-assembly or self-sorting. White-light exposure autonomously operates one helicate as a molecular ratchet, promoting the selective formation of an out-of-equilibrium structure. This ratchet mechanism furthermore accelerates regioselective metal-cation exchange from a homometallic to a heterometallic helicate.

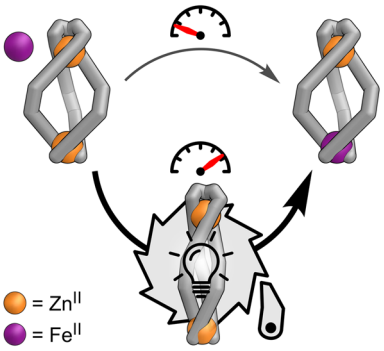

Supporting Information

for

Light-driven ratchet mechanism accelerates regioselective metal-cation exchange in a heterobimetallic helicate

Maximilian J. Notheis,[a] Gregor Schnakenburg,[b] and Larissa K. S. von Krbek*,[a]

a. Kekulé-Institut für Organische Chemie and Biochemie,
Rheinische Friedrich-Wilhelms-Universität Bonn,
Gerhard-Domagk-Str. 1, 53121 Bonn, Germany.
E-mail: larissa.vonkrbek@uni-bonn.de.

b. Institut für Anorganische Chemie,
Rheinische Friedrich-Wilhelms-Universität Bonn,
Gerhard-Domagk-Str. 1, 53121 Bonn, Germany.

Content

S1 General procedures

Reagents and materials. Commercial solvents and reagents were obtained from the following suppliers and used without further purification unless specified otherwise: Sigma Aldrich, Alfa Aesar, abcr, Acros Organics, BLD-Pharm, Fluorochem, Merck, TCI, Carbolution, Thermo Fisher Scientific.

Dry solvents (acetonitrile, tetrahydrofuran, methanol) were dried using an MP-SPS 800 (MBraun) drying apparatus. Solvents used for column chromatography were distilled at atmospheric pressure prior to use.

Schlenk techniques. All reactions using chemicals sensitive to air were carried out under argon using established Schlenk techniques. If chemicals were also sensitive to moisture, glassware was flame-dried prior to use.

Column chromatography. Column chromatography was carried out either using a puriFlash 5.020 (Interchim) flash chromatography machine with PuriFlash 15 µm Si HP (Interchim) flash cartridges or by hand using Silica gel ultra pure (Thermo scientific, 60 µm).

NMR spectroscopy. All NMR spectroscopic measurements were carried out using 300 MHz, 400 MHz, 500 MHz or 700 MHz spectrometers (Bruker Avance I 300, Bruker Avance I 400, Bruker Avance I 500, Bruker Avance III HD Prodigy 500, Bruker Avance III HD Ascend 700). ^{1}H and ^{13}C NMR spectra are referenced to the residual solvent peak for CD_3CN (^{1}H: 1.94 ppm, ^{13}C: 1.32 ppm), CD_2Cl_2 (^{1}H: 5.32 ppm, ^{13}C: 53.5 ppm) or $CDCl_3$ (^{1}H: 7.26 ppm, ^{13}C: 77.16 ppm). NMR signals are reported in terms of chemical shift (δ) in ppm, relative integral, multiplicity, coupling constants (in Hz) and assignment, in that order. The following abbreviations for multiplicity are used: s, singlet; d, doublet; t, triplet; qu, quartet; qn, quintet; m, multiplet; br, broad. Spectra were digitally processed (phase and baseline corrections, integration, peak analysis) using MestReNova 14.2.1 (Mestrelab) and TopSpin 4.05 (BrukerBioSpin). All processing operations were manually checked to ensure that the processed spectra accurately represented the raw data.

Mass spectrometry. Mass spectra were acquired using an Orbitrap XL (Thermo Fischer Scientific) and evaluated and plotted using XCalibur 4.2 (Thermo Fischer Scientific).

UV-vis spectroscopy. UV-vis spectroscopy was carried out using a Cary 60 (Agilent) utilizing a flash lamp style spectrometer with a temperature-controlled sample holder.

FTIR spectroscopy. FTIR spectroscopy was carried out using a Nicolet Summit (Thermo Fisher). A droplet of the sample solution was placed on the measurement window (ATR crystal) and left to dry on air and a spectrum of the resulting thin film was measured.

Elemental analysis. Elemental analysis was carried out using a Vario Micro Cube (Elementar). Approximately 2 mg of compound were used, and all measurements were carried out in duplicate.

HPLC analysis. HPLC chromatography was carried out using a PLATINblue (Knauer) system using a Nucleodur 100-3 Gravity C18 column (3 µm; 2,0 x 100 mm, Machery Nagel).

Light sources. Illumination experiments (NMR and MS) were carried out using portable built-in-house light sources incorporating commercial LED chips (Table S1, for further details see Section S7.1). *In-situ* illumination experiments (NMR and UV-vis) were carried out using *Prizmatrix* fibre collimated LEDs (Table S2, for further details see Section S7.1).

Table S1. Light output of non-collimated LEDs.

λ [nm]	**385**	**405**	**515**	**white**
Manufacturer	Nichia	Nichia	Roithner LaserTechnik GmbH	Nichia
Type	NVSU233B(T) – U385	NVSU233B(T) - U405	SMB1N-515V-02	NVSWE21AT
Light output (as specified by manufacturer)	1.7 W	370 mW	250 mW	297 lm

Table S2. Light output of fibre-collimated LEDs.

λ [nm]	**365**	**390**	**405**	**430**	**450**	**500**	**590**	**660**	**white**
Output power [mW] (1 m optical fibre)	170	220	260	160	440	165	230	140	74

S2 Ligand Synthesis

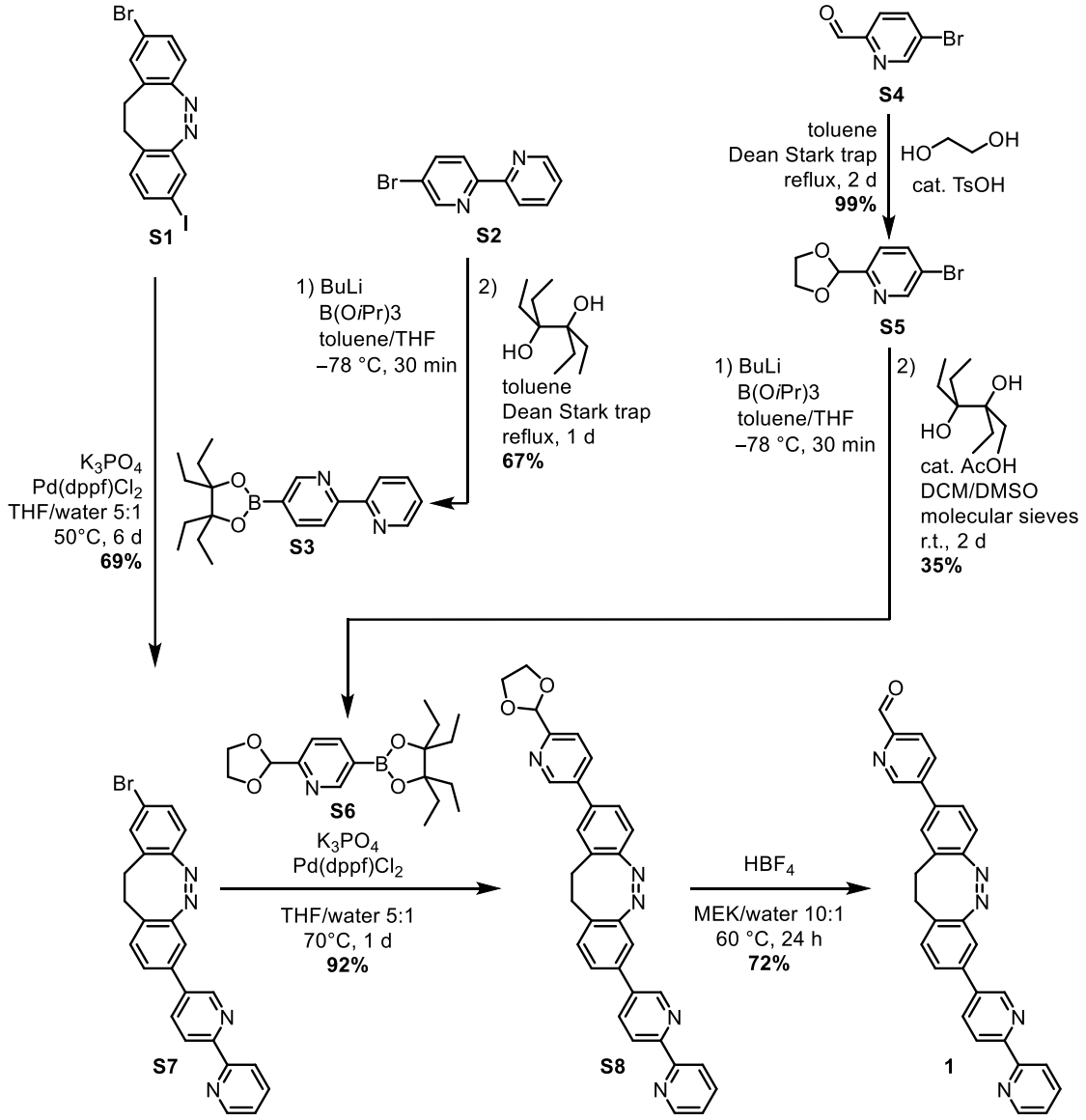

Scheme S1. Synthesis of aldehyde **1** from asymmetric diazocine **S1**, which was previously reported by our group.[1]

S2.1 5-(4,4,5,5-tetraethyl-1,3,2-dioxaborolan-2-yl)-2,2'-bipyridine (**S3**)

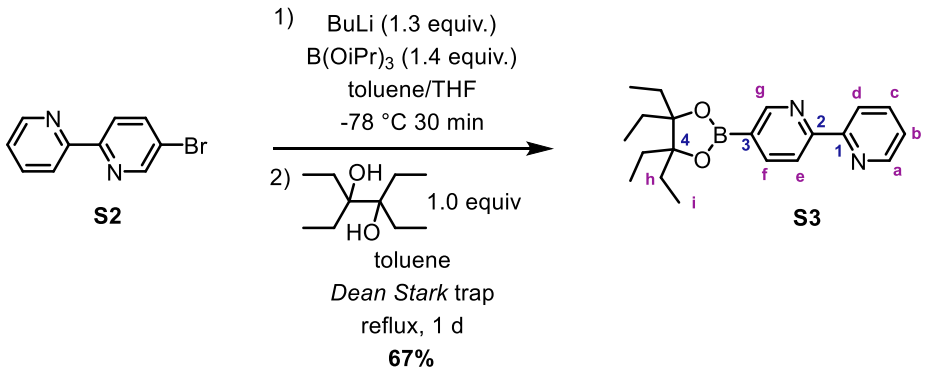

The borylation was carried out following a modified procedure for the borylation of a pyridine acetal.[2]

Under an argon atmosphere, in a heat-gun dried round bottom flask, dry toluene (20 mL) was cooled to −78 °C in an acetone/dry ice bath and *n*-Butyl lithium (2.5 M in hexanes, 5.53 mL, 13.82 mmol, 1.3 equiv.) was added to the cod toluene. A solution of 5-bromo-2,2′-bipyridine (**S2**, 2.50 g, 10.63 mmol, 1.0 equiv.) in 9 mL of dry toluene was added dropwise to the *n*-butyl lithium solution at −78 °C and the mixture was stirred for 15 minutes. Then dry THF (7 mL) was added and the mixture was stirred at −78 °C for 10 minutes. Triisopropylborate (3.41 mL, 14.89 mmol,1.4 equiv.) was added dropwise to the mixture andhe reaction mixture was stirred for an additional 15 minutes at −78 °C. The cooling bath was removed and the reaction was allowed to warm up under stirring for 15 minutes. Then NaOH (40 mL, 3.5 M in water) were added to the reaction mixture, which turned red upon addition of the base. It was allowed to warm up to room temperature and the aqueous phase was acidified to pH = 4 by the addition of HCl (4 M in water) and then extracted with a mixture of DCM/MeOH (10:1 (v/v), 3 × 200 mL). The combined organic layers were dried over magnesium sulfate and the solids were filtered off. The solvent was removed on a rotary evaporator to afford [2,2′-bipyridin]-5-ylboronic acid, which was subjected to the next reaction step without further purification.

The crude [2,2′-bipyridin]-5-ylboronic acid (2.13 g, 10.63 mmol, 1.0 equiv.) and 3,4-diethylhexane-3,4-diol (2.01 mL, 10.63 mmol, 1.0 equiv.) were added to a round bottom flask equipped with a *Dean-Stark* apparatus. The solids were suspended in of

toluene (30 mL) and the reaction was heated to reflux for 24 hours. Approximately 1 mL of water was collected in the trap over the course of the reaction. All volatiles were removed on a rotary evaporator and the oily residue was purified via column chromatography (silica gel, dichloromethane/ethyl acetate 100:0→50:50 (v/v) over 15 column volumes). Product **S3** was obtained as a brown oil with an overall yield of 67% (2.40 g,7.09 mmol).

R_F value (dichloromethane/ethyl acetate; 1:1 (v/v)) = 0.68

^{1}HNMR(500 MHz, CD_2Cl_2, 298 K): δ [ppm] = 0.99 (t, J = 7.5 Hz, 12H, H-i), 1.86 - 1.73 (m, 8H, H-h), 7.33 (ddd, J = 7.5, 4.8, 1.2 Hz, 1H, H-b), 7.83 (ddd, J = 8.0, 7.5, 1.8 Hz, 1H, H-c), 8.17 (dd, J = 7.9, 1.8 Hz, 1H, H-f), 8.41 (dd, J = 7.9, 1.0 Hz, 1H, H-g), 8.47 (dt, J = 8.0, 1.1 Hz, 1H, H-d), 8.67 (ddd, J = 4.8, 1.8, 0.9 Hz, 1H, H-a), 8.97 (dd, J = 1.8, 1.0 Hz, 1H, H-e).

^{13}C NMR (126 MHz, CD_2Cl_2, 298 K): δ [ppm] = 9.01 (C-i), 26.83 (C-h), 89.71 (C-4), 120.33 (C-g), 121.58 (C-d), 124.35 (C-b), 137.21 (C-c), 143.41 (C-f), 149.60 (C-a), 155.33 (C-e), 156.47 (C-1), 158.29 (C-2).

Due to the proximity to the boron atom the signal for C-3 is not visible.

HRMS (ESI$^+$ Orbitrap): m/z (relative intensity) = 339.2239 (100%, $[M+H]^+$, calcd. 339.2242), 361.205 (5%, $[M+Na]^+$, calcd. 361.206).

FTIR (ATR, thin film from CD_2Cl_2: $\tilde{\nu}$ [cm^{-1}] = 751.8 (m), 800.8 (vw), 826.2 (vw), 861.3 (vw), 918.4 (s), 954.5 (w), 1023.2 (w), 1102.7 (vs), 1292.2 (m), 1365.7 (vs), 1459.8 (m), 1546.4 (w), 1595.2 (s), 2883.0 (vw), 2942.7 (w), 2973.2 (m).

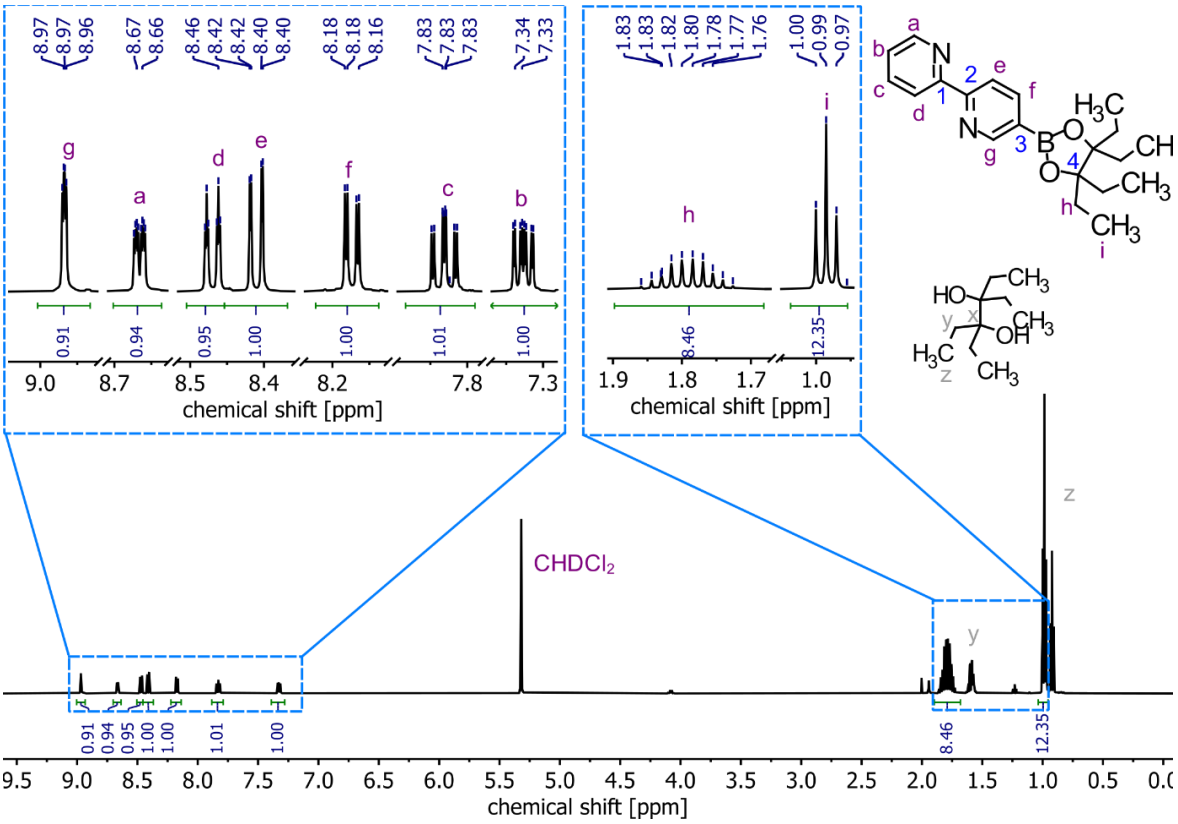

Figure S1. ^{1}H NMR spectrum (500 MHz, CD_2Cl_2, 298 K) of EPin ester **S3**. Signals denoted with y and z correspond to 3,4-diethylhexane-3,4-diol, which could be successfully removed after the next reaction step.

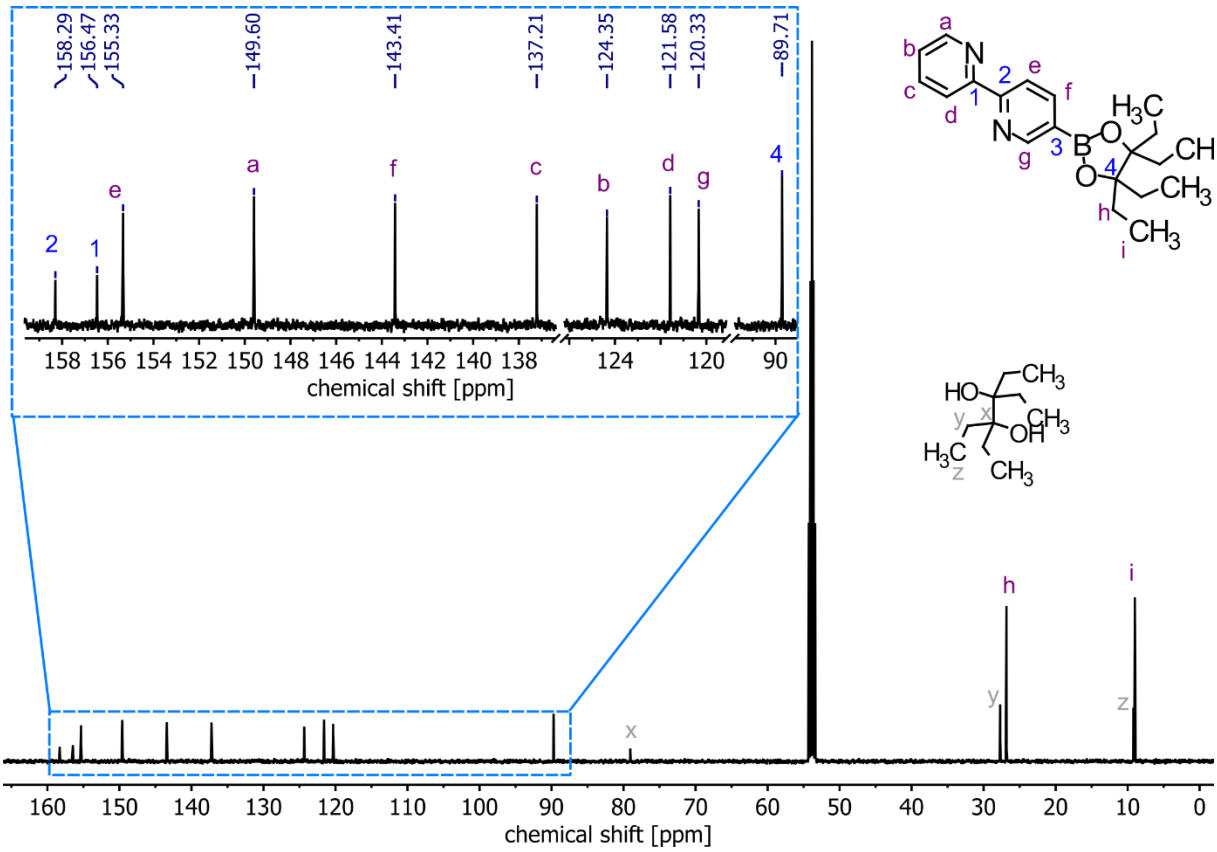

Figure S2. ^{13}C NMR spectrum (126 MHz, CD_2Cl_2, 298 K) of EPin ester **S3**. Signals denoted with x, y, and z correspond to 3,4-diethylhexane-3,4-diol, which could be successfully removed after the next reaction step.

S2.2 5-bromo-2-(1,3-dioxolan-2-yl)pyridine (**S5**)

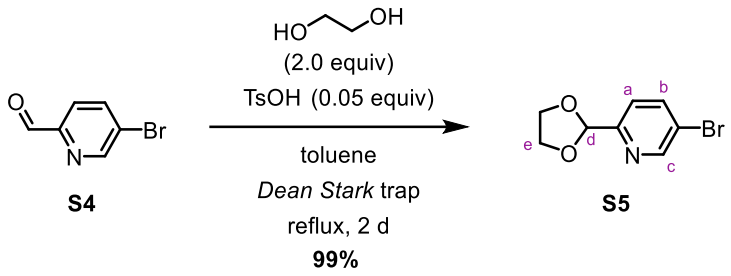

The acetal protection was carried out following a literature procedure.[3]

5-Bromopicolinaldehyde (**S4**, 5.00 g, 26.9 mmol, 1.00 equiv.), ethylene glycol (3.00 mL, 3.34 g, 54.8 mmol, 2.00 equiv.), and *p*-toluenesulfonic acid monohydrate (0.26 g, 1.3 mmol, 0.05 equiv.) were added to a round bottom flask equipped with a *Dean-Stark* apparatus. The solids were suspended in toluene (100 mL) and the reaction was heated to reflux for 2 days. Approximately 2 mL of water were collected in the trap over the course of the reaction. The reaction mixture was extracted with saturated aqueous sodium bicarbonate solution (2 × 50 mL). The organic phase was dried with magnesium sulfate, and all volatiles were removed under reduced pressure to afford product **S5** as a pale-yellow oil in 99% yield (6.10 g, 26.9 mmol).

^{1}H NMR (400 MHz, $CDCl_3$) δ [ppm] = 4.02 – 4.21 (m, 4H, H-e), 5.83 (s, 1H, H-d), 7.44 (dd, J = 8.3, 0.7 Hz, 1H, H-a), 7.87 (dd, J = 8.3, 2.3 Hz, 1H, H-b), 8.68 (dd, J = 2.3, 0.8 Hz, 1H, H-c).

^{1}H NMR data is in agreement with literature reported data.[3]

S2.3 2-(1,3-dioxolan-2-yl)-5-(4,4,5,5-tetraethyl-1,3,2-dioxaborolan-2-yl)pyridine (**S6**)

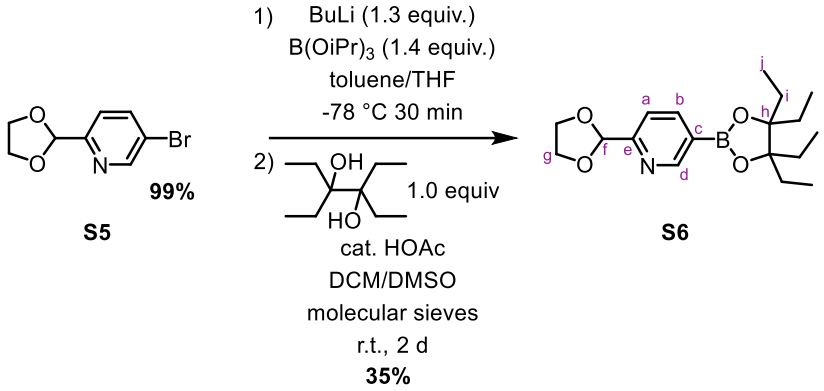

The borylation was carried out following a literature procedure[2] and the esterification following a modified procedure for the esterification of pyridyl boronic acids.[4]

Under an argon atmosphere, in a heat-gun dried round bottom flask, dry toluene (40 mL) was cooled to −78 °C in an acetone/dry ice bath and *n*-butyl lithium (2.5 M in hexanes, 11.2 mL,1.79 g, 28.0 mmol, 1.30 equiv.) was added to the cold toluene. A solution of protected bromo-pyridine (**S5**, 4.96 g, 21.6 mmol, 1.00 equiv.) in of dry toluene (10 mL) was added dropwise to the *n*-butyl lithium solution at −78 °C and the mixture was subsequently stirred for 15 minutes. Dry THF (15 mL) was added to the reaction mixture and the mixture was stirred for 10 minutes at −78 °C. Triisopropylborate (7.17 mL, 31.2 mmol,1.45 equiv.) was added dropwise to the reaction mixture and the reaction mixture was stirred for an additional 15 minutes at −78 °C. The cooling bath was removed, and the reaction was allowed to warm up under stirring for 15 minutes. Then aqueous NaOH solution (40 mL, 3.5 M) was added to the reaction mixture, upon which the reaction mixture turned red. After the addition was completed, the still-cold reaction mixture was brought to room temperature. The aqueous phase was acidified to pH = 4 by the addition of HCl (4 M in water) and then extracted with a mixture of DCM/MeOH (10:1 (v/v), 3 × 200 mL). The combined organic layers were dried over magnesium sulfate and the solids were filtered off. The solvent was removed on a rotary evaporator to afford the crude boronic acid (2.96 g, approx. 15.2 mmol). This was used without further purification in the next step.

The crude boronic acid (2.96 g, approx. 15.2 mmol, approx. 1.00 equiv.), 3,4-diethylhexane-3,4-diol (2.87 mL, 15.18 mmol, 1.00 equiv.), and acetic acid (0.09 g,

1.5 mmol, 0.10 equiv.) dissolved in a mixture of dry dimethylsulfoxide and dry dichloromethane (1:2 (v:v), 150 mL). 3 Å Molecular sieves (approx. 10 g) were added, the reaction mixture was purged with argon for 5 minutes, and the mixture was stirred at room temperature for 2 days. The reaction mixture was extracted with a mixture of saturated aqueous NaCl solution and water (1:3 (v/v), 3 × 200 mL). The organic phase was dried over magnesium sulfate. All volatiles were removed on a rotary evaporator and the residue was purified via column chromatography (silica gel, dichloromethane/ethyl acetate 100:0→70:30 (v/v) over 15 column volumes). Boronic ester **S6** was obtained as a brown oil with an overall yield of 35% (2.39 g, 7.16 mmol).

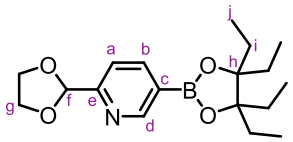

R_F value (dichloromethane/ethyl acetate 4:1 (v/v)) = 0.52.

^{1}H NMR (499 MHz, CD_2Cl_2) δ [ppm] = 0.96 (t, J = 7.5 Hz, 12H, H-j), 1.69 – 1.85 (m, 8H, H-i), 3.99 – 4.18 (m, 4H, H-g), 5.79 (s, 1H, H-6), 7.50 (dd, J = 7.7, 1.0 Hz, 1H, H-a), 8.09 (dd, J = 7.8, 1.7 Hz, 1H, H-b), 8.87 (dd, J = 1.7, 1.0 Hz, 1H, H-d).

^{13}C NMR[*] (126 MHz, CD_2Cl_2) δ [ppm] = 9.0 (C-j), 26.8(C-i), 66.0 (C-h), 89.8 (C-g), 104.3 (C -f), 120.1 (C-a), 143.3 (C-b), 155.2 (C-d), 159.9 (C-e).

HRMS (ESI$^+$ Orbitrap): m/z (relative intensity) = 333.2217 (100%, $[M+H]^+$, calcd. 333.2220).

FTIR (ATR, thin film from CD_2Cl_2): $\tilde{\nu}$ [cm^{-1}] = 401.9 (vw), 632.8 (vw), 665.2 (w), 771.4 (w), 811.6 (w), 843.3 (w), 917.2 (s), 1024.5 (s), 1099.5 (vs), 1290.3 (m), 1366.8 (vs), 1458.6 (m), 1561.1 (vw), 1599.8 (m), 2883.7 (m), 2974.5 (w).

[*] Due to the proximity to the boron atom, the signal for C-c is not resolved.

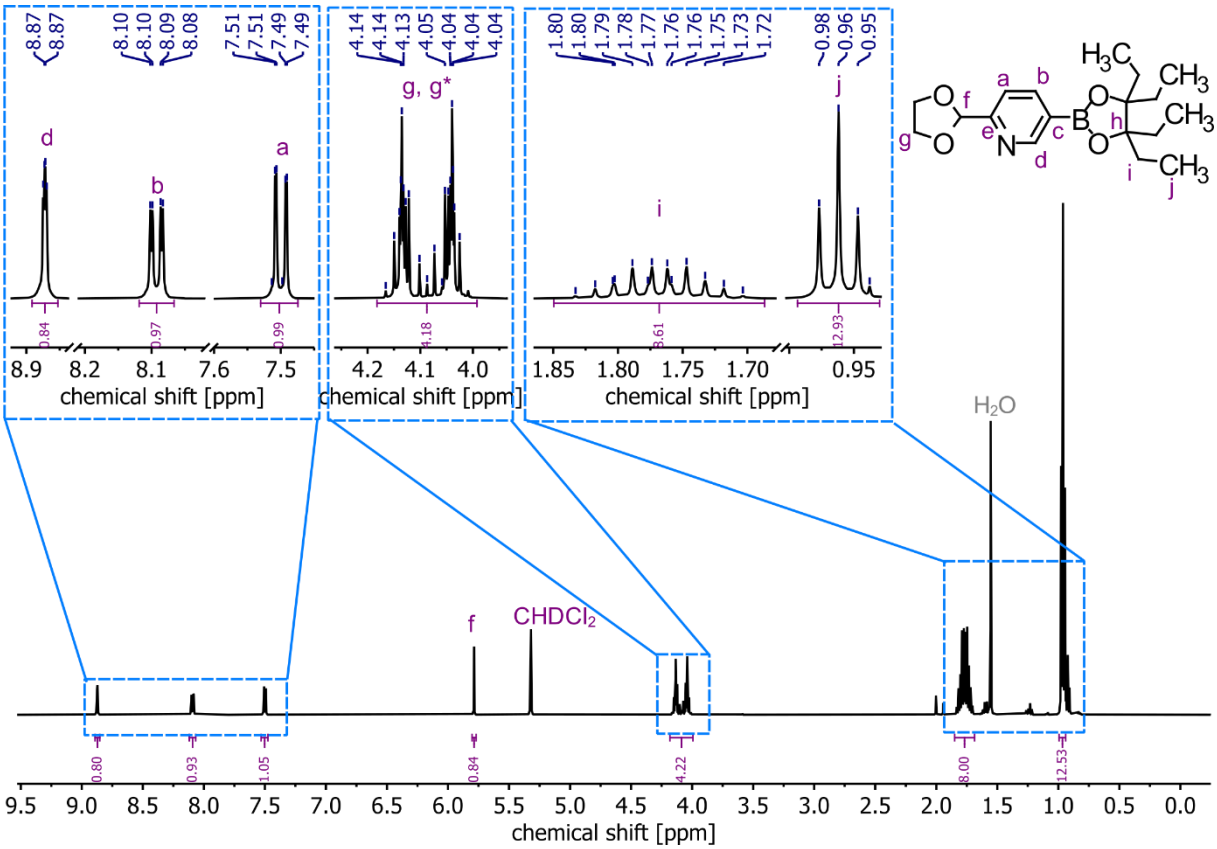

Figure S3. ^{1}H NMR spectrum (500 MHz, CD_2Cl_2, 298 K) of EPin ester **S6**.

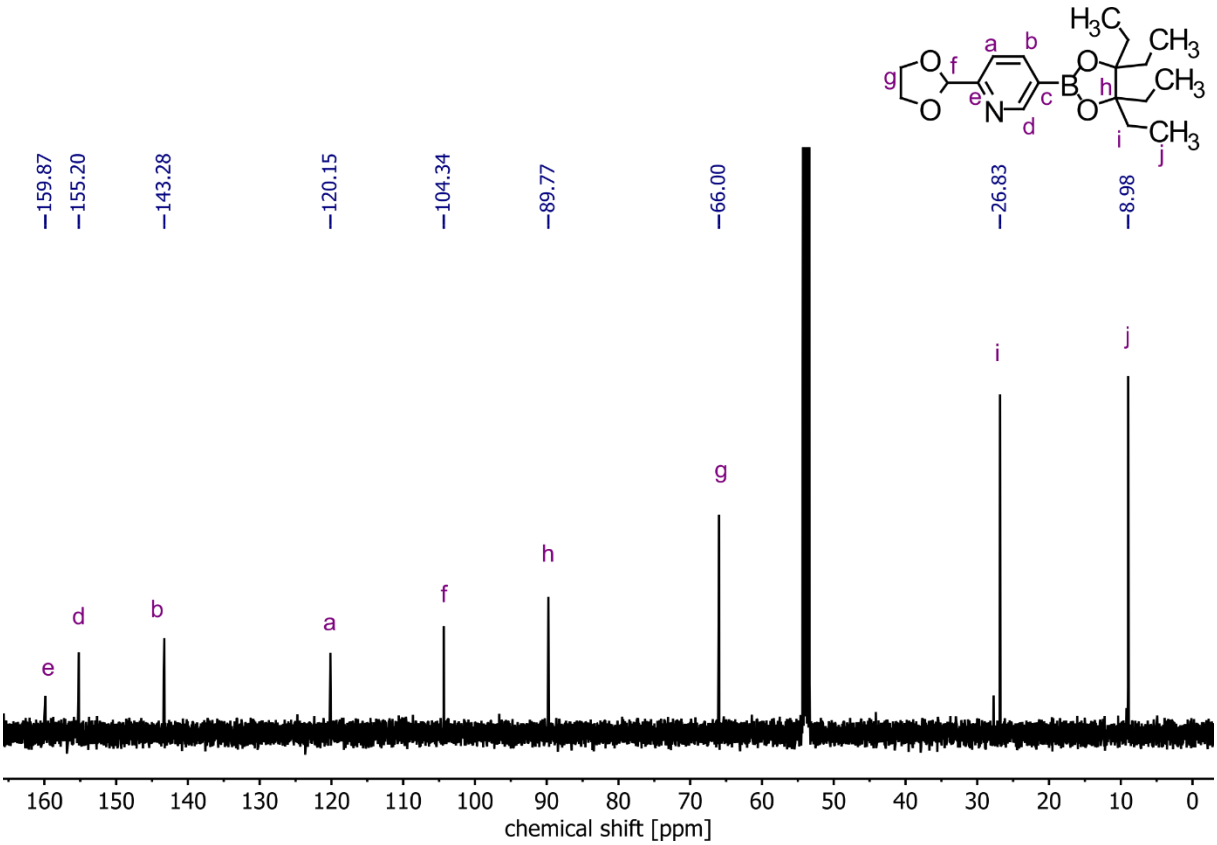

Figure S4. ^{13}C NMR spectrum (126 MHz, CD_2Cl_2, 298 K) of EPin ester **S6**.

S2.4 (*Z*)-8-([2,2'-bipyridin]-5-yl)-2-bromo-11,12-dihydrodibenzo[*c*,*g*][1,2] diazocine (**S7**)

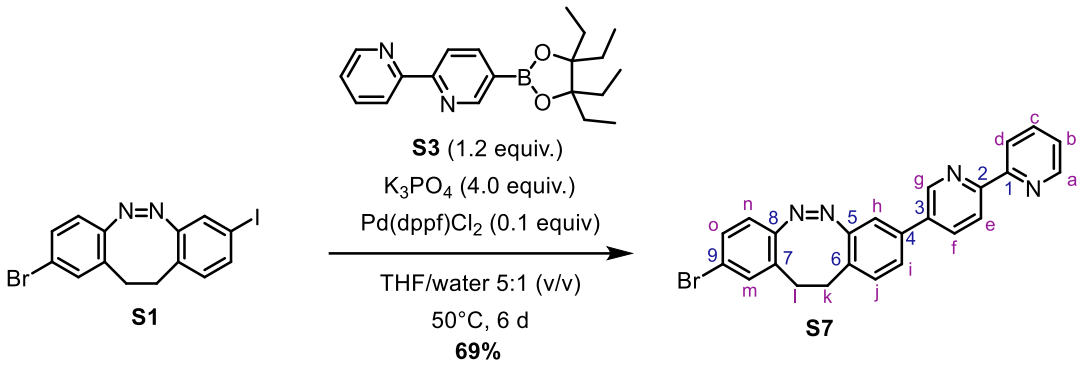

Diazocine **S1**[1] (200 mg, 484 µmol, 1.0 equiv.), boronic ester **S3** (197 mg, 581 µmol, 1.2 equiv.), potassium phosphate (257 mg, 1.21 mmol, 4.0 equiv.), $Pd(dppf)Cl_2$, (35 mg, 48 µmol, 0.1 equiv.), and a magnetic stirring bar were added into a screw cap vial. The open vial was transferred into an argon-filled oxygen-free glovebox and a deoxygenated tetrahydrofuran/water mixture (5:1 (v/v), 3 mL) was added. The vial containing the reaction mixture was closed and removed from the glovebox. The reaction mixture was stirred at 50 °C for 6 days under the vial's remaining Argon atmosphere. After cooling to room temperature, water (10 mL) and ethyl acetate (20 mL) were added to the reaction mixture and the phases were separated. The organic phase was washed with water (1 × 15 mL) and saturated aqueous NaCl solution (1 × 15 mL) and dried over magnesium sulfate. After all volatiles were removed by rotary evaporation, the residue was subjected to column chromatography (silica gel, cyclohexane/ethyl acetate 100:0 → 0:100 (v/v) over 18 column volumes) to afford product **S7** as a yellow solid in 69% yield (146 mg, 331 µmol).

R_F value (dichloromethane/ethyl acetate 1:1 (v/v)) = 0.61.

^{1}H NMR (500 MHz, CD_2Cl_2) δ [ppm] = 2.78 – 3.12 (m, 3H, H-k,l), 6.82 (d, J = 8.3 Hz, 1H, H-n), 7.18 – 7.23 (m, 2H, H-h,j), 7.26 (d, J = 2.1 Hz, 1H, H-m), 7.33 (dd, J = 8.4, 2.1 Hz, 1H, H-o), 7.36 (ddd, J = 7.5, 4.8, 1.2 Hz, 1H, H-b), 7.44 (dd, J = 7.9, 2.0 Hz, 1H, H-i), 7.87 (td, J = 7.7, 1.8 Hz, 1H, H-c), 8.00 (dd, J = 8.3, 2.4 Hz, 1H, H-f), 8.48 (dt, J = 8.0, 1.1 Hz, 1H, H-d), 8.51 (dd, J = 8.3, 0.9 Hz, 1H, H-e), 8.70 (ddd, J = 4.8, 1.9, 1.0 Hz, 1H, H-a), 8.87 (dd, J = 2.4, 0.9 Hz, 1H, H-g).

^{13}C NMR (126 MHz, CD_2Cl_2) δ [ppm] = 31.3 (C-k), 31.3 (C-l), 117.0 (C-h), 120.2 (C-9), 120.7 (C-n), 120.7 (C-e), 120.8 (C-d), 123.8 (C-b), 125.7 (C-i), 127.9 (C-6), 129.8 (C-o), 130.6 (C-7), 130.8 (C-j), 132.4 (C-m), 134.9 (C-f), 134.9 (C-3), 136.4 (C-4), 136.8 (C-c), 147.3 (C-g), 149.2 (C-a), 154.4 (C-8), 155.2 (C-2), 155.6 (C-1), 155.9 (C-5).

HRMS (ESI$^+$ Orbitrap): m/z (relative intensity) = 441.0706 (75%, $[M+H]^+$, calcd. 441.0709).

FTIR (ATR, thin film from CD_2Cl_2): $\tilde{\nu}$ [cm^{-1}] = 558.2 (vw), 628.6 (vw), 711.0 (w), 749.5 (m), 795.4 (s), 833.2 (m), 899.1 (vw), 924.4 (vw), 953.3 (w), 992.1 (vw), 1016.5 (vw), 1096.0 (w), 1243.7 (vw), 1361.7 (w), 1397.3 (vw), 1435.1 (m), 1457.9 (vs), 1563.4 (w), 1573.6 (w), 1588.5 (m), 2853.1 (vw), 2948.1 (vw), 3008.1 (vw), 3050.3 (vw).

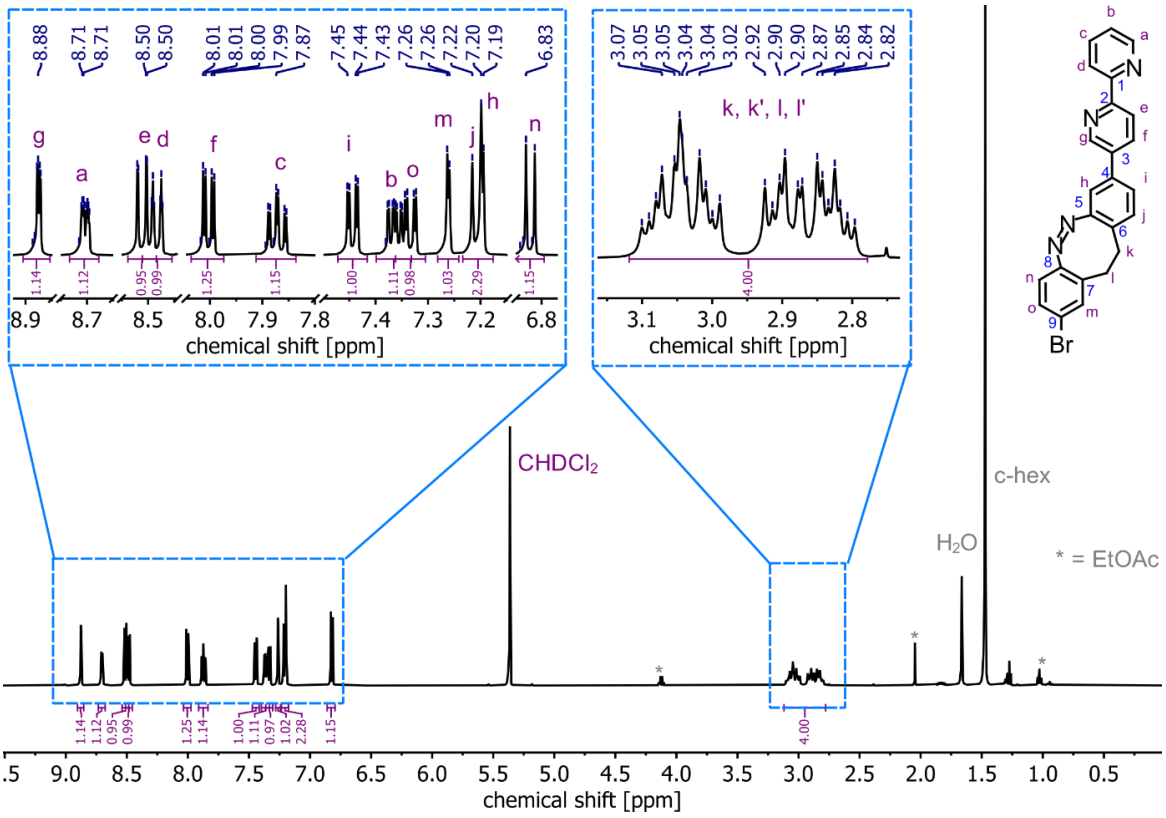

Figure S5. ^{1}H NMR spectrum (500 MHz, CD_2Cl_2, 298 K) of diazocine **S7**.

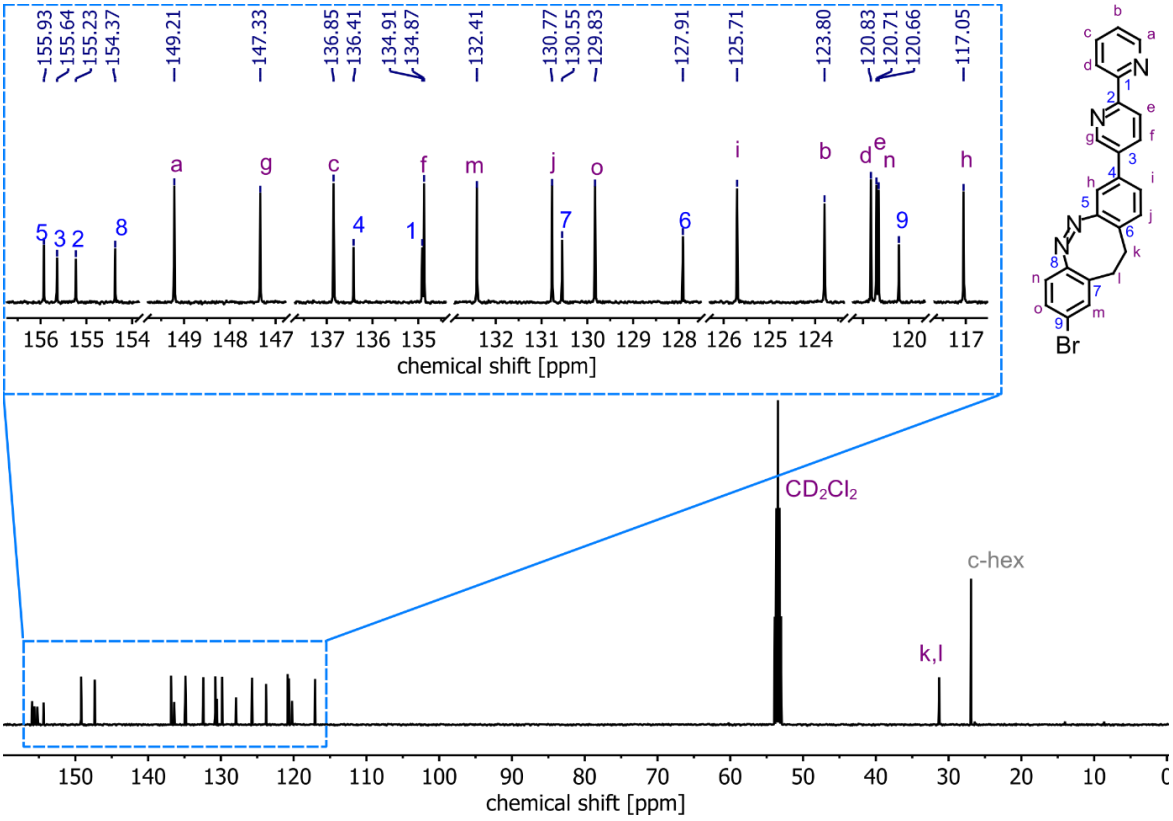

Figure S6. ^{13}C NMR spectrum (126 MHz, CD_2Cl_2, 298 K) of diazocine **S7**.

S2.5 (*Z*)-2-(6-(1,3-dioxolan-2-yl)pyridin-3-yl)-8-([2,2'-bipyridin]-5-yl)-11,12-dihydrodibenzo[*c*,*g*][1,2]diazocine (**S8**)

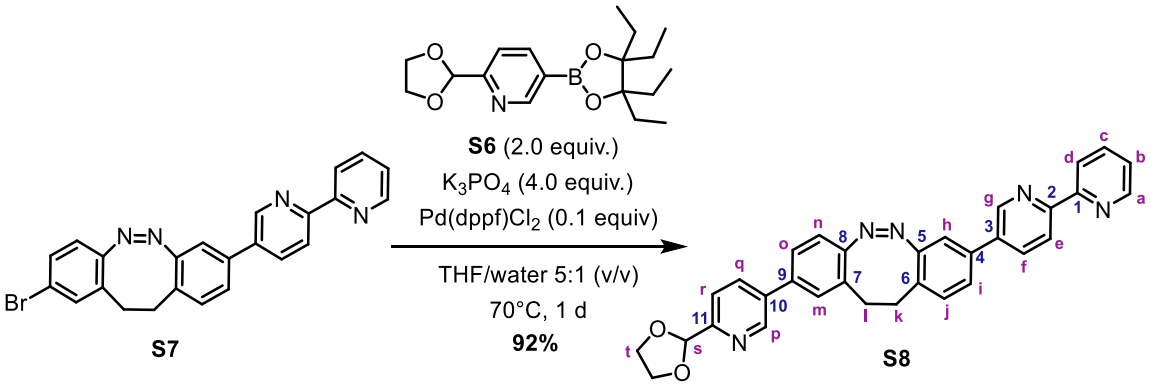

Diazocine **S7** (64.0 mg, 145 µmol, 1.0 equiv.), boronic ester **S6** (96.7 mg, 290 µmol, 2.0 equiv.), potassium phosphate (123 mg, 580 µmol, 4.0 equiv.), $Pd(dppf)Cl_2$ (11 mg, 15 µmol, 0.1 equiv.), and a magnetic stirring bar were added into a screw cap vial. The open vial was transferred into an argon-filled oxygen-free glovebox and a deoxygenated tetrahydrofuran/water mixture (5:1 (v/v), 3 mL) was added. The vial containing the reaction mixture was closed and removed from the glovebox. The reaction mixture was stirred at 70 °C for 1 day under the vial's remaining Argon atmosphere. After cooling to room temperature, water (10 mL) and ethyl acetate (20 mL) were added to the reaction mixture and the phases were separated. The organic phase was washed with water (1 × 15 mL) and saturated aqueous NaCl solution (1 × 15 mL) and dried over magnesium sulfate. After all volatiles were removed by rotary evaporation, the residue was subjected to column chromatography (silica gel, dichloromethane/*iso*-propanol 100:0 → 80:20 (v/v) over 15 column volumes) to afford product **S8** as a yellow solid in 92% yield (68 mg, 133 µmol).

R_F value (dichloromethane/ethyl acetate 1:1 (v/v)) = 0.19.

^{1}H NMR (500 MHz, CD_2Cl_2) δ [ppm] = 2.83 – 3.11 (m, 4H, H-k,l), 4.00 – 4.19 (m, 4H, H-t), 5.80 (s, 1H, H-s), 7.02 (d, J = 8.1 Hz, 1H, H-q), 7.19 (d, J = 8.0 Hz, 1H, H-j), 7.21 (d, J = 1.9 Hz, 1H, H-h), 7.29 – 7.34 (m, 2H, H-b,m), 7.40 (dd, J = 7.9, 2.0 Hz, 1H, H-i), 7.43 (dd, J = 8.2, 1.9 Hz, 1H, H-o), 7.55 (dd, J = 8.1, 0.9 Hz, 1H, H-r), 7.83 (td, J = 7.7, 1.8 Hz, 1H, H-c), 7.86 (dd, J = 8.2, 2.3 Hz, 1H, H-q), 7.97 (dd, J = 8.3, 2.4 Hz, 1H, H-f), 8.43 (dt, J = 8.0 Hz, 1.1, 1H, H-d), 8.46 (dd, J = 8.3, 0.9 Hz, 1H, H-e), 8.66 (ddd, J = 4.8, 1.8, 1.0 Hz, 1H, H-a), 8.73 (dd, J = 2.4, 0.9 Hz, 1H, H-p), 8.84 (dd, J = 2.4, 0.9 Hz, 1H, H-g).

^{13}C NMR (126 MHz, CD_2Cl_2) δ [ppm] = 31.4 (C-k), 31.7 (C-l), 65.6 (C-t), 103.7 (C-s), 117.2 (C-h), 119.8 (C-n), 120.4 (C-r), 120.7 (C-e), 120.8 (C-d), 123.7 (C-b), 125.6 (C-o), 125.6 (C-i), 128.1 (C-6), 128.4 (C-m), 128.9 (C-), 130.8 (C-j), 134.8 (C-q), 134.8 (C-f), 134.9 (C-3), 135.6 (C-10), 136.2 (C-4), 136.3 (C-9), 136.8 (C-c), 147.3 (C-g,p), 149.1 (C-a), 155.1 (C-2), 155.3 (C-8), 155.6 (C-1), 156.0 (C-5), 156.3 (C-11).

HRMS (ESI$^+$ Orbitrap): m/z (relative intensity) = 512.2080 (100%, $[M+H]^+$, calcd. 512.2080), 534.1895 (30%, $[M+Na]^+$, calcd. 534.1900).

FTIR (ATR, thin film from CD_2Cl_2): $\tilde{\nu}$ [cm^{-1}] = 668.2 (m), 750.2 (m), 796.4 (s), 841.4 (m), 943.5 (w), 1021.5 (m), 1092.9 (vs), 1242.9 (w), 1363.1 (w), 1387.6 (w), 1457.9 (vs), 1521.0 (vw), 1588.9 (m), 2851.4 (w), 2893.1 (w), 2922.0 (m), 3049.6 (w).

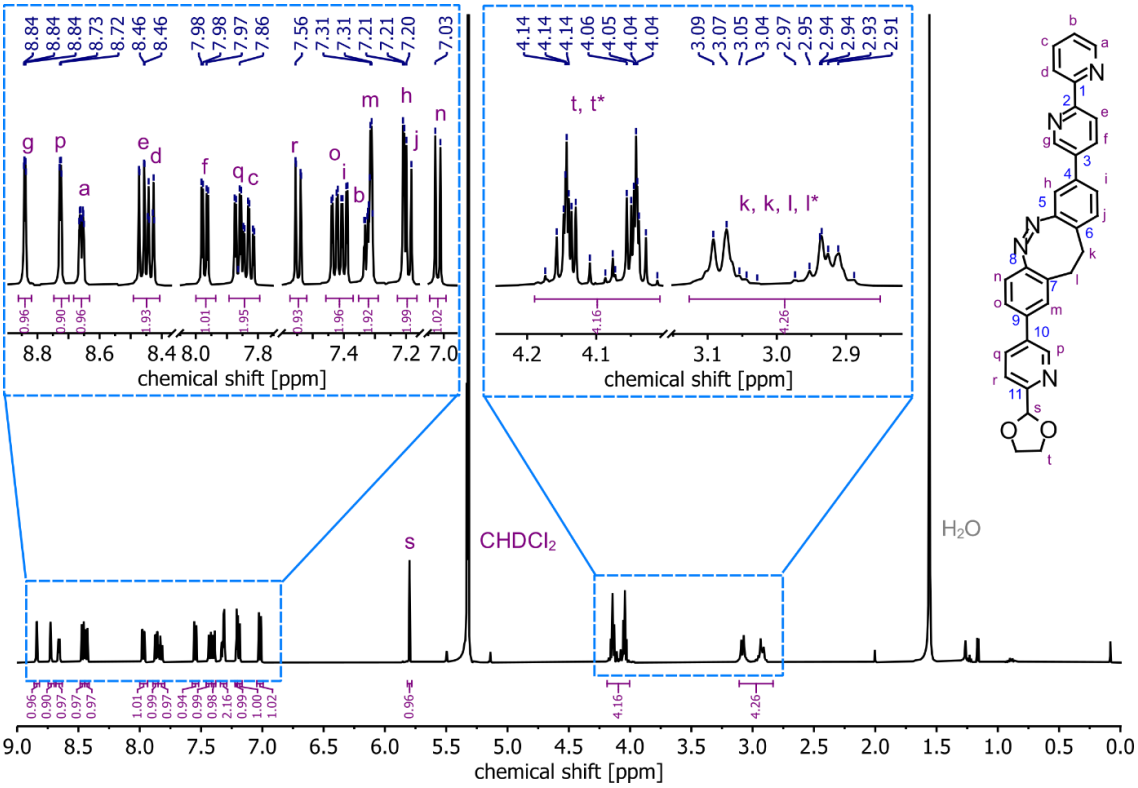

Figure S7. ^{1}H NMR spectrum (500 MHz, CD_2Cl_2, 298 K) of diazocine **S8**.

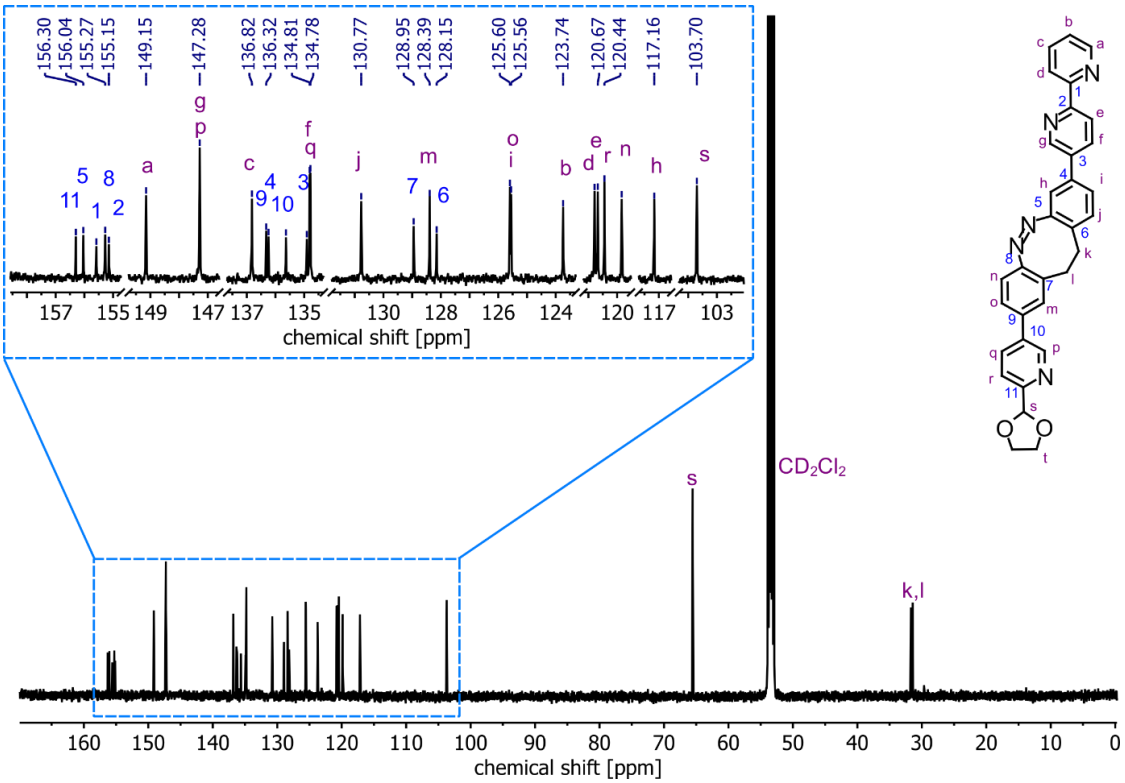

Figure S8. ^{13}C NMR spectrum (126 MHz, CD_2Cl_2, 298 K) of diazocine **S8**.

S2.6 (*Z*)-5-(8-([2,2'-bipyridin]-5-yl)-11,12-dihydrodibenzo[*c*,*g*][1,2]diazocin-2-yl)picolinaldehyde (**1**)

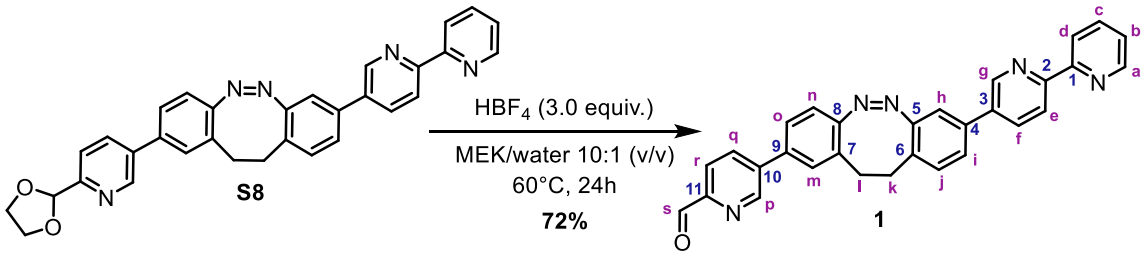

Diazocine **S8** (37.5 mg, 73 µmol, 1.0 equiv.) was dissolved in 10 mL of a mixture of methyl ethyl ketone and water (10:1, v/v) and HBF_4 (32.5 µL, 50 wt% in water, 19.3 mg, 220 µmol, 3.0 equiv.) was added. The reaction vessel was purged with argon for 5 minutes and the reaction mixture stirred at 60°C for 24 hours. After cooling to room temperature, water (10 mL) and ethyl acetate (20 mL) were added to the reaction mixture, and the phases were separated. The organic phase was washed with water (1 × 15 mL) and saturated aqueous NaCl solution (1 × 15 mL) and dried with magnesium sulfate. All volatiles were removed by rotary evaporation, and the residue was subjected to column chromatography (silica gel, dichloromethane/*iso*-propanol 100:0 → 80:20 (v/v) over 15 column volumes) to afford product **1** as a yellow solid in 72% yield (24.6 mg, 53 µmol).

R_F value (dichloromethane/ethyl acetate 1:1 (v/v)) = 0.54.

^{1}H NMR (500 MHz, CD_2Cl_2) δ [ppm] = 2.87 – 3.15 (m, 4H, H-k,l), 7.06 (d, J = 8.2 Hz, 1H, H-n), 7.19 (d, J = 8.0 Hz, 1H, H-j), 7.21 (d, J = 1.9 Hz, 1H, H-h), 7.32 (ddd, J = 7.5, 4.8, 1.2 Hz, 1H, H-b), 7.38 (d, J = 2.0 Hz, 1H, H-m), 7.40 (dd, J = 7.9, 2.0 Hz, 1H, H-i), 7.50 (dd, J = 8.2, 2.0 Hz, 1H, H-o), 7.83 (ddd, J = 8.1, 7.5, 1.8 Hz, 1H, H-c), 7.94 – 7.98 (m, 2H, H-f,q), 8.00 (ddd, J = 8.1, 2.2, 0.8 Hz, 1H, H-r), 8.43 (dt, J = 8.0, 1.1 Hz, 1H, H-d), 8.47 (dd, J = 8.3, 0.8 Hz, 1H, H-e), 8.66 (ddd, J = 4.8, 1.8, 0.9 Hz, 1H, H-a), 8.84 (dd, J = 2.4, 0.9 Hz, 1H, H-g), 8.94 (dd, J = 2.2, 0.9 Hz, 1H, H-p), 10.05 (d, J = 0.7 Hz, 1H, H-s).

^{13}C NMR (126 MHz, CD_2Cl_2) δ [ppm] = 31.4 (C-k), 31.7 (C-l), 117.1 (C-h), 120.0 (C-n), 120.7 (C-e), 120.8 (C-d), 121.5 (C-r), 123.8 (C-b), 125.6 (C-i), 125.9 (C-o), 128.0 (C-6), 128.7 (C-m), 129.3 (C-9), 130.8 (C-j), 134.8 (C-f), 134.8 (C-3), 134.9 (C-q), 135.4

(C-7), 136.3 (C-4), 136.8 (C-c), 139.3 (C-10), 147.3 (C-g), 148.4 (C-p), 149.2 (C-a), 151.7 (C-11), 155.2 (C-2), 155.6 (C-1), 155.9 (C-8), 156.0 (C-5), 192.9 (C-s).

HRMS (ESI$^+$ Orbitrap): m/z (relative intensity) = 468.1818 (100%, $[M+H]^+$, calcd. 468.1819).

FTIR (ATR, thin film from CD_2Cl_2): $\tilde{\nu}$ [cm^{-1}] = 750.5 (w), 796.5 (m), 1017.9 (w), 1095.3 (vw), 1211.2 (w), 1363.1 (w), 1458.1 (vs), 1585.9 (m), 1708.8 (vs) (C=O), 2851.0 (w), 2922.9 (m), 3051.5 (vw).

Elemental analysis ($C_{30}H_{21}N_5O_1$):

Calcd. (%)	C: 77.07	H: 4.53	N: 14.98
Found (%)	C. 77.39	H: 4.70	N: 14.77

HPLC chromatography (reverse phase (C18), water / acetonitrile 65:35 (v/v) + 1% Et_2NH):

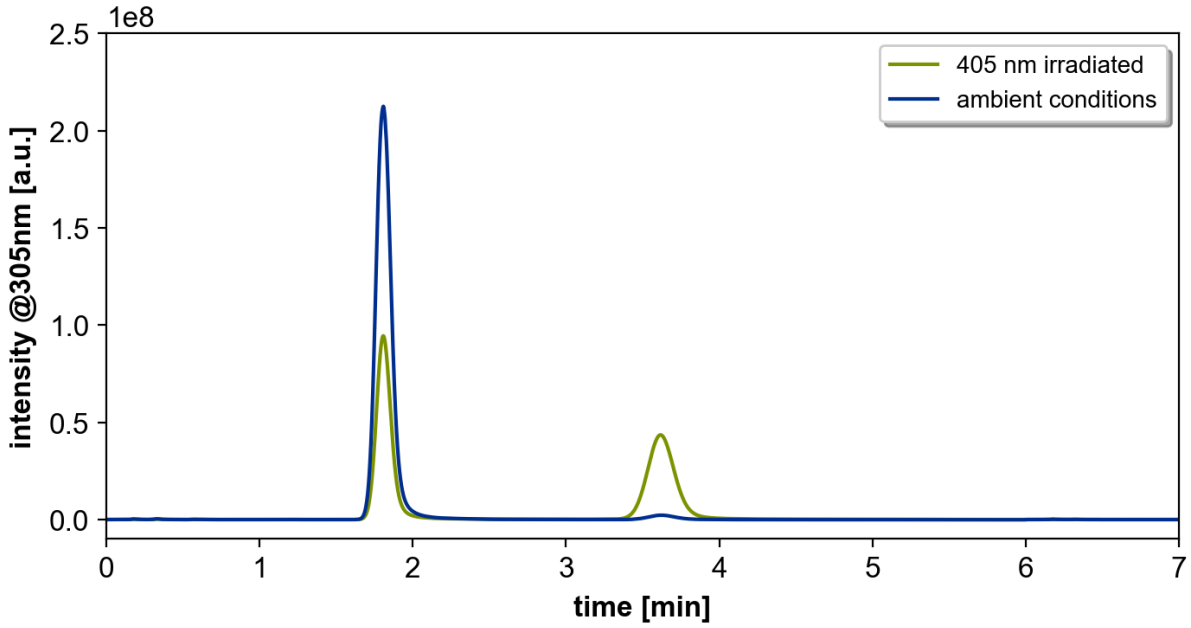

Figure S9. HPLC chromatogram showing the absorbance at 305 nm of aldehyde **1** before and after irradiation with 405 nm light. The sample shows a major peak corresponding to *Z*-**1** (retention time approx. 1.8 min) and a minor peak corresponding to the *E*-**1** (retention time approx. 3.6 min). The increased intensity of the second peak after irradiating the sample with 405 nm light confirms peak assignment.

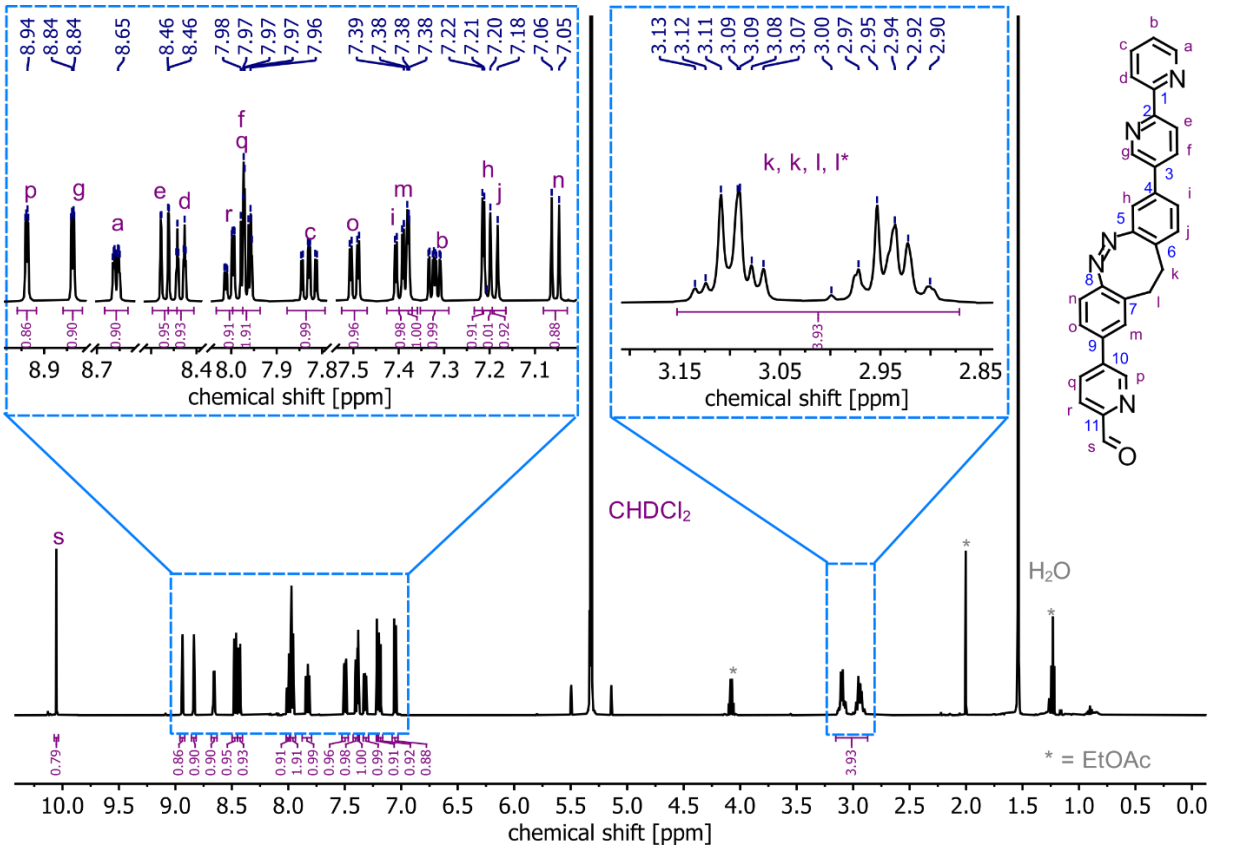

Figure S10. ^{1}H NMR spectrum (500 MHz, CD_2Cl_2, 298 K) of diazocine **1**.

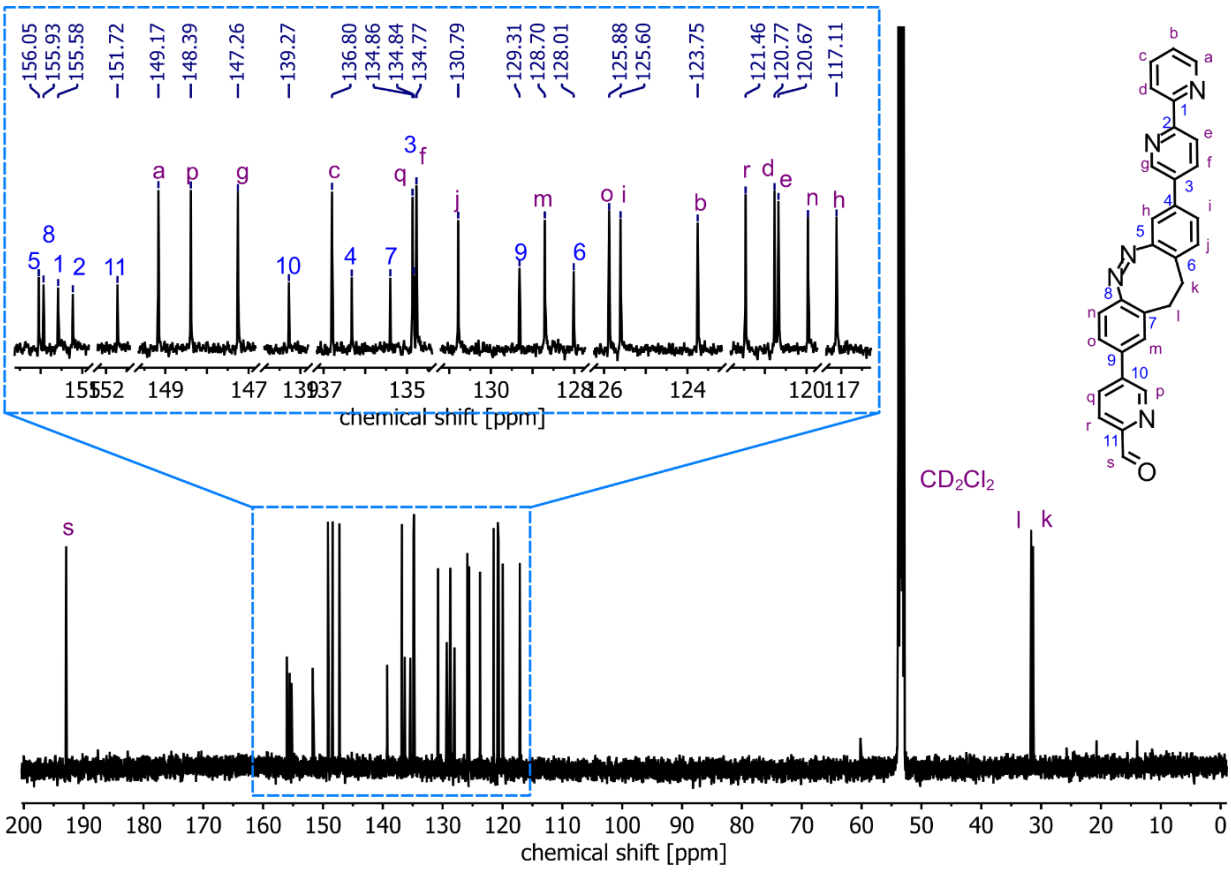

Figure S11. ^{13}C NMR spectrum (126 MHz, CD_2Cl_2, 298 K) of diazocine **1**.

S3 Synthesis of the bimetallic helicates

S3.1 Use of stock solutions

The use of stock solutions was essential for the synthesis of the bimetallic helicates presented herein. Some key aspects include:

1) The stoichiometry must be accurate for successful helicate formation and especially for the self-sorting experiments. The weight disparity between the ligand and the amine of 10:1 made this impossible at small scale.
2) The compounds must be fully dissolved in or miscible with the chosen solvent.
3) Solvents other than acetonitrile should be kept at a minimum, as the presence of excess protic solvents such as water or methanol hinder the formation of the complexes.
4) All fluid transfers were carried out using *Gilson* pipettes.
5) Stock solutions remained usable for months when stored in closed screw cap vials in a fridge at 6 °C.

S3.2 General procedure

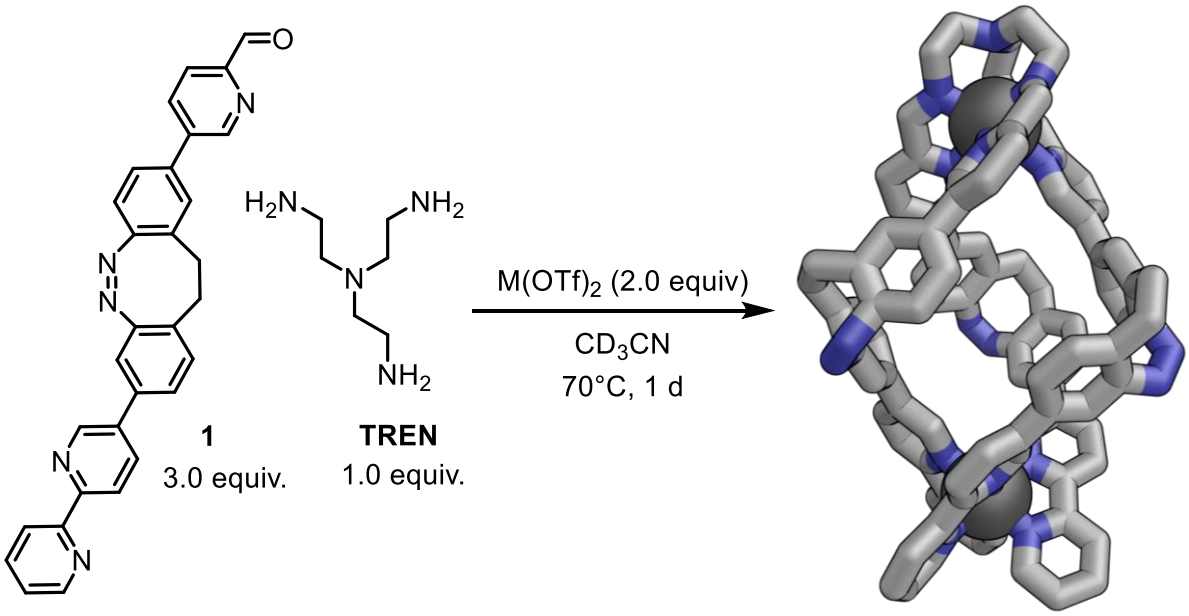

Aldehyde **1** (approx. 1–5 mg, 3.0 equiv.) was weighed into a screw-cap vial as a solid and a highly concentrated stock solution of tris(2-aminoethyl)amine (1.0 equiv.) in deuterated methanol (>50 mg mL^{-1}) was added to the bottom of the vial. Subsequently, a stock solution of metal salt in deuterated acetonitrile (2.0–2.2 equiv., 2–40 mg/mL, depending on the solubility of metal salt) was added. If the vial was not

filled with at least 0.5 mL of solvent, more deuterated acetonitrile was added. Finally, a magnetic stir bar was added, and the vial was closed and heated (to between 45 °C and 65 °C as specified) overnight. A ^{1}H NMR spectrum was measured to confirm successful complex formation. The complexes reported herein could be synthesized in a highly reproducible manner, if reaction time (>12 h) and temperature (>45° C) were sufficiently long and high, respectively, and the targeted stoichiometry was hit accurately.

If the spectrum was not sufficiently clean and impurities were present, the complex was purified by precipitation from diethyl ether. For this, the crude reaction mixture was filtered through a pipette stuffed with an extra fine glass fibre filter (pore size 1.6 µm). The filtrate was added in portions not larger than 0.2 mL (for triflates, perchlorates, and tetrafluoroborates) or no larger than 0.1 mL (for triflimides) to a 2 mL *Eppendorf* centrifuge vial filled with 1.7 mL of diethyl ether. The vial was shaken vigorously and centrifuged (14000 rpm, 1 minute). The supernatant was carefully discarded into a clean beaker to catch any solid in case the precipitate plug fell out. Another portion of 1.7 mL of diethyl ether was added to the residue and a second portion of the filtrate was added. This process was repeated until the filtrate was used up completely. If this was the case, the residue was suspended in 0.1 mL of acetonitrile and 1.9 mL of diethyl ether were added. The suspension was centrifuged (14000 rpm, 1 minute), the supernatant carefully decanted, and the residue suspended in 2.0 mL of diethyl ether. The centrifuge vial was sonicated for 1 minute and centrifuged (14000 rpm, 1 minute). This was repeated twice. The final residue was left open to air to dry for a few hours. Decomposition on air was not observed, but drying under reduced pressure resulted in decomposition. Drying on air resulted in mostly dry samples, but the last traces of solvent and/or water proved difficult to remove for the helicates investigated herein.

Complex formation is typically quantitative, lower yields can be attributed to losses during extraction/precipitation cycles.

S3.3 Zn_2**L**

Zn_2**L** was synthesized according to the general procedure (Section S3.2) using $Zn(OTf)_2$ (1.19 mg, 3.28 µmol, 2.00 equiv.), aldehyde **1** (2.30 mg, 4.92 µmol, 3.00 equiv.), and TREN (0.24 mg, 1.64 µmol, 1.00 equiv.) with a reaction time of 1 day at a temperature of 70 °C. After precipitation the product was obtained as a yellow powder in 83% yield (3.27 mg, 1.39 µmol).

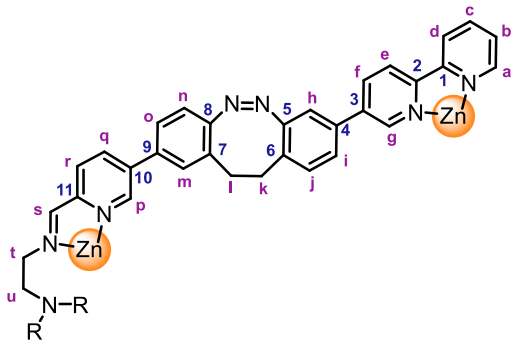

$[C_{96}H_{75}N_{19}Zn_2](CF_3O_3S)_4$

^{1}H NMR (700 MHz, CD_3CN) δ [ppm] = 2.74 (dt, J = 15.1, 7.6 Hz, 3H, H-l), 2.86 (q, J = 7.2 Hz, 6H, H-k), 2.91 – 3.00 (m, 6H, H-l′,u), 3.26 (dd, J = 13.7, 3.9 Hz, 3H, H-u′), 3.68 (dd, J = 11.9, 3.6 Hz, 3H, H-t), 3.86 (t, J = 12.8 Hz, 3H, H-t′), 6.42 (d, J = 1.9 Hz, 3H, H-h), 6.50 (d, J = 2.2 Hz, 3H, H-p), 6.71 (d, J = 1.9 Hz, 3H, H-m), 6.90 (d, J = 8.1 Hz, 3H, H-n), 7.03 (dd, J = 8.2, 1.9 Hz, 3H, H-o), 7.49 – 7.54 (m, 6H, H-g,j), 7.60 – 7.64 (m, 6H, H-b,i), 8.02 (ddd, J = 5.2, 1.7, 0.8 Hz, 3H, H-a), 8.20 (d, J = 8.0 Hz, 3H, H-r), 8.29 (td, J = 7.9, 1.7 Hz, 3H, H-c), 8.39 (dd, J = 8.0, 2.2 Hz, 3H, H-q), 8.56 (dd, J = 8.5, 2.3 Hz, 3H, H-f), 8.65 (dt, J = 8.3, 1.1 Hz, 3H, H-d), 8.69 (d, J = 8.6 Hz, 3H, H-e), 8.79 (d, J = 1.9 Hz, 3H, H-s).

^{13}C NMR (176 MHz, CD_3CN) δ [ppm] = 31.6 (C-l), 32.6 (C-k), 54.9 (C-u), 56.6 (C-t), 119.0 (C-h), 121.9 (C-n), 124.4 (C-e), 125.1 (C-d), 126.0 (C-o), 126.8 (C-b), 128.6 (C-i), 129.4 (C-r), 129.7 (C-m), 130.1 (C-7), 130.2 (C-6), 132.0 (C-j), 134.9 (C-4,9), 138.8 (C-3), 139.3 (C-q), 140.5 (C-f), 140.9 (C-10), 142.9 (C-c), 146.3 (C-p), 146.4 (C-g), 147.2 (C-11), 149.2 (C-2,a), 149.6 (C-1), 156.1 (C-8), 156.3 (C-5), 163.4 (C-s).

HRMS (ESI$^+$ Orbitrap): m/z (relative intensity) = 406.3756 (77%, $[Zn_2\mathbf{L}]^{4+}$, calcd. 406.3751), 591.4843 (100%, $[Zn_2\mathbf{L}$ + OTf$]^{3+}$, calcd. 591.4843), 961.7037 (45%, $[Zn_2\mathbf{L}$ + 2OTf$]^{2+}$, calcd. 961.7027).

FTIR (ATR, thin film from CD_3CN): $\tilde{\nu}$ [cm^{-1}] = 417.3 (vw), 517.6 (w), 574.0 (w), 638.0 (vs) (δ_s F_3C**SO_3**), 756.1 (w), 797.5 (w), 843.8 (w), 901.5 (vw), 931.6 (vw), 1029.6 (vs) (υ_s F_3C**SO_3**), 1161.0 (s) (υ_{as} **F_3C**SO_3), 1256.8 (vs) (υ_{as} F_3C**SO_3**), 1369.4 (vw), 1441.0 (w),

1473.1 (w), 1569.7 (w), 1599.2 (w), 1655.8 (w), 2857.1 (vw), 2926.8 (vw), 2947.5 (vw), 3069.3 (vw).

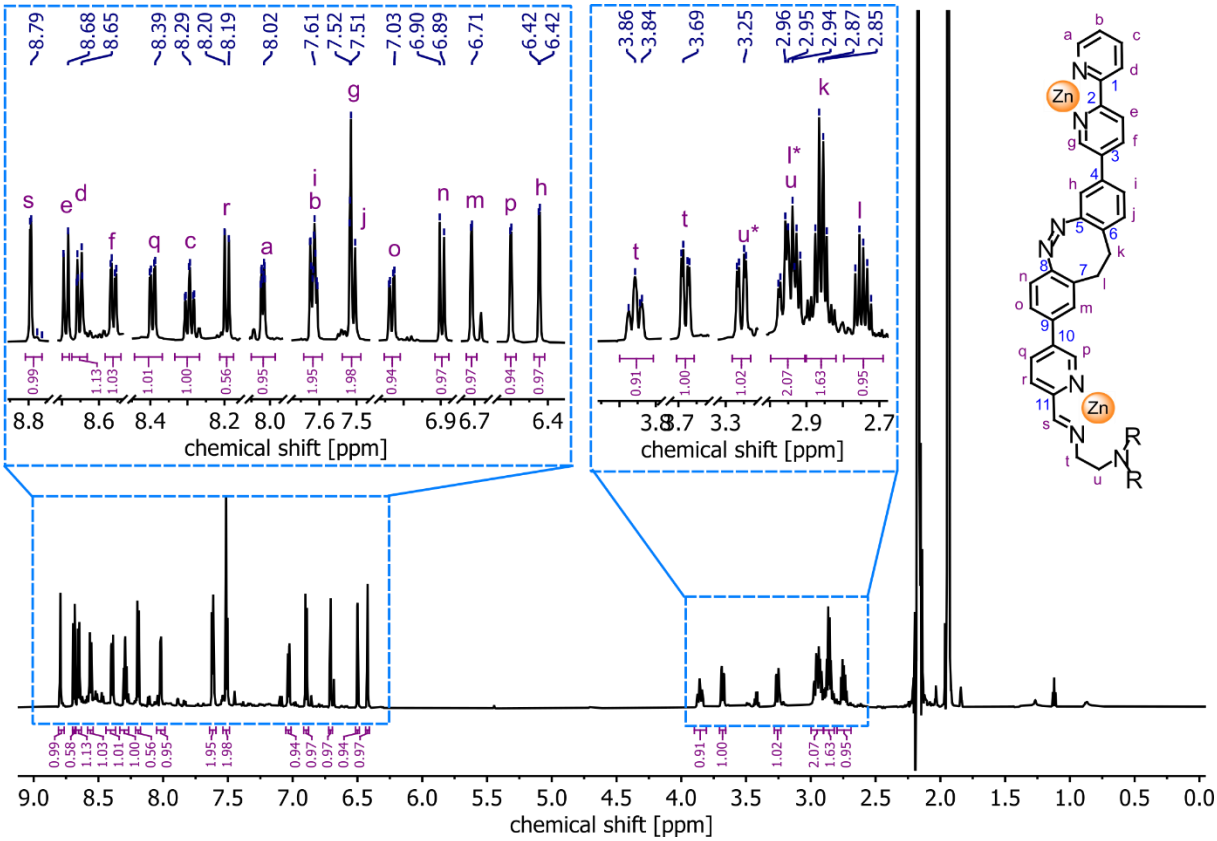

Figure S12. ^{1}H NMR spectrum (700 MHz, CD_3CN, 298 K) of Zn_2**L**.

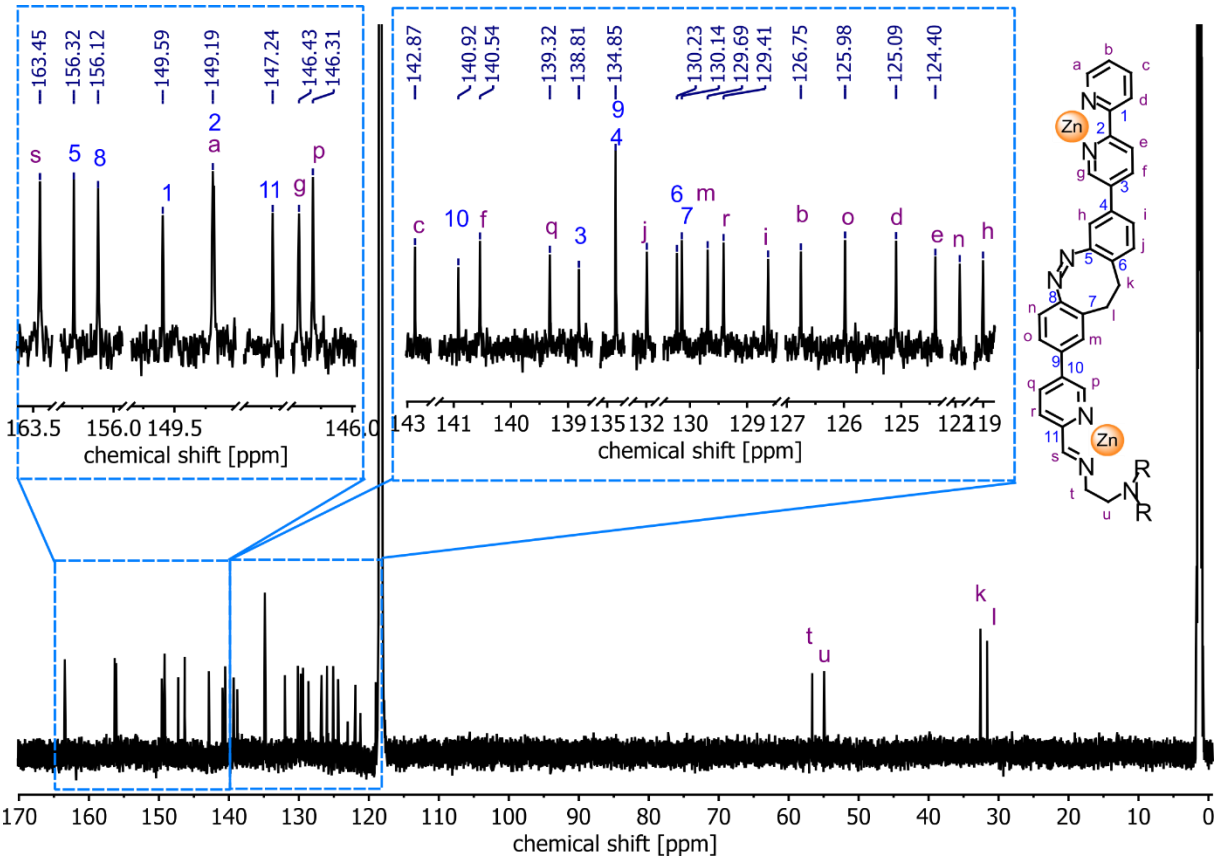

Figure S13. ^{13}C NMR spectrum (176 MHz, CD_3CN, 298 K) of Zn_2**L**.

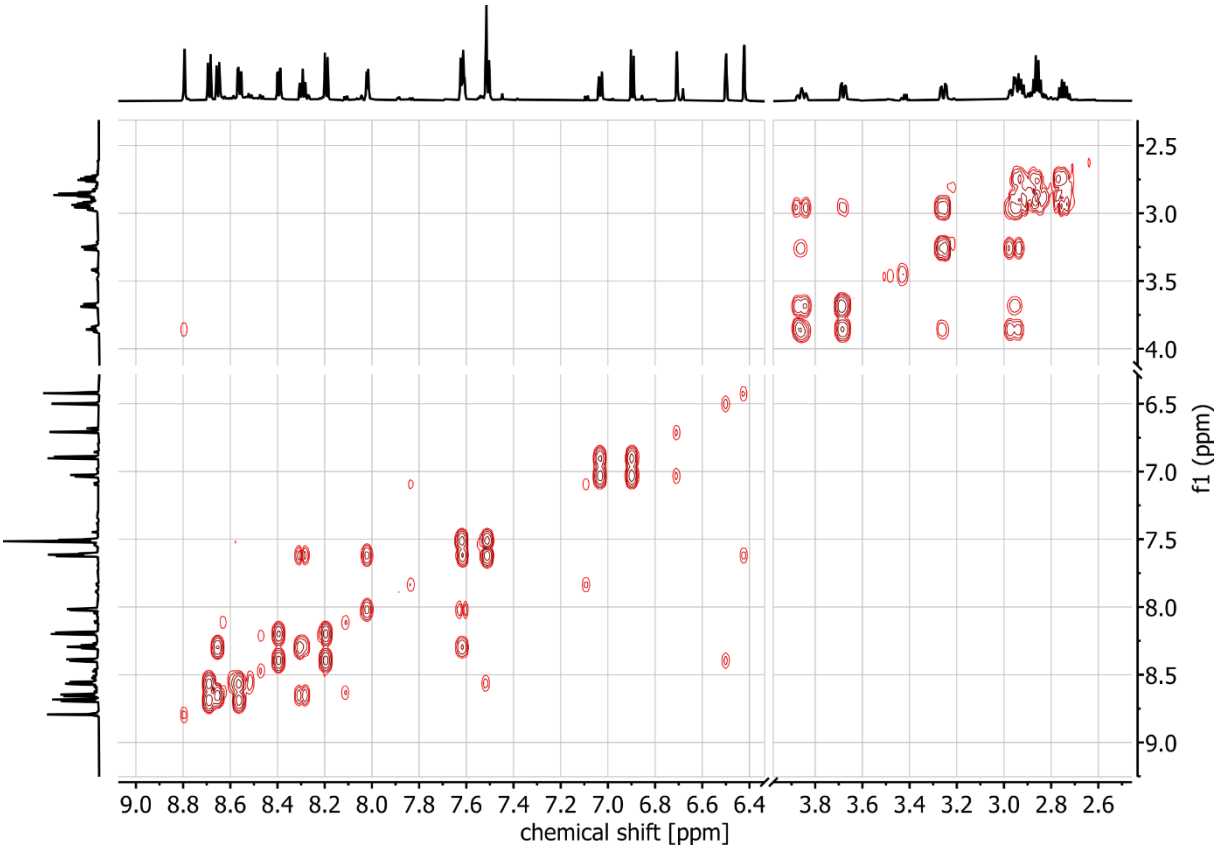

Figure S14. ^{1}H,^{1}H COSY spectrum (700 MHz, CD_3CN, 298 K) of Zn_2**L**.

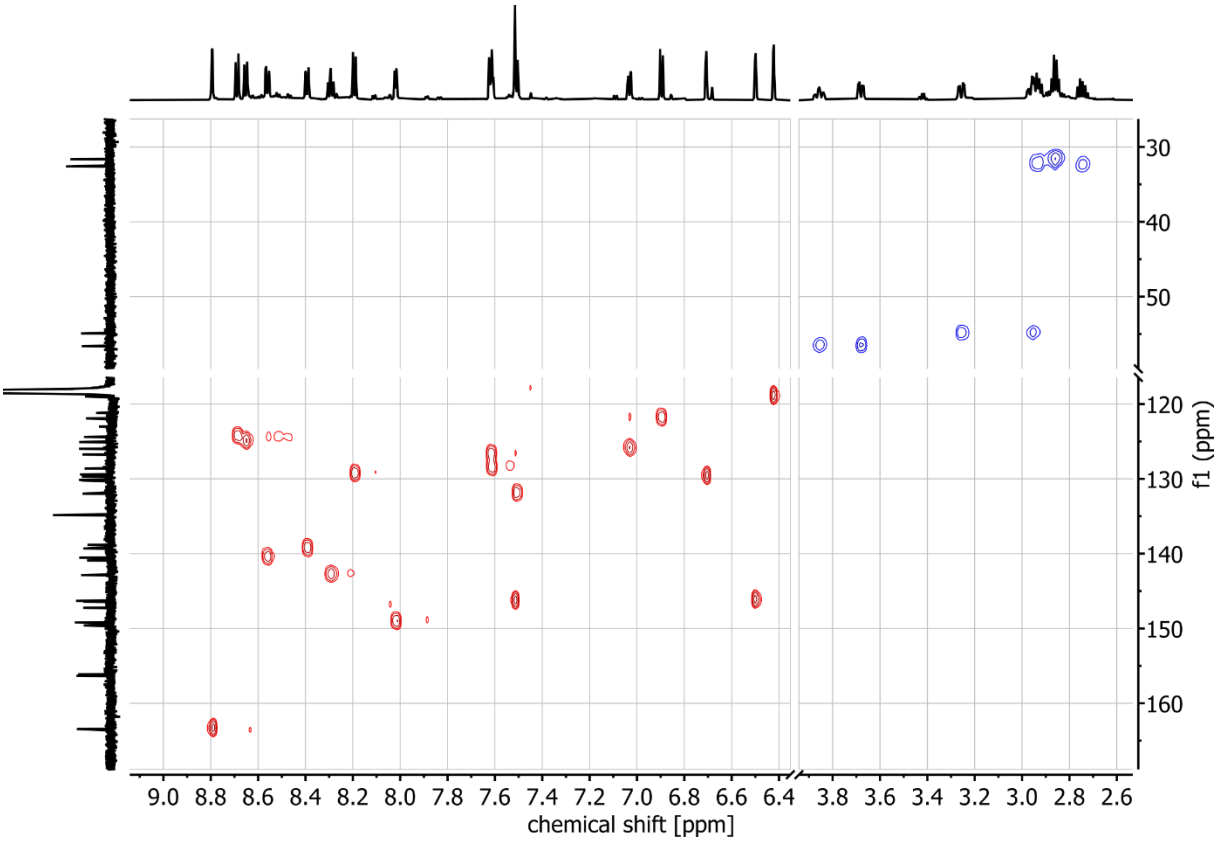

Figure S15. ^{1}H,^{13}C HSQC spectrum (700/176 MHz, CD_3CN, 298 K) of Zn_2**L**.

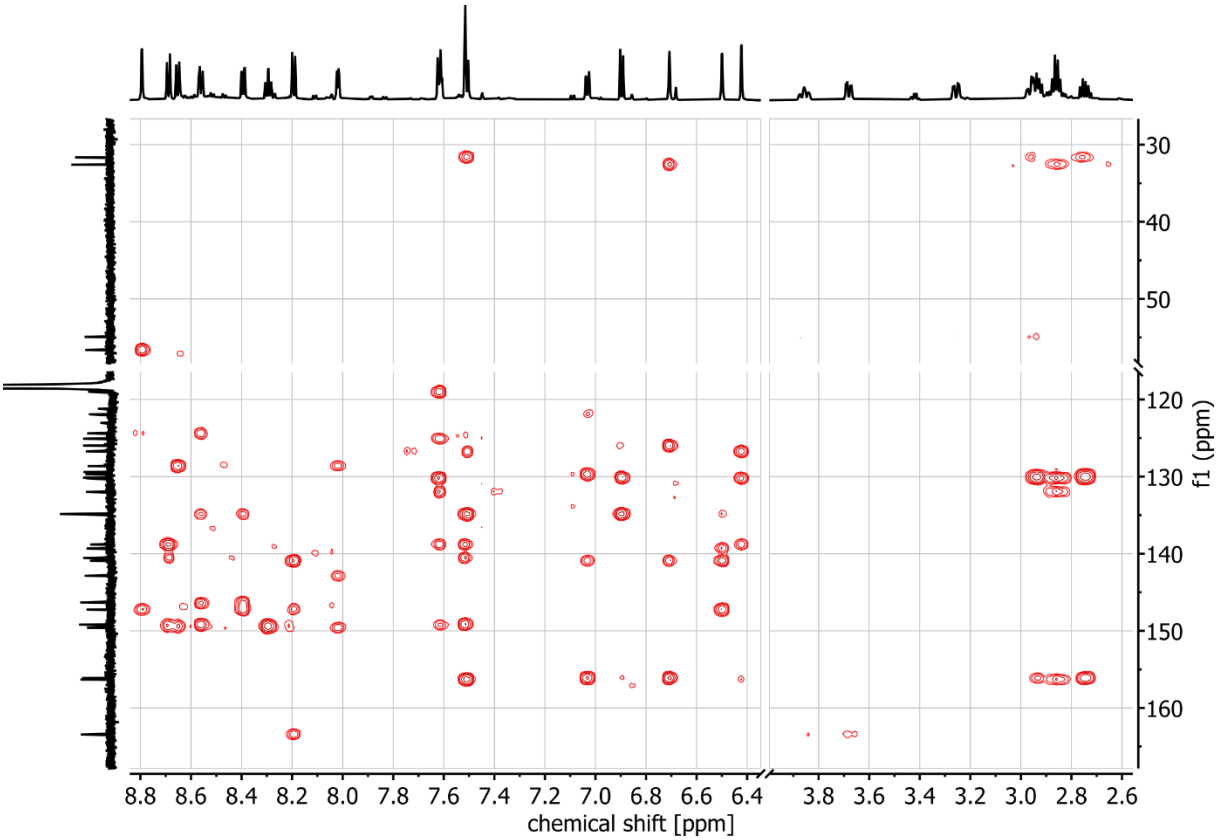

Figure S16. $^{1}H,^{13}C$ HMBC spectrum (700/176 MHz, CD_3CN, 298 K) of Zn_2**L**.

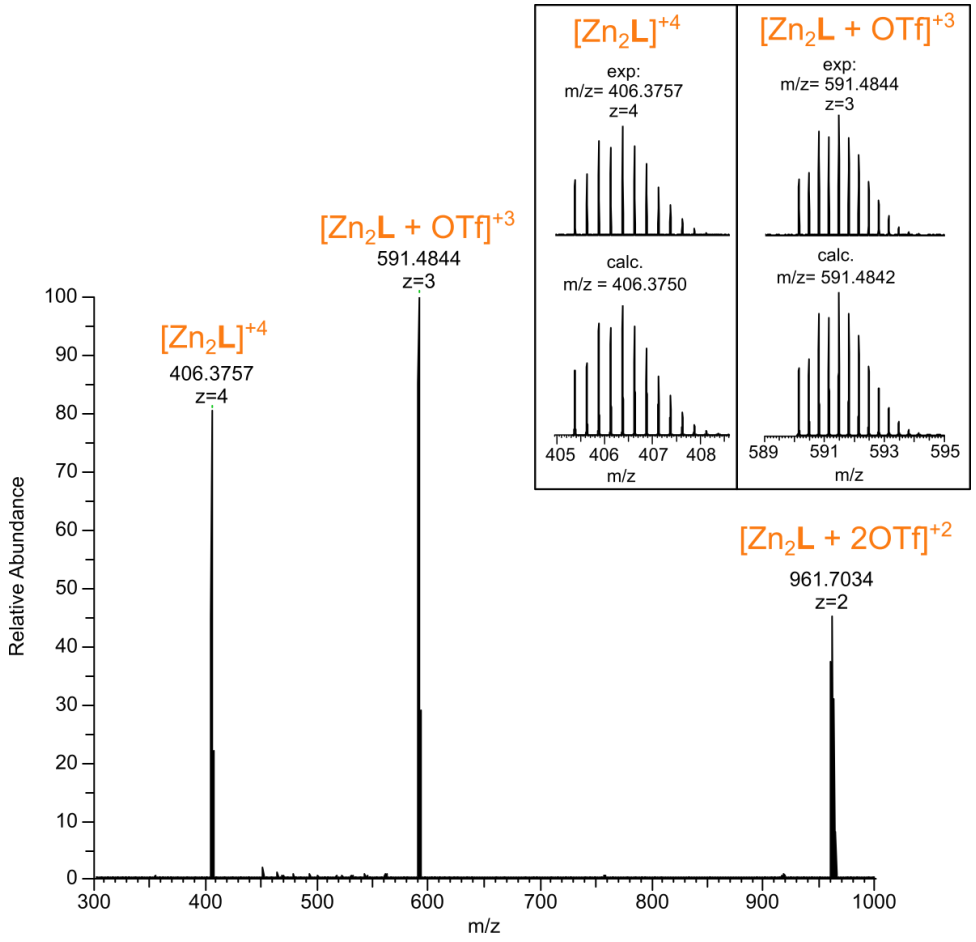

Figure S17. ESI^+ mass spectrum (CH_3CN) of Zn_2**L**.

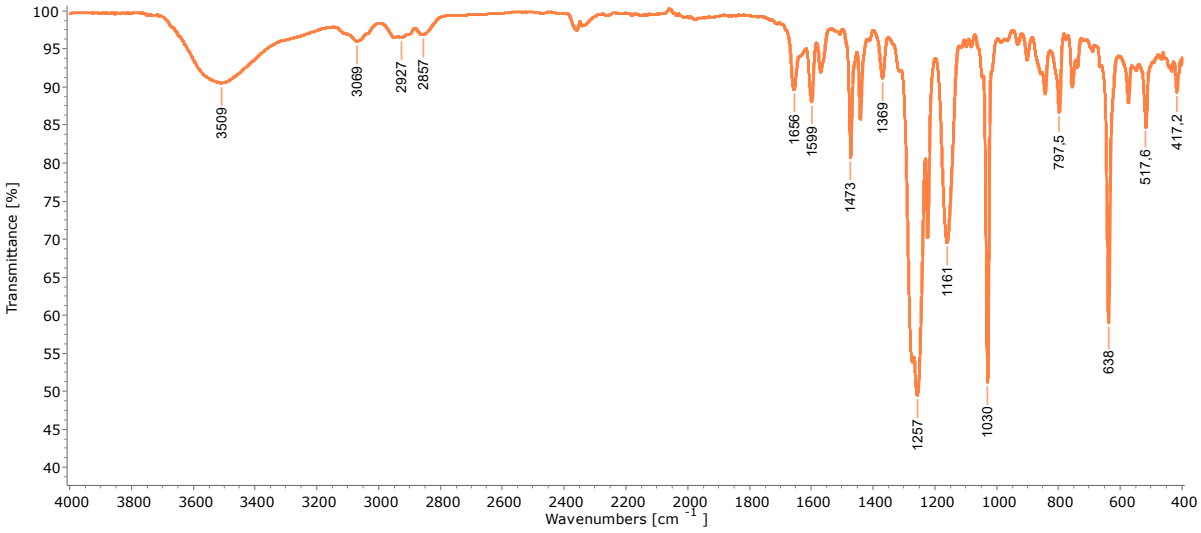

Figure S18. FTIR spectrum (ATR, thin film from evaporation of a CD_3CN solution) of Zn_2**L**.

S3.4 Fe_2**L**

Fe_2**L** was synthesized according to the general procedure (Section S3.2) using $Fe(OTf)_2$ (0.63 mg, 1.78 µmol, 2.00 equiv.), aldehyde **1** (1.25 mg, 2.67 µmol, 3.00 equiv.), and TREN (0.13 mg, 0.89 µmol, 1.00 equiv.) with a reaction time of 1 day at a temperature of 70 °C. After precipitation the product was obtained as a black powder in 90% yield (1.92 mg, 0.81 µmol).

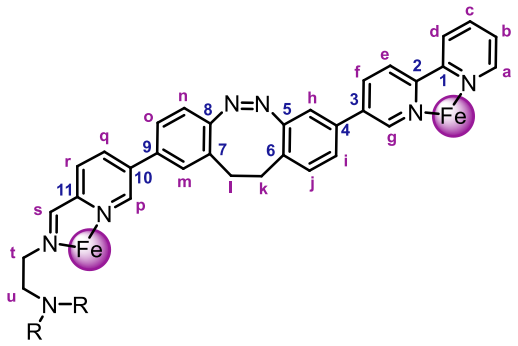

$[C_{96}H_{75}N_{19}Fe_2](CF_3O_3S)_4$

^{1}H NMR (700 MHz, CD_3CN) δ [ppm] = 2.67 – 2.77 (m, 3H, H-l), 2.77 – 2.89 (m, 6H, H-k), 2.96 (ddd, J = 14.8, 8.7, 5.6 Hz, 3H, H- l′), 3.22 (t, J = 13.8 Hz, 3H, H-u), 3.33 (t, J = 12.0 Hz, 3H, H-t), 3.90 (s(br), 3H, H-u′[†]), 4.03 (s(br), 3H, H-t′[*]), 6.30 (d, J = 1.9 Hz, 3H, H-h), 6.45 (s(br), 3H, H-p[*]), 6.60 (d, J = 1.9 Hz, 3H, H-m), 6.97 (d, J = 2.1 Hz, 3H, H-g), 7.00 (d, J = 8.1 Hz, 3H, H-n), 7.11 (dd, J = 8.1, 1.9 Hz, 3H, H-o), 7.41 (dt, J = 5.7, 1.4 Hz, 3H, H-a), 7.44 – 7.46 (m, 3H, H-b), 7.47 (d, J = 7.8 Hz, 3H, H-j), 7.53 (dd, J = 8.0, 2.0 Hz, 3H, H-i), 8.17 (td, J = 7.8, 1.5 Hz, 3H, H-c), 8.36 (dd, J = 8.2, 1.6 Hz, 3H, H-q), 8.44 (dd, J = 8.6, 2.1 Hz, 3H, H-f), 8.51 (d, J = 8.1 Hz, 3H, H-r), 8.65 (dt, J = 8.1, 1.1 Hz, 3H, H-d), 8.70 (d, J = 8.5 Hz, 3H, H-e), 9.59 (s(br), 3H, H-s[*]).

^{13}C NMR (176 MHz, CD_3CN) δ [ppm] = 31.3 (C-k), 32.6 (C-l), *53.9[‡] (C-u), 60.5[†] (C-t), 117.8[§] (C-h),* 121.6 (C-n), 125.0 (C-e), 125.9 (C-d), 126.4 (C-o), 126.7 (C-i), 128.7 (C-b), 129.8 (C-m,r), 130.5 (C-7), 131.0 (C-6), 132.0 (C-j), 134.3 (C-4), 135.2 (C-9), 136.9 (C-q), 137.7 (C-f), 138.9 (C-3), 139.9 (C-c), *141.6[†] (C-10),* 151.6 (C-g), 152.5 (C-11), 155.2 (C-a), 156.3 (C-8), 156.5 (C-5), 159.3 (C-1), 159.4 (C-2).

No signals or cross peaks could be observed for C-s and C-p as the corresponding ^{1}H NMR signals are already strongly broadened.

[†] The signals corresponding to H-p, H-s, H-u′ and H-t′ are strongly broadened.
[‡] The signals corresponding to C-10, C-u, and C-t are not visible in the ^{13}C NMR spectrum and could only be found by their cross-peaks in ^{1}H,^{13}C HSQC and HMBC NMR.
[§] The signal for C-h is underneath the solvent peak and could only be found by its cross-peak in ^{1}H,^{13}C HSQC NMR.

HRMS (ESI$^+$ Orbitrap): m/z (relative intensity) = 401.6297 (100%, $[Fe_2\mathbf{L}]^{+4}$, calcd. 401.6290).

MS (ESI$^+$ Orbitrap): m/z (relative intensity) = 401.631 (100%, $[Fe_2\mathbf{L}]^{+4}$, calcd. 401.629), 585.160 (34%, $[Fe_2\mathbf{L} + OTf]^{+3}$, calcd. 585.154), 952.217 (4%, $[Fe_2\mathbf{L} + 2OTf]^{+2}$, calcd. 952.208).

FTIR (ATR, thin film from CD_3CN): $\tilde{\nu}$ [cm^{-1}] = 518.6 (w), 576.7 (vw), 638.6 (s) (δ_s $F_3C\mathbf{SO_3}$), 756.7 (vw), 792.4 (w), 894.5 (w), 1030.1 (vs) (υ_s $F_3C\mathbf{SO_3}$), 1163.0 (m) (υ_{as} $\mathbf{F_3C}SO_3$), 1258.1 (vs) (υ_{as} $F_3C\mathbf{SO_3}$), 1367.0 (w), 1466.9 (m), 2851.8 (vw), 2928.1 (vw), 3080.1 (vw).

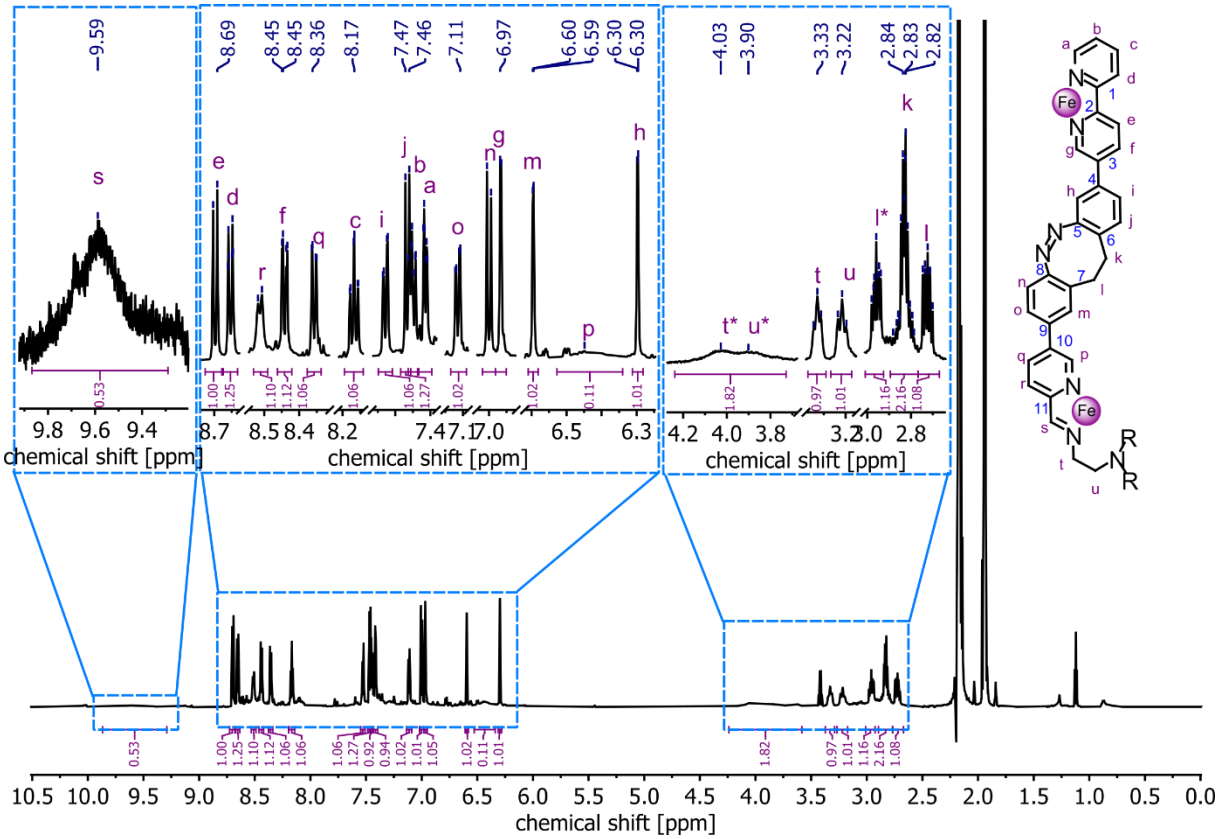

Figure S19. ^{1}H NMR spectrum (700 MHz, CD_3CN, 298 K) of Fe_2**L**.

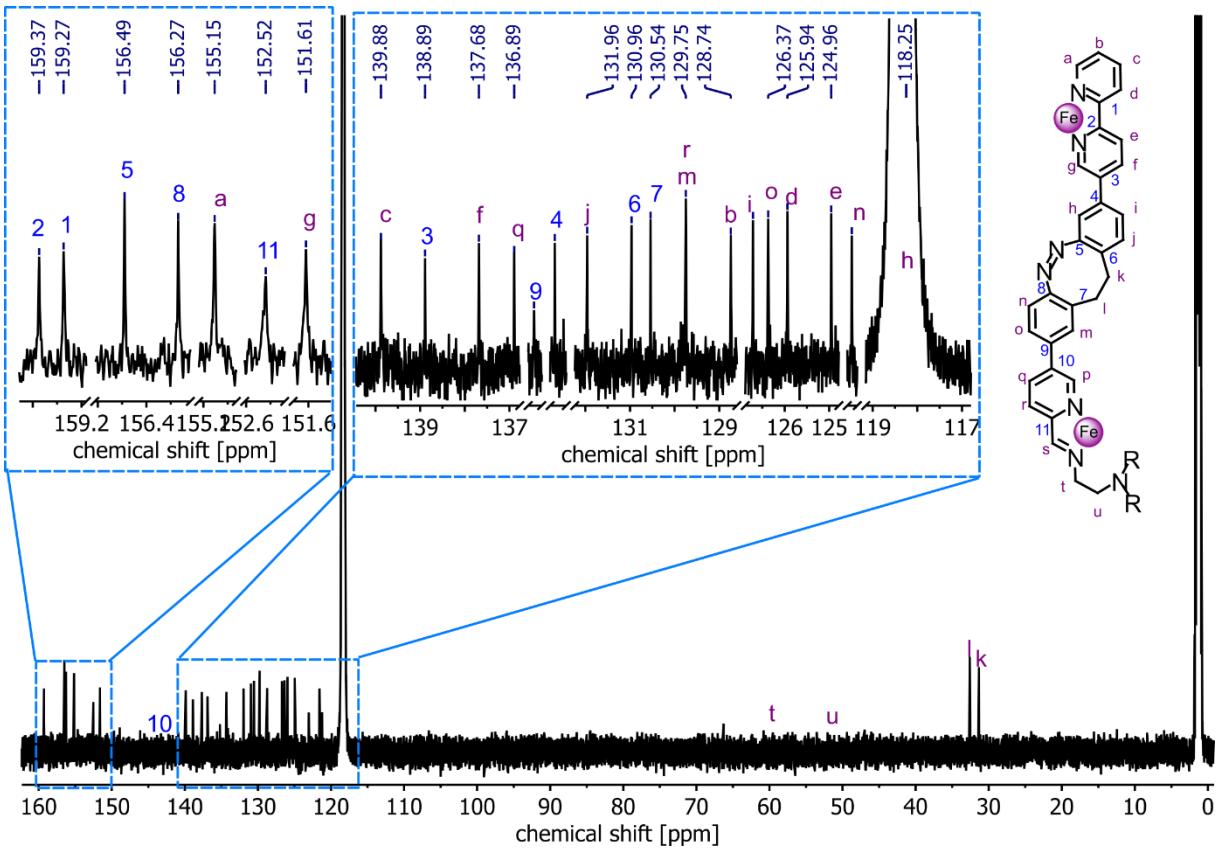

Figure S20. ^{13}C NMR spectrum (176 MHz, CD_3CN, 298 K) of Fe_2**L**.

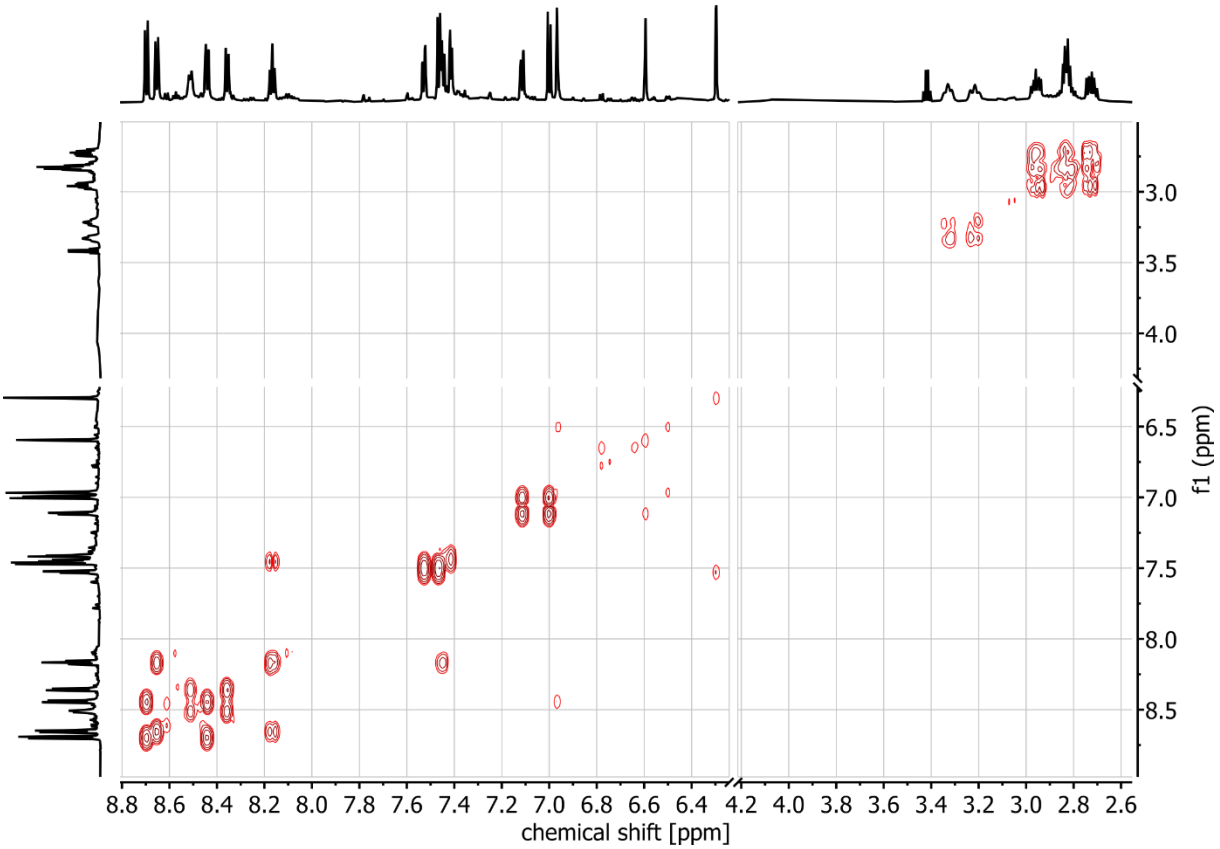

Figure S21. ^{1}H,^{1}H COSY spectrum (700 MHz, CD_3CN, 298 K) of Fe_2**L**.

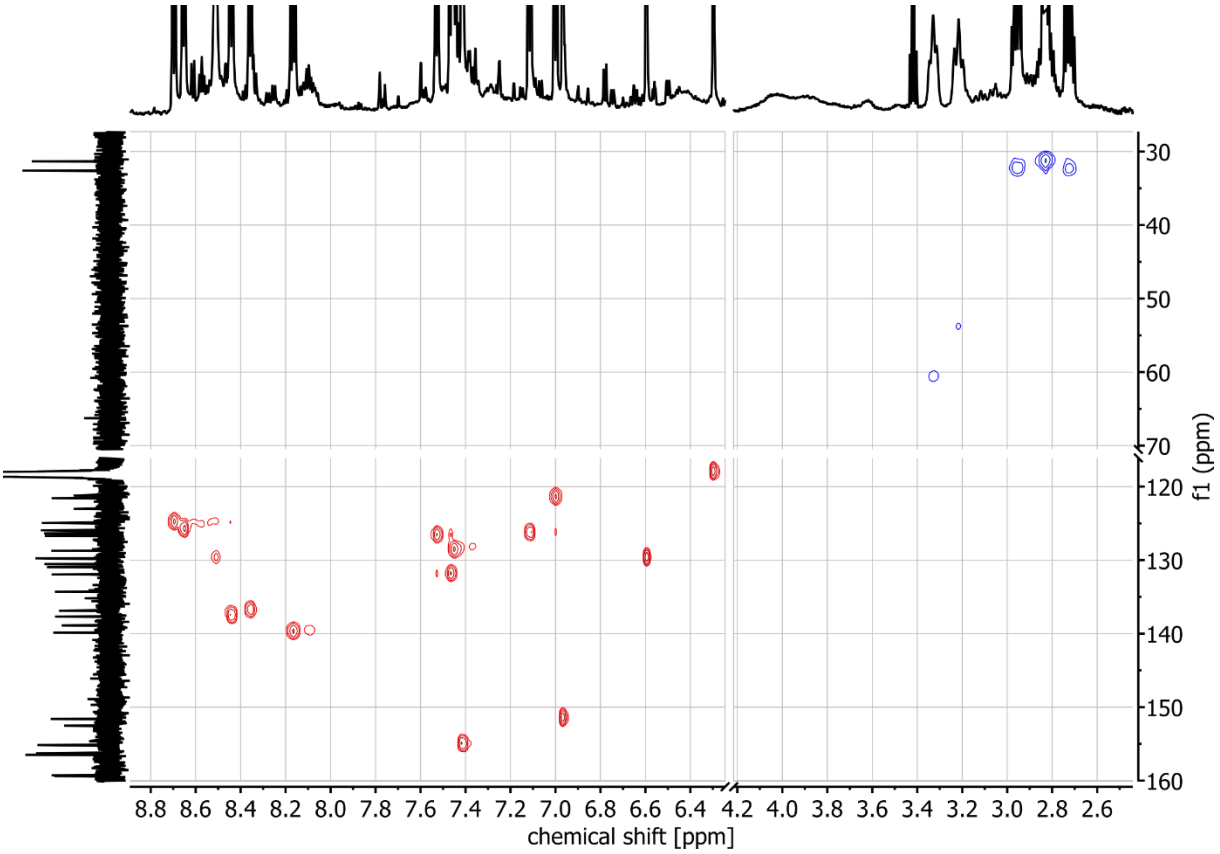

Figure S22. ^{1}H,^{13}C HSQC spectrum (700/176 MHz, CD_3CN, 298 K) of Fe_2**L**.

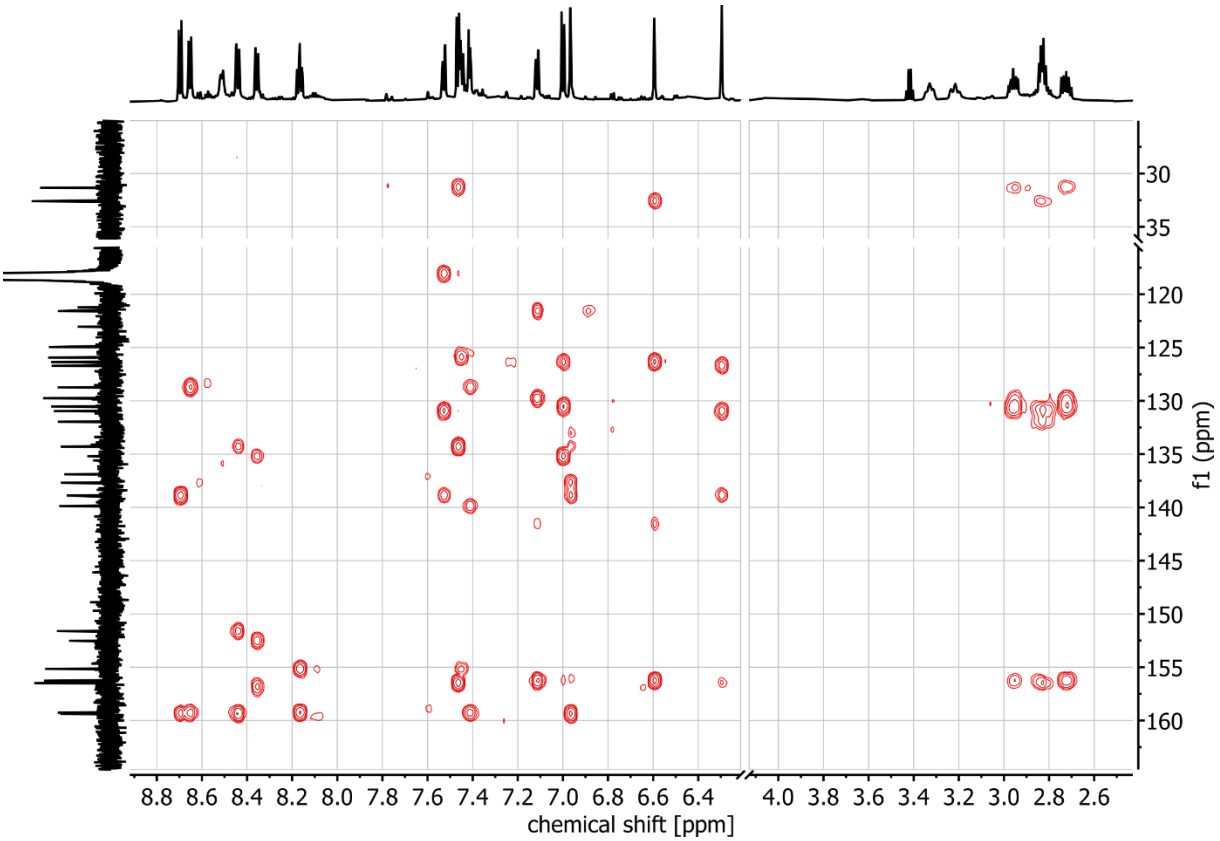

Figure S23. ^{1}H –^{13}C HMBC spectrum (700/176 MHz, CD_3CN, 298 K) of Fe_2**L**.

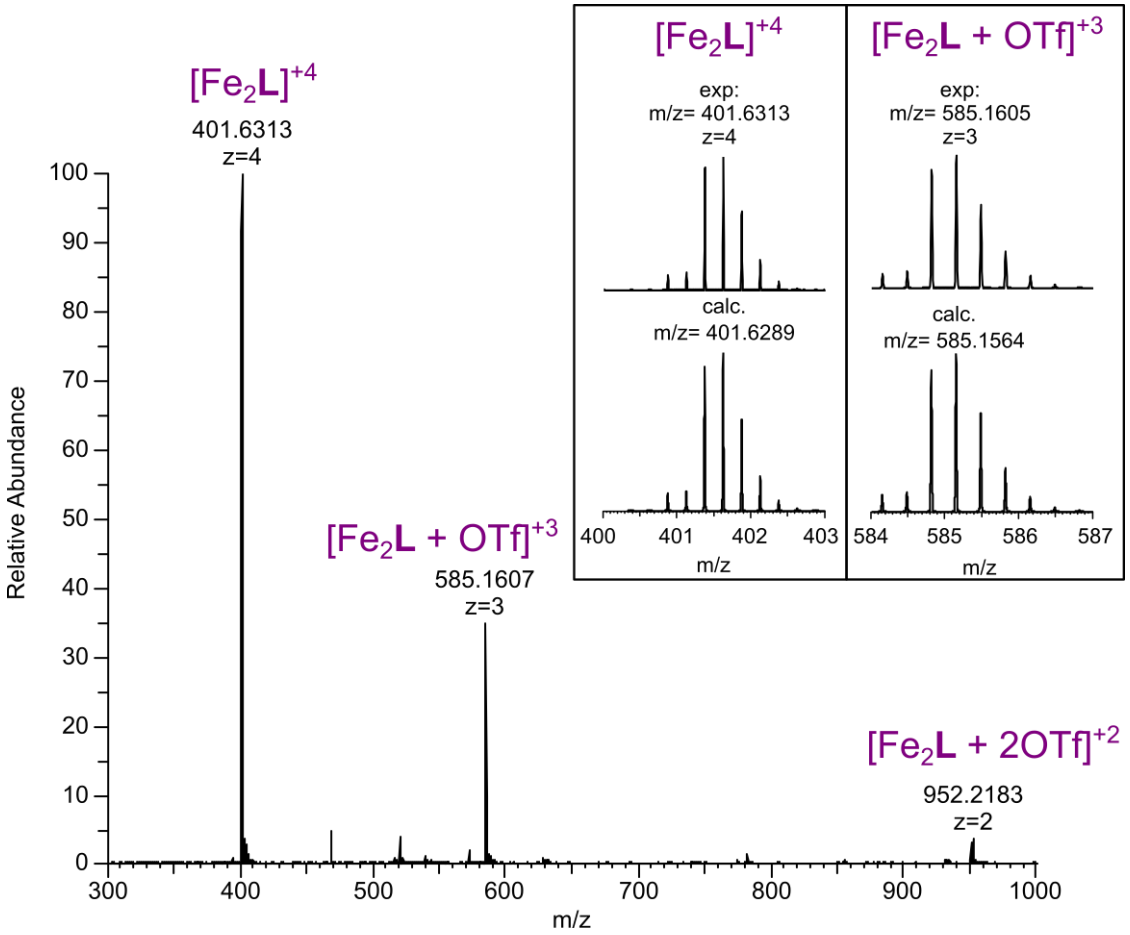

Figure S24. ESI^+ mass spectrum (CH_3CN) of Fe_2**L**.

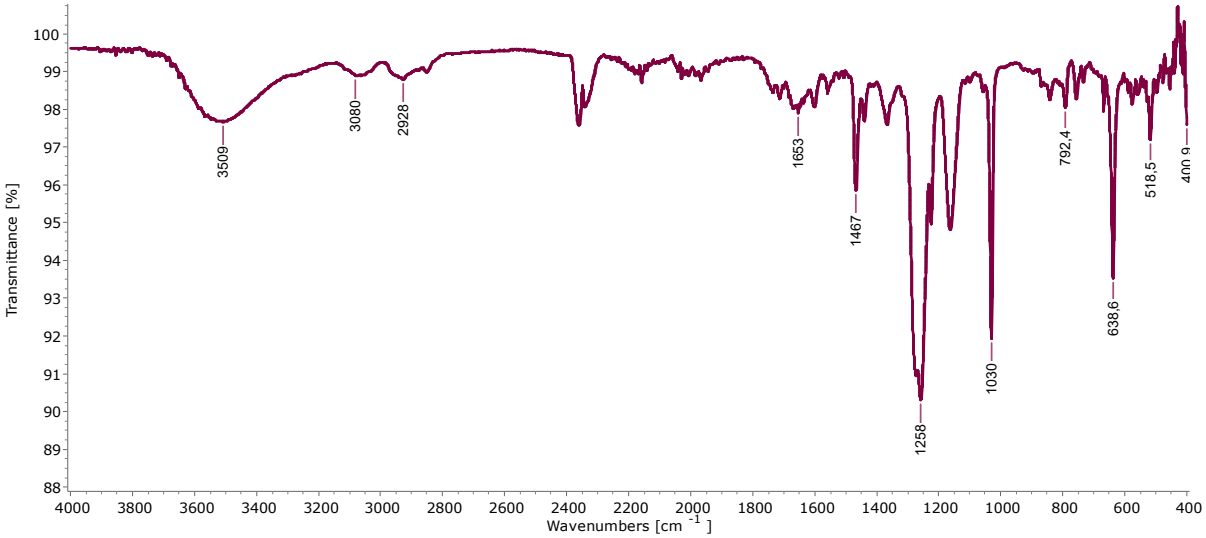

Figure S25. FTIR spectrum (ATR, thin film from evaporation of a CD_3CN solution) of Fe_2**L**.

S3.5 Co_2**L**

Co_2L 2as synthesized according to the general procedure (Section S3.2) using $Co(OTf)_2$ (1.20 mg, 3.4 µmol, 2.20 equiv.), aldehyde **1** (2.14 mg, 4.6 µmol, 3.00 equiv.), and TREN (0.22 mg, 1.5 µmol, 1.00 equiv.) with a reaction time of 1 day at a temperature of 70 °C. After precipitation the product was obtained as a yellow powder in 90% yield (1.92 mg, 0.81 µmol).

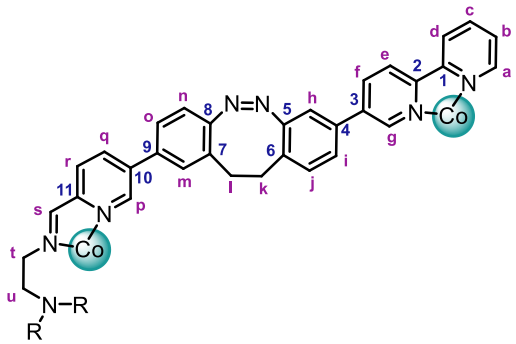

$[C_{96}H_{75}N_{19}Co_2](CF_3O_3S)_4$

^{1}H NMR (400 MHz, CD_3CN) δ [ppm] = 13.79 (H-c/f), 14.99 (H-c/f), 44.83 (H-b), 48.10 (H-q), 82.78 (H-d/e), 83.79 (H-d/e), 85.56 (H-a/g), 90.44 (H-a/g), 112.03 (H-r), 171.59 (H-s), 184.16 (H-p).

Due to the strong paramagnetism of the compound not all assignments could be made and not all signals could be observed.

HRMS (ESI$^+$ Orbitrap): *m/z* (relative intensity) = 402.8771 (100%, $[Co_2\mathbf{L}]^{+4}$, calcd. 402.8774), 586.8212 (15%, $[Co_2\mathbf{L}$ + OTf$]^{+3}$, calcd. 586.8207).

MS (ESI$^+$Orbitrap): *m/z* (relative intensity) = 403.131 (100%, $[Co_2\mathbf{L}]^{+4}$, calcd. 403.8772), 519.927 (9%, $[Co_2\mathbf{L}$ + **1**$]^{+4}$, calcd. 519.930), 587.161 (58%, $[Co_2\mathbf{L}$ + OTf$]^{+3}$, calcd. 587.163), 955.218 (2%, $[Co_2\mathbf{L}$+ 2OTf$]^{+2}$, calcd. 955.206).

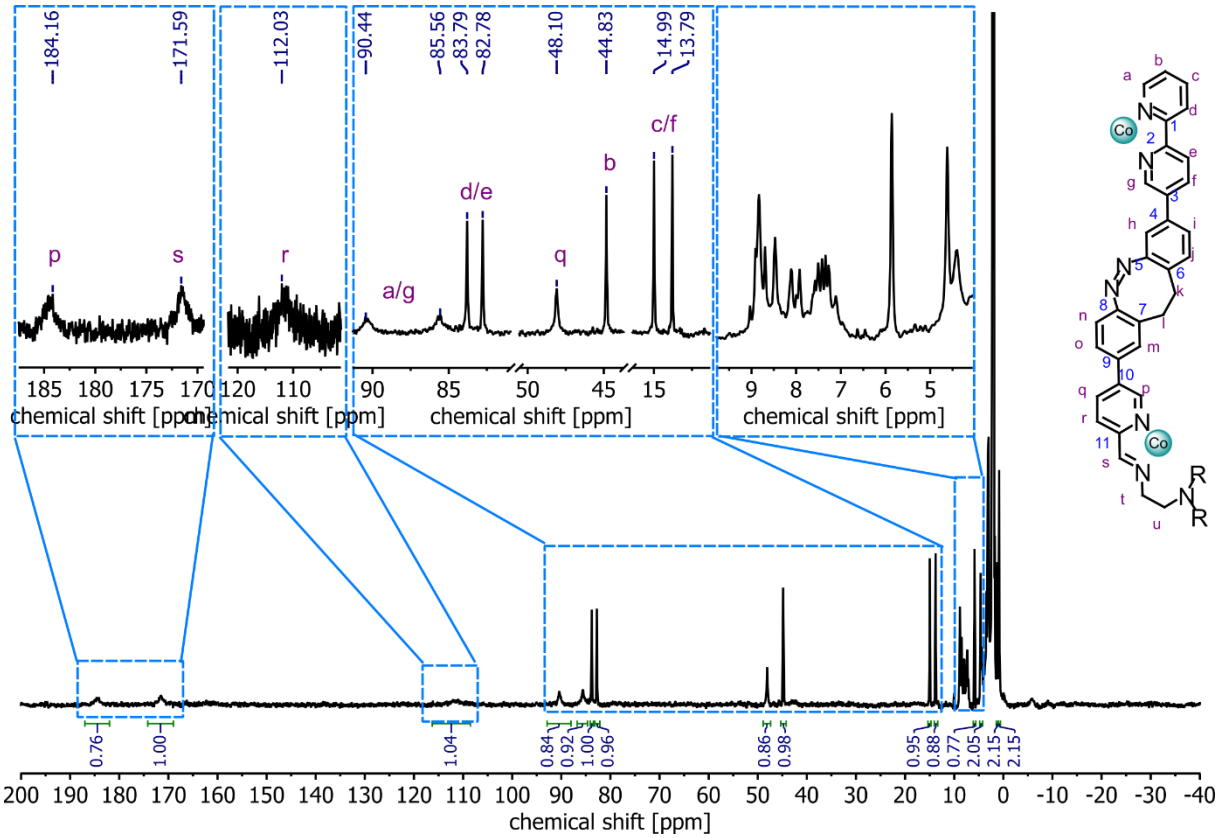

Figure S26. ^{1}H NMR spectrum (500 MHz, CD_3CN, 298 K) of Co_2**L**.

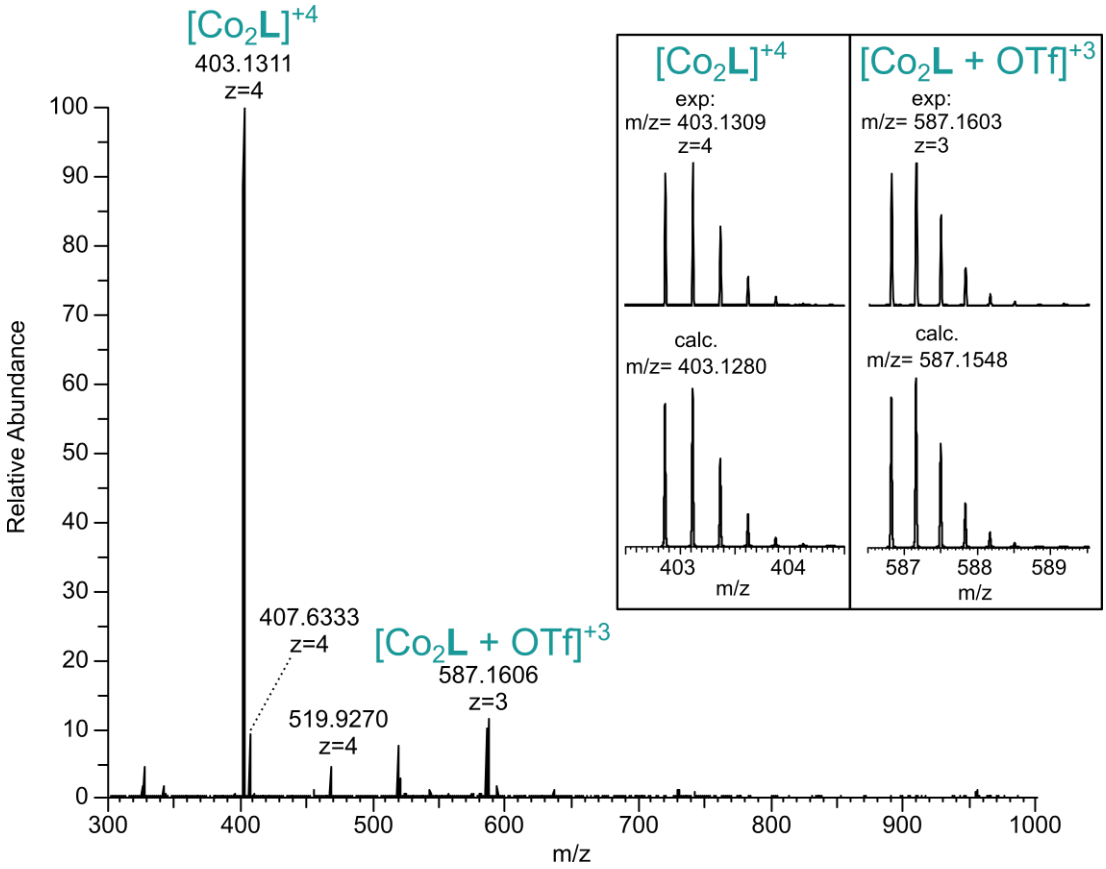

Figure S27. ESI^{+} mass spectrum (CH_3CN) of Co_2**L**.

S3.6 Fe**L**

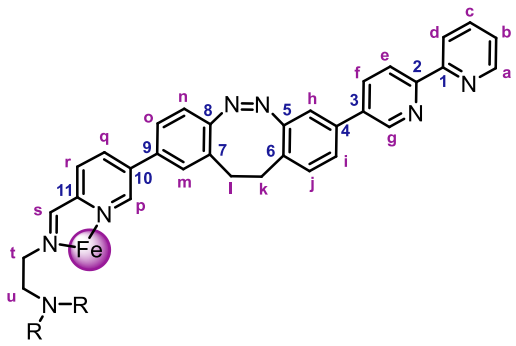

Fe**L** was synthesized according to the general procedure (Section S3.2) using $Fe(OTf)_2$ (0.34 mg, 0.96 µmol, 1.00 equiv.), aldehyde **1** (1.34 mg, 2.87 µmol, 3.00 equiv.), and TREN (0.14 mg, 0.96 µmol, 1.00 equiv.) with a reaction time of 1 day at a temperature of 70 °C. The crude product was used in the next step without workup.

Fe**L** exists as a mixture of conformational isomers with ^{1}H NMR and ESI(+) MS showing the formation of approximately 25% of the Fe_2**L** helicate as a side product.

HRMS (ESI$^+$ Orbitrap): *m/z* (relative intensity) = 774.7901 (100%, $[Fe\mathbf{L}]^{+2}$, calcd. 774.7898).

MS (ESI$^+$ Orbitrap): *m/z* (relative intensity) = 401.628 (57%, $[Fe_2\mathbf{L}]^{+4}$, calcd. 401.629), 585.156 (18%, $[Fe_2\mathbf{L} + OTf]^{+3}$, calcd. 585.154), 775.289 (100%, $[Fe\mathbf{L}]^{+2}$, calcd. 775.288), 952.210 (5%, $[Fe_2\mathbf{L} + 2OTf]^{+2}$, calcd. 952.208), 1699.535 (5%, $[Fe\mathbf{L} + OTf]^{+}$, calcd. 1699.528).

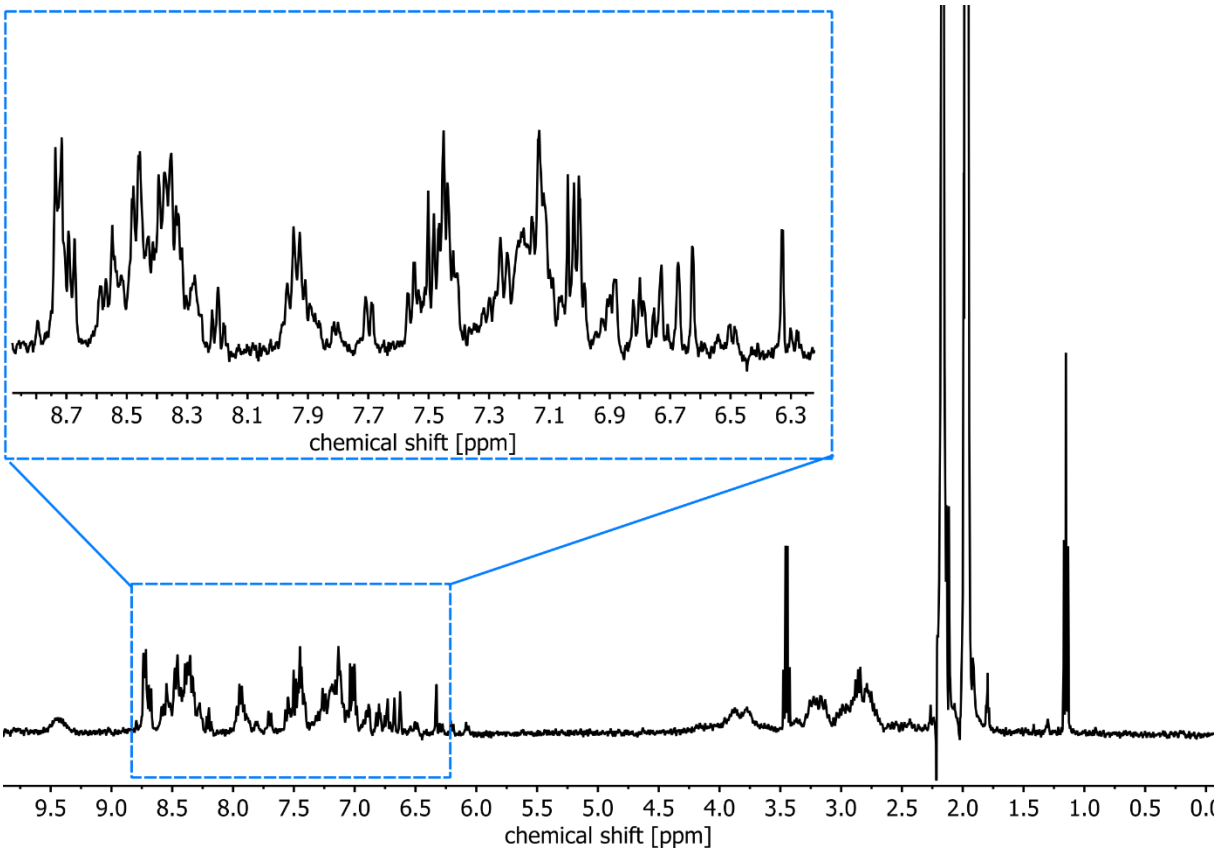

Figure S28. ^{1}H NMR spectrum (400 MHz, CD_3CN, 298 K) of Fe**L**.

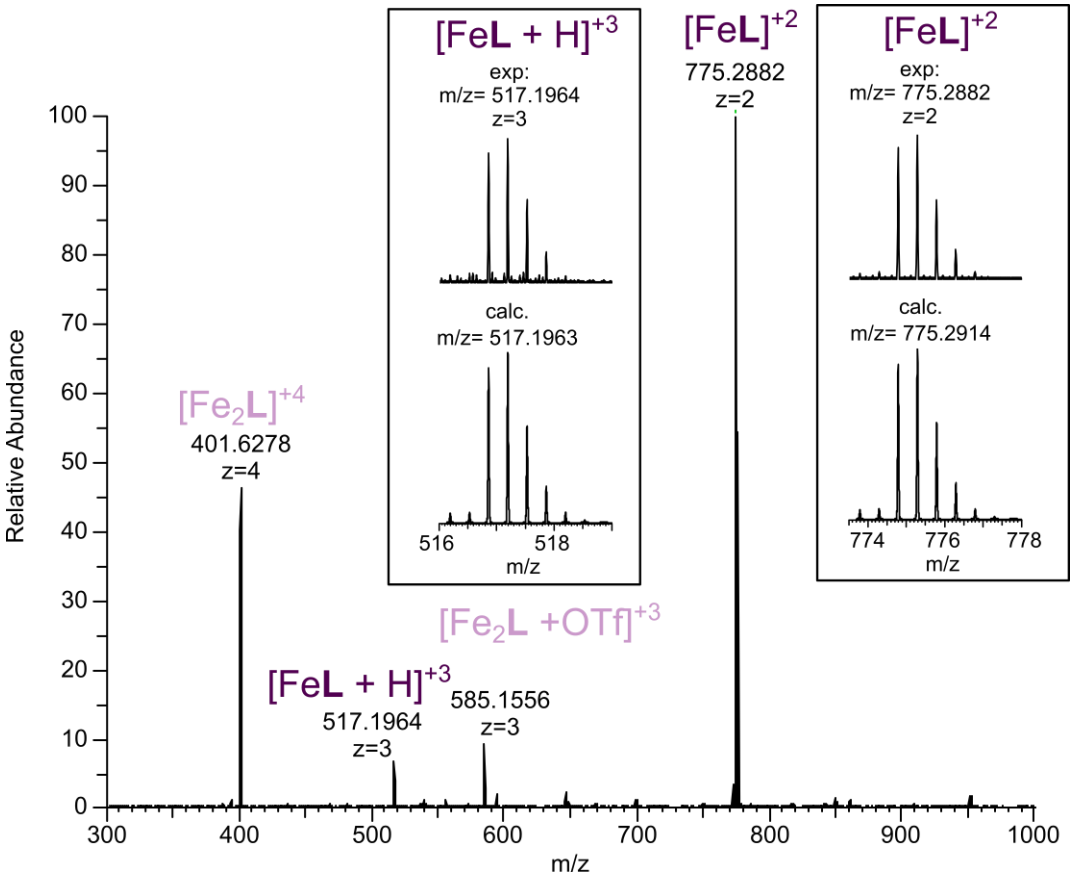

Figure S29. ESI^{+} mass spectrum (CH_3CN) of Fe**L**.

S3.7 FeZn**L**

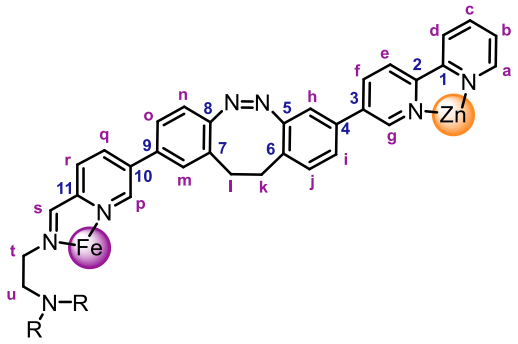

$[C_{96}H_{75}N_{19}ZnFe](CF_3O_3S)_4$

FeZn**L** was synthesized according to the general procedure (Section S3.2) using crude Fe**L** (approx. 0.96 µmol, 1.00 equiv.) and $Zn(OTf)_2$ (0.35 mg, 0.96 µmol, 1.00 equiv.) with a reaction time of 1 hour at a temperature of 30 °C. Even after precipitation no pure product could be obtained, only a mixture containing 65% of the desired FeZn**L** with 25% Fe_2**L** and 10% Zn_2**L** present.

^{1}H NMR (400 MHz, CD_3CN) δ [ppm] = 2.76 (dd, J = 15.4, 6.7 Hz, 3H), 2.80 – 2.88 (m, 6H), 2.94 (dd, J = 10.5, 5.6 Hz, 6H), 3.23 (s, 3H), 3.35 (s, 3H), 4.09 (s, 6H), 6.42 (s, 3H), 6.5 (s (br), 3H), 6.64 (s, 3H), 6.95 (d, J = 8.1 Hz, 3H), 7.08 (d, J = 8.3 Hz, 3H), 7.42 (s, 3H), 7.50 (d, J = 8.5 Hz, 3H), 7.55 (t, J = 9.2 Hz, 3H), 7.59 – 7.65 (m, 3H), 8.03 (d, J = 4.4 Hz, 3H), 8.30 (t, J = 7.1 Hz, 3H), 8.37 (t, J = 6.9 Hz, 3H), 8.54 (d, J = 7.0 Hz, 6H), 8.66 (d, J = 8.2 Hz, 3H), 8.70 (d, J = 8.5 Hz, 3H), 9.7 (s (br), 3H).

Since the helicates could not be separated and a significant signal overlap was observed, no assignments were made in the ^{1}H NMR spectrum.

HRMS (ESI$^+$ Orbitrap): m/z (relative intensity) = 591.4826 (100%, [FeZn**L** + OTf]$^{+3}$, calcd. 591.4843).

MS (ESI$^+$ Orbitrap): m/z (relative intensity) = 401.631 (80%, [Fe_2**L**]$^{+4}$, calcd. 401.629), 403.878 (100%, [FeZn**L**]$^{+4}$, calcd. 403.877), 406.374 (10%, [Zn_2**L**]$^{+4}$, calcd. 405.375), 585.159 (44%, [Fe_2**L** + OTf]$^{+3}$, calcd. 585.156), 588.155 (68%, [FeZn**L** + OTf]$^{+3}$, calcd. 588.154), 591.485 (10%, [Zn_2**L** + OTf]$^{+3}$, calcd. 591.484), 952.214 (6%, [Fe_2**L** + 2OTf]$^{+2}$, calcd. 952.215), 956.710 (9%, [FeZn**L** + 2OTf]$^{+2}$, calcd. 956.705), 961.705 (1%, [Zn_2**L** + 2OTf]$^{+2}$, calcd. 961.700).

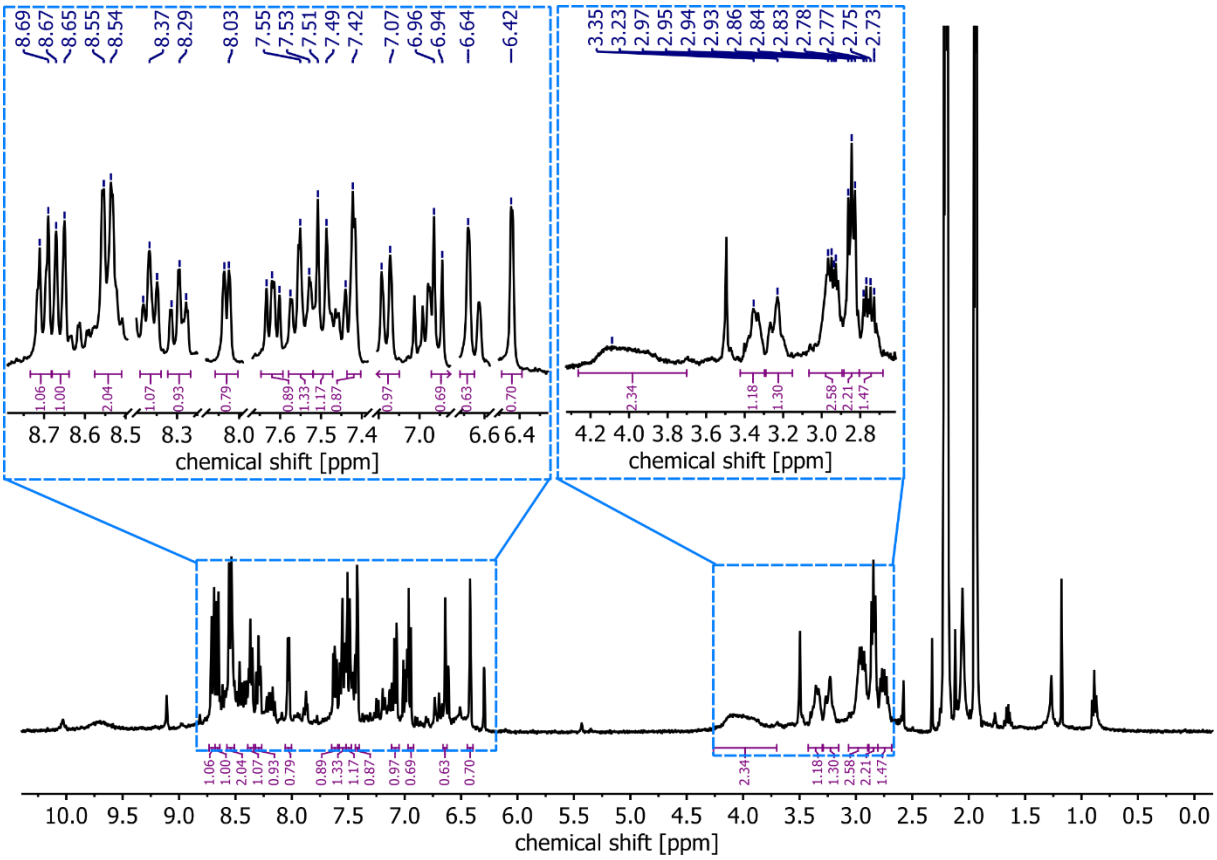

Figure S30. ^{1}H NMR spectrum (400 MHz, CD_3CN, 298 K) of FeZn**L**.

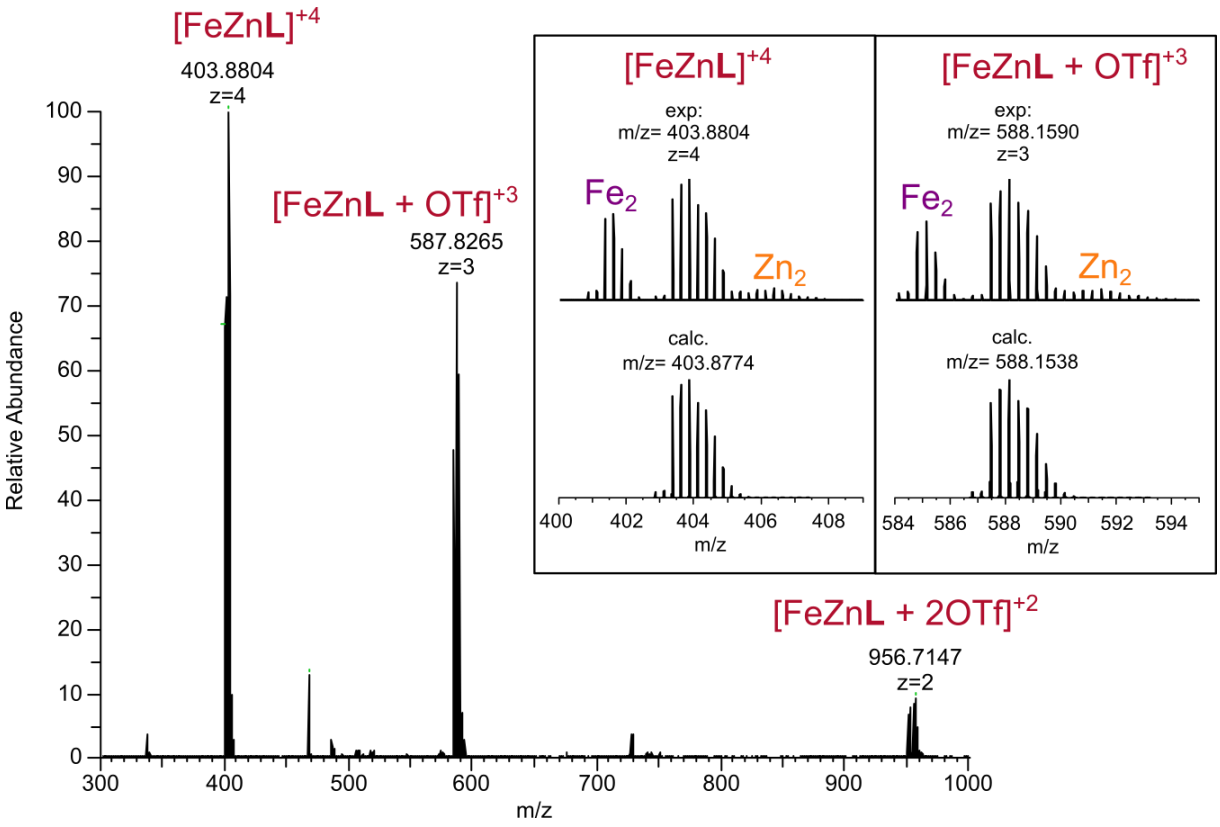

Figure S31. ESI(+) mass spectrum of FeZn**L** (CH_3CN).

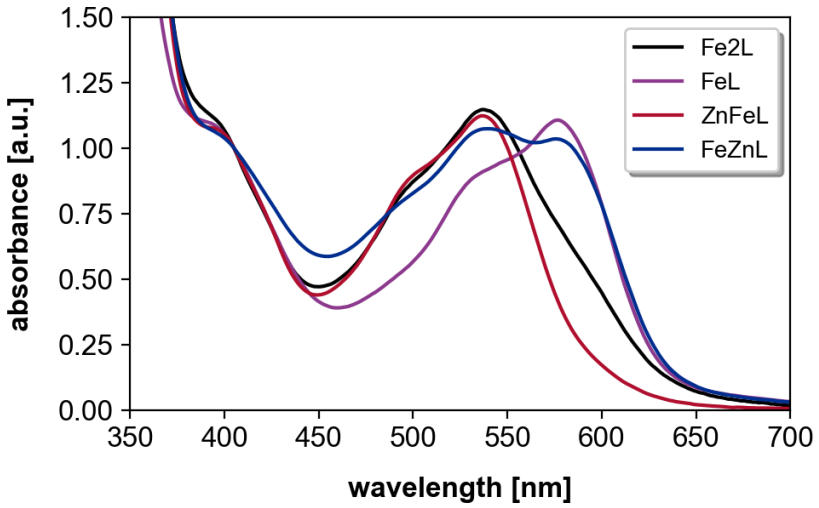

Figure S32. UV-vis spectra (CH_3CN, 0.06 mM) of Fe_2**L**, Fe**L**, ZnFe**L**, and FeZn**L**.

S3.8 ZnFe**L** via Zn→Fe exchange

ZnFe**L** was synthesized by adding $Fe(OTf)_2$ (0.44 mg, 1.23 µmol, 1.50 equiv.) to a solution of Zn_2**L** (1.98 mg, 0.82 µmol, 1.00 equiv.) in CD_3CN and heating the mixture to 65 °C for 2 days. The transformation occurred quantitatively.

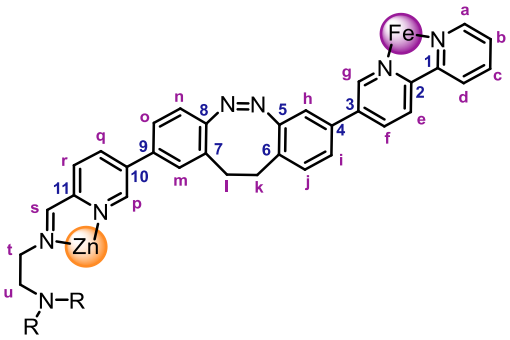

$[C_{96}H_{75}N_{19}ZnFe](CF_3O_3S)_4$

^{1}H NMR (700 MHz, CD_3CN) δ [ppm] = 2.70 – 2.77 (m, 3H, H-l), 2.80 – 2.89 (m, 6H, H-k), 2.91 – 2.99 (m, 6H, H-l′,u), 3.25 (dd, J = 13.7, 3.9 Hz, 3H, H-u′), 3.67 (dd, J = 12.0, 3.6 Hz, 3H, H-t), 3.85 (t, J = 11.6 Hz, 3H, H-t′), 6.31 (d, J = 2.0 Hz, 3H, H-h), 6.50 (d, J = 2.2 Hz, 3H, H-p), 6.69 (d, J = 2.0 Hz, 3H, H-m), 6.95 (d, J = 8.1 Hz, 3H, H-n), 7.06 (d, J = 2.0 Hz, 3H, H-g), 7.09 (dd, J = 8.1, 2.0 Hz, 3H, H-o), 7.41 (dd, J = 5.7, 1.5 Hz, 3H, H-a), 7.45 (ddd, J = 7.4, 5.7, 1.3 Hz, 3H, H-b), 7.48 (d, J = 8.0 Hz, 3H, H-j), 7.58 (dd, J = 8.0, 2.0 Hz, 3H, H-i), 8.16 (td, J = 7.8, 1.5 Hz, 3H, H-c), 8.19 (d, J = 8.0 Hz, 3H, H-r), 8.42 (dd, J = 8.1, 2.3 Hz, 3H, H-q), 8.46 (dd, J = 8.5, 2.1 Hz, 3H, H-f), 8.65 (dt, J = 8.2, 1.0 Hz, 3H, H-d), 8.69 (d, J = 8.5 Hz, 3H, H-e), 8.79 (d, J = 1.9 Hz, 3H, H-s).

^{13}C NMR (176 MHz, CD_3CN) δ [ppm] = 31.0 (C-k), 32.3 (C-l), 54.6 (C-u), 56.3 (C-t), *118.2[**] (C-h),* 121.4 (C-n), 124.4 (C-e), 125.5 (C-d), 125.6 (C-o), 126.3 (C-i), 128.3 (C-b), 129.1 (C-r), 129.3 (C-m), 129.9 (C-7), 130.3 (C-6), 131.5 (C-j), 134.0 (C-4), 134.4 (C-9), 137.0 (C-f), 138.3 (C-3), 138.9 (C-q), 139.4 (C-c), 140.5 (C-10), 145.8 (C-p), 146.9 (C-11), 152.0 (C-g), 154.7 (C-a), 155.8 (C-8), 156.0 (C-5), 158.8 (C-2), 159.0 (C-1), 163.1 (C-s).

HRMS (ESI$^+$ Orbitrap): m/z (relative intensity) = 403.8763 (100%, [ZnFe**L**]$^{4+}$, calcd. 403.8772).

[**] The signal for C-h is underneath the solvent peak and could only be found by its cross-peak in ^{1}H,^{13}C HSQC NMR.

MS (ESI$^+$ Orbitrap): m/z (relative intensity) = 403.880 (100%, [ZnFe**L**]$^{+4}$, calcd. 403.877), 588.159 (58%, [ZnFe**L** + OTf]$^{3+}$, calcd. 588.152), 956.718 (9%, [ZnFe**L** + 2OTf]$^{2+}$, calcd. 956.705).

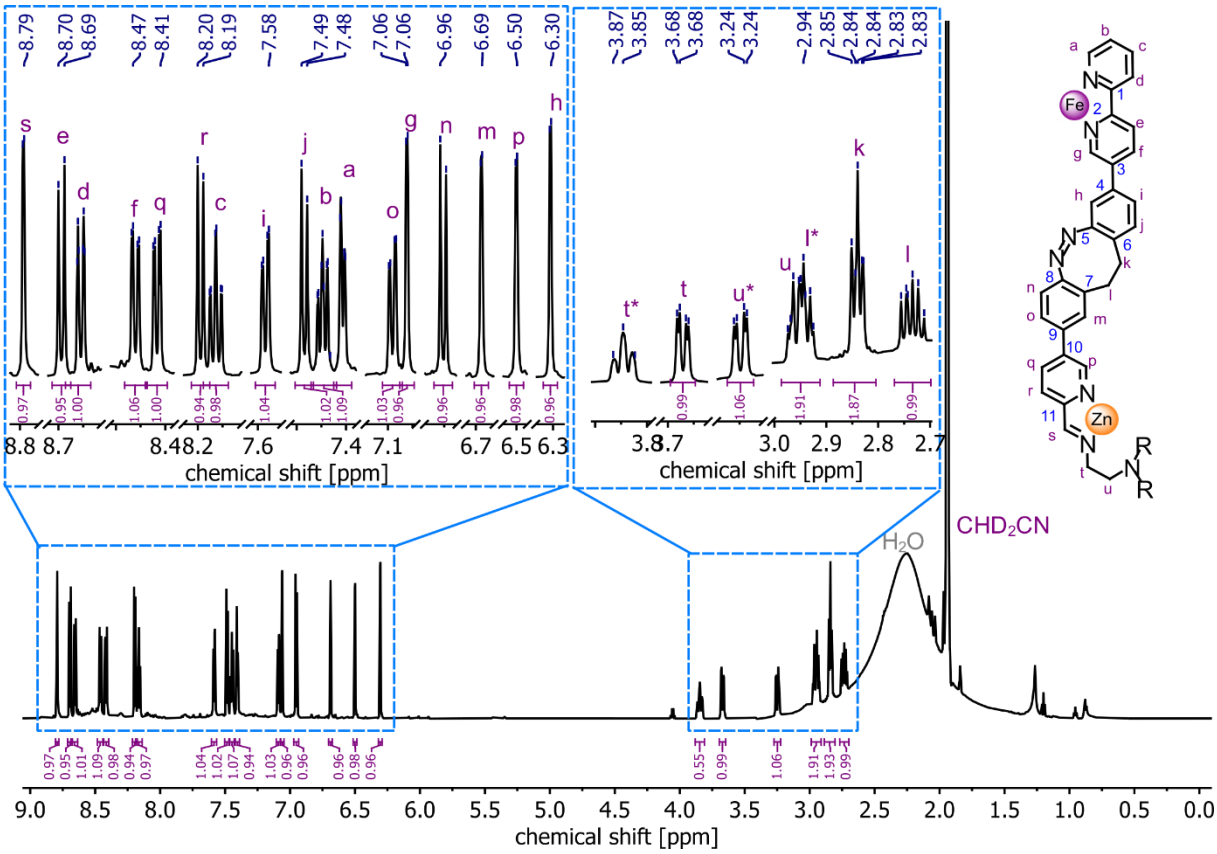

Figure S33. ^{1}H NMR spectrum (700 MHz, CD_3CN, 298 K) of ZnFe**L**.

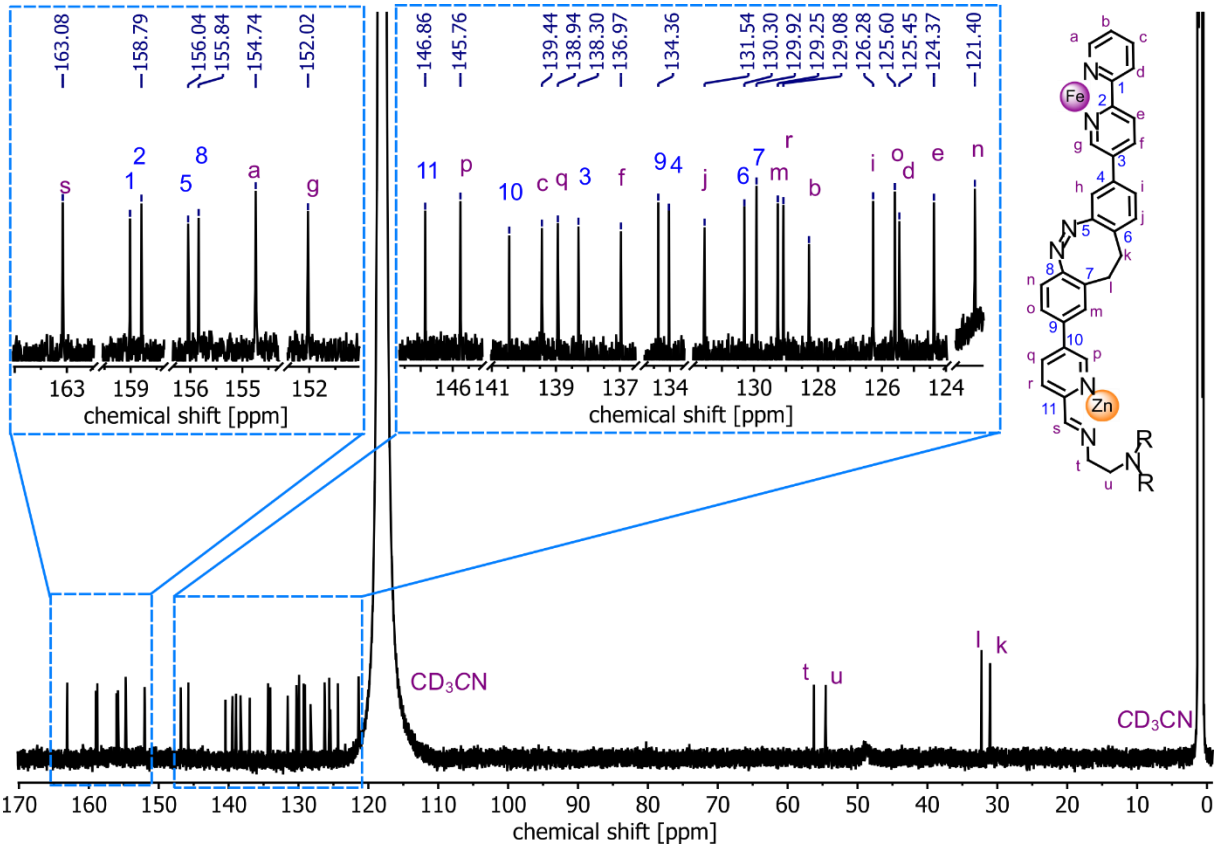

Figure S34. ^{13}C NMR spectrum (176 MHz, CD_3CN, 298 K) of ZnFe**L**.

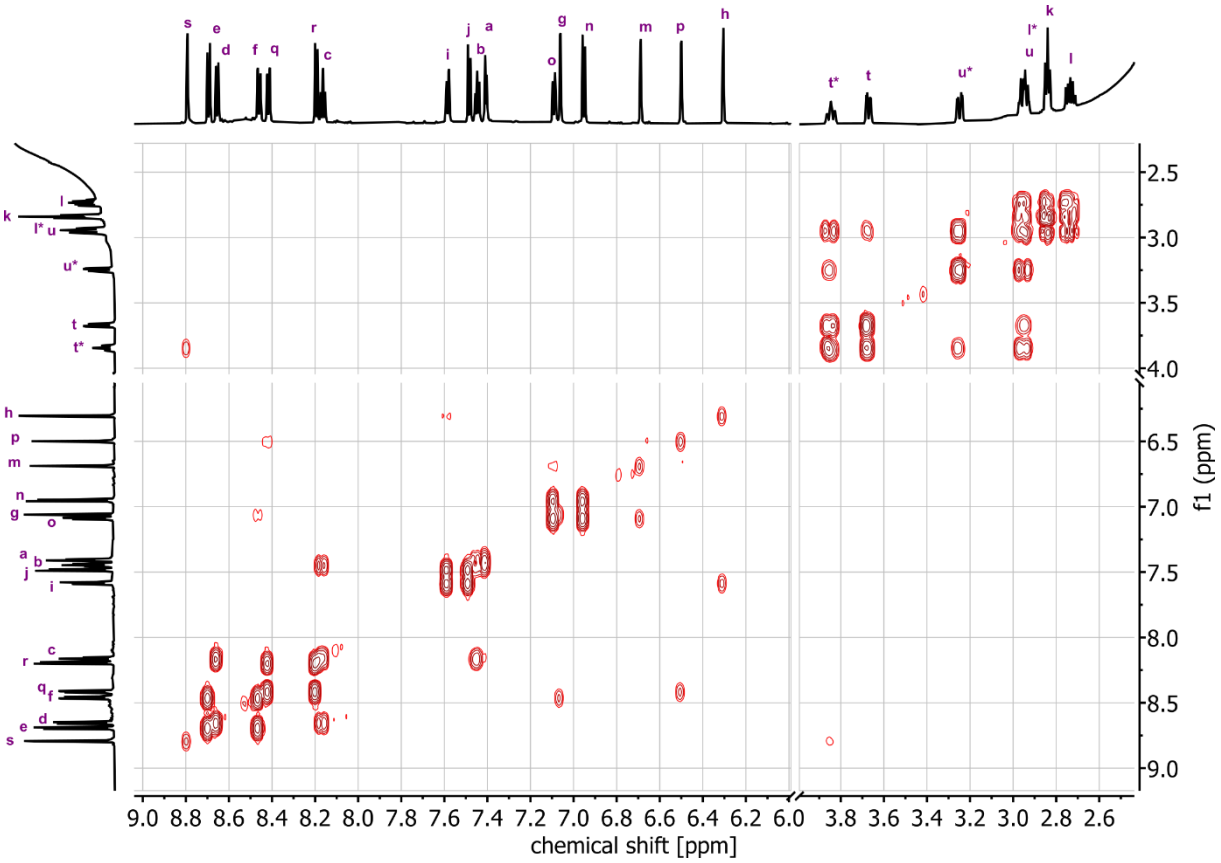

Figure S35. ^{1}H,^{1}H COSY spectrum (700 MHz, CD_3CN, 298 K) of ZnFe**L**.

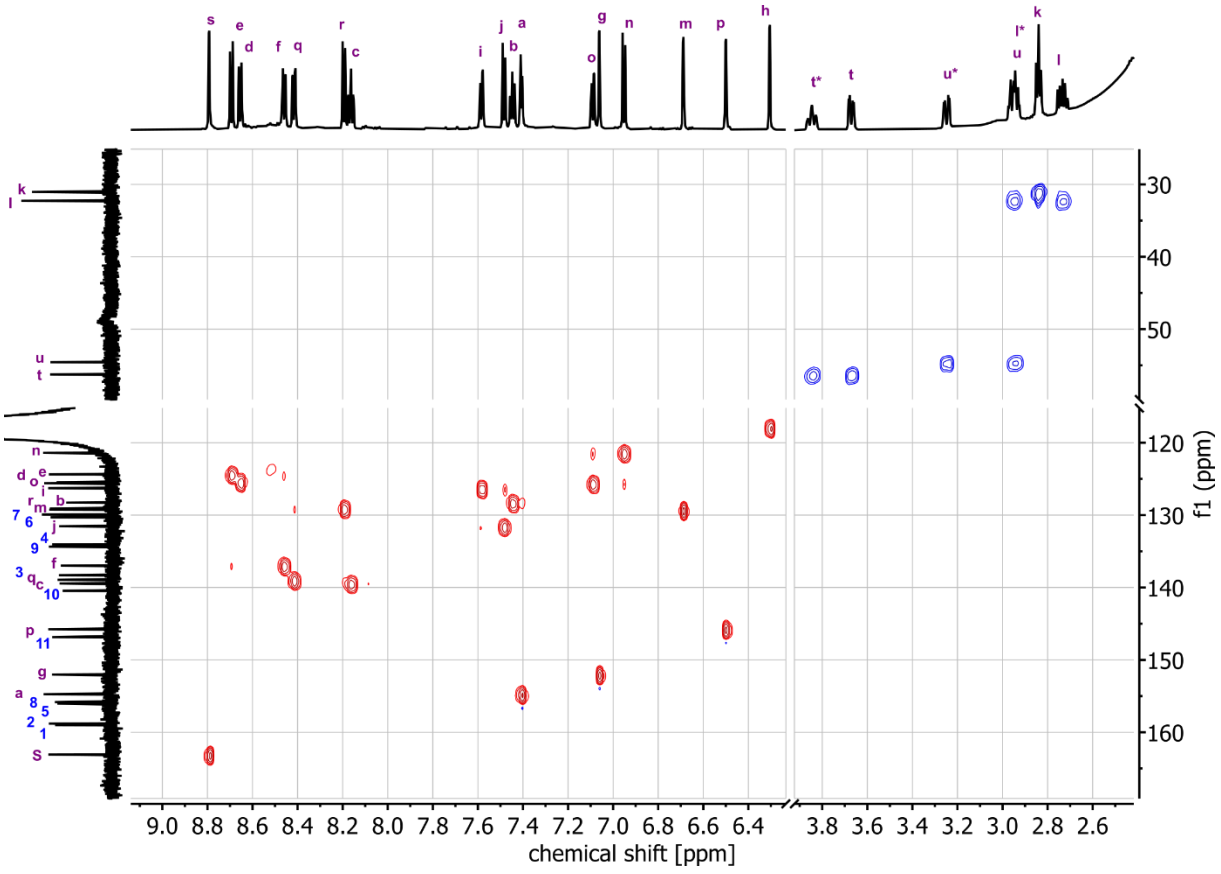

Figure S36. ^{1}H,^{13}C HSQC spectrum (700/176 MHz, CD_3CN, 298 K) of ZnFe**L**.

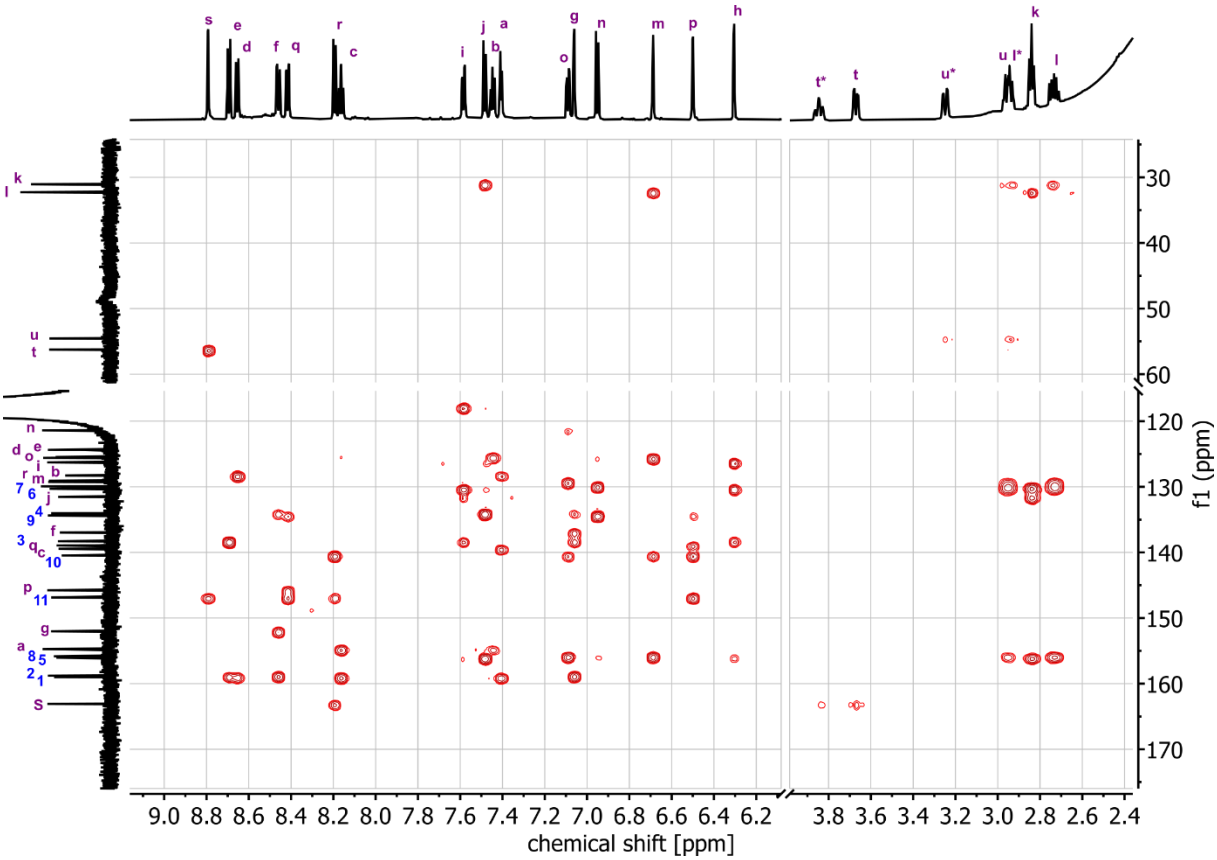

Figure S37. $^{1}H,^{13}C$ HMBC spectrum (700/176 MHz, CD_3CN, 298 K) of ZnFe**L**.

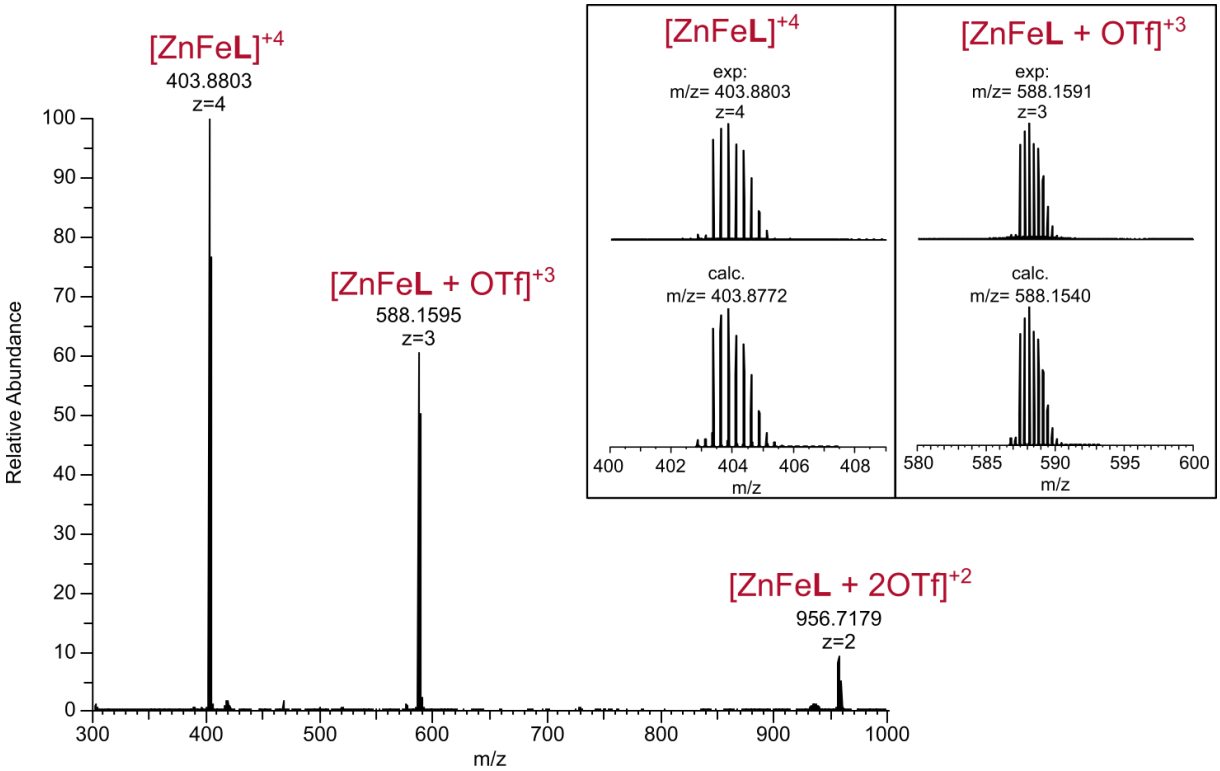

Figure S38. ESI^{+} mass spectrum (CH_3CN) of FeZn**L**.

S4 Heterobimetallic self-sorting

S4.1 Experimental procedures

The self-sorting experiments were carried out as described in the general procedure from Section S3.2 with the samples being investigated by ^{1}H NMR, ESI$^+$ MS, and UV-vis without any further workup.

S4.1.1 ZnFe**L**

ZnFe**L** was synthesized according to the general procedure (Section S3.2) using $Zn(OTf)_2$ (0.39 mg, 1.07 µmol, 1.00 equiv.), $Fe(OTf)_2$ (0.38 mg, 1.07 µmol, 1.00 equiv.), aldehyde **1** (1.50 mg, 3.21 µmol, 3.00 equiv.), and TREN (0.16 mg, 1.07 µmol, 1.00 equiv.) with a reaction time of 1 day at a temperature of 70 °C. This experiment yields exclusively the desired ZnFe**L** helicate, as evidenced by ESI MS and ^{1}H NMR (Main text, Figure 2, bottom).

After precipitation the product was obtained as a dark red powder in 89% yield (2.54 mg, 0.95 µmol).

Analytical data of ZnFe**L** obtained via one-pot self-sorting is the same as for ZnFe**L** obtained from Zn_2**L** via Zn→Fe metal exchange (see Section S3.8).

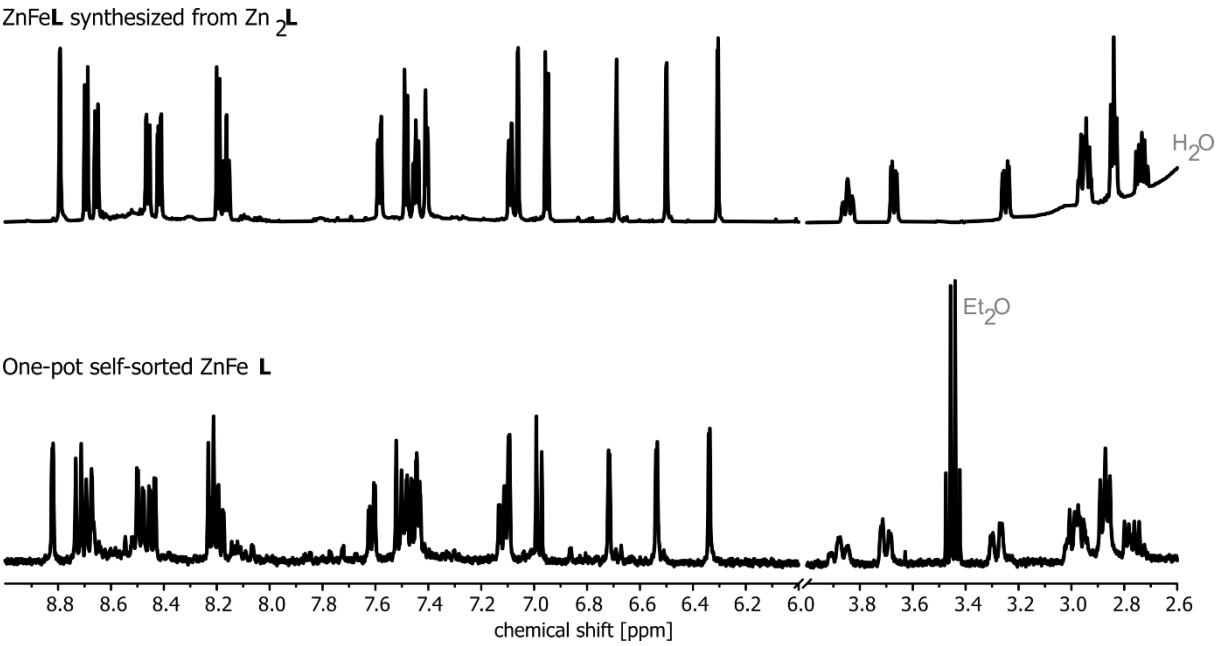

Figure S39. ^{1}H NMR spectra (CD_3CN, 298 K) of ZnFe**L** synthesized from Zn_2**L** via metal exchange (top, 700 MHz) and by one-pot self-sorting (bottom, 400 MHz).

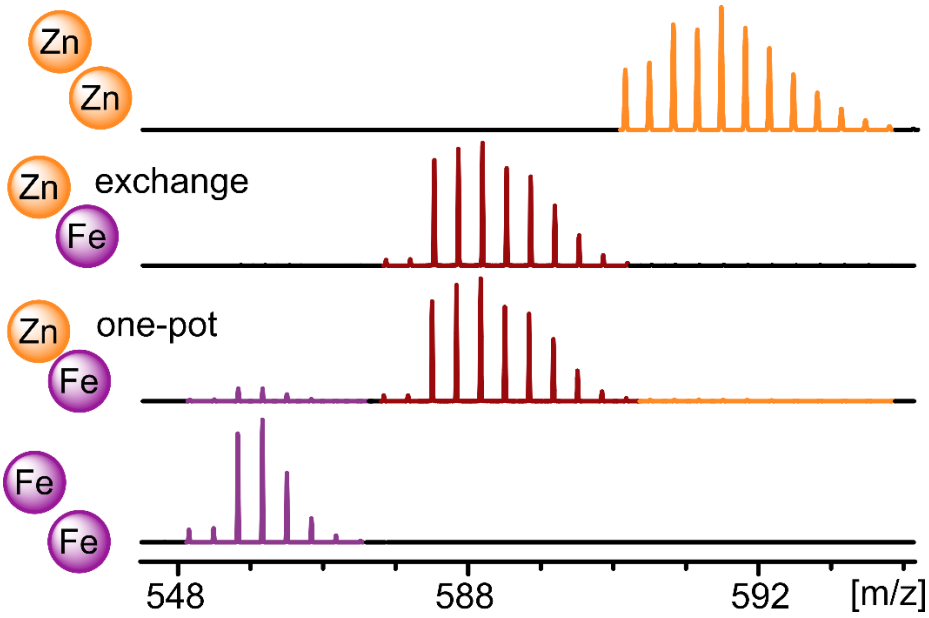

Figure S 40. ESI$^+$ mass spectra (CH_3CN) of Zn_2**L**, Fe_2**L**, and FeZn**L** synthesized via metal exchange and by one-pot self-sorting.

S4.1.2 ZnCo**L**

ZnCo**L** was synthesized according to the general procedure (Section S3.2) using $Zn(OTf)_2$ (0.67 mg, 1.85 µmol, 1.00 equiv.), $Co(OTf)_2$ (0.66 mg, 1.85 µmol, 1.00 equiv.), aldehyde **1** (2.60 mg, 5.56 µmol, 3.00 equiv.), and TREN (0.27 mg, 1.85 µmol, 1.00 equiv.) with a reaction time of 1 day at a temperature of 70 °C.

This experiment yields exclusively the desired ZnCo**L** helicate, as evidenced by ESI MS and the absence of the characteristic broadened ^{1}H NMR signals typically observed for Co^{TREN} are absent (Section S4.4).

$[C_{96}H_{75}N_{19}CoZn](CF_3O_3S)_4$

^{1}H NMR (500 MHz, CD_3CN) δ [ppm] = 14.26 (H-c/f), 15.11 (H-c/f), 45.03 (H-b), 83.01 (H-d/e), 83.75 (H-d/e), 86.59 (H-a/g), 91.58 (H-a/g).

Due to the strong paramagnetism of the compound not all assignments could be made and not all signals could be observed.

HRMS (ESI$^+$ Orbitrap): m/z (relative intensity) = 404.6277 (100%, $[ZnCo\mathbf{L}]^{+4}$, calcd. 404.6267), 589.1548 (15%, $[ZnCo\mathbf{L} + OTf]^{+3}$, calcd. 589.3150).

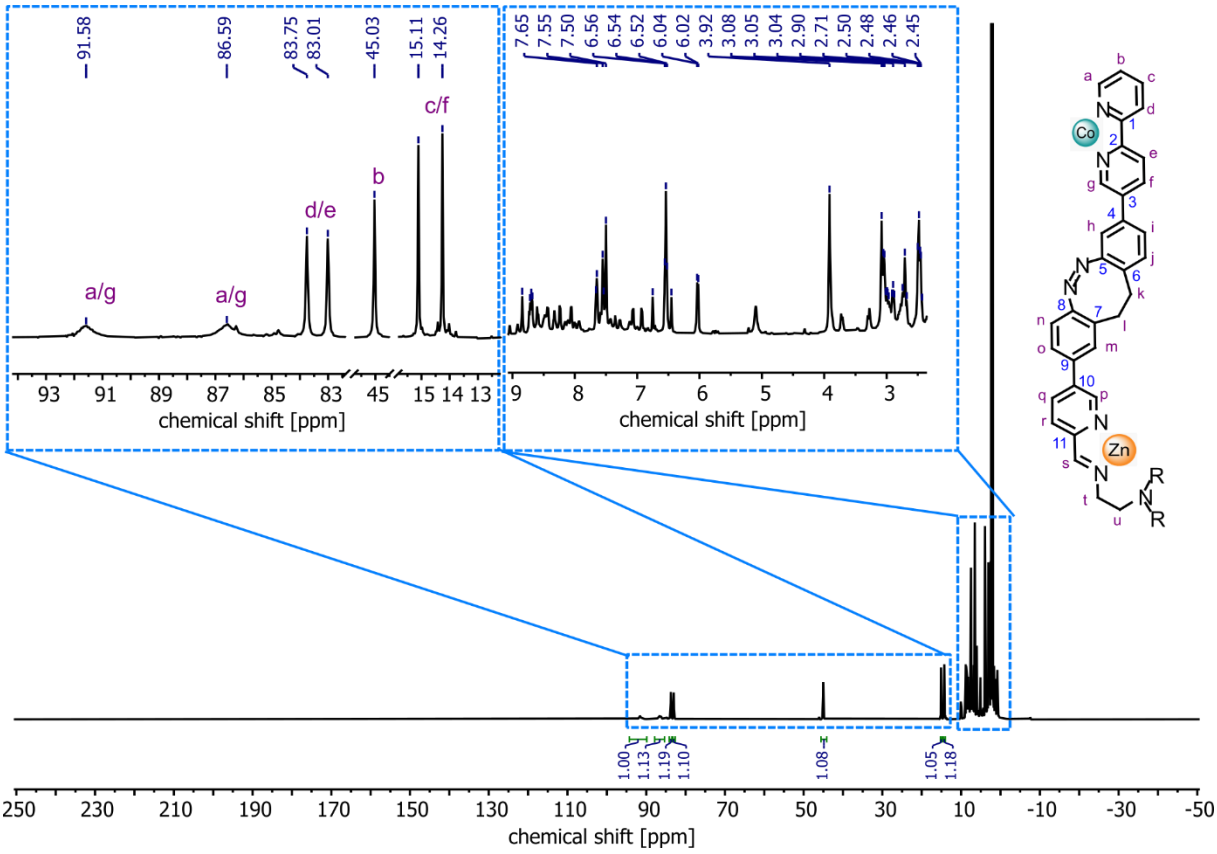

Figure S41. ^{1}H NMR spectrum (500 MHz, CD_3CN, 298 K) of ZnCo**L**.

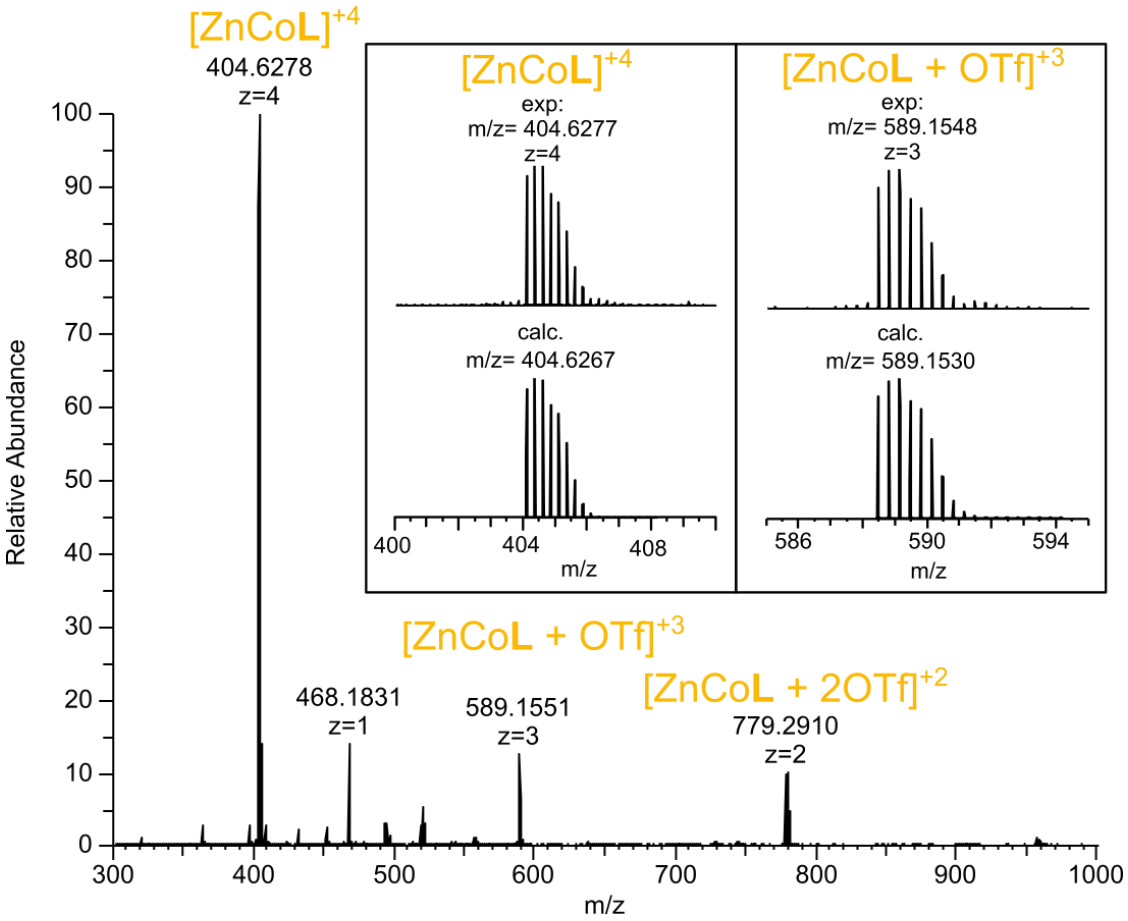

Figure S42. ESI^{+} mass spectrum (CH_3CN) of ZnCo**L**.

S4.1.3 CoFe**L**

CoFe**L** was synthesized according to the general procedure (Section S3.2) using $Co(OTf)_2$ (0.31 mg, 0.86 µmol, 1.00 equiv.), $Fe(OTf)_2$ (0.31 mg, 0.86 µmol, 1.00 equiv.), aldehyde **1** (1.22 mg, 2.60 µmol, 3.00 equiv.), and TREN (0.13 mg, 0.86 µmol, 1.00 equiv.) with a reaction time of 1 day at a temperature of 70 °C.

The product mixture contained minor amounts of Fe_2**L**, Co_2**L**, and FeCo**L**. For details see Section S4.3and Section S4.4.

$[C_{96}H_{75}N_{19}FeCo](CF_3O_3S)_4$

^{1}H NMR (500 MHz, CD_3CN) δ [ppm] = 10.14 (H-m), 48.75 (H-q), 113.74 (H-r), 171.75 (H-s), 183.48 (H-p).

Due to the strong paramagnetism of the compound not all assignments could be made and not all signals could be observed.

HRMS (ESI$^+$ Orbitrap): m/z (relative intensity) = 402.3817 (100%, $[CoFe\mathbf{L}]^{+4}$, calcd. 402.3786), 586.1603 (35%, $[CoFe\mathbf{L} + OTf]^{+3}$, calcd. 586.1558).

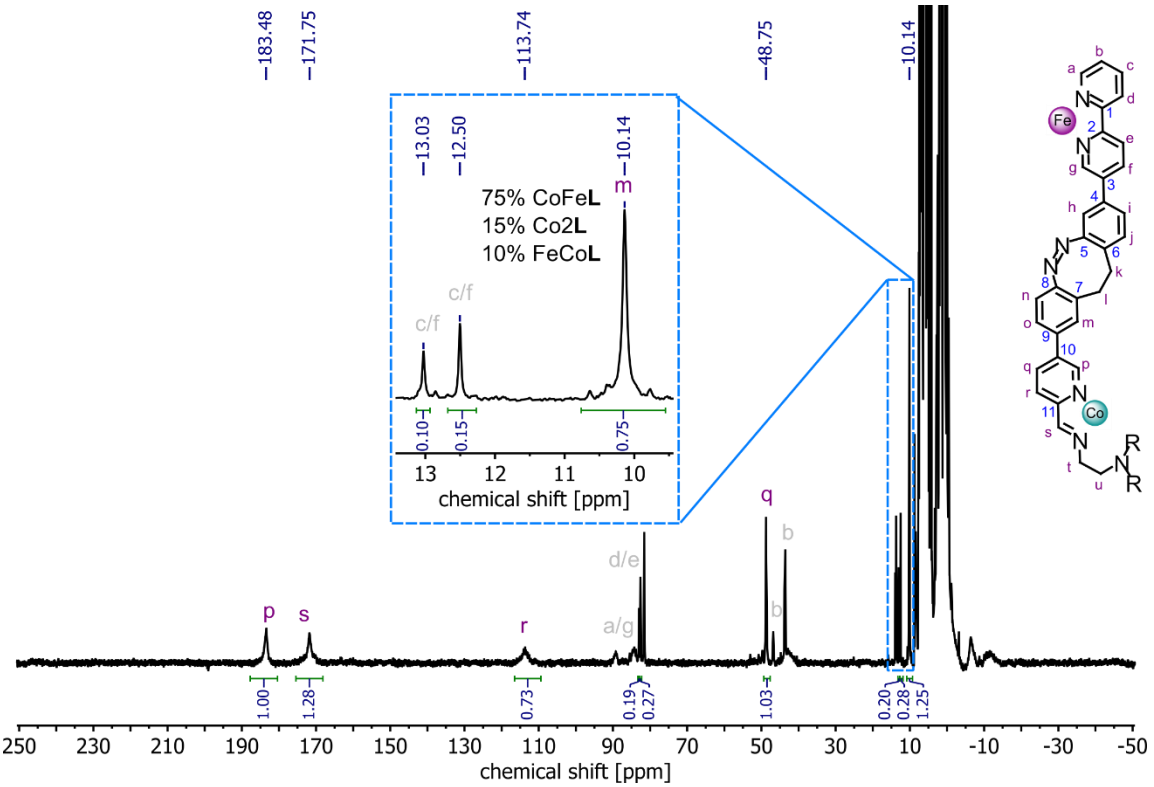

Figure S43. ^{1}H NMR spectrum (500 MHz, CD_3CN, 298 K) of CoFe**L**.

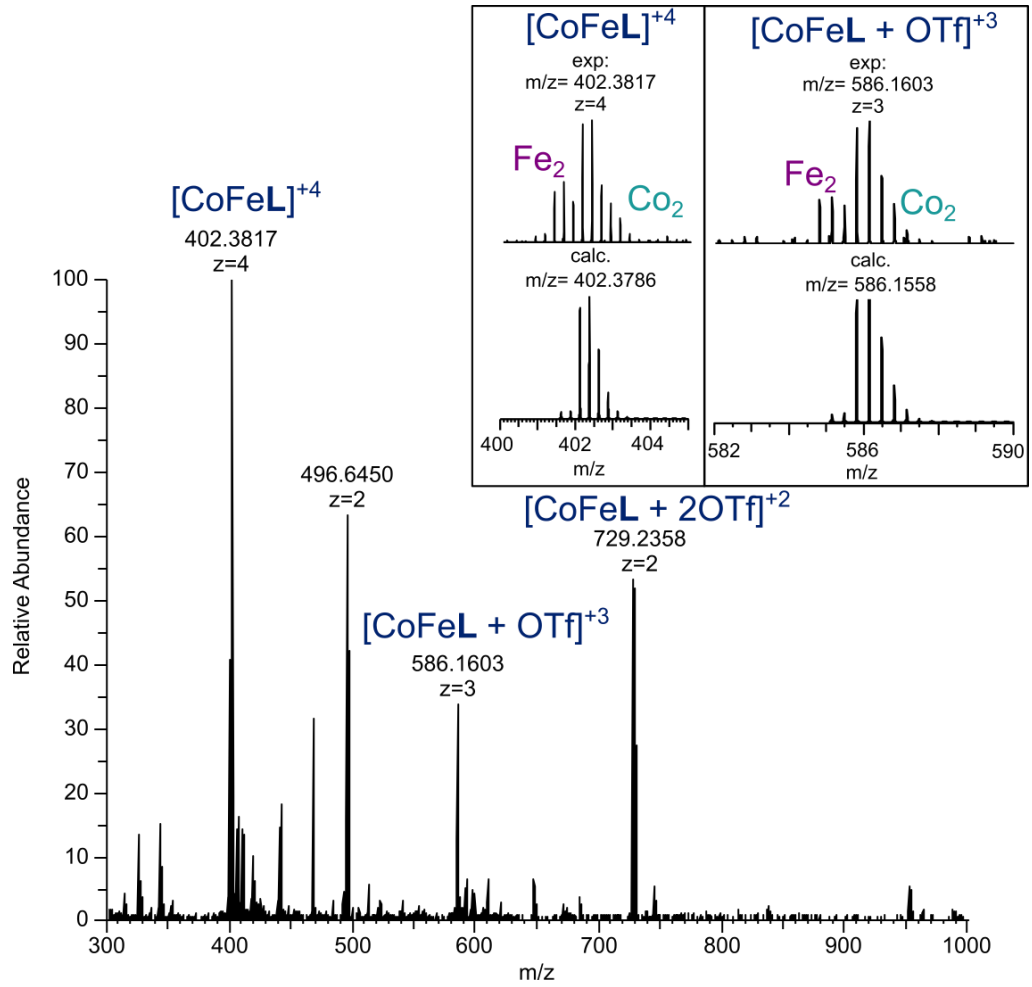

Figure S44. ESI^{+} mass spectrum (CH_3CN) of CoFe**L**.

S4.2 Overview of one-pot self-sorting results

Table S3. Overview of the results of one-pot self-sorting experiments showing that the kinetically more labile metal ends up in the M^{TREN} binding site with the M^{bipy} binding site occupied by the metal forming stronger N−M ligand bonds.

	Zn(II) + Fe(II)	**Zn(II) + Co(II)**	**Co(II) + Fe(II)**
			(major product)
M^{TREN}	Zn(II)	Zn(II)	Co(II)
	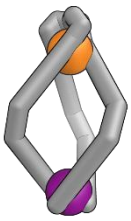	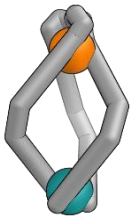	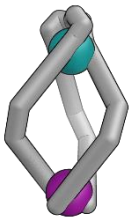
M^{bipy}	Fe(II)	Co(II)	Fe(II)
			(major product)

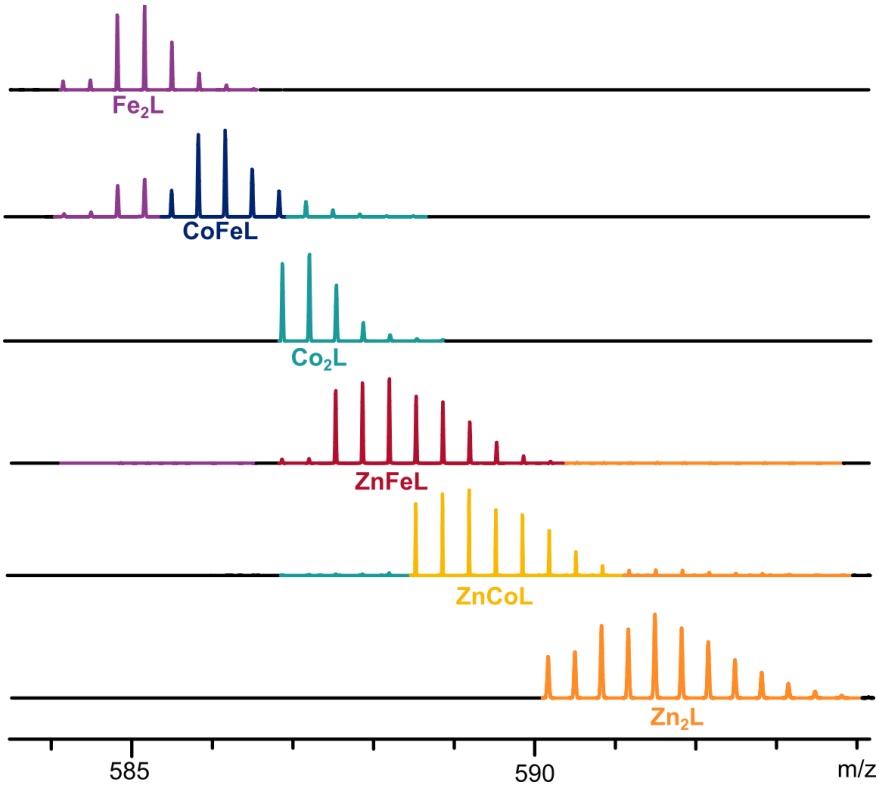

Figure S45. ESI⁺ MS spectra (298 K, CH_3CN) of Fe_2**L**, CoFe**L**, Co_2**L**, ZnFe**L**, ZnCo**L**, and Zn_2**L**. The main product of the Co(II)/Fe(II) self-sorting experiment is the heterometallic CoFe**L** complex with the homometallic Co_2**L** and Fe_2**L** complexes being formed as minor side products. The Zn(II)/Co(II) and Zn(II)/Fe(II)self-sorting experiments selectively produced only the heterometallic ZnCo**L**/ZnFe**L** complexes.

S4.3 CoFe**L** – UV-vis

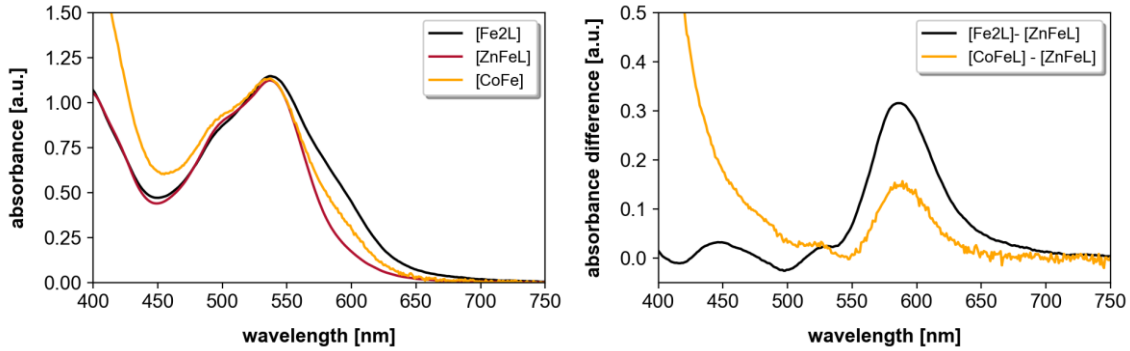

Figure S46. UV-vis spectra of Fe_2**L**, ZnFe**L** and CoFe**L** (CH_3CN, 0.06 mM) (*left*) and plot after subtracting the spectrum of ZnFe**L** from Fe_2**L** and CoFe**L** (*right*). Since Fe_2**L** contains Fe^{Bipy} and Fe^{TREN} in exactly the same amounts, the relative absorbances can be used as a benchmark for a 1:1 mixture of the two iron chromophores. Assuming the extinction coefficients of the Fe chromophores in the mixed complexes are similar to those in Fe_2**L**, it can be estimated that in the CoFe**L** mixture three quarters of all Fe(II) ions are in the bipy coordination site (Fe^{bipy}) with the remainder in the TREN coordination site (Fe^{TREN}), as the shoulder at 590 nm is about 1/3 as intense in CoFe**L** than it is counterpart in Fe_2**L**. This is just a rough estimate, indicating that CoFe**L** is the major product.

S4.4 ZnCo**L** and CoFe**L** – ^{1}H NMR

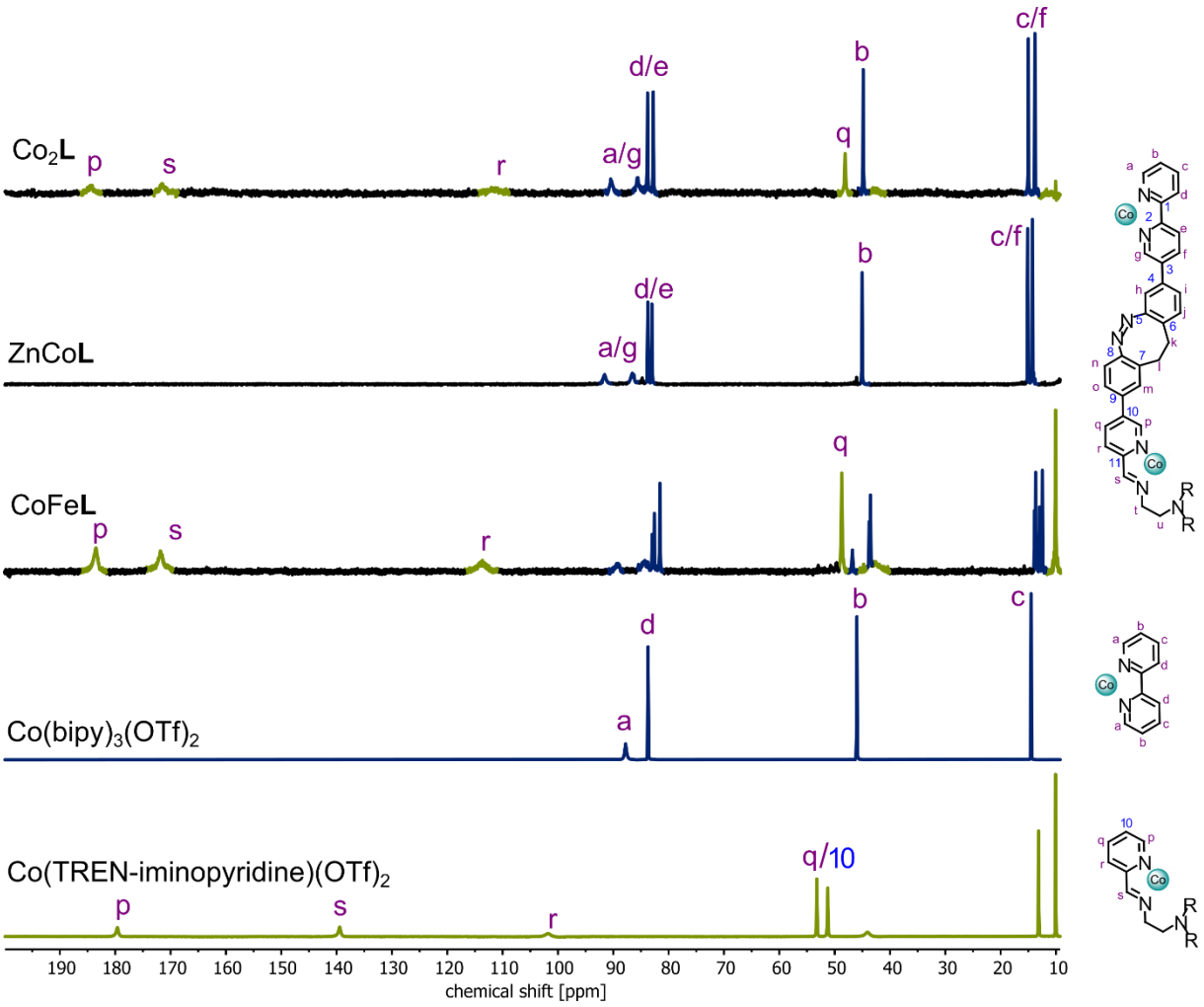

Figure S47. Wide-sweep ^{1}H NMR spectra (400 MHz, CD_3CN, 298 K) of Co2**L**, ZnCo**L**, CoFe**L**, Co(bipy)$_3$, and Co^{TREN} (top to bottom). Signals referring to Co(II) ions in a bipy coordination environment (Co^{bipy}) are highlighted in blue, Co(II) ions in a TREN-pyridylimine corrdination evironment are highlighted in green (Co^{TREN}). For ZnCo**L**, no signals for Co^{TREN} can be observed, indicating successful self-sorting into $Zn^{TREN}Co^{bipy}$**L**. For CoFe**L**, the signal at δ = 48 ppm belonging to H-q in Co^{TREN} is much more intense than the neighbouring signal at δ = 45 ppm belonging to H-b Co^{bipy}. When comparing the relative intensities to the spectrum of Co_2**L**, this indicates Co^{TREN} having been formed preferentially over Co^{bipy} with an estimated ratio of around 3:1. This is in good agreement from the estimates made from the UV-vis data (Figure S46).

S5 UV-vis kinetics of the complexation reactions

The kinetics of complex formation were investigated using UV-vis spectroscopy, as the Fe(II) MLCT bands are readily observable. Initially, a stock solution of the ligand in acetonitrile was prepared at a concentration of either 0.4 or 0.2 mg/mL and added to a 1 mL screw-capped cuvette and positioned in the spectrometer at 25 °C.

Subsequently, a stock solution of TREN in methanol was added, using 3.5 or 7 µL of the solution. Following this, a stock solution of the metal salt(s) in acetonitrile was added to the mixture. The cuvette was then securely capped and thoroughly shaken to ensure complete homogenization of the solution before being returned to the spectrometer.

The sample was initially maintained at a constant temperature of 25 °C for 20 minutes. Subsequently, the temperature was raised to 65 °C to simulate the conditions used during helicate synthesis. Throughout the experiment, the progression of the reaction was monitored by measuring absorbance spectra at regular intervals. The data presented displays one spectrum captured every 30 minutes over a total duration of 5 hours.

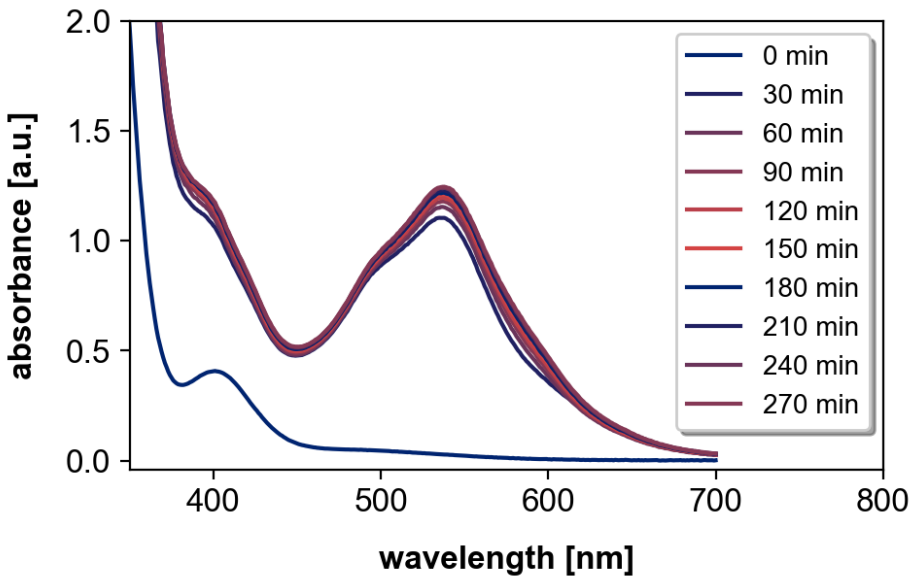

Figure S48. Fe_2**L** formation (0.4 mg/mL aldehyde **1**, 1.0 equiv. TREN, 2.0 equiv. $Fe(OTf)_2$) as followed by UV-vis at 25 °C to 65 °C with one scan every 30 minutes. Very fast formation of a band at 540 nm corresponding to Fe^{bipy} and slow formation of a second band at 590 nm, corresponding to Fe^{TREN}, were observed.

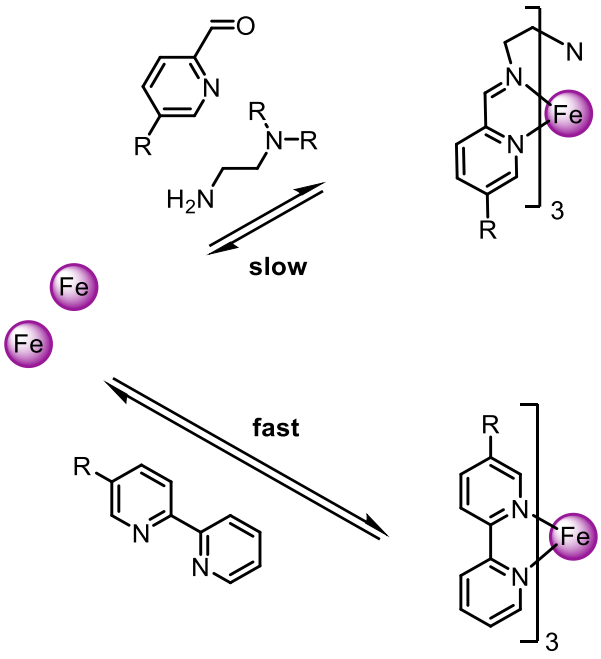

Figure S49. Mechanistic representation of the formation of Fe_2**L** based on the UV-vis experiment (Figure S48). The formation of Fe^{bipy} is rapid and therefore complete within the first 30 minutes, whereas Fe^{TREN} forms much slower over the course of multiple hours.

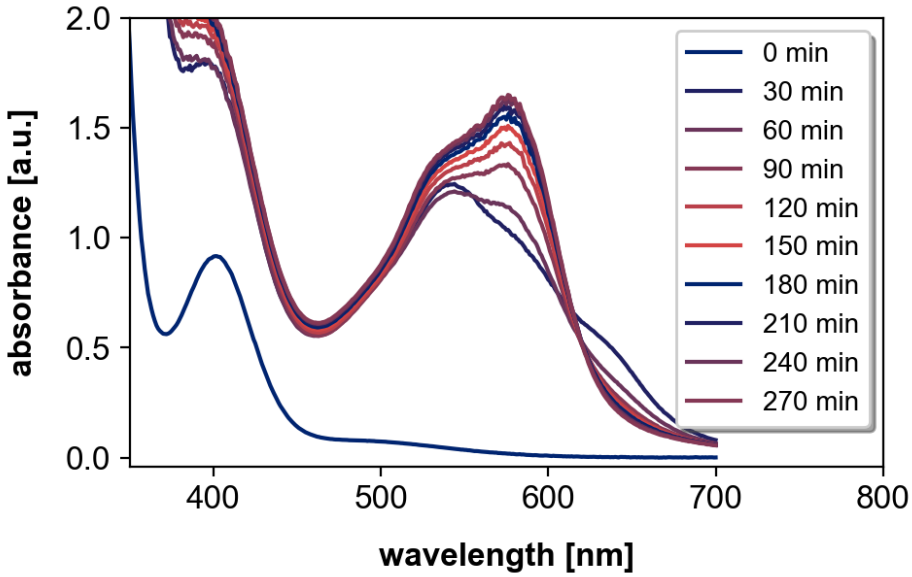

Figure S50. Fe**L** formation (0.2 mg/mL aldehyde **1**, 1.0 equiv. TREN, 1.0 equiv. $Fe(OTf)_2$) as followed by UV-vis at 25 °C to 65 °C with one scan every 30 minutes. Slow formation of a band at 590 nm (Fe^{TREN}), with transient absorbance bands visible at 540 nm (Fe^{bipy}) and 620 nm being observed.

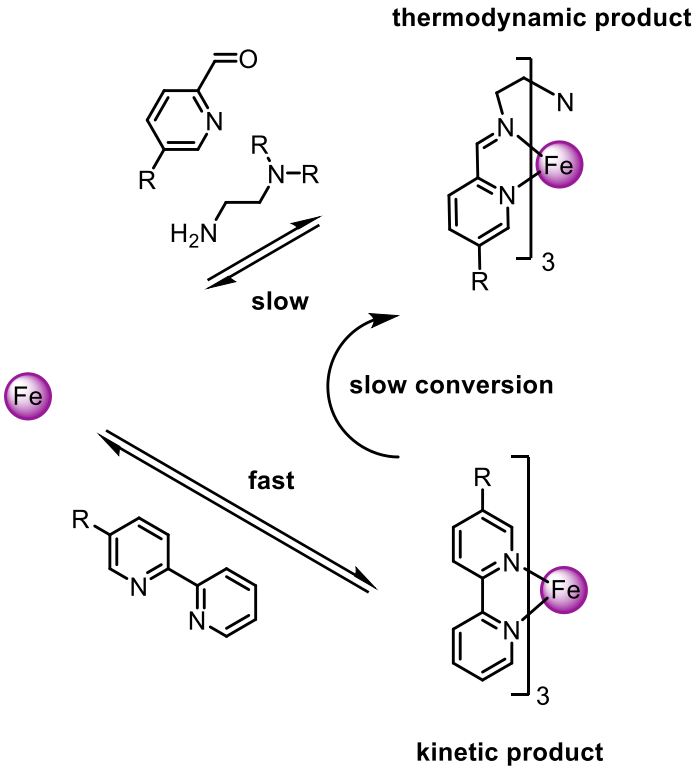

Figure S51. Mechanistic representation of the formation of Fe**L** based on the UV-vis experiment (Figure S50). The formation of Fe^{bipy} is fast, but over time the iminopyridine binding site is formed and the iron atom migrates to the Fe^{TREN} site, indicating that Fe^{Bipy} is a kinetic product, but Fe^{TREN} is the thermodynamic product.

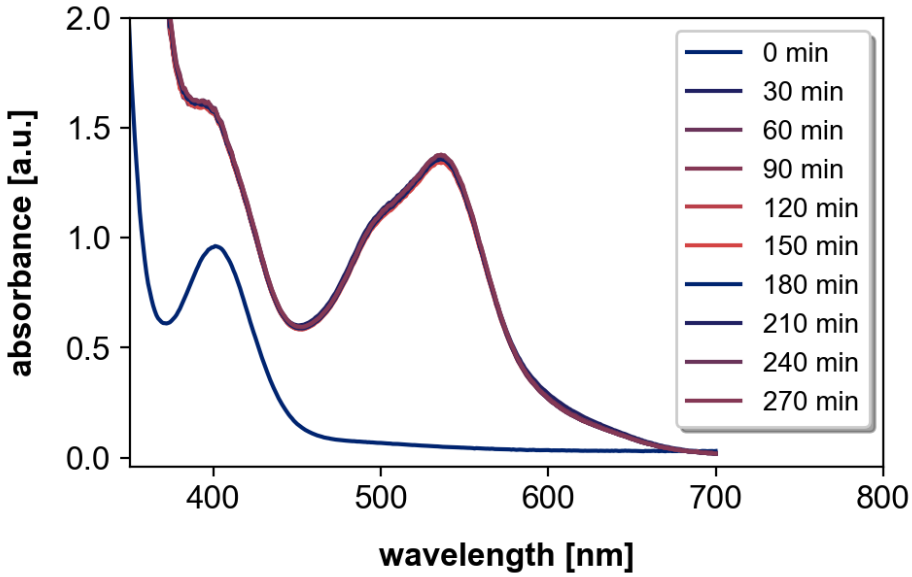

Figure S52. ZnFe**L** formation (0.4 mg/mL aldehyde **1**, 1.0 equiv. TREN, 1.0 equiv. $Fe(OTf)_2$, 1.0 equiv. $Zn(OTf)_2$) as followed by UV-vis at 25 °C to 65 °C with one scan every 30 minutes. Very fast formation of a band at 540 nm corresponding to Fe^{bipy} and no absorbance band at 590 nm (Fe^{TREN}) were observed.

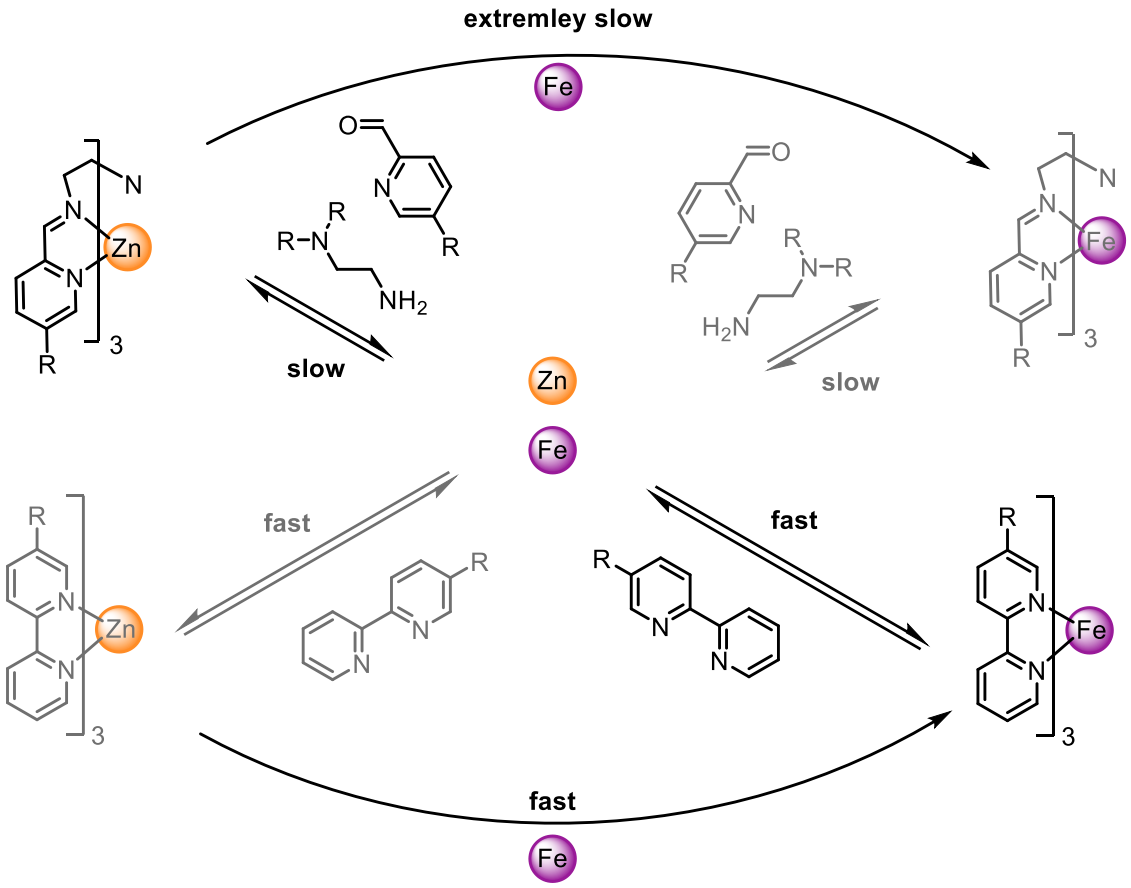

Figure S53. Mechanistic representation of the formation of ZnFe**L** based on the UV-vis experiment (Figure S52) The formation of the bipyridine binding site is fast. The stronger binding affinity of Fe(II) over Zn(II) results in the exclusive formation of Fe^{bipy} over Zn^{bipy}, leaving the uncoordinated and therefore more lewis acidic Zn(II) ions to template and catalyse the formation of the iminopyridine binding site, forming Zn^{TREN}. Replacing the Zn(II) ions in the Zn^{TREN} site with Fe(II) ions to form Fe^{TREN} is a thermodynamically downhill, but extremely slow process (5% over two months, see Section S9.4 for details).

S6 Structural characterization of the complexes

S6.1 A note on the helicate nomenclature used

The helicates are composed of five chiral building blocks: three ligand arms (Figure S54) and two octahedral metal coordination sites, resulting in a multitude of possible stereoisomers.

This multitude of potential stereoisomers raises the question of finding a clear, straightforward way to name all these stereoisomers. Since the aim of this work is not to establish the perfect nomenclature that encompasses all aspects of chirality but rather to visualise and explain the observed stereoisomers in an accessible manner for the reader, we have defined the following specific nomenclature for the helicates (Figure S55):

(i) The direction of view in the helicates is from the M^{TREN} to the M^{bipy} metal centre.
(ii) The helical chirality of the metal centres is defined as Δ and Λ for right- and left-handed helicity, respectively, when looking along this axis.
(iii) The directionality in the ligand-arm orientation is defined by the diazocine units, looking from the ethylene bridge to the azo bridge. The diazocine moieties can either point with their azo nitrogens clockwise or anticlockwise when looking along the M^{TREN}–M^{bipy} axis, which is denoted as P and M, respectively.

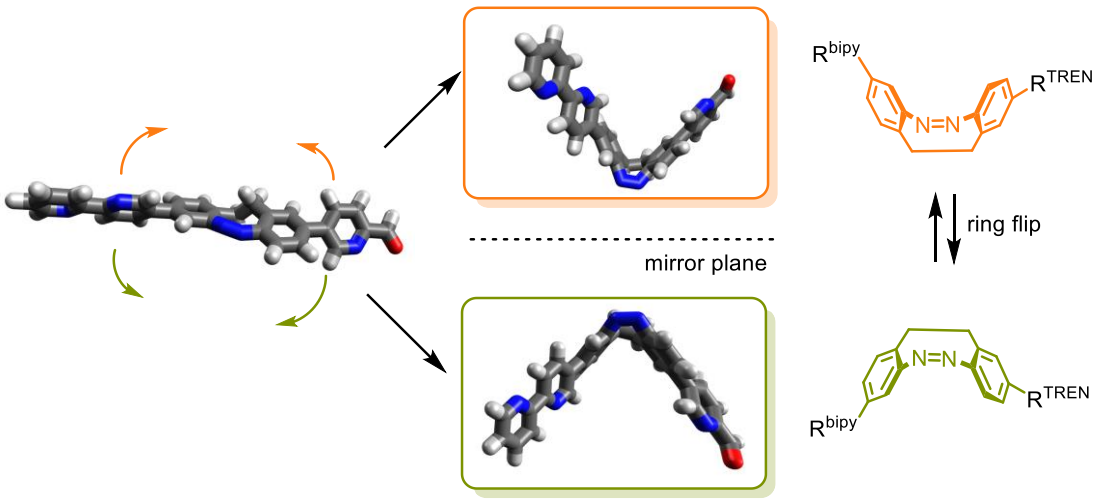

Figure S54. Chirality in the *Z* ground state of aldehyde **1**.

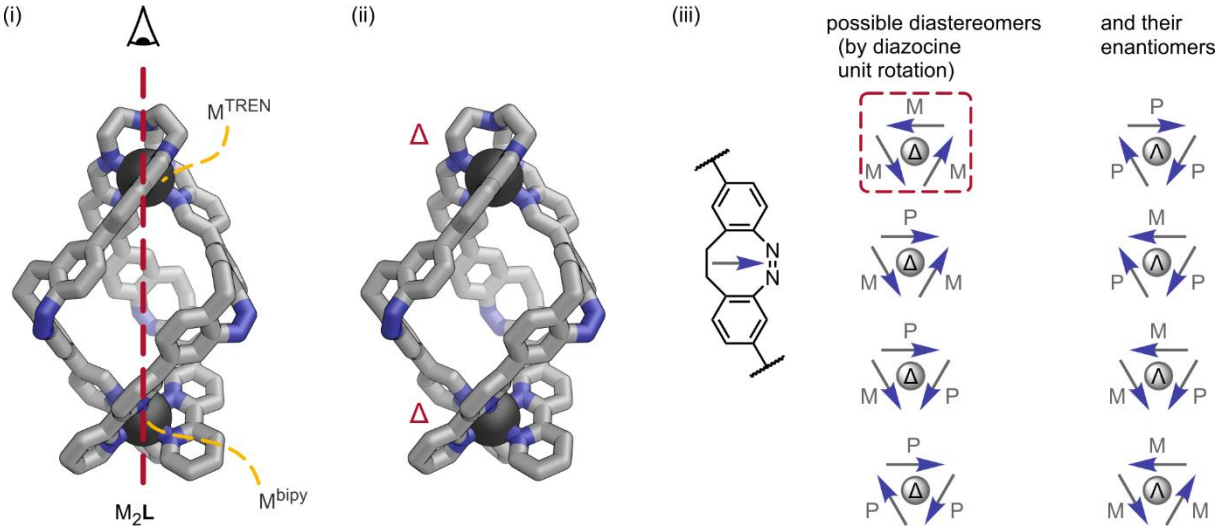

Figure S55. How to derive the nomenclature used in this work, following three steps: (i) The direction of view in the helicates is from the MTREN to the Mbipy metal centre. (ii) The helical chirality of the metal centres is defined as Δ and Λ for right- and left-handed helicity, respectively, when looking along this axis. (iii) The directionality in the ligand-arm orientation is defined by the diazocine units, looking from the ethylene bridge to the azo bridge. The diazocine moieties can either point with their azo nitrogens clockwise or anticlockwise when looking along the MTREN−Mbipy axis, which is denoted as P and M, respectively. Right: Possible diastereomers derived from different diazocine unit orientations within the helicates and their enantiomers. Cartoon representing the structure on the left is highlighted in red.

With two chiral metal centres and three chiral ligand arms, eight diastereomers (plus eight enantiomers) are possible:

(i) The two metal centres can be homochiral, resulting in a helicate structure, or heterochiral, resulting in a pseudo-mesocate.

(ii) The three ligand arms could exist with four different diazocine orientations: (MMM), (PMM), (PPM), and (PPP; Figure S55, right).

Thus, both the helicate and the pseudo-mesocate can have four distinct ligand-arm orientations, leading to eight possible diastereomers. Each of these exists as a racemic mixture of two enantiomers.

S6.2 X-ray crystallography

Suitable single crystals of Fe_2**L** and ZnFe**L** were grown by vapour diffusion. An acetonitrile solution of the respective helicate (approx. 2 mM, 0.3 mL) was filtered and added to a 2.0 mL GC vial. The GC vial was left open and placed in a 10 mL glass vial containing approx. 2 mL of 1,2-dimethoxyethane as the anti-solvent. The outer vial was closed with a snap lid and stored in a dark fridge at approx. 6 °C for five weeks.

The data collections were performed on a STOE Stadivari Eulerian 4-circle diffractometer using Cu-K_α radiation (λ = 1.54186 Å). The diffractometer was equipped with a low–temperature device (Cryostream 800er series, Oxford Cryosystems, 100(1) K). Intensities were measured by fine-slicing ω-scans and corrected for background, polarization and Lorentz effects. An absorption correction by scaling of reflection intensities with a subsequent spherical absorption correction was performed with STOE LANA programme.[5]

The structures were solved by intrinsic phasing methods[6] and refined anisotropically by the least-squares procedure implemented in the SHELX programme system.[7]

The hydrogen atoms were included isotropically using a riding model on the bound carbon atoms.

Some of the disordered triflate anions as well as some of the heavily disordered co-crystallised solvent molecules had to be modelled by using PLATON's squeeze methodology in order to account for their contributions to the calculated structure factors.[8]

Even if the final R-values of the structural model are not of outstanding quality, we consider the refined structural models of both samples to be valid and worth publishing. Due to the very high number of atoms in the asymmetric unit (high F(000) value) combined with small crystal size and poor scattering properties, ωR_2 values of about 40-45% are in our opinion not in the good, but still in the acceptable range.

CCDC numbers 2442413 (**Fe_2L**) and 2442414 (**ZnFeL**) contain the supplementary crystallographic data for this paper, which can be obtained free of charge from the Cambridge Crystallographic Data Centre via http://www.ccdc.cam.ac.uk/data_request/cif.

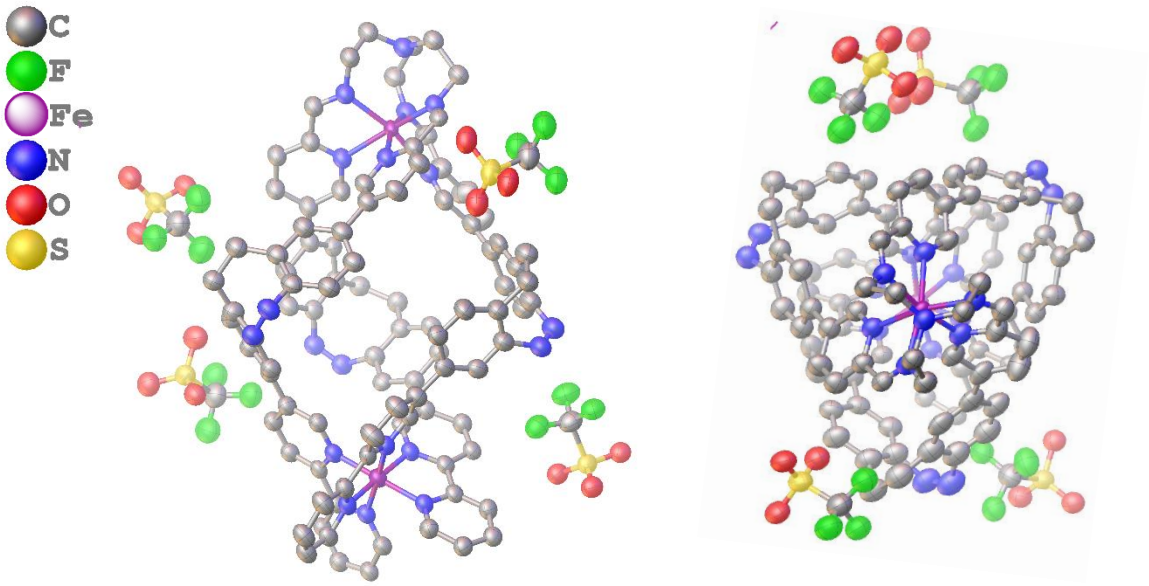

Figure S56. Asymmetric unit of helicate Fe_2**L** as observed in the crystal structure, plotted from two different viewing angles. Hydrogen atoms omitted for clarity. Displacement ellipsoids are drawn at 50% probability.

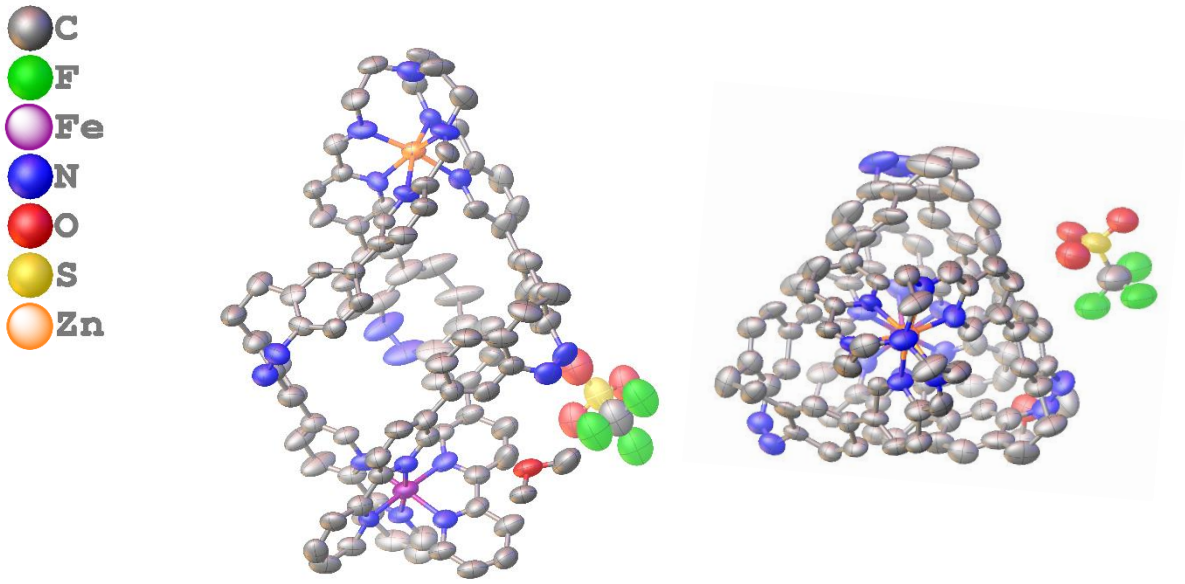

Figure S57. Asymmetric unit of helicate ZnFe**L** as observed in the crystal structure, plotted from two different viewing angles. Hydrogen atoms omitted for clarity. Displacement ellipsoids are drawn at 50% probability.

Table S4. Crystal data and refinement parameters for helicate Fe_2**L**.

Crystal Habitus	clear red plate
Device Type	STOE STADIVARI
Empirical formula	$C_{100}H_{75}F_{12}Fe_2N_{19}O_{12}S_4$
Moiety formula	$C_{96}H_{75}Fe_2N_{19}$, $4(CF_3O_3S)$
Formula weight	2202.73
Temperature/K	100
Crystal system	triclinic
Space group	P-1
a/Å	13.868(6)
b/Å	13.993(8)
c/Å	27.609(12)
α/°	84.79(4)
β/°	88.59(4)
γ/°	75.32(4)
Volume/Å^3	5162(4)
Z	2
ρ_{calc}g/cm^3	1.417
μ/mm^{-1}	3.791
F(000)	2256.0
Crystal size/mm^3	0.1 × 0.1 × 0.03
Absorption correction	multi-scan
T_{min}; T_{max}	0.3511; 0.8080
Radiation	Cu Kα (λ = 1.54186)
2Θ range for data collection/°	9.218 to 146.854°
Completeness to theta	0.993
Index ranges	-16 ≤ h ≤ 17, -17 ≤ k ≤ 16, -13 ≤ l ≤ 32
Reflections collected	98477
Independent reflections	19469 [R_{int} = 0.3935, R_{sigma} = 0.2458]
Data/restraints/parameters	19469/1319/1342
Goodness-of-fit on F^2	1.019
Final R indexes [I>=2σ (I)]	R_1 = 0.1411, wR_2 = 0.3055
Final R indexes [all data]	R_1 = 0.3092, wR_2 = 0.4099
Largest diff. peak/hole / e Å^{-3}	1.11/-0.56
Crystal Habitus	clear red plate
Device Type	STOE STADIVARI
Empirical formula	$C_{100}H_{75}F_{12}Fe_2N_{19}O_{12}S_4$
Moiety formula	$C_{96}H_{75}Fe_2N_{19}$, $4(CF_3O_3S)$

Table S5. Crystal data and refinement parameters for helicate ZnFe**L**.

Crystal Habitus	clear dark red block
Device Type	STOE STADIVARI
Empirical formula	$C_{102}H_{80}F_{12}FeN_{19}O_{13}S_4Zn$
Moiety formula	$C_{96}H_{75}FeN_{19}Zn$, CF_3O_3S, $0.5(C_4H_{10}O_2)$
Formula weight	1810.13
Temperature/K	100.15
Crystal system	triclinic
Space group	P-1
a/Å	13.2445(6)
b/Å	13.7646(8)
c/Å	29.9758(16)
α/°	87.839(5)
β/°	83.823(4)
γ/°	83.708(4)
Volume/Å^3	5398.4(5)
Z	2
ρ_{calc}g/cm^3	1.114
μ/mm^{-1}	2.008
F(000)	2314.0
Crystal size/mm^3	0.35 × 0.2 × 0.14
Absorption correction	multi-scan
T_{min}; T_{max}	0.2195; 0.8261
Radiation	Cu Kα (λ = 1.54186)
2Θ range for data collection/°	8.892 to 135.492°
Completeness to theta	0.990
Index ranges	-15 ≤ h ≤ 15, -7 ≤ k ≤ 16, -34 ≤ l ≤ 35
Reflections collected	100689
Independent reflections	19366 [R_{int} = 0.1942, R_{sigma} = 0.1081]
Data/restraints/parameters	19366/65/1154
Goodness-of-fit on F^2	1.403
Final R indexes [I>=2σ (I)]	R_1 = 0.1658, wR_2 = 0.4095
Final R indexes [all data]	R_1 = 0.2397, wR_2 = 0.4637
Largest diff. peak/hole / e Å^{-3}	1.36/-0.93
Crystal Habitus	clear dark red block
Device Type	STOE STADIVARI
Empirical formula	$C_{102}H_{80}F_{12}FeN_{19}O_{13}S_4Zn$
Moiety formula	$C_{96}H_{75}FeN_{19}Zn$, CF_3O_3S, $0.5(C_4H_{10}O_2)$

S6.3 Quantum chemical structure optimizations

S6.3.1 Structures of Zn_2**L** with unidirectional diazocine orientation within the ligand arms in the *Z* state

Input structures for four diastereomers with the two possible unidirectional diazocine orientations within the ligand arms (PPP and MMM, i.e. Zn^ΔZn^Δ**L**^{MMM}, Zn^ΔZn^Δ**L**^{PPP}, Zn^ΛZn^Δ**L**^{PPP}, Zn^ΛZn^Δ**L**^{MMM}) were generated using the stk python library (Version 2024.9.23.1),[9–11] which enabled the rapid creation of the initial molecular geometries. These structures were then preoptimized in Avogadro[12] (Version 1.2.0) using the Universal Force Field (UFF).[13] Following this, Grimme's CREST[14] algorithm at the GFN-FF[15] level was employed to perform a comprehensive exploration of the potential energy surface. The best structure identified from the conformer search was subsequently reoptimized on GFN2-xTB[16] level using the ALPB[17] model for implicit solvation in acetonitrile. The final structures were visualized using PyMol[18] (Version 3.1.0a OpenSource, Table S6).

Table S6. Overview GFN2-xTB optimized structures of the four diastereomers of Zn_2**L** containing only unidirectional diazocine orientation of the *Z*-ligand arms. The filenames for the structures are listed below with the files available as supporting information.

Zn^ΔZn^Δ**L**^{MMM}	Zn^ΔZn^Δ**L**^{PPP}	Zn^ΛZn^Δ**L**^{PPP}	Zn^ΛZn^Δ**L**^{MMM}
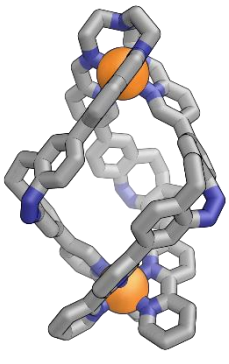	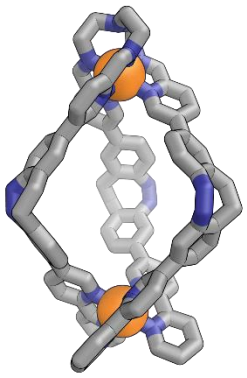	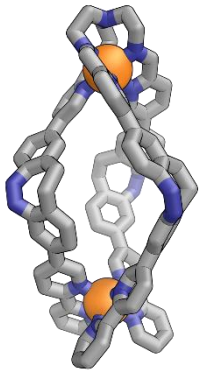	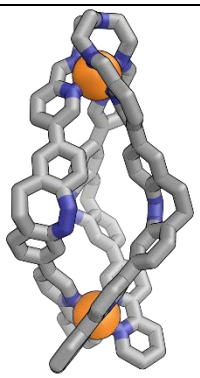
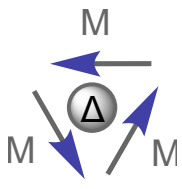	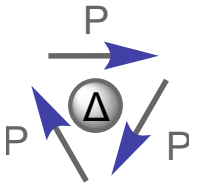	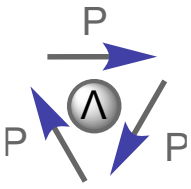	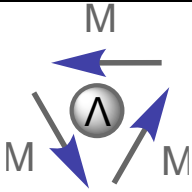
Zn2-Z-Helicate-1.xyz	Zn2-Z-Helicate-4.xyz	Zn2-Z-Mesocate-1.xyz	Zn2-Z-Mesocate-4.xyz

S6.3.2 Structures of Zn_2**L** with other ligand configurations

Input structures for structures containing more than one orientation of the Z-ligand arms or *E*-diazocines were generated using Avogadro[12] (Version 1.2.0) by manipulating the homochiral *Z*-diazocine Zn_2**L** structures listed in Table S6 and subsequent reoptimized on GFN2xTB[16] level using the ALPB[17] model for implicit solvation in acetonitrile. This gave rise to the mixed ligand chirality structures (Table S7) and the four all-E-Structures (Table S8). When an enantiomer of a structure was needed, the structure was mirrored using the "invert chirality" function built into Avogadro. The final structures were visualized using PyMol[18] (Version 3.1.0a OpenSource).

Table S7. Overview of GFN2-xTB optimized structures of the four diastereomers (atropisomers) for the $Zn^{\Delta}Zn^{\Delta}$ helicate. The filenames for the structures are listed below with the files available as supporting information.

$Zn^{\Delta}Zn^{\Delta}$**L**^{MMM}	$Zn^{\Delta}Zn^{\Delta}$**L**^{PMM}	$Zn^{\Delta}Zn^{\Delta}$**L**^{PPM}	$Zn^{\Delta}Zn^{\Delta}$**L**^{PPP}
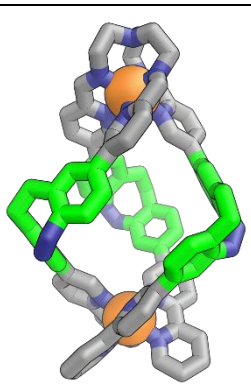	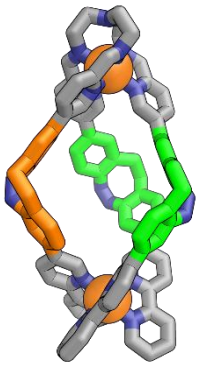	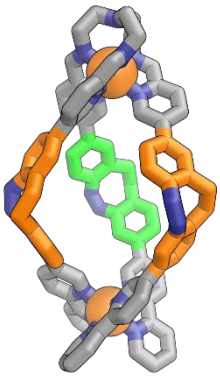	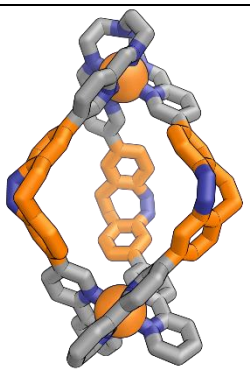
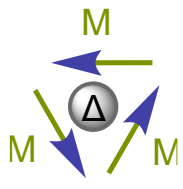	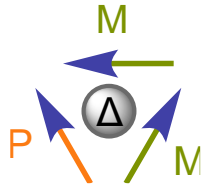	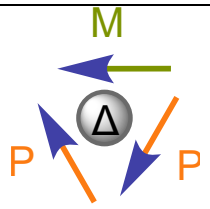	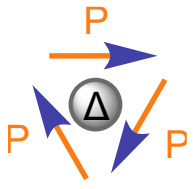
Zn2-Z-Helicate-1.xyz	Zn2-Z-Helicate-2.xyz	Zn2-Z-Helicate-3.xyz	Zn2-Z-Helicate-4.xyz

Table S8. Overview of GFN2-xTB optimized structures of six diastereomers of *E*-Zn_2**L**. The filenames for the structures are listed below with the files available as supporting information.

$Zn^{\Delta}Zn^{\Delta}\mathbf{L}^{PPP}$	$Zn^{\Delta}Zn^{\Delta}\mathbf{L}^{PPM}$	$Zn^{\Delta}Zn^{\Delta}\mathbf{L}^{PMM}$	$Zn^{\Delta}Zn^{\Delta}\mathbf{L}^{MMM}$	$Zn^{\Lambda}Zn^{\Delta}\mathbf{L}^{PPP}$	$Zn^{\Lambda}Zn^{\Delta}\mathbf{L}^{MMM}$
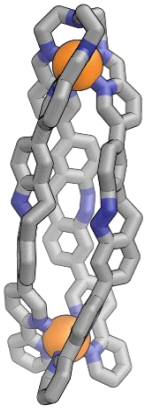	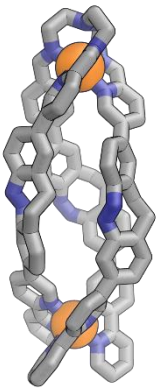	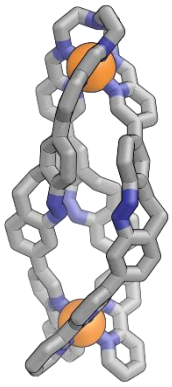	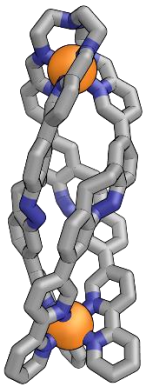	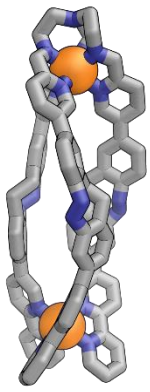	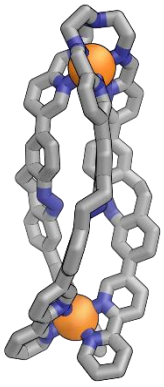
Zn2-E-Helicate-1.xyz	Zn2-E-Helicate-2.xyz	Zn2-E-Helicate-3.xyz	Zn2-E-Helicate-4.xyz	Zn2-E-Mesocate-1.xyz	Zn2-E-Mesocate-4.xyz

S6.3.3 Structures of complexes with metals other than zinc

Structures with metals other than zinc were generated by replacing the zinc atom with the respective element and reoptimized on GFN2-xTB[16] level using the ALPB[17] model for implicit solvation in acetonitrile. Complexes that contained iron atoms did not converge when using ALPB solvation and were optimized without implicit solvation. No significant structural changes were observed for iron and cobalt derivatives. The final structures were visualized using PyMol[18] (Version 3.1.0a OpenSource). Some examples are listed in (Table S9).

Table S9. Overview of GFN2-xTB optimized structures of four example diastereomers of ZnFe**L**. The filenames for the structures are listed below with the files for these and other diastereomers available as supporting information.

$Zn^{\Delta}Fe^{\Delta}\mathbf{L}^{MMM}$	$Zn^{\Delta}Fe^{\Delta}\mathbf{L}^{PPP}$	$Zn^{\Lambda}Fe^{\Delta}\mathbf{L}^{PPP}$	$Zn^{\Lambda}Fe^{\Delta}\mathbf{L}^{MMM}$
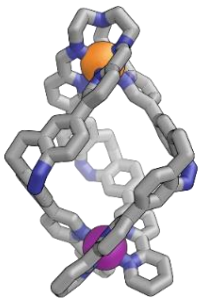	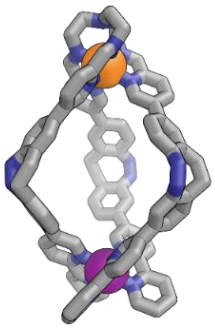	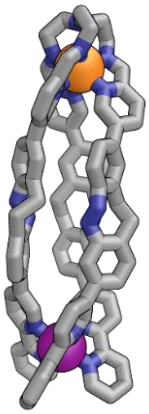	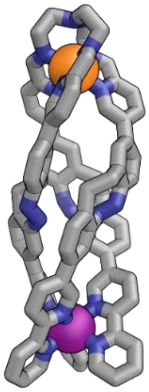
ZnFe-Z-Helicate-1.xyz	ZnFe-Z-Helicate-4.xyz	ZnFe-E-Helicate-1.xyz	ZnFe-E-Helicate-4.xyz

S6.3.4 Comment on energy calculations on metal-organic helicates

All structures were optimized using Grimme's GFN2-xTB[16] as this semi-empirical method shows a great cost-to-benefit ratio for large metallo-supramolecular systems. It is optimized to yield reasonable structures, vibrational frequencies, and noncovalent interactions, but higher-level DFT methods are necessary for accurate energies. Despite resulting in generally more accurate energies, energy calculations of large, porous, flexible, and charged molecules using high-level DFT methods will not necessarily result in accurate energies. Approximating these as static structures in single-molecule models without explicit solvation and anions will likely result in inaccurate results.[19] The complexity and high computational cost of these advanced calculations lead us not to pursue the calculation of accurate relative energies of the structures.

S6.4 Determination of solution stereochemistry of the helicates

As mentioned above, the helicates and pseudo-mesocates are composed of five chiral building blocks, three ligand arms and two octahedral metal coordination sites, resulting in a multitude of possible stereoisomers.

With two chiral metal centres and three possible ligand-arm orientations, eight diastereomers (plus eight enantiomers) are possible. Firstly, the two metal centres can be homochiral, leading to helicates, or heterochiral, resulting in pseudo-mesocates. Secondly, the three ligand arms could exist in four diazocine orientations: (MMM), (PMM), (PPM), and (PPP). Out of these, only the two homochiral arrangements (MMM) and (PPP) would lead to a single set of signals in the NMR spectrum (Table S10).

This leaves four possible structures (Table S11). Three of these structures can be ruled out by the findings from ^{1}H ROESY NMR experiments (Section S6.4.1) as the observed H−H through-space couplings are only possible in the $Zn^{\Delta}Fe^{\Delta}\mathbf{L}^{MMM}$ structure (and its enantiomer). This structure is the same as the one observed in the solid state, as confirmed by the single crystal X-ray structure (Section S6.2). This arrangement of the ligand arms could be confirmed for both $Zn_2\mathbf{L}$ (Figure S63) and $Fe_2\mathbf{L}$ (Figure S62).

Table S10. Computational structures for the four possible ligand configurations in $Zn^{\Delta}Fe^{\Delta}$**L** (for computational details see Section S6.3). Since just one set of signals is observed by NMR, structures containing heterochiral ligands can be ruled out for the ground state of the complexes.

$Zn^{\Delta}Zn^{\Delta}$**L**^{MMM}	$Zn^{\Delta}Zn^{\Delta}$**L**^{PMM}	$Zn^{\Delta}Zn^{\Delta}$**L**^{PPM}	$Zn^{\Delta}Zn^{\Delta}$**L**^{PPP}
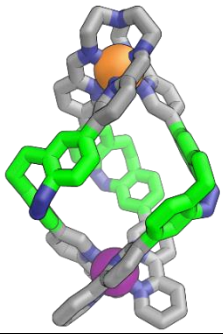	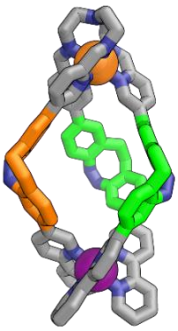	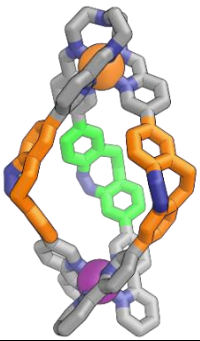	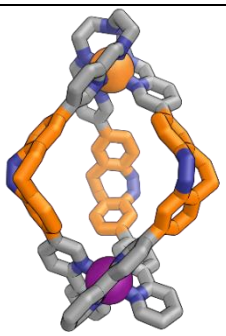
1 set of signals in NMR	3 sets of diastereotopic signals in NMR	3 sets of diastereotopic signals in NMR	1 set of signals in NMR

Table S11. Computational structures for the four remaining diastereomers of ZnFe**L** after ruling out mixed diazocine orientations within the ligand arms (Table S10) and ChemDraw representations of the ligand folding (for computational details see Section S6.3). Only $Zn^{\Delta}Fe^{\Delta}$**L**^{MMM} (and its enantiomer) show the correct folding that could give rise to the ^{1}H ROESY cross-peaks observed in Section S6.4. The same diastereomer was observed in the solid state (Section S6.2).

$Zn^{\Delta}Fe^{\Delta}$**L**^{MMM}	$Zn^{\Delta}Fe^{\Delta}$**L**^{PPP}	$Zn^{\Delta}Fe^{\Delta}$**L**^{MMM}	$Zn^{\Delta}Fe^{\Delta}$**L**^{PPP}
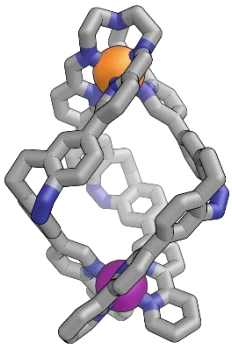	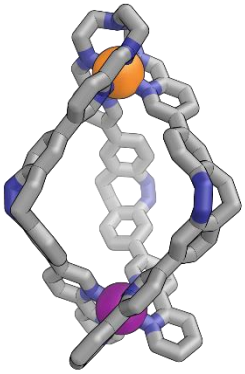	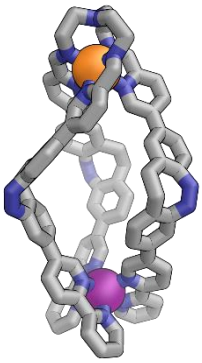	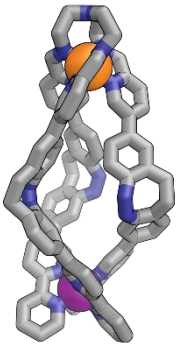
(+ enantiomer)	(+ enantiomer)	(+ enantiomer)	(+ enantiomer)
Ligand conformation in computational structure:			
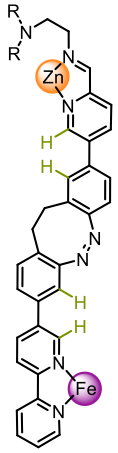	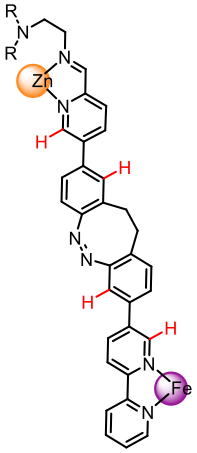	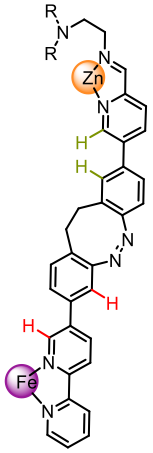	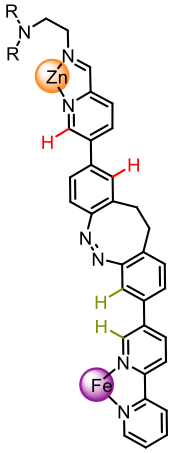
H-p and H-m are adjacent H-g and H-h are adjacent	H-p and H-m not adjacent H-g and H-h not adjacent	H-p and H-m are adjacent H-g and H-h not adjacent	H-p and H-m not adjacent H-g and H-h are adjacent

S6.4.1 1D ROESY NMR of ZnFe**L**

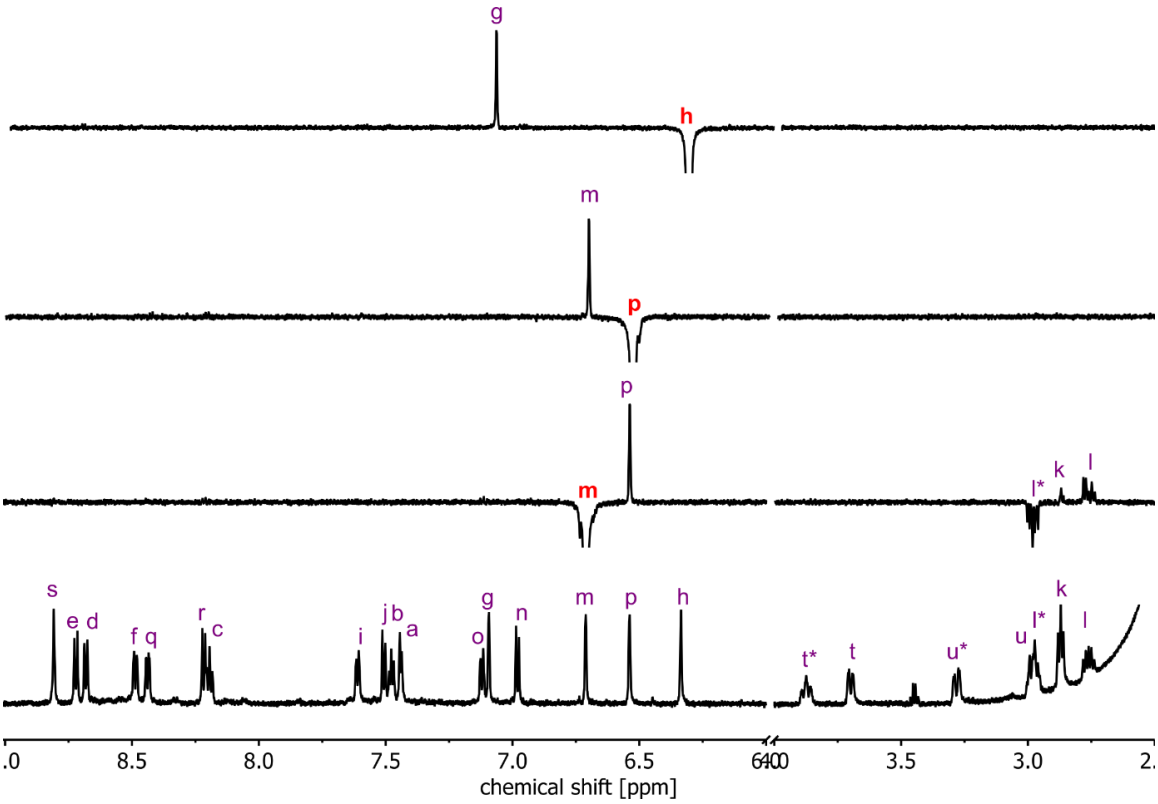

Figure S58. One dimensional ^{1}H ROESY spectra (700 MHz, CD_3CN, 1 mM, 298 K) of ZnFe**L** for signals H-h, H-p and H-m with results summarized in Figure S60 and Table S12.

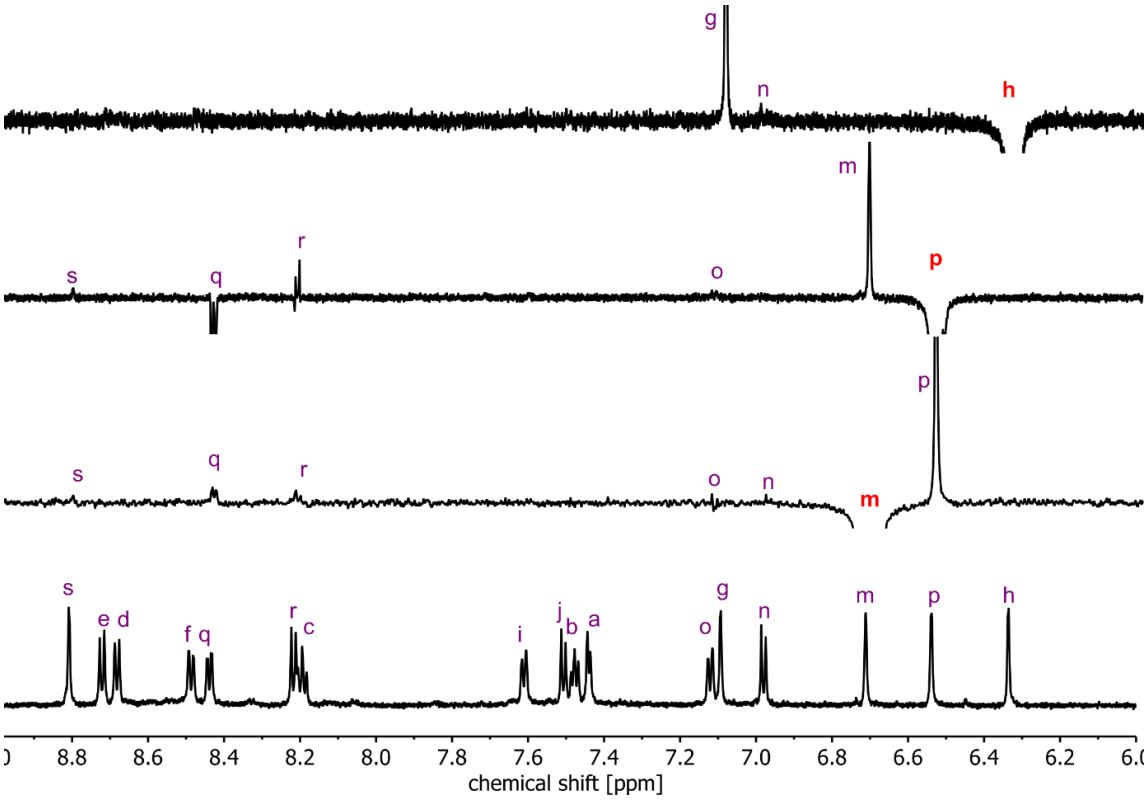

Figure S59. One dimensional ^{1}H ROESY spectra (700 MHz, CD_3CN, 1 mM, 298 K) of ZnFe**L** for signals H-h, H-p and H-m, measured with a small signal width (SW = 3 ppm) to observe just the aromatic region with results summarized in Figure S60 and Table S12.

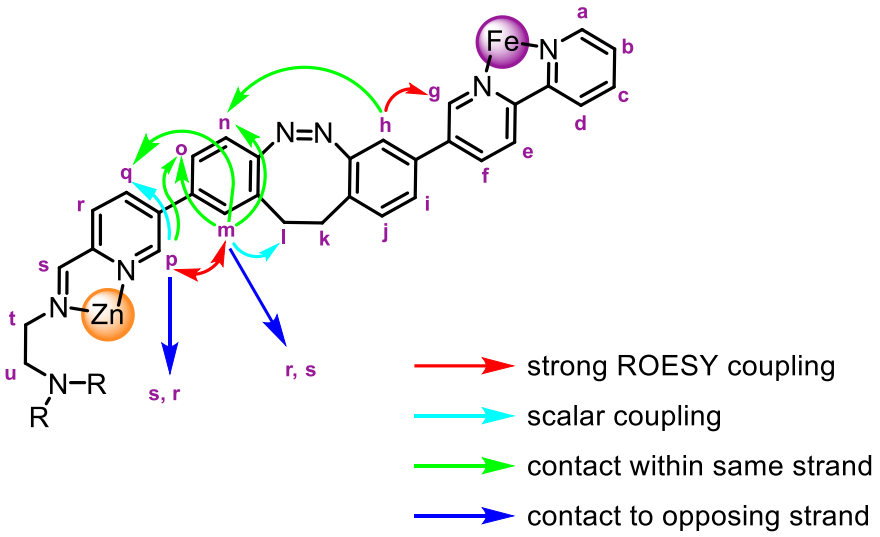

Figure S60. Contacts in ZnFe**L** according to one-dimensional ^{1}H ROESY spectra for signals H-h, H-p and H-m.

Table S12. List of observed ^{1}H ROESY couplings and measured distances in computational solution model of ZnFe**L**. The three intense cross peaks (marked red) can be used to determine the relative stereochemistry of ZnFe**L** (see Section S6.4). Some of the weak signals can likely be assigned to interactions between different ligand strands (distances marked red).

Protons	^{1}H ROESY cross peak	Distance [Å]
h–g	**strong**	2.2
h–n	weak	4.8
m–p	**strong**	2.3
m–l	weak	2.4/2.7
m–q	weak	4.8 (same strand) 4.8 (second ligand)
m–r	weak	5.9 (same strand) 4.7 (second ligand)
m–s	weak	7.0 (same strand) 5.0 (second ligand)
m–o	weak	4.3 (same strand) 4.7 (second ligand)
m–n	weak	4.9 (same strand) 6.7 (second ligand)
p–m	**strong**	2.3
p–q	weak	4.3 (same strand) 4.8 (second ligand)
p–s	weak	5.4 (same strand) 4.4 (second ligand)
p–r	weak	4.9 (same strand) 4.5 (second ligand)
p–o	weak	4.5 (same strand) 5.0 (second ligand)

S6.4.2 2D ROESY NMR of redissolved Fe_2**L** single crystals

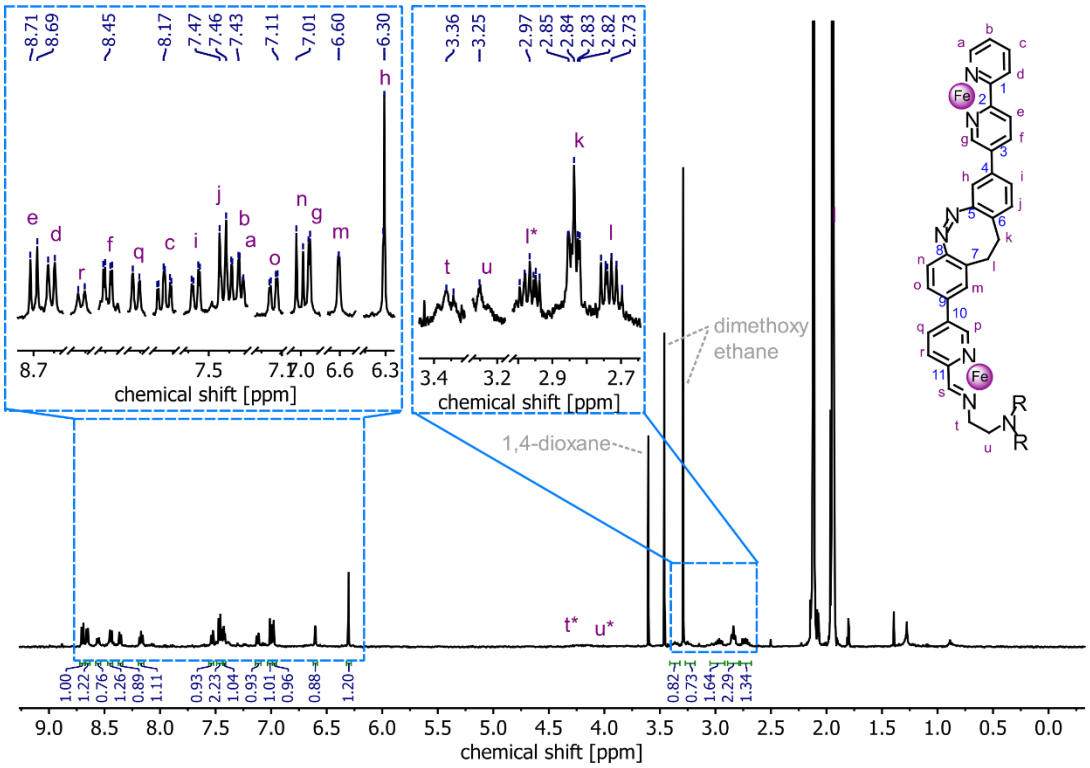

Figure S61. ^{1}H NMR spectrum (500 MHz, CD_3CN, 298 K) of redissolved single crystals of Fe_2**L** showing residual 1,2-dimethoxyethane and its decomposition product 1,4-dioxane that were used during crystallization. No differences to previous spectra are observed.

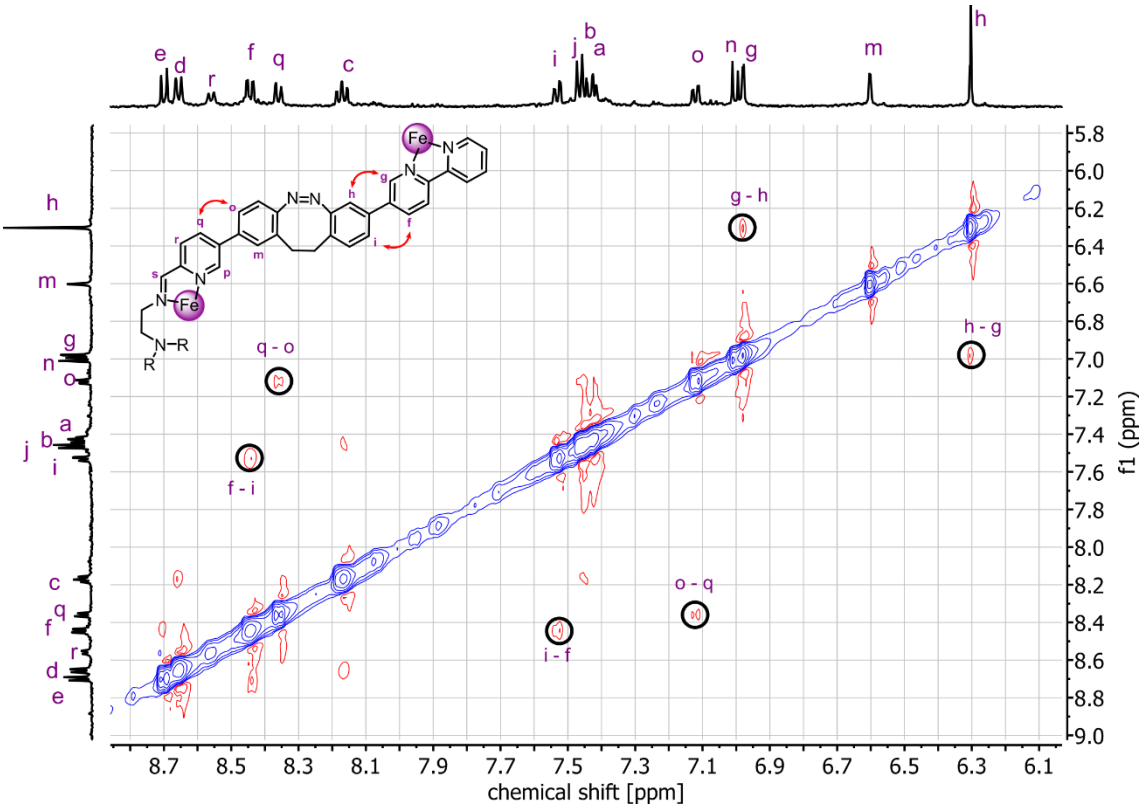

Figure S62. Partial ^{1}H,^{1}H ROESY NMR spectrum (500 MHz, CD_3CN, 298 K) of redissolved single crystals of Fe_2**L** showing through-space coupling between protons H-g and H-h, H-q and H-o, and H-f and H-i, as is expected for the diastereomer observed in the solid-state structure.

S6.4.3 2D ROESY NMR of Zn_2**L**

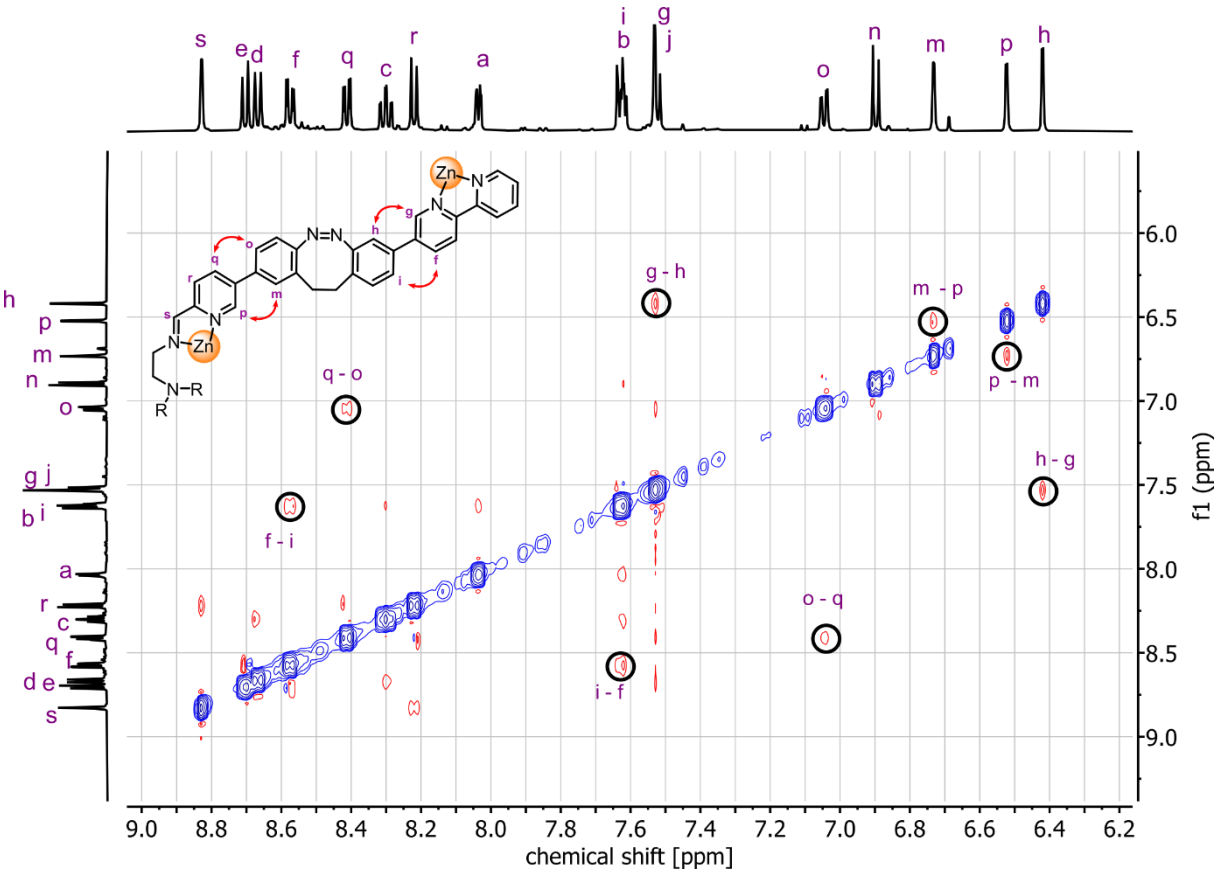

Figure S63. Partial ^{1}H,^{1}H ROESY NMR spectrum (500 MHz, CD3CN, 298 K) of Zn_2**L** showing through-space coupling between protons H-p and H-m, H-g and H-h, H-q and H-o, and H-f and H-i, as is expected for the diastereomer observed in the solid-state structures of Fe_2**L** and ZnFe**L**.

S7 Photochemical characterisation

S7.1 General procedures for the illumination of different types of samples

***Ex-situ* illumination (NMR and MS).** Portable, built-in-house light sources equipped with custom 3D-printed adapters were used to irradiate NMR and MS samples (Figure S60). The samples were promptly subjected to measurement, following irradiation to reduce thermal relaxation to a minimum.

Figure S64. Pictures of the *ex-situ* illumination setup with USB-powered homemade light sources using commercial LED chips with 3D printed adaptors for 2 mL GC vials and 5 mm NMR-tubes.

***In-situ* illumination (NMR).** The NMR sample was fitted with an insert tube made from quartz glass and a quartz glass optical fibre was pushed down into the insert. The end of this fibre was non-terminated, and the exposed surface had been roughened to ensure even and omnidirectional illumination (Figure S61). This construction was lowered into the NMR device using an aluminium rod to avoid damage to the fibre. The other end of the optical fibre was connected to the light source so the sample could be irradiated inside the spectrometer.[20,21]

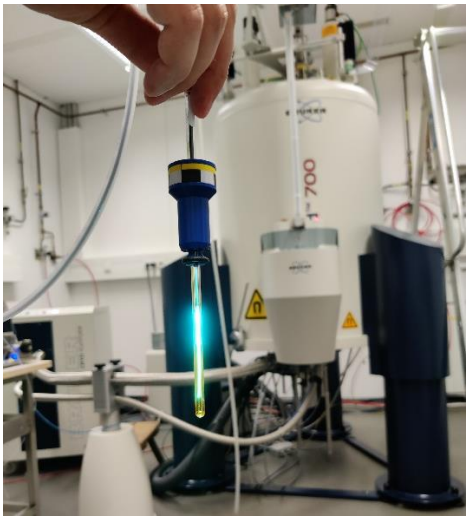

Figure S65. NMR sample with quartz glass insert and optical fibre for in-situ illumination during NMR experiments.

***In situ* illumination (UV-vis).** Samples were irradiated perpendicularly to the measurement axis within the UV-vis spectrometer using optical fibres connected to an LED light source (see Section S1; Figure S62). To facilitate the irradiation of the cuvettes perpendicularly to the spectrometer's measurement axis, a hole matching the diameter of the quartz glass fibre was drilled at the centre of the Teflon stopper used to seal the UV-vis cuvettes. This configuration enabled the connection of an optical fibre to the cuvette, allowing the irradiation of the samples from above.

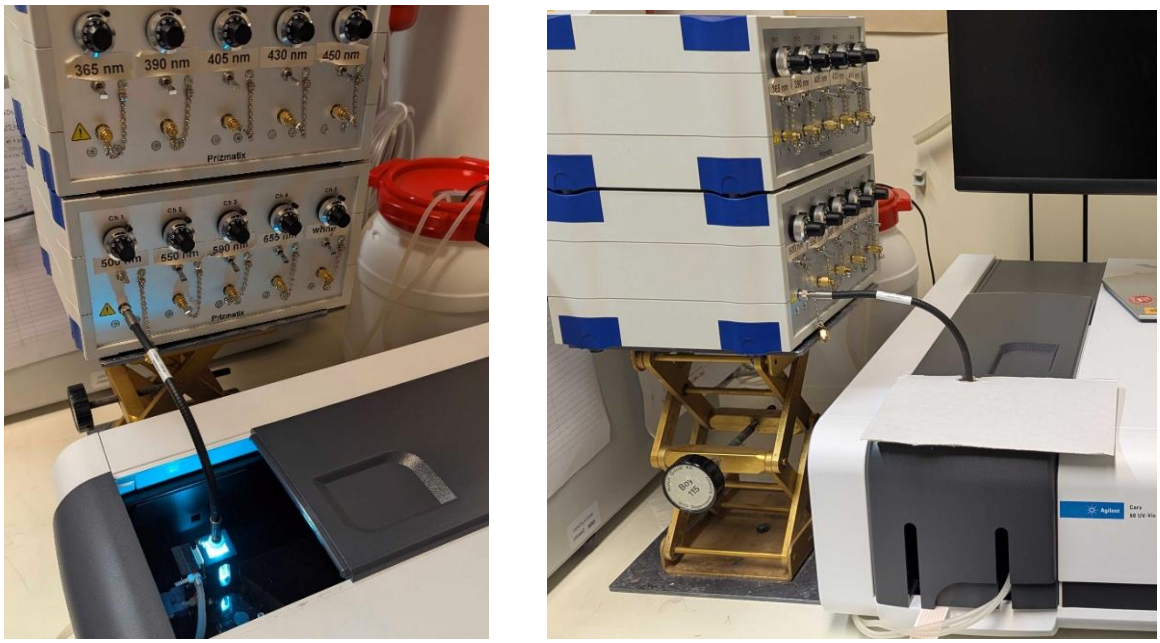

Figure S66. Pictures of the *in-situ* illumination setup showing fibre collimated LED-sources connected to the cuvette with open (left) and closed measurement chamber (right).

Determination of the photo stationary state (PSS). Photostationary states of the photoswitches were determined using ^{1}H NMR spectroscopy. For this purpose, two signals corresponding to the same proton were integrated, and the PSS was calculated based on the resulting integral ratios. To ensure the highest accuracy, well-separated and clearly resolved signals were selected for the analysis, as recommended in the literature.[22,23]

S7.2 Geometry changes of aldehyde **1** during photoswitching

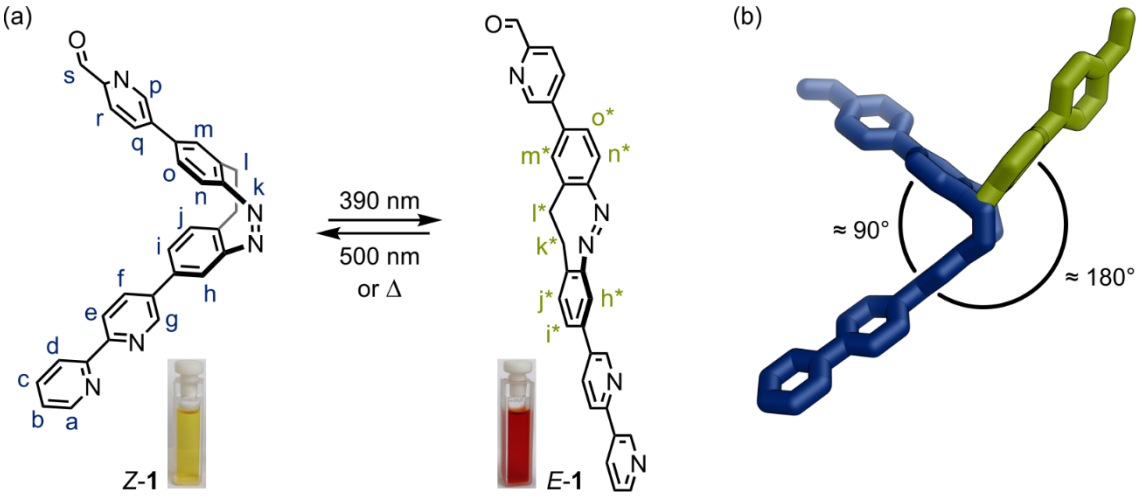

Figure S67. (a) ChemDraw representations of aldehyde **1** in its *E* and *Z*-states with photographs of an acetonitrile solution of **1** before and after irradiation with 405 nm light, showing a drastic colour change from yellow to red. (b) Three-dimensional representation of aldehyde **1** in its *E* and *Z*-states (green and blue, respectively), showcasing the difference in substituent orientation that changes from 90° in the *Z*-state to 180° in the *E*-state. The three-dimensional representations were modelled and pre-optimized using Avogardo[12] (Version 1.2.0) on UFF[13] level before final geometry optimisations were performed on GFN2-xTB[16] level (Version 6.6.0) and the resulting structures visualized using PyMol[18] (Version 3.1.0a OpenSource). The structures are available as supporting information.

S7.3 Photoswitching and thermal relaxation (UV-vis)

Table S13. Overview over photophysical properties of aldehyde **1** and helicates.

structure	$\lambda_{irr}(Z \rightarrow E)$ [nm]	$\lambda_{irr}(E \rightarrow Z)$ [nm]	$\tau_{½}$(298 K) [min]
1	390	500	165
Zn_2**L**	405	500	114
Co_2**L**	390	500	115
Fe_2**L**	405	500	68
ZnFe**L**	405	500	94

S7.3.1 Aldehyde subcomponent **1**

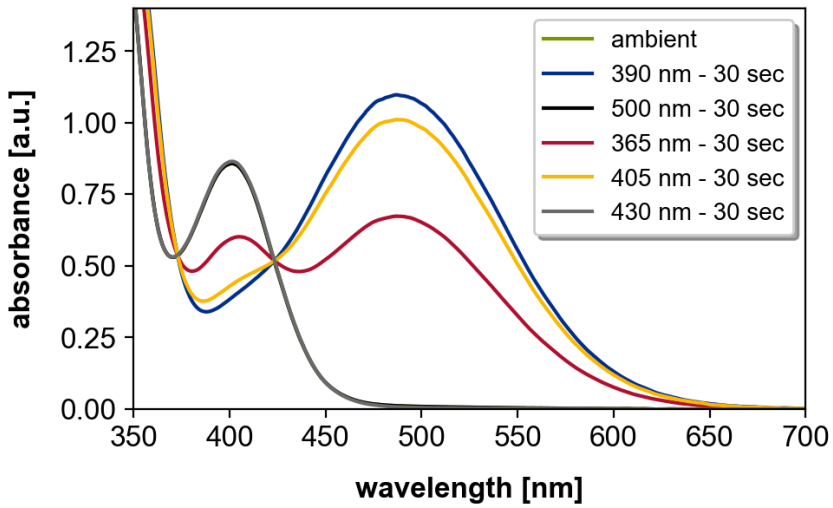

Figure S68. UV-vis spectra of aldehyde **1** (CH_3CN, 0.06 mM) before and after irradiation with different wavelengths.

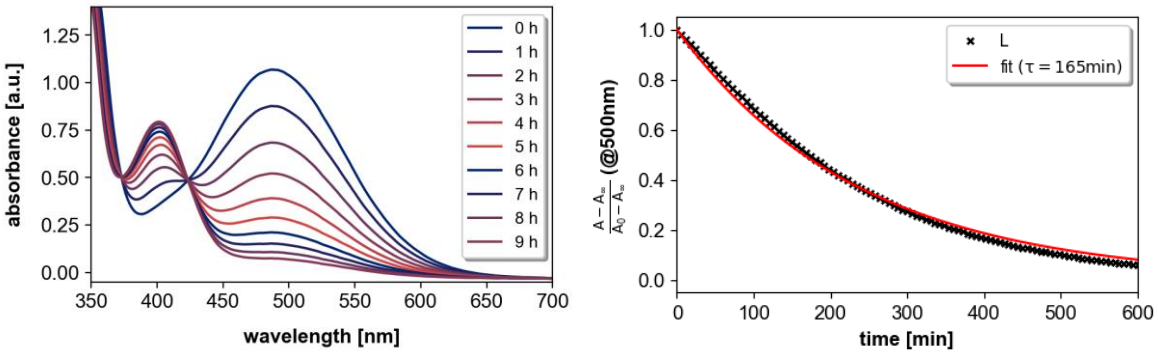

Figure S69. UV-vis spectra (left) and fit (right) of the thermal relaxation of aldehyde **1** (CH_3CN, 0.06 mM, 25 °C) after irradiation at 390 nm for 1 minute. Thermal half-life of **1** was determined to be $\tau_{1/2}$ = 165 min.

S7.3.2 Zn_2**L**

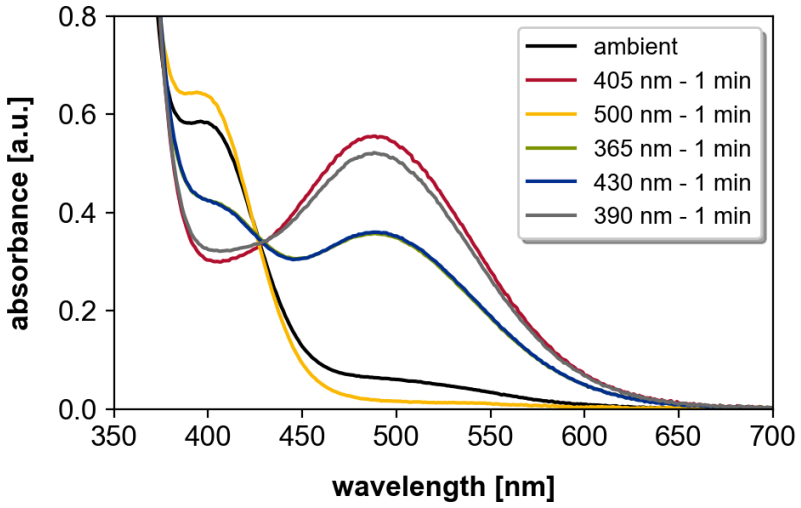

Figure S70. UV-vis spectra of Zn_2**L** (CH_3CN, 0.03 mM) before and after irradiation with different wavelengths.

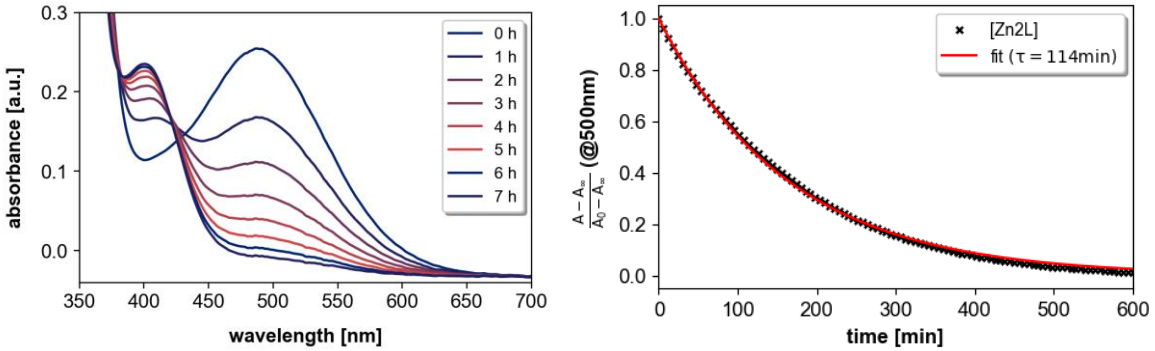

Figure S71. UV-vis spectra (left) and fit (right) of the thermal relaxation of Zn_2**L** (CH_3CN, 0.03 mM, 25 °C) after irradiation at 405 nm for 1 minute. Thermal half-life of Zn_2**L** was determined to be $\tau_{1/2}$ = 114 min.

S7.3.3 Co_2**L**

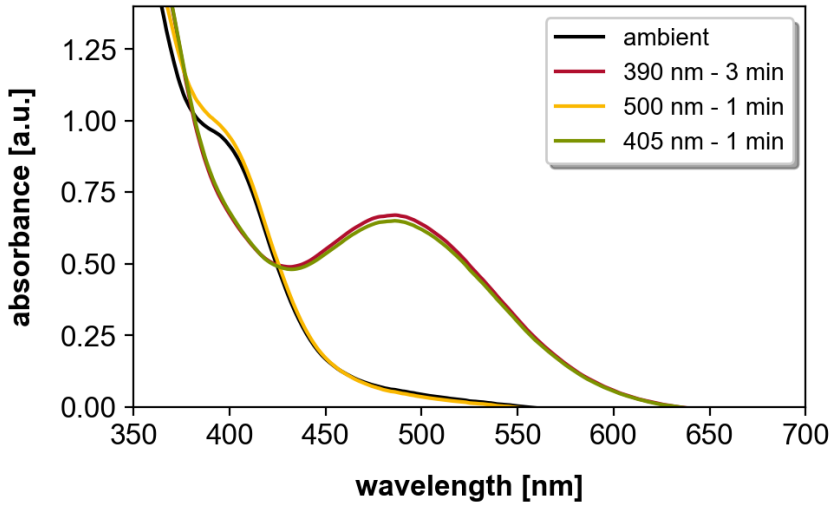

Figure S72. UV-vis spectra of Co_2**L** (CH_3CN, 0.03 mM) before and after irradiation with different wavelengths.

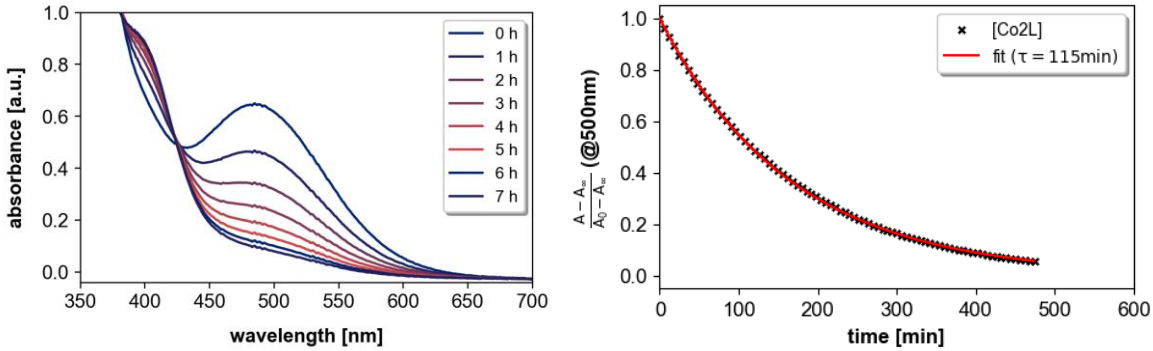

Figure S73. UV-vis spectra (left) and fit (right) of the thermal relaxation of Co_2**L** (CH_3CN, 0.03 mM, 25 °C) after irradiation at 405 nm for 1 minute. Thermal half-life of Co_2**L** was determined to be $\tau_{1/2}$ = 115 min.

S7.3.4 Fe_2**L**

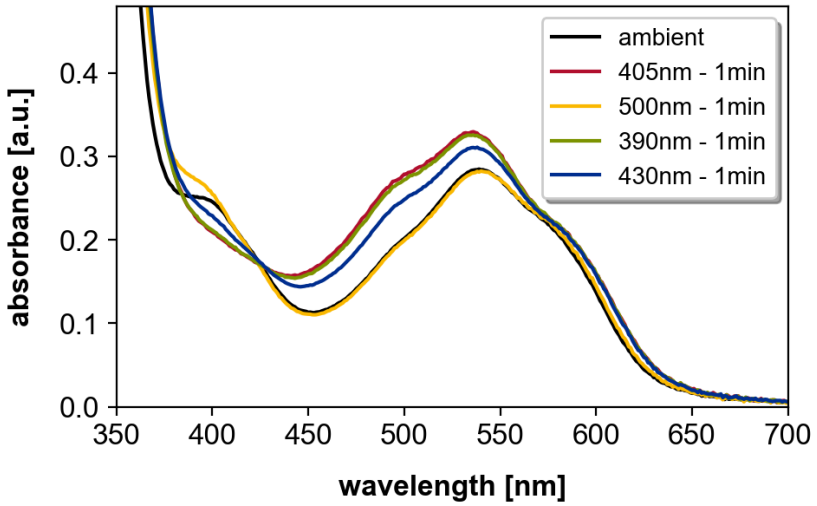

Figure S74. UV-vis spectra of Fe_2**L** (CH_3CN, 0.03 mM) before and after irradiation with different wavelengths.

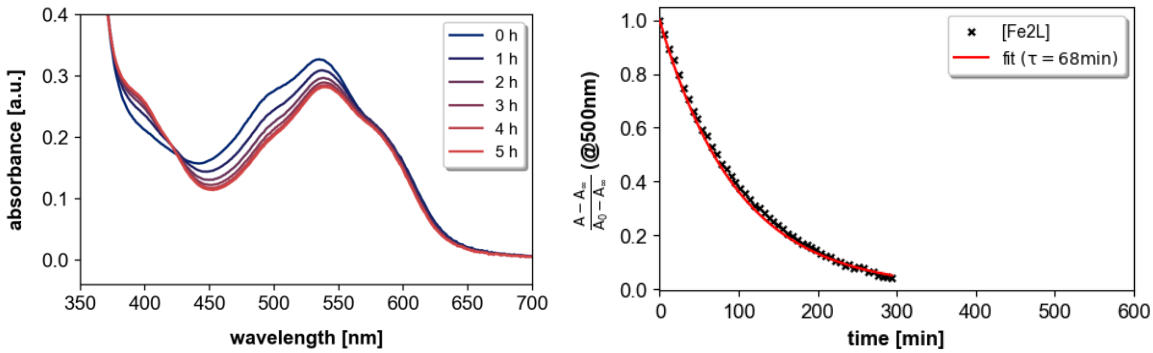

Figure S75. UV-vis spectra (left) and fit (right) of the thermal relaxation of Fe_2**L** (CH_3CN, 0.03 mM, 25 °C) after irradiation at 405 nm for 1 minute. Thermal half-life of Fe_2**L** was determined to be $\tau_{1/2}$ = 68 min.

S7.3.5 ZnFe**L**

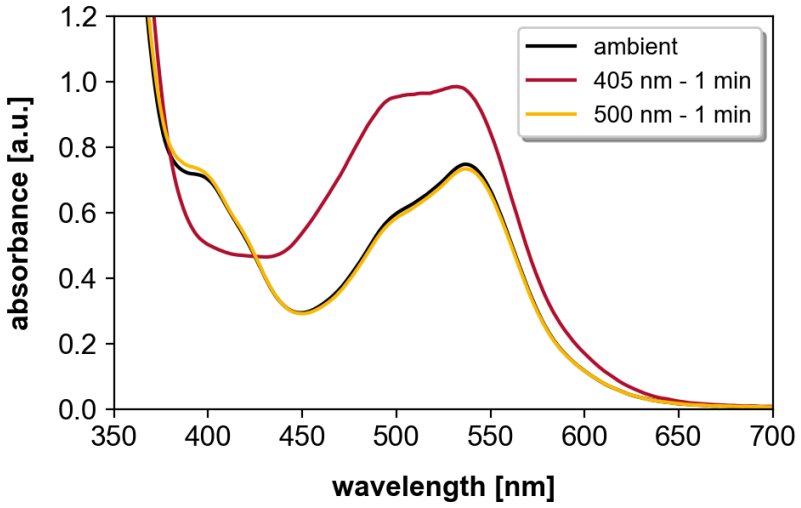

Figure S76. UV-vis spectra of ZnFe**L** (CH_3CN, 0.03 mM) before and after irradiation with different wavelengths.

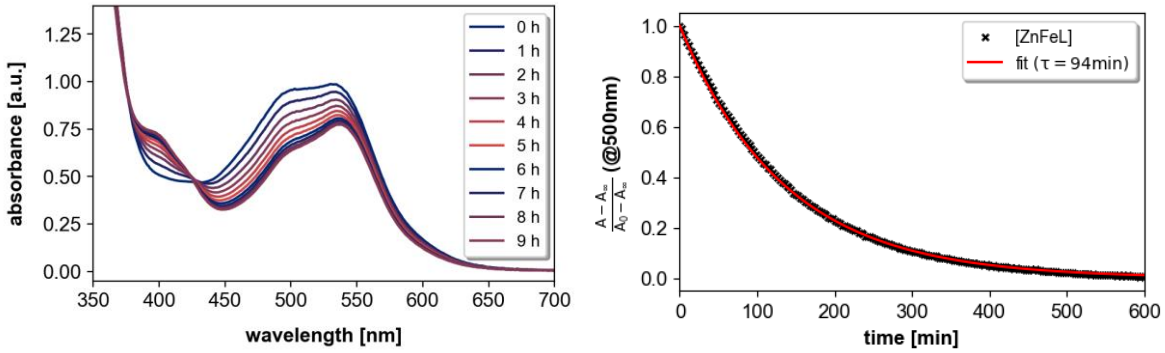

Figure S77. UV-vis spectra (left) and fit (right) of the thermal relaxation of ZnFe**L** (CH_3CN, 0.03 mM, 25 °C) after irradiation at 405 nm for 1 minute. Thermal half-life of ZnFe**L** was determined to be $\tau_{½}$ = 94 min.

S7.3.6 Photochemical fatigue of Zn_2**L**

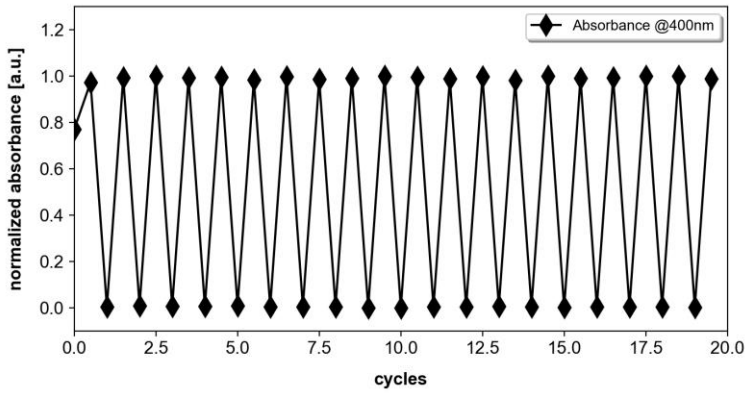

Figure S78. Absorbance of Zn_2**L** (0.03 mM, CH_3CN) at 400 nm after alternating irradiations at 405 nm and 500 nm demonstrating reversible photoisomerization cycles of Zn_2**L**.

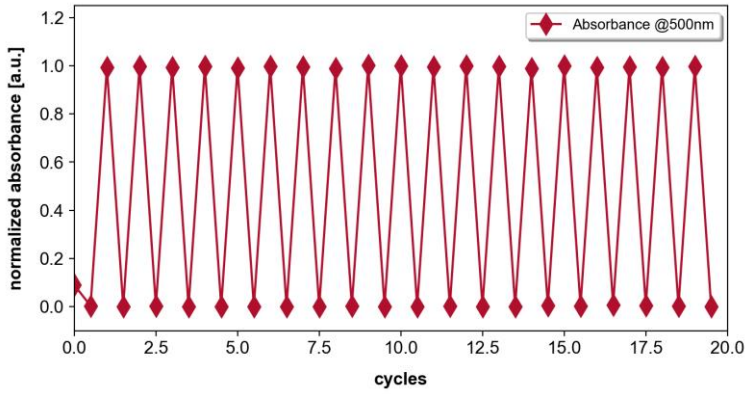

Figure S79. Absorbance of Zn_2**L** (0.03 mM, CH_3CN) at 500 nm after alternating irradiations at 405 nm and 500 nm demonstrating reversible photoisomerization cycles of Zn_2**L**.

S7.3.7 Difference in UV-vis spectra before and after photoswitching

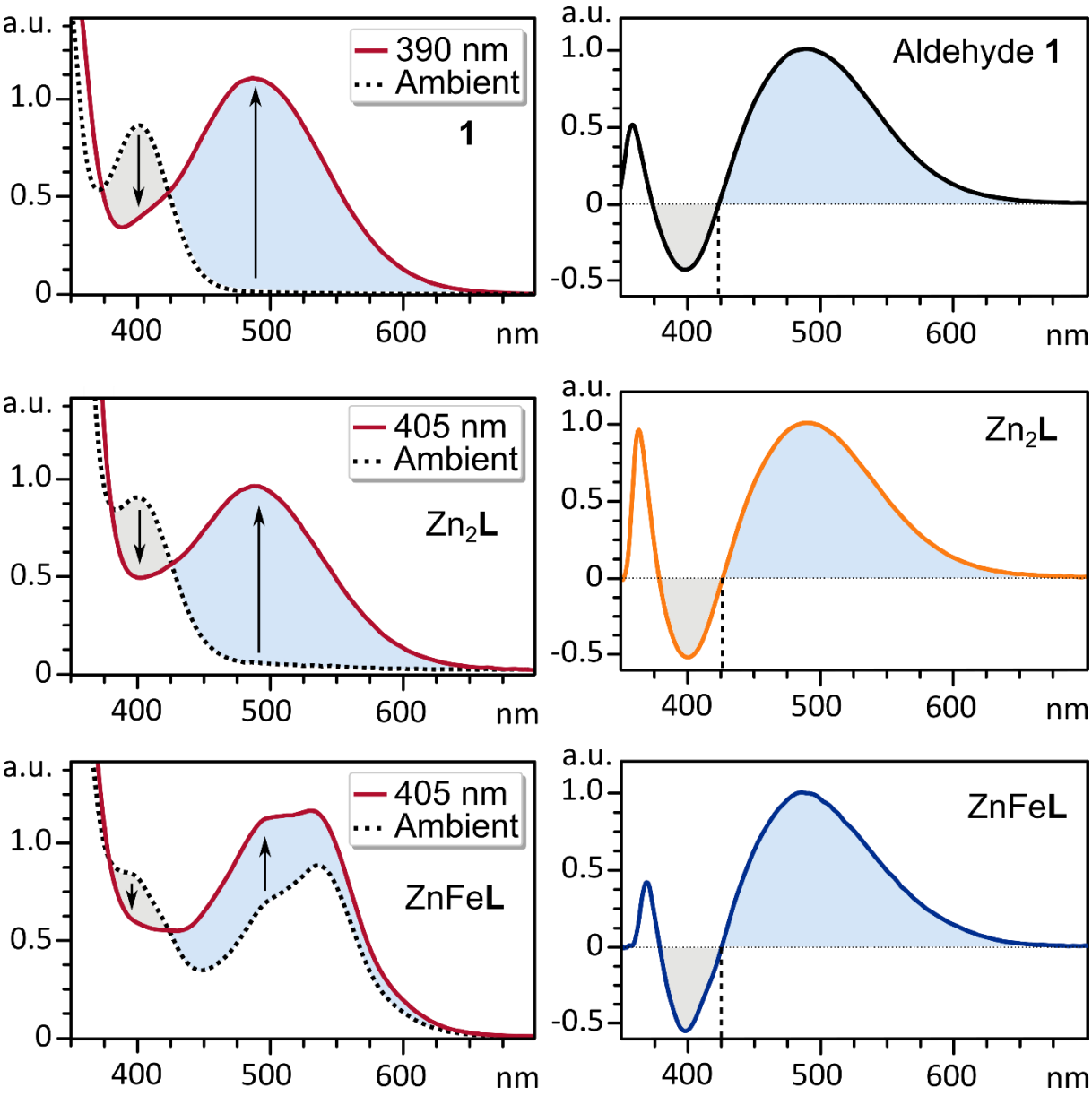

Figure S80. Comparison of the UV-vis spectra of under ambient conditions and at the photostationary state of aldehyde **1**, Zn_2**L**, and ZnFe**L** (left) as well as the normalized difference between the ambient spectrum and the spectrum at the PSS (right), indicating that all changes in the UV-vis spectra during switching arise from the diazocine chromophore.

S7.4 Photoswitching (^{1}H NMR)

S7.4.1 Photostationary states (*ex-situ* illumination)

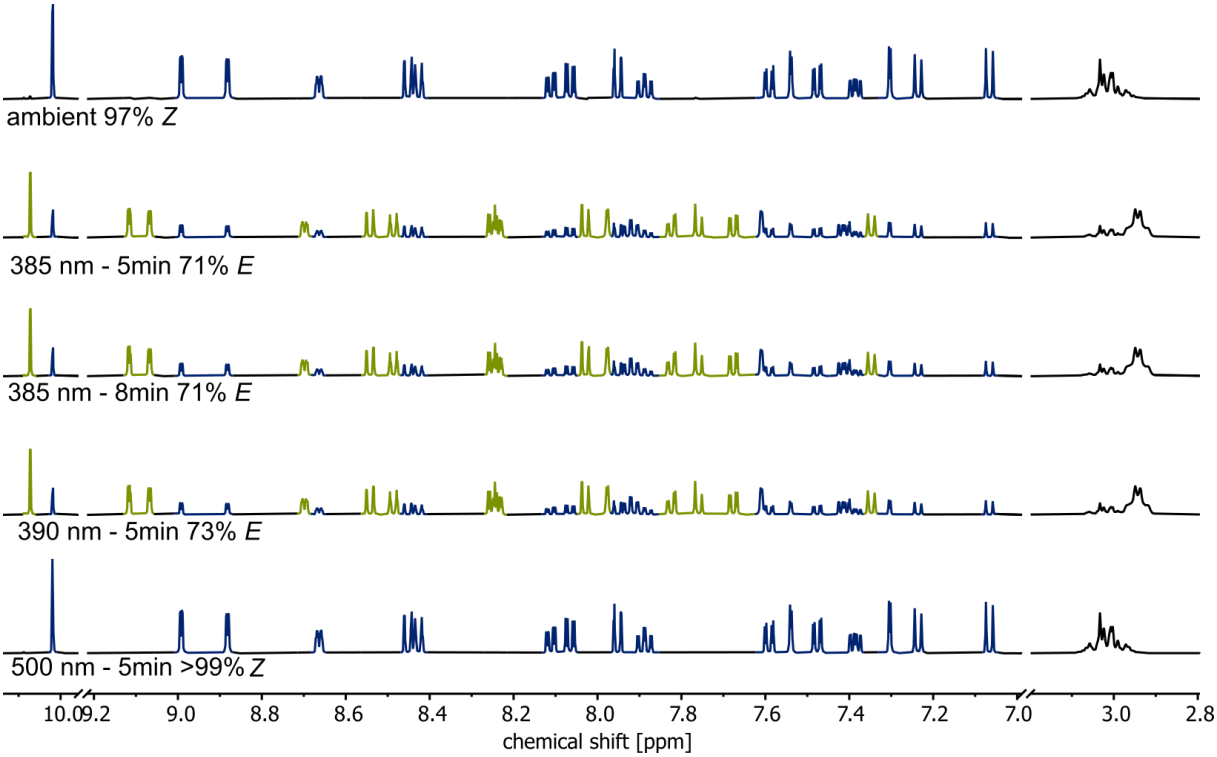

Figure S81. ^{1}H NMR spectra (500 MHz, CD_3CN, 1 mM, 298 K) of ligand precursor **1** before and after irradiation with 385 nm (5 min and 8 min), 390 nm (5 min), and 500 nm (5 min, top to bottom).

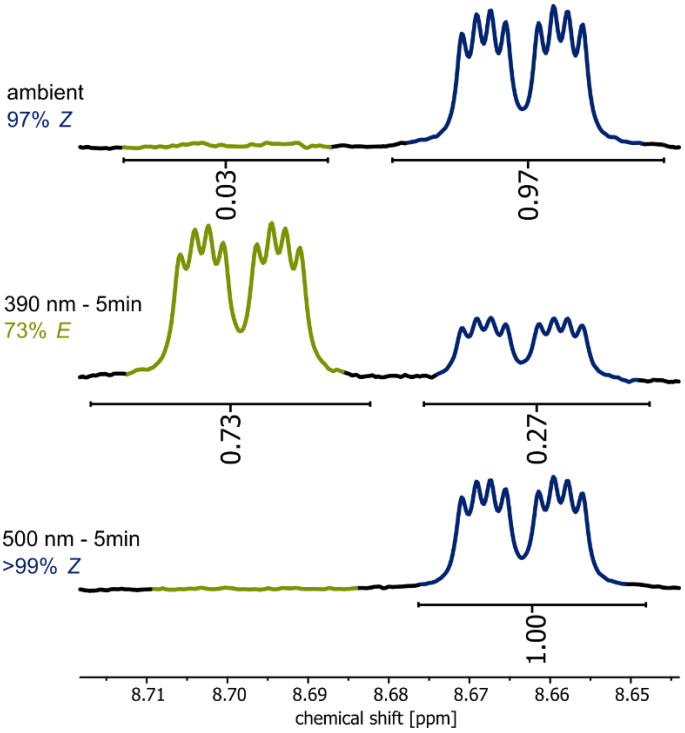

Figure S82. Partial ^{1}H NMR spectra (500 MHz, CD_3CN, 1 mM, 298 K) of ligand precursor **1** before and after irradiation. Integration of H-a proton signals indicates 3% *E*-**1** under ambient conditions (before irradiation) and 73% *E*-**1** after irradiation with 390 nm light for 5 minutes and <<1% *E*-**1** after irradiation with 500 nm light for 5 minutes.

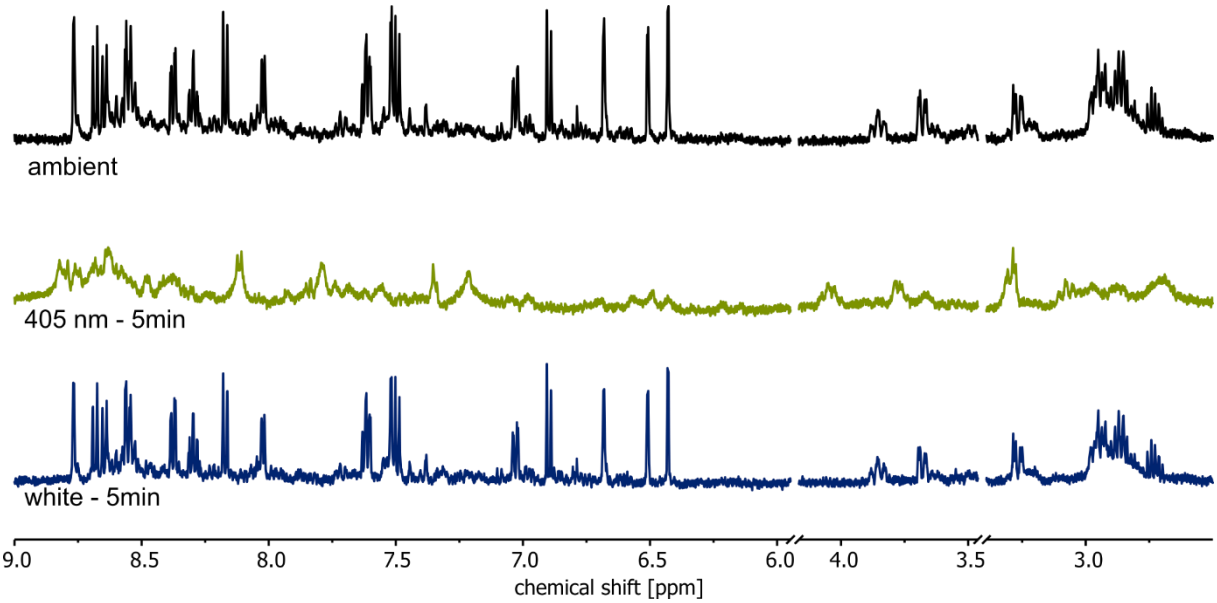

Figure S83. ^{1}H NMR spectra (500 MHz, CD_3CN, 1 mM, 298 K) of Zn_2**L** before and after irradiation with 405 nm (5 min) and white light (5 min, top to bottom).

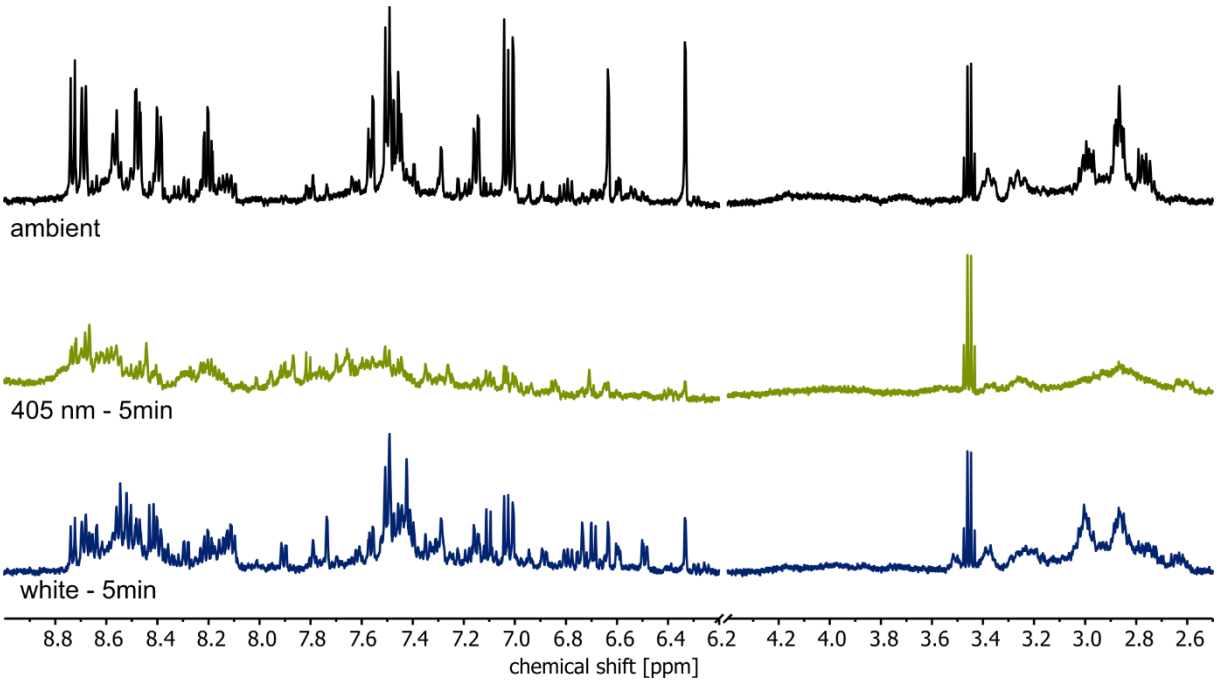

Figure S84. ^{1}H NMR spectra (500 MHz, CD_3CN, 1 mM, 298 K) of Fe_2**L** before and after irradiation with 405 nm (5 min) and white light (5 min, top to bottom).

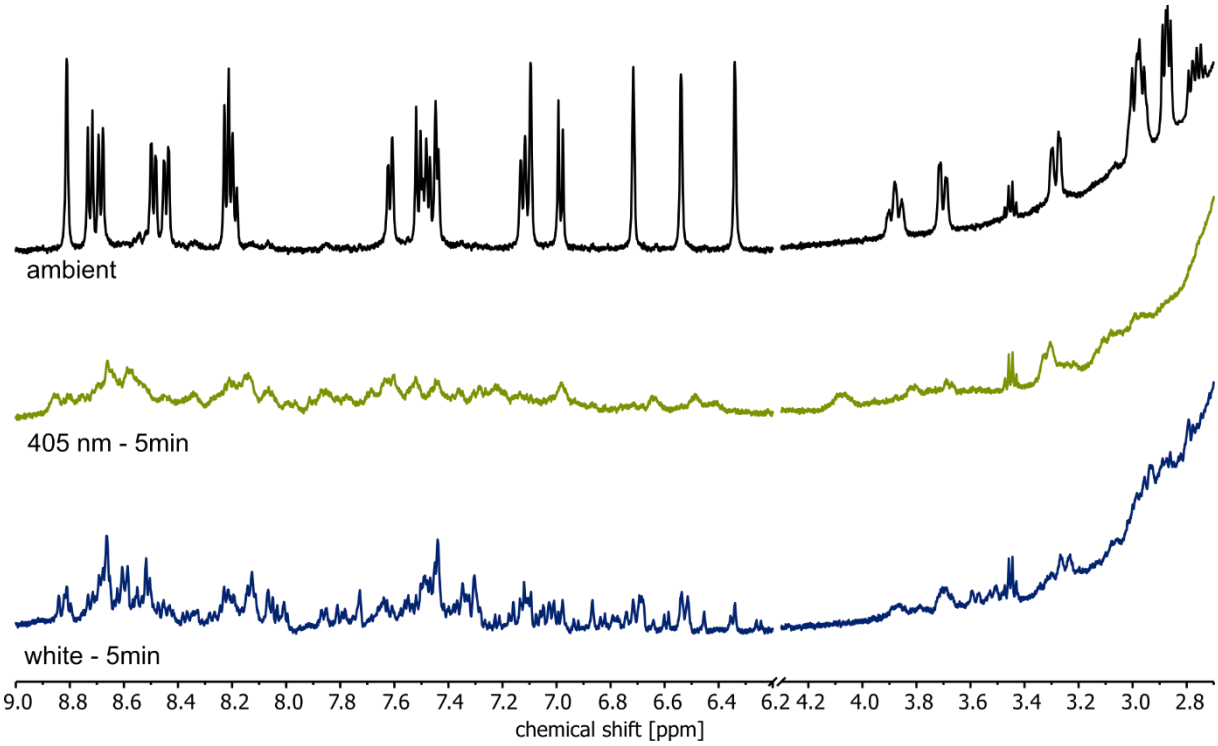

Figure S85. ^{1}H NMR spectra (500 MHz, CD_3CN, 1 mM, 298 K) of ZnFe**L** before and after irradiation with 405 nm (5 min) and white light (5 min, top to bottom).

S7.4.2 DOSY NMR of switched states

Table S14. Diffusion constants *D* and solvodynamic diameters *d* as determined by ^{1}H DOSY NMR experiments

structure	***D*** [10^{-10} m^2s^{-1}]			***d*** (=2*r*) [Å]		
	ambient	after 405 nm irr.	after 515 nm irr.	ambient	after 405 nm irr.	after 515 nm irr.
Zn_2**L**	5.402	5.450	–	20.7	20.5	–
ZnFe**L**	5.716	5.747	5.497	19.6	20.5	20.3

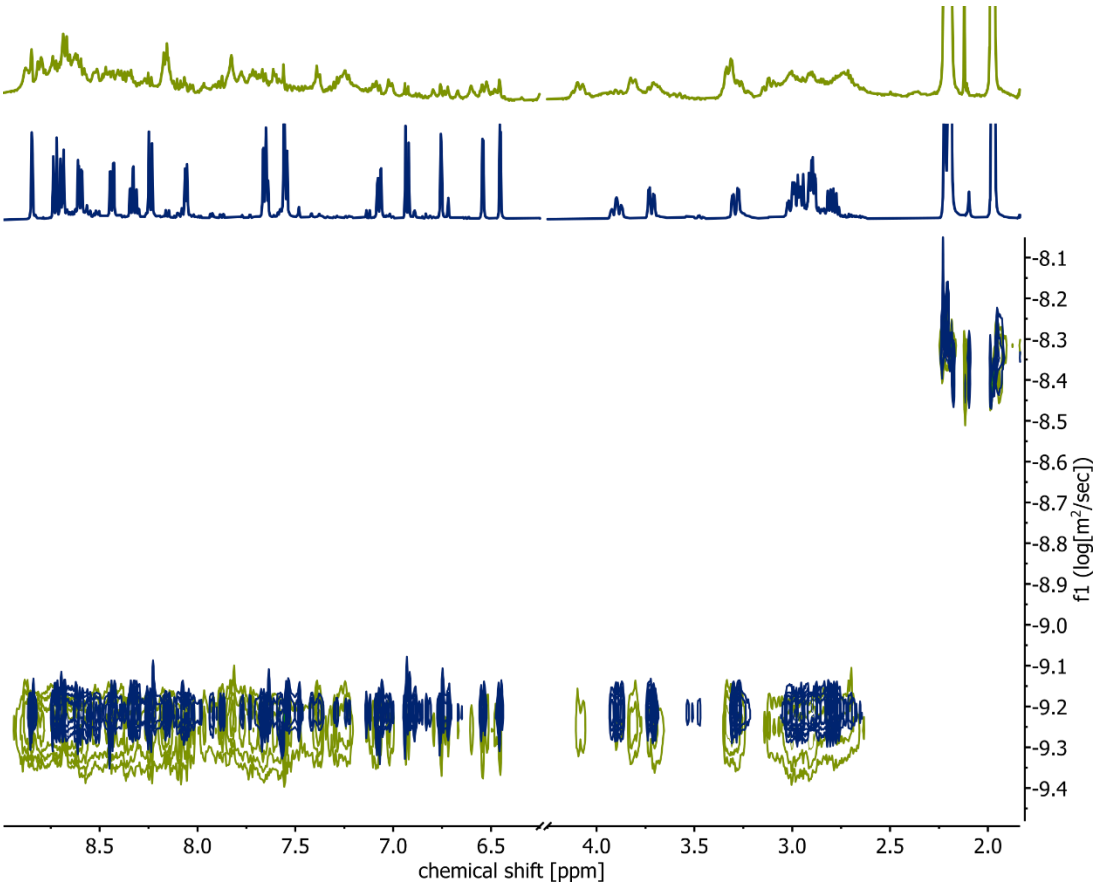

Figure S86. Two dimensional ^{1}H DOSY NMR spectra (500 MHz, CD_3CN, 8 mM, 298 K, D_{20} = 75 ms) of Zn_2**L** before (blue, $D_{amb.}$ = 5.402 · 10^{-10} m^2s^{-1}, $d_{amb.}$ = 20.7 Å) and after irradiation with 405 nm (green, D_{405} = 5.450 · 10^{-10} m^2s^{-1}, d_{405} = 20.5 Å).

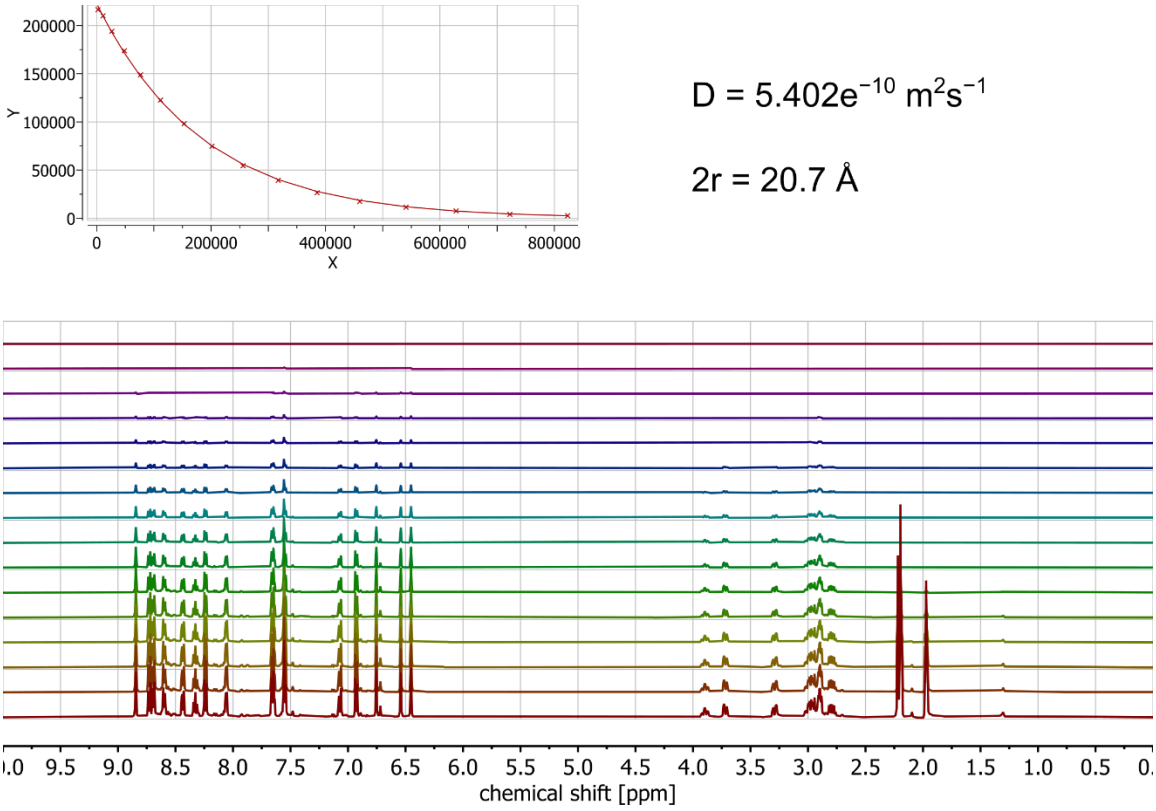

Figure S87. ^{1}H DOSY NMR spectra (500 MHz, CD_3CN, 8 mM, 298 K, D_{20} = 75 ms) of Zn_2**L** under ambient conditions with the diffusion parameter *D* fitted manually to afford $D_{amb.}$ = 5.402 · 10^{-10} m^2s^{-1} ($d_{amb.}$ = 20.7 Å).

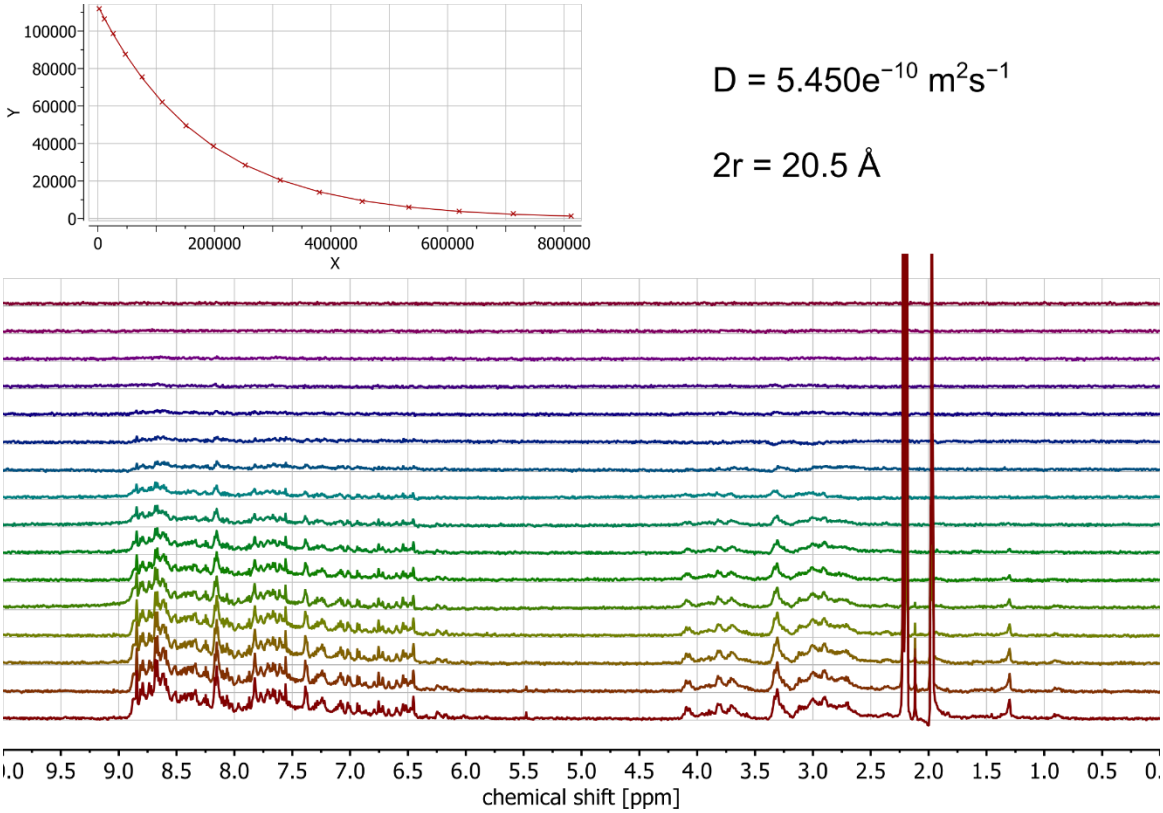

Figure S88. ^{1}H DOSY NMR spectra (500 MHz, CD_3CN, 8 mM, 298 K, D_{20} = 75 ms) of Zn_2**L** after *ex-situ* irradiation with 405 nm for 5 minutes with the diffusion parameter *D* fitted manually to afford D_{405} = 5.450 10^{-10} m^2s^{-1} (d_{405} = 20.5 Å).

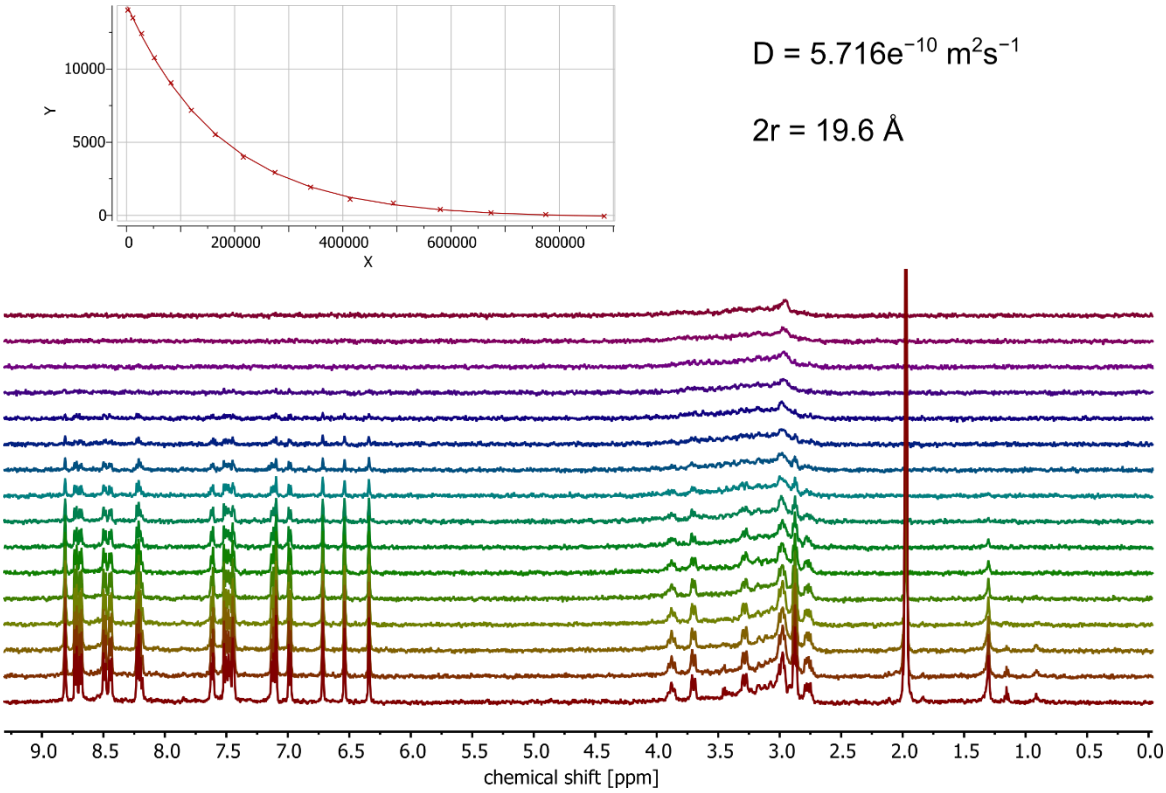

Figure S89. ^{1}H DOSY NMR spectra (500 MHz, CD_3CN, 1 mM, 298 K, D_{20} = 75 ms) of ZnFe**L** under ambient conditions. Due to the low concentration, the conversion to a 2D plot fails and the diffusion parameter *D* was fitted manually to afford $D_{amb.} = 5.716 \cdot 10^{-10}$ m^{2}s^{-1} ($d_{amb.}$ = 19.6 Å).

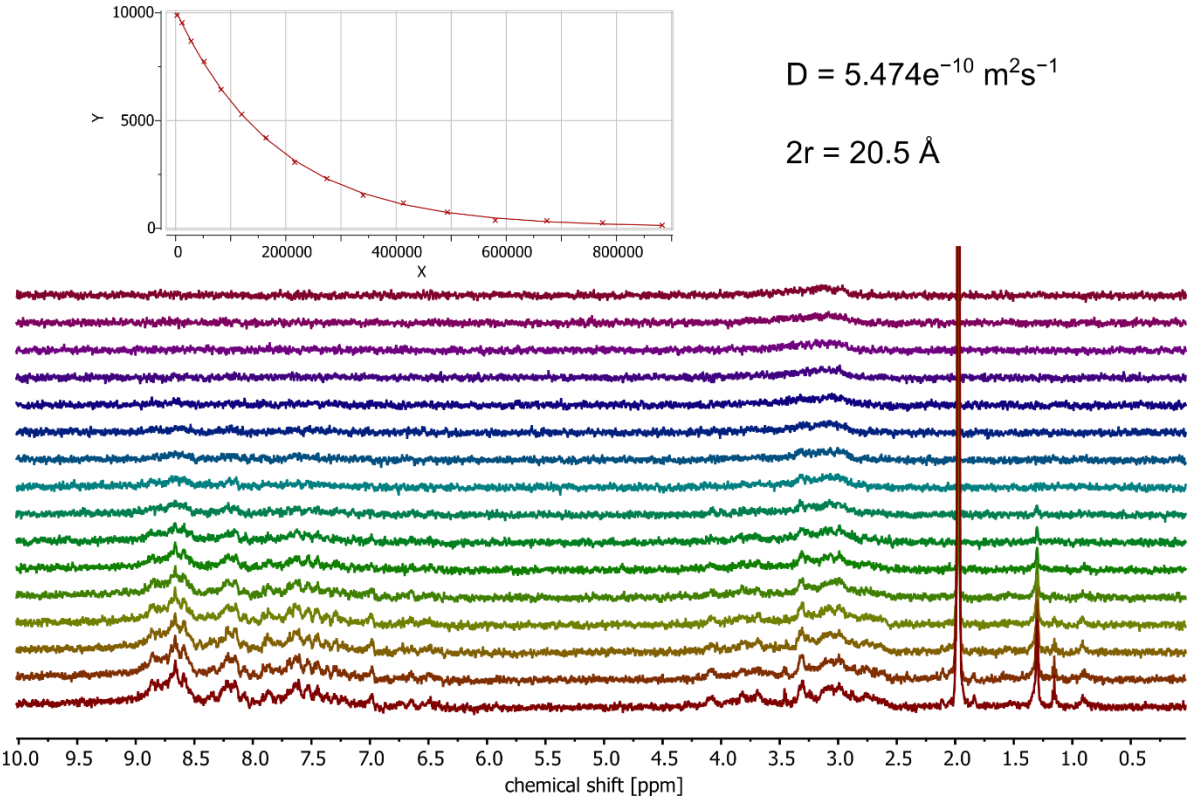

Figure S90. ^{1}H DOSY NMR spectra (500 MHz, CD_3CN, 1 mM, 298 K, D_{20} = 75 ms) of ZnFe**L** after irradiation with 405 nm for 5 minutes. Due to the low concentration, the conversion to a 2D plot fails and the diffusion parameter *D* was fitted manually to afford $D_{405} = 5.474 \cdot 10^{-10}$ m^{2}s^{-1} (d_{405} = 20.5 Å).

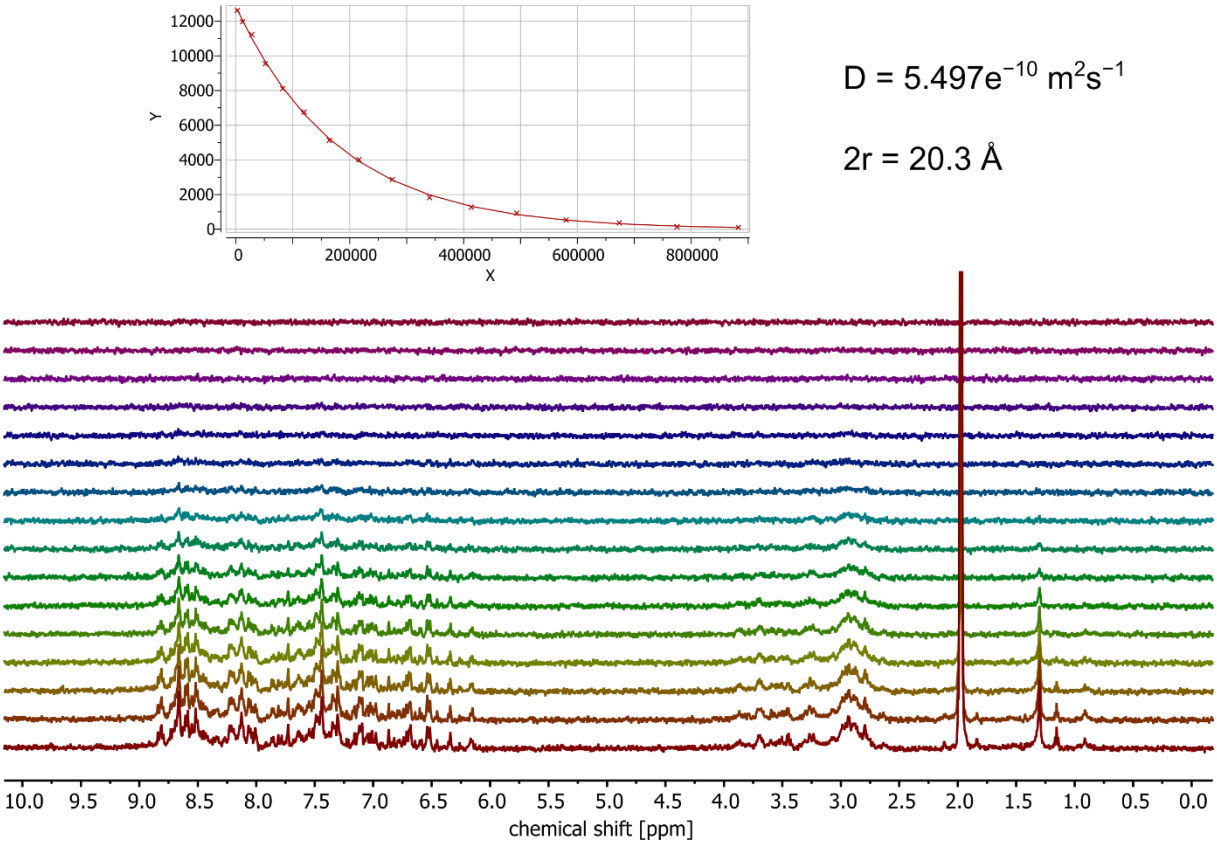

Figure S91. ^{1}H DOSY NMR spectra (500 MHz, CD_3CN, 1 mM, 298 K, D_{20} = 75 ms) of ZnFe**L** after *ex-situ* irradiation with 515 nm for 5 minutes. Due to the low concentration, the conversion to a 2D plot fails and the diffusion parameter *D* was fitted manually to afford $D_{515} = 5.497 \cdot 10^{-10}$ m^{2}s^{-1} (d_{515} = 20.3 Å).

S7.4.3 Photoswitching of ZnFe**L** followed by *in-situ* illumination NMR

To gain further insights into the kinetics of the photoisomerization processes within ZnFe**L** upon irradiation with 405 nm and white light, both processes were investigated via *in-situ* illumination of the samples inside the NMR spectrometer with spectra being recorded every 25 seconds (Figure S92 and Figure S93).

During 405 nm-light irradiation (Figure S92), the signals corresponding to ZnFe**L** disappeared following apparent first-order kinetics (Figure S92, bottom left, all traces). At the same time, at least three new species were formed (Figure S92, bottom right, purple (appears fast), teal (transient), yellow (appears slowly)). Two species appear immediately following apparent first-order kinetics (purple and teal, Figure S92, bottom right), with one of them disappearing again during the reaction (teal, Figure S92, bottom right). This disappearance coincides with the formation of the third species (yellow, Figure S92, bottom right), also following apparent first-order kinetics, indicating that the third species is formed out of the second species. Due to strong signal overlap, no further insights could be gained.

During irradiation of i-*E*-ZnFe**L** with white light (Figure S93), the signals corresponding to the two species formed in the first irradiation step (i-*E*-ZnFe**L**, compare Figure S92) disappear following apparent first-order kinetics (green, teal, Figure S93, bottom left). At the same time, at least two new species are formed (yellow, green, Figure S93, bottom right). One species appears slowly (yellow, bottom right), while the second species is the main product of the white-light irradiation and appears following apparent first-order kinetics (i-*Z*-ZnFe**L**; green, Figure S93, bottom right). Due to strong signal overlap, no further insights could be gained.

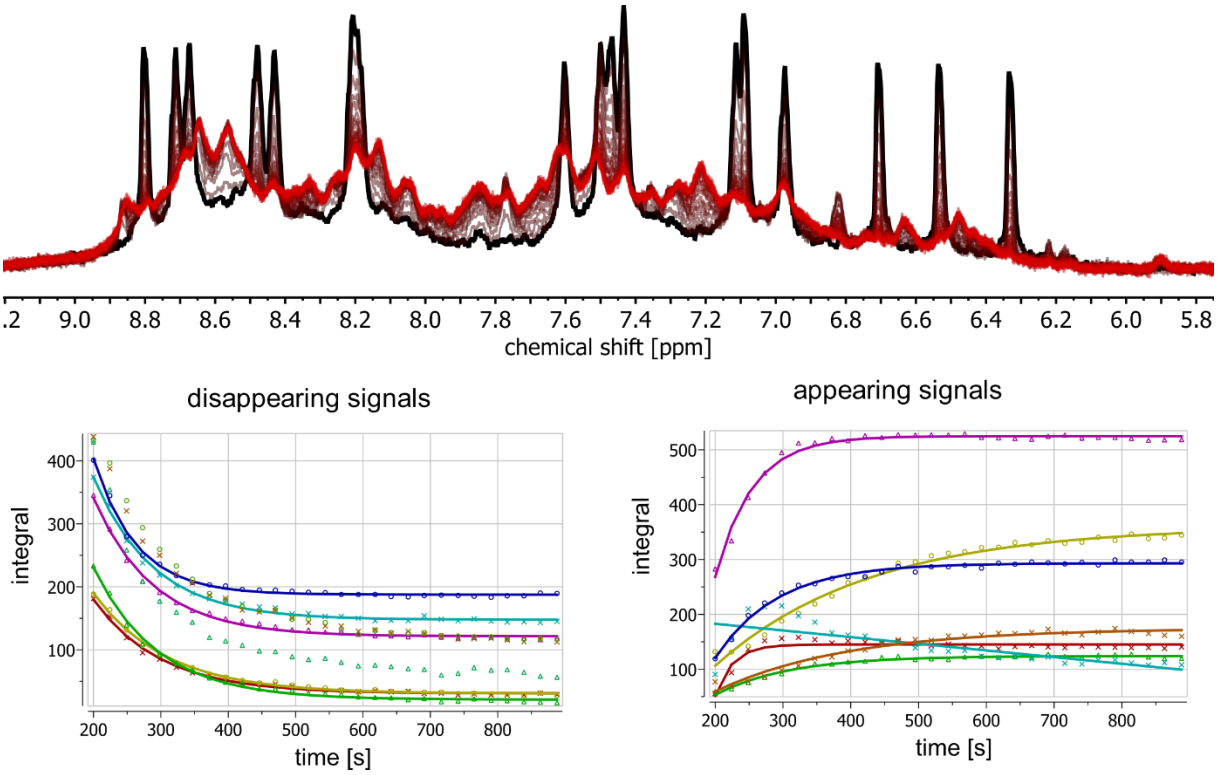

Figure S92. ^{1}H NMR spectra (700 MHz, CD_3CN, 1 mM, 298 K) of ZnFe**L** during *in-situ* irradiation with 405 nm (maroon to red, top) with spectra being measured every 25 seconds for a duration of 15 minutes. Bottom left: Plotted integrals of ZnFe**L** proton signals over time with data points fitted to first-order kinetics. Bottom right: Plotted integrals of appearing proton signals over time with data points fitted to first-order kinetics.

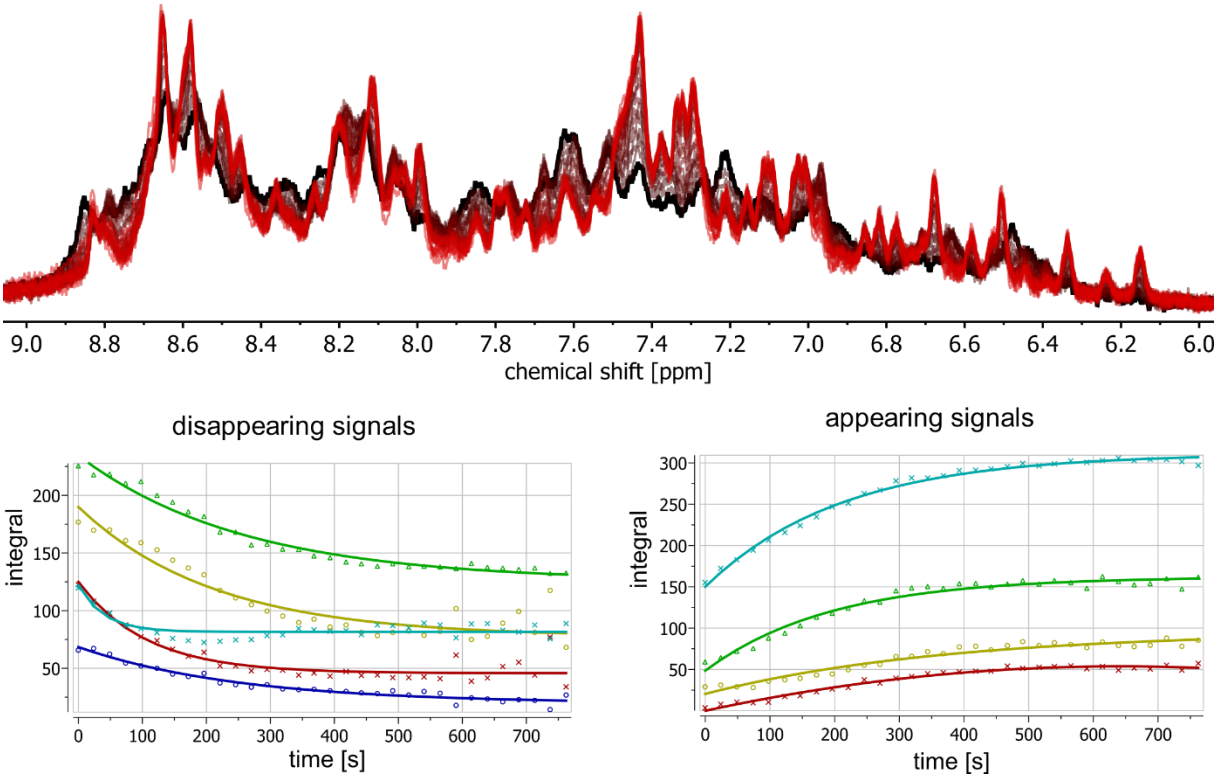

Figure S93. ^{1}H NMR spectra (700 MHz, CD_3CN, 1 mM, 298 K) of ZnFe**L** previously irradiated with 405 nm light following *in-situ* irradiation with white light (maroon to red, top) with a spectrum being recorded every 25 seconds for a duration of 13 minutes. Bottom left: Plotted integrals of i-*E*-ZnFe**L** proton signals over time with data points fitted to first-order kinetics. Bottom right: Plotted integrals of appearing proton signals over time with data points fitted to first-order kinetics.

S7.4.4 NMR kinetics of reforming ZnFe**L** from kinetically trapped state i-*Z*-ZnFe**L**

After the irradiation with 405 nm (Figure S92) and white light (Figure S93) the irradiation ceased and the dark state kinetics of the sample were observed (Figure S94). Over the course of 4.5 hours, only small changes were observed. One group of signals decreased in intensity (green, Figure S94, bottom left) while another group of signals increased in intensity (teal, Figure S94, bottom right), both following apparent first-order kinetics. No significant amount of the starting species ZnFe**L** is observed, and it is not the species that appears, indicating that a stable kinetic trap has been reached, and the mixture of isomers slowly converts into a more stable isomer, that is not the thermodynamic ground state.

In a separate experiment, a sample was consecutive irradiated *ex-situ* with 405 nm and white light and the relaxation was followed by high-temperature ^{1}H NMR at 65 °C (Figure S95). Due to the time required for shimming the magnetic field, the measurement started slightly delayed, and a significant amount of the thermodynamic ground state was already present when the measurement started (approx. 40%). All signals disappear and appear following apparent first-order kinetics (Figure S96).

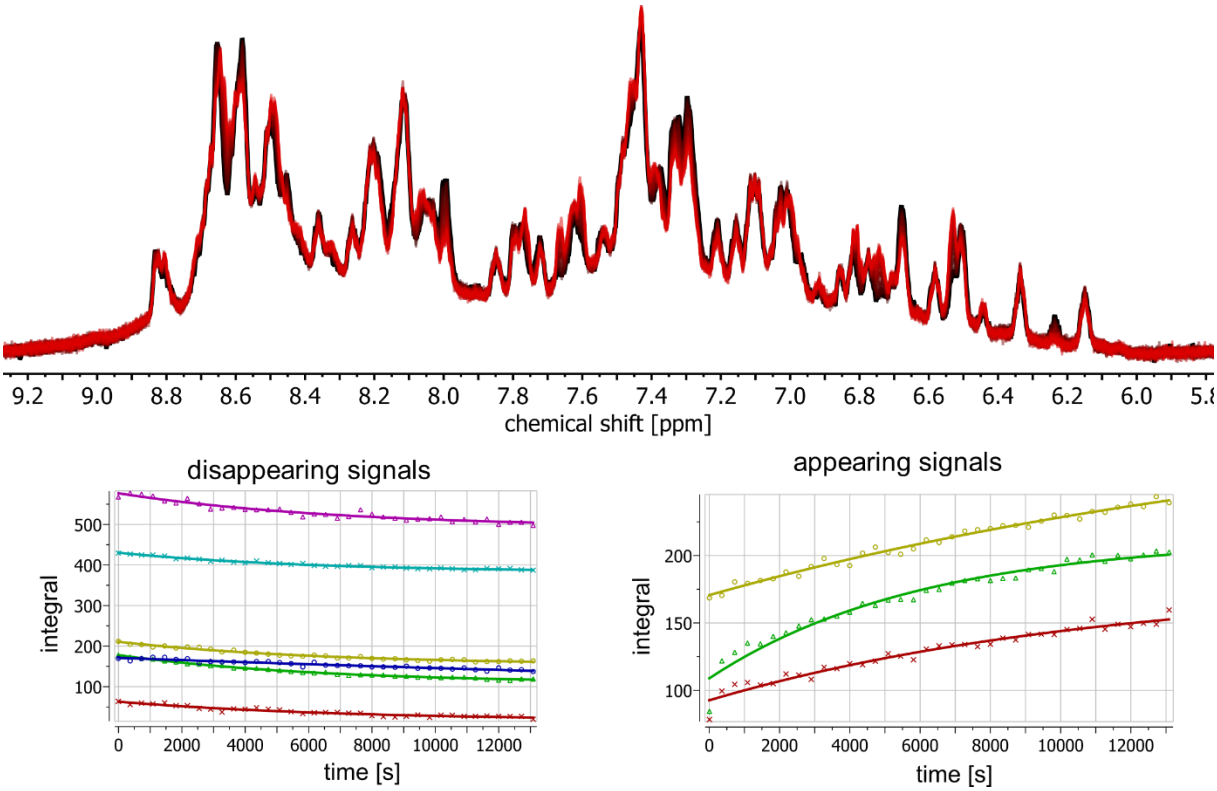

Figure S94. ^{1}H NMR spectra (700 MHz, CD_3CN, 1 mM, 298 K) of ZnFe**L** after consecutive 405 nm and white-light irradiation following thermal structure conversion at 298 K over 230 minutes with a spectrum recorded every 5 minutes (top, maroon to red). Bottom left: Plotted integrals of i-*Z*-ZnFe**L** proton signals over time with data points fitted to first-order kinetics. Bottom right: Plotted integrals of appearing proton signals over time with data points fitted to first-order kinetics. In the dark, a slow conversion of all signals into a second set of signals can be observed. This process follows apparent first-order kinetics.

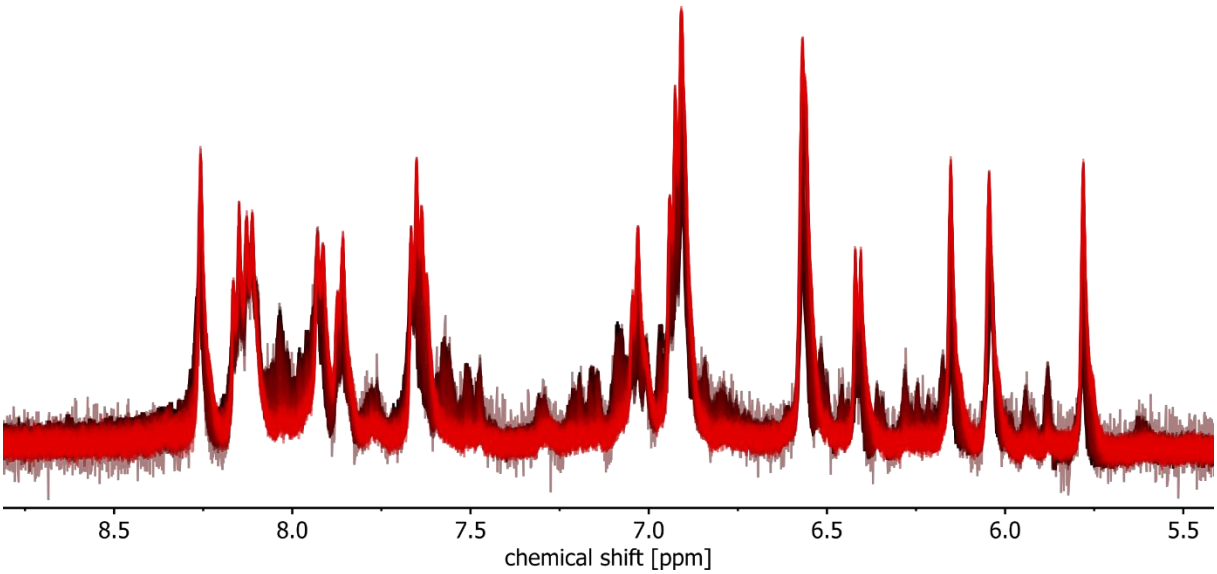

Figure S95. High-temperature ^{1}H NMR spectra (500 MHz, CD_3CN, 1 mM, 338 K) of ZnFe**L** after consecutive *ex-situ* irradiation with 405 nm and white light following conversion of i-*Z*-ZnFe**L** to ZnFe**L** over 4 hours with a spectrum being recorded every minute for the first hour and every 3 minutes after that (maroon to red). At 338 K, the conversion of the formerly kinetically trapped species into the ground state of ZnFe**L** can be observed to follow apparent first-order kinetics (Figure S96).

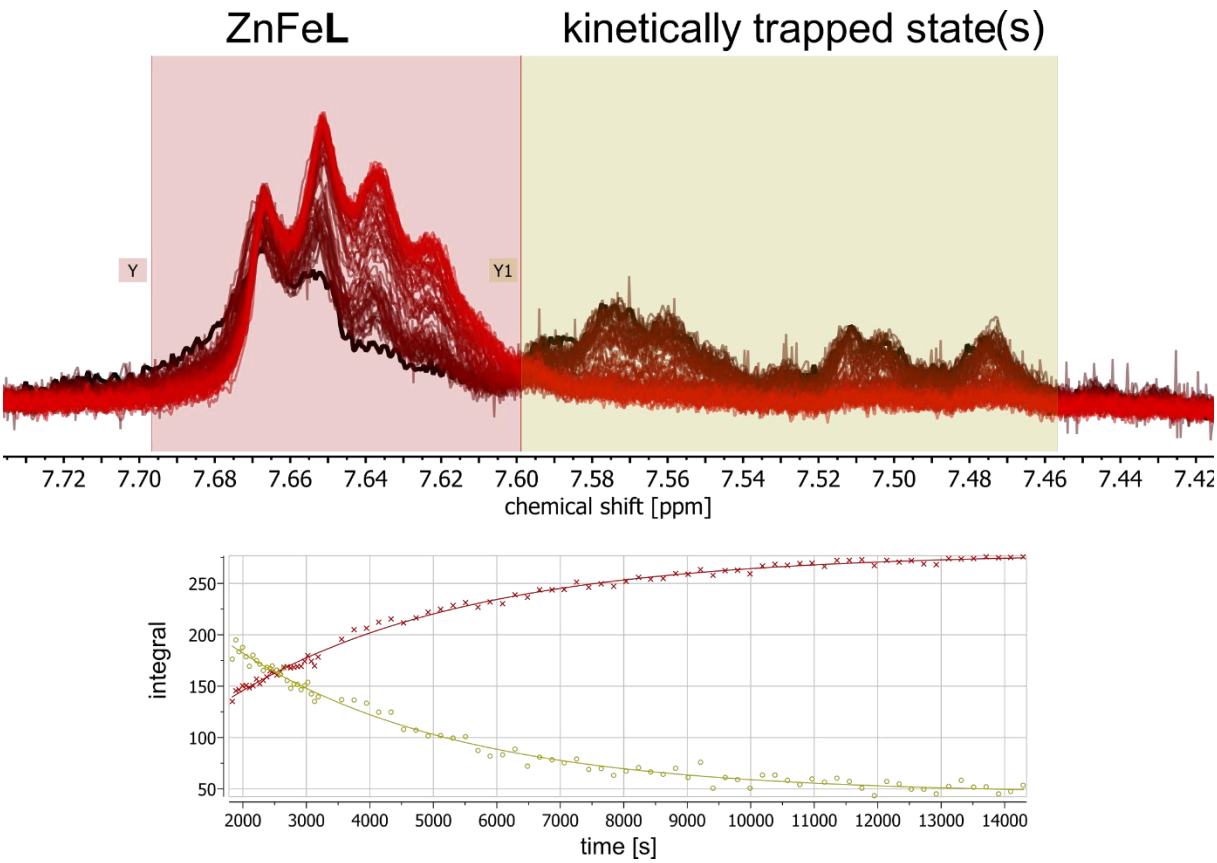

Figure S96. Partial high-temperature ^{1}H NMR spectra (500 MHz, CD_3CN, 1 mM, 338 K) of ZnFe**L** after consecutive *ex-situ* irradiation with 405 nm and white light following conversion of i-*E*-ZnFe**L** to ZnFe**L** over 4 hours with a spectrum being recorded every minute for the first hour and every 3 minutes after that (top, maroon to red, compare Figure S95). Bottom: Plotted integrals of i-*Z*-ZnFe**L** (yellow) and ZnFe**L** (red) proton signals over time with data points fitted to first-order kinetics. Formation of ZnFe**L** helicate follows apparent first-order kinetics with no intermediates being observed

S7.4.5 Low-temperature NMR of the switched states

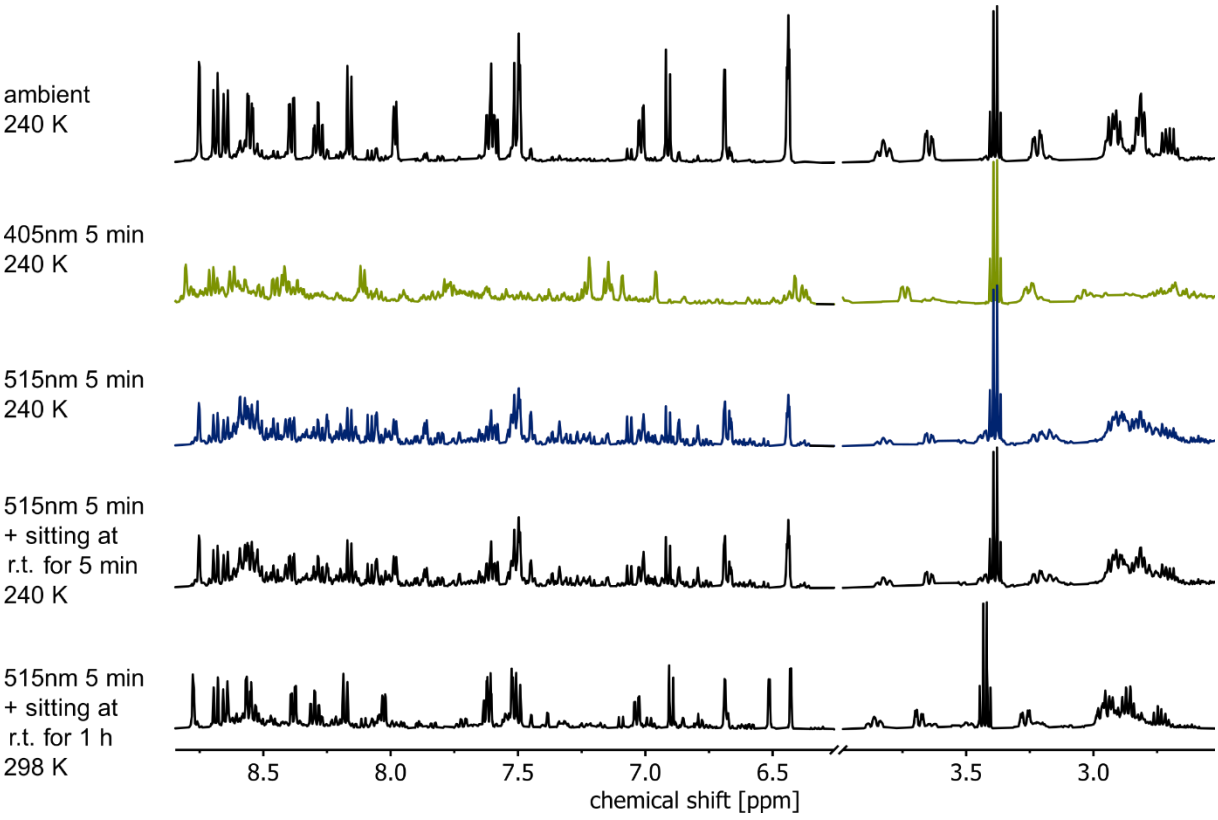

Figure S97. Variable-temperature ^{1}H NMR spectra (500 MHz, CD_3CN, 1 mM) of Zn_2**L** under ambient conditions (240 K), after *ex-situ* irradiation with 405 nm light for 5 min (240 K), after *ex-situ* 515 nm light irradiation for 5 min (240 K), and after leaving the irradiated sample at room temperature for 5 min and 1 hour (240 K and 298 K, respectively; top to bottom). Compared to switching experiments at room temperature (Figure S83), the spectrum after 405 nm irradiation shows many sharp and well-defined signals instead of broadened signals, indicating that a dynamic process was occurring at room temperature. Back-switching was fully reversible at room temperature. In contrast, a spectrum similar to that of kinetically trapped ZnFe**L** is observed after back-switching at low temperatures. Warming the sample up to room temperature reforms the initial spectrum for Zn_2**L**. This indicates that the M_2**L** complexes undergo an isomerization during the photoswitching process, resulting in a kinetically trapped state. Reforming the initial state likely involves dissociation of bipyridine ligands, as the much more labile zinc complex already reforms at a much lower temperature (5 min at 25°C as compared to 5 hours at 65 °C for ZnFe**L**).

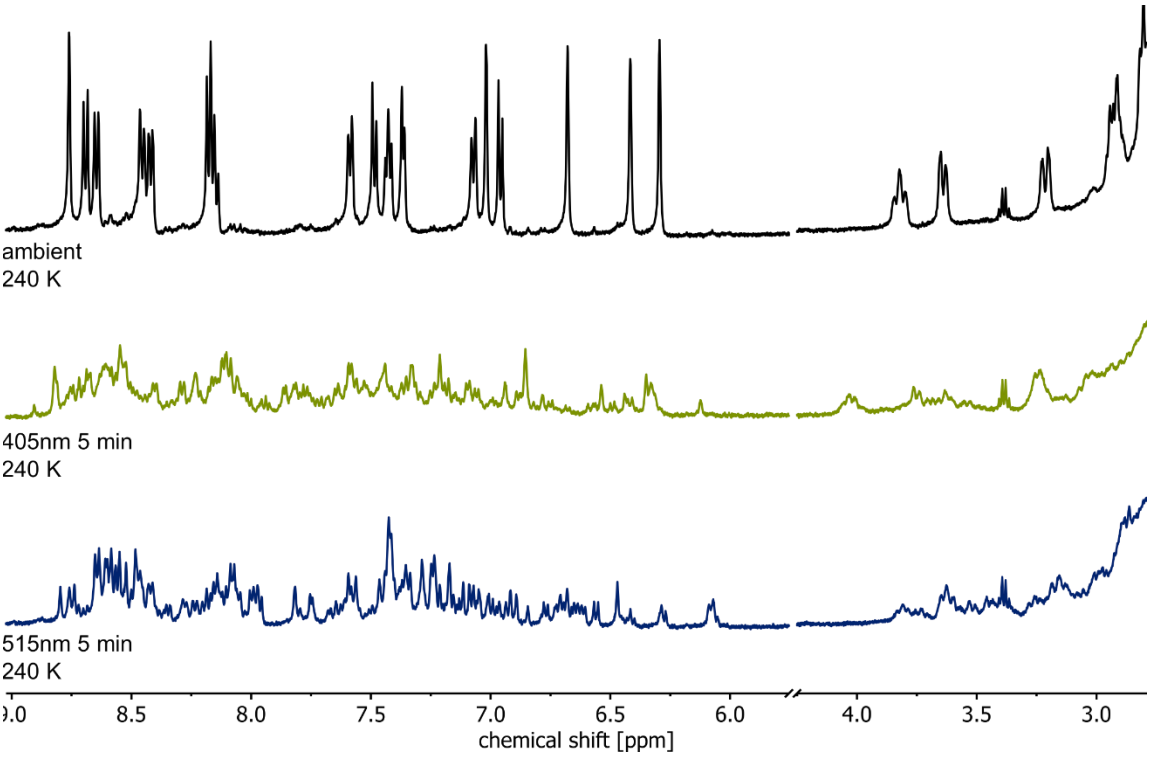

Figure S98. Low temperature ^{1}H NMR spectra (500 MHz, CD_3CN, 1 mM, 240 K) of ZnFe**L** under ambient conditions, after irradiation with 405 nm light for 5 min, and after 515 nm light irradiation for 5 min (top to bottom). Compared to switching experiments at room temperature (Figure S85), the spectrum after 405 nm irradiation shows many sharp and well-defined signals instead of broadened signals, indicating that a dynamic process was occurring at room temperature. The spectrum obtained after back-switching looks very similar to the one observed at room temperature, indicating that the irreversible transformation of the complex to the kinetically trapped state during photoswitching remains fast at low temperatures.

S7.5 Photoswitching of helicates investigated by ESI$^+$ MS

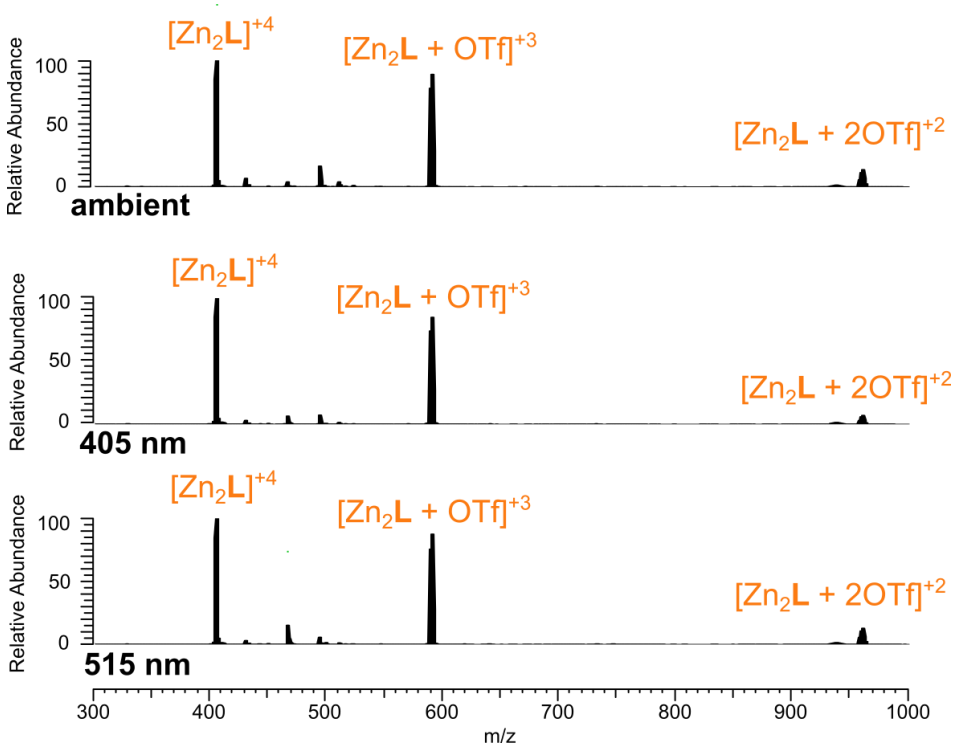

Figure S99. ESI$^+$ mass spectra (CH_3CN, 0.1 mM) of Zn_2**L** under ambient conditions and after irradiation with 405 nm and 515 nm light, respectively (top to bottom). After irradiation, no new peaks are observed, but the relative intensity of the $[Zn_2$**L** + 2OTf$]^{2+}$ peak decreases slightly after irradiating with 405 nm and recovers when switching back with 515 nm.

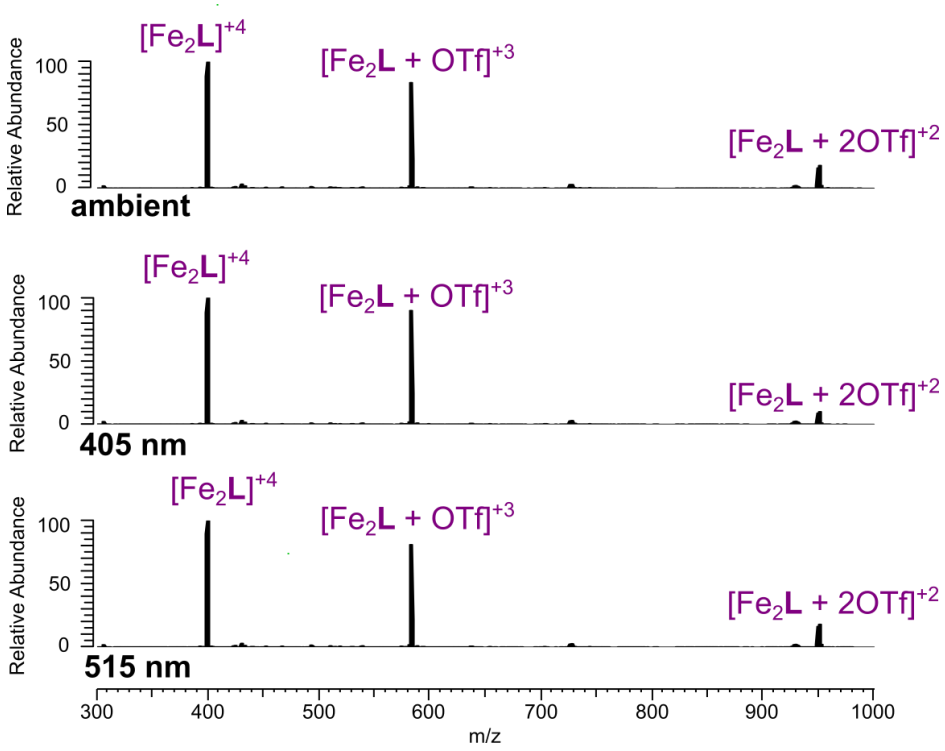

Figure S100. ESI$^+$ mass spectra (CH_3CN, 0.1 mM) of Fe_2**L** under ambient conditions and after irradiation with 405 nm and 515 nm light, respectively (top to bottom). No new peaks are observed after irradiation but the relative intensity of the $[Fe_2$**L** + 2OTf$]^{2+}$ peak decreases slightly after irradiating with 405 nm and recovers when switching back with 515 nm.

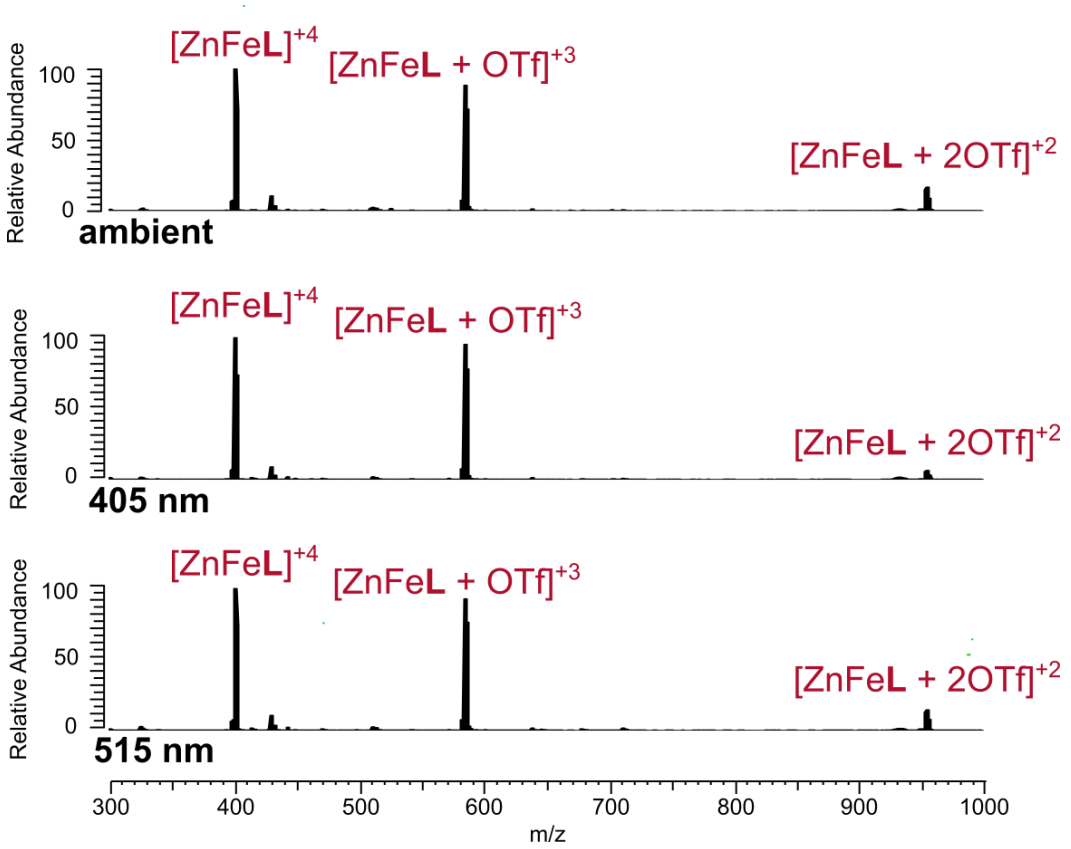

Figure S101. ESI(+) mass spectra (CH_3CN, 0.1 mM) of ZnFe**L** under ambient conditions and after irradiation with 405 nm and 515 nm light, respectively (top to bottom). No new peaks are observed after irradiation but the relative intensity of the $[ZnFe\mathbf{L} + 2OTf]^{2+}$ peak decreases slightly after irradiating with 405 nm and recovers when switching back with 515 nm.

S7.6 Possible isomerisations observed during photoswitching

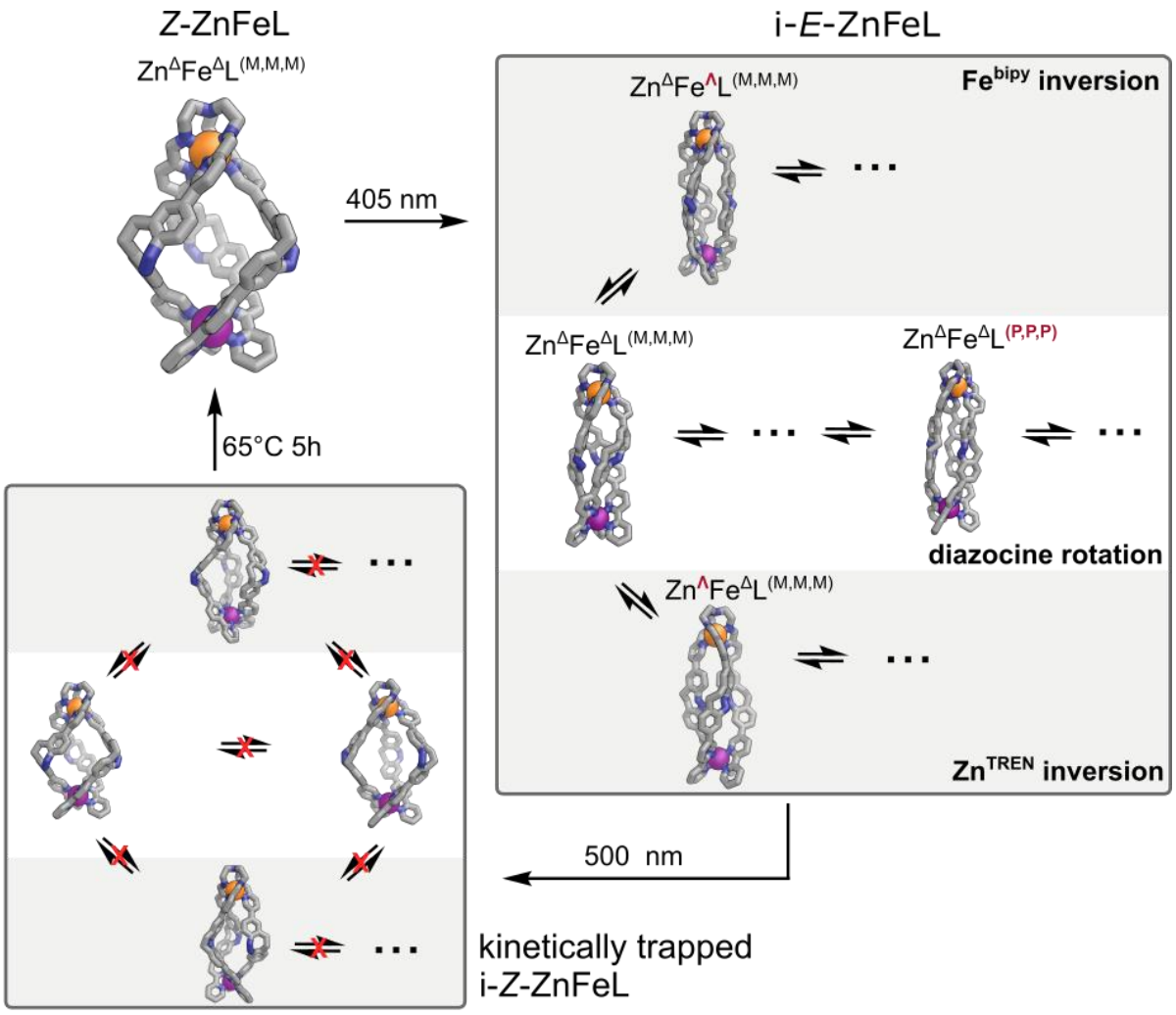

Figure S102. Potential isomerisations of the helicate during photoswitching, using ZnFe**L** as an example. Mass spectrometry (see section S7.5) and DOSY NMR (see section S7.4.2) indicate that both approximate size and molecular formula are retained, but in-situ illuminated NMR spectroscopy (see section S7.4.3) indicates that photoswitching with 405 nm forces an isomerisation reaction, producing multiple products. Back-switching with 500 nm/white light brings the photoswitches back into the *Z* state, and the isomerisation of the helical structure is kinetically trapped. Reforming the initial structure requires heating with the temperature and time of heating strongly depending on the metal in the bipyridine binding site, indicating that breaking of the M−bipy bonds is the rate determining step for the reformation of the initial helicate. Potential isomerisations could occur at the two metal centres that could invert their stereochemistry or by rotation of the diazocines around sigma bonds which should exhibit a much lower barrier in the *E* state than in the *Z* state, where the inversion of the N=N double bond would be required.

S8 Irradiation of ZnFe**L** with full spectrum light for long periods

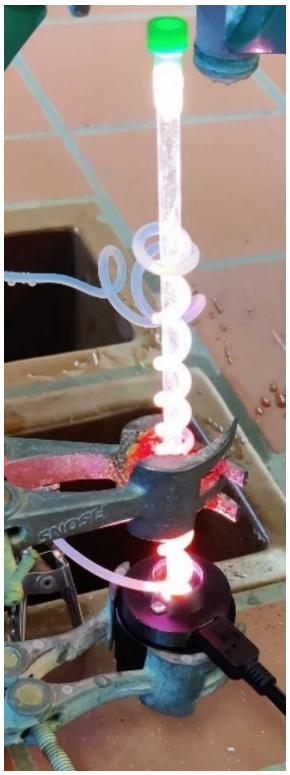

Figure S103. Experimental setup for the long-term irradiation of ZnFe**L** with white light. An NMR sample (1 mM, CD_3CN) was placed on the white LED and flexible tubing was wrapped around the NMR tube. Cold water (approximately 15 °C) was circulated through the tubing to prevent the sample from overheating during the prolonged irradiation time.

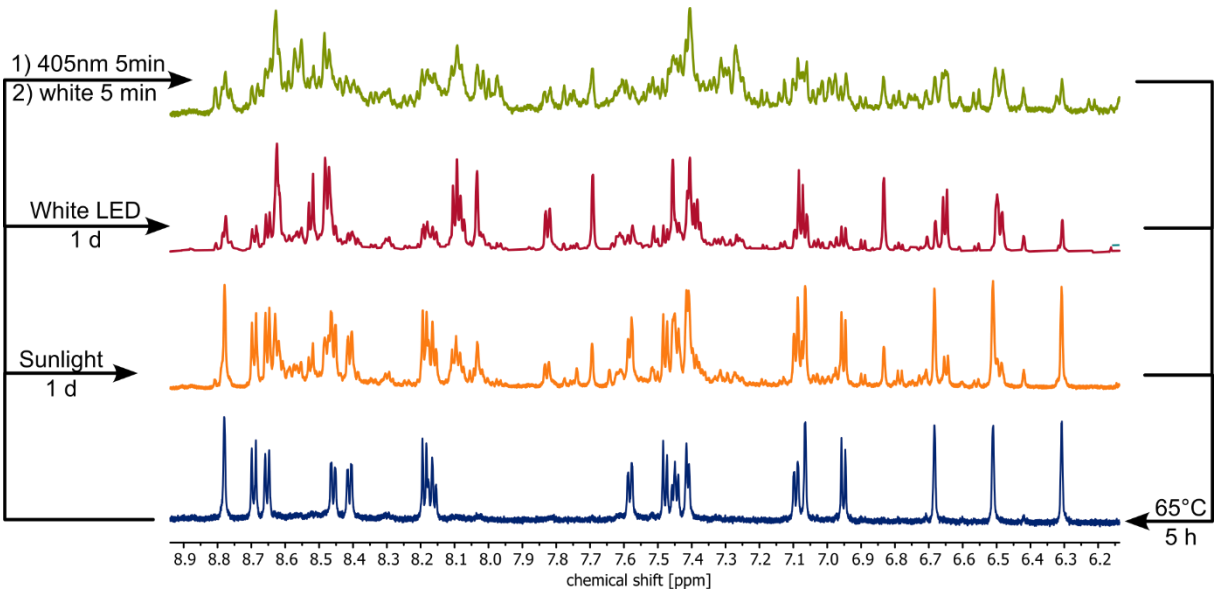

Figure S104. Partial ^1H NMR spectra (700 MHz, CD_3CN, 1 mM, 298 K) of ZnFe**L** before and after irradiation with sunlight for one winter day, a white LED for 24 hours, and consecutive irradiation with 1) 405 nm for 5 minutes and 2) white light for 5 minutes. Despite visible light being unable to accumulate meta-stable *E*-diazocines, a drastic photoinduced change is observed.

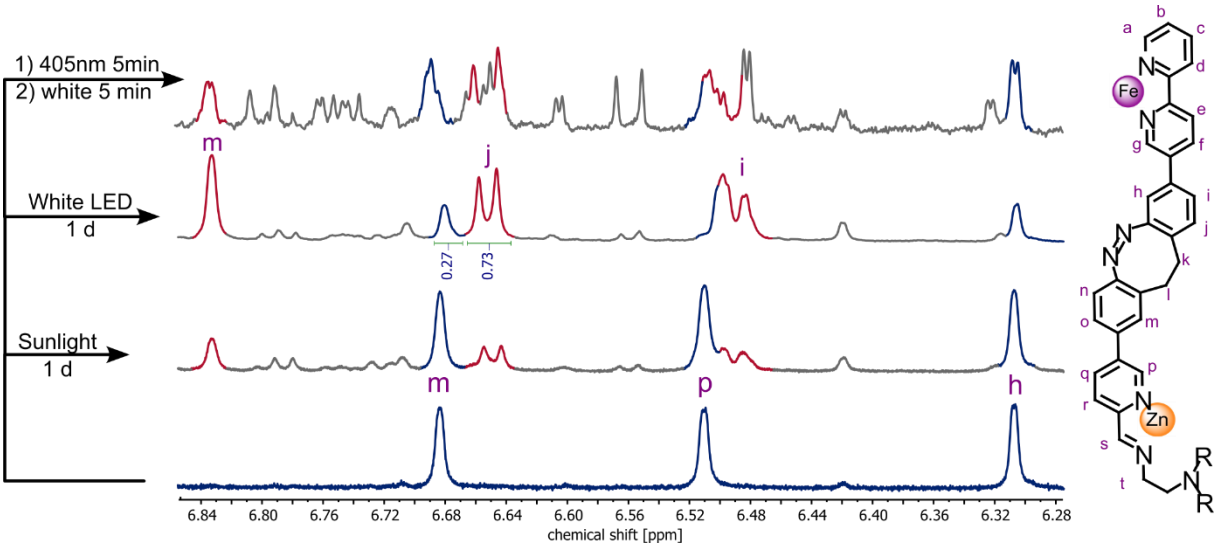

Figure S105. Partial ^{1}H NMR spectra (700 MHz, CD_3CN, 1 mM, 298 K) of ZnFe**L** before and after irradiation with sunlight for one winter day, a white LED for 24 hours, and consecutive irradiation with 1) 405 nm for 5 minutes and 2) white light for 5 minutes. The ground state structure and the new structure are highlighted in blue and red, respectively.

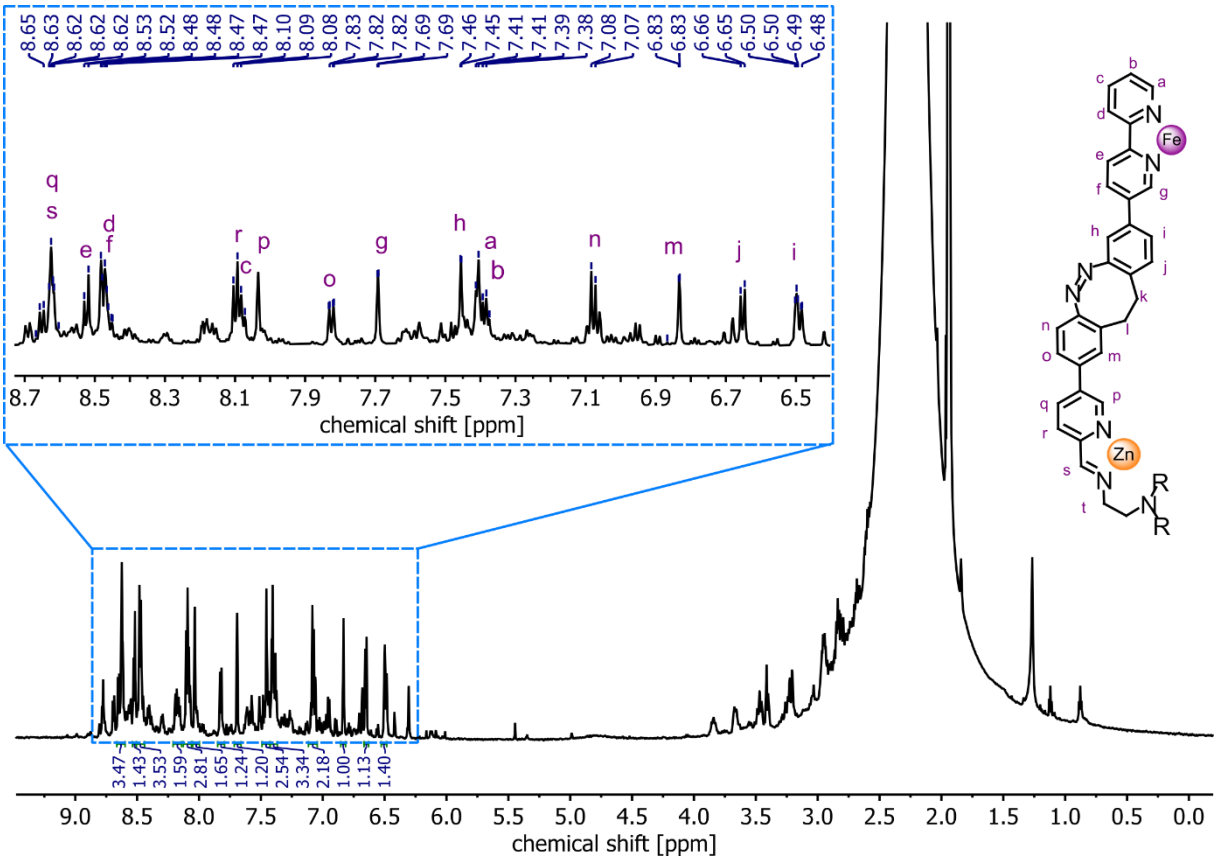

Figure S106. ^{1}H NMR spectrum (700 MHz, CD_3CN, 298 K) of Fe_2**L** after 24 hours white light irradiation.

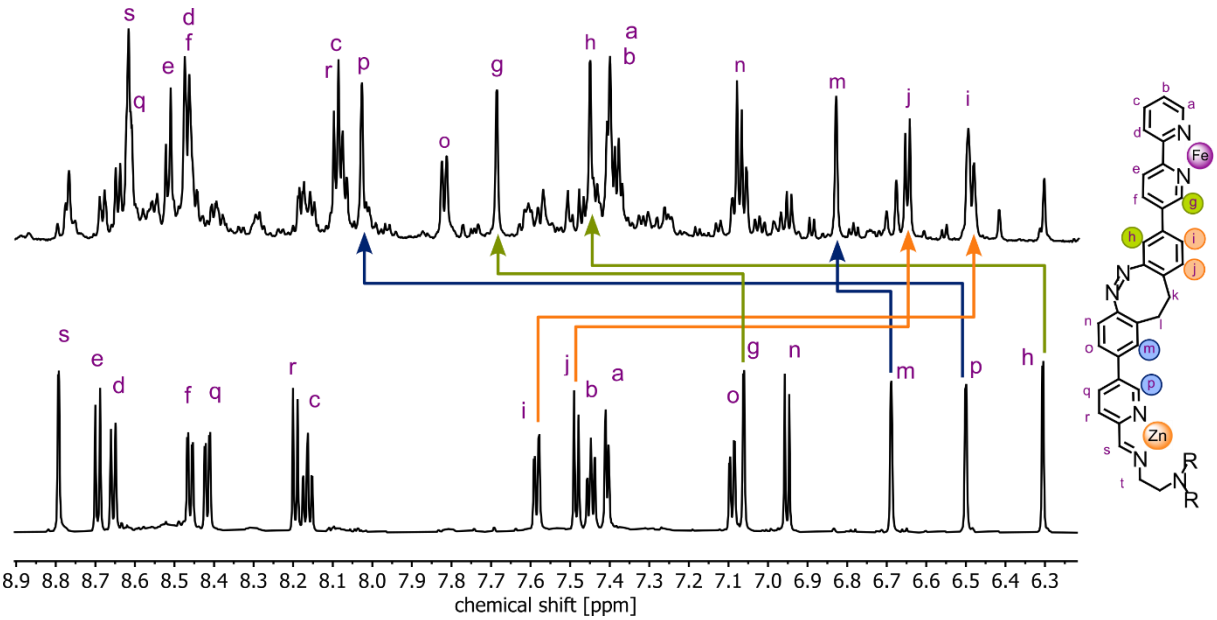

Figure S107. Partial ^{1}H NMR spectra (700 MHz, CD_3CN, 1 mM, 298 K) of ZnFe**L** before (bottom) and after white light irradiation for 24 hours (top) with arrows indicating the changes for highlighted proton signals.

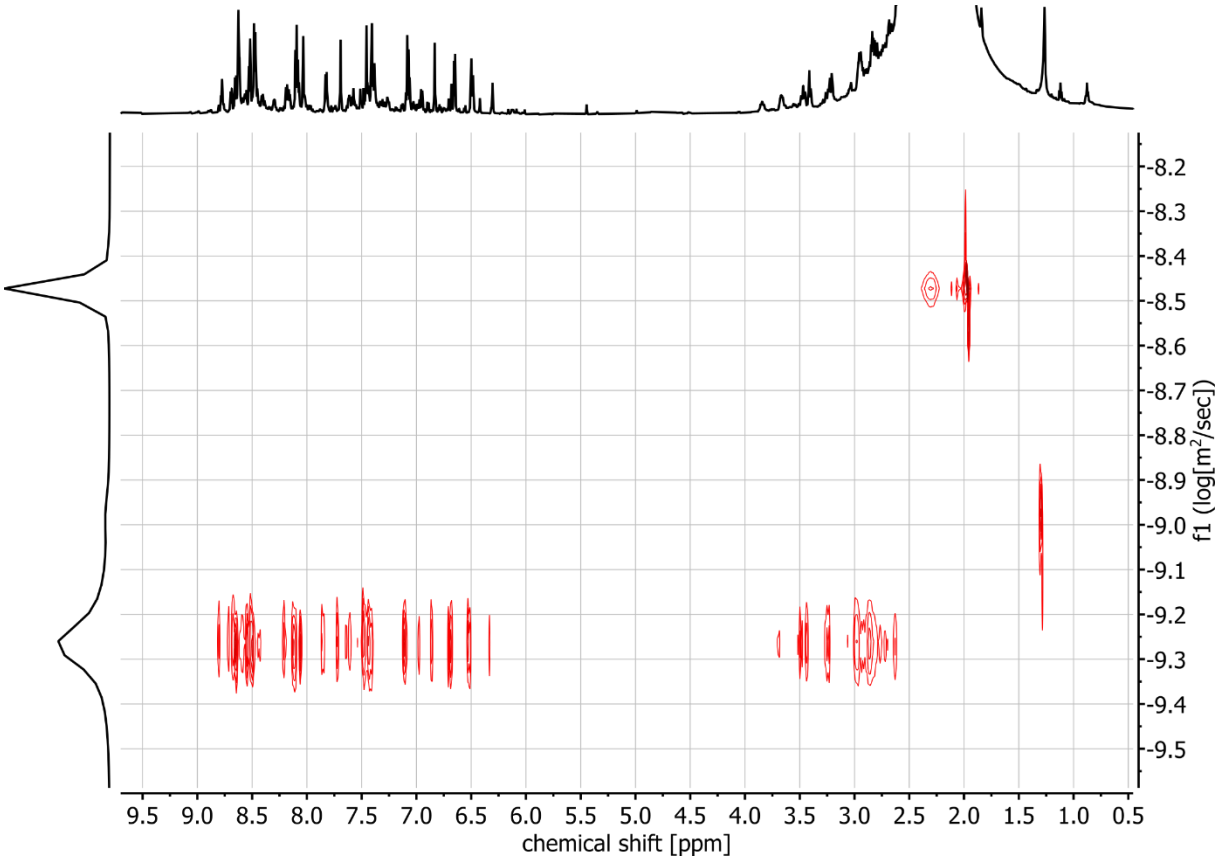

Figure S108. ^{1}H DOSY spectrum (700 MHz, CD_3CN, 1 mM, 298 K, D_{20} = 50 ms) of ZnFe**L** after 24 hours white light irradiation.

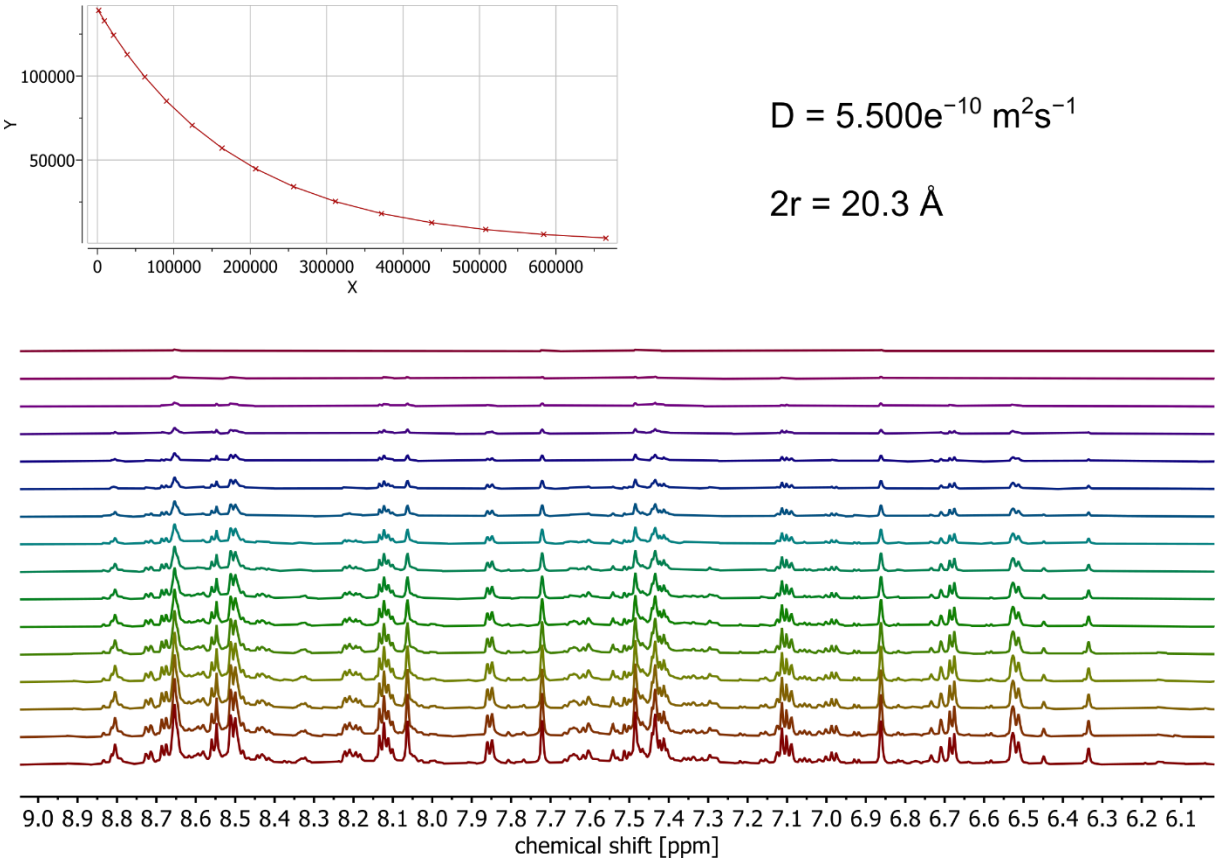

Figure S109. ^{1}H DOSY spectrum (700 MHz, CD_3CN, 1 mM, 298 K, D_{20} = 50 ms) of ZnFe**L** after 24 hours white light irradiation.

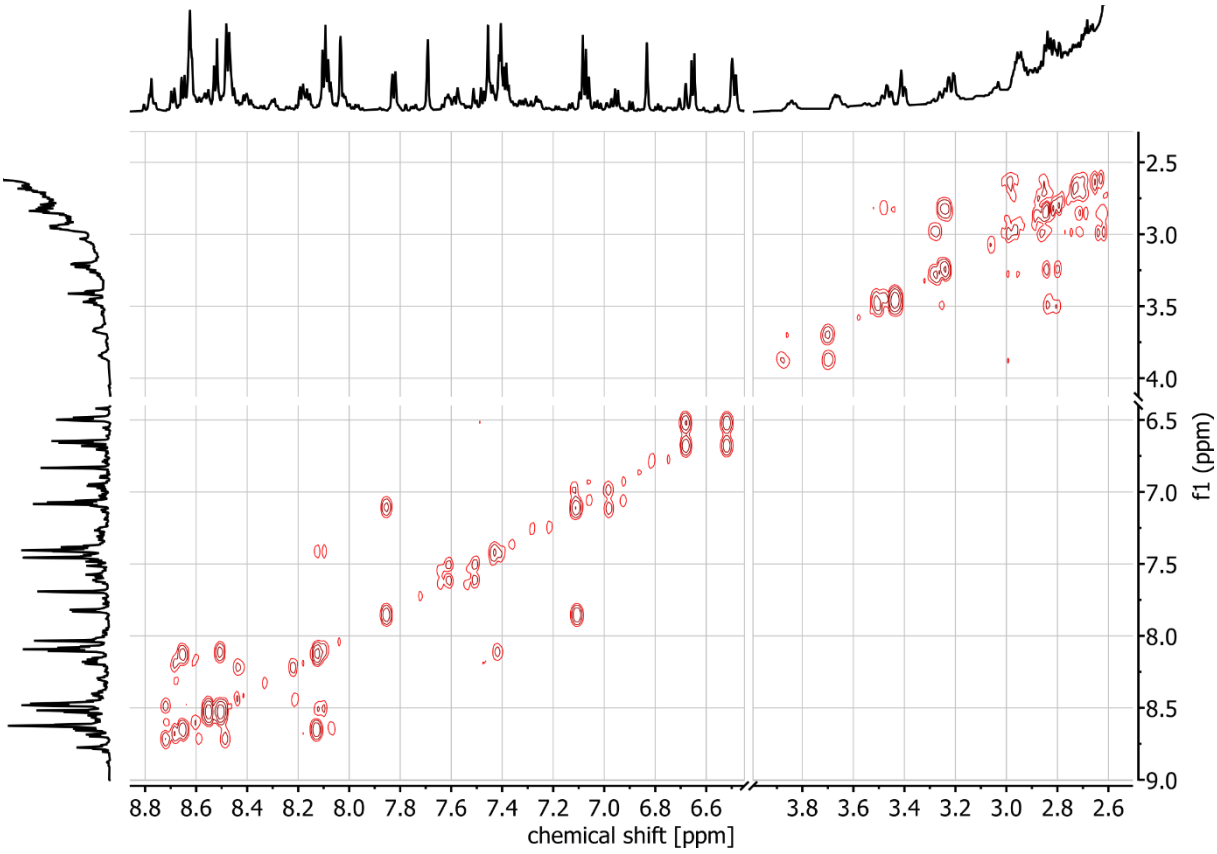

Figure S110. $^{1}H,^{1}H$ COSY spectrum (700 MHz, CD_3CN, 298 K) of ZnFe**L** after 24 hours white light irradiation.

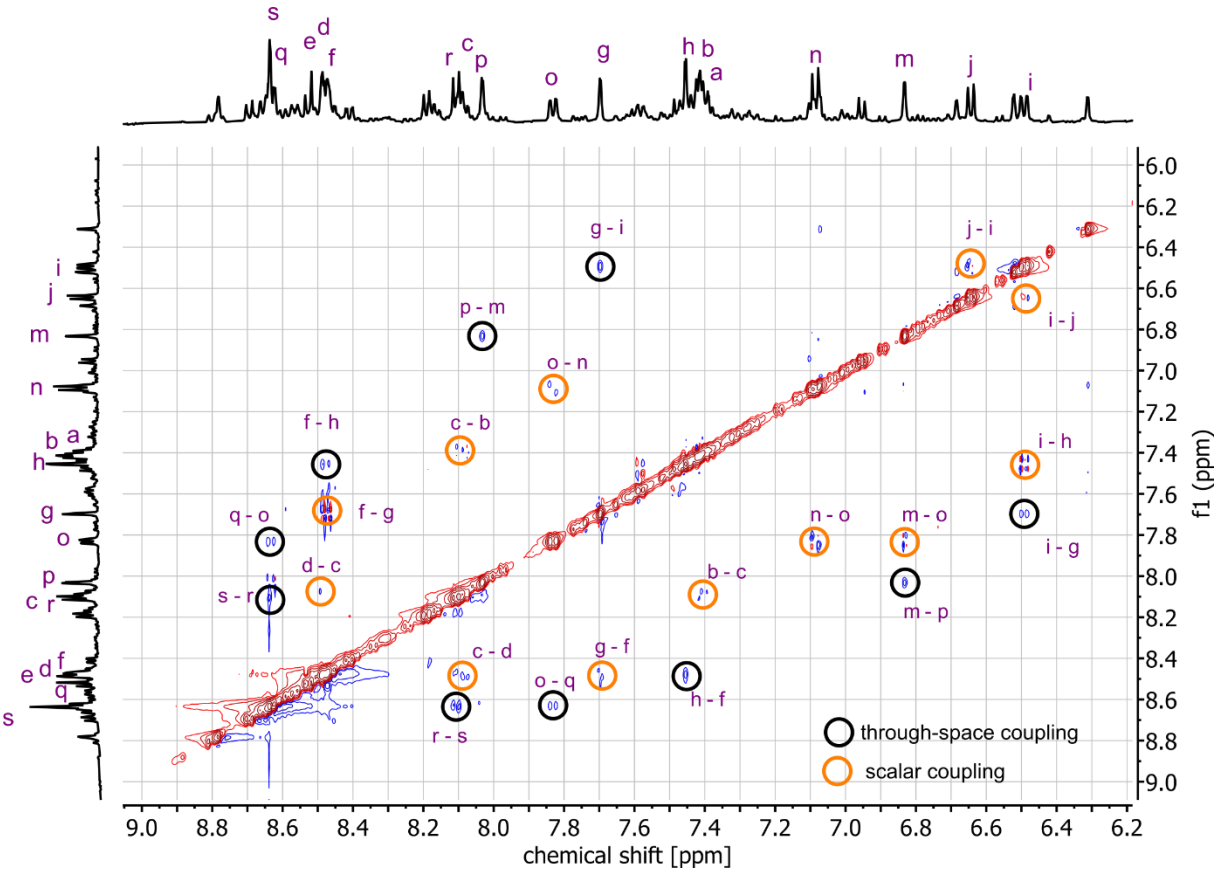

Figure S111. $^{1}H,^{1}H$ ROESY spectrum (500 MHz, CD_3CN, 298 K) of ZnFe**L** after 24 hours white light irradiation.

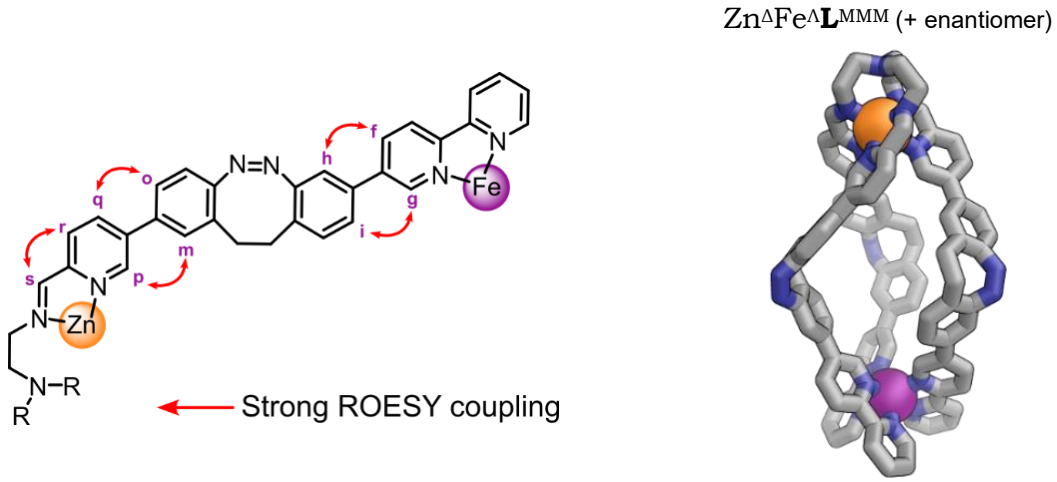

Figure S112. Through space interactions observed by ROESY NMR (Figure S111) show that white light irradiation results in the ZnΔFeΛ**L**^{MMM} diastereomer (and its enantiomer), based on neighbouring hydrogen atoms in the computational structures (Table S15).

Table S15. Computational structures for the four remaining diastereomers of ZnFe**L** after ruling out mixed chirality ligands (Table S10) and ChemDraw representations of the ligand folding (for computational details see Section S6.3). Only ZnΔFeΛ**L**^{MMM} (and its enantiomer) show the correct folding that could give rise to the ^{1}H ROESY cross-peaks observed in Figure S111.

ZnΔFeΔ**L**^{MMM}	ZnΔFeΔ**L**^{PPP}	ZnΔFeΛ**L**^{MMM}	ZnΔFeΛ**L**^{PPP}
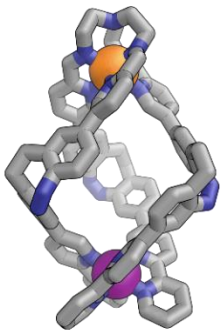 (+ enantiomer)	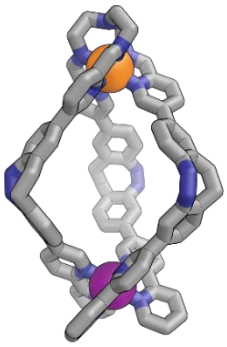 (+ enantiomer)	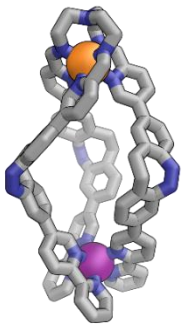 (+ enantiomer)	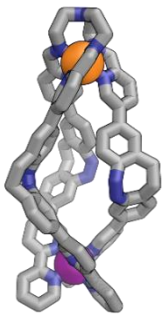 (+ enantiomer)
Ligand conformation in computational structure:			
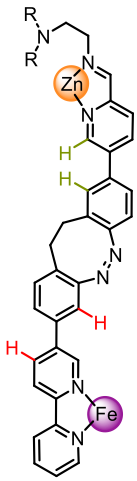	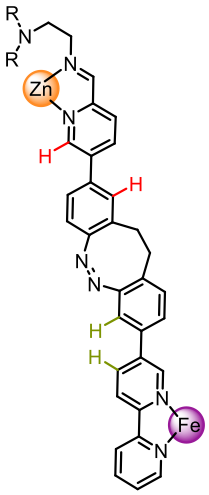	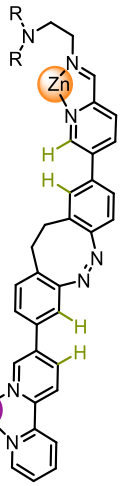	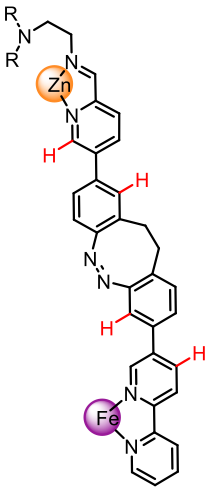
H-p and H-m are adjacent H-g and H-i are not adjacent	H-p and H-m not adjacent H-g and H-i are not adjacent	H-p and H-m are adjacent H-g and H-i are adjacent	H-p and H-m not adjacent H-g and H-i are not adjacent

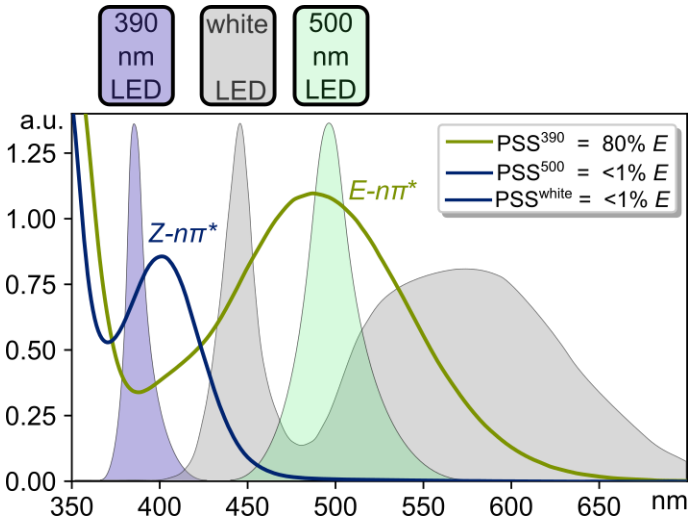

Figure S113. UV-vis spectrum of the diazocine chromophore (0.1 mM, CH_3CN) at the photostationary states after irradiation with 390 nm, 500 nm, and white light with an overlay of the normalized emission spectra of the LEDs used for irradiation, showing a small overlap of the white LED's emission spectrum with the *Z*-nπ* band and a large overlap with the *E*-nπ* band. This means that at the photostationary state of the white LED, the diazocine is constantly being switched into the *E*-state, but back switching is much faster due to the better spectral overlap, resulting in no significant accumulation of *E*-diazocine and a photostationary state identical to PSS^{500}.

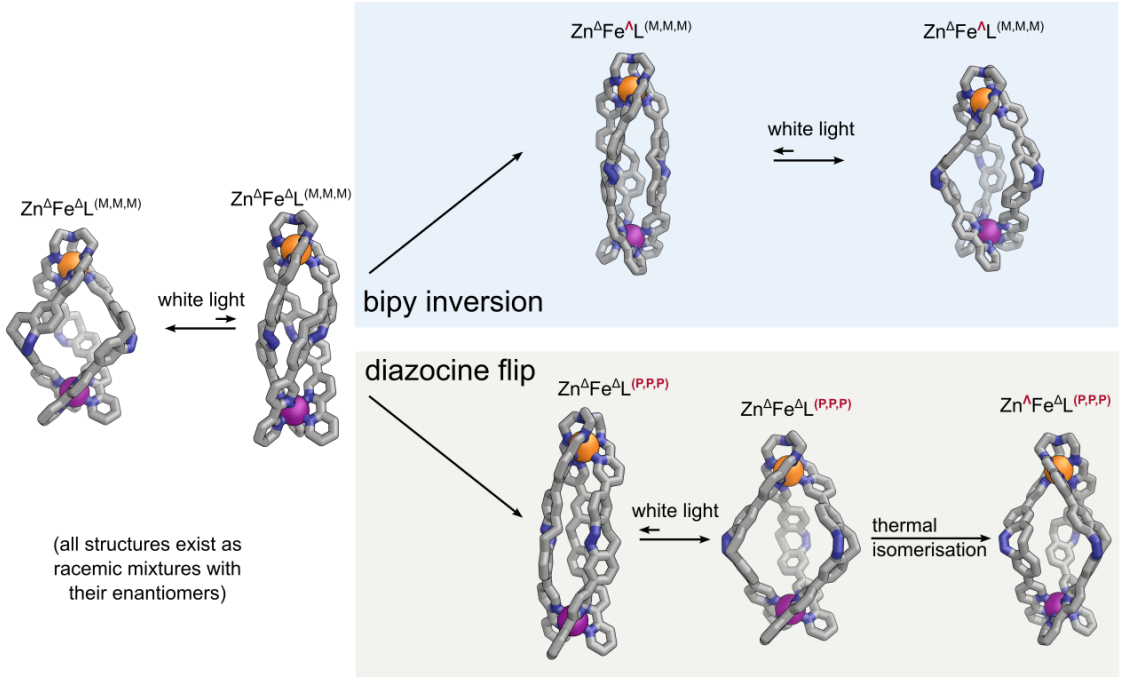

Figure S114. Postulated isomerisation pathways for the white light induced isomerisation of ZnFe**L** occurring at room temperature. Experimental data suggests the conversion of $Zn^{\Delta}Fe^{\Delta}\mathbf{L}^{MMM}$ (and its enantiomer) into $Zn^{\Delta}Fe^{\wedge}\mathbf{L}^{MMM}$ (and its enantiomer).

$Zn^{\Delta}Fe^{\Delta}L^{MMM}$ to $Zn^{\Delta}Fe^{\wedge}L^{MMM}$ isomerization may occur either by the inversion of the stereochemistry at the Fe^{bipy} centre in the switched *E*-helicate or by the rotation of the diazocine moieties in the *E*-helicate, followed by a stereoinversion at the Zn^{TREN} centre. The bipy-inversion path is supported by the observation that this binding site is destabilised in the *E*-state (Section S9), which would also accelerate Fe^{bipy} stereo isomerisation. However, the ligand dissociation/association potentially involved in the inversion of the Fe^{bipy} moiety seems to occur on a slower timescale spanning multiple hours at elevated temperatures (Section S9). The diazocine-flip Zn^{TREN}-inversion pathway is supported by the observation that isomerisation occurs within minutes, even at ambient temperature (Figure S85 and Figure S98), indicating that only low-energy barriers must be overcome in the process. Rotation around two single bonds, necessary for flipping the *E*-diazocine moieties, does not present a high energetic barrier, and the relatively labile coordinative bonds of Zn(II) do not create a significant barrier for Zn^{TREN} stereoisomerization. Additionally, the diazocine-flip mechanism may generate mixed chirality structures, potentially accounting for the complex spectra observed following the 405nm/white light switching. ^{1}H NMR data of Fe_2**L** (Figure S19) show strongly broadened signals for hydrogen atoms near the Fe^{TREN} centre, suggesting that dynamic processes may be occurring at room

temperature and that the M^{TREN} moiety might be relatively flexible, allowing for possible chiral inversion at room temperature. Comparing the two potentially isomerised metal centres, Zn^{TREN} presents a stronger coordination pocket but is a much more labile metal compared to Fe^{bipy}. The strongly distorted coordination sphere surrounding Zn^{TREN}, with a seventh nitrogen in close proximity to the Zn(II) cation in the crystal structure (Section S6.2), might further suggest the possibility of chirality inversion at room temperature. While these considerations may hint at the diazocine-flip Zn^{TREN}-inversion mechanism, there is no definitive experimental evidence for either reaction pathway, and the precise nature of the isomer conversion mechanism remains unclear.

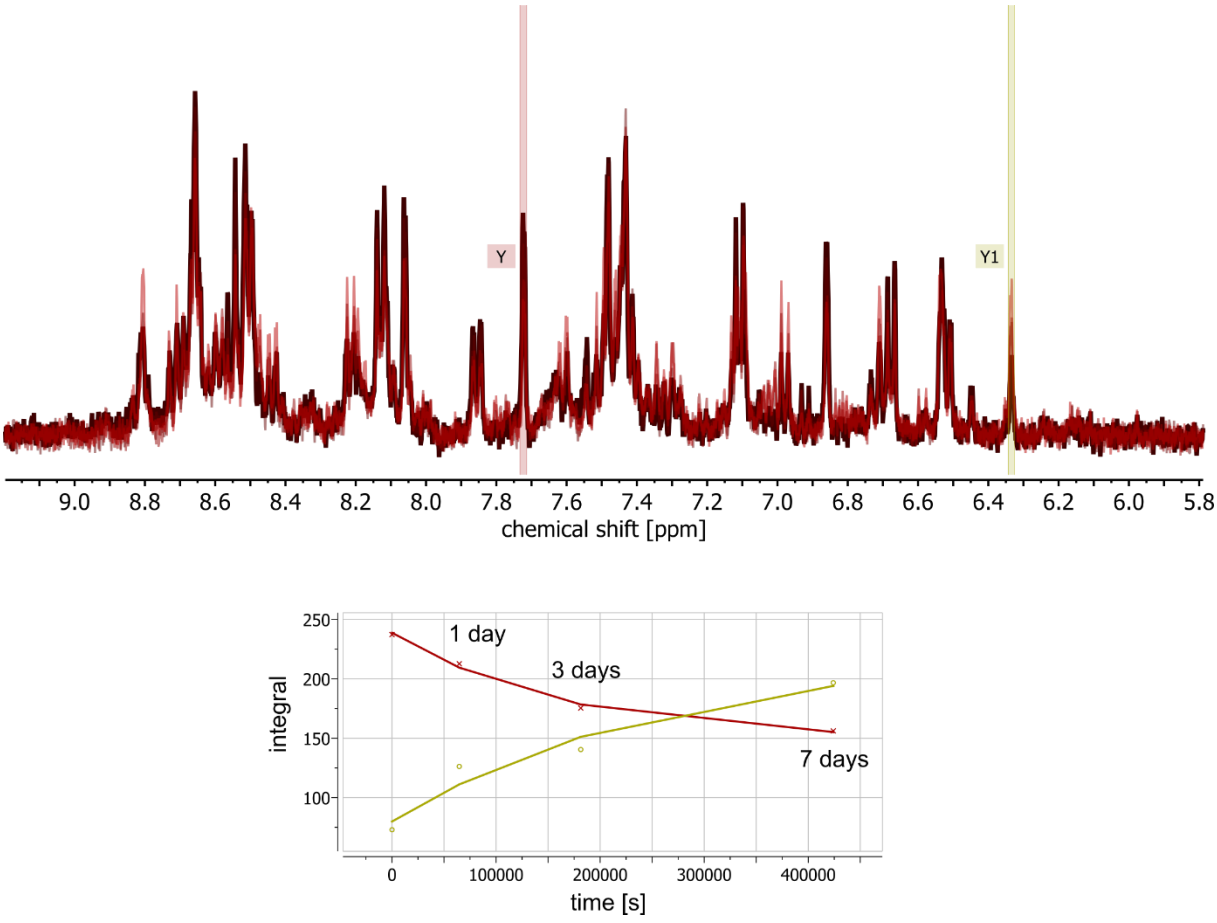

Figure S115. Thermal back-isomerisation of ZnFe**L** after 24 hours of white light irradiation as followed by ^{1}H NMR spectrometry (400 MHz, CD_3CN, 1 mM, 298 K). Bottom: Plotted integrals of meta-stable diastereomer of ZnFe**L** (red, Y) and stable isomer ZnFe**L** (yellow, Y1) proton signals over time with data points fitted to first-order kinetics. Reforming of lowest energy isomer ZnFe**L** helicate follows apparent first-order kinetics with no intermediates being observed.

S9 Metal Exchange

S9.1 Thermal relaxation of ZnFe**L** at 65 °C for reference

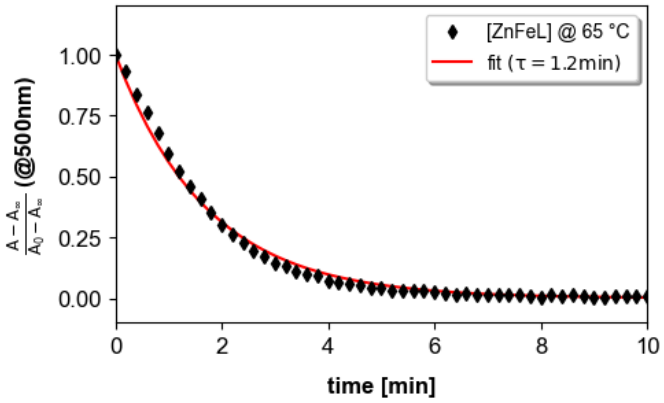

Figure S116. UV-vis kinetics and fit of the thermal relaxation of ZnFe**L** (CH_3CN, 0.06 mM, 65 °C) after irradiation at 405 nm for 1 minute. The thermal half-life of ZnFe**L** was determined to be $\tau_{½}$ = 1.2 min at 65 °C (compare Figure S117).

S9.2 Metal-exchange kinetics by UV-Vis

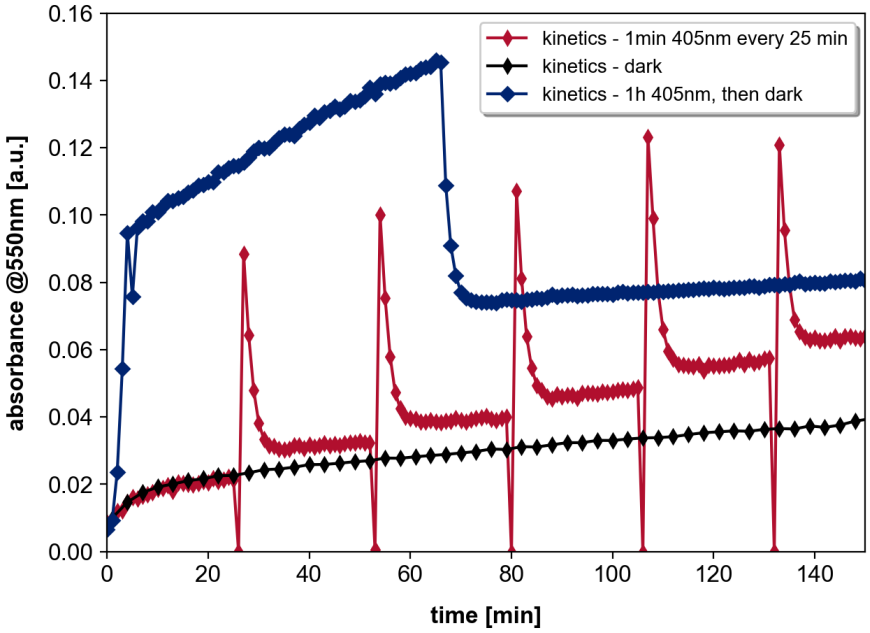

Figure S117. UV-vis kinetics of the metal exchange of Zn_2**L** to ZnFe**L**, following the formation of Fe^{bipy} by the appearance of its MLCT band at 550 nm. A stock solution of Zn_2**L** (CH_3CN, 0.06 mM) was cooled to 6°C and 1.5 equiv. of $Fe(OTf)_2$ were added. Three aliquots were consecutively taken from this mixture and transferred to a UV-vis cuvette, which was then immediately placed into the UV-vis spectrometer that had been preheated to 65°C. The first sample was measured in the dark (black), the second sample was irradiated at 405 nm for 1 minute every 25 minutes (red), and the last sample was continuously irradiated for 1 hour (blue).

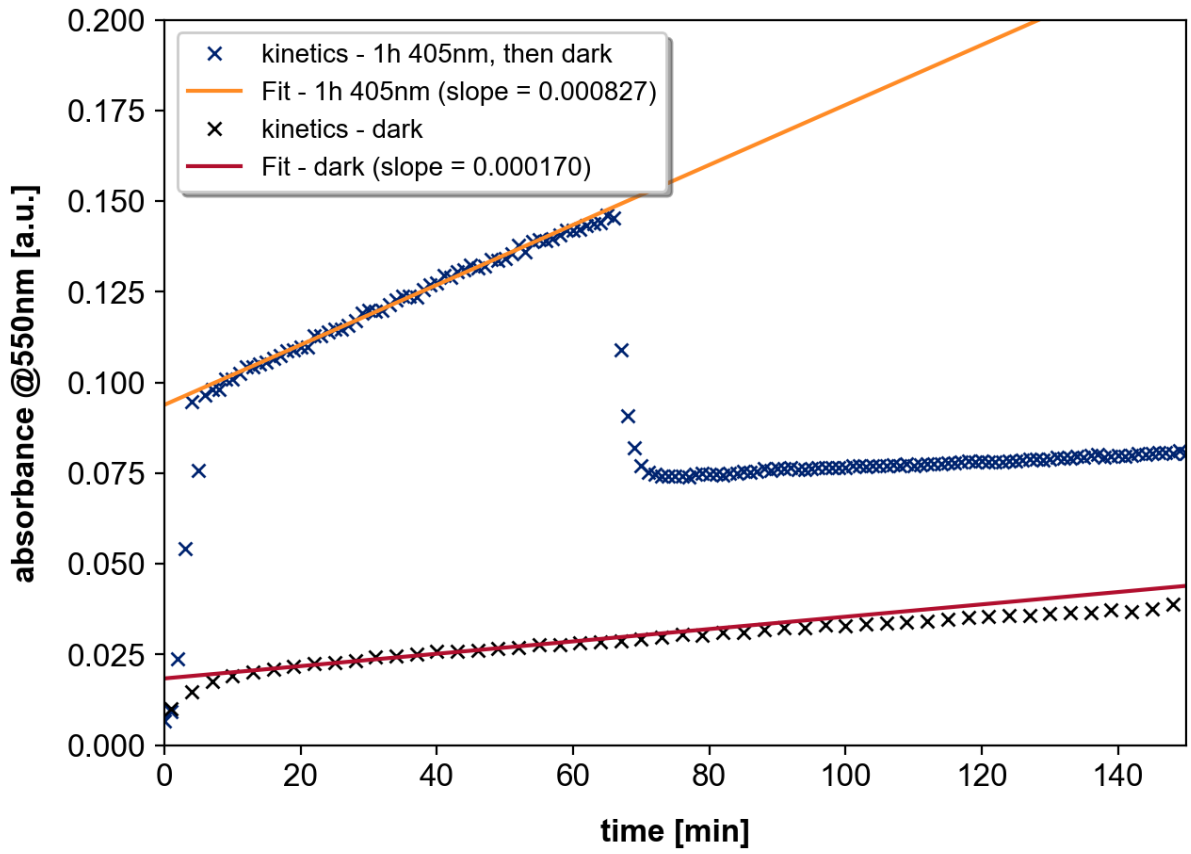

Figure S118. Fitted linear regressions to the experimental UV-vis data Zn_2**L** to ZnFe**L** metal exchange experiment (Figure S117, 1 h 405 nm irradiation, then 1h dark). The linear regression was performed using the data from *t* = 10 min to *t* = 60 min. The fit for the irradiated rate yielded a slope of 0.000827. In contrast, the reaction without irradiation had a slope of 0.000170, indicating that irradiation accelerates the metal exchange reaction by a factor of approximately 5.

S9.3 Metal-exchange kinetics by NMR

The kinetics of the Zn_2**L** to ZnFe**L** metal exchange reaction were investigated using high-temperature ^{1}H NMR spectroscopy (Figure S119, 700 MHz, CD3CN, 1 mM, 338 K). Besides the signals belonging to the starting material and the product, a third group of signals appeared and disappeared again (Figure S120). The experimental data suggests that the reaction kinetics did not follow first-order rate laws and that a transient intermediate or side product, tentatively assigned to a "Zn_2Fe**L**" state (Figure S122), was formed. This state seems unable to directly form the ZnFe**L** product and may be considered an unproductive resting state. The kinetics modeling program COPASI (version 4.44)[24] was used to fit this two-equilibria, three-state model (Figure S121) to the data obtained from the NMR experiments (Figure S122 and Table S16). The results of this fit seem reasonable and can explain the rapid disappearance of the starting material, as both the product and resting state are formed through equilibrium reactions. The overall equilibrium lays on the side of the desired ZnFe**L**, which appears to be the thermodynamically most stable species. Over time, the slow backreaction of "Zn_2Fe**L**" to Zn_2**L** pulls the mixture into the thermodynamic minimum, resulting in the predominant formation ZnFe**L**. The exact structure or nature of the "Zn_2Fe**L**" species could not be ascertained from the available data.

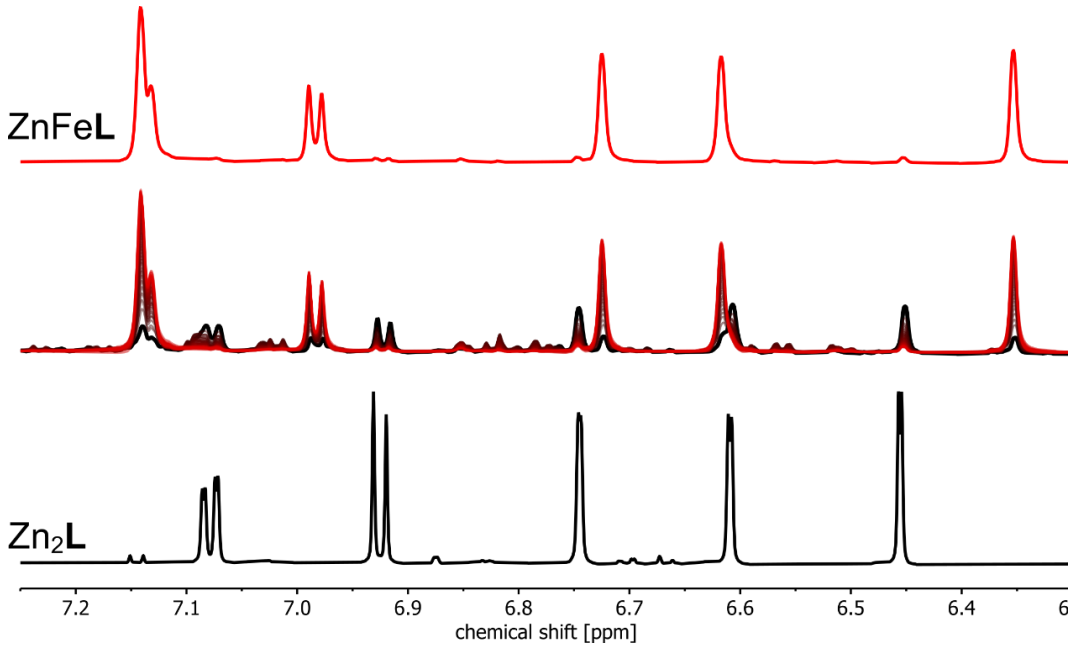

Figure S119. High-temperature ^{1}H NMR spectra (700 MHz, CD_3CN, 1 mM, 338 K) of ZnFe**L**, Zn_2**L** after the addition of 1.5 equiv. $Fe(OTf)_2$ with spectra being recorded every 5 minutes for 5.5 hours (maroon to red), and Zn_2**L** (top to bottom).

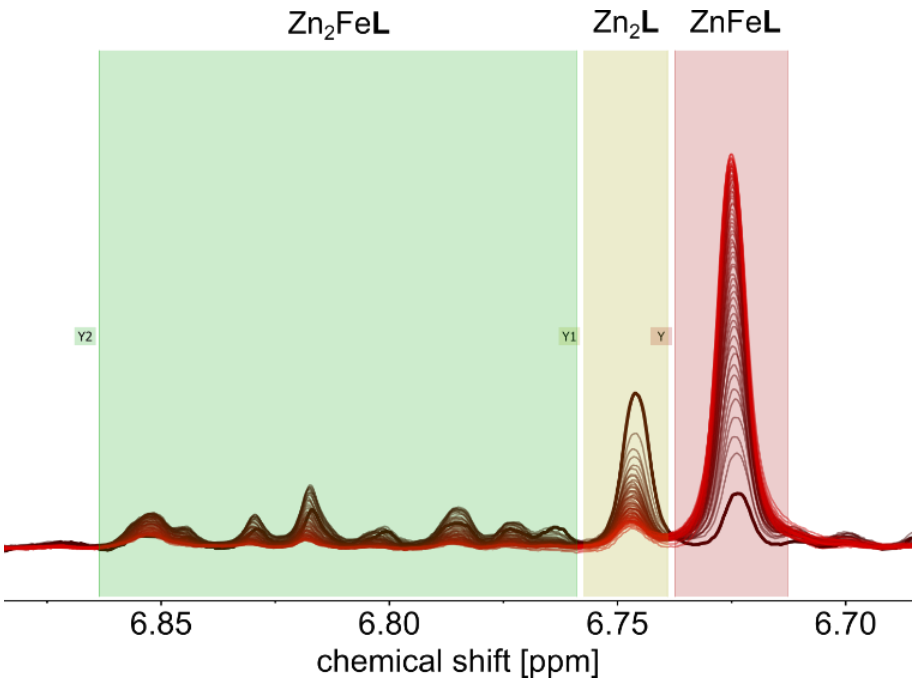

Figure S120. Partial high-temperature ^{1}H NMR spectra (700 MHz, CD_3CN, 1 mM, 338 K) of Zn_2**L** after the addition of 1.5 equiv. $Fe(OTf)_2$. Coloured panels show the signals assigned to different species for the evaluation of the kinetics of the metal exchange process.

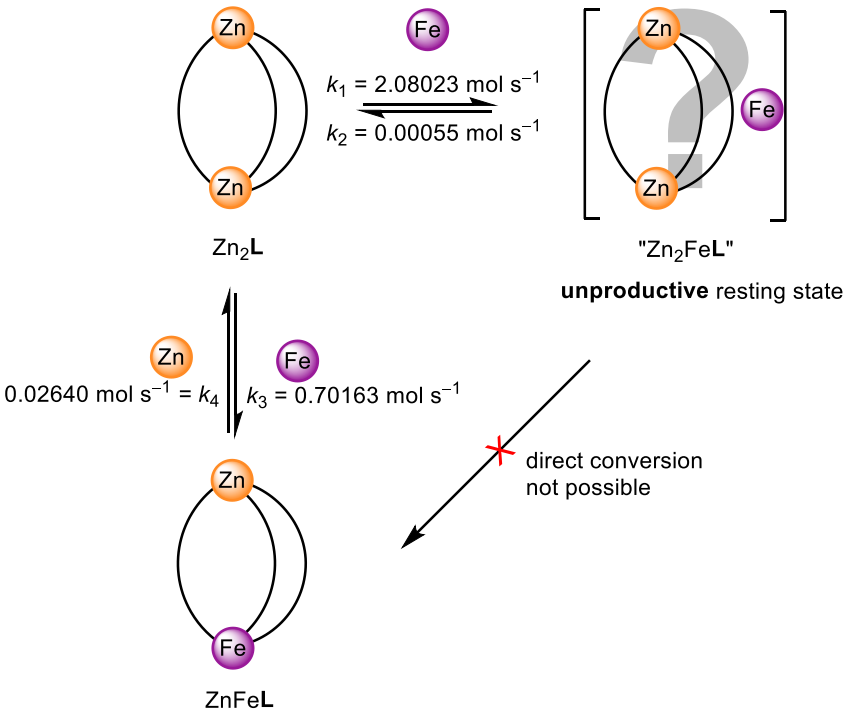

Figure S121. Kinetics model used for fitting of the NMR data (Figure S120). At first glance, the experimental data indicated that the reaction kinetics did not follow first-order rate laws and that a transient intermediate or side product was formed. Since this only forms after the addition of Fe(II) ions, the additional NMR signals were tentatively assigned to a "Zn_2Fe**L**" state. Kinetic modelling indicated that this state was unable to directly form the ZnFe**L** product and can be regarded as an unproductive resting state.

Table S16. Parameter estimation results for the kinetic model (Figure S121) using the genetic algorithm built into the kinetics modelling software COPASI.[24]

Parameter	Lower Bound	Upper Bound	Value [mol s^{-1}]	Std. Deviation
k_1	1.00E-06	10000	2.08023	0.050440
k_2	1.00E-06	10000	0.00055	0.000013
k_3	1.00E-06	10000	0.70163	0.008606
k_4	1.00E-06	10000	0.02640	0.001452

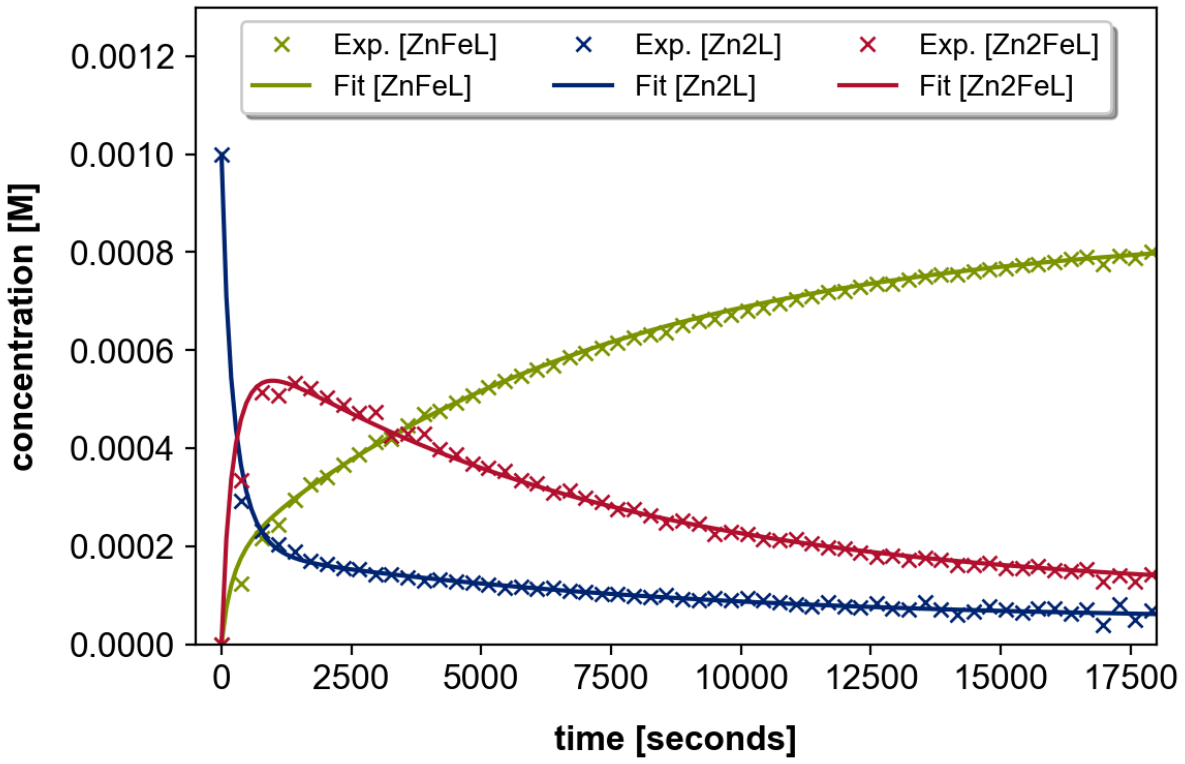

Figure S122. Kinetic model (Figure S121) fitted to experimental data (Figure S120) using the COPASI program.[24]

S9.4 Stability of ZnFe**L** and metal scrambling

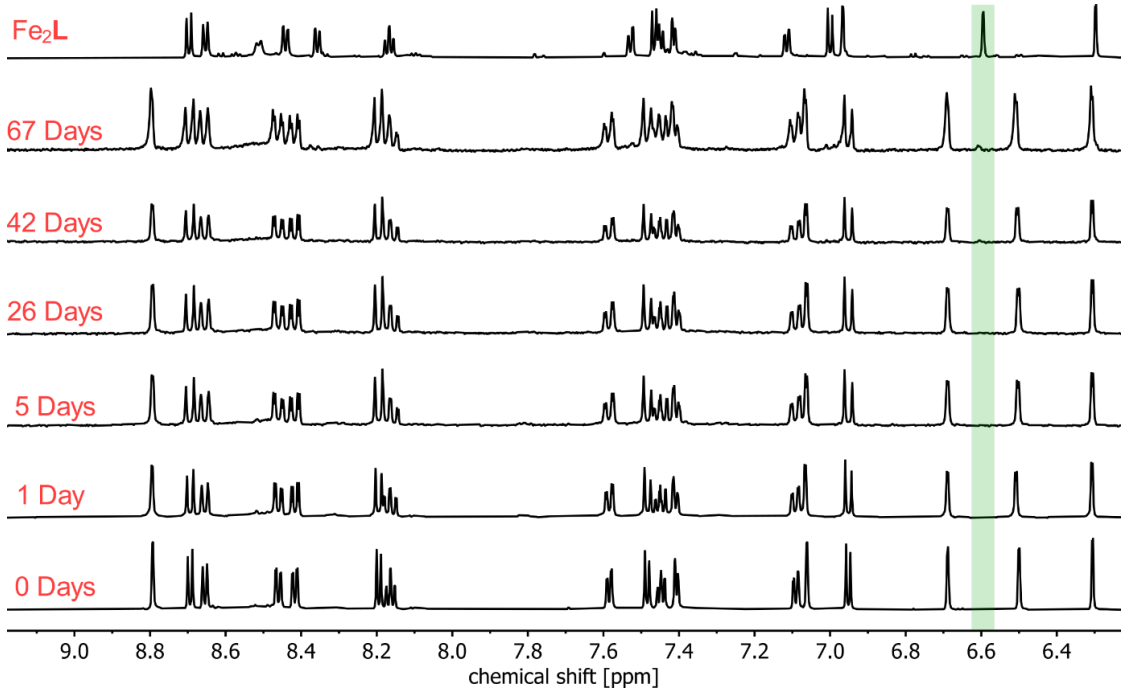

Figure S123. Partial ^{1}H NMR spectra (400 MHz, CD_3CN, 1 mM, 298 K) of ZnFe**L** during stability tests. The sample was synthesised using the metal exchange reaction of Zn_2**L** with 1.5 equiv. $Fe(OTf)_2$. The sample was heated to 65 °C, with measurements taken periodically after 0, 1, 5, 26, 42, and 62 days (bottom to top). The very slow emergence of signals belonging to Fe_2**L** (green box) due to metal exchange at the Zn^{TREN} site was observed. No signals corresponding to Zn_2**L** are observed, indicating that traces of free Fe(II) ions remaining from the synthesis were involved in the exchange, and the Zn(II) ions ended up as solvated ions in solution rather than in any complex.

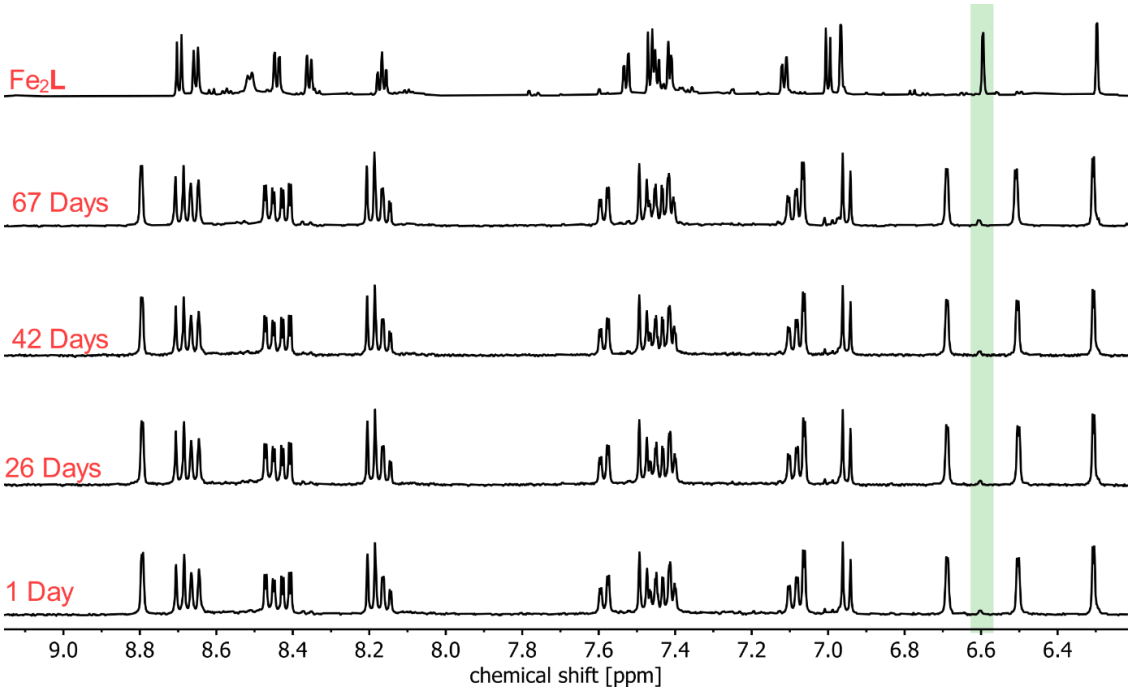

Figure S124. Partial ^{1}H NMR spectra (400 MHz, CD_3CN, 1 mM, 298 K) of ZnFe**L** (derived from the one-pot reaction, therefore containing 6% Fe_2**L**) during stability tests. 3.0 equiv. of $Fe(OTf)_2$ were added to the sample and it was heated to 65 °C, with measurements taken periodically after 1, 26, 42, and 62 days (bottom to top). The very slow increase of signals belonging to Fe_2**L** (green box) due to metal exchange was observed. No signals corresponding to Zn_2**L** are observed, indicating that excess Fe(II) ions were involved in the exchange, and the Zn(II) ions ended up as solvated ions in solution rather than in any complex.

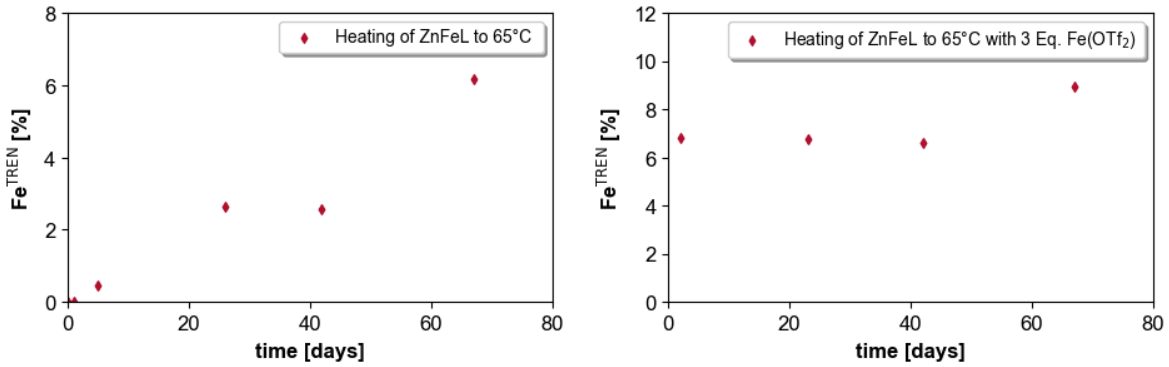

Figure S125. Plot of the percentage of TREN coordination sites occupied by Fe(II) (Fe^{TREN}) in % over time, derived from the signals in the green boxes from Figure S123 (left) and Figure S124 (right).

S10 Dilution experiment for Zn_2L

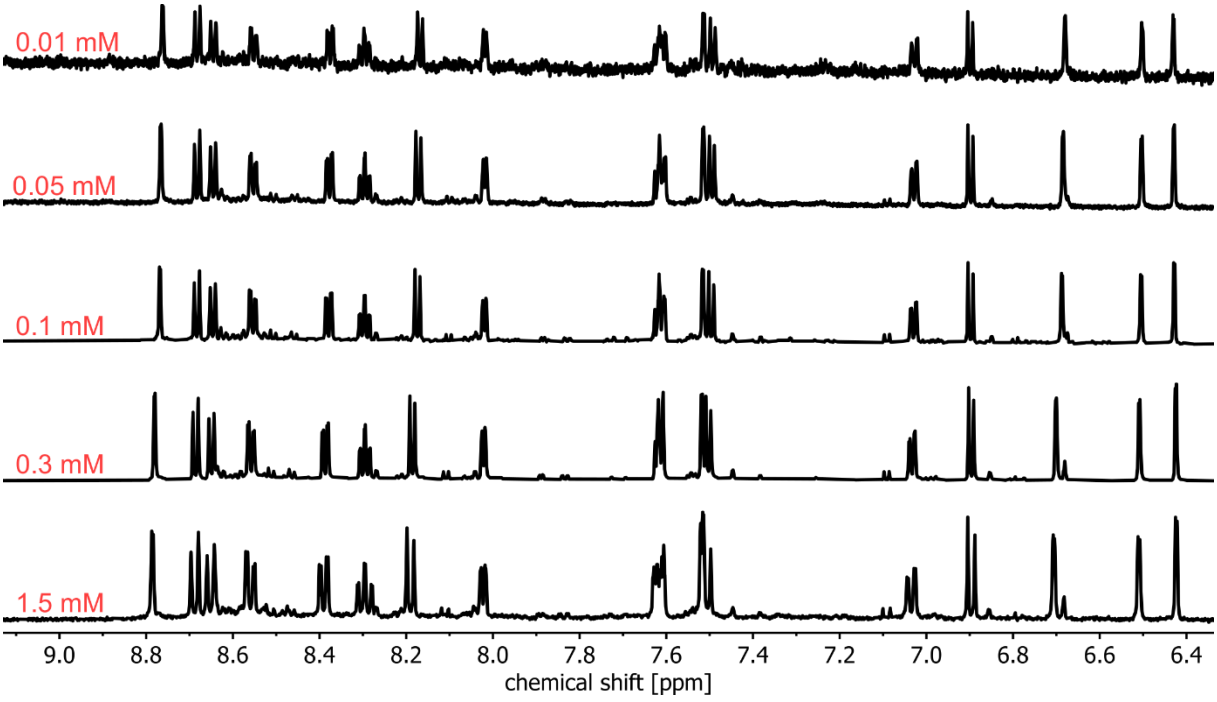

Figure S126. ^{1}H NMR spectra (700 MHz, CD_3CN, 298 K, up to 128 scans) of Zn_2**L** at concentrations from 0.01 mM to 1.5 mM (top to bottom) showing no observable disassembly upon dilution of the samples, because no signals corresponding to the free ligand or any other species could be observed.

S11 Literature

[1] M. J. Notheis, V. Sahiti, V. Prangenberg, J. S. Kruse, L. von Krbek, *Synlett* **2025**, DOI 10.1055/a-2567-1399.

[2] M. Kieffer, B. S. Pilgrim, T. K. Ronson, D. A. Roberts, M. Aleksanyan, J. R. Nitschke, *J. Am. Chem. Soc.* **2016**, *138*, 6813–6821.

[3] D. A. Roberts, B. S. Pilgrim, J. D. Cooper, T. K. Ronson, S. Zarra, J. R. Nitschke, *J. Am. Chem. Soc.* **2015**, *137*, 10068–10071.

[4] N. Oka, T. Yamada, H. Sajiki, S. Akai, T. Ikawa, *Org. Lett.* **2022**, *24*, 3510–3514.

[5] X-Area LANA 2.7.9.0 (STOE&Cie, **2022**.)

[6] G. M. Sheldrick, *Acta Crystallogr. Sect. C: Struct. Chem.* **2015**, *71*, 3–8.

[7] G. M. Sheldrick, *Acta Crystallogr. Sect. A* **2015**, *71*, 3–8.

[8] A. L. Spek, *Acta Crystallogr. Sect. C* **2015**, *71*, 9–18.

[9] L. Turcani, A. Tarzia, F. T. Szczypiński, K. E. Jelfs, *J. Chem. Phys.* **2021**, *154*, 214102.

[10] L. Turcani, A. Tarzia, *Stk*, https://github.com/lukasturcani/stk.

[11] A. Tarzia, K. E. Jelfs, *Chem. Commun.* **2022**, *58*, 3717–3730.

[12] M. D. Hanwell, D. E. Curtis, D. C. Lonie, T. Vandermeersch, E. Zurek, G. R. Hutchison, *J. Cheminformatics* **2012**, *4*, 17.

[13] A. K. Rappe, C. J. Casewit, K. S. Colwell, W. A. Goddard, W. M. Skiff, *J. Am. Chem. Soc.* **1992**, *114*, 10024–10035.

[14] P. Pracht, S. Grimme, C. Bannwarth, F. Bohle, S. Ehlert, G. Feldmann, J. Gorges, M. Müller, T. Neudecker, C. Plett, S. Spicher, P. Steinbach, P. A. Wesołowski, F. Zeller, *J. Chem. Phys.* **2024**, *160*, 114110.

[15] S. Spicher, S. Grimme, *Angew. Chem. Int. Ed.* **2020**, *59*, 15665–15673.

[16] C. Bannwarth, S. Ehlert, S. Grimme, *J. Chem. Theory Comput.* **2019**, *15*, 1652–1671.

[17] S. Ehlert, M. Stahn, S. Spicher, S. Grimme, *J. Chem. Theory Comput.* **2021**, *17*, 4250–4261.

[18] L. Schrödinger, *The PyMOL Molecular Graphics System, Version~1.8*, **n.d.**

[19] A. Tarzia, W. Shan, V. Posligua, C. J. T. Cox, L. Male, B. D. Egleston, R. L. Greenaway, K. E. Jelfs, J. E. M. Lewis, *Chem. A Eur. J.* **2025**, *31*, e202403336.

[20] C. Feldmeier, H. Bartling, E. Riedle, R. M. Gschwind, *J. Magn. Reson.* **2013**, *232*, 39–44.

[21] Y. Ji, D. A. DiRocco, J. Kind, C. M. Thiele, R. M. Gschwind, M. Reibarkh, *ChemPhotoChem* **2019**, *3*, 984–992.

[22] S. Ghosh, C. Eschen, N. Eleya, A. Staubitz, *J. Org. Chem.* **2022**, *88*, 3372–3377.

[23] M. S. Maier, K. Hüll, M. Reynders, B. S. Matsuura, P. Leippe, T. Ko, L. Schäffer, D. Trauner, *J. Am. Chem. Soc.* **2019**, *141*, 17295–17304.

[24] S. Hoops, S. Sahle, R. Gauges, C. Lee, J. Pahle, N. Simus, M. Singhal, L. Xu, P. Mendes, U. Kummer, *Bioinformatics* **2006**, *22*, 3067–3074.